Advances in Materials Science and Engineering

# Non-destructive Testing for Performance Evaluation of Civil Materials and Structures

Lead Guest Editor: Yubo Jiao
Guest Editors: Xiangxiong Kong and Qinglin Guo

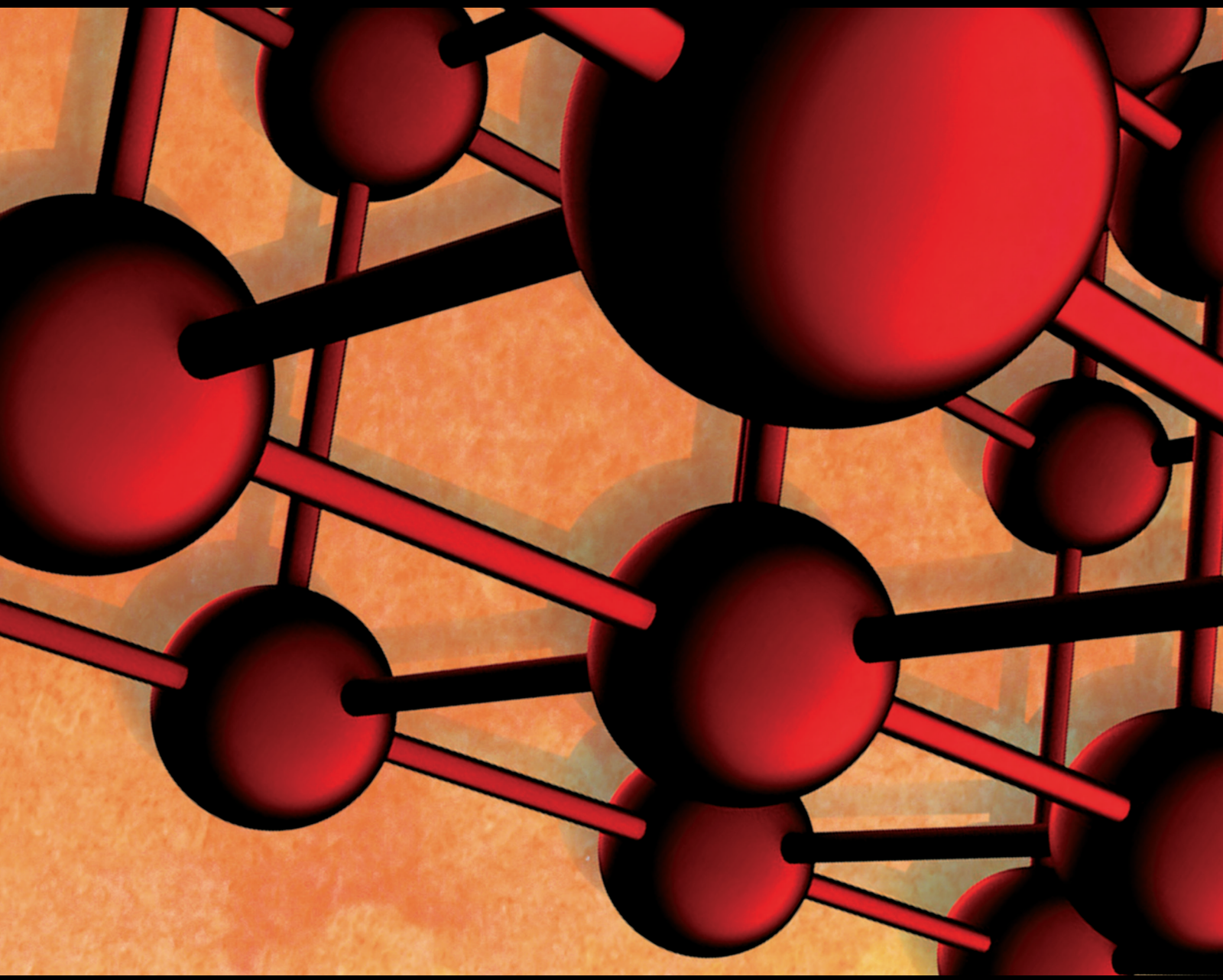

# Non-destructive Testing for Performance Evaluation of Civil Materials and Structures

Advances in Materials Science and Engineering

# Non-destructive Testing for Performance Evaluation of Civil Materials and Structures

Lead Guest Editor: Yubo Jiao
Guest Editors: Xiangxiong Kong and Qinglin Guo

# Contents

# Contents

Hindawi
Advances in Materials Science and Engineering
Volume 2022, Article ID 6636959, 11 pages
https://doi.org/10.1155/2022/6636959

*Research Article*

# Study on Evaluation Theory of Bridge Damage State and Methodology on Early Warning of Danger

**Guofu Jiang**[1], **Qianxue Liang**[1], **Hua Wang**[1], **Yucai Ju**[1], **Haihua Wang**[1], **Xirui Wang**[1], **Longlin Wang**[1] and **Wensheng Wang**[2,3]

[1]*Guangxi Transportation Science and Technology Group Co. Ltd., Nanning 530007, China*
[2]*College of Transportation, Jilin University, Changchun 130022, China*
[3]*College of Construction Engineering, Jilin University, Changchun 130026, China*

Correspondence should be addressed to Hua Wang; wanghua15@mails.jlu.edu.cn and Wensheng Wang; wangws@jlu.edu.cn

Received 13 January 2021; Revised 22 April 2021; Accepted 26 April 2021; Published 28 March 2022

Academic Editor: Luigi Di Sarno



When evaluating and prewarning the damage state of bridges, the observation equation and state equation of bridge systems are not constructed in the existing methods, which would cause the evaluation results to be inconsistent with the actual damage state of bridges. Therefore, the existing methods have the problems of low evaluation accuracy, high false alarm rate, and poor real-time performance. In order to solve the above problems, this paper proposes a novel evaluation and judgment theory of bridge damage state and methodology on early warning of danger. The wavelet packet analysis method is used to construct the observation equation and state equation of bridge systems, which could provide a relevant basis for evaluating the damage state of bridges. Then, the fuzzy comprehensive evaluation method is used to construct the fuzzy evaluation model of the bridge damage state to evaluate and judge the damage state of bridges. According to the evaluation results, combined with mathematical-statistical analysis methods and principal component analysis methods, the methodology on early warning of danger for bridge structures can be realized. The experimental results showed that the proposed method has high evaluation and judgment accuracy, low false alarm rate, and good real-time performance and reliability.

## 1. Introduction

In the bridge operation process, monitoring the durability, integrity, and safety of bridge structures is an important part of bridge safety evaluation [1–5]. The bridge's structural safety is affected by not only natural disasters such as earthquakes and sudden accidents but also a brittle failure due to the damage accumulation of nodes [6–11]. Therefore, the main purpose of monitoring the durability and safety of bridge structures is to evaluate the bridge damage state under the effect of load [12–14]. The long-term structural health monitoring data contains quite a few structural information and could play significant roles in detecting damages in early stage, and neutral axis indicator and machine learning method have been used in the long-term structural health monitoring [15, 16]. At present, most of the bridge structures in China were made of steel, and the design life of most bridges is about to be due. Therefore, it is an urgent problem to evaluate and judge the damage state of such bridges and early warning of dangers [17–20].

So far, some progress has been made in the research of bridge damage state assessment and early warning methods of danger. For example, Geng et al. proposed a method for the bridge damage state assessment and early warning method based on lateral acceleration monitoring [21]. In this method, the root mean square of the lateral acceleration of main girders was taken as a monitoring parameter to analyze the dynamic characteristics of bridges, and the bridge damage state would be evaluated by the correlation model. The principal component analysis was used to analyze the changes of the correlation model due to the changes in environmental factors. According to the analysis results, the early warning index of bridges is determined to realize the early warning of dangers. However, this method does not

build the observation equation of the system, and it takes a long time to detect the change of the principal component correlation coefficient of bridge structures, which has the problem of poor real-time performance. In addition, Hua et al. proposed a long-term monitoring and early warning method of bridge structure modal frequency formed by combining principal component analysis and support vector regression [22]. Yabe et al. also proposed a combination of state representation and frequency slice wavelet transform for monitoring and evaluating bridge conditions [23]. Liu et al. proposed a method for the bridge damage state assessment and early warning method based on the improved Bayesian method [24]. This method is based on the analytic hierarchy process (AHP) theory in the existing evaluation systems and decomposes the whole bridge hierarchy according to different parts and functions of bridges. Each subcomponent of bridges is converted into a node in the Bayesian probability network so that the state score of each subcomponent corresponds to the state probability of the node in the Bayesian network one by one, and then the overall state of the bridge at a certain time is determined. Thus, real-time update, transmission, evaluation, and early warning can be carried out on the status information of bridges at different times. However, this method has the problem of poor real-time performance for early warning of bridge damage due to its slow information update speed.

On the other hand, Dong et al. proposed a method for the bridge damage state assessment and early warning method based on a sliding window subspace algorithm [25]. This method combines a data-driven random subspace identification algorithm and sliding window technology to track and identify bridge modal parameters in real time and evaluates the bridge damage state. According to the evaluation results of the bridge damage state, the danger warning for the bridge could be realized based on frequency change rate and frequency value. However, this method does not construct the state equation of the system, which leads to a large error between the evaluation result and the actual bridge damage state, and there is a problem of a high false alarm rate. Huang et al. proposed a method of bridge damage state assessment and early warning method based on finite element analysis [26]. Taking the tested deflection value of a slab girder as a guide, given the law that reducing the elastic modulus of concrete or increasing the bending moment caused by the load will increase the deflection, this method is used to evaluate the damage state of existing bridges. Then, Midas FEA software is used to simulate the bridge damage, and the damage warning method of bridges is designed based on it. However, there is a large gap between the simulated value and the actual value for this method, which causes the problem of high false alarm rate in this method.

In summary, most of the current researches on the damage state assessment and danger warning methods of bridges have problems with poor real-time performance of bridge damage warning or high false alarm rate. In order to solve the problems in the above methods, this paper proposes a novel evaluation and judgment theory of bridge damage state and methodology on early warning of danger. This bridge damage state assessment and early warning method is constructed based on the integration of wavelet packet analysis method, fuzzy comprehensive evaluation method, and principal component analysis method.

## 2. Dynamic System of Bridge Structure

In the process of studying the evaluation and judgment theory of bridge damage state and methodology on early warning of danger, it is necessary to first construct the dynamic system of bridge structure based on the wavelet packet analysis method. The dynamic system is used to decompose the bridge structure at multiple scales to obtain the observation equation and state equation of bridge structures, which could provide relevant basis and data for evaluating and judging the damage state of bridges.

Assuming that the degree of freedom of the dynamic system is $n$, the differential equation of motion could be obtained based on the mathematical theory of wavelet packet analysis [27]:

$$\mathbf{M}\ddot{x} + \mathbf{C}\dot{x} + \mathbf{K}x(t) = F(t), \tag{1}$$

where $\boldsymbol{M}$ describes the mass matrix, $\mathbf{M} \in R^{n\times n}$; $x$ is the displacement response vector, $x \in R^{n\times 1}$; $\boldsymbol{C}$ is the damping matrix, $\mathbf{C} \in R^{n\times n}$; $\boldsymbol{K}$ is the stiffness matrix, $\mathbf{K} \in R^{n\times n}$; $F$ is the system excitation vector, $F \in R^{n\times 1}$.

Let $\overline{x}(t)$ be the state vector; the state equation can be used to describe the above equation of motion:

$$\overline{x}(t) = A\overline{x}(t) = B\overline{F}(t), \tag{2}$$

in which

$$\begin{cases} A = \begin{bmatrix} 0 & I \\ -M^{-1}K & -M^{-1}C \end{bmatrix}, \\ B = \begin{bmatrix} 0 & 0 \\ -M^{-1} & 0 \end{bmatrix}, \\ \overline{F}(t) = \begin{bmatrix} F(t) \\ 0 \end{bmatrix}. \end{cases} \tag{3}$$

The $p$-dimensional continuous signal ($f(t) \in R^{n\times 1}$) is obtained by the acceleration sensor, and the dynamic response of the observed structure can be expressed as

$$f(t) = \mathbf{T}\ddot{x}(t) + v(t), \tag{4}$$

where $v(t)$ describes the observation noise; $\boldsymbol{T}$ describes the observation matrix. Then the continuous signal $f(t)$ can be described as

$$f(t) = \overline{\mathrm{Cx}}(t) + \overline{\mathrm{DF}}(t) + v(t), \tag{5}$$

The output equation and the state equation are discretized in the time domain. Let $\Delta t$ represent the time interval of the system sampling, and it will obtain the time-domain solution of the state equation in the time domain:

$$\overline{x}(t) = e^{A\Delta t}\overline{x}(t - \Delta t) + \int_{t-\Delta t}^{t} e^{A(t-f)}B\overline{F}(f)\mathrm{d}f, \tag{6}$$

Then, the discrete observation equation and state equation in the time domain are expressed as follows:

$$\begin{cases} \overline{x}(N,k+1) = \overline{A}(N)\overline{x}(N,k) + \overline{B}(N)\overline{F}(N,k), \\ f(N,k) = \overline{C}(N)\overline{x}(N,k) + D(N)\overline{F}(N,k) + v(N,k), \\ \overline{A} = e^{A\Delta t}, \\ \overline{B} = \int_{t-\Delta t}^{t} e^{A(t-f)}B. \end{cases} \tag{7}$$

Suppose that the wavelet packet decomposition scale is $i$; the observation equation and state equation of the structural system are defined as follows:

$$\begin{cases} f(i,k) = \overline{C}(i)\overline{x}(i,k) + \overline{D}(i)\overline{F}(i,k) + v(i,k), \\ \overline{x}(i,k+1) = \overline{A}(i)\overline{x}(i,k) + \overline{B}(i)\overline{F}(i,k). \end{cases} \tag{8}$$

The state equation of the dynamic system in the case of scale $i$ can be decomposed into the scale $(i-1)$ through the wavelet transform method, and then the system state equation in coarse-scale signal space $V_{i-1}$ is obtained:

$$\begin{aligned} \overline{x}_v^i(i-1,k+1) &= \sum_l h(l)\overline{x}(i,2k-l+2) \\ &= \overline{A}_v^i(i-1)\overline{x}_v^i(i-1,k+1) \\ &\quad + \overline{B}_v^i(i-1)\overline{F}_v^i(i-1,k+1), \end{aligned} \tag{9}$$

where the subscript $v$ describes the projection corresponding to the signal sequence $\overline{x}(i,k)$ of scale $i$ in the coarse-scale signal space $V_{i-1}$.

The observation equation of the dynamic system is decomposed from scale $i$ to scale $(i-1)$ by wavelet transform method, and the observation equation of the system in the coarse-scale signal space $V_{i-1}$ is obtained:

$$\begin{cases} f_v^i(i-1,k) = \sum_l h(l)f(i,2k-l) = \overline{C}_v^i(i-1) \times \overline{x}_v^i(i-1,k) + \overline{D}_v^i(i-1)\overline{F}_v^i(i-1,k) + v^i v(i-1,k), \\ \overline{C}_v^i(i-1) = \overline{C}(l), \\ \overline{D}_v^i(i-1) = \overline{D}(l), \\ \overline{F}_v^i(i-1,k) = \sum_l h(l)\overline{F}(i,2k-l), \\ v^i v(i-1,k) = \sum_l h(l)v(i,2k-l), \end{cases} \tag{10}$$

In the same way, the state equation of the dynamic system in the fine-scale signal space $W_{i-1}$ is obtained:

$$\begin{aligned} \overline{x}_W^i(i-1,k+1) &= \sum_l g(l)\overline{x}(i,2k-l+2) \\ &= \overline{A}_W^i(i-1)\overline{x}_W^i(i-1,k) \\ &\quad + \overline{B}_W^i(i-1)\overline{F}_W^i(i-1,k), \end{aligned} \tag{11}$$

where the subscript $W$ describes the projection corresponding to the signal sequence $\overline{x}(i,k)$ of scale $i$ in the coarse-scale signal space.

Similarly, the observation equation of the dynamic system is decomposed from scale $i$ to scale $(i-1)$ by wavelet transform method, and the observation equation of the system in the coarse-scale signal space $W_{i-1}$ is obtained:

$$\begin{cases} f_W^i(i-1,k) = \sum_l g(l)f(i\cdot 2k-l) = \overline{C}_W^i(i-1)\overline{x}_W^i(i-1,k) + \overline{D}_W^i(i-1)\overline{F}_W^i(i-1,k) + v_W^i(i-1,k), \\ \overline{C}_W^i(i-1) = \overline{C}(i), \\ \overline{D}_W^i(i-1) = \overline{D}(i), \\ v_W^i(i-1,k) = \sum_l g(l)v(i,2k-l). \end{cases} \tag{12}$$

## 3. Evaluation and Judgment of Bridge Damage State

Based on the observation equation and state equation of the system, the fuzzy comprehensive evaluation method is used to evaluate and judge the damage state of bridges.

*3.1. First-Level Evaluation.* The first-level evaluation refers to the fuzzy comprehensive evaluation and judgment for the most basic components including bridge support, deck pavement, bridge piers, and main force-bearing components [28–30].

Let $m$ represent the total number of damaged items that can affect the technical state of components and evaluate

each damaged item of bridges. The corresponding impact evaluation matrix $\boldsymbol{R}$ of components can be constructed as follows:

$$\mathbf{R} = \begin{bmatrix} r_{11} & r_{12} & \cdots & r_{15} \\ r_{21} & r_{22} & \cdots & r_{25} \\ \cdots & \cdots & \cdots & \cdots \\ r_{m1} & r_{m2} & \cdots & r_{m5} \end{bmatrix}. \tag{13}$$

Suppose that the fuzzy subset on the domain $U_1$ is the factor existing in the factor set $U$ of the component $S_{ij}$, which is called $\mathrm{AS}_{ij} = (a_1, a_2, \ldots, a_m)$ for short. Let $\mathrm{BS}_{ij}$ be the fuzzy comprehensive evaluation set of damage state corresponding to the component $S_{ij}$; $\mathrm{AS}_{ij}$ and $\mathrm{RS}_{ij}$ are used to evaluate the damage state of a single component, which is calculated by

$$\mathrm{BS}_{ij} = \mathrm{AS}_{ij} \cdot \mathbf{R} = \left(b_1', b_2', b_3', b_4', b_5'\right). \tag{14}$$

*3.2. Second-Level Fuzzy Comprehensive Evaluation.* Let $R'$ represent the evaluation matrix of a single factor corresponding to the substructure $S_i$, and $R'$ is composed of fuzzy comprehensive evaluation sets of various damage states [29, 31–33], which is expressed as follows:

$$R' = \begin{bmatrix} b_{11} & b_{12} & \cdots & b_{15} \\ b_{21} & b_{22} & \cdots & b_{25} \\ \cdots & \cdots & \cdots & \cdots \\ b_{n1} & b_{n2} & \cdots & b_{n5} \end{bmatrix}. \tag{15}$$

Assume that $\mathrm{AS}_i$ represents the fuzzy subset existing in the domain $U_1$, and its expression is $\mathrm{AS}_i = (a_1, a_2, \ldots, a_i, \ldots, a_n)$, in which $a_i$ is the distribution weight of the $i$-th subcomponent in the substructure $S_i$; $n$ is the number of the components in the substructure $S_i$. $\mathrm{BS}_i$ is assumed to represent the fuzzy subset existing in $\boldsymbol{V}$, that is, the fuzzy comprehensive evaluation set corresponding to the damage state of substructure $S_i$, and its expression is as follows:

$$\mathrm{BS}_i = \mathrm{AS}_i \times R' = \left(b_1', b_2', b_3', b_4', b_5'\right), \tag{16}$$

*3.3. Third-Level Fuzzy Comprehensive Evaluation.* The first-level and second-level fuzzy comprehensive evaluation values are combined to form an evaluation matrix of a single factor $R''$:

$$R'' = \begin{bmatrix} r_{11} & r_{12} & \cdots & r_{15} \\ r_{21} & r_{22} & \cdots & r_{25} \\ \cdots & \cdots & \cdots & \cdots \\ r_{51} & r_{52} & \cdots & r_{55} \end{bmatrix}. \tag{17}$$

The fuzzy subset $\mathrm{AB}_i = (a_1, a_2, a_3, a_4, a_5)$ existing in the domain $U_1$ is the assigned weight of the bridge substructure.

Based on the fuzzy subset $AB$ and evaluation matrix of a single factor $R''$, the evaluation model $BB$ of bridge damage state is constructed:

$$\mathrm{BB} = \mathrm{AB} \times R'' = \left(b_1', b_2', b_3', b_4', b_5'\right). \tag{18}$$

## 4. Methodology on Early Warning of Danger

According to the evaluation results, combined with mathematical-statistical analysis methods and principal component analysis methods, the methodology on early warning of danger for bridge structures can be realized.

In practice, environmental factors such as wind speed and temperature will affect the modal parameters of bridge structures [34, 35]. The nonlinear principal component analysis method is used to extract the parameters of wind speed and temperature, and the modal parameters are projected in the characteristic parameter space of environmental factors. Then, the hypothesis testing is carried out on the basis of statistical theory to realize the judgment of the operating state of bridge structures for further danger warning.

The nonlinear relationships between the reconstruction vector $\hat{x}$ and feature vector $\boldsymbol{y}$ as well as the feature vector $\boldsymbol{y}$ and initial data vector $\boldsymbol{x}$ are described as follows:

$$\begin{cases} \hat{x}_i^{(k)} = \sum_{j=1}^{M} W_{4ij} \Xi \left( \sum_{r=1}^{m} W_{3jr} y_r^{(k)} + b_{3j} \right) + b_{4i}, \\ \hat{y}_i^{(k)} = \sum_{p=1}^{M} W_{2rp} \Xi \left( \sum_{q=1}^{n} W_{1pq} x_q^{(k)} + b_{1p} \right) + b_{2r}. \end{cases} \tag{19}$$

The square prediction error of statistics ($\boldsymbol{Q}$) describes the deviation degree of modal test value from the principal component model at the $k$-th moment [36]. Let $Q_k$ represent the statistics of the modal parameters corresponding to $\boldsymbol{Q}$ at the $k$-th moment, and its calculation equation is as follows:

$$Q_k = \sum_{i=1}^{n} \left( x_i^{(k)} - \hat{x}_i^{(k)} \right)^2 = \sum_{i=1}^{n} \left[ x_i^{(k)} - \sum_{j=1}^{M} W_{4ij} \Xi \left( \sum_{r=1}^{m} W_{3jr} y_r^{(k)} + b_{3j} \right) + b_{4i} \right]^2, \tag{20}$$

and when the value of $Q_k$ is too large, it indicates that the bridge structure is abnormal [37].

The principal component analysis method is used to test the square prediction error of statistics ($\boldsymbol{Q}$). Let

$x = [x_1, x_2, \ldots, x_n]$ represent the covariance matrix corresponding to the collected modal parameters of bridge structures under the normal operating state at a certain time, and its principal component decomposition is carried out:

$$\mathrm{x}\mathrm{x}^T = \mathrm{u}\mathbf{d}\mathrm{u}^T, \tag{21}$$

where $u = [u_1, u_2, \ldots, u_n]$, and $u_i$ is the standard orthogonal eigenvector; $\mathbf{d} = \mathrm{diag}(\lambda_1, \lambda_2, \ldots, \lambda_n)$ is the eigenvalue matrix.

Considering the influence of environmental factors including wind speed and temperature, the principal components of these two environmental factors are selected in the process of danger warning, which can be expressed as

$$\begin{cases} \theta_k = \sum_{i=3}^{n} \lambda_i^k, h_0 = 1 - \dfrac{2\theta_1\theta_3}{\theta_2^2}. \end{cases} \tag{22}$$

When the test level i $\alpha$, the upper limit of confidence interval ($Q_\alpha$) for the system is calculated by the following equation:

$$Q_\alpha = \theta_1 \left[ \frac{c_\alpha \sqrt{2\theta_2 h_0^2}}{\theta_1} + \frac{\theta_2 h_0 (h_0 - 1)}{\theta_1^2} + 1 \right]^{1/h_0}, \tag{23}$$

where $c_\alpha$ represents the critical value of the normal distribution at the test level of $\alpha$. When the statistic is less than the upper limit of confidence interval ($Q_\alpha$), it indicates that the bridge structure is normal; otherwise, the bridge structure is abnormal, and a danger warning is required.

## 5. Experiment and Analysis

In order to verify the overall effectiveness of evaluation and judgment theory of bridge damage state and methodology on early warning of danger, it is necessary to carry out the field tests. The operating system for this test is Windows XP Professional, MATLAB simulation platform was used in this test, and MIDAS software was used for the finite element model of the bridge structure. In this paper, the Nanfeihe Bridge in Hefei, China, was taken as the experimental test object. Its total length is about 764.5 m and the total width is about 40.5 m. The tower of Nanfeihe Bridge is a cable-stayed bridge of a double-cable plane with a total of 84 stay cables. The main bridge of this cable-stayed bridge is divided into two spans, in which the left span is about 160 m long, the right span is about 120 m long, and the total height of the bridge tower is about 90 m away from the bridge deck. The actual view of the Nanfeihe Bridge is shown in Figure 1(a), its plan graph is shown in Figure 1(b), and its elevation is in Figure 1(c).

Based on the design and measured data of Nanfeihe Bridge, the finite element model diagram of its bridge structure can be constructed, and the corresponding finite element model results are illustrated in Figure 2.

The abovementioned finite element model (in Figure 2) was input into the simulation software, and five damage parts (including bridge tower crack, broken cable, concrete crack) were set in the simulation software by reducing Young's modulus. The specific layout of damaged parts is presented in Figure 3, in which the 1st damage part is bridge tower crack, the 2nd damage part is bridge deck crack, the 3rd damage part is concrete crack, the 4th damage part is broken cable, and the 5th damage part is reinforcement corrosion.

In the field tests, the acceleration sensors were arranged at six measure points (i.e., the left, middle, and right endpoints of the main bridge and the lower, middle, and upper endpoints of the cable tower). The signal wave of the measuring point is as shown in Figure 4. Then, the time history function of environmental load could be set in MIDAS software, and the dead weight of the bridge was converted in the model, in which the gravity acceleration is 9.806 m/s$^2$ and the initial temperature is 0°C. On this basis, the node dynamic load of the bridge was set, the node spacing was 0.5 m, and the vehicle speed was set as 80 km/h.

According to the damage degree of a bridge, the damage of bridge structure could be divided into three levels with three grades, that is, first-level damage (★-I, II, III) only with local surface damages, second-level damage (★★-I, II, III) with serious section damage or steel strength reduction and without structural plastic deformation, and third-level damage (★★★-I, II, III) representing that the component is partially or completely disabled. Three methods have been used to evaluate and judge the damage state of the bridge at different positions:

(1) Method I is the presented evaluation and judgment theory of bridge damage state and methodology on early warning of danger in this paper

(2) Method II is the bridge damage state assessment and early warning method based on lateral acceleration monitoring in [21]

(3) Method III is the bridge damage state assessment and early warning method based on the sliding window subspace algorithm in [25]

The evaluation test results by these three methods are listed in Table 1.

According to the evaluation test results of the damage state of five bridge components in Table 1, it can be seen that the evaluation results of method I are consistent with the actual damage grade of different bridge components, while there are certain errors between the evaluation results of method II [21] or method III [25] and the actual damage grade. This is because method I presented in this paper uses the fuzzy comprehensive evaluation method to construct the evaluation model of bridge damage state based on the observation equation and state equation of bridge systems, which would improve the accuracy of the evaluation and judgment.

When the bridge structure is damaged, the principal component correlation coefficient will increase. These three methods (i.e., methods I, II, and III) were used to evaluate and judge the damage state of the bridge, respectively. The corresponding principal component correlation coefficients calculated by methods I, II, and III are presented in Figure 5. It can be seen from the data analysis in Figure 5 that the principal component correlation coefficient obtained by

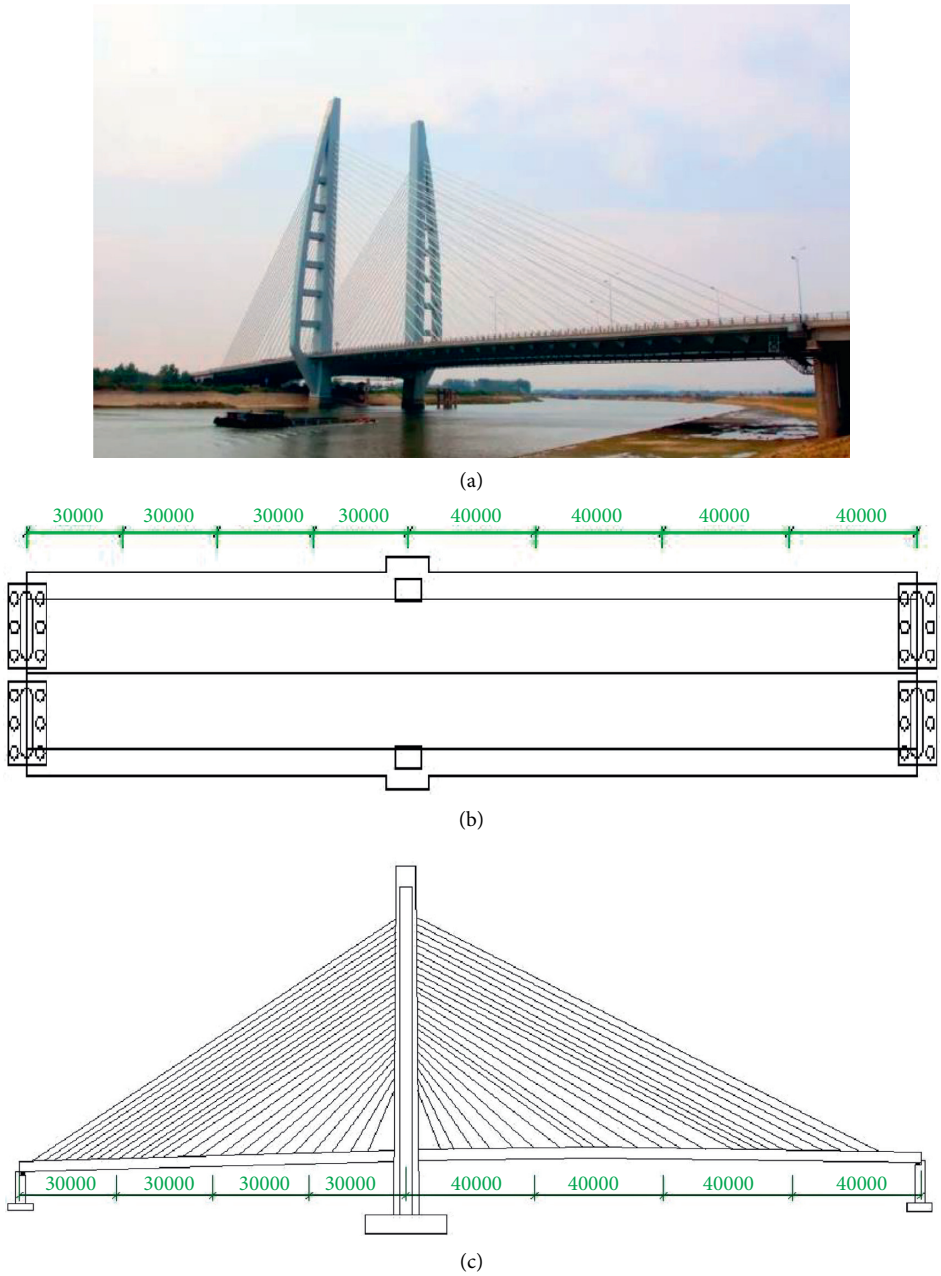


Figure 1: The Nanfeihe Bridge tested in this paper. (a) The actual view of Nanfeihe Bridge. (b) The plain graph of Nanfeihe Bridge. (c) The elevation of Nanfeihe Bridge.

method I in this paper of the bridge structure fluctuates greatly around the 60th test. This shows that method I presented in this paper detected and judged the damage of the bridge structure around the 60th test. However, methods II and III showed that the principal component correlation coefficients of the bridge structure increased significantly during the tests of 100~150 and 150~200, respectively, indicating that the damage of the bridge structure was detected until the tests of 100~150 and 150~200.

In order to further compare and analyze the evaluation efficiency of bridge damage for different methods, a time-consumption comparison of damage evaluation was then carried out, and the results are shown in Figure 6. From the above comparison analysis, it can be seen that the consumed time of evaluating the bridge damage state is between 2.7 and 3.9 s for method II in [21], and the consumed time of evaluating the bridge damage state is between 1.5 and 3.0 s for method III in [25]. In contrast, the consumed time of evaluating the bridge damage state is always less than 0.6 s for method I presented in this paper. This fully shows that the presented method in this paper can quickly realize the evaluation and judgment of bridge state damage. The reason is that the presented method I obtains the damage information of bridge system structure through the observation matrix and the state matrix, which provides a basis for the bridge damage evaluation and shortens the evaluation time.

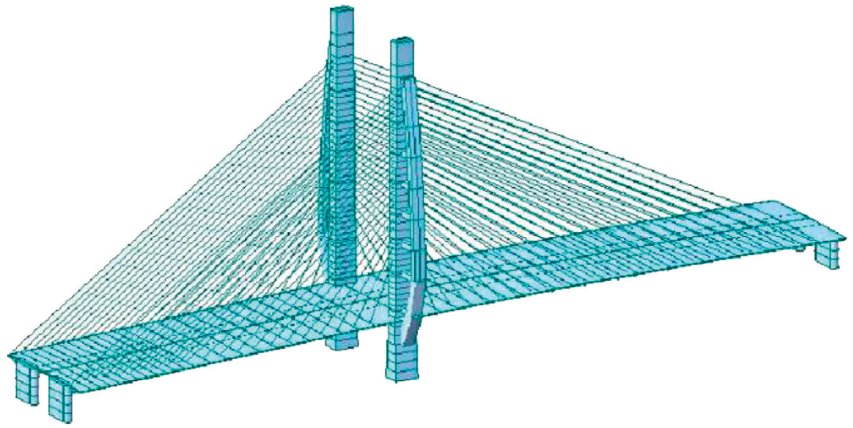

Figure 2: The finite element model of Nanfeihe Bridge structure.

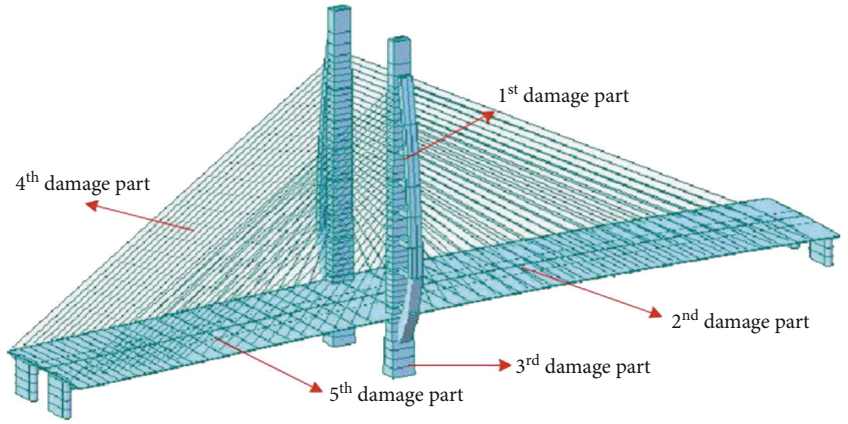


Figure 3: The layout of five damage parts in the finite element model.

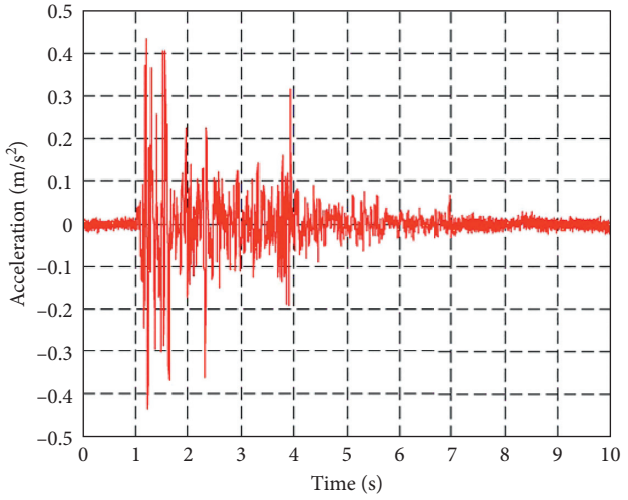


Figure 4: The signal wave of the measuring point.

Table 1: Comparison of evaluation test results among methods I, II, and III.

| Bridge components | Actual damage grade | Method I | Method II | Method III |
|---|---|---|---|---|
| 1st damage part | ★-II | ★-II | ★-III | ★-I |
| 2nd damage part | ★★★-I | ★★★-I | ★★-III | ★★★-II |
| 3rd damage part | ★★-II | ★★-II | ★★★-I | ★★★-I |
| 4th damage part | ★-I | ★-I | ★-II | ★-II |
| 5th damage part | ★-III | ★-III | ★★-I | ★★-II |

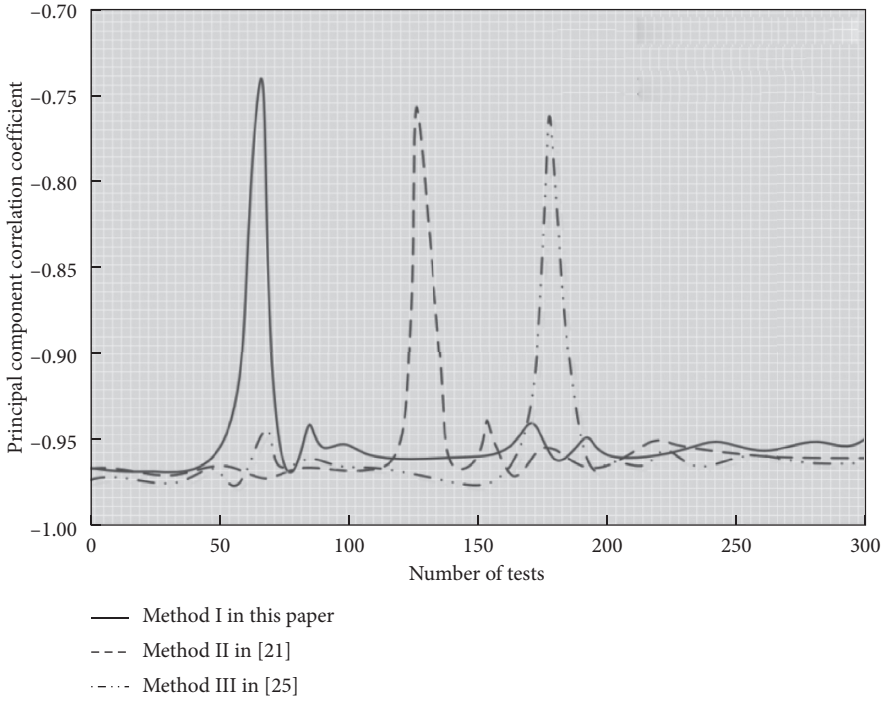


Figure 5: The principal component correlation coefficients calculated by methods I, II, and III.

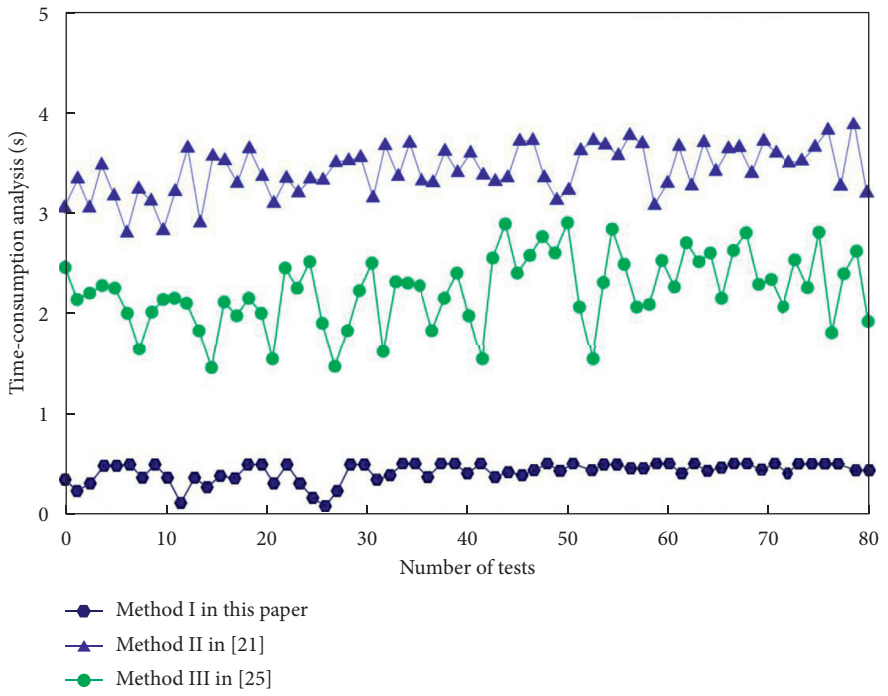


Figure 6: The time-consumption comparison of damage evaluation by methods I, II, and III.

Table 2: Comparison of *FAR* and *WT* among methods I, II, and III.

| Test no. | Method I | | Method II | | Method III | |
|---|---|---|---|---|---|---|
| | FAR (%) | WT (min) | FAR (%) | WT (min) | FAR (%) | WT (min) |
| 1 | 2.1 | 8.34 | 10.7 | 20.45 | 11.4 | 24.77 |
| 2 | 2.4 | 7.98 | 11.0 | 20.47 | 12.0 | 29.03 |
| 3 | 1.9 | 7.88 | 9.7 | 22.01 | 10.8 | 26.74 |
| 4 | 1.7 | 9.01 | 9.9 | 23.14 | 10.5 | 25.64 |
| 5 | 2.0 | 8.45 | 11.5 | 25.16 | 12.4 | 23.33 |

The false alarm rate (*FAR*) represents the proportion of negative samples divided into positive samples in all negative samples and its calculation equation is as follows:

$$\mathrm{FAR} = \frac{N_{\mathrm{NF}}}{N_{\mathrm{NF}} + N_{\mathrm{NT}}}, \tag{24}$$

where $N_{NF}$ is the number of misclassified negative samples and $N_{NT}$ is the number of negative samples correctly classified. The warning time (WT) refers to the time that the warning signal will be issued according to the fault condition.

Table 2 shows the comparison results of FAR and WT among method I presented in this paper, method II in [21], and method III in [25]. From the comparative analysis in Table 2, it can be seen that the FAR of method I in this paper is below 2.5%, which is much lower than those of methods II and III. At the same time, the WT of method I in this paper is within 10 min, which is half of those of methods II and III. Therefore, the presented method I has a low FAR and good WT. The reason is that the presented method I can accurately evaluate and judge the bridge damage state and detect the change of principal component correlation coefficient of bridges in a short time, thereby shortening the WT.

## 6. Conclusions

Bridges occupy an important position in the process of national economic construction, and their operation safety is one of the basic conditions for stable economic development. When a bridge accident occurs, it will have an adverse impact on society, especially the transportation field, and cause huge economic losses. In order to grasp the actual condition of bridges in time, it is necessary to evaluate and judge and the damaged condition of bridges and perform the early warning of danger. The existing damage state assessment and early warning methods of bridges cannot accurately assess the damage level of bridges, and the existing methods have the problems of low evaluation accuracy, high false alarm rate, and poor real-time performance. Therefore, this paper proposed a novel evaluation and judgment theory of bridge damage state and methodology on early warning of danger. Based on the observation equation and state equation of bridge systems by wavelet packet analysis method, the fuzzy comprehensive evaluation method is used to evaluate and judge the damage state of bridges. Then, according to mathematical-statistical analysis methods and principal component analysis methods, the methodology on early warning of danger for bridge structures can be realized. The Nanfeihe Bridge was taken as the experimental test object to analyze and verify the proposed method in this paper. The experimental results showed that the proposed method can accurately evaluate and judge the bridge damage state in a short time, reduce the false alarm rate, and improve the performance and reliability of the real-time early warning. The proposed method can effectively solve the problems of long warning time and evaluation accuracy of the current methods. Besides, due to the used basic methods, the proposed methodology on early warning of danger can be further promoted in practice. However, this study also has some limitations; for example, it does not use other cases to test the effectiveness of this method. In the future, we will conduct in-depth research on this problem to improve the applicability of this method.

## Data Availability

The data used to support the findings of this study are available from the corresponding author upon request.

## Conflicts of Interest

The authors declare that they have no conflicts of interest.

## Acknowledgments

This work was partially financially supported by the Scientific and Technological Project of Science and Technology Department of Jilin Province (Grant no. 20190303052SF), Nanning Excellent Young Scientist Program (Grant no. RC20180108), Nanning Excellent Young Scientist Program and Guangxi Beibu Gulf Economic Zone Major Talent Program (Grant no. RC20190206), Science and Technology Base and Talent Special Project of Guangxi Province (Grant no. AD19245152), and "Yongjiang plan" of Nanning leading talents in innovation and entrepreneurship (Grant no. 2018-01-04).

## References

[1] Q. Al-Kaseasbeh, Z. B. Lin, Y. C. Wang et al., "Electrochemical characterization of steel bridge welds under simulated durability test," *Journal of Bridge Engineering*, vol. 23, no. 10, 2018.

[2] G. J. Tan, W. S. Wang, and Y. B. Jiao, "Flexural free vibrations of multistep nonuniform beams," *Mathematical Problems in Engineering*, vol. 2016, Article ID 7314280, 12 pages, 2016.

[3] H. B. Liu, H. Wang, G. J. Tan et al., "Vibration analysis of reinforced concrete simply supported beam versus variation

temperature," *Shock and Vibration*, vol. 2017, Article ID 4931749, 20 pages, 2017.

[4] H. B. Liu, H. Wang, G. J. Tan et al., "Effect of temperature and spring-mass systems on modal properties of timoshenko concrete beam," *Structural Engineering and Mechanics*, vol. 65, no. 4, pp. 389–400, 2018.

[5] M. J. Osmolska, T. Kanstad, M. A. N. Hendriks, K. Hornbostel, and G. Markeset, "Durability of pretensioned concrete girders in coastal climate bridges: basis for better maintenance and future design," *Structural Concrete*, vol. 20, no. 6, pp. 2256–2271, 2019.

[6] S. Mangalathu, S. H. Hwang, E. Choi et al., "Rapid seismic damage evaluation of bridge portfolios using machine learning techniques," *Engineering Structures*, vol. 201, 2019.

[7] K. R. Karim and F. Yamazaki, "Effect of earthquake ground motions on fragility curves of highway bridge piers based on numerical simulation," *Earthquake Engineering & Structural Dynamics*, vol. 30, no. 12, pp. 1839–1856, 2001.

[8] B. G. Nielson and R. DesRoches, "Seismic fragility methodology for highway bridges using a component level approach," *Earthquake Engineering & Structural Dynamics*, vol. 36, no. 6, pp. 823–839, 2007.

[9] G. J. Tan, J. H. Shan, C. L. Wu et al., "Free vibration analysis of cracked timoshenko beams carrying spring-mass systems," *Structural Engineering and Mechanics*, vol. 63, no. 4, pp. 551–565, 2017.

[10] G. Tan, Y. Liu, Y. Gong, Y. Shen, and Z. Liu, "Free vibration of the cracked non-uniform beam with cross section varying as polynomial functions," *Ksce Journal of Civil Engineering*, vol. 22, no. 11, pp. 4530–4546, 2018.

[11] Y. Jiao, Y. Zhang, W. Shan, Q. Han, Y. Zhao, and S. Liu, "Damage fracture characterization of reinforced concrete beam subjected to four-point bending with parametric analysis of static, dynamic, and acoustic properties," *Structural Health Monitoring*, vol. 19, no. 4, pp. 1202–1218, 2020.

[12] W. C. Shan, X. Q. Wang, and Y. B. Jiao, "Modeling of temperature effect on modal frequency of concrete beam based on field monitoring data," *Shock and Vibration*, vol. 2018, Article ID 8072843, 12 pages, 2018.

[13] G. Tan, W. Wang, Y. Jiao, and Z. Wei, "Free vibration analysis of continuous bridge under the vehicles," *Structural Engineering and Mechanics*, vol. 61, no. 3, pp. 335–345, 2017.

[14] G. J. Tan, W. S. Wang, Y. C. Cheng et al., "Dynamic response of a nonuniform timoshenko beam with elastic supports, subjected to a moving spring-mass system," *International Journal of Structural Stability and Dynamics*, vol. 18, no. 5, 2018.

[15] Y. Xia, X. M. Lei, P. Wang et al., "Long-term performance monitoring and assessment of concrete beam bridges using neutral axis indicator," *Structural Control & Health Monitoring*, vol. 27, no. 12, 2020.

[16] G. V. Demarie and D. Sabia, "A machine learning approach for the automatic long-term structural health monitoring," *Structural Health Monitoring*, vol. 18, no. 3, pp. 819–837, 2019.

[17] S. Ye, X. Lai, I. Bartoli, and A. E. Aktan, "Technology for condition and performance evaluation of highway bridges," *Journal of Civil Structural Health Monitoring*, vol. 10, no. 4, pp. 573–594, 2020.

[18] Y. Q. Ni, Y. W. Wang, and C. Zhang, "A bayesian approach for condition assessment and damage alarm of bridge expansion joints using long-term structural health monitoring data," *Engineering Structures*, vol. 212, 2020.

[19] A. J. Reiff, M. Sanayei, and R. M. Vogel, "Statistical bridge damage detection using girder distribution factors," *Engineering Structures*, vol. 109, pp. 139–151, 2016.

[20] F. Soleimani, "Propagation and quantification of uncertainty in the vulnerability estimation of tall concrete bridges," *Engineering Structures*, vol. 202, 2020.

[21] F. F. Geng, Y. L. Ding, H. W. Zhao et al., "Early warning method of abnormal dynamic performance of high speed railway bridge based on transverse acceleration monitoring," *Railway Engineering*, vol. 9, pp. 1–5, 2016.

[22] X. G. Hua, Y. Q. Ni, J. M. Ko, and K. Y. Wong, "Modeling of temperature-frequency correlation using combined principal component analysis and support vector regression technique," *Journal of Computing in Civil Engineering*, vol. 21, no. 2, pp. 122–135, 2007.

[23] A. Yabe, A. Miyamoto, and E. Brühwiler, "Characteristics of a bridge condition assessment method based on state representation methodology (srm) and damage detection sensitivity," *Journal of Civil Structural Health Monitoring*, vol. 9, no. 2, pp. 233–251, 2019.

[24] L. J. Liu, D. Wu, X. Zhang et al., "Application of improved bayesian method in bridge state assessment," *Journal of Chang'an University: Natural Science Edition*, vol. 37, no. 6, pp. 47–53, 2017.

[25] J. Dong, L. Chen, G. J. Yang et al., "Study on early bridge structure operational warning based on sliding window technique and data-driven stochastic subspace identification algorithm," *Railway Standard Design*, vol. 3, pp. 68–74, 2018.

[26] H. X. Huang, Z. L. Li, and L. Y. Fang, "Research on the simulation methods and criteria of damage state of existing bridges," *Journal of Hebei University of Technology*, vol. 47, no. 2, pp. 60–66, 2018.

[27] Y. Yamamoto and J. W. Baker, "Stochastic model for earthquake ground motion using wavelet packets," *Bulletin of the Seismological Society of America*, vol. 103, no. 6, pp. 3044–3056, 2013.

[28] L. An, "A construction risk early warning model of long-span cable-stayed bridge based on mcmc-ccraa," *Journal of Highway and Transportation Research and Development*, vol. 34, no. 10, pp. 42–50, 2017.

[29] S. Q. Yang, M. Guo, X. L. Liu et al., "Highway performance evaluation index in semiarid climate region based on fuzzy mathematics," *Advances in Materials Science and Engineering*, vol. 2019, Article ID 6708102, 7 pages, 2019.

[30] J. G. Cai, F. H. Dong, and Z. L. Luo, "Durability of concrete bridge structure under marine environment," *Journal of Coastal Research*, vol. 83, pp. 429–435, 2018.

[31] S. J. Hormozabad and A. K. Ghorbani-Tanha, "Semi-active fuzzy control of lali cable-stayed bridge using mr dampers under seismic excitation," *Frontiers of Structural and Civil Engineering*, vol. 14, no. 3, pp. 706–721, 2020.

[32] H. Pragalath, S. Seshathiri, H. Rathod et al., "Deterioration assessment of infrastructure using fuzzy logic and image processing algorithm," *Journal of Performance of Constructed Facilities*, vol. 32, no. 2, 2018.

[33] L. Liang, S. Sun, M. Li et al., "Data fusion technique for bridge safety assessment," *Journal of Testing and Evaluation*, vol. 47, no. 3, pp. 2080–2100, 2019.

[34] F. Magalhaes and A. Cunha, "Automated identification of the modal parameters of a cable-stayed bridge: influence of the wind conditions," *Smart Structures and Systems*, vol. 17, no. 3, pp. 431–444, 2016.

[35] H. Sohn, M. Dzwonczyk, E. G. Straser, A. S. Kiremidjian, K. H. Law, and T. Meng, "An experimental study of

temperature effect on modal parameters of the alamosa canyon bridge," *Earthquake Engineering & Structural Dynamics*, vol. 28, no. 8, pp. 879–897, 1999.

[36] M. R. Hashemi, Z. Ghadampour, and S. P. Neill, "Using an artificial neural network to model seasonal changes in beach profiles," *Ocean Engineering*, vol. 37, no. 14-15, pp. 1345–1356, 2010.

[37] C. Tong, T. Lan, H. Yu, and X. Peng, "Distributed partial least squares based residual generation for statistical process monitoring," *Journal of Process Control*, vol. 75, pp. 77–85, 2019.

Hindawi
Advances in Materials Science and Engineering
Volume 2021, Article ID 6678261, 10 pages
https://doi.org/10.1155/2021/6678261

*Research Article*

# Experimental Study on Reasonable Horizontal Load Value on the Top of Railings of Glass Bridges or Gallery Roads in Scenic Area

**Qingwen Sun**,[1] **Qiushi Yan**,[2] **Liqu Liu**,[3] **and Haowei Wang**[3]

[1]*China Academy of Building Research, State Key Laboratory of Building Safety and Environment, Beijing 100013, China*
[2]*Key Laboratory of Urban Security and Disaster Engineering, Ministry of Education, Beijing University of Technology, Beijing 100024, China*
[3]*National Center for Quality Supervision and Test of Building Engineering, Beijing 100013, China*

Correspondence should be addressed to Qiushi Yan; yqs2011@bjut.edu.cn

Received 30 December 2020; Accepted 26 July 2021; Published 6 August 2021

Academic Editor: Ivan Giorgio



With the increase of glass bridges or glass walkways in the scenic area, the safety protection provided by railings cannot be neglected. However, there is a difference between the demands for a horizontal load on the top of railings in the present design specifications. Especially, it does not give specific advice on the horizontal load on the top of railings of glass bridges or glass roads in the scenic area. In this study, experimental research is conducted on railing columns based on the investigation of common railings of glass bridges or glass roads in the scenic area. The type of railing columns includes finished products and field production. The number of railing columns is 12. The displacement and strain results of the railing columns under different loads are obtained. The rigidity and strength are analyzed by numerical simulation combined with test results. A reasonable horizontal load on the top of the railings of a glass bridge or glass road is advised. These results provide a reference for the design, inspection, and evaluation of railings of glass bridges or gallery roads in the scenic area.

## 1. Introduction

On March 2, 2021, in a public university in El Alto, Bolivia, the corridor railings suddenly broke, causing seven students to fall and one student to be seriously injured. In the Lantern Festival, in 2004, a crush and stampede accident occurred on the Rainbow Bridge in Mihong Park in Miyun District, Beijing, resulting in 37 deaths and 15 injuries [1]. There have also been many accidents with casualties on campus and shopping malls being caused by collapsed railings [2–4]. At present, glass bridge and gallery road railing systems in scenic areas are designed and manufactured according to the standards of railing systems of civil buildings. Tourists will stop to enjoy and take photos in the steep and dangerous places. Thus, the safety protection of the railing cannot be neglected. It is important to ensure the reliability of railings.

In the existing literature [5–9], different railing systems are verified to satisfy the requirements by the loading test. Fan et al. [10] test the horizontal thrust and vertical pressure of a bridge railing. According to the analysis of the finite element method, the most disadvantageous loading control position of the railing is determined by the design uniform load which is equivalent to the test concentrated load. Zhang and Guo [11] studied the long rail at a bus station by the overall detection method and the cut-off test method. And, the horizontal load of 2.5 kN/m was advised for the railing with two people above. In the existing literature, the study of the horizontal load of railings has not been found.

The load of railings is specifically advised in the present specification. On the top of a railing, the horizontal load value is 1.0 kN/m, and the vertical load value is 1.2 kN/m, according to *Load Code for the Design of Building Structures* (GB 50009-2012) [12]. The horizontal load value is 2.5 kN/m and the vertical load value is 1.2 kN/m e according to *Technical Specifications of Urban Pedestrian Overcrossing and Underpass* (CJJ 69-95) [13]. In addition, according to *Design Specifications for Highway Safety Facilities* (JTG D81-2017) [14], the standard horizontal loading value on the

top of sidewalk or bicycle lane railings is 0.75 kN/m and the standard vertical load value is 1.0 kN/m. According to the uniform building code [15], the load of railings outside the exit is 292 N/m, and the load of railings at the exit is 730 N/m. According to Eurocode [16], both the horizontal load and vertical load are 1.0 kN/m. There is a difference between the horizontal load values in different specifications. Then, the maximum value of the horizontal load is advised in *Technical Specifications of Urban Pedestrian Overcrossing and Underpass* (CJJ 69-95).

For human safety, Hopkins et al. [17] investigated the average pressure of a crowd in a New Year's party and a popular concert in New York, USA. The results showed that people will die in ten minutes in body pressure of 2.1 kN/m and will die in 15 to 30 seconds in a body of 11.68 kN/m. Smith [18] developed an inclined crowd model to quantify the pressure exerted by the crowd on the guard railings. Huang et al. [19] analyzed the pressure bearing capacity of people and individuals by the aforementioned inclined crowd model. The results showed that the safe design load value of human bearing capacity increases from 0.75 to 1.0 kN/m. Therefore, the design value of the horizontal load of railings should be limited.

For railings, structural safety and human safety both should be satisfied. It is necessary to study the reasonable horizontal load value of railings of glass bridges or gallery roads. In this study, experimental research was conducted on railing columns. The type of railing columns includes finished products and field production. The displacement and strain results of the railing columns under different loads are obtained. The rigidity and strength are analyzed by numerical simulation combined with test results. A reasonable horizontal load on the top of the railings of a glass bridge or glass road is advised.

## 2. Experiment Details

*2.1. Simplified Model of Railings.* In a railing system, the railing bars are firmly combined with the post which is fixed on the bottom support. The horizontal distributed load $F$ is applied to the railing bars outwards. And, the load is transferred to the post through bar-post joints. The post is the main bearing component. This study focuses on a single post. The horizontal distributed load $F$ of the railing bars is equivalent to concentrated load $P$ applied to the post, as given in equation (1) and Table 1.

The concentrated load:

$$P = F \cdot L, \tag{1}$$

where $L$ is post spacing, calculated as $L = 1$ m.

*2.2. Test Methods.* There are two types of railing posts for glass bridges or gallery roads in scenic areas based on an investigation. Type I is steel pipe railing posts which are rectangular steel tubes with a thickness of 2 mm–6 mm and a width of 60 mm–120 mm, as shown in Figure 1. Generally, the railing posts and the bottom support are connected by fillet welds which are 4–6 mm in length. Type II is finished railing posts, assembled on site by the manufacturer, as shown in Figure 2. Type II are single-piece posts made of stainless steel with a thickness of 5 mm–15 mm and a width of 60 mm–120 mm. The bottom gasket of a post is fixed on the bottom support through bolts or welds.

Table 1: Load value.

| Load steps | Initial | 1 | 2 | 3 | 4 | 5 | 6 | 7 | 8 | 9 | 10 | 11 | 12 |
|---|---|---|---|---|---|---|---|---|---|---|---|---|---|
| $P$ (kN) | 0 | 0.5 | 0.75 | 1 | 1.25 | 1.5 | 2 | 2.5 | 3 | 3.5 | 4 | 4.5 | 5 |
| $F$ (kN/m) | 0 | 0.5 | 0.75 | 1 | 1.25 | 1.5 | 2 | 2.5 | 3 | 3.5 | 4 | 4.5 | 5 |

Figure 1: Example of railings constructed on site.

There are two differences between the aforementioned two types of railings. First, the cross sections of the two types of railing posts are different. Second, two types of railing posts are connected to the bottom support in different ways. Finished railings are generally fastened by bolts or spot welding. The steel pipe posts are generally connected by full welding.

Two types of railing posts were tested. Material properties of the selected steel pipe post and the finished post are shown in Table 2 and detailed size parameters are shown in Table 3. The steel pipe post is made of Q235 steel, while the finished post is made of 304 stainless steel. Posts are fixed on the bottom support by welding with 6 mm fillet welds. The nodes at the bottom of the railing posts are fixed with the actual condition consistent. A horizontal loading test was conducted on the top of the post. The displacement, stress, and other test phenomena were recorded. The maximum test load is 5 kN/m.

As shown in Figure 3, the loading system equipment includes a counterforce frame, a load gauge, a displacement sensor, and a strain gauge. The bottom of the post is fixed on the test platform while the top of the post is welded with two railing bars. Displacement measuring points are arranged on the top of the post. Strain measuring points are arranged on its bottom.

*2.3. Test Results.* The test results of 12 railing posts are summarized in Figure 4. The maximum load, maximum strain, and test phenomena are recorded in Table 4. Posts 1

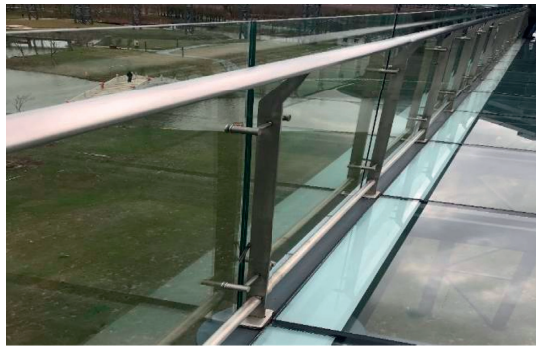

Figure 2: Example of finished railings.

to 8 are steel pipe posts made on site. The steel pipe posts were not collapsed during loading. The maximum load $F_{max}$ applied is 5.0 kN/m. Posts 9 to 12 are finished stainless steel posts. The connections and finished post were damaged due to excessive deformation. The gasket welds at the bottom of the posts were also pulled apart. The maximum load $F_{max}$ applied ranged from 1.5 kN/m to 3.5 kN/m.

At the same displacement, loads of steel pipe posts were compared. As the steel pipe post height increased, both the stiffness of the post and the load value decreased. The load value increased with post section thickness increasing. The load value also increased with post section size increasing. At the same displacement, loads of finished posts were compared. The results showed that the effect of post height, section thickness, and size on the load values of posts can be neglected. The maximum load $F_{max}$ applied for post 1 and 2 was 3.5 kN/m. $F_{max}$ applied for post 3 to 8 was 5.0 kN/m. $F_{max}$ applied for post 9 and 10 was 1.5 kN/m. $F_{max}$ applied for post 11 and 12 was 2.5 kN/m.

The results showed that, for the steel pipe post, the strain under the maximum load was acceptable. For the finished post, the strain increased even under a low load. The load of post 10 was smaller compared with other posts. The possible explanation was that the weld cracking between the post bottom and the gasket lead to a mild increase in the strain of the post.

To sum up, firstly, the effect of post height on the horizontal load value of the steel pipe post is obvious. With the height increase, both the post rigidity and the horizontal load value decreased. Secondly, the maximum test load of the steel pipe post is bigger compared to that of the finished post. At the same load, the strain of the steel pipe post is smaller compared to that of the finished post. Thirdly, the stress of support of the finished post is large with the horizontal load applied.

*2.4. Parametric Analysis.* Method of normalization was adopted to analyze the test results of steel pipe post 1 to 8 to study the relationship between railing load at the top $P$, post height $H$, section property $W$, material strength $f_y$, displacement $\Delta$, and strain $\varepsilon$.

(1) The correlation curve of $(FH/W \cdot fy) \propto \Delta/H$ is shown in Figure 5(a). According to *Technical Code for Test and Evaluation of City Bridges* (CJJ/T 233-2015) [20], H/120 was taken as the horizontal displacement limit. When $\Delta/H = 1/120$, the value of $(FH/W \cdot fy)$ ranged from 0.15 to 0.31. The correlation curve of $(FH/W \cdot fy) \propto \varepsilon$ is shown in Figure 5(b). When $(FH/W \cdot fy)<1$, $\varepsilon < 778(\times 10^{-6})$, the maximum strain of components 2, 4, and 7 exceed 500. The maximum strain of other components was less than $400(\times 10^{-6})$. When the value range of $(FH/W \cdot fy)$ ranged from 0.15 to 0.31, the maximum strain is $330(\times 10^{-6})$.

(2) When the displacement limit is $H/120$, the load curve of the steel pipe post is shown in Figure 6. The load value of post 5 was 0.8 kN/m which was the lowest load among posts. The load value of post 8 was 1.9 kN/m which was the highest load. The average load of posts is around 1.2 kN/m.

## 3. Numerical Analysis

The numerical analysis method was adopted to research more sizes of steel pipe posts in this study. The model of Qi et al. [21] was adopted. In the study of Qi et al. [21], a comparative study was conducted on the between element model and overall model applied on the analysis of the middle part of the column.

The results showed that the results of the internal force and displacement of the middle part column obtained by the element model and overall model are consistent. The element model was proved to analyze the railing system well. The finite element analysis model was developed with *Midas*, as shown in Figure 7(a).

The element model included a post and two half-span railings. One railing is at the left of the post and the other is at the right side. The post bottom was designed to be fixed support. For ends of the railings, the displacement of $x$, $y$, and $z$ directions of the node was constrained. Connections between the railing and the post were rigid. The displacement in $x$, $y$, and $z$ directions of connections was constrained. The upper node of the post was adopted as the main node. A nodal load was applied on the post based on the element model. And, loading conditions were the same as the test conditions. The material parameters were taken according to the results of material property experiments, as shown in Table 2, and the type of finite element is the bar element. Calculated results are shown in Figures 7(b) and 7(c).

Figure 8 shows the comparison between numerical analysis results and test results.

Compared to the results obtained by the experiment, calculated results of deformation and displacement of the railing post using the element model are consistent. Especially, the calculated results' displacement values are the same as the results from the experiment. Therefore, the element model can be used for numerical simulation of the railing posts of glass bridges or gallery roads in the scenic area.

Post height and section size of the post were analyzed. Based on the investigation, most of the steel pipe posts of

Table 2: Material properties of samples.

| No. | Sample specifications | Elastic modulus $E$ (MPa) | Yield strength $f_y$ (MPa) | Tensile strength (MPa) | Elongation at break (%) |
|---|---|---|---|---|---|
| 1 | Steel pipe post | $2.06 \times 10^5$ | 356 | 503 | 23.0 |
| 2 | Finished post | $1.93 \times 10^5$ | 700 | 789 | 36.5 |

Table 3: Size parameters of samples (mm).

| Type | No. | Height | Component size | Thickness |
|---|---|---|---|---|
| Steel pipe post | 1 | 1200 | 60 * 60 | 2 |
| | 2 | 1200 | 60 * 60 | 3 |
| | 3 | 1200 | 80 * 80 | 2 |
| | 4 | 1200 | 80 * 80 | 3 |
| | 5 | 1500 | 60 * 60 | 2 |
| | 6 | 1500 | 60 * 60 | 3 |
| | 7 | 1500 | 80 * 80 | 2 |
| | 8 | 1500 | 80 * 80 | 3 |
| Finished post | 9 | 1050 | 60 | 7 |
| | 10 | 1050 | 45–80 | 14 |
| | 11 | 1000 | 80 | 8 |
| | 12 | 1100 | 60–80 | 10 |

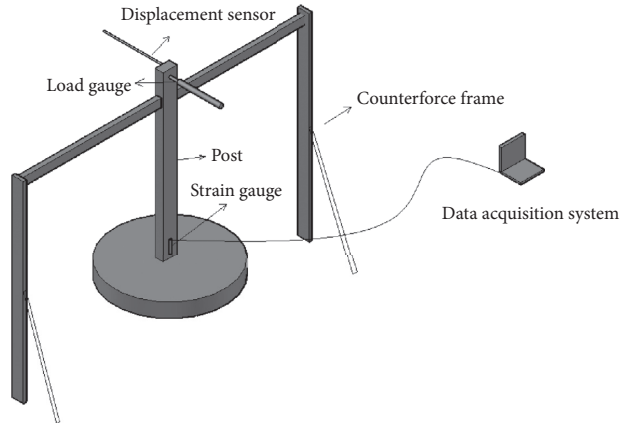


Figure 3: Schematic diagram of the loading system.

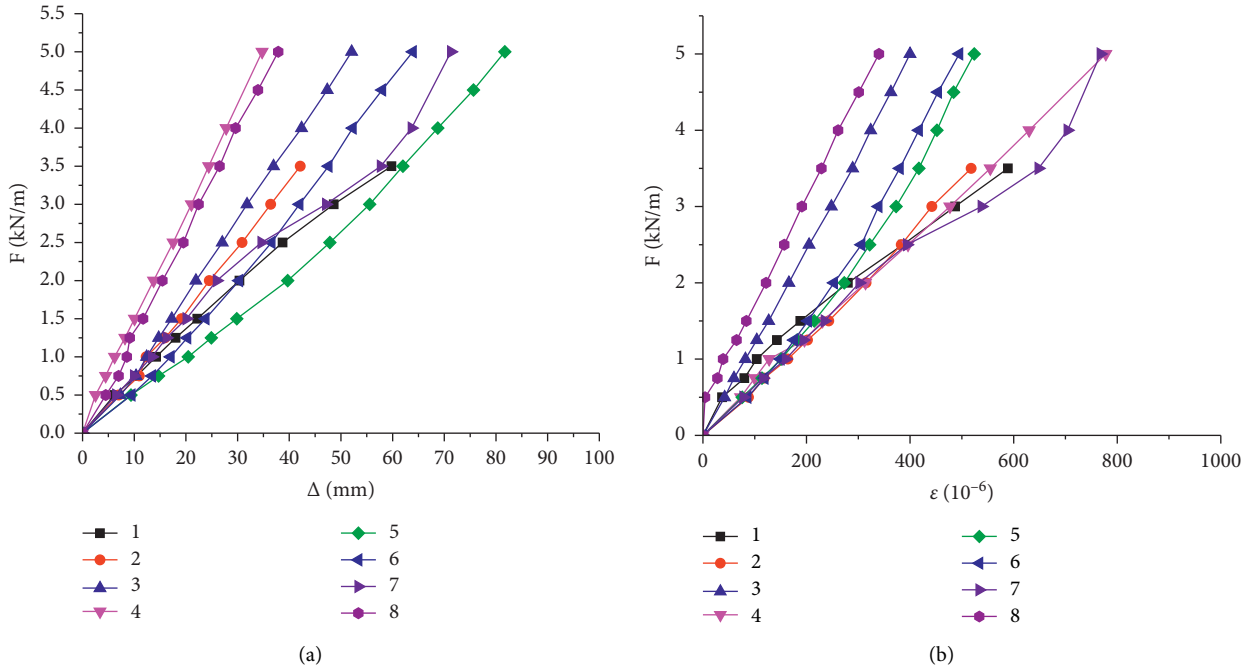


Figure 4: Continued.

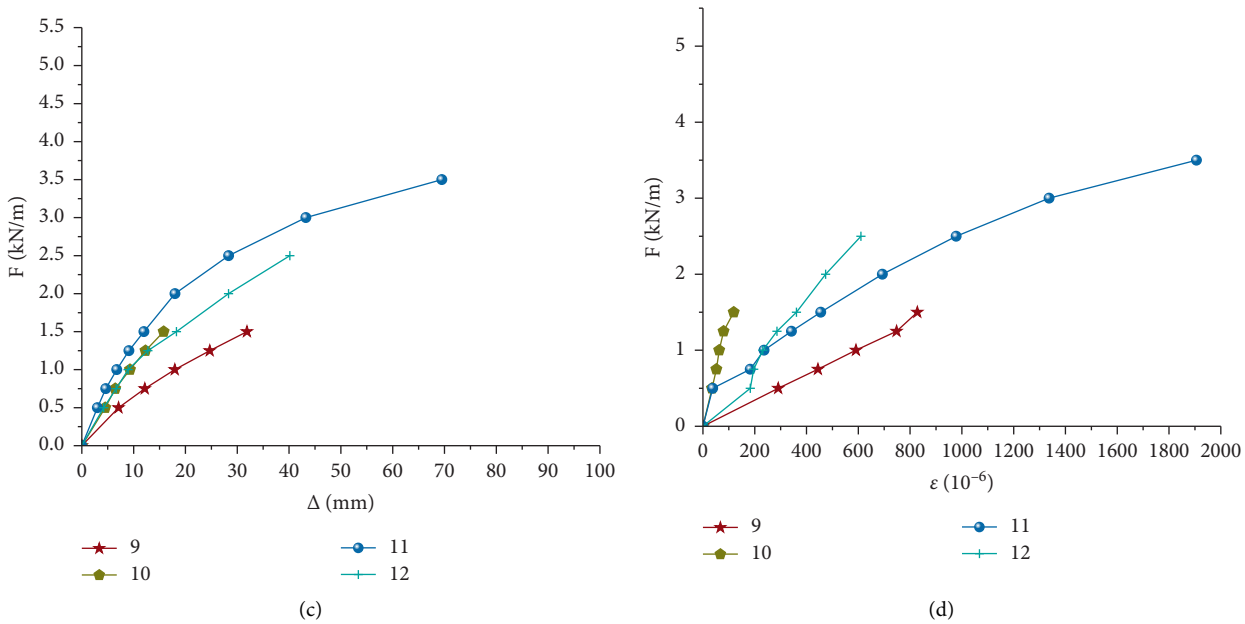


Figure 4: Load-displacement and load-strain test results of post components. (a) Load-displacement test results of steel pipe post components. (b) Load-strain test results of steel pipe post components. (c) Load-displacement test results of finished post components. (d) Load-strain test results of finished post components.

Table 4: Test phenomena.

| Type | No. | Maximum load $F_{max}$ (kN/m) | Maximum strain $\varepsilon$ ($10^{-6}$) | Description of phenomena |
|---|---|---|---|---|
| Steel pipe posts | 1 | 3.5 | 589 | The Jack slid out, the test ended; no weld cracked, no post collapsed |
| | 2 | 3.5 | 518 | The Jack slid out, the test ended, no weld cracked, no post collapsed |
| | 3 | 5 | 400 | The Jack reached its maximum, the test ended, no weld cracked, no post collapsed |
| | 4 | 5 | 778 | The Jack reached its maximum, the test ended, no weld cracked, no post collapsed |
| | 5 | 5 | 524 | The Jack reached its maximum, the test ended, no weld cracked, no post collapsed |
| | 6 | 5 | 495 | The Jack reached its maximum, the test ended, no weld cracked, no post collapsed |
| | 7 | 5 | 768 | The Jack reached its maximum, the test ended, no weld cracked, no post collapsed |
| | 8 | 5 | 340 | The Jack reached its maximum, the test ended, no weld cracked, no post collapsed |
| Finished posts | 9 | 1.5 | 828 | Welds at the bottom of posts cracked |
| | 10 | 1.5 | 119 | The upper support broke, the surface of the stainless steel post cracked, and welds between posts and gaskets at the pulling side failed |
| | 11 | 2.5 | 1906 | The upper support broke, the surface of the stainless steel post cracked |
| | 12 | 2.5 | 610 | The upper support broke, the surface of the stainless steel post cracked, and welds between posts and gaskets at the pulling side failed |

glass bridges and gallery roads in the scenic area were square steel tubes. The height of square steel tubes ranged from 1000 mm to 2000 mm. The section dimension of square steel tubes was (40-100) mm * (2-5) mm. Detailed parameters of the element model are displayed in Table 5. As shown in Table 5, 3 height values and 6 section dimensions of steel pipe posts were adopted, and subsequently, 18 element models were developed for numerical calculation.

The results obtained from 18 element models were analyzed by the method of normalization. The results show that

(1) The relationship of $(FH/W \cdot fy) \propto \Delta/H$ and $(FH/W \cdot fy) \propto \varepsilon$ is shown in Figure 9. The horizontal displacement limit is $H/120$. When $\Delta/H = 1/1201/120$, $(FH/W \cdot fy)$ has a value range

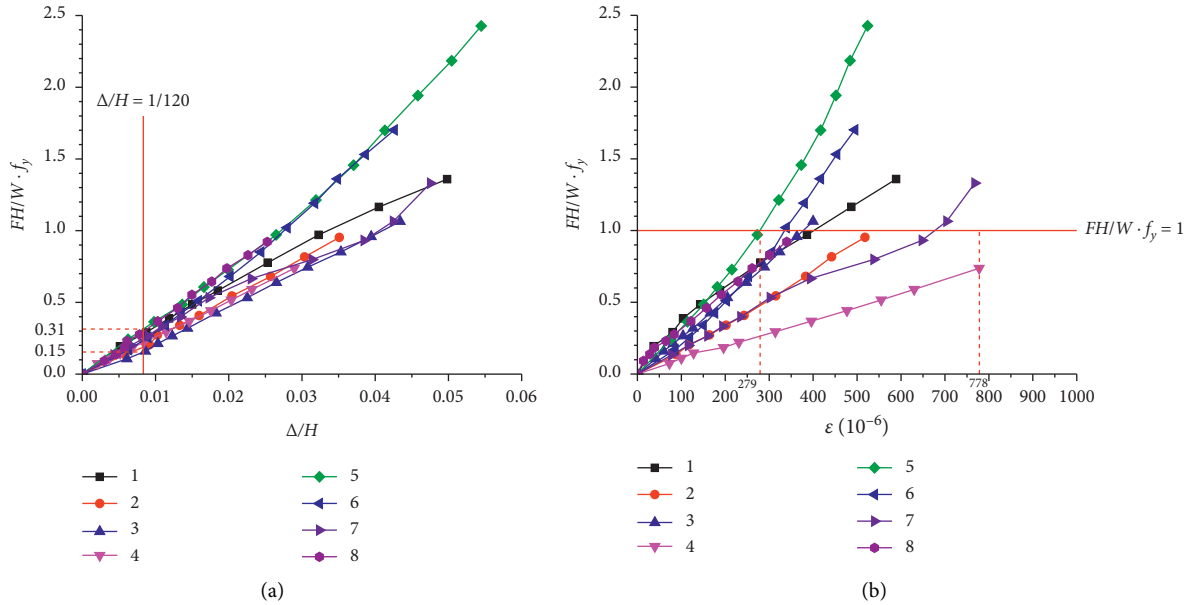


Figure 5: (a) Correlation curve (test results) of $(FH/W \cdot fy) \propto \Delta/H$. (b) Correlation curve (test results) of $(FH/W \cdot fy) \propto \varepsilon$.

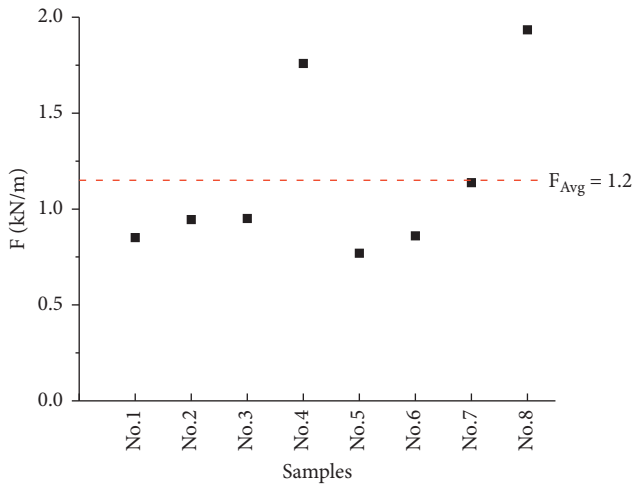


Figure 6: Load of steel pipe post with the displacement limit of $H/120$.

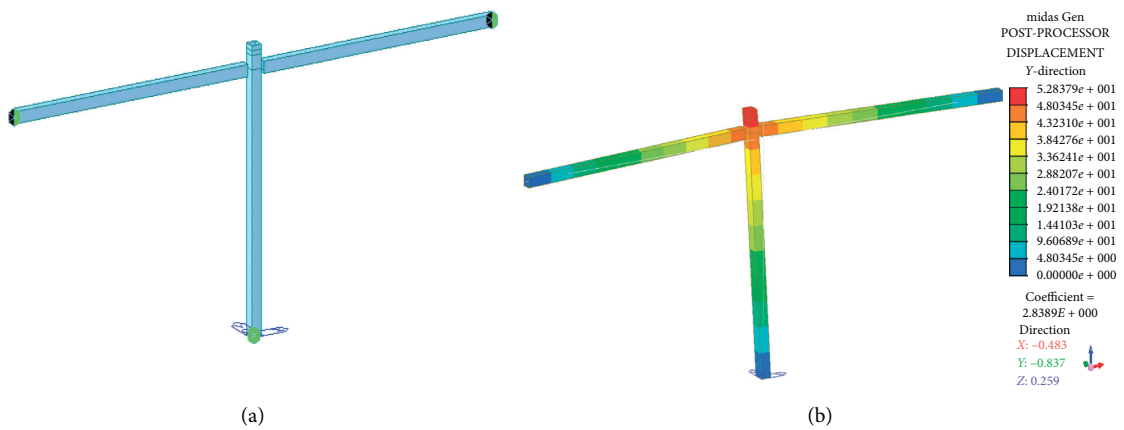


Figure 7: Continued.

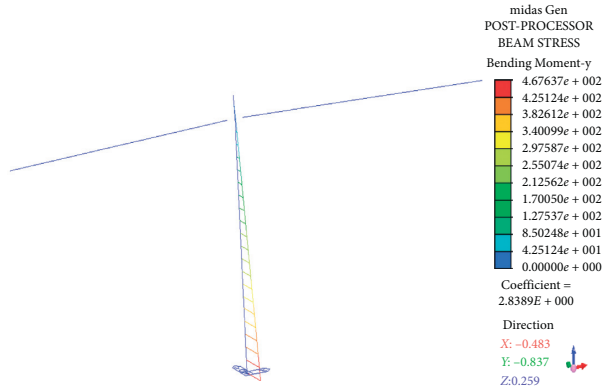


(c)

Figure 7: Finite element checking model of railing posts. (a) Element model of a post. (b) Checking results of displacement (post 1). (c) Checking results of stress (post 1).

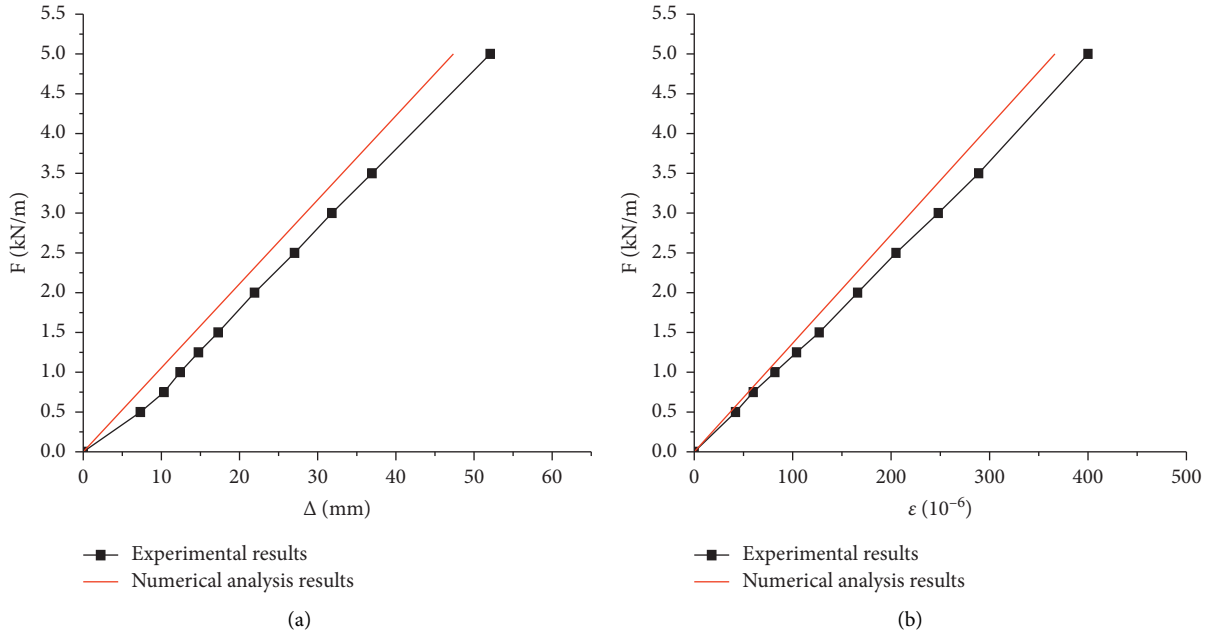


Figure 8: Comparison of experimental results and numerical analysis results of post 3 ((a) load-displacement; (b) load-strain).

Table 5: Size parameters of element models.

| | | | | | | | |
|---|---|---|---|---|---|---|---|
| Height | No. | H1 | H2 | H3 | — | — | — |
| | Parameter (mm) | 1000 | 1500 | 2000 | — | — | — |
| Section size | No. | B1 | B2 | B3 | B4 | B5 | B6 |
| | Parameter (mm) | 50 * 50 * 2 | 50 * 50 * 5 | 70 * 70 * 2 | 70 * 70 * 5 | 100 * 100 * 2 | 100 * 100 * 5 |
| | No. | B7 | B8 | B9 | B10 | B11 | B12 |
| | Parameter (mm) | 60 * 60 * 2 | 60 * 60 * 5 | 80 * 80 * 2 | 80 * 80 * 5 | 90 * 90 * 2 | 90 * 90 * 5 |

Note: an element model with a height of 1000 mm and a section size of 50 * 50 * 2 are regarded as H1B1.

from 0.10 to 0.56. The equation $(FH/W \cdot fy)$ can be considered as the ratio between post function $S$ and resistance $R$. It implied that $S/R$ ranged from 0.10 to 0.56, and equation (2) can be obtained:

$$\text{When } \frac{FH}{W \cdot fy} < 1\left(\text{that is } \frac{S}{R} < 1\right), \quad \varepsilon < 230\left(\times 10^{-6}\right). \tag{2}$$

(2) When the horizontal displacement limit is $H/120$, the relationship of element model load $F$ and $\Delta/H$ is shown in Figure 10. It can be seen that the load of H1B5, H1B6, H2B6, H1B10, and H1B12 were higher than 5.0 kN/m. The load of H3B12 was 0.1 kN/m which was the minimum value. Load values under $\Delta/H = 1/120$ were summarized in Figure 11. The average load was around 1.3 kN/m.

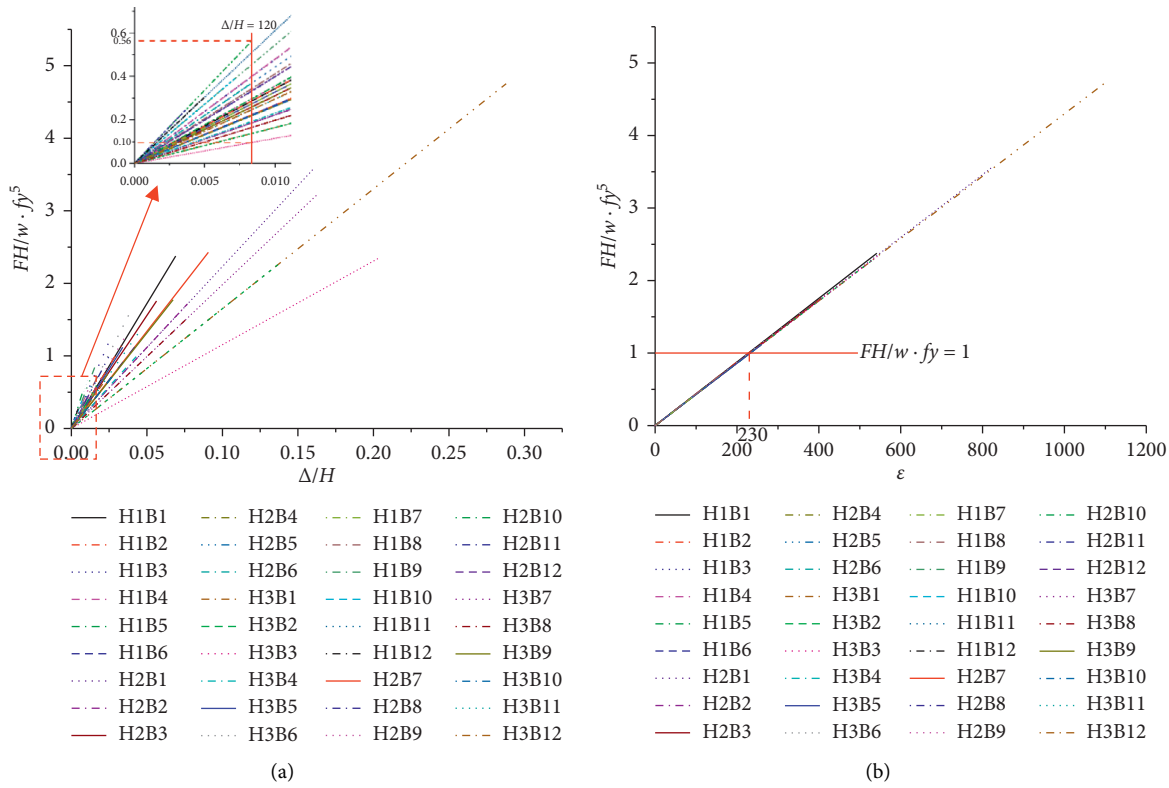


Figure 9: (a) Correlation curve (numerically calculated results) of $FH/W \cdot fy \propto \Delta/H$. (b) Correlation curve (numerically calculated results) of $FH/W \cdot fy \propto \varepsilon$.

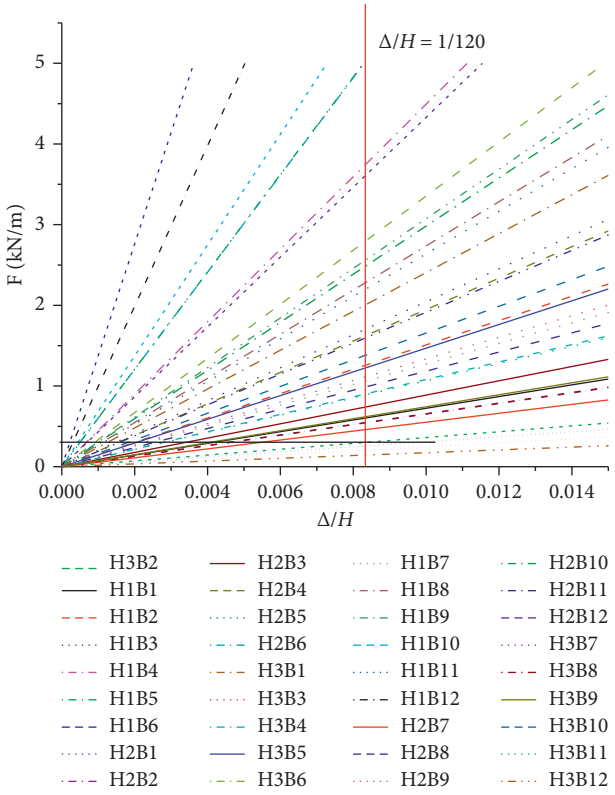


Figure 10: Correlation curve of $F$ and $\Delta/H$.

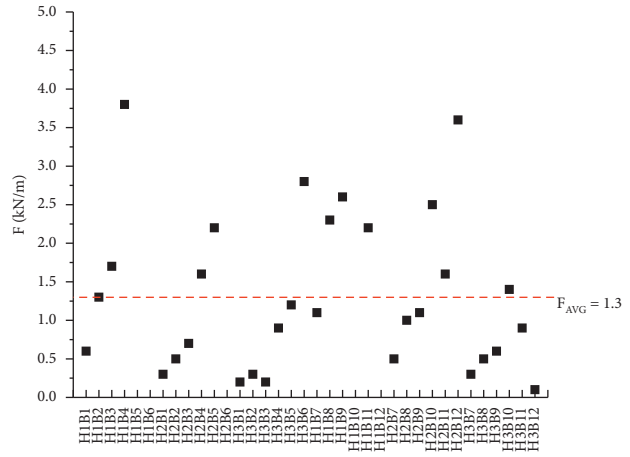


FIGURE 11: Element model loads under the displacement limit of $H/120$.

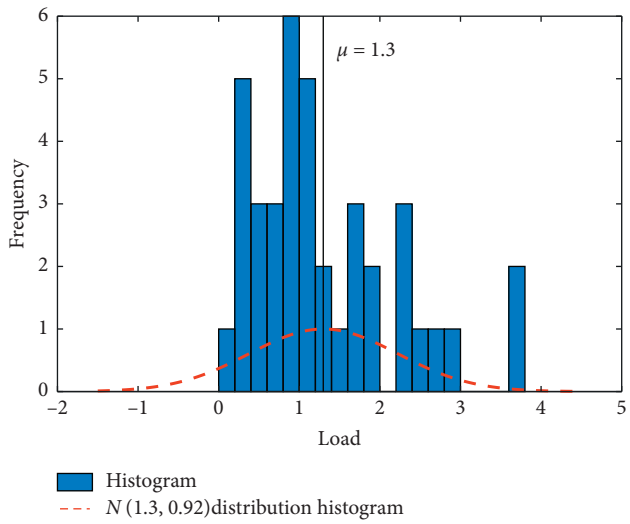


FIGURE 12: Histogram of horizontal load frequencies.

(3) Based on the results of the experiment and simulation, 39 sets of data were used to estimate the averaged horizontal load. The estimated value of averaged horizontal load was 1.3 kN/m. According to results of statistical analysis, the confidence interval of the averaged horizontal load with a confidence level of 95% is given:

$$<\mu>_{0.95} = \left(1.3 - 2.02\frac{0.92}{\sqrt{39}}; 1.3 + 2.02\frac{0.92}{\sqrt{39}}\right) = (1.0; 1.6)\,\text{kN/m}. \quad (3)$$

## 4. Conclusion

(1) A simplified test model of railings' post was proposed and load tests were carried out on railing posts of different sizes. The results showed that the maximum load of steel pipe posts was 5 kN/m, and the maximum load of finished posts was 2.5 kN/m. Compared with that of finished posts, the maximum load of steel pipe posts was higher and the strain value of steel pipe posts was smaller. Therefore, it is not recommended to choose finished posts as the main stress components in the railing systems of glass bridges and gallery roads in the scenic area.

(2) Results calculated by element models have the same tendency as that of railing posts. Therefore, it is acceptable to use element models for railing post simulation.

(3) Test results of 8 steel pipe posts and 18 steel pipe element models were numerically analyzed. When the displacement limit of the top of the post was $H/120$, $FH/W \cdot fy$ ranged from 0.10 to 0.56, and $\varepsilon$ was smaller than $230(\times 10^{-6})$. Therefore, $H/120$ is considered as the displacement limit of the top of the post to ensure that the bearing capacity of the post satisfied the requirements.

(4) With the displacement limit of $H/120$, the average horizontal load of 8 steel pipe posts was 1.2 kN/m and the averaged horizontal load of 18 steel pipe post element models was 1.3 kN/m. Based on analyzing the two sets of data, the confidence interval of the averaged horizontal load with a confidence level of 95% is $<\mu>_{0.95} = (1.0; 1.6)$ kN/m. Therefore, the reasonable value of the horizontal load on the top of the glass bridge or gallery road railings ranged from 1.0 kN/m to 1.6 kN/m.

## Data Availability

The data used to support the findings of the study can be obtained upon request (13691371229@163.com).

## Conflicts of Interest

The authors declare that they have no conflicts of interest.

## Acknowledgments

The authors deeply appreciate the support from compilation group of technical specification for glass trestle engineering and compilation group of inspection and evaluation standard for glass bridges in scenic spots.

## References

[1] D. Zhang, "Design of safe evacuation: thoughts on the accident of the rain bowl bridge in Miyun county," *Archi-creation*, no. 6, pp. 124–127, 2004.

[2] D. Huang, M. Dong, and Z. Wang, "Analysis and prevention of staircase accidents in primary and secondary schools," *Architectural Technology*, vol. 35, no. 4, pp. 278-279, 2004.

[3] C. Liu, "The Importance of safety design of non-structural building components," *Anhui Architecture*, vol. 11, no. 6, 69 pages, 2004.

[4] J. Liu and W. Xu, "Discussion on firmness and durability of metal railings in civil buildings," *Engineering quality*, vol. 29, no. 8, pp. 5–7, 2011.

[5] L. Chen, "Load test analysis of residential railings," *Shanghai construction technology*, no. 5, pp. 66–70, 2011.
[6] P. Chen, "Horizontal thrust test of pedestrian bridge railing," *Municipal technology*, vol. 29, no. 3, pp. 123-124, 2011.
[7] X. Wang, "Horizontal push load test and analysis of indoor railing of a commercial complex," *Shanxi architecture*, no. 11, pp. 36-37, 2017.
[8] F. Peng, Y. Qi, Y. Lieping et al., "Study on mechanical properties and structural safety of GFRP railings," *FRP/ Composites*, no. 6, pp. 48–54, 2010.
[9] X. Cui, X. Zhang, and Z. Wu, "Research on application effect of FRP Bridge sidewalk railing engineering," *Journal of Chongqing Jianzhu University: Natural Science Edition*, vol. 35, no. 3, pp. 22–26, 2016.
[10] M. Fan, X. Liang, and J. Gao, "Study on the load effect of urban bridge railings," *Highways & Automotive Applications*, no. 3, pp. 190–193, 2014.
[11] A. Zhang and S. Guo, "Research of the overall detection method of railing thrust strength," *Municipal Engineering Technology*, no. 1, pp. 47–49, 2012.
[12] GB50009-2012, *Load Code for the Design of Building Structures*, China Architecture and Building Press, Beijing, China, 2002.
[13] CJJ69-1995, *Technical Specifications of Urban Pedestrian Overcrossing and Underpass*, The Standardization Administration of the People's Republic of China, Beijing, China, 1995.
[14] Jtg D81-2017, *Design Specifications for Highway Safety Facilities*, 2017.
[15] International Council of Building Official, *Uniform Building Code 1997*, ICC, California, LA, USA, 1997.
[16] European Committee for Standardization, *EN-1991-2. European 1 Part 2*, CEN, Brussels, Belgium, 2002.
[17] I. H. Hopkins, G. Pountney, S. J. Hayes et al., *Crowd Pressure Monitoring. Engineering for Crowd Safety*, pp. 389–398, Elsevier, Amsterdam, Netherland, 1993.
[18] R. A. Smith, "The Hillsborough football disaster: stress analysis and design codes for crush barriers," *Engineering Failure Analysis*, vol. 1, no. 3, pp. 183–192, 1994.
[19] L. Huang, D. Liu, J. Hao et al., "Experimental research on barriers design load based on body safety," *China Satefy Science Journal*, vol. 23, no. 3, pp. 22–26, 2013.
[20] China Academy of Building Research, *Technical Code for Test and Evaluation of City Bridges*, China Architecture&Building Press, Beijing, China, 2016.
[21] Y. Qi, F. Peng, and L. Ye, "Study on mechanical properties and design of railing structures," *Industrial Construction*, vol. 41, no. 5, pp. 71–79, 2011.

Hindawi
Advances in Materials Science and Engineering
Volume 2021, Article ID 9913297, 11 pages
https://doi.org/10.1155/2021/9913297

*Research Article*

# Fatigue Performance of Rubber Concrete in Hygrothermal Environment

**Yushan Liu**,[1,2] **Jianyong Pang**,[1,2] **and Weijing Yao**[1,2]

[1]*State Key Laboratory of Mining Response and Disaster Prevention and Control in Deep Coal Mines, Anhui University of Science and Technology, Huainan, Anhui 232001, China*
[2]*School of Civil Engineering and Architecture, Auhui University of Science and Technology, Huainan, Anhui 232001, China*

Correspondence should be addressed to Jianyong Pang; pangjyong@163.com

Received 19 March 2021; Accepted 7 July 2021; Published 16 July 2021

Academic Editor: Shazim A. Memon



It is widely accepted that the rubber concrete (RC) originating from waste is a promising material that can contribute to the conservation and rational use of natural resources and the protection of the environment. However, the fatigue performance in a hygrothermal environment is a major concern because little pertinent information is available in the relevant literature. In this study, a cyclic loading test was carried out on RC subjected to different wet-dry cycles at different temperatures. The loading strain, plastic strain, and elastic strain of the concrete were compared and analyzed. The results revealed that the loading strain and plastic strain of the RC were obvious after the 1st loading cycle. As the number of loading cycles increased, the stress-strain curve became denser and the RC exhibited good elasticity. As the wet-dry cycles increased, the average plastic strain in the 10th–60th loading cycle increased while the elastic strain decreased. After 28 wet-dry cycles, the average plastic strain at 60°C increased by 42.31% compared with 20°C. In fact, as the temperature became higher, the plastic damage incurred by the RC became more severe. Finally, the damage variable was defined based on the elastic modulus and plastic strain to evaluate the fatigue performance of the RC in a hygrothermal environment. The findings of this study can provide a useful reference for RC applications.

## 1. Introduction

With the rapid development of the automobile industry and the rapid increase in automobile demand, tire rubber waste, which is toxic and hazardous, has increased, and the recycling and disposal of end-of-life tires are considered as "black pollution" [1–3]. Most waste tires are piled up in landfills without any particular treatment, which poses a risk to the wellbeing of the ecological environment and creates fire hazards [4, 5]. With regard to the recycling of rubber tires and reduction of environmental pollution, studies have attempted to introduce processed rubber aggregates as elastic materials into concrete to prepare rubber concrete (RC) [6, 7]. Notably, RC can not only make use of waste tires with high added value but also improve the ductility, toughness, wear resistance, and skid resistance of concrete. Moreover, RC exhibits excellent performance in vibration reduction and noise reduction [8–10]. Although the addition of rubber reduces the compressive strength of concrete, its plastic deformation ability and fatigue performance are significantly improved [11, 12].

Nowadays, RC is widely used in bridges, tunnels, railways, airport runways, nuclear structures, and so on [7, 12]. These structures are subjected to fatigue loading over long time periods while in service, and the antifatigue performance of the structure plays a vital role in its effective use in engineering applications [13, 14]. Therefore, many studies have investigated the mechanical properties and damage of RC under cyclic loading [15–21]. Pang et al. [18] found that the total strain, elastic strain, and plastic strain of RC are significantly higher compared with those of ordinary concrete in the process of cyclic loading, while the relative strain is extremely small, which indicates good ductility and stability. Lv et al. [20] investigated the effect of rubber particles on the fatigue performance of self-compacting lightweight rubber aggregate concrete. Their results revealed that the

fatigue life and strain increased as the replacement of rubber particles increased. Pacheco-Torres et al. [21] investigated the suitability of using discarded waste tire rubber particles in concrete rigid road pavements and presented an optimal combination of the size and proportion of rubber particles that improves the performance of the material subjected to cyclic loading stresses, which makes the material suitable for use in the construction of rigid concrete pavements.

However, in practical applications, tunnels, railways, and bridges are often subjected to two main groups of actions: traffic loadings and hygrothermal actions [22–24]. Multiple studies indicate that the strength, durability, and fatigue performance of the material rapidly decline in a hygrothermal environment [24–28]. Morshed et al. [26] found out the hygrothermal environments are deleterious to the durability of the interfacial bonding between concrete and CFRP. Tuakta and Büyüköztürk [27] observed a significant degradation of the bond strength when exposed to prolonged moisture condition, which can be up to 70% when specimens are conditioned for 8 weeks. Tang et al. [28] concluded that the higher the temperature, the lower the cohesive strength of the surrounding rock supporting structure under hygrothermal environments. Additionally, in areas with high temperature and humidity, a considerable proportion of highways suffer fatigue damage soon after being put into use, and this phenomenon develops rapidly [29–31]. Hence, it is understood that the fatigue performance of concrete in a hot and humid environment is somewhat different from that under normal conditions. Thus, it is necessary to investigate the fatigue performance of RC in a hygrothermal environment.

The objective of this study was to investigate the fatigue performance of RC in a hygrothermal environment. To this end, a cyclic loading test was carried out on the RC after different wet-dry cycles at different temperatures. Moreover, to quantify the fatigue damage of RC under the coupled action of the hygrothermal environment and loading, the damage variable was defined based on the elastic modulus and plastic strain. This has important practical significance for the promotion of RC engineering applications, natural resource preservation, and environmental protection.

## 2. Materials and Methods

*2.1. Raw Materials.* The cement used in this study was Chinese standard Portland cement; the chemical composition is presented in Table 1. The coarse aggregate was crushed limestone with continuous grading, particle size of 5–15 mm, and an apparent density of 2780 kg/m$^3$. The fine aggregate was river sand with a fineness modulus of 2.6. A high-performance water reducer (HPWR) with a water-reducing rate of 30% was employed to ensure fluidity and water retention. The rubber particles had a size of 0.85 mm and density of 1030 kg/m$^3$. Table 2 represents the technical indexes of rubber particle, used for preparing the concrete. The appearance and microstructure of the rubber particle are presented in Figure 1.

Table 1: Chemical composition of cement.

| Composition | $SiO_2$ | $Al_2O_3$ | $Fe_2O_3$ | CaO | MgO | $SO_3$ | Ignition loss |
|---|---|---|---|---|---|---|---|
| Content (%) | 22.60 | 5.03 | 4.38 | 63.11 | 1.46 | 2.24 | 1.18 |

*2.2. Preparation of Specimens.* The mix proportions of RC are presented in Table 3. The dimensions of the cylindrical specimens were $\Phi 50 \times 100$ mm.

The materials were measured using an electronic balance and mixed in a double-horizontal-shaft forced-type concrete mixer. First, preweighted aggregate and rubber were mixed for 1 min; then, binder material was added and mixed for 1 min. Subsequently, the already measured water and water reducer were poured into the properly mixed dry materials and stirred for 3 min to ensure a mix with uniform plastic consistency. The mold was filled in three layers and consolidated using a vibratory table. Additionally, the top surface was smoothed with a trowel. The specimens were subjected to the laboratory conditions of $20 \pm 2^{\circ}$C and 70% relative humidity. After hardening, the specimens were released from the molds and were cured in a saturated $Ca(OH)_2$ solution at $20 \pm 2^{\circ}$C for 90 d.

*2.3. Test and Characterization.* To prevent the moisture content from affecting the result of wet-dry cycles, all specimens were placed in an oven at the temperature of $105 \pm 5^{\circ}$C for 24 h before testing. After cooling, the specimens were divided into two groups and placed into thermostatic water bath box at the temperatures of 20°C and 60°C, respectively. In order to investigate the influence of hygrothermal environment on the fatigue performance of RC accurately, a wet-dry cycle test (soaking 16 h + drying 6 h + cooling 2 h) was used in lab conditions to simulate the humid and hot environment. The number of wet-dry cycles was 7, 14, and 28, respectively. Subsequently, the treated specimens were preserved in sealed polyethylene bags until the day of testing. The details of the test process are illustrated in Figure 2.

Using the RDL-200 electronic creep machine, uniaxial compression and cyclic loading tests were carried out on the RC specimens subjected to different wet-dry cycles. The uniaxial compression test was carried out at a rate of 1 mm/min until the specimen failed, so as to obtain the compressive strength, which is denoted as $f_c$. In the cyclic loading test, a small preload of 500 N was applied to the specimen before the test to ensure that the specimen and test device were properly aligned and centred. The equal amplitude cyclic loading method was used; the upper load was 30 kN and the lower unloading limit was 0 kN. The rate of loading and unloading was set to 30 kN/min. One loading and unloading process was considered as one cycle, and 60 cycles were carried out in total. The residual compressive strength was obtained at the rate of 1 mm/min after cyclic loading and is denoted as $f_c'$. The cyclic loading path of the test is shown in Figure 3.

Table 2: Technical indexes of rubber particle.

| Moisture content (%) | Ash content (%) | Acetone extract (%) | Metal content (%) | Fiber content (%) | Sieve residue content (%) | Tensile strength (MPa) | Elongation at break (%) |
|---|---|---|---|---|---|---|---|
| 0.62 | 8.75 | 5.12 | 0.02 | 0.00 | 0.014 | 16.8 | 564 |

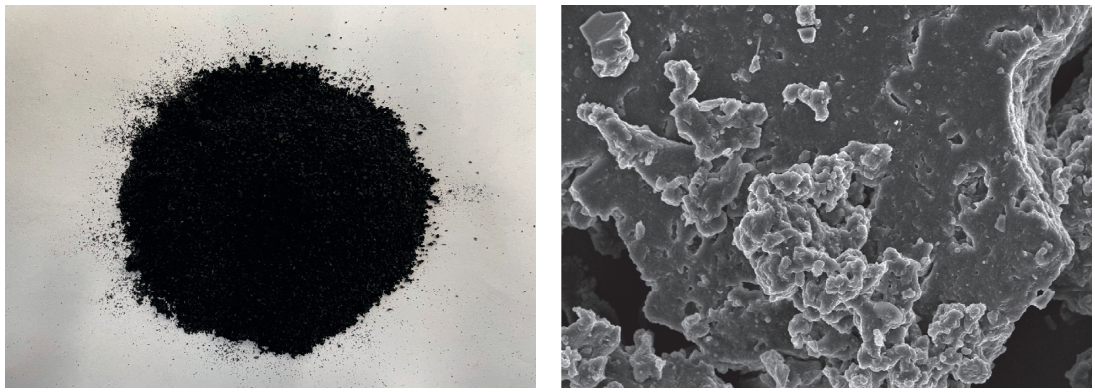

(a) (b)

Figure 1: The (a) appearance and (b) microstructure of the rubber particles.

Table 3: Mix proportions of RC (kg/m$^3$).

| Cement | Limestone | Sand | Rubber | Water | Water reducer | Water cement ratio |
|---|---|---|---|---|---|---|
| 322 | 1225 | 689 | 275 | 161 | 3.21 | 0.5 |

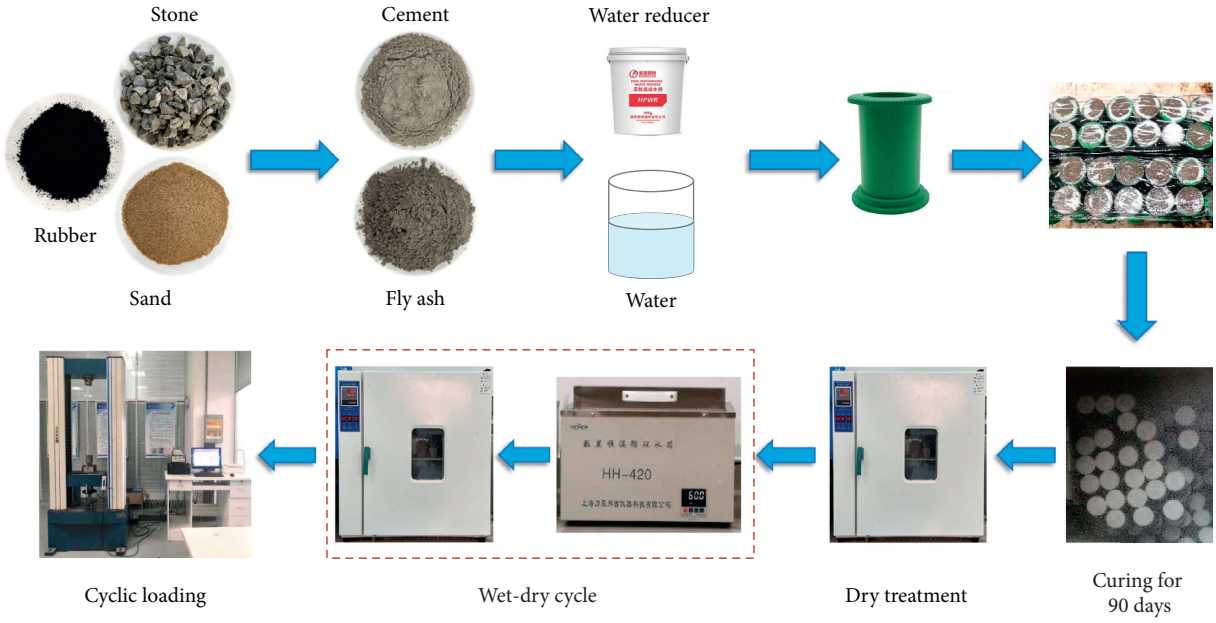


Figure 2: Details of test process.

## 3. Results and Discussion

*3.1. Compressive Strength Analysis.* The influence of wet-dry cycles and cyclic loading on the compressive strength of RC is demonstrated in Figure 4. The compressive strength of RC decreases and the pace of decline is prone to be faster with increasing wet-dry cycles. When the temperature was 20°C, the compressive strength of RC after 7, 14, 21, and 28 wet-dry cycles decreased by 5.63%, 16.90%, 30.99%, and 38.03%, while that of RC after cyclic loading declined by 10.28%, 23.00%, 37.87%, and 45.99%, respectively. After the same wet-dry cycles, the higher the temperature, the poorer the residual compressive strength.

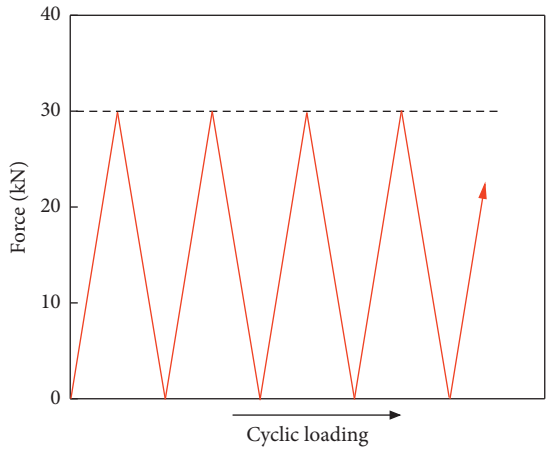


Figure 3: Cyclic loading path.

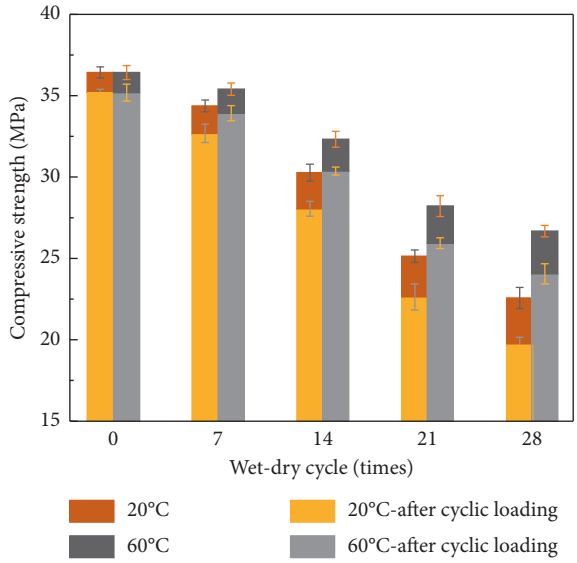


Figure 4: Compressive strength under different wet-dry cycles.

*3.2. Typical Cyclic Loading Curves.* The typical curve of RC under cyclic loading is shown in Figure 5(a). As can be seen, the stress-strain curve of RC is first sparse and then becomes dense. The deformation of RC under cyclic loading mainly occurs in the first cycle and is observed as a large opening at the bottom of the curve. The hydrophobicity of the rubber particles resulted in a weak interface between the rubber particles and the cement matrix, which led to many initial pores in the specimen. Once the specimen was loaded, the internal pores of RC were compressed and microcracks quickly appeared, mainly with plastic deformation. Because rubber particles have better elasticity and toughness, the addition of rubber particles into concrete is equivalent to the introduction of an elastomer to some extent [32, 33]. Hence, the deformation of RC is mainly elastic deformation after the primary pores have been gradually compacted, which indicates that there exists a reduced hysteretic loop area and a denser curve.

As can be seen from the single-cycle curve in Figure 5(b), the loading period is mainly divided into three stages: the compaction stage, approximate elastic stage, and crack evolution stage [34]. In Figure 5(b), $\varepsilon_l$ represents the loading strain, $\varepsilon_p$ represents the plastic strain (also called plastic strain), and $\varepsilon_e$ represents the elastic strain during each loading-unloading cycle. The curve in the compaction stage is concave, which indicates that the stress is kept at a low value and grows very slowly as the strain increases. This stage corresponds to the process of compacting and closing the internal pores. As the pores are gradually compacted, the specimen is uniformly compressed and the stress-strain curve increases approximately linearly, which indicates the approximate elastic stage. As the load and strain increase, the stress slowly increases and the curve exhibits a convex shape, which indicates the stage of microcrack evolution. As the load continues to increase, the curve exhibits a convex shape and the strain continues to increase, which indicates the stage of crack evolution. This is attributed to the breaking of the internal pores as the load increases, and the generation and expansion of microcracks with the breaking of the pores. The brittleness of concrete was weakened while its ductility is enhanced, and ductile deformation becomes the main deformation type.

*3.3. Loading Strain Analysis.* The relationships between the loading strain and the number of loading cycles are shown in Figure 6. As can be seen, the variation trend of the loading strain of the RC specimen with the number of loading cycles is essentially the same, although the number of wet-dry cycles is different. The loading strain increased with the number of cyclic loading, and the loading strain rate in the 0th–10th loading was obvious. After 10 loading cycles, the strain slowly increased and the curve tended to be flat. When the number of wet-dry cycles of the RC at 20°C was 0, 7, 14, 21, and 28, the loading strain in the 0th–10th cycle accounted for 97.22%, 96.36%, 96.86%, 91.2%, and 89.93% of the total strain, respectively.

Additionally, the loading strain increased with the wet-dry cycles under the same number of loading cycles. At 20°C, compared with the RC specimens without soaking, the loading strain in the 0th–10th loading cycle of the specimens, which had been subjected to 7, 14, 21, and 28 wet-dry cycles, increased by 7.14%, 17.62%, 25.95%, and 46.67%, respectively, and the loading strain in the 0th–60th loading cycle increased by 8.10%, 18.06%, 34.26%, and 58.56%. The influence of the wet-dry cycles on the loading strain was more significant as the number of loading cycles increased.

*3.4. Plastic Strain Analysis.* Figure 7 presents the average plastic strain within the 10th–60th loading cycle under different wet-dry cycles. As can be seen, the average plastic strain increased with the wet-dry cycles. When the temperature was 20°C, compared with the untreated RC specimens, the average plastic strain increased by 31.82% after 7 wet-dry cycles. As the wet-dry cycles increased, the average plastic strain increased by 40.91%, 77.27%, and 254.55%.

When the number of wet-dry cycles was the same, the average plastic strain at 60°C was larger compared with that

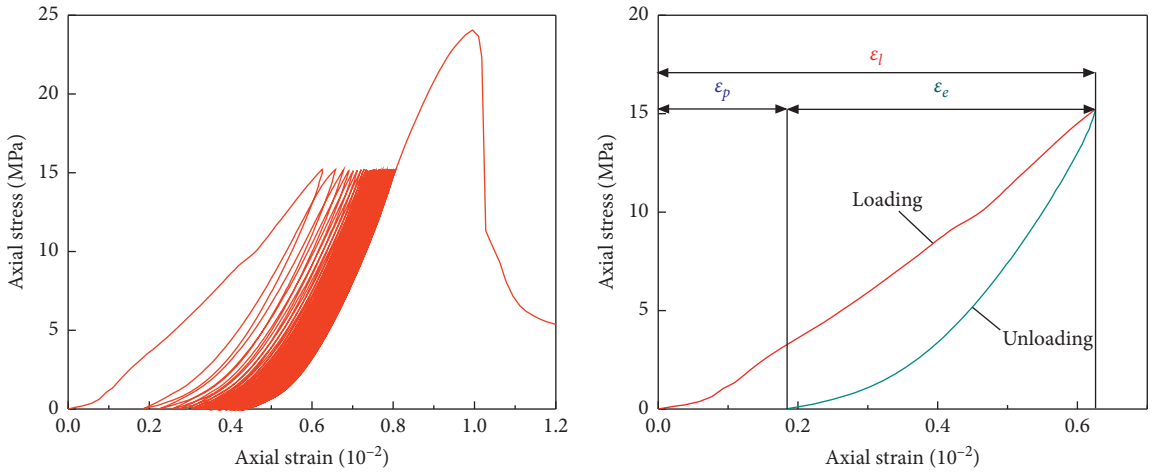


Figure 5: Typical RC curves under cyclic loading: (a) full strain curve under cyclic loading; (b) single-cycle curve.

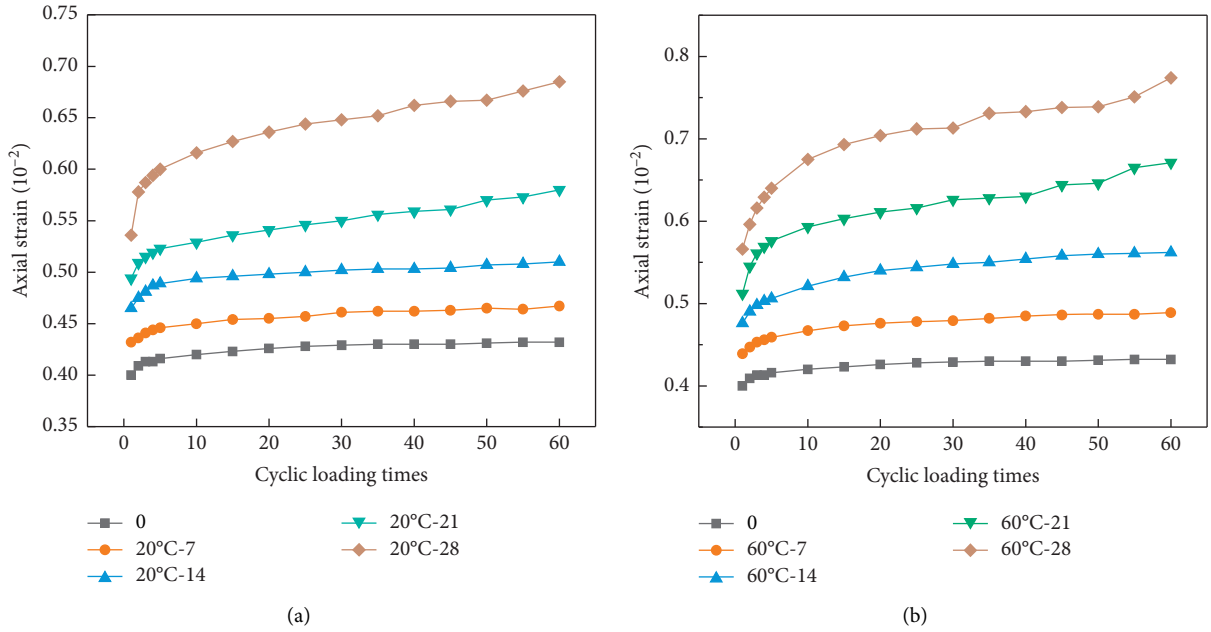


Figure 6: Relationships between loading strain and number of loading cycles: (a) 20°C; (b) 60°C.

at 20°C. This suggests the growth rate of the irreversible plastic strain was greater under higher temperature. Because rubber particles have good elasticity, the plastic deformation was mainly caused by the pores and cracks in the cement matrix. In a humid and hot environment, high temperature accelerates the wet-dry erosion, which further weakens the bonding of the rubber particles and cement matrix. Therefore, under cyclic loading, the accumulation of plastic deformation occurs owing to the internal crack propagation and damage evolution.

*3.5. Elastic Strain Analysis.* The deformation of concrete under loading, which can be recovered after unloading, is called elastic deformation. The difference between the loading strain $\varepsilon_l$ at the maximum axial stress of 30 kN and the plastic strain $\varepsilon_p$ when the specimen is unloaded to 0 kN is defined as the elastic strain $\varepsilon_e$. The average elastic strain within the 10th–60th loading cycle under different wet-dry cycles is shown in Figure 8.

It can be deduced from Figure 8 that the average elastic strain shows a fluctuating reduction. Obviously, the average elastic strain after the first seven wet-dry cycles is dropped at most, which is up to 3.79% at 20°C, and 5.96% at 60°C. As wet-dry cycles increased, the pace of the decline tended to be slow. It is attributed to the fact that the deterioration of RC is a continuing process induced by the wet-dry cycles. During the initial wet-dry cycles, the rearrangement of aggregates and cement matrix promotes the development of crack quickly.

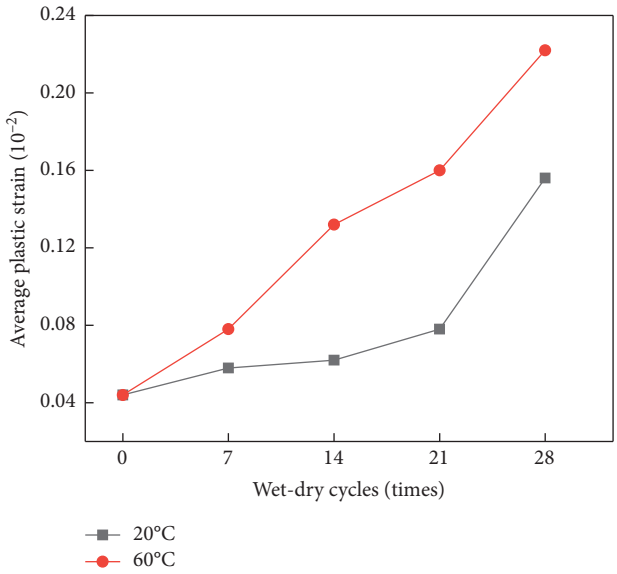


Figure 7: Average plastic strain in 10th–60th loading cycle under different wet-dry cycles.

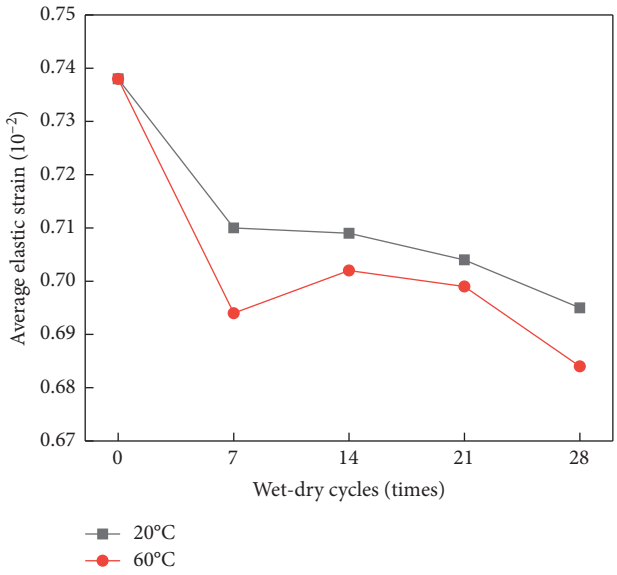


Figure 8: Average elastic strain in 10th–60th loading cycle under different wet-dry cycles.

As can be seen, the average elastic strains at 20°C were higher than those at 60°C, which confirms that the coupled corrosion of the hygrothermal environment and loading makes the process of durability performance deterioration easier, resulting in partial elastic strain transformed into plastic strain.

*3.6. Damage Evolution.* Damage refers to the microdefects or microcracks that exist inside the material as a result of manufacturing or external factors and results in the attenuation of mechanical properties and increase of deformation [35, 36]. A damage variable is a reference physical quantity, such as the stress, strain, elastic modulus, density, and energy density, and can be used to describe the internal damage of the material [37]. The damage variable can be selected according to the research object.

*3.6.1. Damage Variable of Elastic Modulus.* The elastic modulus $E_0$ reflects the deformation resistance of concrete and is essential for evaluating the material performance. The elastic modulus $E_0$ is calculated using the elastic stage of the unloading curve, which can be expressed as follows:

$$E_0 = \frac{\sigma}{\varepsilon_e}. \tag{1}$$

The elastic modulus $E_0$ of the RC subjected to various wet-dry cycles after 10, 20, 30, 40, 50, and 60 loading cycles is shown in Figure 9. As can be seen, $E_0$ of the RC specimen after 10, 20, 30, 40, 50, and 60 loading cycles fluctuated within a certain range. Therefore, the average $\overline{E}_0$ value was used to investigate the influence of the wet-dry cycles on the elastic modulus of RC [38]. According to Ma et al. [39], the increase of $\overline{E}_0$ after different wet-dry cycles was defined as the total damage variable $D_{En}$, and the average increase of $\overline{E}_0$ after each adjacent wet-dry cycle was defined the phase damage variable $\Delta D_E$, as follows:

$$D_{En} = \frac{\overline{E}_{0n} - \overline{E}_{00}}{\overline{E}_{00}}, \tag{2}$$

$$\Delta D_E = \frac{D_{En} - D_{Em}}{n - m}, \tag{3}$$

where $\overline{E}_{00}$ is the average elastic modulus of RC without soaking and $\overline{E}_{0n}$ is the average elastic modulus of RC when the wet-dry cycle is $n$. When the number of the wet-dry cycle $n$ is 7, 14, 21, and 28, the corresponding $m$ value is 0, 7, 14, and 21.

According to the definition in (2) and (3), the trend of the total damage variable $D_{En}$ and the phase damage variable $\Delta D_E$ of the RC specimen subjected to various wet-dry cycles are shown in Figure 8.

As shown in Figures 9 and 10, as the wet-dry cycles increased, the elastic modulus increased, and its total deterioration gradually increased. This is attributed to the fact that the amount of damage and energy dissipation increased, which accelerated the fatigue process. When the temperature was 20°C, the total damage variable of RC was 16.28% after seven wet-dry cycles. As the wet-dry cycles increased, the total degradation variables were 19.73%, 21.18%, and 22.60%.

However, during this process, the phase deterioration gradually decreased: the 0–7 phase of damage decreased up to 2.33%, and the 21–28 phase of damage decreased by the minimum amount of only 1.41%, which indicates that the wet-dry cycles result in the gradual deterioration of RC.

*3.6.2. Damage Variable of Plastic Strain.* Considering that the concrete is brittle and ductile, and its failure is mainly caused by excessive deformation, strain is one of the important indices for controlling the structural deformation

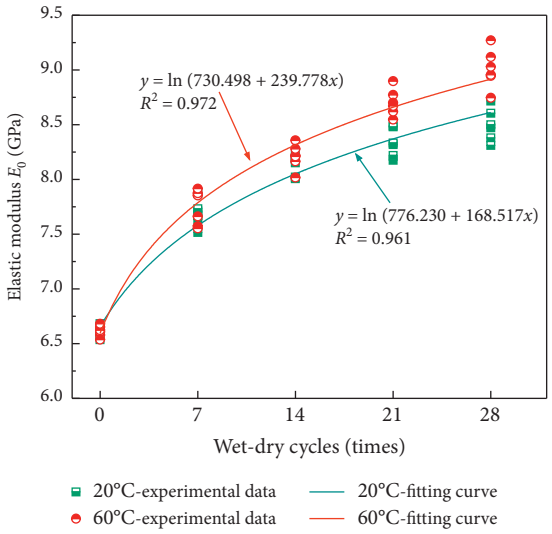


Figure 9: Elastic modulus of RC after being subjected to different wet-dry cycles.

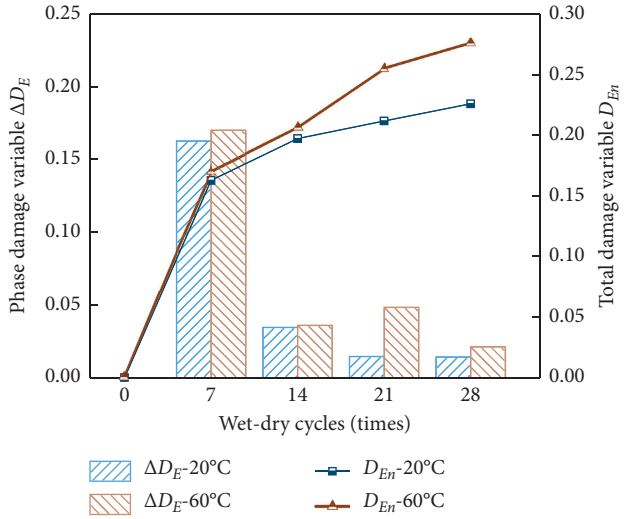


Figure 10: Total damage variable and phase damage variable of RC after being subjected to different wet-dry cycles.

and investigating the safety of concrete. The failure strain, which is also known as peak strain, is the strain that indicates structural failure and is denoted as $\varepsilon_f$. The plastic strain $\varepsilon_p$ refers to the deformation that cannot be recovered, which is known as residual deformation. To measure the fatigue plastic damage of RC specimens under cyclic loading, the ratio of the plastic strain $\varepsilon_p$ to the peak strain $\varepsilon_f$ in 0–60 loading cycles is defined as the damage variable $D_\varepsilon$ and is expressed as follows [19]:

$$D_\varepsilon = \frac{\varepsilon_p}{\varepsilon_f}. \tag{4}$$

Figure 11 shows the variation of $D_\varepsilon$ under different wet-dry cycles. Under the coupling action of wet-dry cycles and cyclic loading, the damage variable of the RC specimen increased with the number of wet-dry cycles. When the

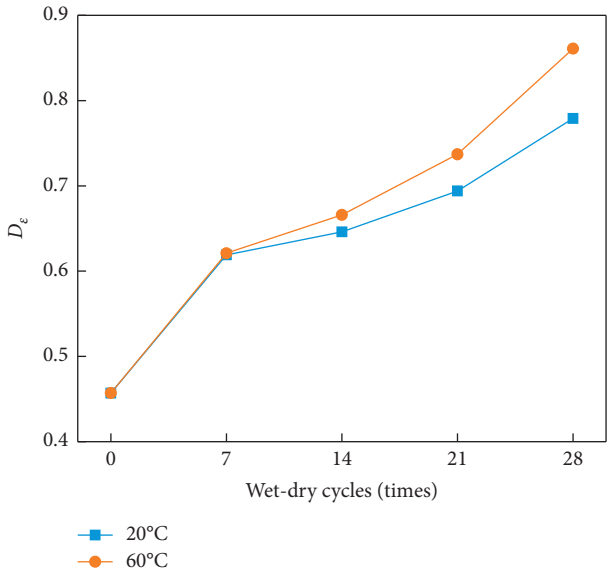


Figure 11: Damage variable $D_\varepsilon$ of RC subjected to different wet-dry cycles.

temperature was 20°C, the $D_\varepsilon$ values of RC after 0, 7, 14, 21, and 28 wet-dry cycles were 0.457, 0.617, 0.626, 0.651, and 0.679, respectively. Comparing the specimen without wet-dry cycle, the $D_\varepsilon$ values of RC at 20°C after 7, 14, 21, and 28 wet-dry cycles increased by 35.01%, 36.98%, 42.45%, and 48.58%, while those of 60°C increased by 35.89%, 45.73%, 61.27%, and 88.40%, respectively. After the same wet-dry cycles, the $D_\varepsilon$ values increased with the temperature. After 7, 14, 21, and 28 wet-dry cycles, compared with 20°C, the $D_\varepsilon$ value increased by 0.32%, 3.19%, 6.61%, and 11.76%, respectively.

*3.6.3. Damage Mechanism Analysis.* From the results we have obtained, one can conclude that the damage caused by the wet-dry cycles to the concrete is not negligible. Figure 12 shows the schematic diagram of internal structure, and Figure 13 displays the microstructure of the interfacial zone in the hygrothermal environment. The repeated soaking and high temperature drying precipitated the internal microcracks through. The soluble particles in the specimen were lost through the leftover pores, while the remaining particles expanded during the drying process and formed new internal voids and cracks. With the increase of wet-dry cycles, the pores left by the loss of soluble components accumulate (Figures 13(g) and 13(h)). Under repeated loading, the slip distance between the particles increased, and the cracks had sufficient time to develop and expand, which led to a loose internal structure and increased deformation. After 21 wet-dry cycles, wider fractures can be observed at the interface zone compared to the microstructure without wet-dry cycles (Figures 13(e) and 13(f)), illustrating the fact that the formation of fractures and pores significantly aggravates the deformation.

Comparing the specimens subjected to the same wet-dry cycles, it can be seen that the higher the temperature, the

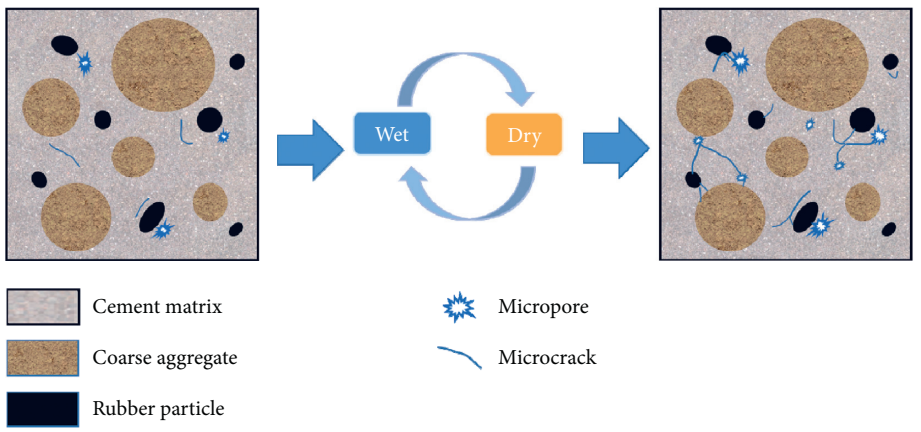


Figure 12: The internal structure schematic diagram of RC subjected to different wet-dry cycles.

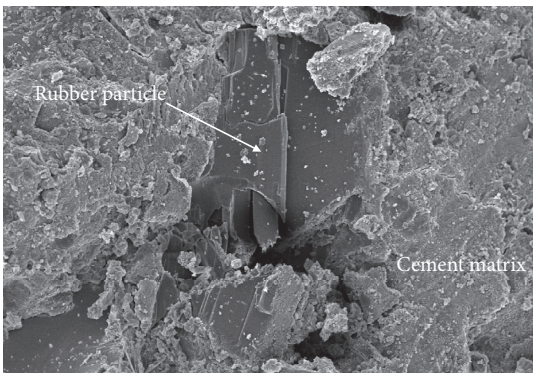


(a)

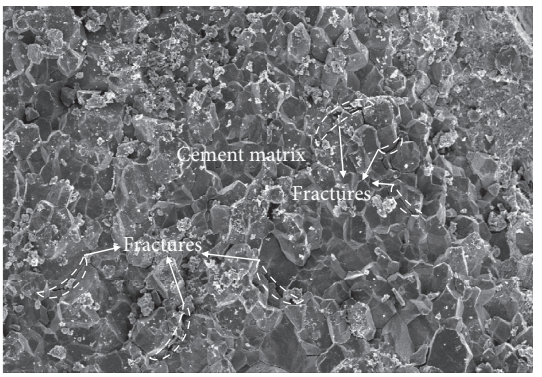


(b)

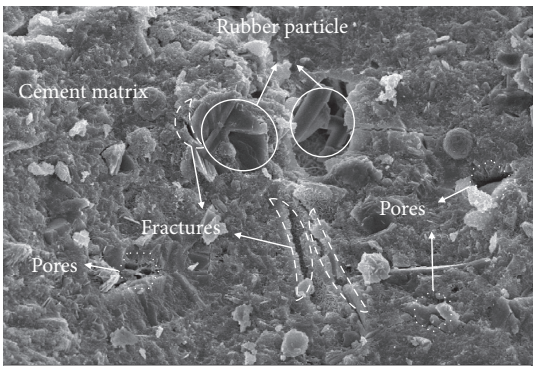


(c)

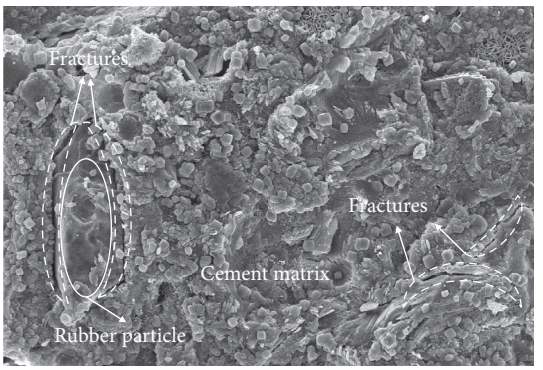


(d)

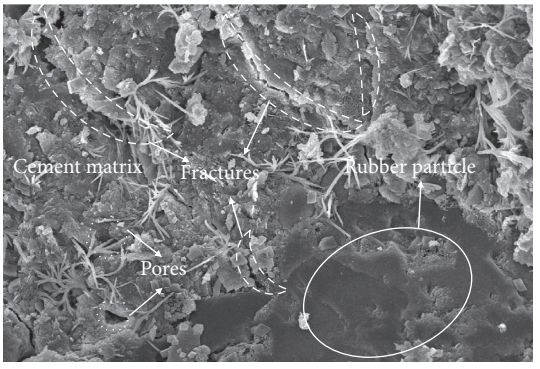


(e)

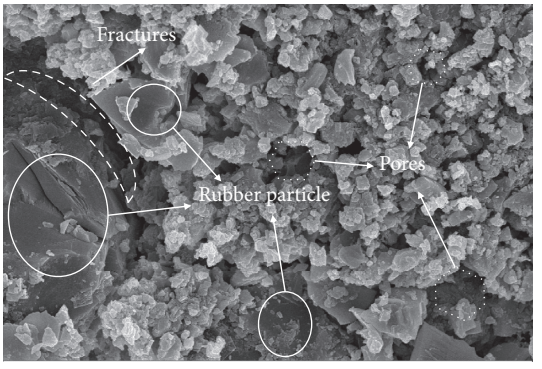


(f)

Figure 13: Continued.

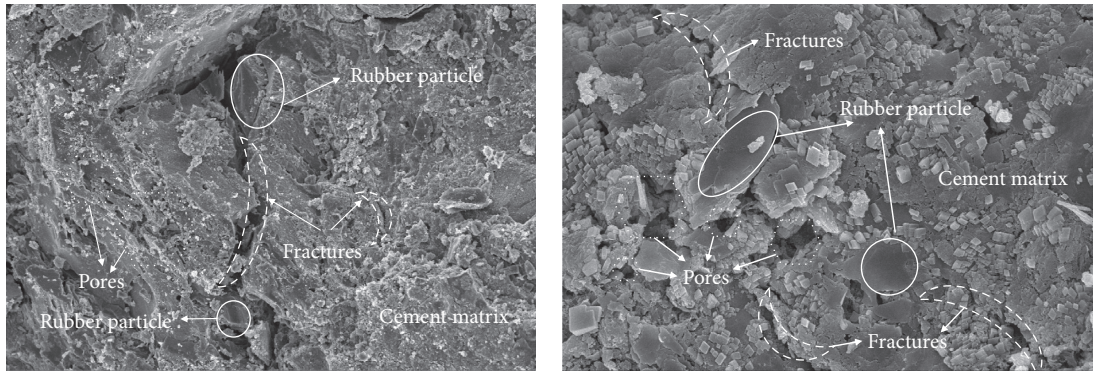


(g) (h)

Figure 13: Microstructures of the interfacial transition zone, subjected to (a) 0 wet-dry cycles, (b) 0 wet-dry cycles, (c) 14 wet-dry cycles at 20°C, (d) 14 wet-dry cycles at 60°C, (e) 21 wet-dry cycles at 20°C, (f) 21 wet-dry cycles at 60°C, (g) 28 wet-dry cycles at 20°C, and (h) 28 wet-dry cycles at 60°C.

looser the cement matrix and the longer the fracture length. The interaction effect caused by the negative influence of the temperature and wet-dry cycles resulted in the differential deformation and internal stress of the rubber particles and cement paste, and the internal structure was not as dense as before. This resulted in the more severe fatigue plastic damage of RC in the hygrothermal environment.

## 4. Conclusions

In this study, a cyclic loading test was carried out on RC subjected to different wet-dry cycles at different temperatures. The loading strain, plastic strain, and elastic strain of the specimens were compared and analyzed. Additionally, the damage variable was defined based on the elastic modulus and plastic strain. The main findings of this study are as follows:

(1) There existed primary pores and microcracks in the RC owing to the addition of hydrophobic rubber particles. The loading strain and plastic strain of the RC were obvious after the 1st loading cycle. As the number of loading cycles increased, the stress-strain curve became denser and the RC exhibited good elasticity.

(2) As the number of wet-dry cycles increased, the average plastic strain in the 10th–60th increased while the average elastic strain declined. Compared with the RC specimens without soaking, the average plastic strain in the 0th–60th loading cycle of the specimens, which were subjected to 7, 14, 21, and 28 wet-dry cycles at 20°C, increased by 31.82%, 40.91%, 77.27%, and 254.55%, respectively.

(3) The elastic modulus of RC increased logarithmically with the number of wet-dry cycles. The total damage variable gradually increased, which indicates that the deterioration of RC is a continuing process induced by the wet-dry cycles. The damage variable of the elastic modulus was maximum during the 0th–7th wet-dry cycles, that is, 16.27% at 20°C and 17.01% at 60°C, respectively.

(4) The comparison of the damage variable, which was defined based on the elastic modulus and plastic strain, revealed that the coupled corrosion of the hygrothermal environment and cyclic loading made the deterioration of durability performance easier, and fatigue damage accumulated faster.

## Data Availability

The datasets generated and analyzed during the current study are available from the corresponding author upon reasonable request.

## Conflicts of Interest

The authors declare that there are no conflicts of interest regarding the publication of this paper.

## Acknowledgments

This work was supported by China Postdoctoral Science Foundation (2020M681974), Natural Science Foundation of Anhui Province (KJ2020A0297), and Anhui University of Science and Technology (2020CX1004). Thanks are due to the State Key Laboratory of Mining Response and Disaster Prevention and Control in Deep Coal Mines, Engineering Research Center of Underground Mine Construction, for providing the experiment conditions.

## References

[1] J. Xu, Z. Yao, G. Yang, and Q. Han, "Research on crumb rubber concrete: From a multi-scale review," *Construction and Building Materials*, vol. 232, Article ID 117282, 2020.

[2] X. Chen, Z. Liu, S. Guo, Y. Huang, and W. Xu, "Experimental study on fatigue properties of normal and rubberized self-compacting concrete under bending," *Construction and Building Materials*, vol. 205, pp. 10–20, 2019.

[3] F. Liu, L.-y. Meng, G.-F. Ning, and L.-J. Li, "Fatigue performance of rubber-modified recycled aggregate concrete (RRAC) for pavement," *Construction and Building Materials*, vol. 95, pp. 207–217, 2015.

[4] Y.-F. Wu, S. M. S. Kazmi, M. J. Munir, Y. Zhou, and F. Xing, "Effect of compression casting method on the compressive strength, elastic modulus and microstructure of rubber concrete," *Journal of Cleaner Production*, vol. 264, Article ID 121746, 2020.

[5] Y. C. Zhang and L. L. Gao, "Mechanical performance test of rubber-powder modified concrete," *E3S Web of Conferences*, vol. 38, Article ID 03006, 2018.

[6] O. Youssf, M. A. Elgawady, J. E. Mills, and X. Ma, "An experimental investigation of crumb rubber concrete confined by fibre reinforced polymer tubes," *Construction and Building Materials*, vol. 53, pp. 522–532, 2014.

[7] G. Xue, X. Zhang, and M. Cao, "Tests for damping energy-dissipation performance of rubber concrete considering temperature effect," *Journal of Vibration and Shock*, vol. 39, no. 19, pp. 94–100, 2020.

[8] C. M. Copetti, P. M. Borges, J. Z. Squiavon, S. R. da Silva, and J. J. de Oliveira Andrade, "Evaluation of tire rubber surface pre-treatment and silica fume on physical-mechanical behavior and microstructural properties of concrete," *Journal of Cleaner Production*, vol. 256, Article ID 120670, 2020.

[9] E. Eltayeb, X. Ma, Y. Zhuge, O. Youssf, and J. E. Mills, "Influence of rubber particles on the properties of foam concrete," *Journal of Building Engineering*, vol. 30, Article ID 101217, 2020.

[10] K. A. Stallings, S. A. Durham, and M. G. Chorzepa, "Effect of cement content and recycled rubber particle size on the performance of rubber-modified concrete," *International Journal of Sustainable Engineering*, vol. 12, no. 3, pp. 189–200, 2019.

[11] S. Guo, Q. Dai, R. Si, X. Sun, and C. Lu, "Evaluation of properties and performance of rubber-modified concrete for recycling of waste scrap tire," *Journal of Cleaner Production*, vol. 148, pp. 681–689, 2017.

[12] B. S. Thomas, R. C. Gupta, P. Kalla, and L. Cseteneyi, "Strength, abrasion and permeation characteristics of cement concrete containing discarded rubber fine aggregates," *Construction and Building Materials*, vol. 59, pp. 204–212, 2014.

[13] W. Bai and J. Lv, "Experimental on damping capacity of rubber lightweight aggregate concrete," *Journal of Chang'an University (Natural Science Edition)*, vol. 38, no. 3, pp. 27–33, 2018.

[14] T. Gupta, S. Chaudhary, and R. K. Sharma, "Mechanical and durability properties of waste rubber fiber concrete with and without silica fume," *Journal of Cleaner Production*, vol. 112, pp. 702–711, 2016.

[15] T. Gupta, A. Tiwari, S. Siddique, R. K. Sharma, and S. Chaudhary, "Response assessment under dynamic loading and microstructural investigations of rubberized concrete," *Journal of Materials in Civil Engineering*, vol. 29, no. 8, Article ID 04017062, 2017.

[16] R. Yang, Y. Xu, and Q. Zheng, "Fatigue and damage evolution characteristics of rubber cement mortar under graded constant load cyclic compression," *Journal of Building Materials*, vol. 7, pp. 1–12, 2020.

[17] Y. Zhang and Z. Zhao, "Internal stress development and fatigue performance of normal and crumb rubber concrete," *Journal of Materials in Civil Engineering*, vol. 27, 2015.

[18] J. Pang, Y. Chen, and X. Huang, "Effect of high stress equal-amplitude cyclic loading on mechanical and deformation properties of rubberized concrete," *Journal of Yangtze River Scientific Research Institute*, vol. 37, no. 10, pp. 142–148, 2020.

[19] D. Y. Jiang, W. H. Liu, and J. Chen, "Fatigue performance of ordinary concrete subjected to stepwise discontinuous cyclic loading," *Journal of Southeast University (Natural Science Edition)*, vol. 49, no. 4, pp. 631–637, 2019.

[20] J. Lv, T. Zhou, Q. Du, and K. Li, "Experimental and analytical study on uniaxial compressive fatigue behavior of self-compacting rubber lightweight aggregate concrete," *Construction and Building Materials*, vol. 237, Article ID 117623, 2020.

[21] R. Pacheco-Torres, E. Cerro-Prada, F. Escolano, and F. Varela, "Fatigue performance of waste rubber concrete for rigid road pavements," *Construction and Building Materials*, vol. 176, pp. 539–548, 2018.

[22] C. Hu, H. Zeng, and Y. Que, "Characteristics of concrete pavement temperature field and temperature stress in hot and humid areas," *Journal of Fuzhou University (Natural Science Edition)*, vol. 39, no. 5, pp. 727–737, 2011.

[23] A. Abouhouraira, A. Ouali, O. Elhammoumi, L. Kassoumi, and A. Fekri, "Effect of accelerated ageing by cyclic variations of temperature and humidity on shrinkage of concretes," *Materials Today*, vol. 31, 2020.

[24] A. Mateos, J. Harvey, J. Bolander, R. Wu, J. Paniagua, and F. Paniagua, "Structural response of concrete pavement slabs under hygrothermal actions," *Construction and Building Materials*, vol. 243, Article ID 118261, 2020.

[25] S. A. Morshed, T. J. Young, W. M. Chirdon, Q. Zhang, and J. Tatar, "Durability of wet lay-up FRP bonded to concrete with nanomodified epoxy adhesives," *The Journal of Adhesion*, vol. 96, no. 13, pp. 1141–1166, 2020.

[26] S. A. Morshed, A. Sinha, Q. Zhang, and J. Tatar, "Hygrothermal conditioning of wet-layup CFRP-concrete adhesive joints modified with silane coupling agent and core-shell rubber nanoparticles," *Construction and Building Materials*, vol. 227, Article ID 116531, 2019.

[27] C. Tuakta and O. Büyüköztürk, "Deterioration of FRP/concrete bond system under variable moisture conditions quantified by fracture mechanics," *Composites Part B: Engineering*, vol. 42, no. 2, pp. 145–154, 2011.

[28] Y. Tang, H. Su, and H. Zhang, "Cohesive strength and micro failure mechanism of high geothermal diversion tunnel shotcrete surrounding rock," *Water Resources Research*, vol. 33, no. 4, pp. 127–129, 2015.

[29] E. I. Egba, M. Ismail, and N. Bakhary, "Temperature response in hardened concrete subjected to tropical rainforest environment," *Engineering, Technology & Applied Science Research*, vol. 7, no. 3, pp. 1623–1628, 2017.

[30] S. N. Shoukry, G. W. William, B. Downie, and M. Y. Riad, "Effect of moisture and temperature on the mechanical properties of concrete," *Construction and Building Materials*, vol. 25, no. 2, pp. 688–696, 2011.

[31] M. Qin, N. Liang, and Z. Lu, "Fatigue property analysis of asphalt mixture in water-temperature action," *Journal of Central South University*, vol. 42, no. 4, pp. 1126–1132, 2011.

[32] H. Xin, J. Pang, G. Liu, and C. Yu, "The influence of equal amplitude high stress repeated loading on the mechanical and deformation characteristics of rubber concrete," *Construction and Building Materials*, vol. 266, Article ID 121135, 2021.

[33] A. Gholampour, T. Ozbakkaloglu, and R. Hassanli, "Behavior of rubberized concrete under active confinement," *Construction and Building Materials*, vol. 138, pp. 372–382, 2017.

[34] G. Hu, Q. Zhao, and Y. He, "Elastic modulus's evolution law of plangiogranite under cyclic loading," *Journal of Engineering Geology*, vol. 24, no. 5, pp. 881–890, 2016.

[35] M. N. Noorsuhada, "An overview on fatigue damage assessment of reinforced concrete structures with the aid of acoustic emission technique," *Construction and Building Materials*, vol. 112, pp. 424–439, 2016.
[36] M. Liu, J. Lu, P. Ming, and J. Liu, "Effect of fatigue load on damage and fracture properties of rubber concrete," *Acta Materiae Compositae Sinica*, vol. 38, pp. 1594–1603, 2020.
[37] D. Jiang, Y. Cui, and J. Fan, "Experimental study of mechanical characteristics of salt rock under discon- tinuous cyclic loading," *Rock and Soil Mechanics*, vol. 38, no. 5, pp. 1327–1334, 2017.
[38] X. Liu, D. Li, Z. Wang, and L. Zhang, "The effect of dry-wet cycles with acidic wetting fluid on strength deterioration of shaly sandstone," *Chinese Journal of Rock Mechanics and Engineering*, vol. 35, pp. 1543–1554, 2016.
[39] Q. Ma, P. Yu, and P. Yuan, "Experimental study on creep properties of deep siltstone under cyclic wetting and drying," *Chinese Journal of Rock Mechanics and Engineering*, vol. 37, pp. 593–600, 2018.

Hindawi
Advances in Materials Science and Engineering
Volume 2021, Article ID 5526171, 10 pages
https://doi.org/10.1155/2021/5526171

*Research Article*

# Residual Mode Vector-Based Structural Damage Identification with First-Order Modal Information

**Shuai Luo, Zhenxin Zhuang, Wei Wang, and Ping Jiang**

*School of Civil Engineering, Shaoxing University, Shaoxing, Zhejiang 312000, China*

Correspondence should be addressed to Ping Jiang; jiangping@usx.edu.cn

Received 15 February 2021; Accepted 16 June 2021; Published 3 July 2021

Academic Editor: Qinglin Guo



Damage identification based on the change of dynamic properties is an issue worthy of attention in structure safety assessment, nevertheless, only a small number of discontinuous members in existing structure are damaged under service condition, and the most remaining members are in good condition. According to this feather, we developed an effective damage location and situation assessment algorithm based on residual mode vector with the first mode information of targeted structure, which utilized the quantitative relationship between first natural modes of global structure with the change of the element stiffness. Firstly, the element damage location is determined with exploitation of the sparseness of element stiffness matrices based on the discontinuity of damaged members. Then, according to the distribution characteristics of the corresponding residual mode vector, the nodal equilibrium equation about the damage parameter is established based on the residual mode vector, and the damage coefficients of structural elements are evaluated with the proposed equations. Two numerical examples are given to verify the proposed algorithm. The results showed that the proposed damage identification method is consistent with the preset damage. It can even accurately identify large-degree damages. The proposed algorithm only required the first-order modal information of the target structures and held few requirements of analysis resource; hence when compared with existing methods, it has obvious advantages for structural damage identification.

## 1. Introduction

Structural damage identification technology shows its strong vitality in many engineering fields such as civil engineering, mechanical engineering, and aerospace engineering, which has benefited from the combination with modal measurement technology and finite-element analysis [1–3]. Various damage location and detection technologies have been developed based on structural vibration properties. The principle for vibration-based damage identification is that the damage-induced changes in the physical properties of element stiffness will cause detectable changes in system modal properties (natural frequencies and mode shapes).

The investigation of mode eigen values for damage detection is common as the natural frequencies can be conveniently measured from just a few accessible points on the structure [4–7]. However, this method could not detect the subtle damage on structure. Damage detection methods have also been developed for the identification of damage directly based on measured mode shapes or mode shape curvatures [8–10]. A drawback of many mode shape-based methods is the complexity of having measurements from a large number of locations for higher order modal shapes [11–13]. For the purpose of fully utilized mode information, Kaouk and Zimmerman [14–16] defined the residual mode equation for damage detection based on mode information of structure, which can accomplish the dual tasks of determining the damage location and solving the damage situation effectively. This kind of damage detection method has received the widespread attention over the last decade [17–21]. There exists a common obstacle in the aforementioned detection methods, which is to obtain higher order of structural modal shapes. This requirement limits the practical application of the residual mode method. Recently, with the development of high-speed camera and sensitive sensor and vision recognition technology, the modal parameter

identification technology of engineering structure has made remarkable progress [22–25]. We can effectively realize the accurate identification of the finite-order natural mode shapes (usually the first order) and natural frequencies (usually the first order) of the structural system. As such, more advanced analysis procedures are required to make the best use of first-order modal information from structural health monitoring.

In this paper, the authors develop a damage detection method originally proposed by Kaouk et al. based on the residual mode equation with only the first order of structure mode information. The residual mode vector is developed based on the residual mode equation for structural element damage detection, in which the relationship between the stiffness matrix of damaged element and first-order mode information is derived from the residual mode equation. Then based on the relationship, the element damage location is determined with exploitation of the sparseness of element stiffness matrices. Finally, according to the distribution characteristics of residual mode vector, a new damage assessment algorithm is proposed.

The presentation of this work is organized as follows: in Section 2, the proposed algorithm based on the residual mode vector is developed. In Section 3, the process of structural damage identification using the established method is introduced numerically in detail with a simple supported beam. Moreover, the source of the accelerated formula is also discussed in detail. A two-story framework example is shown in Section 3.2 to show the feasibility and the superiority of the proposed method. The conclusions of this work are summarized in Section 4.

## 2. Problem Formulation

*2.1. Fundamental Assumptions.* In the following theoretical development, the following assumptions are made in damaged structures:

(1) Structural damages only reduce the system stiffness matrix, and structural refined numerical model has been developed before damage occurrence.

(2) It is assumed that the effect of damage on the mass properties of the structure is negligible, and we assume that the structure under consideration is undamped.

(3) The crack-induced structural member damage is not continuous in the finite-element model, this is reasonable in the previous study [26–29], and furthermore we could change the scale of element size in the numerical model.

*2.2. Theoretical Development.* One basic approach to obtain a qualitative feel for the effect of the damage on an individual mode is to monitor the change in mode information between the damaged structures and the undamaged structures. With the above assumptions, considering an initial design, the first-mode eigen equation of an $n$-DOF finite-element model of the undamaged structure exists and is given as

$$\lambda_1 \mathbf{M}\phi_1 = \mathbf{K}\phi_1, \tag{1}$$

where $\lambda_1$ and $\phi_1$ are the first-mode eigen value and corresponding eigenvector separately and $\mathbf{M}$ and $\mathbf{K}$ are the $n \times n$ analytical mass and stiffness matrices. In this paper, only the first-order modal information of the system will be used to identify the damage location and damage situation, and this is also the important motivation for conducting this research. Let $\Delta\mathbf{K}$ be the exact perturbation matrices that reflect the nature of the structural damage. Thus, the exact perturbation matrices are sparse matrices with the nonzero elements reflecting the state of damage. The eigen equation for the damaged structure is then

$$\lambda_{1\mathrm{d}} \mathbf{M}\phi_{1\mathbf{d}} = (\mathbf{K} - \Delta\mathbf{K})\phi_{1\mathbf{d}}, \tag{2}$$

where $\lambda_{1d}$ and $\phi_{1\mathbf{d}}$ are the first-mode eigen value and corresponding eigenvector measured precisely, as the first-order modal parameters of structures are the most easily obtained dynamic information in experimental process. $\Delta\mathbf{K}$ is the $n \times n$ analytical mass and stiffness matrices:

$$\Delta\mathbf{K} = \sum_m \alpha_m \mathbf{K}_{\mathbf{m}}, \tag{3}$$

where $\alpha_m$ is a scalar denoting the damage extent corresponding to the $m$-th element and the $\Delta\mathbf{K}$ matrices represent the effect of damage on the structural property matrices. Thus, the exact damage matrices are sparse matrices with the nonzero elements reflecting the state of damage. Now equation (2) can be rewritten in the dynamic residual form:

$$\Delta\mathbf{K}\phi_{1\mathbf{d}} = (\mathbf{K} - \lambda_{1\mathrm{d}}\mathbf{M})\phi_{1\mathbf{d}} = \mathbf{D}, \tag{4}$$

where $\mathbf{D}$ is the defined residual mode vector related to the first mode about the damaged system, and it could be depicted as

$$\mathbf{D} = [\ d_1,\ d_2,\ \cdots\ d_n\ ]^T, \tag{5}$$

where superscript $T$ means transpose, and the same below, the proposed residual mode vector is $n \times 1$ column vector. Then the location of damage element could be easily processed based on the distribute regulation of the proposed residual mode vector. Sort the elements in residual mode vector in absolute descending order, and then one can easily find that there is a great deal of differences: The amplitude of $d_i$ in the proposed residual mode vector corresponding to the damaged element is much larger than that of the undamaged element; even, the elements in the proposed residual mode vector corresponding to undamaged element tends to 0, which could be used as the basis of filtering in the analysis process.

Obviously, equation (4) is composed of $n$ equilibrium equations at nodes; based on the assumption that there is only one element damaged at each node, for the node location of the damage element, the stiffness of the independent damage element is strictly proportional to the right-hand side of equation (4), and its ratio is the damage

coefficient to be calculated. Based on this principle, the damage situation could be evaluated quantitatively.

In the end, this section summarizes the key steps as follows:

*Step 1:* calculating the residual mode vector

For the target structure, calculate residual mode vector by substituting the experimental results of first-order modal information $\lambda_{1\,d}$ and $\phi_{1\mathbf{d}}$ into equation (4).

*Step 2:* locating the damage element in structure and filter

Arrange the elements in the residual mode vector in the descending order of their absolute values. Divide the previous element by the next, and the last damage element is where the result tends to infinity, so as to locate the damage element; then the element in residual mode vector corresponding to the undamaged unit after positioning is artificially set to 0 to realize filtering.

*Step 3:* Verifying the results of location identification

List the elements in residual mode vector after filtering according to their corresponding structural elements. Divide the elements in residual mode vector corresponding to the symmetrical node in the element, and the result whose quotient is −1 is the damaged component, so as to *verify* the results of location identification in Step 3, and prepare a new list for identification of the damage situation quantitatively.

*Step 4:* Evaluating the damage coefficient

Take out the stiffness matrix of the damage element after positioning, establish the balance equation on the node position one by one according to the damage element code, and complete the damage identification by evaluating the damage coefficient of the balance equation.

To conclude this section, the process of the proposed vibration measurements using only first-order modal information mainly involves two key influence factors: precise of first mode information and sparse of element stiffness matrix. More details are explained in the following numerical examples.

## 3. Numerical Examples

*3.1. Simply Supported Beam.* A 12-element simply supported beam used in this example shown in Figure 1 is employed to exercise the proposed method. The basic parameters of the beam are as follows: Young's modulus $E = 200$ GPa, density $\rho = 7.8 \times 10^3$ kg/m$^3$, length of each element $L = 0.1$ m, and cross-sectional area $A = 2.5 \times 10^{-3}$ m$^2$. The finite-element model of the structure has 26 degrees of freedom.

Let the beam element stiffness matrix in local coordination can be represented as

$$\mathbf{K_e} = \frac{EI}{L^3}\begin{bmatrix} 12 & 6L & -12 & 6L \\ 6L & 4L^2 & -6L & 2L^2 \\ -12 & -6L & 12 & -6L \\ 6L & 2L^2 & -6L & 4L^2 \end{bmatrix}. \tag{6}$$

The corresponding element mass matrix is

$$\mathbf{M_e} = \frac{\rho A}{420}\begin{bmatrix} 156L & 22L^2 & 54L & -13L \\ 22L^2 & 4L^3 & 13L^2 & -3L^3 \\ 54L & 13L^2 & 156L & -22L^2 \\ -13L & -3L^3 & -22L^2 & 4L^3 \end{bmatrix}. \tag{7}$$

The local coordinate of each element is consistent with the global coordination; hence, the coordination transformation is unnecessary; the element stiffness matrix represented by all element node displacements in the global coordinate system is derived directly as equation (1). The deformation vector of each node in the overall coordinate system is set as

$$\mathbf{V} = [\, v_1 \;\; \theta_1 \;\; v_2 \;\; \theta_2 \;\; \ldots \;\; v_{12} \;\; \theta_{12} \;\; v_{13} \;\; \theta_{13} \,]^{\mathrm{T}}. \tag{8}$$

Take element 3, for example, the deformation vector corresponding to $K_3^e$ can be expressed as

$$\mathbf{V_{3e}} = [\, v_3 \;\; \theta_3 \;\; v_4 \;\; \theta_4 \,]^{\mathrm{T}}. \tag{9}$$

According to the relationship of the deformation vector between local and global coordination, the element matrix under global coordination system is given by

$$\mathbf{V_{3e}} = \mathbf{SV}, \tag{10}$$

where the connective matrix $\mathbf{S}$ is $4 \times 26$, the element in row 1 and column 5 of $\mathbf{S}$ is 1; the element in row 2 and column 6 of $\mathbf{S}$ is 1; the element in row 3 and column 7 of $\mathbf{S}$ is 1; the element in row 4 and column 8 of $\mathbf{S}$ is 1; and the rest of the elements of $\mathbf{S}$ is 0. The connective matrix $\mathbf{S}$ can be expressed as

$$\mathbf{S} = \begin{bmatrix} 0 & \ldots & 0 & 1 & 0 & 0 & 0 & 0 & \ldots & 0 \\ 0 & \ldots & 0 & 0 & 1 & 0 & 0 & 0 & \ldots & 0 \\ 0 & \ldots & 0 & 0 & 0 & 1 & 0 & 0 & \ldots & 0 \\ 0 & \ldots & 0 & 0 & 0 & 0 & 1 & 0 & \ldots & 0 \end{bmatrix}_{4\times 26}. \tag{11}$$

The elastic strain energy of element 3 can be derived based on the energy theorem as

$$\mathbf{U}_3 = \mathbf{V_{3e}^T K_3^e V_{3e}}. \tag{12}$$

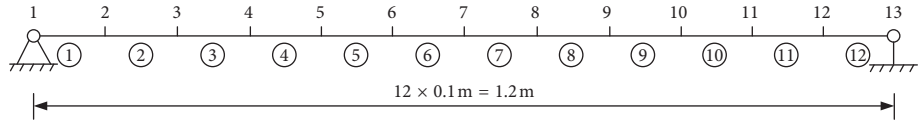


Figure 1: The finite element model of simply supported beam.

Substitute equation (10) into equation (12), we can get

$$\begin{aligned} \mathbf{U}_3 &= \mathbf{V}^{\mathbf{T}}\mathbf{S}_3^{\mathbf{T}}\mathbf{K}_3^{\mathbf{e}}\mathbf{S}_3, \\ \mathbf{V} &= \mathbf{V}^{\mathbf{T}}\mathbf{K}_3^{\mathbf{g}}\mathbf{V}. \end{aligned} \tag{13}$$

Hence, the element stiffness matrix of element 3 under the global coordination can be expressed as

$$K_3^g = S_3^T K_3^e S_3. \tag{14}$$

The element stiffness matrix under the global coordination could be derived similarly; then the whole stiffness matrix of the beam is obtained as

$$\mathbf{K} = \sum_{i=1}^{12} (1 - \alpha_i)\mathbf{K}_\mathbf{i}^\mathbf{g}, \tag{15}$$

where $\alpha_i (0 \le \alpha_i < 1)$ is taken as an unknown variable expressed as a damage coefficient of the corresponding element $i$, and for undamaged theoretical model, these damage coefficients are all zeros.

With the same procedure, the whole mass matrix $\mathbf{M}$ could be derived; then the modal equilibrium equation of the undamaged structural system shown in equation (1) is obtained, and the damage identification of the structure will be studied with this equation. Obviously, for single element in the global system, its element stiffness matrix is sparse, which provides important clues for damage identification.

For the damaged beam, preset the damage coefficient artificially as $\alpha_2 = 0.15$, $\alpha_4 = 0.6$, $\alpha_8 = 0.13$, and $\alpha_{10} = 0.3$, and the rest elements are intact. Figure 2 shows the measured first eigenvector $\phi_{1d}$ of the damaged system, with which the corresponding eigen value $\lambda_{1d} = 1033.5$.

Then the first-order eigen value $\lambda_{1d}$ and eigenvector $\boldsymbol{\phi}_{\mathbf{1d}}$ of the damaged beam are substituted into equation (4) to obtain the residual mode vector. Figure 3 shows the distribution diagram of residual mode vector obtained from equation (4). The vector is numbered according to the degrees of freedom (abscissa) of the element. Since each element is statically self-balanced according to mode shape, the residual mode vector corresponding to each element is symmetric about the $x$-axis; hence the sum is 0.

The first purpose in this analysis is to determine the location of the damage. Arrange the absolute value of the obtained residual mode vector from large to small in accordance with Step 2. It should be noted that for the absolute value of residual mode vector from large to small, the number of the corresponding abscissa in Figure 3 of each ordered element of residual mode vector must be marked first before the sorting, which is important for the subsequent damage detection work. Then, according to Step 3, obtain the location map of damage element as shown in Figure 4. The abscissa is the number of degrees of freedom of

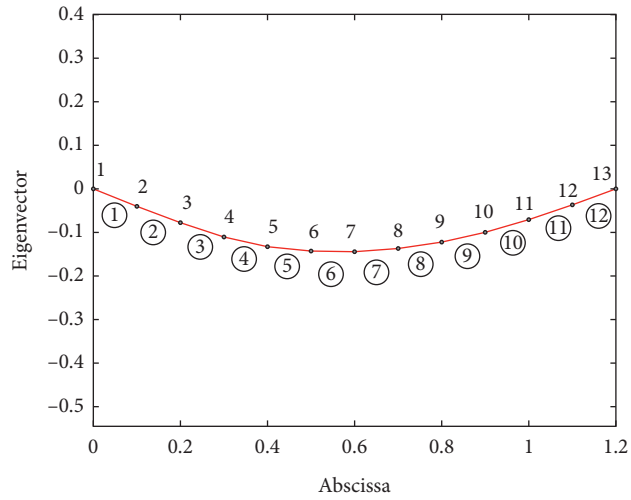


Figure 2: The measured first modal eigenvector.

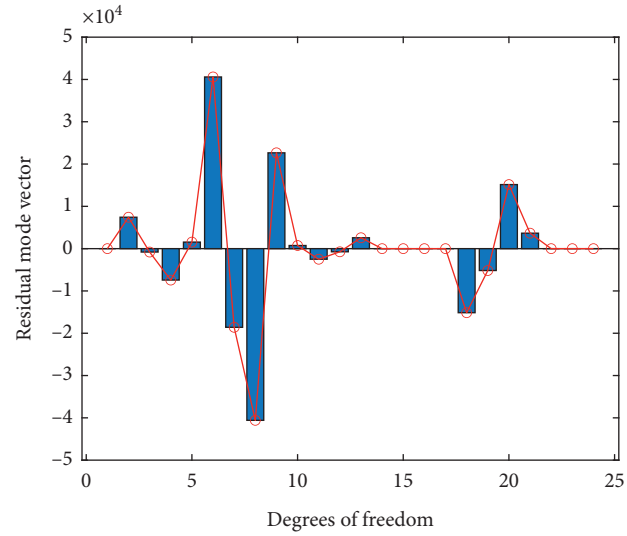


Figure 3: The distribution diagram of residual mode vector.

the unit, the ordinate is the ratio, the peak position in the figure is 16, and each unit corresponds to four degrees of freedom. Therefore, it is clear that four damaged elements are present in the simply supported beam, which is consistent with the presetting.

The next step of this analysis is to verify the location of the structural damage. Referring to Step 4, the residual mode vector of the corresponding elements is arranged in Table 1 according to the node code of each element, and the first variable of each element is divided by the third variable. The element whose quotient equals minus is the damage

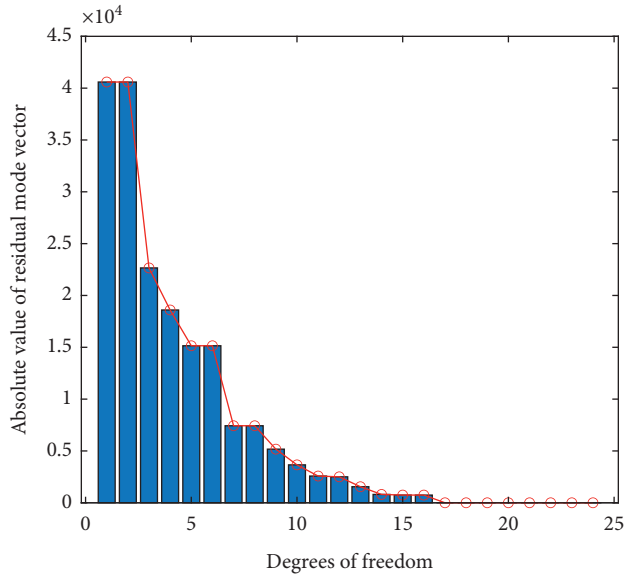


Figure 4: The location map of the damage element.

component, so as to verify the results of damage element location in the third step. Obviously, the results of damage location are consistent with the presetting, which verifies the results of Step 3 again.

The last step of this analysis is to determine the extent of structural damage with the damage location according to Step 4. Take out the stiffness matrix of the element after damage location, and calculate $\mathbf{K_m}\phi_{1d}$ in the left-hand side of equation (4), respectively, as shown in Figure 5. At the same time, take out the residual mode vector of the damage element located in Table 1, and express it in Figure 5. By comparison, for the given damage element, the elements in $D_m$ are proportional to the product vector of the element stiffness matrix $\mathbf{K_m}$ and the first-mode shape $\phi_{1d}$, and the ratio is the damage degree $\alpha_m$.

As the located elements, 2, 4, 6, and 10 are discontinuous members in this study, and the following formula can be used to solve the damage coefficient:

$$\boldsymbol{\alpha}_{\mathbf{m}}\mathbf{K_m}\phi_{1d} = \mathbf{D_m}. \tag{16}$$

Finally, the damage parameters obtained are listed in Table 2. From the table, it can be easily seen that the results calculated by this method are accurate solutions with Equation (16) which reflects the advantage of the proposed algorithm.

The results in this section indicate that only the first mode of the structure needs to be provided by the algorithm proposed in this paper. Compared with the commonly used identification methods, the experimental requirements were not strict. Therefore, the proposed method has obvious advantages for structural damage identification. This paper will continue to use an example of a frame structure to further verify the results.

*3.2. Two-Story Frame Structure.* The second example is a two-story frame structure as shown in Figure 6. This frame was modeled with 24 equal elements of 0.2 m in length. Every node has 3 DOFs, an axial displacement, a transverse displacement, and a rotation. The properties of this structure are as follows: cross-sectional area $A = 0.0336\,\mathrm{m}^2$; moment of inertia $I = 1.6128 \times 10^{-4}\,\mathrm{m}^4$; Young's modulus $E = 200\,\mathrm{GPa}$; and density $\rho = 2500\,\mathrm{kg/m}^3$.

The stiffness matrix of frame element considering axial deformation can be expressed as

$$\mathbf{K_{ef}} = \frac{EA}{L}\begin{bmatrix} 1 & 0 & 0 & -1 & 0 & 0 \\ 0 & 0 & 0 & 0 & 0 & 0 \\ 0 & 0 & 0 & 0 & 0 & 0 \\ -1 & 0 & 0 & 1 & 0 & 0 \\ 0 & 0 & 0 & 0 & 0 & 0 \\ 0 & 0 & 0 & 0 & 0 & 0 \end{bmatrix} + \frac{EI}{L^3}\begin{bmatrix} 0 & 0 & 0 & 0 & 0 & 0 \\ 0 & 12 & 6L & 0 & -12 & 6L \\ 0 & 6L & 4L^2 & 0 & -6L & 2L^2 \\ 0 & 0 & 0 & 1 & 0 & 0 \\ 0 & -12 & -6L & 0 & 12 & -6L \\ 0 & 6L & 2L^2 & 0 & -6L & 4L^2 \end{bmatrix}. \tag{17}$$

The corresponding element mass matrix is

$$\mathbf{M_{ef}} = \frac{\rho AL}{6}\begin{bmatrix} 2 & 0 & 0 & 1 & 0 & 0 \\ 0 & 0 & 0 & 0 & 0 & 0 \\ 0 & 0 & 0 & 0 & 0 & 0 \\ 1 & 0 & 0 & 2 & 0 & 0 \\ 0 & 0 & 0 & 0 & 0 & 0 \\ 0 & 0 & 0 & 0 & 0 & 0 \end{bmatrix} + \frac{\rho AL}{420}\begin{bmatrix} 0 & 0 & 0 & 0 & 0 & 0 \\ 0 & 156 & 22L & 0 & 54 & -13L \\ 0 & 22L & 4 & 0 & 13L & -3L^2 \\ 1 & 0 & 0 & 0 & 0 & 0 \\ 0 & 54 & 13L & 0 & 156 & -22L \\ 0 & -13L & -3L^2 & 0 & -22L & 4L^2 \end{bmatrix}. \tag{18}$$

Table 1: Residual mode vector according to elements.

| Element no. | 1 | 2 | 3 | 4 | 5 | 6 | 7 | 8 | 9 | 10 | 11 | 12 |
|---|---|---|---|---|---|---|---|---|---|---|---|---|
| Residual | 0 | 7431.3 | −7431.3 | 40591.4 | −40591.4 | 743.4 | −743.4 | 0 | 0.0 | −15147.5 | 15147.5 | 0 |
| Force | 0 | −805.2 | 1548.4 | −18598.0 | 22657.1 | −2504.3 | 2578.6 | 0 | 0.0 | −5172.5 | 3657.8 | 0 |
| Vector | 7431.3 | −7431.3 | 40591.4 | −40591.4 | 743.4 | −743.4 | 0.0 | 0 | −15147.5 | 15147.5 | 0.0 | 0 |
| Residual mode vector | −805.2 | 1548.4 | −18598.0 | 22657.1 | −2504.3 | 2578.6 | 0.0 | 0 | −5172.5 | 3657.8 | 0.0 | 0 |

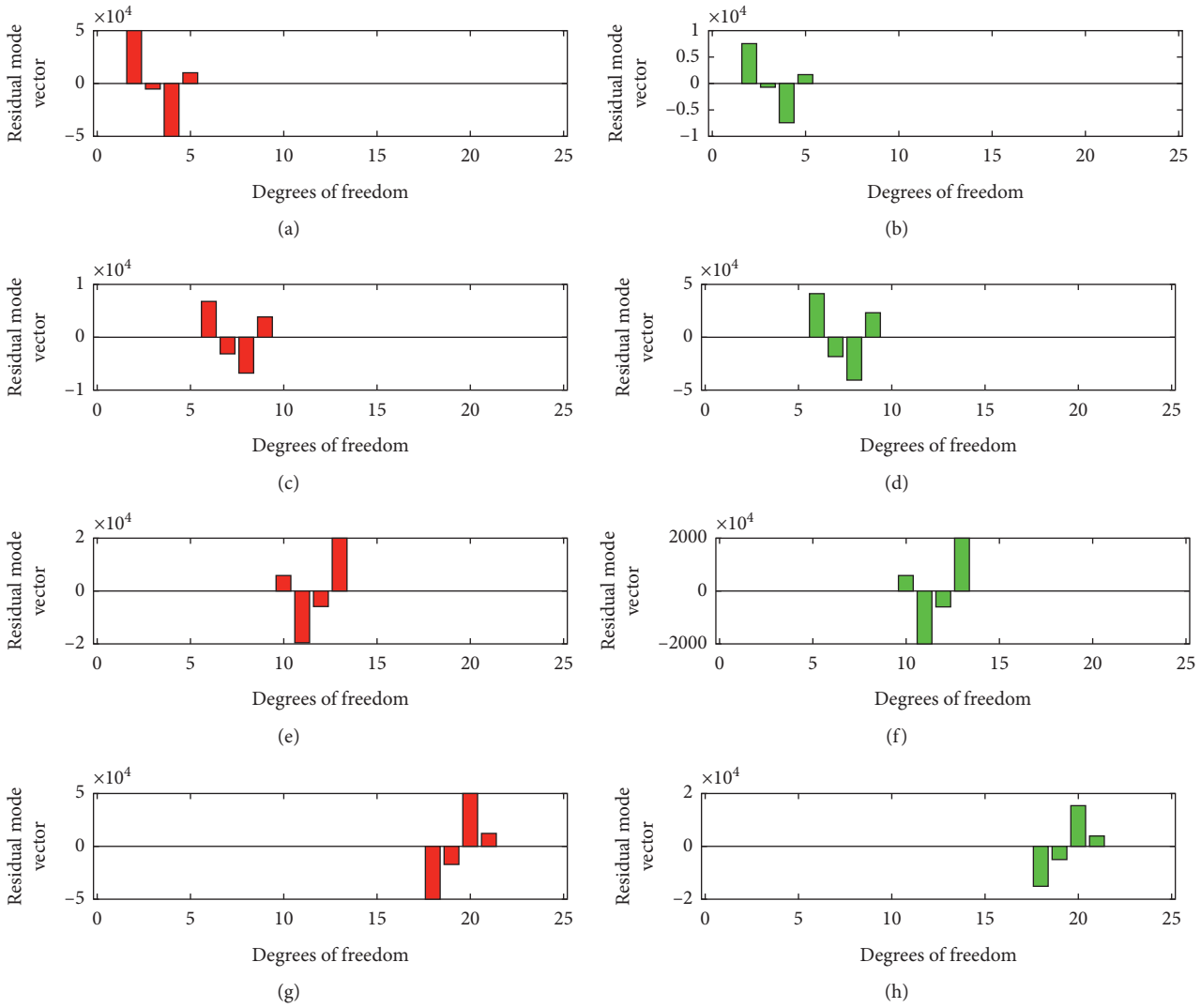


Figure 5: Residual mode vector according to damage location.

Table 2: The evaluated damage parameters.

| Element no 2 | | | Element no 4 | | | Element no 6 | | | Element no 10 | | |
|---|---|---|---|---|---|---|---|---|---|---|---|
| $\mathbf{K}_2\phi_{1\mathbf{d}}$ | $\mathbf{D}_2$ | $\alpha_2$ | $\mathbf{K}_4\phi_{1\mathbf{d}}$ | $\mathbf{D}_4$ | $\alpha_4$ | $\mathbf{K}_6\phi_{1\mathbf{d}}$ | $\mathbf{D}_6$ | $\alpha_6$ | $\mathbf{K}_{10}\phi_{1\mathbf{d}}$ | $\mathbf{D}_{10}$ | $\alpha_{10}$ |
| 7431.2 | 49541.8 | 0.15 | 40591.3 | 67652.2 | 0.6 | 743.3 | 5718.2 | 0.13 | −15147.5 | −50491.6 | 0.3 |
| −805.2 | −5368.2 | 0.15 | −18598 | −30996.6 | 0.6 | −2504.2 | −19263.6 | 0.13 | −5172.5 | −17241.8 | 0.3 |
| −7431.2 | −49541.9 | 0.15 | −40591.4 | −67652.3 | 0.6 | −743.3 | −5718.2 | 0.13 | 15147.4 | 50491.6 | 0.3 |
| 1548.3 | 10322.4 | 0.15 | 22657.1 | 37761.8 | 0.6 | 2578.6 | 19835.4 | 0.13 | 3657.7 | 12192.6 | 0.3 |

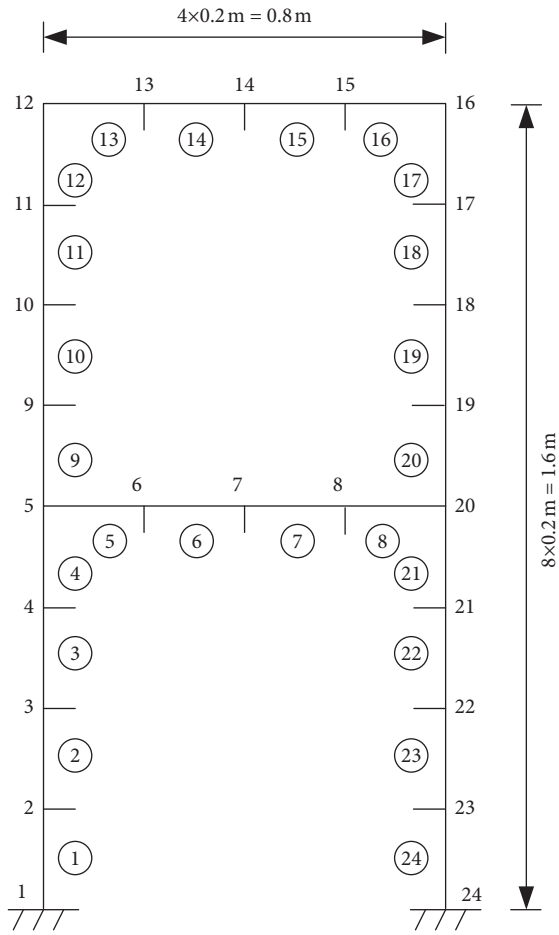


Figure 6: Two-story frame structure.

Taking element 3 as an example, suppose the element stiffness matrix in the local coordinate system is $\mathbf{K}_{3ef}$, and the displacement vector in the local coordinate system can be expressed as

$$\mathbf{V}_{3ef} = [\ u_{3a}\ \ v_{3a}\ \ \theta_{3a}\ \ u_{4b}\ \ v_{4b}\ \ \theta_{4b}\ ]^{T}. \tag{19}$$

According to the energy theorem, the elastic strain energy of the third element is known to be

$$\mathbf{U}_{3ef} = \mathbf{V}_{3ef}^{T}\mathbf{K}_{3ef}\mathbf{V}_{3ef}. \tag{20}$$

The relationship between the deformation of element component 3 in the local coordination and the global coordination needs to transform in the numerical model as the local coordinate of each element is inconsistent with the global coordination, which is different from the simply supported beam example.

The displacement vector in the global coordinate system can be expressed as

$$\mathbf{V}_{3g} = [\ u_3\ \ v_3\ \ \theta_3\ \ u_4\ \ v_4\ \ \theta_4\ ]^{T}. \tag{21}$$

Then the mapping relationship between local coordinates and global coordinates can be found as [30]

$$\mathbf{V}_{3g} = \mathbf{P}\mathbf{V}_{3ef}, \tag{22}$$

where the matrix $P$ representing the mapping relationship is a $6\times6$ matrix as

$$\mathrm{P}_3 = \begin{bmatrix} \cos(\alpha_3) & -\sin) & 0 & 0 & 0 & 0 \\ \sin(\alpha_3) & \cos(\alpha_3) & 0 & 0 & 0 & 0 \\ 0 & 0 & 1 & 0 & 0 & 0 \\ 0 & 0 & 0 & \cos(\alpha_3) & -\sin(\alpha_3) & 0 \\ 0 & 0 & 0 & \sin(\alpha_3) & \cos(\alpha_3) & 0 \\ 0 & 0 & 0 & 0 & 0 & 1 \end{bmatrix}, \tag{23}$$

where $a_3$ is the rotation angle of element 3 in the frame, and obviously the angle is $\pi/2$. By substituting equation (22) into equation (20), the following equations can be obtained by energy theorem as

$$\mathbf{U}_{3ef} = \mathbf{V}_{3g}^{T}\left(\mathbf{P}_3^{-1}\right)^{T}\mathbf{K}_{3ef}\mathbf{P}_3^{-1}\mathbf{V}_{3g}. \tag{24}$$

Thus, the stiffness matrix of element 3 under the global coordination can be derived as

$$\mathbf{K}_{3eg} = \left(\mathbf{P}_3^{-1}\right)^{T}\mathbf{K}_{3ef}\mathbf{P}_3^{-1}. \tag{25}$$

Furthermore, the stiffness matrix of element 3 represented by the overall displacement vector of the frame structure in the global coordination is derived directly. The deformation vector of each node in the global coordination is set as

$$\mathbf{V}_f = [\ u_1\ \ v_1\ \ \theta_1\ \ \ldots\ u_{24}\ \ v_{24}\ \ \theta_{24}\ ]^{T}. \tag{26}$$

As the simple supported beam model in example 1, the connective relationship between the element displacement vector and the overall displacement vector is given by

$$\mathbf{V}_{3g} = \mathbf{S}\mathbf{V}_f, \tag{27}$$

where the connective matrix $\mathbf{S}$ is $6\times72$. According to the corresponding relationship of $\mathbf{V}_f$ and $\mathbf{V}_{3g}$, the connective matrix $\mathbf{S}_3$ can be expressed as

$$\mathbf{S}_3 = \begin{bmatrix} 0\ \ldots\ 0 & 1 & 0 & 0 & 0 & 0 & 0 & 0\ \ldots\ 0 \\ 0\ \ldots\ 0 & 0 & 1 & 0 & 0 & 0 & 0 & 0\ \ldots\ 0 \\ 0\ \ldots\ 0 & 0 & 0 & 1 & 0 & 0 & 0 & 0\ \ldots\ 0 \\ 0\ \ldots\ 0 & 0 & 0 & 0 & 1 & 0 & 0 & 0\ \ldots\ 0 \\ 0\ \ldots\ 0 & 0 & 0 & 0 & 0 & 1 & 0 & 0\ \ldots\ 0 \\ 0\ \ldots\ 0 & 0 & 0 & 0 & 0 & 0 & 1 & 0\ \ldots\ 0 \end{bmatrix}, \tag{28}$$

where the element in row 1 and column 7 of $\mathbf{S_3}$ is 1; the element in row 2 and column 8 of $\mathbf{S_3}$ is 1; the element in row 3 and column 9 of $\mathbf{S_3}$ is 1; the element in row 4 and column 10 of $\mathbf{S_3}$ is 1; the element in row 5 and column 11 of $\mathbf{S_3}$ is 1; the element in row 6 and column 12 of $\mathbf{S_3}$ is 1; and rest of the elements of $\mathbf{S}$ is zero. Substitute equation (27) into equation (24), the strain energy can be deduced as

$$\begin{aligned} \mathbf{U}_{3e} &= \mathbf{V}^{T}\mathbf{S}_3^{T}\mathbf{K}_{3eg}, \\ \mathbf{S}_3\mathbf{V} &= \mathbf{V}^{T}\mathbf{K}_3^{g}\mathbf{V}. \end{aligned} \tag{29}$$

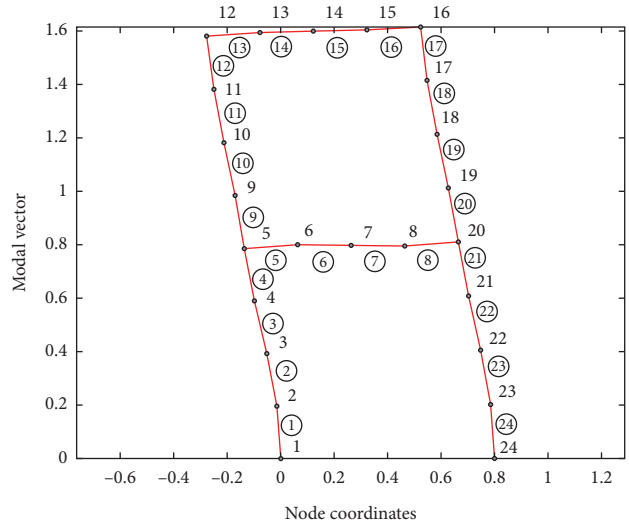


Figure 7: The measured first eigenvector of the frame structure.

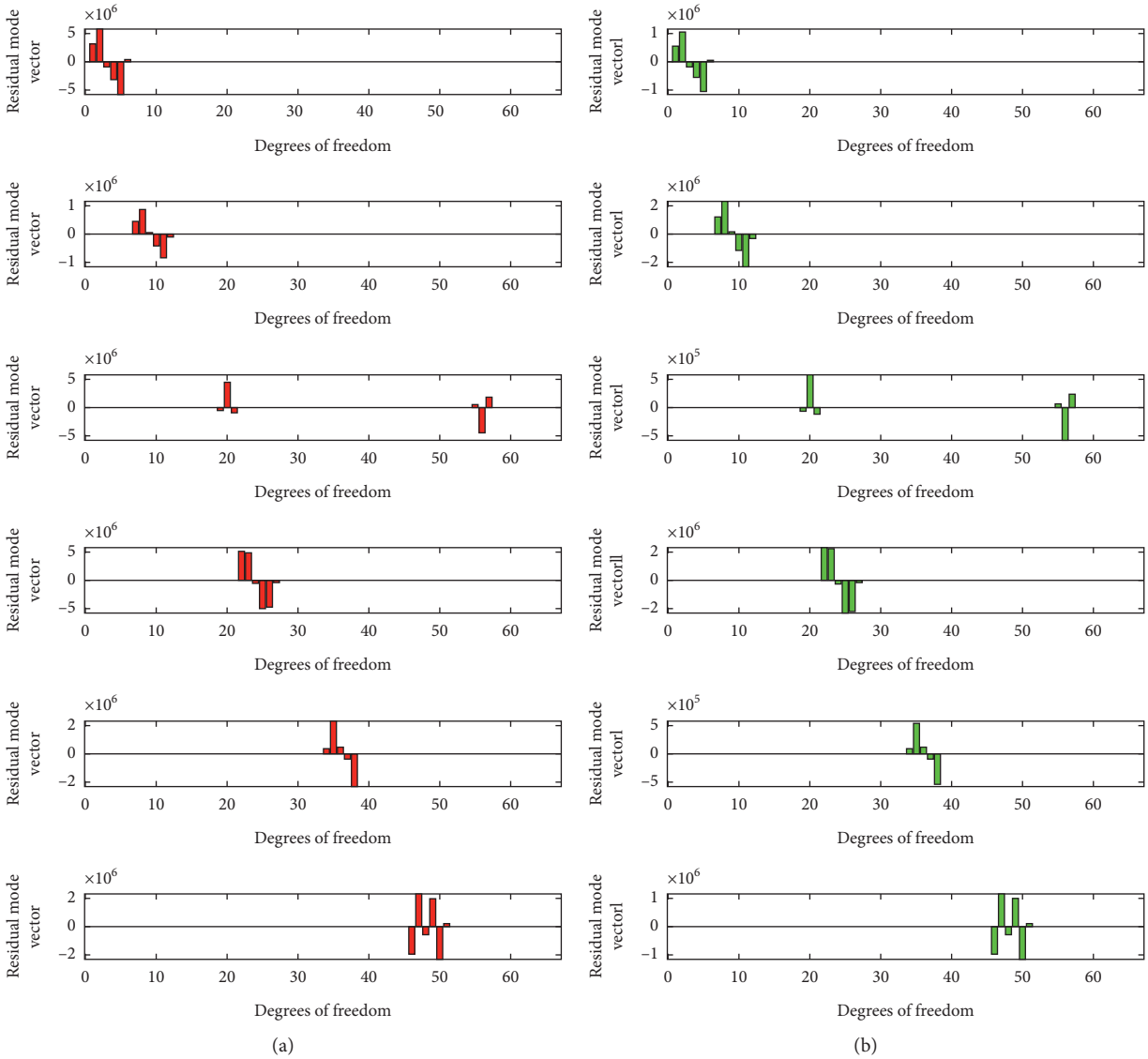


Figure 8: Component schematic diagram: (a) the amount of $K_m\phi_{1\,d}$. (b) The residual mode vector of the damage element.

Table. 3: The evaluated damage parameters.

| Element no 2 | | Element no 4 | | Element no 8 | | Element no 10 | | Element no 14 | | Element no 18 | |
|---|---|---|---|---|---|---|---|---|---|---|---|
| $K_2\phi_{1\,d}$ | $D_2$ | $K_4\phi_{1\,d}$ | $D_4$ | $K_8\phi_{1\,d}$ | $D_8$ | $K_{10}\phi_{1\,d}$ | $D_{10}$ | $K_{14}\phi_{1\,d}$ | $D_{14}$ | $K_{18}\phi_{1\,d}$ | $D_{18}$ |
| 3211025 | 481653.7 | 3581720 | 1074516 | −440108 | −57214 | 4332774 | 2599664 | 321187.5 | 73873.12 | −2235587 | −894235 |
| 5930163 | 889524.4 | 7166890 | 2150067 | 3836174 | 498702.6 | 4061953 | 2437172 | 2002432 | 460559.4 | 2652865 | 1061146 |
| −993756 | −149063 | 330389.7 | 99116.92 | −765979 | −99577.2 | −524497 | −314698 | 419546.6 | 96495.72 | −681415 | −272566 |
| −3211025 | −481654 | −3581720 | −1074516 | 440108 | 57214.04 | −4332774 | −2599664 | −321187 | −73873.1 | 2235587 | 894234.8 |
| −5930163 | −889524 | −7166890 | −2150067 | −3836174 | −498703 | −4061953 | −2437172 | −2002432 | −460559 | −2652865 | −1061146 |
| 351551.4 | 52732.71 | −1046734 | −314020 | 1533214 | 199317.8 | −342058 | −205235 | −19060.2 | −4383.84 | 234297.8 | 93719.13 |
| $\alpha_2 = 0.15$ | | $\alpha_4 = 0.3$ | | $\alpha_8 = 0.13$ | | $\alpha_{10} = 0.6$ | | $\alpha_{14} = 0.23$ | | $\alpha_{18} = 0.4$ | |

Substitute equation (25) into equation (29), then the stiffness matrix of element 3 under the global coordination can be expressed by the overall displacement vector as

$$\mathbf{K}_3^{\mathbf{g}} = \mathbf{S}_3^{\mathbf{T}}\left(\mathbf{P}_3^{-1}\right)^{\mathbf{T}}\mathbf{K}_{3\mathbf{ef}}\mathbf{P}_3^{-1}\mathbf{S}_3. \tag{30}$$

The element stiffness matrix of the rest elements in global coordination can be obtained by the same procedure. Obviously, for each single element component, the stiffness matrix is a sparse matrix, and its sparse property is the key foundation of the proposed damage identification method.

As the next step is establishing the whole stiffness matrix of the structure system in global matrix, the element stiffness matrix under the global coordination could be derived similarly, and the whole stiffness matrix of the frame structure can be expressed as

$$\mathbf{K} = \sum_{i=1}^{24}(1-\alpha_i)\mathbf{K}_{\mathbf{i}}^{\mathbf{g}}, \tag{31}$$

where $\alpha_i\,(0 \le \alpha_i < 1)$ is taken as an unknown variable expressed as the damage coefficient corresponding to element $i$, and for undamaged theoretical model these damage coefficients are all zeros. With the same procedure, the whole mass matrix $\mathbf{M}$ could be derived by the element mass matrix in equation (18), then the modal equilibrium equation of undamaged structural system shown in formula (1) is obtained, and the damage identification of the structure could be studied based on it. The stiffness of the single element in the global system is spare, whose nodal points are coupled. Thus, it would provide important clues for damage identification obviously.

For the damaged frame structure, we could preset the damage coefficients artificially as $\alpha_2 = 0.15$, $\alpha_4 = 0.3$, $\alpha_8 = 0.13$, $\alpha_{10} = 0.6$, $\alpha_{14} = 0.23$, and $\alpha_{18} = 0.4$, and the rest elements are intact. Figure 7 shows the measured first eigenvector $\boldsymbol{\phi}_{\mathbf{1d}}$ of the damaged system, with which the corresponding eigen value $\lambda_{1d} = 58814.7$. The same operation could be operated for damage identification of frame structures, which takes an example of the previous proposed beam.

The first-order eigen value $\lambda_{1\mathrm{d}}$ and eigenvector $\phi_{\mathbf{1d}}$ of the damaged beam are substituted into equation (4) to obtain the residual mode vector. Take out the stiffness matrix of the element after damage location, and calculate the amount of $\mathbf{K_m}\phi_{\mathbf{1d}}$ in the left-hand side of equation (4), respectively, as shown in Figure 8(a) and take out the residual mode vector of the damage element and express it in Figure 8(b). By comparison, for the given damage element, the element value in residual mode vector is proportional to the product vector of the element stiffness matrix $\mathbf{K_m}$ and the first mode shape $\phi_{\mathbf{1d}}$, and the ratio is the damage degree $\alpha_m$.

The damage coefficients can be evaluated by equation (16). Table 3 shows the amount of $\mathbf{K_m}\phi_{\mathbf{1d}}$ in the left-hand side of equation (16), and the residual mode vector corresponding to the located damage members of the frame structure. From the table, it can be seen that the results calculated by this method are accurately the same as those preset, which further proves the reliability of this proposed method.

According to the solution results of the two numerical examples, only the first-order mode of the structure needs to be measured by the method developed in this paper. Compared with the commonly used identification method, the experimental requirements are not strict, and the measured results are accurate solutions, so the solution results are better than the approximate methods such as sensitivity method, which is worth popularizing. Therefore this research develops a new strategy of structural damage identification based on first-order mode and opens up a new way for structural damage identification based on the dynamic test.

## 4. Conclusions

This study presents an accurate algorithm for structural damage identification and location based on the measured first-order modal information of structure according to the sparse characteristics of the element stiffness matrix. The only location results required in determining the damage in the first-order modal equilibrium equation is the common residual mode vector whose nonzero elements are corresponding to the damaged member in the structure system. Finally based on the location results, the mechanical balance equation of the residual deformation of the located element is formulated for determining the damage extent. The proposed method has the advantages of low calculation resource requirement, fast positioning speed, and high recognition accuracy. As the higher order modal information could not be acquired sufficiently with the current technology, the process of computing the extent of structural damage using the proposed algorithm is shown to be computationally attractive and hence suitable for large-scale problems.

## Data Availability

The data used to support the findings of this study are available from the corresponding author upon request.

## Conflicts of Interest

The authors declare that they have no conflicts of interest.

## References


[1] S. W. Doebling, C. R. Farrar, and M. B. Prime, "A summary review of vibration-based damage identification methods," *The Shock and Vibration Digest*, vol. 30, no. 2, pp. 91–105, 1998.

[2] W. Wei Fan and P. Z. Pizhong Qiao, "Vibration-based damage identification methods: a review and comparative study," *Structural Health Monitoring*, vol. 10, no. 1, pp. 83–111, 2011.

[3] A. D. Dimarogonas, "Vibration of cracked structures: a state of the art review," *Engineering Fracture Mechanics*, vol. 55, no. 5, pp. 831–857, 1996.

[4] A. Mehrisadat Makki, G. Linlin, K. Kamyar, Z. Yincai, H. Bruce, and D. Zheyuan, "Non-contact structural health monitoring of a cable-stayed bridge: case study," *Structure and Infrastructure Engineering*, vol. 15, pp. 1119–1136, 2019.

[5] Z. Li, M. Q. Feng, L. Luo, D. Feng, and X. Xu, "Statistical analysis of modal parameters of a suspension bridge based on Bayesian spectral density approach and SHM data," *Mechanical Systems and Signal Processing*, vol. 98, pp. 352–367, 2018.

[6] D. Ribeiro, R. Calçada, R. Delgado, M. Brehm, and V. Zabel, "Finite element model updating of a bowstring-arch railway bridge based on experimental modal parameters," *Engineering Structures*, vol. 40, pp. 413–435, 2012.

[7] W. Di and S. S. Law, "Eigen-parameter decomposition of element matrices for structural damage detection," *Engineering Structures*, vol. 29, no. 4, pp. 519–528, 2007.

[8] Y. B. Yang, B. Zhang, Y. Qian, and Y. Wu, "Contact-point response for modal identification of bridges by a moving test vehicle," *International Journal of Structural Stability and Dynamics*, vol. 18, no. 5, Article ID 1850073, 2018.

[9] Y. Oshima, K. Yamamoto, and K. Sugiura, "Damage assessment of a bridge based on mode shapes estimated by responses of passing vehicles," *Smart Structures and Systems*, vol. 13, no. 5, pp. 731–753, 2014.

[10] Y. Zhang, S. T. Lie, and Z. Xiang, "Damage detection method based on operating deflection shape curvature extracted from dynamic response of a passing vehicle," *Mechanical Systems and Signal Processing*, vol. 35, no. 1-2, pp. 238–254, 2013.

[11] A. Malekjafarian and E. J. Obrien, "Identification of bridge mode shapes using short time frequency domain decomposition of the responses measured in a passing vehicle," *Engineering Structures*, vol. 81, pp. 386–397, 2014.

[12] M. Frizzarin, M. Q. Feng, P. Franchetti, S. Soyoz, and C. Modena, "Damage detection based on damping analysis of ambient vibration data," *Structural Control and Health Monitoring*, vol. 17, pp. 368–385, 2010.

[13] M. Brehm, V. Zabel, and C. Bucher, "An automatic mode pairing strategy using an enhanced modal assurance criterion based on modal strain energies," *Journal of Sound and Vibration*, vol. 329, no. 25, pp. 5375–5392, 2010.

[14] M. Kaouk and D. C. Zimmerman, "Structural damage assessment using a generalized minimum rank perturbation theory," *AIAA Journal*, vol. 32, no. 4, pp. 836–842, 1994.

[15] D. C. Zimmerman and M. Kaouk, "Structural damage detection using a minimum rank update theory," *Journal of Vibration and Acoustics*, vol. 116, no. 2, pp. 222–231, 1994.

[16] S. W. Doebling, "Minimum-rank optimal update of elemental stiffness parameters for structural damage identification," *AIAA Journal*, vol. 34, no. 12, pp. 2615–2621, 1996.

[17] Q. Yang, C. Wang, N. Li, S. Luo, and W. Wang, "Model-free method for damage localization of grid structure," *Applied Sciences*, vol. 9, no. 16, p. 3252, 2019.

[18] B. Zhang, Y. Qian, Y. Wu, and Y. B. Yang, "An effective means for damage detection of bridges using the contact-point response of a moving test vehicle," *Journal of Sound and Vibration*, vol. 419, pp. 158–172, 2018.

[19] J. Høgsberg and S. Krenk, "Calibration of piezoelectric RL shunts with explicit residual mode correction," *Journal of Sound and Vibration*, vol. 386, pp. 65–81, 2017.

[20] W. Zhang, J. Li, H. Hao, and H. Ma, "Damage detection in bridge structures under moving loads with phase trajectory change of multi-type vibration measurements," *Mechanical Systems and Signal Processing*, vol. 87, pp. 410–425, 2017.

[21] W. Zuo, J. Bai, and J. Yu, "Sensitivity reanalysis of static displacement using taylor series expansion and combined approximate method," *Structural and Multidisciplinary Optimization*, vol. 53, no. 5, pp. 953–959, 2016.

[22] J. Guo, J. Jiao, K. Fujita, and I. Takewaki, "Damage identification for frame structures using vision-based measurement," *Engineering Structures*, vol. 199, Article ID 109634, 2019.

[23] Y. B. Yang, Y. C. Li, and K. C. Chang, "Constructing the mode shapes of a bridge from a passing vehicle: a theoretical study," *Smart Structures and Systems*, vol. 13, no. 5, pp. 797–819, 2014.

[24] D. Feng, M. Feng, E. Ozer, and Y. Fukuda, "A vision-based sensor for noncontact structural displacement measurement," *Sensors*, vol. 15, no. 7, pp. 16557–16575, 2015.

[25] E. J. OBrien and A. Malekjafarian, "A mode shape-based damage detection approach using laser measurement from a vehicle crossing a simply supported bridge," *Structural Control and Health Monitoring*, vol. 23, no. 10, pp. 1273–1286, 2016.

[26] W. Zhang, Z. Wang, and H. Ma, "Crack identification in stepped cantilever beam combining wavelet analysis with transform matrix," *Acta Mechanica Solida Sinica*, vol. 22, no. 4, pp. 360–368, 2009.

[27] D. G. Kasper, D. C. Swanson, and K. M. Reichard, "Higher-frequency wavenumber shift and frequency shift in a cracked, vibrating beam," *Journal of Sound and Vibration*, vol. 312, no. 1-2, pp. 1–18, 2008.

[28] E. Douka, S. Loutridis, and A. Trochidis, "Crack identification in beams using wavelet analysis," *International Journal of Solids and Structures*, vol. 40, no. 13-14, pp. 3557–3569, 2003.

[29] Y. Narkis, "Identification of crack location in vibrating simply supported beams," *Journal of Sound and Vibration*, vol. 172, no. 4, pp. 549–558, 1994.

[30] R. D. Cook, D. S. Malkus, M. E. Plesha, and R. J. Witt, *Concepts and Applications of Finite Element Analysis*, John Wiley & Sons, New York, NY, USA, 4th ed edition, 2002.

Hindawi
Advances in Materials Science and Engineering
Volume 2021, Article ID 5567873, 18 pages
https://doi.org/10.1155/2021/5567873

*Research Article*

# Durability Evaluation of Concrete with Multiadmixtures under Salt Freeze-Thaw Cycles Based on Surface Resistivity

**Shibin Luo**,[1,2] **Wei Liang**,[3] **Hua Wang**,[4,5] **Wensheng Wang**,[1,6] **and Rongjun Zou**[7]

[1]*College of Transportation, Jilin University, Changchun 130025, China*
[2]*Guangxi Hechi Highway Development Center, Hechi 537000, China*
[3]*Guangxi Communications Investment Logistics Development Co., Ltd., Nanning 530029, China*
[4]*Guangxi Beibu Gulf Investment Group Co., Ltd., Nanning 530029, China*
[5]*Guangxi Transportation Science and Technology Group Co., Ltd., Nanning 530007, China*
[6]*College of Construction Engineering, Jilin University, Changchun 130025, China*
[7]*Guangxi Yanglu Expressway Co., Ltd., Nanning 530007, China*

Correspondence should be addressed to Hua Wang; wanghua15@mails.jlu.edu.cn and Wensheng Wang; wangws@jlu.edu.cn

Received 5 February 2021; Accepted 27 May 2021; Published 15 June 2021

Academic Editor: Xiangxiong Kong



According to the climatic characteristics of seasonal frozen area in northeast China, the concrete strength tests, surface resistivity, rapid chloride permeability, and freeze-thaw test under salt solution were carried out to study the influences of mineral admixtures and air content on the conventional properties and salt freeze-thaw resistance of concretes. Then, the correlation analysis of surface resistivity with strength and rapid chloride permeability were further investigated. Subsequently, the changes of cumulative mass loss and relative dynamic elastic modulus varying with salt freeze-thaw cycles were analyzed to study the influences of mineral admixtures and air content on salt freeze-thaw resistance of concrete. The test results showed that fly ash (FA) was not conducive to improve the strength and salt freeze-thaw resistance of concrete. However, blast furnace slag (BFS) and silica fume (SF) could improve the compressive and flexural strength of concrete, in which SF can improve its strength more significantly. Increasing the air content of concrete will lead to the reduction of its compressive strength, and the flexural strength first increased and then decreased. Nevertheless, the addition of air-entrainment agent (AEA) has the best effect on improving the salt freeze-thaw resistance of concrete. Moreover, surface resistivity of concrete has a good exponential function relationship with strength and a good power function relationship with rapid chloride permeability. Therefore, it is of great significance for engineering quality control and quickly and nondestructive testing.

## 1. Introduction

Due to the high strength, considerable durability, and promising economy, concrete has been one of the most widely used building materials in civil engineering since the 20th century [1–6]. When optimizing mix proportion of concrete in many, if not most engineering construction of China, the trial mix with highest strength is the chosen mix proportion [7–12]. Actually, the durability indexes of concrete deserve the same attention as the strength index, especially when the concrete is working in harsh environment [13–17]. In northeast China, as an example, deicing salt has been invariably used to melt ice and snow on roads for decades [18–20]. Consequently, concrete pavements and bridges suffer from freezing and thawing environment strengthened by salt solution. A large number of cases have shown that the durability of concrete with rosy frost resistance will be greatly reduced when serving in this salt freeze-thaw condition. The presence of salt solutions eventually results in premature spalling of the concrete surface [21, 22], which gives rise to additional maintenance costs every year [23, 24].

In general, air entraining agent (AEA) is undoubtedly the most critical admixture in order to improve the frost resistance of concrete [25, 26]. The addition of air entraining agent brings a large number of tiny, enclosed bubbles inside the concrete. The work of Wellman et al. indicated that these bubbles block the growth of the bodies of ice and the generation of hydraulic pressure as water freezes in capillary cavities, effectively improving the frost resistance of concrete [27]. There are quite a few influential factors impacting air entrainment, in which bubble size and bubble distribution are decisive factors [28–30]. However, it is extremely difficult to obtain the bubble size and distribution in fresh concrete for engineering builders. As a rule, measuring the total air content as a quality control measure of air entrainment is practical [30]. Subsequently, much of research has suggested that the optimal air contents are invariably below 7% when giving consideration to concrete strength, frost resistance, and workability [31]. Recently, super air meter becomes a popular tool for assessing the air void system of fresh concrete. Not only does the total air void content matter, but also the distance between different air bubbles plays an important role in controlling freeze-thaw damage in concrete. Powers indicated that ice growth is restricted and the pore pressure can be readily accommodated by a closely spaced air void system [32]. Yuan et al. used CT to obtain the bubble structure distribution information and proposed the void-to-void distance as a factor to evaluate the freezing-thawing resistance with deicing salt performance of cement concrete [33].

Some environment-friendly mineral admixtures for concrete such as fly ash (FA), blast furnace slag (BFS), and silica fume (SF) are strongly recommended to improve salt freeze-thaw resistance because of their contributions to microstructure of concrete [34, 35]. Studies on mechanism for salt freeze-thaw have suggested that the invasion of chlorides is responsible for damages from salt crystals, high degree of saturation, and additional hydraulic pressure [36, 37]. These damages can be alleviated by rational addition of mineral admixtures, which are pozzolanic and finer than cement, filling pore structure and interfacial transition zone of concrete. Consequently, the chloride penetration coefficient would be reduced significantly [38]. Moreover, the reasonable combination of multimineral admixtures would enable concrete to show better performance than that of single-mineral admixture [39, 40]. For instance, silica fume is better than blast furnace slag in changing the pore structure, and multimineral admixtures would improve the chloride penetration and electrical resistance of concretes [41]. In the case of addition of SF, BFS, and FA at the same time, Sun et al. believed that SF provides main prophase strength amongst these three types of mineral admixtures due to its highly early pozzolanic reaction [42]. Then, BFS begins to develop its pozzolanic effect during transitional period. After 28 days, FA also gradually exhibits its own properties and provides its contributions to the strength of concrete. In terms of improvement of resistance to concrete deteriorating factors, Bapat emphasized that the use of mineral admixtures in concrete is the cheapest alternative [43].

The design strength grade of C40 is sufficient for construction concrete of northeast China in many cases. By contrast, the durability of concrete served in salt-frost environment has been more emphasized heavily recently. When taking the concrete technical factors such as design requirements, construction methods, times, and strength grade into consideration, the high-performance concrete might not be suitable for adoption. Accordingly, the air-entrained concrete with multimineral admixtures would be an overwhelmingly feasible and economical choice to improve the resistance of concrete to salt-frost erosion. However, when using the conventional method to design the mix proportion of air-entrained concrete with multimineral admixtures, a large number of trial mixes are required to select the desired combination of materials that meets special performance, which would be costly, time-consuming, and sometimes uneconomical and wasteful [44, 45]. From these considerations, a simple genetic algorithm was applied to optimize the mix proportion design of this multiconstituent concrete in this paper. The genetic algorithm is a global optimizing method which imitates biological evolution and has an advantage over many other methods on handling multiple objectives [46]. Actually, the fitness functions of different indices such as strength, slump, and material price or else have been adopted by researchers in order to obtain optimum mix proportions for target concrete properties through the genetic algorithm [47, 48]. In this paper, aiming at improving the resistance of concrete to salt-frost erosion, the mix proportion of air-entrained concrete with multimineral admixtures was designed based on the genetic algorithm, in which the fitness functions of salt freeze-thaw resistance indices were adopted.

This paper studied the influences of different mineral admixtures and air contents on the performances of concrete. At the same time, the correlation analysis between mechanical properties and durability of concrete was studied. Several groups of concrete specimens with different mineral admixtures (FA, BFS, and SF) and air contents were designed after determining the water binder ratio, cement dosage, sand ratio, and aggregate dosage. Then, the mechanical properties, physical properties, and salt freeze-thaw resistance of concrete specimens were tested. Subsequently, the influences of mineral admixtures on the mechanical and physical properties as well as surface resistivity of concrete were studied, and the quantitative relationship between strength as well as rapid chloride permeability and surface resistivity of concrete were established.

## 2. Materials and Methods

*2.1. Mixture Materials.* The ordinary Portland cement (OPC) was procured from Jilin Yatai Dinglu Cement Ltd., and the corresponding grade is P.O. 42.5. To achieve the reasonable application of mineral admixtures and AEA in concrete, FA, BFS, SF, and AEA were introduced into cement concrete for a better salt freeze-thaw resistance [49–52]. The main chemical compositions of OPC, FA, BFS, and SF are shown in Figure 1. In this study, AEA was triterpenoid saponin AEA with the type of SJ-2 to achieve

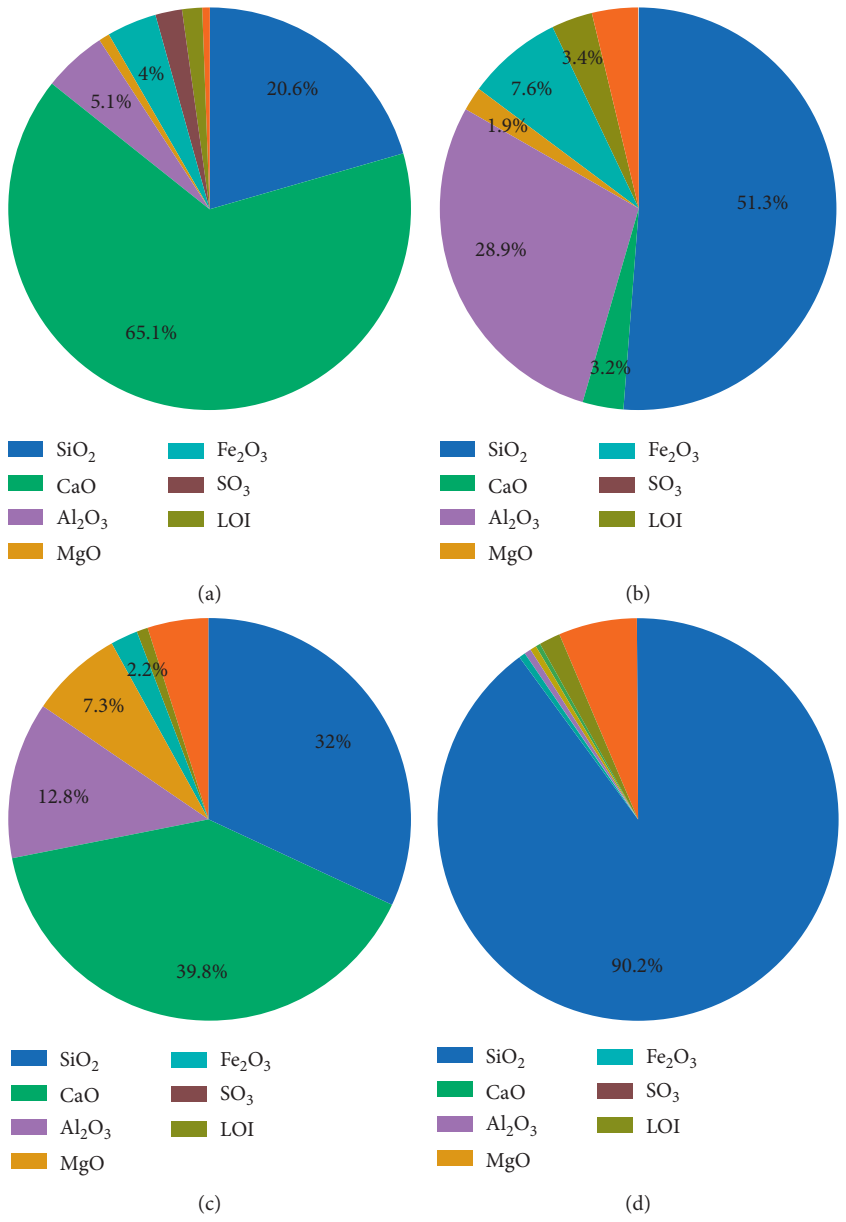


Figure 1: Chemical composition results of binders: (a) OPC. (b) FA. (c) BFS. (d) SF.

different air contents in cement concrete. And naphthalene superplasticizer was also introduced into trial concrete mixes to keep consistent workability, of which the pH value is in the range of 7–9. Following the existing study [53], natural sand with a maximum size of 9.5 mm was used as coarse aggregate and well-graded river sand with a fineness modulus of 2.0 was used as fine aggregates, which were obtained from Jilin Province, China. The specific gravities for natural gravel and river sand are 2.76 and 2.64, respectively.

*2.2. Mixture Proportion and Specimen Preparation.* In order to analyse the influences of FA, BFS, SF, and AEA on the salt freeze-thaw resistance of cement concretes, different dosages of AEA and several mineral admixtures were studied. The dosage of FA or BFS should be controlled within 30% by the total mass of cementitious materials, respectively [54–56]. Meanwhile, the total dosage of FA and BFS was limited to less than 40% by the total mass of cementitious materials. By contrast, the dosage of SF was controlled not to exceed 10% due to its high activity and cost. Besides, considering that the influence of AEA on the frost resistance of concrete is higher than that of multimineral admixtures [31], the AEA content was designed and divided into three feasible range levels of air content, i.e., $(2.5 \pm 0.5)\%$, $(4.5 \pm 0.5)\%$, and $(6.5 \pm 0.5)\%$.

Following the above mixture proportion ranges, a total of 15 groups of concrete proportions with various dosages and combinations of FA, BFS, SF, and AEA were prepared for the concretes used in this study. In the mixture design, OPC, FA, BFS, and SF were used as the main components of binders and the total binder content in all concrete

specimens was kept constant at 423 kg/m$^3$. A target concrete strength grade of C40 was selected for pavement concrete mixtures, and the water-to-binder ratio of all these cement concretes was also kept constant at 0.40. After that, a concrete mixer was applied to mix all the raw materials, and naphthalene superplasticizer was carefully added to the mixture to maintain a slump range of (45 ± 5) mm. The air content range levels in concrete specimens were controlled by AEA with the type of SJ-2 in accordance with the Chinese specification JTG E30-2005. These 15 groups of mixture proportions with various dosages of FA, BFS, SF, and AEA, including single admixture, double admixtures, and triple admixtures, are shown in Table 1. The dosage of AEA is characterized by the air content. Three dosage levels of FA, BFS, SF, and AEA of concrete specimens were determined and applied, for example, FA-10 means replacing 10% of OPC with FA and AEA-2 means air content of (2.5 ± 0.5)%.

Referring to the Chinese specification JTG E30-2005 and existing literature [1, 57, 58], three types of cement concretes were selected and prepared in this paper, in which specimens with 100 mm × 100 mm × 100 mm were used for the 28-day compression test, specimens with 100 mm × 100 mm × 400 mm were used for the 28-day flexural test, and specimens with 40 mm × 40 mm × 160 mm were used for the surface resistivity test and salt freeze-thaw cycle test. For each type of geometric dimensions, the number of each mixture proportion for these 15 groups of cement concretes was determined as three, i.e., three replicate specimens. In accordance with the related specification, after the preparation was completed, all the concrete specimens were firstly placed in the standard curing room with a temperature of 20°C and relative humidity of 95% for 24 h of sealed curing and then demoulded. These concrete specimens will continue to be placed in the standard curing room for 27 days.

### 2.3. Experimental Methods

*2.3.1. Compressive Strength Test and Flexural Strength Test.* The compressive strength and flexural strength at the age of 28 days were tested according to ASTM C39/C39M-18. The specimen sizes of compressive strength test and flexural strength test were described in the above section, and the universal testing machine was performed on three replicate specimens for the mechanical tests, as shown in Figure 2. For the compressive strength test, the loading rate was set as 0.5 MPa/s. For the flexural strength test, the loading rate was set as 0.05 MPa/s. During the whole process of test loading, the load and deflection of the specimens were recorded in real time. Then, the corresponding compressive strength ($S_c$) and flexural strength ($S_f$) could be calculated.

*2.3.2. Surface Resistivity Test and Rapid Chloride Permeability Test.* The four-probe method is used to determine the surface resistivity of concrete specimens. In this paper, the Resitest-400 instrument was adopted to measure the surface resistivity of concrete specimens after 28 days of curing. Before testing, the saturated sponge was put into the sensors, which were connected to the host through a cable. The surface resistivity test is shown in Figure 3(a).

The rapid chloride permeability test of cement concrete was carried out to evaluate the resistance to chloride ion penetration of concrete according to ASTM C1202. These specimens of rapid chloride permeability test were 100 mm in diameter and 50 mm in height. The side surfaces of all specimens were firstly coated with rapid setting epoxy. These specimens were placed inside an automatic vacuum water-soaking machine to saturate for 18 hours, and then the electrical fluxes of concrete specimens were determined. The setups of the surface resistivity test and rapid chloride permeability test are illustrated in Figure 3(b).

*2.3.3. Salt Freeze-Thaw Cycle Test.* In the salt freeze-thaw cycles, the concrete specimens with size of 40 mm × 40 mm × 160 mm were immersed in 3% concentration salt solution and exposed to freeze-thaw condition at the same time. A special freeze-thaw machine was adopted to create temperature conditions, as shown in Figure 4. The duration of one freeze-thaw cycle was 12 hours, in which the lowest and highest temperatures were −18°C and 18°C, respectively. The freeze-thaw test was terminated when any specimen showed considerable surface damage or reduction in relative dynamic modulus of elasticity value of more than 80% of the initial value [23]. After multiple salt freeze-thaw cycles, the mass of concrete specimens and ultrasonic propagation speeds in specimens were also measured, as shown in Figure 4. Then, the mass loss ($M_n$) and variation of relative dynamic elasticity modulus ($R_n$) of specimens can be calculated by using equations (1) and (2), respectively:

$$M_n = \frac{m_0 - m_n}{m_0} \times 100\%, \quad (1)$$

where $m_0$ is the initial mass of concrete specimens before exposed to salt freeze-thaw condition and $m_n$ is the mass of concrete specimens after $n$ salt freeze-thaw cycles:

$$R_n = \frac{(v_n)^2}{(v_0)^2} \times 100\%, \quad (2)$$

where $v_0$ is the ultrasonic propagation speed in specimens before exposed to salt freeze-thaw condition and $v_n$ is the ultrasonic propagation speed in specimens after $n$ salt freeze-thaw cycles.

## 3. Results and Discussion

### 3.1. Influence Analysis of Mineral Admixtures and Air Content on Physical and Mechanical Performances of Concretes

*3.1.1. Influence of Single-Mineral Admixture-FA.* The 28-day compressive strength, flexural strength, surface resistivity, and rapid chloride permeability of concretes with FA are shown in Figure 5. It can be seen from Figure 5(a) that the 28-day compressive strength of control cement concrete is 42.9 MPa. With the increase of FA content, the compressive strength of cement concrete decreases, and FA has a great influence on the compressive strength of concrete, as

Table 1: Mix proportions of concretes with multiadmixtures (kg/m$^3$).

| No. | OPC | FA | BFS | SF | Air content (%) | Fine aggregate | Coarse aggregate | Slump (mm) |
|---|---|---|---|---|---|---|---|---|
| Control | 423 | — | — | — | 1 | 584 | 1240 | 45 ± 5 |
| FA-10 | 381 | 42 | — | — | 1 | 584 | 1240 | 45 ± 5 |
| FA-20 | 338 | 85 | — | — | 1 | 584 | 1240 | 45 ± 5 |
| FA-30 | 296 | 127 | — | — | 1 | 584 | 1240 | 45 ± 5 |
| BFS-10 | 381 | — | 42 | — | 1 | 584 | 1240 | 45 ± 5 |
| BFS-20 | 338 | — | 85 | — | 1 | 584 | 1240 | 45 ± 5 |
| BFS-30 | 296 | — | 127 | — | 1 | 584 | 1240 | 45 ± 5 |
| SF-3 | 410 | — | — | 13 | 1 | 584 | 1240 | 45 ± 5 |
| SF-6 | 398 | — | — | 25 | 1 | 584 | 1240 | 45 ± 5 |
| SF-9 | 385 | — | — | 38 | 1 | 584 | 1240 | 45 ± 5 |
| FA-BFS | 296 | 63.5 | 63.5 | — | 1 | 584 | 1240 | 45 ± 5 |
| FA-BF-BFS | 271 | 63.5 | 63.5 | 25 | 1 | 584 | 1240 | 45 ± 5 |
| AEA-2 | 423 | — | — | — | 2.5 | 584 | 1240 | 45 ± 5 |
| AEA-4 | 423 | — | — | — | 4.5 | 584 | 1240 | 45 ± 5 |
| AEA-6 | 423 | — | — | — | 6.5 | 584 | 1240 | 45 ± 5 |

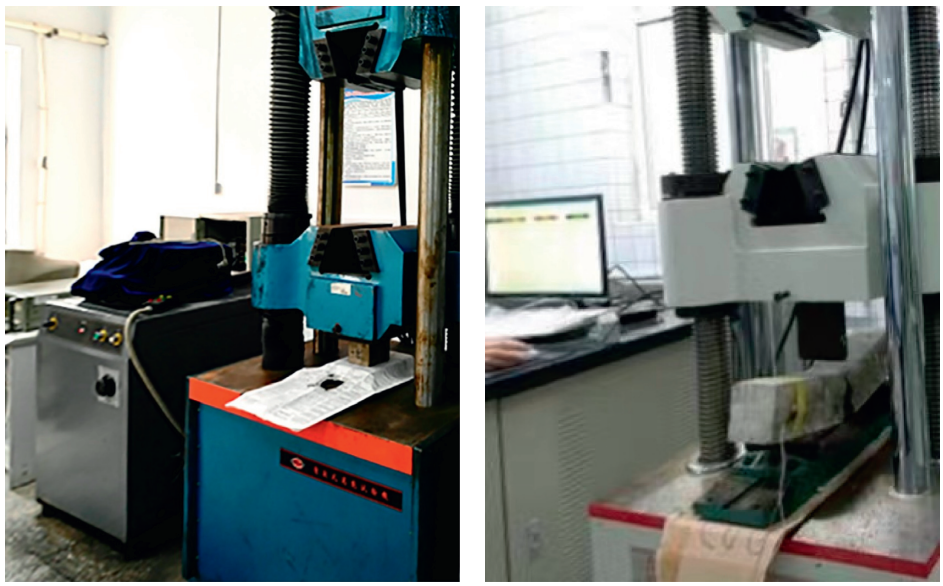

(a) (b)

Figure 2: Mechanical performance tests of cement concretes used in this paper. (a) Compressive strength test. (b) Flexural strength test.

concluded by Mardani-Aghabaglou et al. [51]. When the FA content is 30%, the strength decreases to 34.69 MPa. From Figure 5(b), it can be seen that the 28-day flexural strength of control cement concrete is 4.95 MPa, and the flexural strength of cement concrete is 4.48 MPa, 4.25 MPa, and 3.92 MPa when the FA contents are 10%, 20%, and 30%, which indicates that the flexural strength of cement concrete decreases with the increase of FA content, which is line with the findings of Mardani-Aghabaglou et al. [51]. It can be seen from Figure 5(c) that the surface resistivity increases with the increase of FA content, and the surface resistivity changes slightly with the increase of FA content in the range of 10%~20%, as previously described in [59]. In Figure 5(d), the rapid chloride permeability of control cement concrete in 28 days is 1951.5 C. With the increase of FA content, the rapid chloride permeability decreases. When the FA content is 10%, 20%, and 30%, the rapid chloride permeability of concrete is 1297.5 C, 1192.5 C, and 972.5 C, respectively. When the FA content is within 0%~10%, the rapid chloride permeability decreases the most. When the FA content is higher than 10%, the reduction range of rapid chloride permeability becomes smaller, which indicates that the appropriate content of FA can effectively reduce the rapid chloride permeability of concrete [59].

The mechanical properties of concrete with FA decrease with the increase of FA content, and the decrease range increases with the increase of FA content, which indicates that the secondary hydration degree of FA is low in the 28-day strength formation process, which is not enough to improve the strength of concrete [35]. The surface resistivity

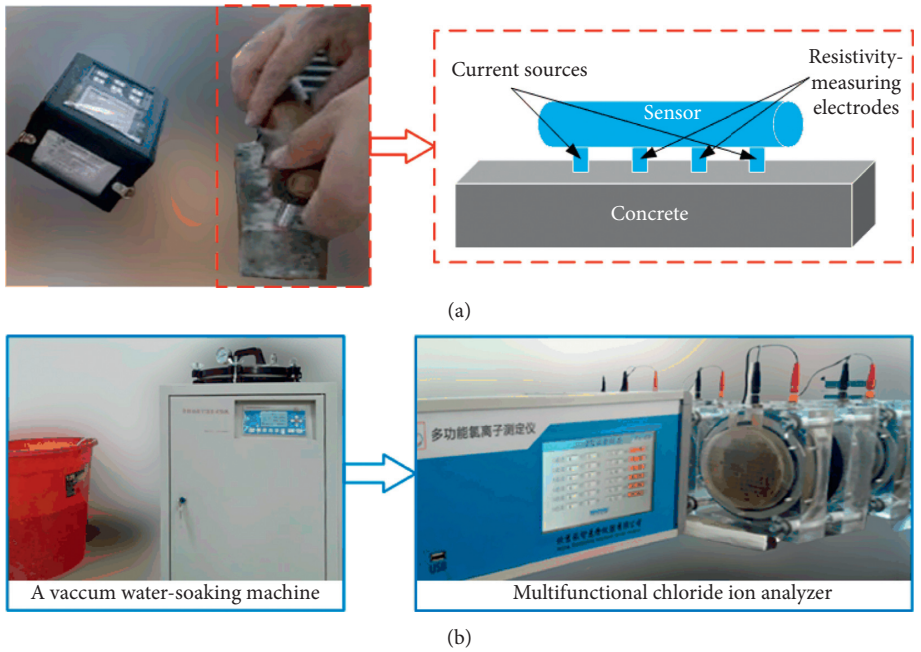


Figure 3: Surface resistivity test and rapid chloride permeability test of cement concretes. (a) Surface resistivity test. (b) Rapid chloride permeability test.

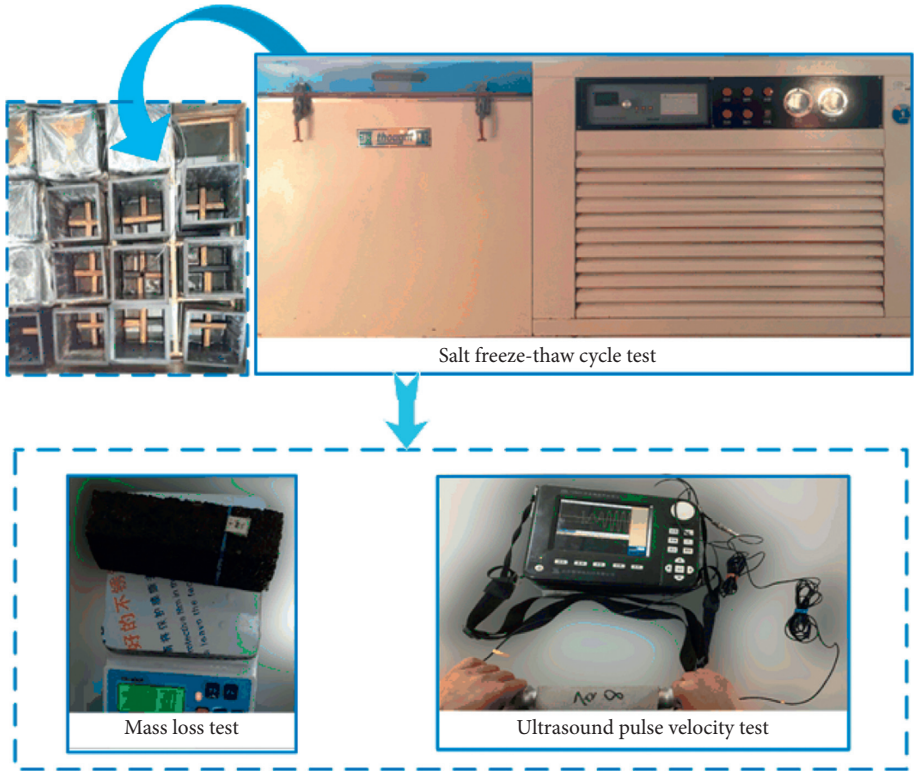


Figure 4: Salt freeze-thaw cycle test of cement concretes.

of concrete increases with the increase of FA content. The electric flux of concrete decreases with the increase of fly ash content. The rapid chloride permeability reflects the chloride penetration resistance of concrete. The higher the rapid chloride permeability, the stronger the chloride ion resistance of concrete. From the surface resistivity and rapid chloride permeability of concrete added with FA, the compactness of concrete has been improved, mainly because

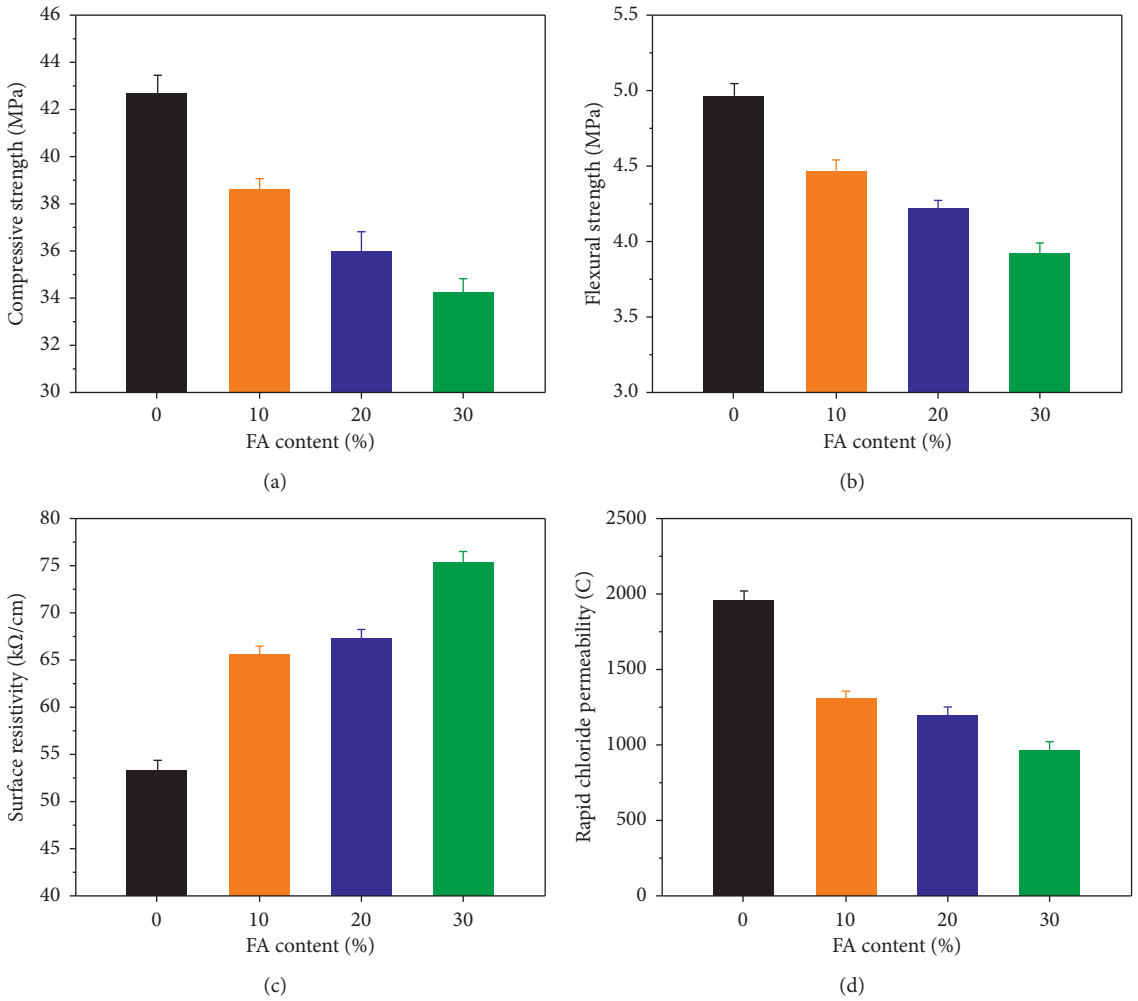


Figure 5: Influence of single-mineral admixture-FA on the performances of concrete. (a) Compressive strength. (b) Flexural strength. (c) Surface resistivity. (d) Rapid chloride permeability.

FA plays the role of microaggregate filling, which can fill the internal defects of concrete [49]. Therefore, the surface resistivity and rapid chloride permeability of concrete are improved.

*3.1.2. Influence of Single-Mineral Admixture-BFS.* The influences of BFS contents on 28-day compressive strength, flexural strength, surface resistivity, and rapid chloride permeability of concrete are shown in Figure 6.

It can be seen from Figure 6(a) that the compressive strength of cement concrete increases with the increase of BFS content in the range of 0%~30%, the compressive strength of concrete increases slowly in the range of 0%~20%, and the compressive strength of concrete increases faster in the range of 20%~30%. When the BFS content is 30%, the compressive strength of concrete is 47.26 MPa. It can be seen from Figure 6(b) that with the increase of BFS content, the flexural strength of concrete increases, and the flexural strength of concrete increases linearly with BFS content. When BFS content is 30%, the flexural strength is 6.05 MPa. The test results indicate that compressive strength and flexural strength are consistent with previous study [43, 59, 60]. From Figure 6(c), it can be seen that the surface resistivity of concrete increases fastest when the BFS content is 0%~10% and slows down when the BFS content is 10%~30%, which indicates that adding a small amount of BFS can improve the surface resistivity of concrete [59]. It can be seen from Figure 6(d) that the rapid chloride permeability of cement concrete decreases linearly with the increase of BFS content in the content range of 0%~30%. When the BFS content is 30%, the rapid chloride permeability is 950.5 C.

In the case of single-mineral admixture-BFS, the mechanical properties of concrete increase with the increase of BFS content, the surface resistivity increases with the

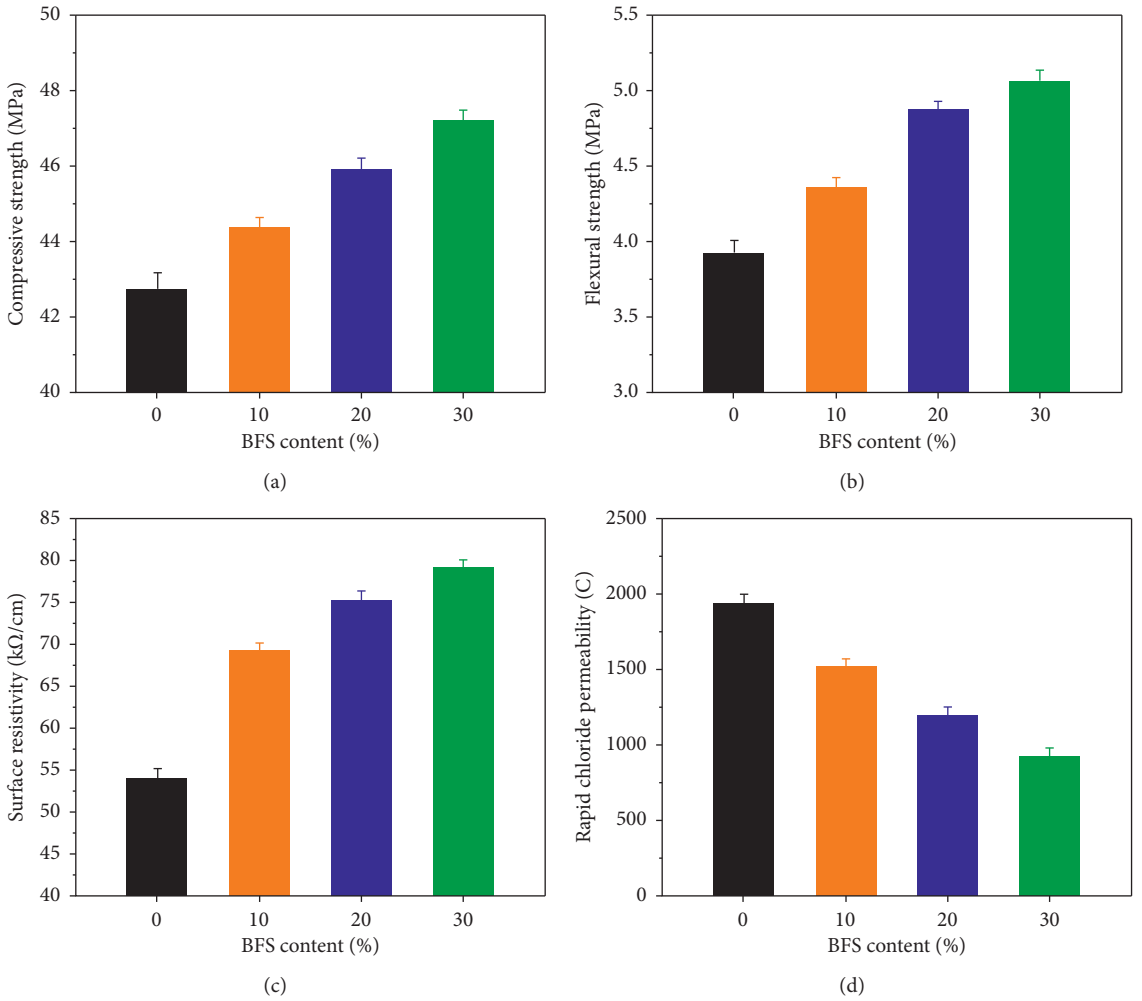


Figure 6: Influence of single-mineral admixture-BFS on the performances of concrete. (a) Compressive strength. (b) Flexural strength. (c) Surface resistivity. (d) Rapid chloride permeability.

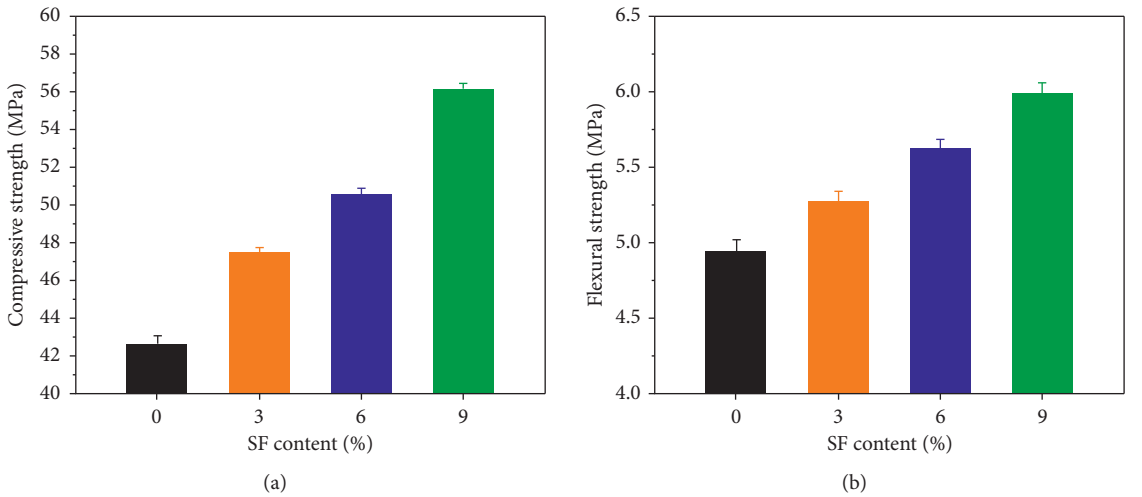


Figure 7: Continued.

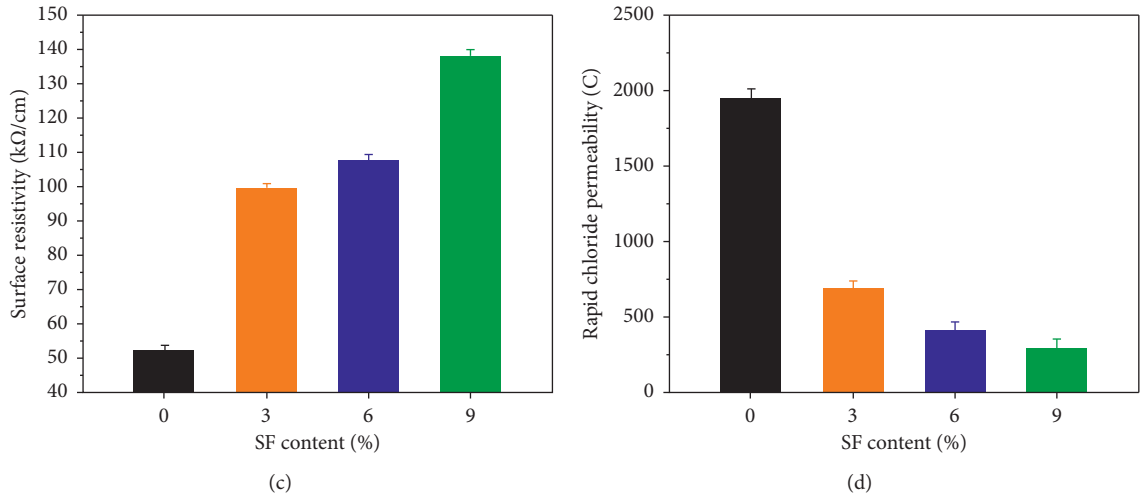


Figure 7: Influence of single-mineral admixture-SF on the performances of concrete. (a) Compressive strength. (b) Flexural strength. (c) Surface resistivity. (d) Rapid chloride permeability.

increase of BFS content, and the rapid chloride permeability decreases with the increase of BFS content. BFS contains a lot of oxides (such as $Al_2O_3$ and CaO), which has high activity in hydration [60]. It can be hydrated more in 28 days to improve the strength of concrete. At the same time, the physical properties of concrete are improved due to the filling effect of microaggregate and secondary hydration.

*3.1.3. Influence of Single-Mineral Admixture-SF.* The influences of SF content on 28-day compressive strength, flexural strength, surface resistivity, and rapid chloride permeability of concrete are shown in Figure 7.

It can be seen from Figure 7(a) that when the SF content is in the range of 0~9%, the concrete strength increases with the increase of SF content, and the concrete strength increases linearly with the SF content. When the SF content is 9%, the concrete strength can reach 56.47 MPa. It can be seen from Figure 7(b) that the flexural strength of concrete increases with the increase of SF content. When the SF content is 6%, the flexural strength of concrete has a maximum value. The strength results are consistent with the analysis results [50, 51, 59]. It can be seen from Figure 7(c) that with the increase of SF content, the surface resistivity of concrete increases. When the SF content is 9%, the resistivity of concrete can reach 137.3 kΩ/cm. It can be seen from Figure 7(d) that the rapid chloride permeability of concrete decreases exponentially with the addition of SF, which indicates that the rapid chloride permeability of concrete can be greatly reduced by adding a small amount of SF.

SF contains more than 90% of silica. In the alkaline environment formed after cement hydration, the secondary hydration degree of SF is larger [50]. In addition, the fineness of SF is larger and the microaggregate is filled more fully, which improves the mechanical and physical properties of concrete.

*3.1.4. Influence of Multimineral Admixtures.* The influences of multimineral admixtures on 28-day compressive strength, flexural strength, surface resistivity, and rapid chloride permeability of concrete are shown in Figure 8.

It can be seen from Figure 8(a) that when the content of FA and BFS is 15%, respectively, the compressive strength of concrete is 45.83 MPa. Under the same proportion of FA and BFS, adding 6% SF, the strength can reach 48.02 MPa. It can be seen from Figure 8(b) that when the content of FA and BFS is 15% respectively, the flexural strength of concrete is 5.46 MPa. Under the same proportion of FA and BFS, adding 6% SF, the strength can reach 5.86 MPa. It can be seen from Figure 8(c) that the surface resistivity of double admixtures is 86.05 kΩ/cm, while that of triple admixtures is 119.35 kΩ/cm, which indicates that SF can effectively improve the resistivity of concrete. It can be seen from Figure 8(d) that the rapid chloride permeability of concrete can be effectively reduced in the case of double mixing, but when 6% SF is added, the rapid chloride permeability is only 287.5 C, which indicates that SF can effectively reduce the rapid chloride permeability of concrete. This is similar to the previous research results [39, 43, 59].

The results showed that the mechanical properties of the concrete are better than that of the control cement concrete, which indicates that the hydration and secondary hydration of mineral admixtures are sufficient in the process of strength formation, which can provide strength for the concrete [1, 34, 58].

*3.1.5. Influence of Air Contents by AEA.* The influences of air contents on 28-day compressive strength, flexural strength, surface resistivity, and rapid chloride permeability of concrete are shown in Figure 9.

It can be seen from Figure 9(a) that the compressive strength of concrete decreases with the increase of air content. When the air content is 2.5%, the compressive strength of concrete is 37.88 MPa. When the air content is 6.5%, the compressive strength of concrete is only 30.6 MPa. It can be seen from Figure 9(b) that with the increase of air

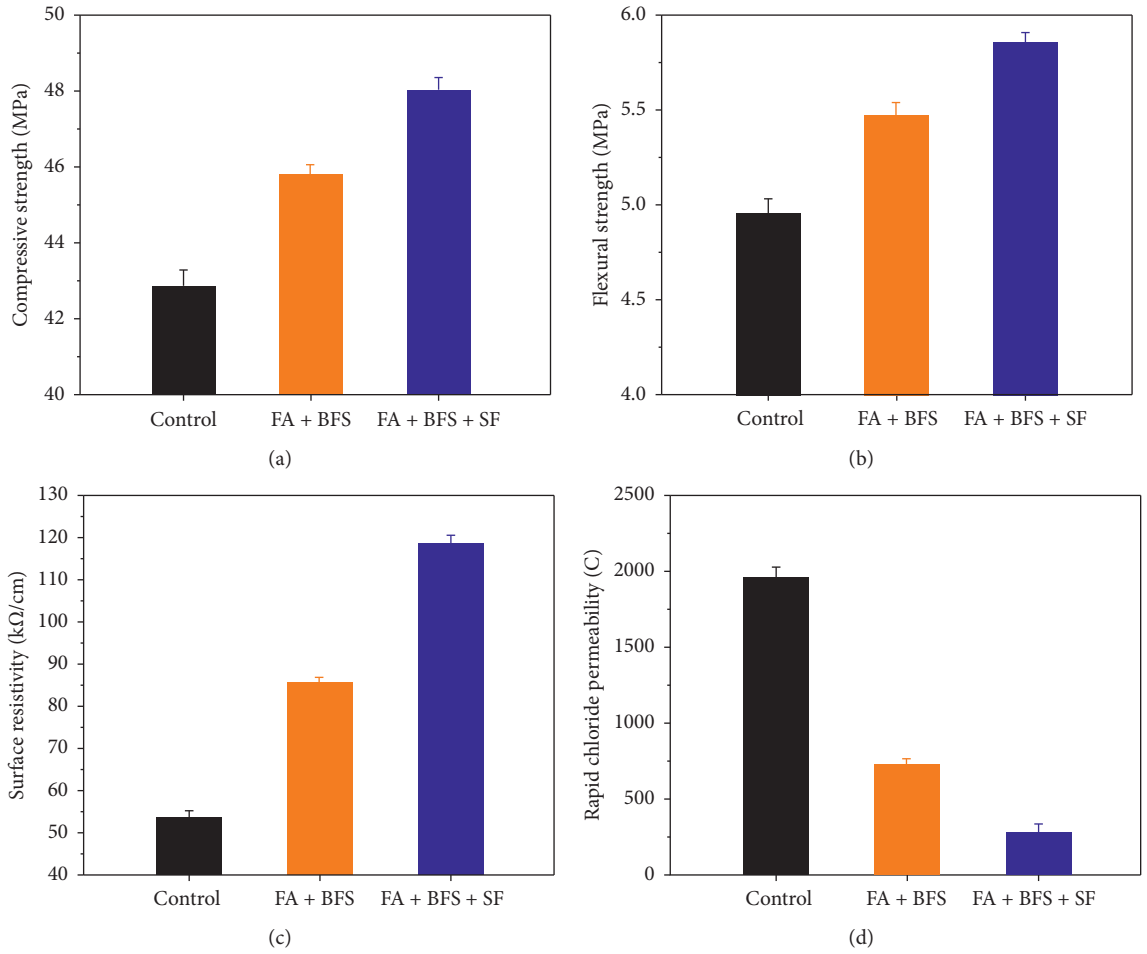


Figure 8: Influence of multimineral admixtures on the performances of concrete. (a) Compressive strength. (b) Flexural strength. (c) Surface resistivity. (d) Rapid chloride permeability.

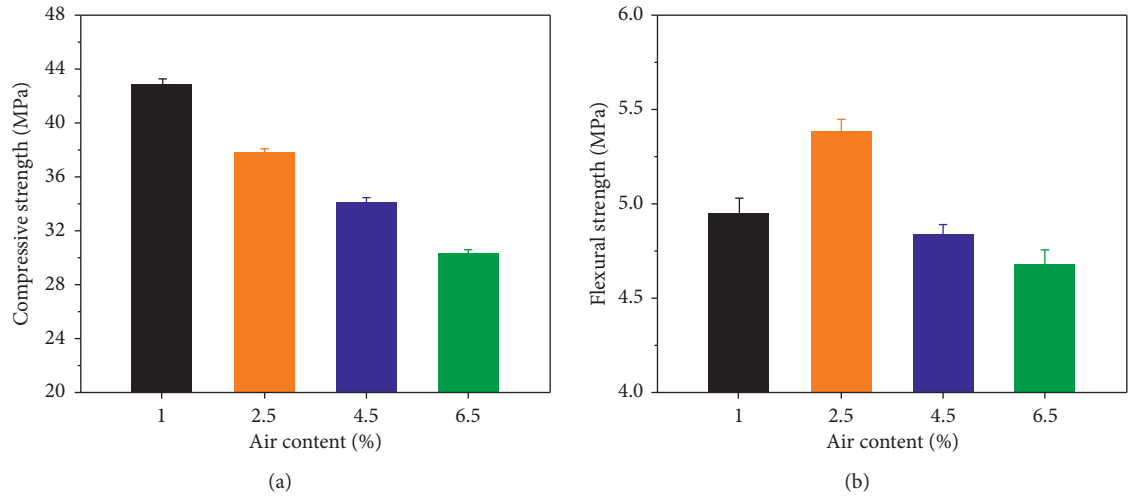


Figure 9: Continued.

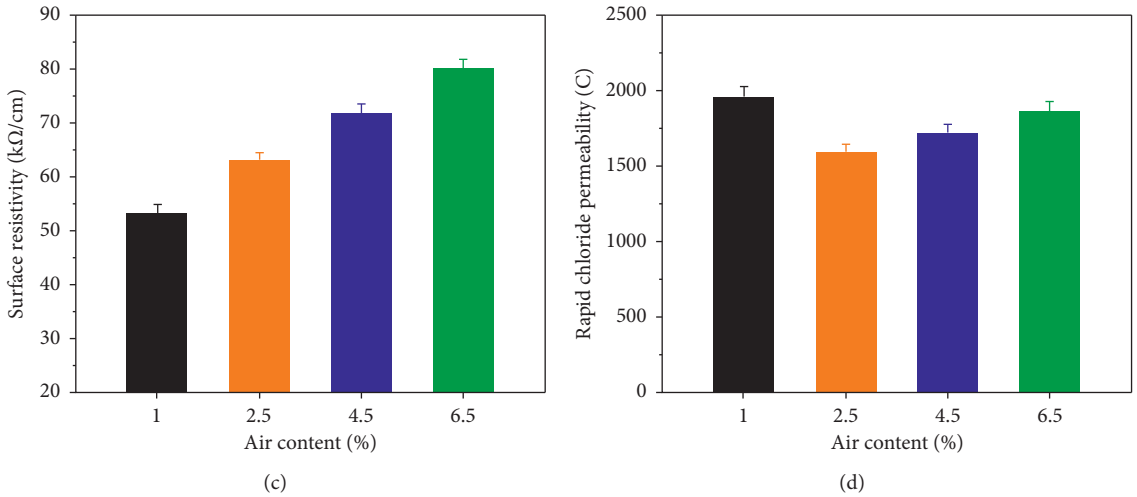


Figure 9: Influence of air contents on the performances of concrete. (a) Compressive strength. (b) Flexural strength. (c) Surface resistivity. (d) Rapid chloride permeability.

content in the range of 1%~6.5%, the flexural strength first increases and then decreases, and there is a maximum value of flexural strength, that is, when the air content is 2.5%, the maximum flexural strength of cement concrete is 5.38 MPa, as previously described in [25]. It can be seen from Figure 9(c) that the surface resistivity of concrete increases with the increase of air content. When the air content is 6.5%, the maximum value of concrete resistivity is 79.35 kΩ/cm. It can be seen from Figure 9(d) that the rapid chloride permeability of concrete decreases with the increase of air content in the air content range of 1%~2.5% and increases with the increase of air content in the air content range of 2.5%~6.5%. When the air content is 2.5%, the minimum rapid chloride permeability of concrete is 1596 C, which is line with the findings of Li et al. [59].

With the increase of air content, the air in concrete increases, and the compressive strength of concrete decreases. The rapid chloride permeability of concrete first decreases and then increases with the increase of air content. This is because with the increase of air content, tiny closed bubbles are formed in concrete, and the capillary channels in concrete are destroyed [2, 31].

### 3.2. Correlation Analysis between Surface Resistivity and Mechanical and Rapid Chloride Permeability Properties

*3.2.1. Correlation Analysis between Surface Resistivity and Compressive and Flexural Strength.* Concrete strength is a comprehensive index to measure the quality of concrete [4]. Concrete resistivity is an important electrochemical parameter of concrete, which can be used to characterize the internal microstructure of concrete and evaluate the permeability of concrete [50]. If the quantitative relationship between concrete compressive strength and resistivity can be established, the development trend of concrete compressive strength can be inferred by concrete resistivity, and vice versa. The relation curves between surface resistivity and strength of concrete (i.e., compressive and flexural strength) are shown in Figure 10.

For single-mineral admixture-FA, the surface resistivity of concrete is negatively correlated with compressive strength and flexural strength [59]. With the increase of strength (compressive and flexural), the surface resistivity decreases gradually. The parameter relationships have good nonlinear correlations, and the correlation coefficients are greater than 0.94. For single-mineral admixture-BFS or SF, the surface resistivity of concrete is positively correlated with compressive strength and flexural strength [49]. With the increase of strength (compressive and flexural), the surface resistivity increases gradually. The parameter relationships have good nonlinear correlations, and the correlation coefficients are greater than 0.93. While in the case of multiple admixtures, the surface resistivity of concrete is still positively correlated with the compressive strength and flexural strength. With the increase of strength, the resistivity increases gradually. The parameter relationship has a good nonlinear correlation, and the correlation coefficients are greater than 0.98. The compressive and flexural strength of concrete with FA would decrease with the increase of surface resistivity; however, the compressive and flexural strength of concrete with BFS, SF, or multimineral admixture would increase with the increase of surface resistivity, i.e., strength = $a \times e^{bx}$. At the same time, it also shows that adding FA instead of cement, the early strength of concrete gradually decreases, and BFS and SF are conducive to the improvement of the early strength of concrete [50, 60]. For the air content, the compressive and flexural strength of concrete change with the increase of surface resistivity in a polynomial power function.

According to the test results, the development trend of concrete strength can be predicted. The surface resistivity of concrete can not only reflect the density and pore structure of concrete statically but also indirectly reflect the correlation between strength and density.

*3.2.2. Correlation Analysis between Surface Resistivity and Rapid Chloride Permeability.* The four-probe method used

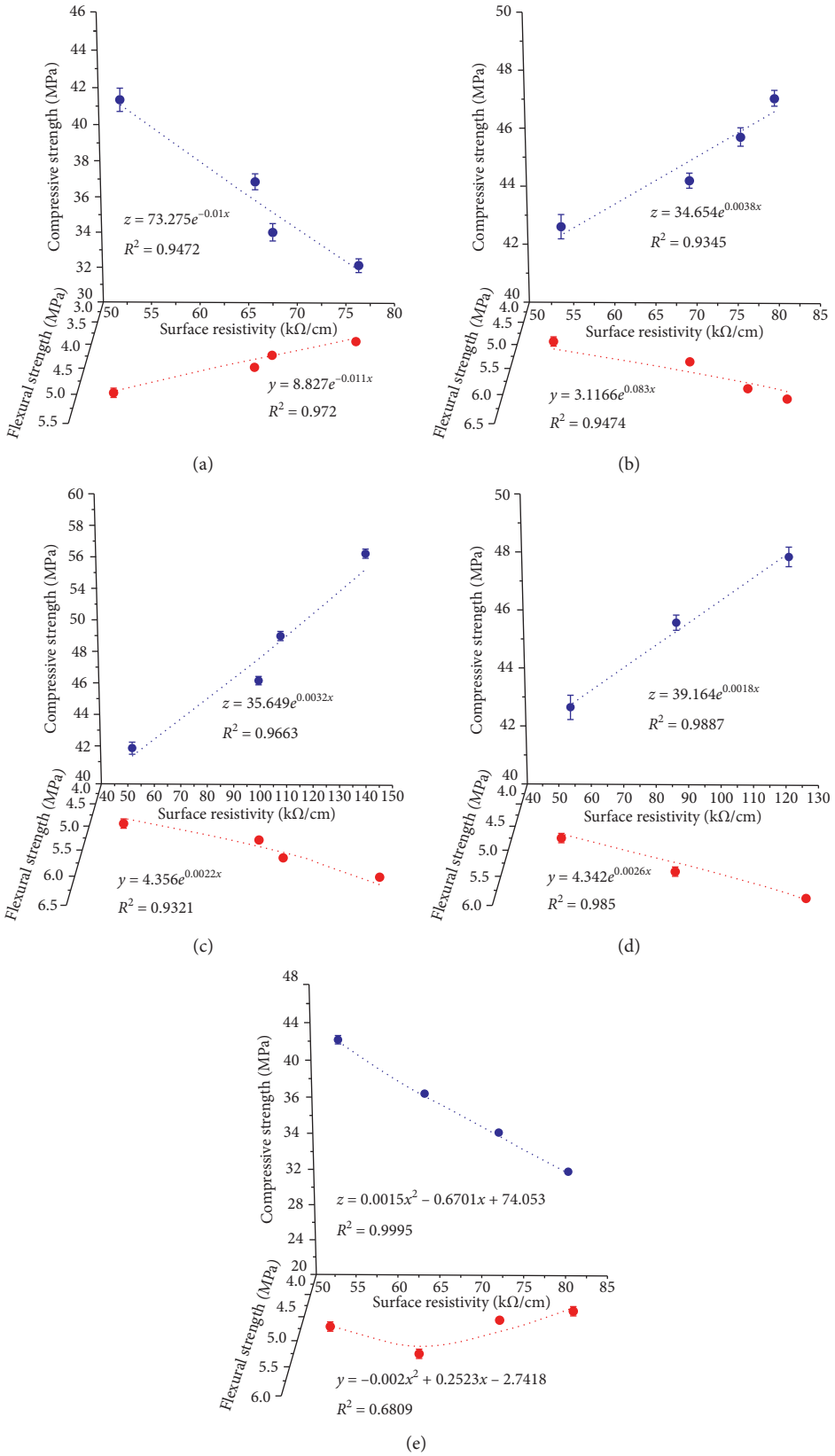


Figure 10: Correlation analysis between surface resistivity and mechanical properties. (a) FA. (b) BFS. (c) SF. (d) Multimineral admixtures. (e) Air contents.

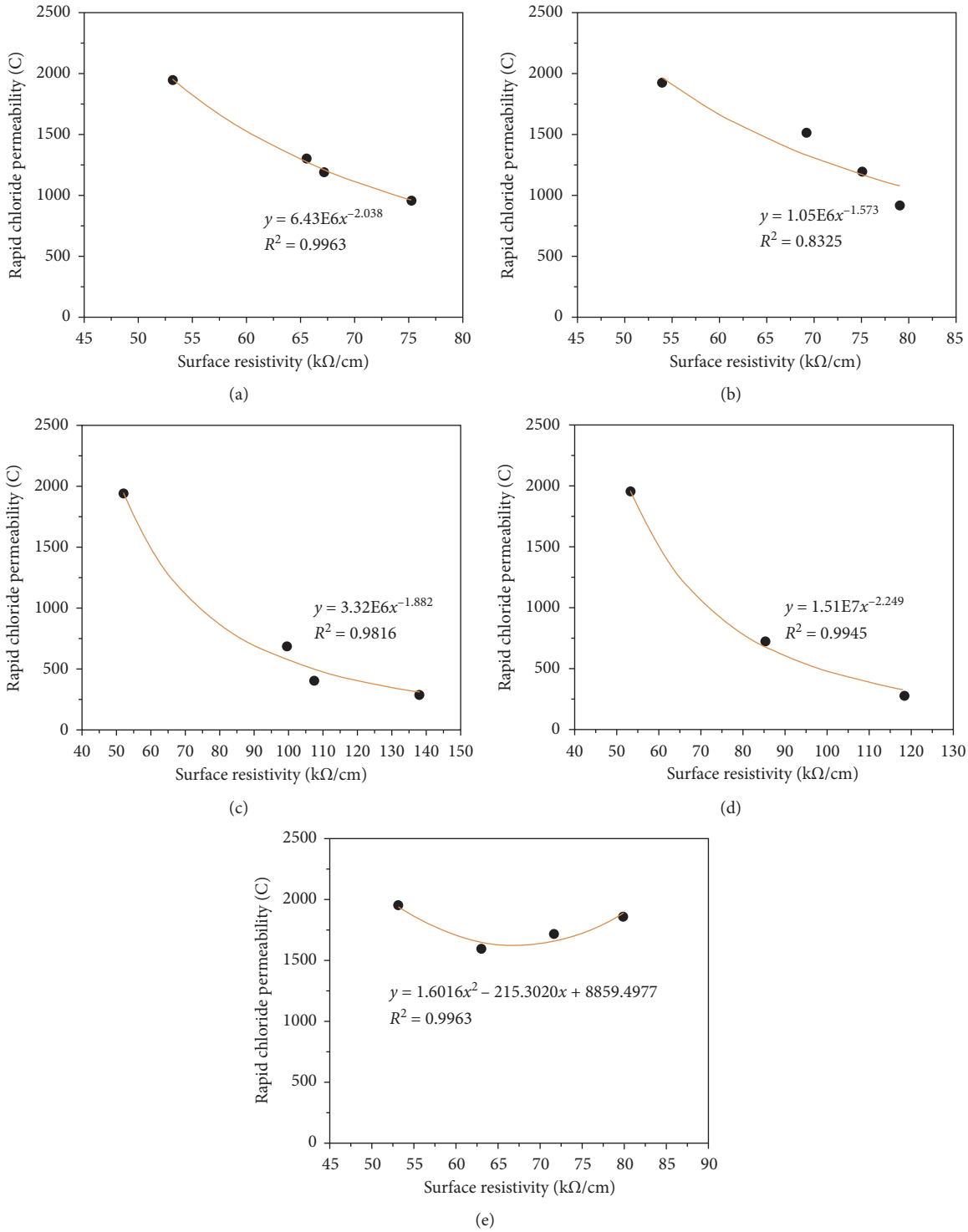


Figure 11: Correlation analysis between surface resistivity and rapid chloride permeability. (a) FA. (b) BFS. (c) SF. (d) Multimineral admixtures. (e) Air contents.

to test the surface resistivity of concrete and the rapid chloride permeability method used to test the chloride ion penetration resistance of concrete are both electrical test methods [59]. Both methods could reflect the compactness of concrete, so these two test results can be fitted and analyzed. The results are shown in Figure 11. It can be seen from Figure 11 that when power function regression is adopted, the correlation coefficient between rapid chloride permeability and surface resistivity reaches around 0.9, which shows that they have a good correlation.

Concrete is a kind of porous medium [33, 41]. There are many kinds of conductive ions in its pore solution, which

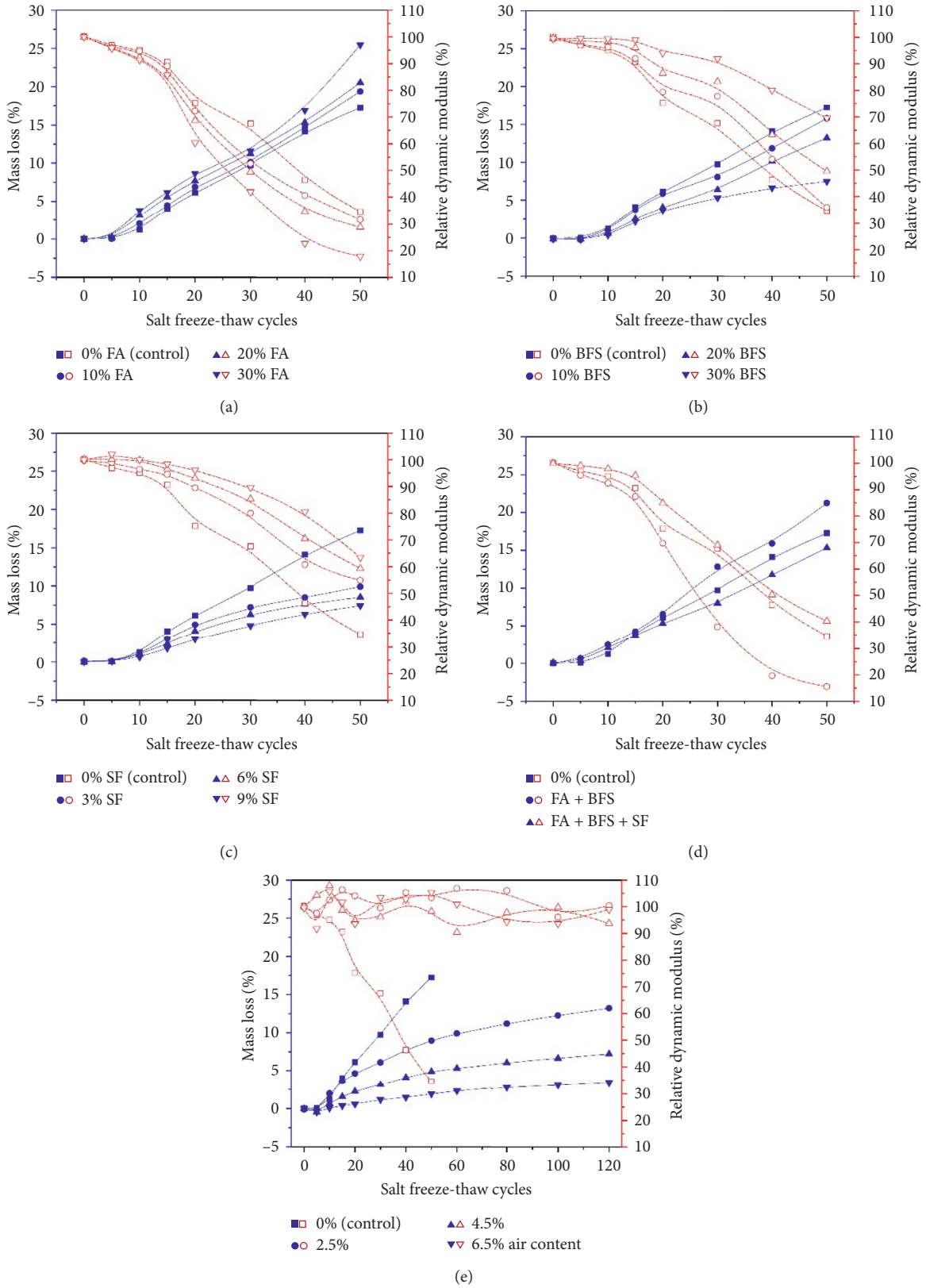


Figure 12: The salt freeze-thaw resistance of concretes with mineral admixtures. (a) FA. (b) BFS. (c) SF. (d) Multimineral admixtures. (e) Air contents.

have great influence on the conductivity of concrete. No matter the rapid chloride permeability method or the four-probe method, it is necessary to apply voltage on the specimen to measure the electric quantity of the corresponding part. The difference is that the rapid chloride permeability method tests the total electric quantity passing through the axial direction of the cylinder specimen, while the four-probe method tests the surface resistivity of the cylinder specimen with a depth of about 30 mm [59]. The two methods are similar but different, and the conversion relationship between them can be obtained by regression analysis. Compared with the rapid chloride permeability method, the surface resistivity test method does not need to cut and keep water, which has the advantages of saving time and labor, and has the potential of popularization and application.

*3.3. Evaluation of Salt Freeze-Thaw Resistance of Concretes with Mineral Admixtures.* Compared with the control group, the cumulative mass loss, and relative dynamic modulus of elasticity of concrete with different single, multiple and air content under salt freeze-thaw cycles are shown in Figure 12.

From Figure 12(a), it can be seen that in the first five salt freeze-thaw cycles, the mass loss of concrete with FA showed negative numbers. After that, the mass loss of the four concretes increased with the increase of salt freeze-thaw cycles. This shows that in the early stage of salt freeze-thaw, because the pores in the concrete were not completely saturated during the immersion period, the ice crystal pressure forced the intrusion of salt water during the freeze-thaw process [22, 57, 58]. At this time, the mass loss of concrete during the salt freeze-thaw process was less than the mass of the invading salt water. When the intruding salt water reaches a state of equilibrium and the mass of the intruding salt water reaches relative saturation, the concrete will experience mass loss, and the situation will occur after 5 salt freeze-thaw cycles. In addition, with the increase of FA content, the mass loss of concrete is greater. With respect to relative dynamic modulus, as the salt freeze-thaw cycle increases, the relative dynamic modulus of concrete decreases. In the first 15 salt freeze-thaw cycles, the relative dynamic modulus of concrete has a small decrease, and the freeze-thaw effects are consistent. The variation of mass loss and relative dynamic modulus with FA has been described in previous publications [50, 51]. When there are more than 15 salt freeze-thaw cycles, the relative dynamic modulus of concretes decreased greatly. With the increase of FA content, the relative dynamic modulus of concrete decreases more greatly. Therefore, with the increase of FA content, the salt freeze-thaw resistance of concrete decreases, as reported by Liu et al. [35].

It can be seen from Figure 12(b) that the mass loss of concrete with BFS increases with the increase of salt freeze-thaw cycles, but in the first 5 salt freeze-thaw processes, the mass loss of concrete decreases with the increase of salt freeze-thaw cycles, and the principle is described above. In the process of the salt freeze-thaw cycle, the mass loss of concrete decreases with the increase of BFS content. In addition, with the increase of salt freeze-thaw cycles, the relative dynamic modulus of concrete decreases. In the BFS content range of 0%~30%, the greater the BFS content, the better the salt freeze-thaw resistance of concrete. This may be due to the high activity of BFS, which contains more oxides, hydration in water, and secondary hydration in alkaline environment will form cementitious substances. At the same time, due to the filling effect of micro-aggregate, the salt freeze-thaw resistance of concrete is improved [60].

In Figure 12(c), it can be seen that the mass loss of concrete increases with the increase of salt freeze-thaw cycles. When the SF content is in the range of 3%~6%, the mass loss trend is the same, which indicates that a small amount of SF can reduce the mass loss of concrete. At the same time, with the increase of salt freeze-thaw cycles, the relative dynamic modulus of concrete decreases. The reason may be that SF contains a lot of silica, in the secondary hydration, there is more silica hydration, and at the same time, due to the filling effect of microaggregate [61], the salt freeze-thaw resistance of concrete is improved.

It can be seen from Figure 12(d) that the mass loss of FA and BFS compound concrete under salt freeze-thaw cycles is not improved compared with that of control concrete, but the spalling resistance is decreased. However, when 6% SF was added, that is, in the case of three mineral admixtures, the mass loss of concrete under salt freeze-thaw cycles is slightly increased. At the same time, with regard to the relative dynamic modulus, the relative dynamic modulus of concrete with FA and BFS decreases more than that of the control concrete in the process of salt freeze-thaw cycles, while the three-mineral admixture concrete shows better salt freeze-thaw resistance than that of the control concrete.

The cumulative mass loss and the relative dynamic modulus with different air contents vary with salt freeze-thaw cycles show that the mass loss of concrete increases with the increase of salt freeze-thaw cycles, and the mass loss of concrete treated by AEA is significantly lower than that of control concrete. When the air content is in the range of 1%~6.5%, the mass loss of concrete will decrease with the increase of air content. When the air content of concrete is 2.5%, 4.5%, and 6.5%, with the increase of salt freeze-thaw cycles, the relative dynamic modulus of concrete is basically stable at 90%, while for the concrete without AEA, at 30 salt freeze-thaw cycles, the relative dynamic modulus has been reduced to 60%. It can be seen that in the appropriate range of air content, with the increase of air content, the number of tiny airtight bubbles in hardened concrete increases, which will greatly improve the salt freeze-thaw resistance of concrete [25, 31].

## 4. Conclusions

The mechanical properties, physical properties, and salt freeze-thaw resistance of concrete specimens were tested in this study. Based on the test results, the influences of mineral admixtures and different air contents on the mechanical properties, physical properties, and salt freeze-thaw

resistance of concrete were analyzed. The following conclusions could be reached:

(1) The mechanical properties of concrete decreased with the increase of FA content, while the mechanical properties tended to increase with the increase of BFS or SF content. The surface resistivity of concrete showed an increasing trend with the increase of FA, BFS, and SF content. The rapid chloride permeability gradually decreased with the increase of mineral admixture content.

(2) The salt freeze-thaw resistance of concrete decreased with the increase of FA content. However, the salt freeze-thaw resistance of concrete increased with the increase of BFS or SF. Especially, adding an appropriate amount of SF can significantly improve the salt freeze-thaw resistance of concrete.

(3) When adding 15% FA and 15% BFS, the mechanical properties, surface resistivity, and rapid chloride permeability of concrete will be improved, but the salt freeze-thaw resistance of concrete will decrease. When adding 15% FA, 15% BFS, and 6% SF, the mechanical properties, resistivity, and rapid chloride permeability of concrete will be greatly improved, and the salt freeze-thaw resistance of concrete will be slightly improved.

(4) Within the air content range of 1%~6.5%, as the air content increased, the compressive strength of concrete decreased, and the flexural strength first increased and then decreased. The surface resistivity of concrete increased with the increase of air content, and the rapid chloride permeability of concrete first decreased and then increased. The air content plays a major role in the salt freeze-thaw resistance of concrete, and the salt freeze-thaw resistance of concrete increased with the increase of air content.

(5) Surface resistivity of concrete has a good exponential function relationship with strength and a good power function relationship with rapid chloride permeability. Therefore, it is of great significance for engineering quality control to use the four-probe method to test surface resistivity. The strength and durability of concrete can be quickly and nondestructively estimated according to the regression equation.

## Data Availability

The data used to support the findings of this study are available from the corresponding author upon request.

## Conflicts of Interest

The authors declare that they have no conflicts of interest.

## Acknowledgments

This research was funded by Nanning Excellent Young Scientist Program (grant number: RC20180108), Nanning Excellent Young Scientist Program and Guangxi Beibu Gulf Economic Zone Major Talent Program (grant number: RC20190206), Science and Technology Base and Talent Special Project of Guangxi Province (grant number: AD19245152), "Yongjiang Plan" of Nanning Leading Talents in Innovation and Entrepreneurship (grant number: 2018-01-04), and Scientific and Technological Project of Science and Technology Department of Jilin Province (grant number: 20190303052SF). This research was also supported by China Postdoctoral Science Foundation (grant number: 2021T140262).

## References

[1] Y. B. Jiao, Y. Zhang, M. Guo, L. Zhang, H. Ning, and S. Liu, "Mechanical and fracture properties of ultra-high performance concrete (UHPC) containing waste glass sand as partial replacement material," *Journal of Cleaner Production*, vol. 277, Article ID 123501, 2020.

[2] C. S. Poon, S. C. Kou, and L. Lam, "Compressive strength, chloride diffusivity and pore structure of high performance metakaolin and silica fume concrete," *Construction and Building Materials*, vol. 20, no. 10, pp. 858–865, 2006.

[3] F. Pacheco-Torgal, Y. Ding, and S. Jalali, "Properties and durability of concrete containing polymeric wastes (tyre rubber and polyethylene terephthalate bottles): an overview," *Construction and Building Materials*, vol. 30, pp. 714–724, 2012.

[4] H. B. Liu, G. B. Luo, H. B. Wei, and H. Yu, "Strength, permeability, and freeze-thaw durability of pervious concrete with different aggregate sizes, porosities, and water-binder ratios," *Applied Sciences-Basel*, vol. 8, no. 8, p. 1217, 2018.

[5] G. Tan, Z. Zhu, W. Wang et al., "Flexural ductility and crack-controlling capacity of polypropylene fiber reinforced ECC thin sheet with waste superfine river sand based on acoustic emission analysis," *Construction and Building Materials*, vol. 277, Article ID 122321, 2021.

[6] X. J. Shi, P. Park, Y. Rew, K. Huang, and C. Sim, "Constitutive behaviors of steel fiber reinforced concrete under uniaxial compression and tension," *Construction and Building Materials*, vol. 233, Article ID 117316, 2020.

[7] W. S. Wang, Y. C. Cheng, and G. J. Tan, "Design optimization of SBS-modified asphalt mixture reinforced with eco-friendly basalt fiber based on response surface methodology," *Materials*, vol. 11, no. 8, 2018.

[8] K. Amini, P. Vosoughi, H. Ceylan, and P. Taylor, "Effect of mixture proportions on concrete performance," *Construction and Building Materials*, vol. 212, pp. 77–84, 2019.

[9] H. B. Liu, S. Q. Liu, P. L. Zhou, and Y. Zhang, "Mechanical properties and crack classification of basalt fiber RPC based on acoustic emission parameters," *Applied Sciences-Basel*, vol. 9, no. 18, p. 3931, 2019.

[10] W.-J. Long, K. H. Khayat, A. Yahia, and F. Xing, "Rheological approach in proportioning and evaluating prestressed self-consolidating concrete," *Cement and Concrete Composites*, vol. 82, pp. 105–116, 2017.

[11] X. Shi, A. Mukhopadhyay, D. Zollinger, and Z. Grasley, "Economic input-output life cycle assessment of concrete pavement containing recycled concrete aggregate," *Journal of Cleaner Production*, vol. 225, pp. 414–425, 2019.

[12] X. Shi, A. Mukhopadhyay, and K.-W. Liu, "Mix design formulation and evaluation of portland cement concrete paving

mixtures containing reclaimed asphalt pavement," *Construction and Building Materials*, vol. 152, pp. 756–768, 2017.
[13] H. J. Wu, Z. Diao, and K. Z. Fan, "Study on durability of non-dispersible concrete in seawater environment," *International Journal of Structural Integrity*, vol. 11, no. 3, pp. 443–452, 2020.
[14] N. Xie, M. Akin, and X. Shi, "Permeable concrete pavements: a review of environmental benefits and durability," *Journal of Cleaner Production*, vol. 210, pp. 1605–1621, 2019.
[15] G. Dimitriou, P. Savva, and M. F. Petrou, "Enhancing mechanical and durability properties of recycled aggregate concrete," *Construction and Building Materials*, vol. 158, pp. 228–235, 2018.
[16] H. B. Liu, G. B. Luo, Y. F. Gong, and H. B. Wei, "Mechanical properties, permeability, and freeze-thaw resistance of pervious concrete modified by waste crumb rubbers," *Applied Sciences-Basel*, vol. 8, no. 10, 2018.
[17] W. S. Wang, G. J. Tan, C. Y. Liang, Y. Wang, and Y. C. Cheng, "Study on viscoelastic properties of asphalt mixtures incorporating SBS polymer and basalt fiber under freeze-thaw cycles," *Polymers*, vol. 12, no. 8, p. 1804, 2020.
[18] N. Xie, X. M. Shi, and Y. Zhang, "Impacts of potassium acetate and sodium-chloride deicers on concrete," *Journal of Materials in Civil Engineering*, vol. 29, no. 3, 2017.
[19] Y. Farnam, M. Krafcik, L. Liston et al., "Evaluating the use of phase change materials in concrete pavement to melt ice and snow," *Journal of Materials in Civil Engineering*, vol. 28, no. 4, 2016.
[20] Z. Sun and G. W. Scherer, "Measurement and simulation of dendritic growth of ice in cement paste," *Cement and Concrete Research*, vol. 40, no. 9, pp. 1393–1402, 2010.
[21] J. Yuan, H. Lu, Q. B. Yang, and J. Ling, "Mechanisms on the salt-frost scaling of concrete," *Journal of Materials in Civil Engineering*, vol. 29, no. 3, 2017.
[22] B. Lei, W. Li, Z. Tang, V. W. Y. Tam, and Z. Sun, "Durability of recycled aggregate concrete under coupling mechanical loading and freeze-thaw cycle in salt-solution," *Construction and Building Materials*, vol. 163, pp. 840–849, 2018.
[23] Q. L. Guo, Q. Liu, P. Zhang et al., "Temperature and pressure dependent behaviors of moisture diffusion in dense asphalt mixture," *Construction and Building Materials*, vol. 246, Article ID 118500, 2020.
[24] Q. Guo, G. Li, Y. Gao et al., "Experimental investigation on bonding property of asphalt-aggregate interface under the actions of salt immersion and freeze-thaw cycles," *Construction and Building Materials*, vol. 206, pp. 590–599, 2019.
[25] G. J. Ke, J. Zhang, B. Tian, and J. Wang, "Characteristic analysis of concrete air entraining agents in different media," *Cement and Concrete Research*, vol. 135, Article ID 106142, 2020.
[26] F. Huang, H. Li, Z. Yi, Z. Wang, and Y. Xie, "The rheological properties of self-compacting concrete containing superplasticizer and air-entraining agent," *Construction and Building Materials*, vol. 166, pp. 833–838, 2018.
[27] D. M. Wellman, K. E. Parker, L. Powers et al., "Effect of iron and carbonation on the diffusion of iodine and rhenium in waste encasement concrete and soil fill material under hydraulically unsaturated conditions," *Applied Geochemistry*, vol. 23, no. 8, pp. 2256–2271, 2008.
[28] G. C. Shan, S. Zhao, M. Qiao, N. Gao, J. Chen, and Q. Ran, "Synergism effects of coconut diethanol amide and anionic surfactants for entraining stable air bubbles into concrete," *Construction and Building Materials*, vol. 237, Article ID 117625, 2020.
[29] M. Khoshroo, A. A. Shirzadi Javid, and A. Katebi, "Effect of chloride treatment curing condition on the mechanical properties and durability of concrete containing zeolite and micro-nano-bubble water," *Construction and Building Materials*, vol. 177, pp. 417–427, 2018.
[30] L. Du and K. J. Folliard, "Mechanisms of air entrainment in concrete," *Cement and Concrete Research*, vol. 35, no. 8, pp. 1463–1471, 2005.
[31] S. Chatterji, "Freezing of air-entrained cement-based materials and specific actions of air-entraining agents," *Cement and Concrete Composites*, vol. 25, no. 7, pp. 759–765, 2003.
[32] Z. Liu and W. Hansen, "Pore damage in cementitious binders caused by deicer salt frost exposure," *Construction and Building Materials*, vol. 98, pp. 204–216, 2015.
[33] J. Yuan, Z. Du, Y. Wu, and F. Xiao, "Freezing-thawing resistance evaluations of concrete pavements with deicing salts based on various surfaces and air void parameters," *Construction and Building Materials*, vol. 204, pp. 317–326, 2019.
[34] P. Duan, Z. Shui, W. Chen, and C. Shen, "Efficiency of mineral admixtures in concrete: microstructure, compressive strength and stability of hydrate phases," *Applied Clay Science*, vol. 83-84, pp. 115–121, 2013.
[35] H. B. Liu, G. B. Luo, L. H. Wang, and Y. Gong, "Strength time-varying and freeze-thaw durability of sustainable pervious concrete pavement material containing waste fly ash," *Sustainability*, vol. 11, no. 1, 2019.
[36] J. J. Valenza and G. W. Scherer, "Mechanism for salt scaling of a cementitious surface," *Materials and Structures*, vol. 40, no. 3, pp. 259–268, 2007.
[37] B. Amini and S. S. Tehrani, "Simultaneous effects of salted water and water flow on asphalt concrete pavement deterioration under freeze-thaw cycles," *International Journal of Pavement Engineering*, vol. 15, no. 5, pp. 383–391, 2014.
[38] S.-H. Han, "Influence of diffusion coefficient on chloride ion penetration of concrete structure," *Construction and Building Materials*, vol. 21, no. 2, pp. 370–378, 2007.
[39] Q. Yuan, D. Zhou, B. Li, H. Huang, and C. Shi, "Effect of mineral admixtures on the structural build-up of cement paste," *Construction and Building Materials*, vol. 160, pp. 117–126, 2018.
[40] C. Wu, L. Li, W. Wang, and Z. Gu, "Experimental characterization of viscoelastic behaviors of nano-$TiO_2$/$CaCo_3$ modified asphalt and asphalt mixture," *Nanomaterials*, vol. 11, no. 1, 2021.
[41] Y. Li, J. Bao, and Y. Guo, "The relationship between autogenous shrinkage and pore structure of cement paste with mineral admixtures," *Construction and Building Materials*, vol. 24, no. 10, pp. 1855–1860, 2010.
[42] W. Sun, Y. Zhang, S. Liu, and Y. Zhang, "The influence of mineral admixtures on resistance to corrosion of steel bars in green high-performance concrete," *Cement and Concrete Research*, vol. 34, no. 10, pp. 1781–1785, 2004.
[43] J. D. Bapat, "Performance of cement concrete with mineral admixtures," *Advances in Cement Research*, vol. 13, no. 4, pp. 139–155, 2001.
[44] C.-H. Lim, Y.-S. Yoon, and J.-H. Kim, "Genetic algorithm in mix proportioning of high-performance concrete," *Cement and Concrete Research*, vol. 34, no. 3, pp. 409–420, 2004.
[45] C. Liang, X. Xu, H. Chen et al., "Machine learning approach to develop a novel multi-objective optimization method for pavement material proportion," *Applied Sciences*, vol. 11, no. 2, 2021.
[46] M. Shahnewaz, R. Machial, M. S. Alam, and A. Rteil, "Optimized shear design equation for slender concrete beams reinforced with FRP bars and stirrups using genetic algorithm

and reliability analysis," *Engineering Structures*, vol. 107, pp. 151–165, 2016.

[47] S. Kim, H. B. Choi, Y. Shin, G.-H. Kim, and D.-S. Seo, "Optimizing the mixing proportion with neural networks based on genetic algorithms for recycled aggregate concrete," *Advances in Materials Science and Engineering*, vol. 2013, Article ID 527089, 10 pages, 2013.

[48] W. J. Park, T. Noguchi, and H. S. Lee, "Genetic algorithm in mix proportion design of recycled aggregate concrete," *Computers & concrete*, vol. 11, no. 3, pp. 183–199, 2013.

[49] H. Yazici, "The effect of silica fume and high-volume class c fly ash on mechanical properties, chloride penetration and freeze-thaw resistance of self-compacting concrete," *Construction and Building Materials*, vol. 22, no. 4, pp. 456–462, 2008.

[50] C.-W. Chung, C.-S. Shon, and Y.-S. Kim, "Chloride ion diffusivity of fly ash and silica fume concretes exposed to freeze-thaw cycles," *Construction and Building Materials*, vol. 24, no. 9, pp. 1739–1745, 2010.

[51] A. Mardani-Aghabaglou, G. İnan Sezer, and K. Ramyar, "Comparison of fly ash, silica fume and metakaolin from mechanical properties and durability performance of mortar mixtures view point," *Construction and Building Materials*, vol. 70, pp. 17–25, 2014.

[52] H. Ziari, P. Hayati, and J. Sobhani, "Airfield self-consolidating concrete pavements (ASCCP): mechanical and durability properties," *Construction and Building Materials*, vol. 72, pp. 174–181, 2014.

[53] M. J. Islam, M. S. Meherier, and A. K. M. R. Islam, "Effects of waste pet as coarse aggregate on the fresh and harden properties of concrete," *Construction and Building Materials*, vol. 125, pp. 946–951, 2016.

[54] W. S. Wang, Y. C. Cheng, H. P. Chen, and G. Tan, "Study on the performances of waste crumb rubber modified asphalt mixture with eco-friendly diatomite and basalt fiber," *Sustainability*, vol. 11, no. 19, 2019.

[55] Q. Guo, L. Li, Y. Cheng, Y. Jiao, and C. Xu, "Laboratory evaluation on performance of diatomite and glass fiber compound modified asphalt mixture," *Materials & Design (1980–2015)*, vol. 66, pp. 51–59, 2015.

[56] Q. L. Guo, H. Y. Wang, Y. Gao, Y. Jiao, F. Liu, and Z. Dong, "Investigation of the low-temperature properties and cracking resistance of fiber-reinforced asphalt concrete using the DIC technique," *Engineering Fracture Mechanics*, vol. 229, 2020.

[57] J. Tian, W. Wang, and Y. Du, "Damage behaviors of self-compacting concrete and prediction model under coupling effect of salt freeze-thaw and flexural load," *Construction and Building Materials*, vol. 119, pp. 241–250, 2016.

[58] M. An, Y. Wang, and Z. Yu, "Damage mechanisms of ultra-high-performance concrete under freeze-thaw cycling in salt solution considering the effect of rehydration," *Construction and Building Materials*, vol. 198, pp. 546–552, 2019.

[59] X. J. Li, W. S. Wang, Z. Q. Zhu, and K. Zhang, "Investigation on durability behaviour and optimization of concrete with triple-admixtures subjected to freeze-thaw cycles in salt solution," *Advances in Materials Science and Engineering*, vol. 2021, Article ID 5572011, 16 pages, 2021.

[60] A. Qi, X. H. Liu, Z. W. Wang, and Z. X. Chen, "Mechanical properties of the concrete containing ferronickel slag and blast furnace slag powder," *Construction and Building Materials*, vol. 231, Article ID 117120, 2020.

[61] H. B. Liu, G. B. Luo, L. H. Wang, W. Wang, W. Li, and Y. Gong, "Laboratory evaluation of eco-friendly pervious concrete pavement material containing silica fume," *Applied Sciences-Basel*, vol. 9, no. 1, p. 73, 2019.

Hindawi
Advances in Materials Science and Engineering
Volume 2021, Article ID 5593040, 17 pages
https://doi.org/10.1155/2021/5593040

*Research Article*

# Consolidation Behavior and Compression Prediction Model of Coastal Cement Soil Modified by Nanoclay

**Wenjie Yu**,[1] **Na Li**,[1] **Mengdan Dai**,[1] **Dongliang An**,[1] **Biao Qian**,[2] **Wei Wang**,[1] **and Ping Jiang**[1]

[1]*School of Civil Engineering, Shaoxing University, Shaoxing 312000, China*
[2]*Tongchuang Engineering Design Co. Ltd., Shaoxing 312000, China*

Correspondence should be addressed to Na Li; lina@usx.edu.cn and Ping Jiang; jiangping@usx.edu.cn

Received 19 February 2021; Revised 13 April 2021; Accepted 16 May 2021; Published 26 May 2021

Academic Editor: Yubo Jiao



Coastal cement soil modified by nanoclay (NCS) has particular research significance as a modification approach to improve the high compressibility of coastal cement soil (CCS). At curing ages of 7 days and 28 days, consolidation and SEM tests were performed on 6 groups of NCS samples with a nanoclay content between 0% and 10% and 6 groups of CCS samples with a cement content between 10 and 20%, and a compression prediction model was established based on the test results. Test results show that (1) there is a linear interval for the improvement effect of the increment of cement content on the compression of CCS samples. In this test, the cement content in this interval is between 12% and 18%. CCS with a cement content of 18% is preferred. (2) The improvement effect on the compression of the sample is better with a nanoclay content of 4% and 8%, but poor with a content of 2%. At a consolidation pressure between 100 kPa and 800 kPa, NCS with a nanoclay content of 4% is preferred. (3) Adhesion is better with a nanoclay content of 4%, and the filling effect is better with a content of 8%. (4) The cosine-power function-exponential model is established, and the measured data are fitted, and a prediction model for the compression amount of CCS and NCS is established.

## 1. Introduction

With the continuous development of economic construction, determining how to carry out engineering construction in coastal soft soil areas has become a problem that many countries need to solve during the development process. For example, due to the current situation of large amounts of coastal areas, China, South Korea, Singapore, and other countries have to carry out engineering construction in these areas to meet their own development needs [1–4]. Coastal soft soil has the characteristics of high natural water content, large compressibility, and low strength [5], which makes it difficult to meet design requirements and requires cement reinforcement [6, 7]. Many studies have shown that cement is an important material to improve the compressibility of soft soil. Generally, improvement increases at the beginning and then decreases with the increase of cement content [8, 9]. Filling and chemical reactions are the main reason for the modification effect of nanomaterials on cement soil [10]. Kwon et al. [11] carried out unconfined compressive strength (UCS) tests on cement soil with different clay content and particle fineness. The research results showed that the particle fineness could affect the compressibility of the sample. The sample strength was high, and the water absorption was low, with a clay content of 14.3%. Existing research results show that high compressibility is the main factor restricting the use of coastal cement soil (CCS) as foundation soil [12, 13], although cement has a better effect on improving the compressibility of soft soil [14, 15].

With the development of nanotechnology [16], nanomaterials with their unique advantages are gradually favored by civil engineers. Although cement can fill most of the pores in the soil, there are still some nanopores that need to be filled with nanomaterials. Therefore, many studies have been focused on nano-modified cement soil (NCS). Nano-$SiO_2$ can improve the durability of CCS [17]. Nano-MgO can

improve shear resistance [18], compression [19, 20], and erosion resistance [21] of cement soil. Nanoclay can improve the frost resistance [22], compressive strength, and flexural strength [23, 24] of concrete. Choobbasti and Kutanaei [25] improved the flexural strength of cement soil by adding nano-$SiO_2$, with the characteristics of higher activity and water absorption. UCS tests were performed on cement soils with different nano-$SiO_2$ content. The research results showed that the improvement of compressive strength was better with 4% content [25]. Zhang et al. [26] analyzed the macroscopic mechanics and microstructure of cement soil mixed with nanoclay utilizing X-ray diffraction (XRD) and mercury injection tests. The results showed that the flexural strength of the sample increased by 25.94% with a nanoclay content of 3%. Nanoclay was uniformly distributed and filled the pores inside the cement soil and combined with hydrated calcium silicate to wrap ettringite and other crystals together to improve the strength. The above results prove that cement content is the main factor affecting the compressibility of cement soil. In addition to filling pores, nanomaterials can also be combined with cement hydration reaction products.

At present, there are fewer studies on the consolidation characteristics of CCS and NCS, and further exploration is needed to provide data support for solving the high compressibility of CCS. In this study, consolidation tests on CCS and NCS samples were conducted. The improvement effect of cement content on the consolidation characteristics of CCS was studied, and a compression prediction model was established based on the test results, providing data references for the application of CCS. The improvement effect of nanoclay content on the consolidation characteristics of CSS was also investigated, and a compression prediction model was established for NCS with better modification effect, which was convenient for the promotion of NCS, and is expected to provide a reference for solving the high compressibility of CCS.

## 2. Test Overview

*2.1. Test Materials and Equipment.* The coastal soft soil used throughout this experimental test was collected from a site in Shangyu Industrial Zone, Binhai New Town, Shaoxing City, Zhejiang Province, China. The specific physical properties are summarized in Table 1. The cement used was PO 32.5 composite Portland cement, and its specific physical and mechanical properties are shown in Table 2. The nanoclay selected has high-purity and ultrafine particle size, and the properties of it are shown in Table 3. The water used was ordinary tap water. This test equipment was a fully automated oedometer (air pressure) (model TKA-STC-1F).

*2.2. Experimental Scheme.* The rapid consolidation test method was adopted in this test, and the loading was from 12.5 kPa to 1600 kPa with the order of the loading ratio of 2, for a total of 8 pressure levels. Consolidation tests of CCS and NCS samples were conducted with 22 groups of 5 samples in each group, for a total of 110 samples.

*2.2.1. Design Scheme of CCS Samples.* The samples were coded as CCS-X-Y, where CCS represents coastal cement soil, *X* represents its curing age, and *Y* represents its cement content. The specific sample design scheme is shown in Table 4.

*2.2.2. Design Scheme of NCS Samples.* The samples were coded as NCS-X-Y(-Z), where NCS represents nano-modified cement soil, *X* represents its curing age, *Y* represents its cement content, and *Z* represents its nanoclay content. The specific sample design scheme is shown in Table 5.

Each set of tests was repeated 5 times, and the obtained results were processed. The investigated compression value of CCS-7-10 was taken as an example, and the results are summarized in Figure 1.

In order to better reflect the test results, two investigated data with the largest and smallest compression amounts were first removed, and then, the relative standard deviation (RSD) of the remaining three investigated data was calculated. If the RSD was less than 5%, the average value of the remaining three sets of data was directly used as the standard to analyze the test results. If the RSD was greater than or equal to 5%, a new set of five samples' test should be carried again until the RSD was less than 5%.

After excluding the two sets of data with the largest and smallest compression amounts, the RSD of the CCS-7-10 group was 1.5% less than 5%, with an average value of 6.995, which was used as the standard value to analyze the test results. The test results of other groups were also processed according to this method.

*2.3. Sample Preparation.* The samples of CCS and NCS were prepared according to the test scheme and geotechnical test standards [27]. The preparation steps are stated as below:

(1) The coastal soft soil was crushed and soaked in water.

(2) The soaked coastal soft soil is filtered by a fine sieve with 2 mm opening, and then, its moisture content is measured.

(3) The bolt-type flow-plastic soil ring vibrator was put on the experimental platform.

(4) The weighed quantities of coastal soft soil, cement, nanoclay, and water were mixed and stirred. Then, the combination of CCS and NCS, which was evenly mixed, was poured into the bolt-type flow-plastic soil ring vibrator with a size of 61.8 mm × 20 mm for self-compacting.

After completion of the self-compacting, the sample was taken out from the vibrator and put into a constant temperature curing box for curing.

*2.4. Test Procedure.* The samples of CCS and NCS were carried out the rapid consolidation test according to the test scheme and geotechnical test standards [27]. The procedure is as below:

Table 1: Coastal soft soil physical properties.

| Density $\rho$ (kN/m$^3$) | Water content (%) | Plastic limit (%) | Liquid limit (%) | Plasticity index | Liquidity index |
|---|---|---|---|---|---|
| 18.2 | 31.7 | 24.6 | 40.9 | 16.3 | 0.44 |

Table 2: Physical and mechanical properties of PO 32.5 composite Portland cement.

| Fineness (%) | Initial setting time (min) | Final setting time (min) | 3 d compressive strength (MPa) | 28 d compressive strength (MPa) | 3 d flexural strength (MPa) | 28 d flexural strength (MPa) |
|---|---|---|---|---|---|---|
| 3.4 | 210 | 295 | 26.9 | 48.1 | 4.9 | 9.0 |

Table 3: Some properties of nanoclay.

| The average particle size (um) | Purity (%) | pH value | Main element |
|---|---|---|---|
| 1–3 | 98 | 7.6 | Si, O, Al, and Fe |

Table 4: Sample design scheme of coastal cement soil (CCS).

| Sample code | Cement content (%) | Water content (%) | Number of samples in 7 d | Number of samples in 28 d |
|---|---|---|---|---|
| CCS-7-10 | 10 | 80 | 5 | |
| CCS-7-12 | 12 | | 5 | |
| CCS-7-14 | 14 | | 5 | |
| CCS-7-16 | 16 | | 5 | |
| CCS-7-18 | 18 | | 5 | |
| CCS-7-20 | 20 | | 5 | |
| CCS-28-10 | 10 | | | 5 |
| CCS-28-12 | 12 | | | 5 |
| CCS-28-14 | 14 | | | 5 |
| CCS-28-16 | 16 | | | 5 |
| CCS-28-18 | 18 | | | 5 |
| CCS-28-20 | 20 | | | 5 |

Table 5: Sample design scheme of coastal cement soil modified by nanoclay.

| Sample code | Cement content (%) | Nanoclay content (%) | Water content (%) | Number of samples in 7 d | Number of samples in 28 d |
|---|---|---|---|---|---|
| NCS-7-10 | 10 | 0 | 80 | 5 | |
| NCS-7-10-2 | | 2 | | 5 | |
| NCS-7-10-4 | | 4 | | 5 | |
| NCS-7-10-6 | | 6 | | 5 | |
| NCS-7-10-8 | | 8 | | 5 | |
| NCS-7-10-10 | | 10 | | 5 | |
| NCS-28-10 | | 0 | | | 5 |
| NCS-28-10-2 | | 2 | | | 5 |
| NCS-28-10-4 | | 4 | | | 5 |
| NCS-28-10-6 | | 6 | | | 5 |
| NCS-28-10-8 | | 8 | | | 5 |
| NCS-28-10-10 | | 10 | | | 5 |

(1) Saturated sample: put the prepared sample into a saturated container for saturation.

(2) Install the sample: put the guard ring, large filter stone, limit ring, filter paper, saturated sample, filter paper, small filter stone, positioning ring, and pressurized cover into the consolidation container in order from bottom to top and add water until it is submerged in the sample.

(3) Install the consolidation vessel: put the assembled consolidation container into the pressurizing device

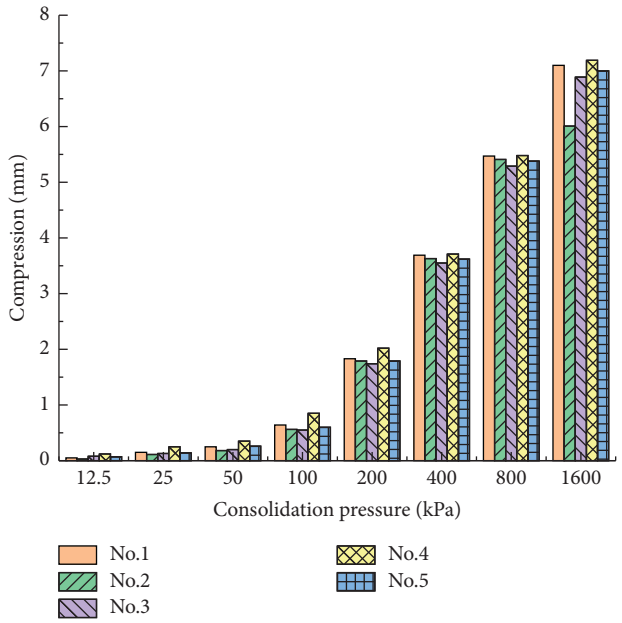


Figure 1: Investigated compression value of five samples of CCS-7-10.

and adjust the fixing bolt to make the bottom of the pressurized cover tightly contact.

(4) Adjust the displacement sensor: touch the displacement pointer of the displacement sensor with the top of the fixing bolt and fix the displacement sensor when the number in the displacement sensor displays a number in the range of 6 to 8.

(5) Select the pressure level: the pressure range is controlled within 12.5 kPa~1600 kPa.

(6) Pressure test: select the test specification, consolidation type, and deformation per hour in sequence on the software. Then, turn on the gas compressor and start the consolidation test.

(7) Organize the instrument: when all pressure levels are completed, stop the test. Quickly remove the consolidated container from the pressurizing device and take out the consolidated sample. Organize the instrument and turn off the software and power.

## 3. Test Results and Analysis of CCS

*3.1. Compression-Pressure Analysis.* The compression amount is the difference between the height of the sample stabilized at a certain consolidation pressure and the initial sample, which is calculated as shown in the following formula:

$$d_i = \sum \Delta h_i, \tag{1}$$

where $d_i$ represents the compression amount (mm) at a certain consolidation pressure and $h_i$ represents the total deformation (mm) of the sample after consolidation and stabilization at the same consolidation pressure.

According to the test results and formula (1), the compression amount of CCS samples at different consolidation pressures was obtained, and the compression amount-consolidation pressure curves (*d-p* curves) of CCS-7 and CCS-28 were drawn, as shown in Figures 2 and 3.

Figure 2 indicates that the *d-p* curves of the CCS-7 samples are all increasing concave-convex curves. When the consolidation pressure is between 0 kPa and 400 kPa, the compression of the sample increases slow at the beginning and then fast; however, between 400 kPa and 1600 kPa, it was first fast and then slow. The compression of the sample decreases continuously with the increase of cement content at the same consolidation pressure. When the consolidation pressure is greater than or equal to 200 kPa and cement content is between 12% and 16%, each 2% increment of cement content has a better improvement effect on the compression of the sample that is reduced by about 0.3 mm. When the cement content is 10% and 18%, 2% increment of cement content has a moderate improvement effect on the compression that is reduced by 0.1 mm.

Figure 3 indicates that the *d-p* curves of CCS-28 are similar to those of CCS-7. As the cement content increases, the compression of the sample decreases continuously at the same consolidation pressure. When the consolidation pressure is greater than or equal to 200 kPa and cement content is 10%, 14%, and 16%, 2% increment of cement content has a better effect on the compression amount of the sample, reducing the compression amount by about 0.4 mm. When the cement content is 12% and 18%, 2% increment of cement content has a moderate effect on the compression amount of the sample, reducing the compression amount by about 0.2 mm.

The compression data of CCS samples at different curing ages were compared, as shown in Table 6. This table indicates that when the cement content is between 10% and 14% and the consolidation pressure is less than or equal to 400 kPa, the differences between the compression amounts of CCS samples at different curing ages gradually increase with consolidation pressure, but decrease with increased cement content. When the pressure is greater than 400 kPa, the differences between the compression amount at different curing ages gradually decrease with pressure increases but increase with cement content. When the cement content is greater than 14%, the difference between the compression amounts of CCS samples at different curing ages gradually increases with increase cement content. The results indicate that the higher the cement content, the better the improvement effect of curing age on the compression of the sample.

The above results show a mutual improvement effect of cement content and curing age on the compression amount of CCS. At a curing age of 7 days with a cement content between 10% and 16% and at a curing age of 28 days with a cement content of 10%, 14%, and 16%, a 2% increment of cement content had a better improvement effect on the compression of the sample. This is because when the cement content exceeds a certain level (12% in this test), a more complete cement-soil skeleton can be formed. When the cement content is too large (18% in this test), the increasing content will make the cement particles wrap each other and slow down the increase rate of hydration reactions.

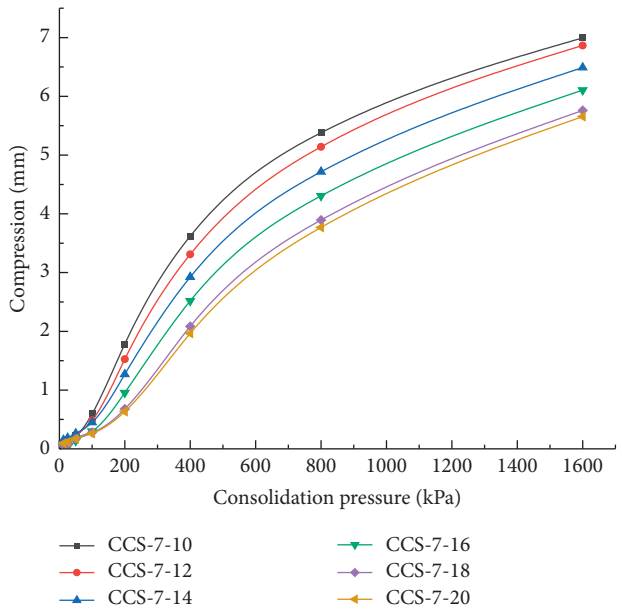


Figure 2: The compression amount-consolidation pressure curves of CCS-7.

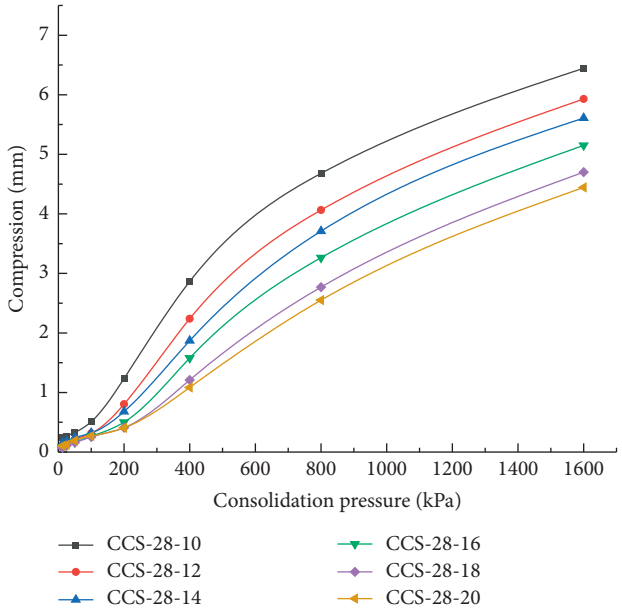


Figure 3: The compression amount-consolidation pressure curves of CCS-28.

Therefore, on the premise of meeting engineering requirements, CCS with a cement content between 12% and 18% is preferred.

*3.2. Analysis of Void Ratio Changes.* The void ratio is the ratio of pore volume to solid volume of the sample, calculated as shown in the following formula:

$$e_0 = \frac{(1 + w_0)G_s p_w}{p_0} - 1, \tag{2}$$

where $e_0$ represents the initial void ratio, $w_0$ represents water content, $G_s$ represents particle specific gravity, $p_w$ represents the density of water at 20°C, and $p_0$ represents the density of the sample.

The void ratio $e_i$ of the sample at a fixed consolidation pressure can be calculated according to the following formula:

$$e_i = e_0 - \frac{1 + e_0}{h_0} - \Delta d_i, \tag{3}$$

where $h_0$ represents the initial height of the sample (20 mm) and $\Delta d_i$ represents the compression amount of the sample after stabilization at a certain consolidation pressure.

Based on the test results and equations (1)–(3), the void ratios of CCS-7 and CCS-28 and their changes were obtained, as shown in Figure 4, where Ivr represents the initial void ratio and Fvr represents the final void ratio.

It can be seen in Figure 4 that the initial void ratio of the sample increases with cement content. For every 2% increase in cement content, the largest increase in initial porosity is in CCS-7-14 and CCS-28-20, with a value of 0.04. In other cases, it remains between 0.02 and 0.03. With the same cement content, the initial and final void ratio of the sample increased with the curing age. The initial void ratio increased the most (4.8%) with a cement content of 10%, and the final void ratio is highest increased the most (20.5%) with a cement content of 20%. The change in the void ratio of the sample decreased with curing age, and this reduction effect increased with cement content. The maximum value is 0.17, with a cement content of 20%. The above research results show that the addition of cement will improve the initial void ratio of the sample, and the improvement effect of the cement increment on the void ratio is approximately the same. The effect of cement on the initial pore ratio can be strengthened by increasing the curing age.

*3.3. Compression Modulus-Pressure Analysis.* The compression modulus is an important index for evaluating the compressibility of soil, which can be calculated according to the following formula:

$$E_s = \frac{1 + e_0}{a_v}, \tag{4}$$

where $a_v$ represents the coefficient of compressibility. In engineering, the compressibility of soil is often distinguished by a coefficient of compressibility between 100 kPa and 200 kPa and is calculated by the following formula:

$$a_v = \frac{e_i - e_{i+1}}{p_{i+1} - p_i},$$
$$a_{1-2} = \frac{e_{100} - e_{200}}{p_{200} - p_{100}}, \tag{5}$$

where $p_i$ represents a certain consolidation pressure. $a_{1\text{-}2}$ of CCS-7 and CCS-28 are obtained according to formula (5), shown in Figures 5 and 6. When $a_{1\text{-}2}$ is less than 0.1 MPa, it refers to low-compressibility soil. When $a_{1\text{-}2}$ is between 0.1 MPa and 0.5 MPa, it refers to medium-compressibility

Table 6: Compression of CCS at different consolidation pressures.

| Cement content (%) | Curing age (d) | The amount of compression under consolidation pressure (mm) | | | | |
|---|---|---|---|---|---|---|
| | | 100 kPa | 200 kPa | 400 kPa | 800 kPa | 1600 kPa |
| 10 | 7 | 0.595 | 1.785 | 3.620 | 5.380 | 6.995 |
| | 28 | 0.510 | 1.235 | 2.865 | 4.680 | 6.445 |
| 12 | 7 | 0.485 | 1.525 | 3.310 | 5.140 | 6.865 |
| | 28 | 0.315 | 0.805 | 2.240 | 4.065 | 5.930 |
| 14 | 7 | 0.450 | 1.270 | 2.925 | 4.715 | 6.490 |
| | 28 | 0.320 | 0.680 | 1.870 | 3.710 | 5.610 |
| 16 | 7 | 0.300 | 0.955 | 2.520 | 4.305 | 6.105 |
| | 28 | 0.265 | 0.500 | 1.580 | 3.265 | 5.150 |
| 18 | 7 | 0.280 | 0.680 | 2.085 | 3.895 | 5.760 |
| | 28 | 0.255 | 0.410 | 1.210 | 2.770 | 4.700 |
| 20 | 7 | 0.260 | 0.635 | 1.965 | 3.770 | 5.655 |
| | 28 | 0.270 | 0.405 | 1.085 | 2.550 | 4.445 |

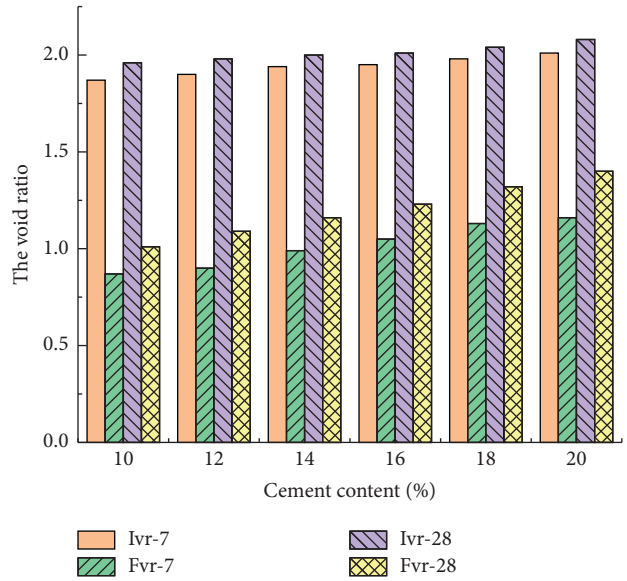


Figure 4: Change in the void ratio of CCS.

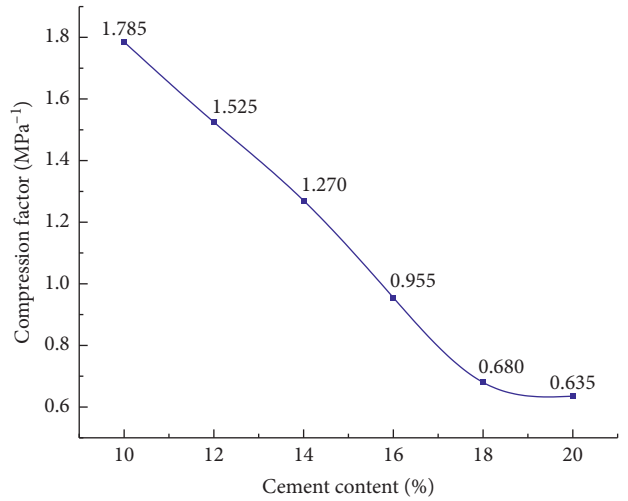


Figure 5: $a_{1\text{-}2}$ of CCS -7 with different cement content.

soil. When $a_{1\text{-}2}$ is greater than 0.5 MPa, it refers to high-compressibility soil.

As shown in Figure 5, when the cement content is between 10% and 18%, the sample decreases approximately linearly with the increased cement content, indicating that cement content in this interval has a better improvement effect on the compressibility of the sample. When the cement content is between 18% and 20%, the change of $a_{1\text{-}2}$ is small at only 0.045 MPa$^{-1}$, indicating that increasing the cement content at this time has an balanced improvement effect. The $a_{1\text{-}2}$ of CCS-7 is more than 0.5 MPa, which means it refers to high-compressibility soil.

As shown in Figure 6, when the cement content is between 10% and 12%, $a_{1\text{-}2}$ changes the most, and the coefficient of compressibility of the sample decreases by 0.343 MPa$^{-1}$, which indicates that increasing the cement content at this time has the best improvement effect. When the cement content is between 18% and 20%, $a_{1\text{-}2}$ changes slightly, only 0.028 MPa$^{-1}$, indicating that increasing the cement content at this time has an average improvement effect. Numerically, the value of $a_{1\text{-}2}$ of CCS at a curing age of 28 days decreases from 1.074 MPa$^{-1}$ to 0.208 MPa$^{-1}$, and the sample changes from high- to medium-compressibility soil. These results show that the improvement effect of cement increment on the compressibility of the sample is better with a cement content between 12% and 18%.

*Es* values of CCS-7 and CCS-28 are obtained from formula (4), and the *Es-p* curve is drawn, as shown in Figures 7 and 8. Regarding the applied consolidation pressure, 12.5 kPa and 25 kPa, which represent prestressing, are not considered. The compression modulus is an important parameter to characterize compressibility in a fixed pressure range. Therefore, the compression modulus is studied with a consolidation pressure between 100 kPa and 1600 kPa in this test. The structure between the particles of cement hydration reaction products will be destroyed when the consolidation pressure is near 800 kPa.

It can be seen from Figure 7 that the change of *Es* of a single sample shows a concave trend. When the cement content is 10% and 12%, the minimum value of *Es* of the sample appears at a consolidation pressure of 200 kPa; when

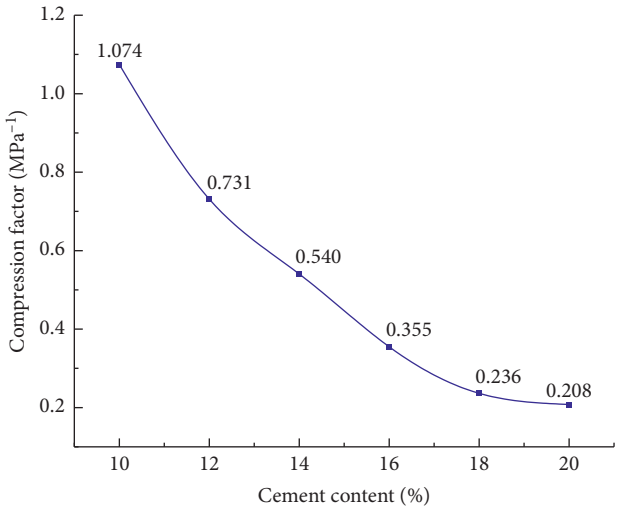


Figure 6: $a_{1\text{-}2}$ of CCS-28 with different cement content.

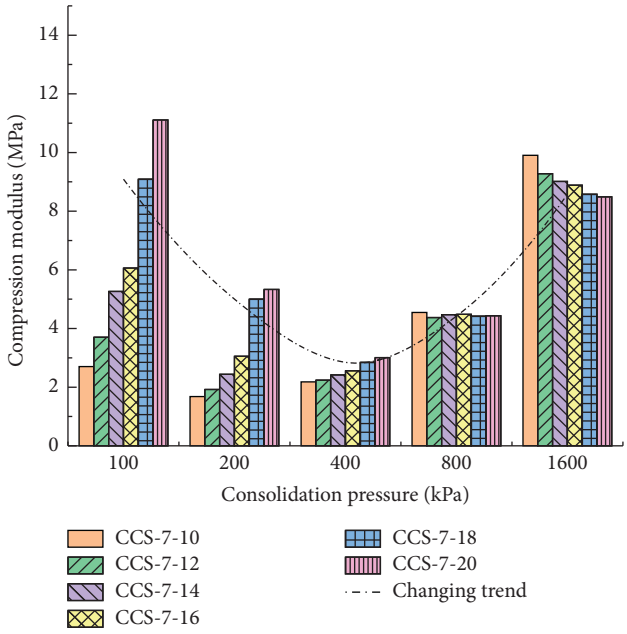


Figure 7: *Es* of CCS-7 with different cement content.

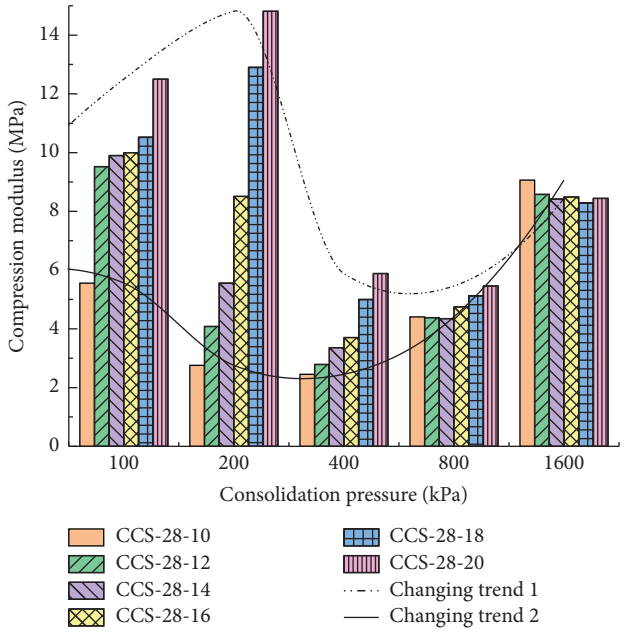


Figure 8: *Es* of CCS-28 with different cement content.

the content is greater than 12%, it appears at a pressure of 400 kPa. When the consolidation pressure is between 100 kPa and 800 kPa, the increasing cement content can increase *Es* of the sample. Overall, the improvement effect on *Es* of the sample is the best with a cement content of 18%. When the consolidation pressure is between 800 kPa and 1600 kPa, the increased cement content will decrease *Es* of the sample.

As can be seen from Figure 8, the change trend of *Es* of a single sample is divided into two types. When the cement content is less than 18%, it shows a concave trend; when the content is greater than or equal to 18%, it shows a convex-concave trend. When the cement content is less than 20%, the minimum value of *Es* of the sample appears at a consolidation pressure of 400 kPa; when the content is 20%, it appears at a pressure of 800 kPa. When the consolidation pressure is between 100 kPa and 800 kPa, the increment of cement content can improve *Es* of the sample. Overall, the improvement effect on *Es* of the sample is the best with a cement content of 18%. When the consolidation pressure is 1600 kPa, the increment of cement content will decrease *Es* of the sample.

The above test results show that when the structure of the particles produced in the cement hydration reaction is not damaged, the increasement of the particles can improve the compression modulus of the sample; when the structure is destroyed and recombined, the compression modulus of the particles after recombination is less than that of coastal soft soil particles. At this time, increasing the cement hydration reaction products will reduce the compression modulus of

the sample. By comprehensive comparison, increasing the cement content by 18% has the best effect on the compression modulus of the sample.

## 4. Test Results and Analysis of NCS

*4.1. Compression-Pressure Analysis.* According to the test results and formula (1), the compression amount of nano-modified cement soil (NCS) samples after stabilization at various consolidation pressures was obtained, and the *d-p* histograms of NCS-7 and NCS-28 were plotted, as shown in Figures 9 and 10.

It can be seen from Figure 9 that the change of the *d-p* histogram of NCS-7 shows a "S" type. As the consolidation pressure increases, first the concave type increases and then the convex type. When the nanoclay content is 2%, the compression amount of the sample increases. When the content is 4% and 8%, the compression amount of the sample decreases. When the content is 6%, there is a general modification effect on the compression. When the content is 10%, the compression amount decreases when the consolidation pressure is between 200 kPa and 400 kPa, and otherwise increases.

It can be seen from Figure 10 that the change of the *d-p* histogram of NCS-28 also shows a "S" type. At the consolidation pressure less than or equal to 800 kPa, the addition of nanoclay can reduce the compression amount of the sample, but the nanoclay content has an effect on the reduction level. At the nanoclay content of 4% and 8%, the reduction effect is better. At the consolidation pressure of 400 kPa and the nanoclay content of 4%, the reduction effect is the best, with a 29% decrease to 0.685 mm. When the consolidation pressure is 1600 kPa, the compression amount decreases with a nanoclay content of 4% and 8%, but otherwise increases.

The compression data of NCS samples in different curing ages are compared, as shown in Table 7.

It can be seen in Table 7 that an increase in the curing age will reduce the compression amount of NCS samples, and the reduction increases at the beginning and then decreases with the increase of consolidation pressure. The above test results show that the modification effect of nanoclay on the compression of CCS is closely related to the curing age. At a curing age of 7 days, the hydroscopicity of nanoclay will hinder the hydration reaction of cement, reducing the hydration reaction products of the cement and the early strength of the sample. The improvement effect is better with a nanoclay content of 4% and 8%. At a curing age of 28 days, the filling and bonding effects of nanoclay play a major role, and the addition of nanoclay can better improve the compressibility of CCS. The degree of the pozzolanic reaction of nanoclay is better with a nanoclay content of 4%, and the filling ability is better with a nanoclay content of 8%.

In order to explore the improvement effect of nanoclay on the compression amount of CCS, the compression amounts of NCS and CCS at a curing age of 28 days and consolidation pressure between 100 kPa and 400 kPa are compared, as shown in Table 8.

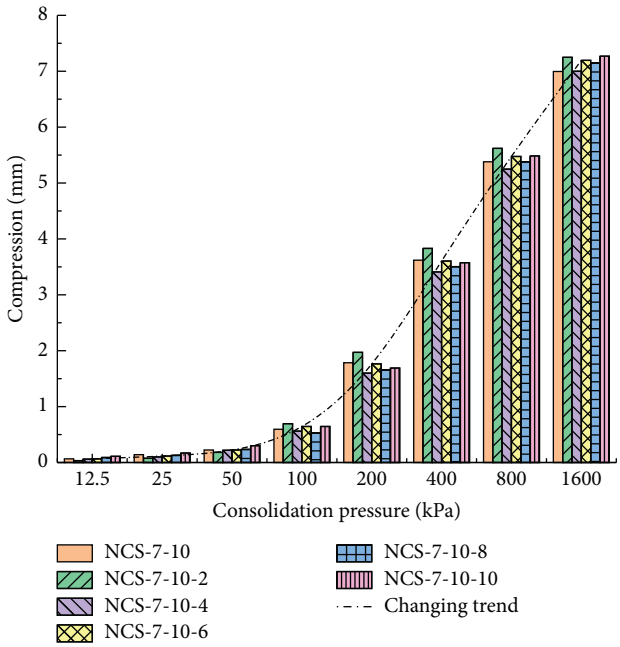


Figure 9: *d-p* histogram of NCS-7 with different consolidation pressure.

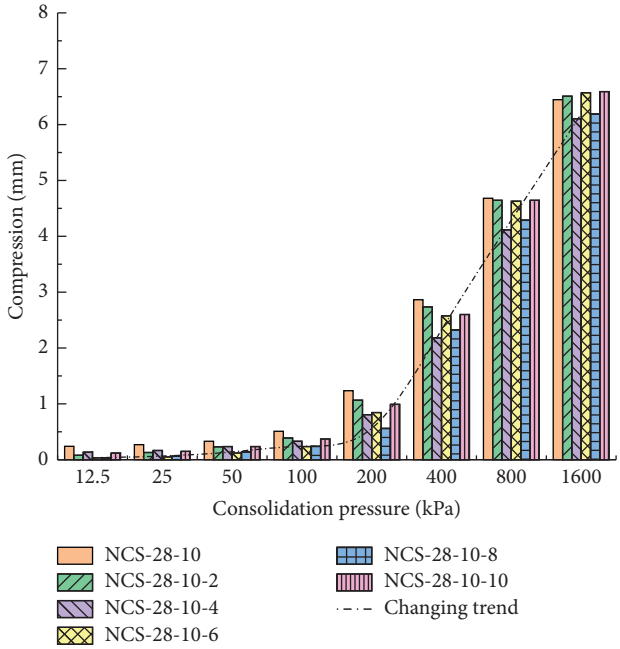


Figure 10: *d-p* histogram of NCS-28 with different consolidation pressure.

As shown in Table 8, at a consolidation pressure of 100 kPa, when the cement content is 18%, the increment of cement content has the best effect on improving the compression of CCS samples, and a 2% increment will decrease the compression amount by 0.255 mm. When the nanoclay content is 6%, the increment of nanoclay content has the best effect, and a 2% increment will decrease the compression amount by 0.275 mm. At this time, the improvement effect

Table 7: Compression of NCS at different consolidation pressures.

| Nanoclay content (%) | Curing age (d) | Compression deformation (mm) | | | | |
|---|---|---|---|---|---|---|
| | | 100 kPa | 200 kPa | 400 kPa | 800 kPa | 1600 kPa |
| 0 | 7 | 0.595 | 1.785 | 3.620 | 5.380 | 6.995 |
| | 28 | 0.510 | 1.235 | 2.865 | 4.680 | 6.445 |
| 2 | 7 | 0.695 | 1.970 | 3.830 | 5.620 | 7.250 |
| | 28 | 0.390 | 1.065 | 2.735 | 4.645 | 6.510 |
| 4 | 7 | 0.560 | 1.600 | 3.410 | 5.250 | 7.000 |
| | 28 | 0.330 | 0.805 | 2.180 | 4.115 | 6.105 |
| 6 | 7 | 0.645 | 1.765 | 3.605 | 5.475 | 7.195 |
| | 28 | 0.235 | 0.845 | 2.575 | 4.630 | 6.570 |
| 8 | 7 | 0.530 | 1.655 | 3.505 | 5.380 | 7.150 |
| | 28 | 0.240 | 0.560 | 2.325 | 4.290 | 6.190 |
| 10 | 7 | 0.645 | 1.690 | 3.575 | 5.485 | 7.270 |
| | 28 | 0.370 | 0.990 | 2.600 | 4.645 | 6.590 |

Table 8: Comparison of compression between NCS and CCS.

| Sample code | Compression and difference (mm) | | | | | |
|---|---|---|---|---|---|---|
| | 100 kPa | $d$-$d_{\text{ccs-28-10}}$ | 200 kPa | $d$-$d_{\text{ccs-28-10}}$ | 400 kPa | $d$-$d_{\text{ccs-28-10}}$ |
| CCS-28-10 | 0.510 | | 1.235 | | 2.865 | |
| CCS-28-12 | 0.315 | 0.195 | 0.805 | 0.430 | 2.240 | 0.625 |
| CCS-28-14 | 0.320 | 0.190 | 0.680 | 0.555 | 1.870 | 0.995 |
| CCS-28-16 | 0.265 | 0.245 | 0.500 | 0.735 | 1.580 | 1.285 |
| CCS-28-18 | 0.255 | 0.255 | 0.410 | 0.825 | 1.210 | 1.655 |
| CCS-28-20 | 0.270 | 0.240 | 0.405 | 0.830 | 1.085 | 1.780 |
| NCS-28-10 | 0.510 | | 1.235 | | 2.865 | |
| NCS-28-10-2 | 0.390 | 0.120 | 1.065 | 0.170 | 2.735 | 0.130 |
| NCS-28-10-4 | 0.330 | 0.180 | 0.805 | 0.430 | 2.180 | 0.685 |
| NCS-28-10-6 | 0.235 | 0.275 | 0.845 | 0.390 | 2.575 | 0.290 |
| NCS-28-10-8 | 0.240 | 0.270 | 0.560 | 0.675 | 2.325 | 0.540 |
| NCS-28-10-10 | 0.370 | 0.140 | 0.990 | 0.245 | 2.600 | 0.265 |

of 6% nanoclay content is 1.08 times that of 10% cement content on the compression of the sample. At a consolidation pressure of 200 kPa, when the cement content is 20%, the increment of cement content has the best effect, and a 2% increment will decrease the compression amount by 0.830 mm. When the nanoclay content is 8%, the increment of nanoclay content has the best effect, and a 2% increment will decrease the compression amount by 0.675 mm. At this time, the improvement effect of 8% nanoclay content is about equal to that of 5% cement content on the compression of the sample. At a consolidation pressure of 400 kPa, when the cement content is 20%, the increment of cement content has the best effect, and a 2% increment will decrease the compression amount by 1.780 mm. When the nanoclay content is 4%, the increment of nanoclay content has the best effect, and a 2% increment will decrease the compression amount by 0.685 mm. At this time, the improvement effect of 4% nanoclay content is equivalent to that of 2% cement content on the compression of the sample. The above research results show that the improvement effect of nanoclay at low consolidation pressure between 100 kPa and 200 kPa is better than that of the equivalent cement, but at high consolidation pressure between 400 kPa and 1600 kPa, nanoclay is less effective at improving the compression than the equivalent amount of cement.

*4.2. Analysis of Void Ratio Change.* Based on the consolidation test results and formulas (1)–(3), the void ratios of NCS-7 and NCS-28 and their changes are obtained, as shown in Figure 11.

Figure 11 indicates that, as nanoclay content increases, the initial void ratio of the sample first increases and then decreases. With the same nanoclay content of less than 8%, the initial void ratio increases with the growth of the curing age; when the nanoclay content is greater than or equal to 8%, the initial void ratio decreases with the growth of the curing age. The change in the void ratio decreases with the growth of the curing age and decreases the most with a nanoclay content of 8%, with a value of 0.14. The final void ratio increases with the growth of the curing age and increases the most with a nanoclay content of 4%, which is 0.17. The above test results show that, at a curing age of 7 days, when the nanoclay content is less than 6%, the addition of nanoclay will increase the initial void ratio; when the content is greater than or equal to 6%, it will reduce the initial void ratio, and the filling effect is the best with a content of 8%. At a curing age of 28 days, when the nanoclay content is less than 6%, the improvement effect of nanoclay increment on the initial void ratio is weakened; when the content is greater than or equal to 6%, the reduction effect of nanoclay increment on the initial void ratio is enhanced.

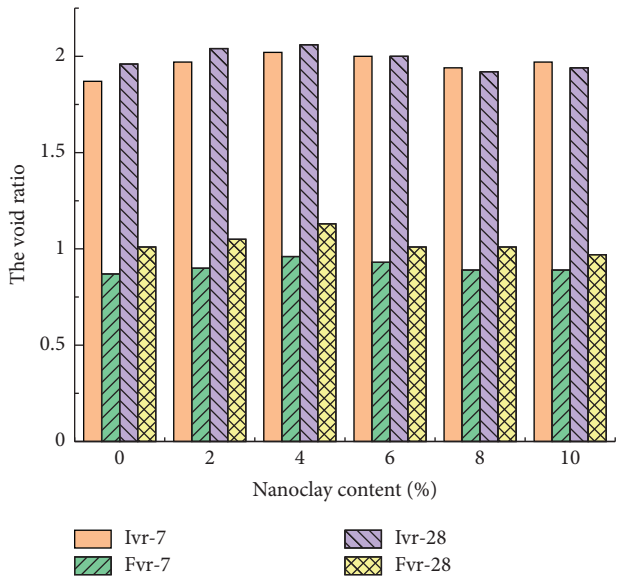


Figure 11: Change in the void ratio of NCS.

In order to investigate the reasons for the different effects of nanoclay content on compression of the samples, SEM tests were performed on 6 groups of NCS samples with different nanoclay content at a curing age of 28 days. The SEM method focuses the electron beam and turns it into an electron probe. Then, the electron probe is scanned by pointing it at the surface of the sample to detect the distribution of particles and pores on the sample, which is then converted into an image [28, 29]. The results of this test method are clear and intuitive. Therefore, it is used to explore the mechanism for the improvement effect of different nanoclay contents on the sample, and the results are shown in Figure 12.

According to the quantitative analysis of microscopic images [30], it is found that small particles in the sample, as shown in Figure 12, increase with increased nanoclay content, and the bonding state between particles shows a state of alternating weakening and strengthening. Specifically, it is weakened in NCS-28-10-2 and NCS-28-10-6 and strengthened in other samples. With the increased nanoclay content, more small particles adhere to the larger particles, and the pore size first increases and then decreases. It increases in NCS-28-10-2 and gradually decreases in other groups of samples.

The above experimental results show that the bonding state of the sample is the best with a nanoclay content of 4%; the filling effect is good with a content of 8% and 10%; both the bonding state and filling effect of the sample are poor with a nanoclay content of 2%.

*4.3. Compression Modulus-Pressure Analysis.* The values of $a_{1\text{-}2}$ for NCS-7 and NCS-28 are deduced according to formula (5), as shown in Figures 13 and 14.

As shown in Figure 13, with the increased nanoclay content, the value of $a_{1\text{-}2}$ of the sample first increases, then decreases, then increases, and finally decreases. The coefficient of compressibility increases with a nanoclay content of 2%, but decreases with other contents. The value of $a_{1\text{-}2}$ of the sample is smaller with a nanoclay content of 4% and 10%, as 1.571 $MPa^{-1}$ and 1.554 $MPa^{-1}$, respectively. It is shown that the compressibility of the sample can be well improved with a nanoclay content of 4% and 10%.

As shown in Figure 14, with the increased nanoclay content, the coefficient of compressibility of the sample first decreases, then increases, then decreases, and finally increases. The minimum value is 0.467 $MPa^{-1}$ with a nanoclay content of 8%. At this time, NCS changes from high- to medium-compressibility soil. Second, the coefficient of compressibility is smaller with a nanoclay content of 4%, which is 0.727 $MPa^{-1}$. It is shown that the compressibility of the sample can be well improved with a nanoclay content of 8% and 4%. This may be due to the combined effects of the physical filling and chemical bonding effects of nanoclay, which causes its compression amount to fluctuate up and down when the content of nanoclay is different.

*Es* values for NCS-7 and NCS-28 are obtained according to formula (4), and *Es-p* diagrams are plotted, as shown in Figures 15 and 16.

As can be seen from Figure 15, the change of *Es* of a single sample shows a concave trend. The minimum values of *Es* are all at a consolidation pressure of 200 kPa. When the consolidation pressure is between 100 kPa and 200 kPa, *Es* of the sample increases with a nanoclay content of 4%, 8%, and 10%, but decreases with a content of 2%. When the pressure is between 400 kPa and 1600 kPa, the addition of nanoclay mainly reduces *Es* of the sample.

As can be seen from Figure 16, the changing trend of *Es* of a single sample shows a concave type. The minimum values of *Es* are all at the consolidation pressure of 400 kPa. The main reason for this phenomenon is that the sample reaches the limit when the consolidation pressure is 400 kPa, and the internal particles are destroyed, resulting in larger pores; as the consolidation pressure continues to increase, the damaged particles are forced to squeeze each other so that the pores become smaller. When the consolidation pressure is less than 800 kPa, the addition of nanoclay can improve *Es*, and when the nanoclay content is 4% and 8%, the improvement effect is the best; when the consolidation pressure is greater than or equal to 800 kPa, the addition of nanoclay can decrease *Es* of the sample. The above test results show that the improvement effect of nanoclay content on *Es* of the sample is related to consolidation pressure. When the consolidation pressure is greater than or equal to 800 kPa, the addition of nanoclay will reduce *Es* of the sample; when the pressure is less than 800 kPa and the sample is at a different curing age, the improvement effect of nanoclay on *Es* is different. By comprehensive comparison, when the consolidation pressure is between 12.5 kPa and 800 kPa with a nanoclay content of 4%, the comprehensive improvement effect on the consolidation characteristics is better.

## 5. Compression Amount Prediction

*5.1. Compression Amount Prediction of CCS.* Compression prediction is based on a combination of the constitutive

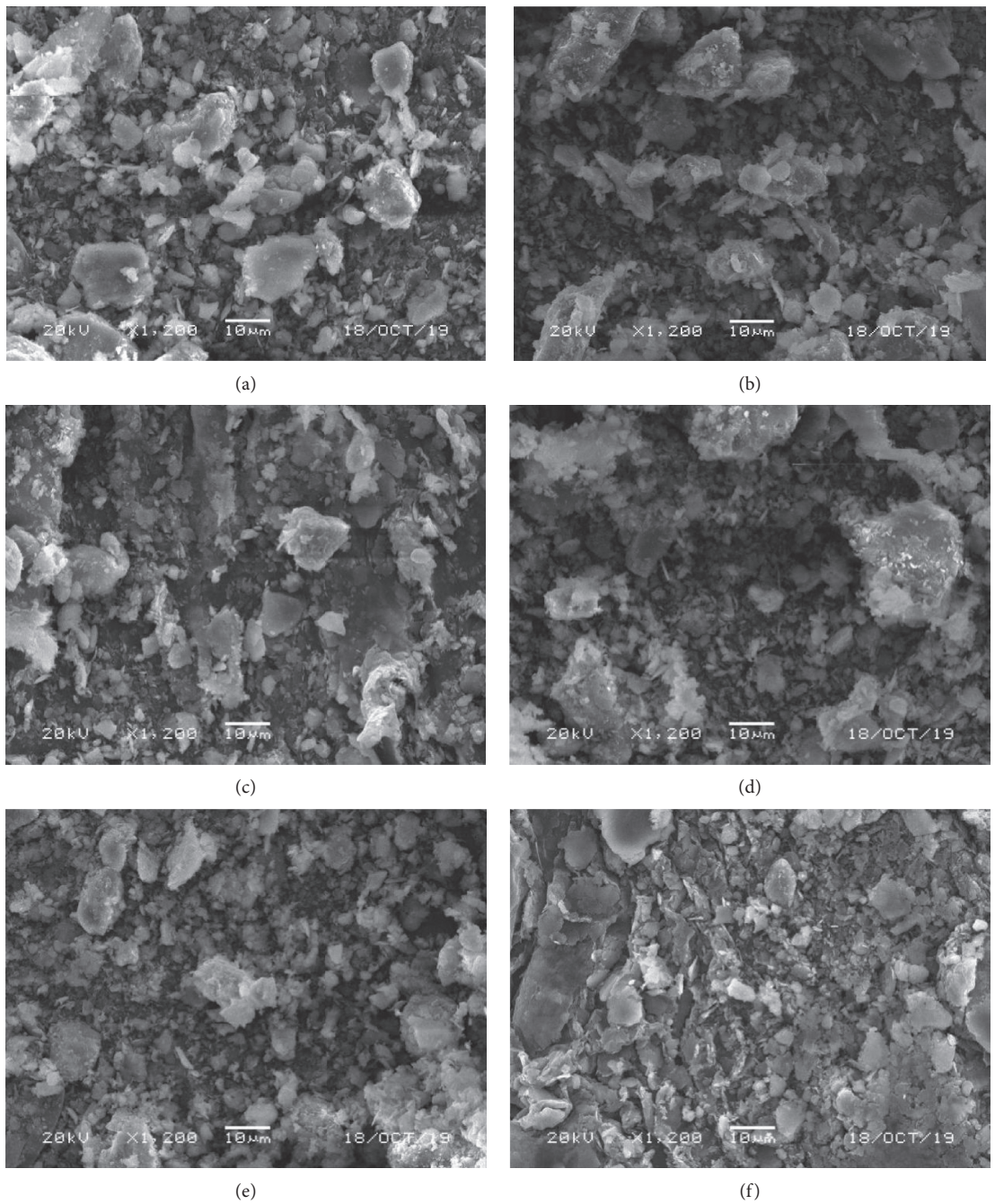


Figure 12: Microstructure of nano-modified cement soil: (a) NCS-28-10; (b) NCS-28-10-2; (c) NCS-28-10-4; (d) NCS-28-10-6; (e) NCS-28-10-8; (f) NCS-28-10-10.

model, consolidation theory, and finite element method for theoretical prediction, or according to the observed trend of the settlement value, to find a mathematical model that fits the trend and performs the reasonable prediction [31, 32]. With the first method, we need to know the stress-strain relationship, boundary conditions, and coefficient of permeability of the sample to derive a mathematical model [33]. These data are relatively easy to measure in the laboratory, but measured data are quite different from actual engineering situations which need further study before it can be popularized and applied. The second method is a prediction based on field data: the settlement data observed in the field are sorted out, the changing trend is analyzed, and the function that can express the changing trend is found and fitted to complete the settlement prediction [34]. This method is simple to operate and has high practicability. Many studies have been conducted based on this method and expanded it from a simple hyperbolic and exponential model [35] to a logical, dynamic, and combinatorial model [36]. Since the *d-p* curves of the CCS and NCS samples in this study are both in the shape of "S," the traditional hyperbolic and exponential models are not well-fitting.

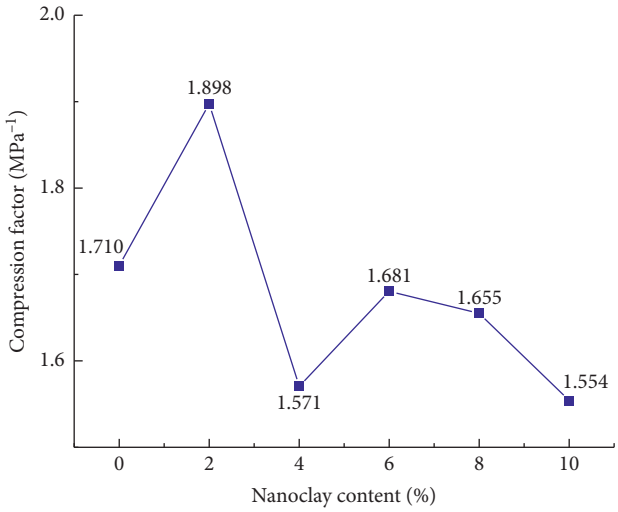


Figure 13: $a_{1\text{-}2}$ of NCS-7 of different nanoclay content.

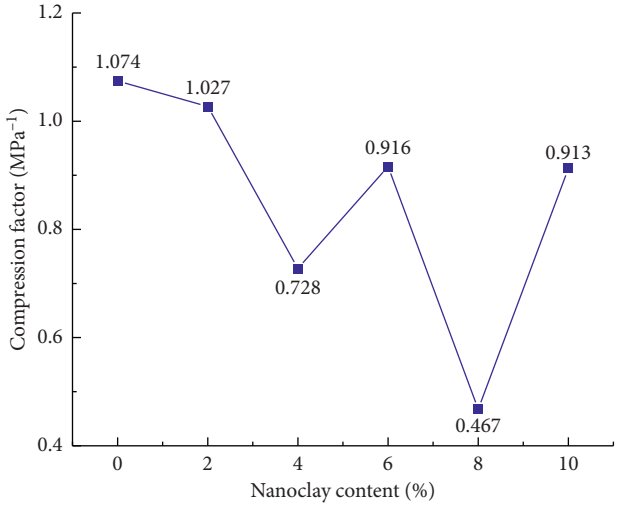


Figure 14: $a_{1\text{-}2}$ of NCS-28 of different nanoclay content.

Consider establishing a new model to better fit the *d*-*p* curve in this experiment.

The second method is used to predict the compression amount. The specific steps are as follows:

(1) Determine the trend line characteristics: the compression pressure curves of CCS and NCS samples were analyzed. It was found that they have the same trends and characteristics; both are "S" type curves. CCS-28-12 was taken as an example, as shown in Figure 17.

As can be seen from Figure 17, the compression amount of the sample is 0 at a consolidation pressure of 0 kPa. The pressure starts from 12.5 kPa, the slope of the curve is greater than 0, and the compression amount increases progressively. Therefore, the minimum value of the compression amount is at 12.5 kPa, and the maximum is 1600 kPa. Because soil particles are incompressible, the volume change of the sample is entirely caused by the pore change, and the compression amount has an upper bound. The curve is concave and convex at first with an "S" type, that is, it slowly increases to a certain value, then increases rapidly, then slowly increases, and then gradually flattens.

(2) Select the function model: the cosine function has an upper bound of 1 and a lower bound of 0, goes through the origin, and increases monotonically between 0 and 1. The composite compression pressure data in the upper and lower bounds and the first derivative are shown in the following formula:

$$y = \cos x. \tag{6}$$

In order to enable the cosine function to simulate the change of the measured data, the first coefficient $s_w$ was increased to improve the upper bound of the function.

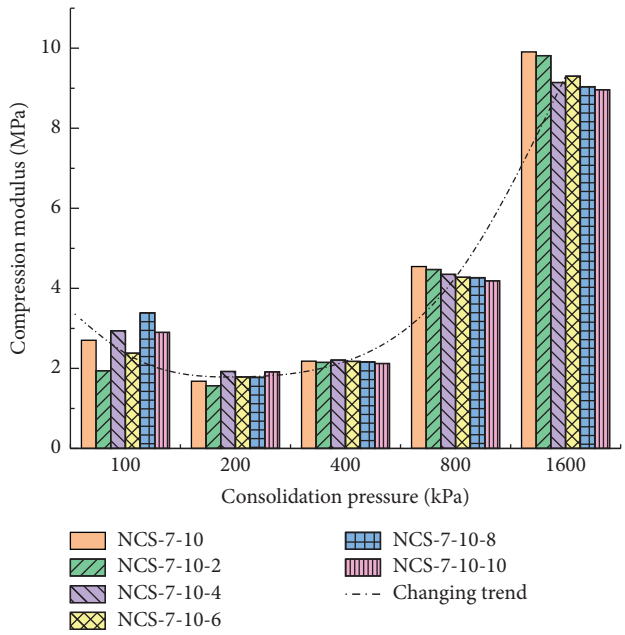


Figure 15: *Es* of NCS-7 with different consolidation pressure.

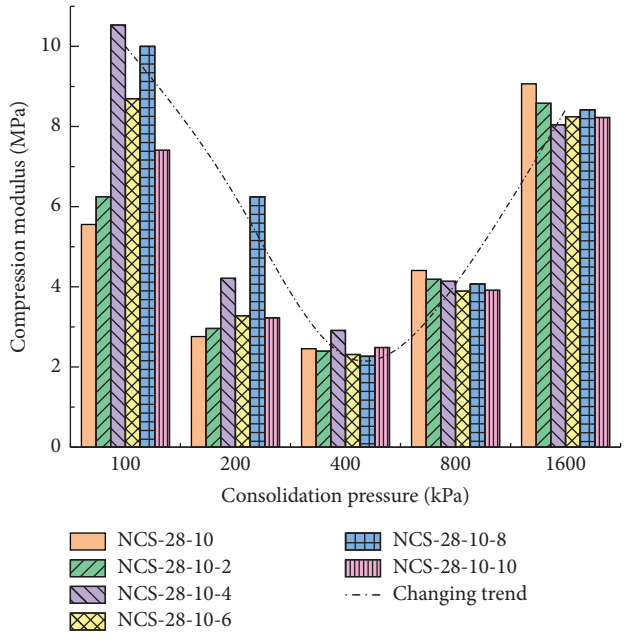


Figure 16: *Es* of NCS-28 with different consolidation pressure.

The power and exponential functions were increased to make the second derivative of the cosine function change to meet the change requirements of the "S" type, to form the cosine-power function-exponential model, as shown in the following formula:

$$s = s_w \cos^k \frac{\pi e^{-bx}}{2}, \tag{7}$$

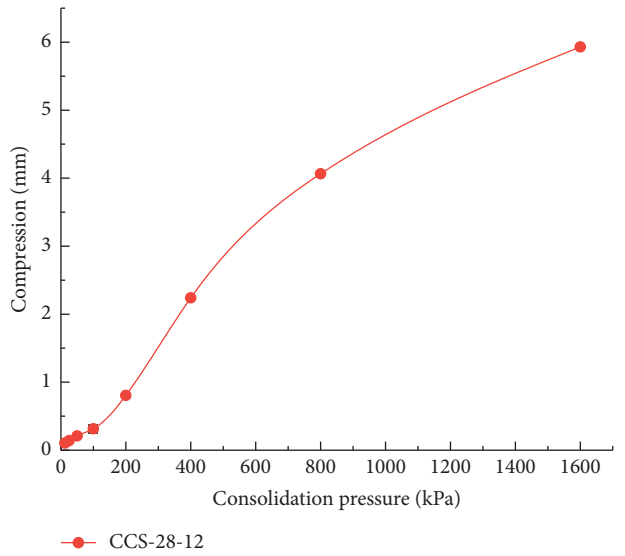


Figure 17: *d-p* curve of CCS-28-12.

where $s$ represents the required amount of compression, $s_w$ represents the upper bound, and $k$ and $b$ are constants.

(3) Conduct function fitting: function fitting was performed in Origin software, and the results are shown in Figure 18.

As shown in Figure 18, the fitted curves pass the measured data points with better fitting effect. Therefore, they can be used to predict the compression of the sample and solve the parameters in the model.

(4) Solve the parameters: Origin software was used to fit the model to convergence, and the values of $s_w$, $k$, and $b$ with different cement content were obtained, as shown in Table 9.

The fitting accuracy $R^2$ of different cement content in Table 9 can reach 0.99, with better fitting result. Therefore, formula (7) can be used to fit the measured value of the compression pressure of CCS samples. After substituting the data of $s_w$ in Table 10 into formula (7), the compression pressure prediction models of CCS samples with a cement content of 10%, 12%, 14%, 16%, 18%, and 20% can be obtain obtained, respectively.

Because the water content of the sample in this test was 80%, the cement content was between 10% and 20%, and the consolidation pressure was between 12.5 kPa and 1600 kPa; formula (8) only had high accuracy for CCS samples that met these conditions.

(5) Verify fitting results: since the compression amount of the sample at a consolidation pressure between 12.5 kPa and 50 kPa was greatly affected by the preparation method, the test results were prone to deviation. Therefore, in the process of verifying

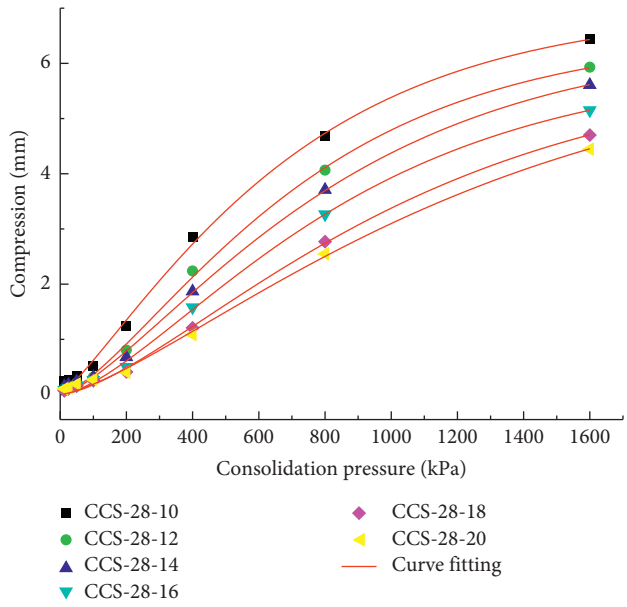


Figure 18: Fitting results with different consolidation pressure.

Table 9: $s_w$, $k$, and $b$ values with different cement content.

| Cement content | 10% | 12% | 14% | 16% | 18% | 20% |
|---|---|---|---|---|---|---|
| $s_w$ | 6.997 | 6.533 | 6.463 | 6.002 | 6.000 | 6.228 |
| $k$ | 1.216 | 1.457 | 1.436 | 1.560 | 1.528 | 1.406 |
| $b$ | 0.000908 | 0.000914 | 0.000802 | 0.000801 | 0.000657 | 0.000538 |

Table 10: $s_w$, $k$, and $b$ values with different nanoclay content.

| Nanoclay content (%) | $s_w$ | $k$ | $b$ |
|---|---|---|---|
| 4 | 6.105 | 1.74375 | 0.00116 |

fitting results, the compression amount at a consolidation pressure between100 kPa and 1600 kPa is mainly verified.

The $x$ values of 100, 200, 400, 800, and 1600 were substituted into formula (7), respectively, and the predicted values of compression of the sample with different cement content were obtained.

Consolidation tests were performed on six groups of CCS samples at a curing age of 28 days and cement content of 10%, 12%, 14%, 16%, 18%, and 20%. The compression value corresponding to the consolidation pressure at each level was taken as the measured value, as shown in Table 11.

As shown in Table 11, the standard deviations are mostly less than 0.05, indicating that the predicted values are closer to the measured values with better fitting results.

### 5.2. Compression Prediction of NCS

*5.2.1. Function Fitting.* The study found that the $d$-$p$ curves of NCS and CCS samples have the same trend and characteristics, both of which are "S"-shaped curves, and when the nanoclay content is 4%, the compression modification effect on CCS is better. Therefore, a compression prediction model was established for NCS samples with a nanoclay content of 4%. Formula (7) was used to fit the function in Origin software. The fitting results are shown in Figure 19.

As can be seen in Figure 19, the fitting results slightly deviate at consolidation pressure of 400 kPa and 800 kPa, but better-fitting at other consolidation pressure values. Therefore, it was determined to use this model to predict the compression of the sample and solve the parameters in the model.

*5.2.2. Parameter Solving.* Origin software was used to solve $s_w$, $k$, and $b$, and the values are shown in Table 10.

According to the model parameters in Table 10, the fitting accuracy $R^2$ is 0.99 when the content of nanoclay is 4%, with good fitting effect. Therefore, the data in Table 10 were substituted into formula (7) to calculate the prediction model of the compression amount of NCS samples at a curing age of 28 days with a nanoclay content of 4%, as shown in the following formula:

Table 11: Calculated value corresponding to different consolidation pressure under different cement content.

| Cement content (%) | Numeric type | 100 kPa | 200 kPa | 400 kPa | 800 kPa | 1600 kPa |
|---|---|---|---|---|---|---|
| 10 | Measured value | 0.640 | 1.310 | 2.940 | 4.770 | 6.470 |
| | Predictive value | 0.622 | 1.351 | 2.728 | 4.735 | 6.434 |
| | Standard deviation | 0.0091 | 0.0203 | 0.1061 | 0.0174 | 0.0180 |
| 12 | Measured value | 0.330 | 0.840 | 2.210 | 4.040 | 5.980 |
| | Predictive value | 0.363 | 0.918 | 2.128 | 4.112 | 5.920 |
| | Standard deviation | 0.0163 | 0.0389 | 0.0408 | 0.0360 | 0.0301 |
| 14 | Measured value | 0.290 | 0.740 | 1.980 | 3.810 | 5.630 |
| | Predictive value | 0.313 | 0.790 | 1.849 | 3.695 | 5.616 |
| | Standard deviation | 0.0117 | 0.0250 | 0.0653 | 0.0577 | 0.0071 |
| 16 | Measured value | 0.250 | 0.570 | 1.550 | 3.260 | 5.170 |
| | Predictive value | 0.224 | 0.611 | 1.540 | 3.267 | 5.151 |
| | Standard deviation | 0.0131 | 0.0207 | 0.0048 | 0.0036 | 0.0095 |
| 18 | Measured value | 0.200 | 0.490 | 1.160 | 2.770 | 4.710 |
| | Predictive value | 0.179 | 0.485 | 1.236 | 2.743 | 4.706 |
| | Standard deviation | 0.0105 | 0.0025 | 0.0378 | 0.0136 | 0.0019 |
| 20 | Measured value | 0.200 | 0.460 | 1.140 | 2.610 | 4.480 |
| | Predictive value | 0.188 | 0.475 | 1.147 | 2.503 | 4.454 |
| | Standard deviation | 0.0059 | 0.0075 | 0.0037 | 0.0537 | 0.0129 |

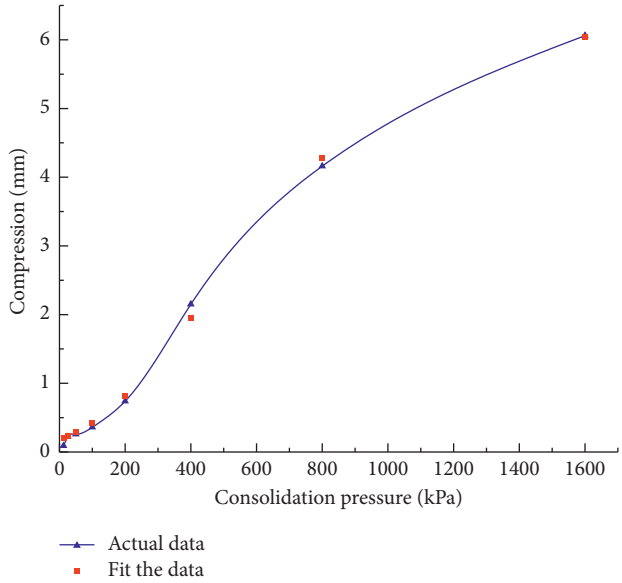


Figure 19: Fitting results with different consolidation pressure.

Table 12: Value of different consolidation pressure.

| Numeric type | 100 kPa | 200 kPa | 400 kPa | 800 kPa | 1600 kPa |
|---|---|---|---|---|---|
| Measured value | 0.25 | 0.77 | 2.19 | 4.13 | 5.94 |
| Predictive value | 0.28 | 0.84 | 2.16 | 4.26 | 5.79 |
| Standard deviation | 0.02 | 0.03 | 0.02 | 0.06 | 0.08 |

$$s = 6.105 \cos^{1.74375} \frac{\pi e^{-0.00116x}}{2}. \quad (8)$$

*5.2.3. Verification of Fitting Results.* The compression amount at a consolidation pressure between 100 kPa and 1600 kPa was verified. The $x$ values of 100 kPa, 200, 400, 800, and 1600, were substituted into the formula. The predicted value of the compression amount of NCS samples at a curing age of 28 days with a nanoclay content of 4% was obtained.

Consolidation tests were performed on NCS samples at a curing age of 28 days with a nanoclay content of 4%. The compression pressure data were obtained. The compression amount corresponding to the consolidation pressure at each level was measured. The predicted value of compression was compared with the measured value, as shown in Table 12.

As shown in Table 12, the standard deviation is smaller with a maximum value of 0.08, indicating that the prediction result of formula (8) is better.

## 6. Conclusions and Discussions

*6.1. Conclusions*

(1) There is a linear interval in the improvement effect of the increment of cement content on the compression of CCS. In this test, cement content in this interval is between 12% and 18%. The improvement effect on the compression amount, compressibility, and compression modulus of CCS is better with a cement content of 18%.

(2) The improvement effect of nanoclay content on the compressibility of the sample is greatly affected by the curing age. When the nanoclay content is 4% and 8%, the improvement effect is better; when the nanoclay content is 2%, the improvement effect is poor. When the consolidation pressure is between 100 kPa and 800 kPa, NCS with a nanoclay content of 4% is preferred.

(3) Microscopic test results show that adhesion is better with a nanoclay content of 4%, and the filling effect is better with a nanoclay content of 8%.

(4) A cosine-power function-exponential model is proposed to fit the measured data, and the fitting effect is better. And, establish a model to predict the compression of CCS and NCS.

*6.2. Discussions.* It should be noted that the samples studied in this study are still limited, and the following topics deserve further in-depth study:

(1) Based on a cement content of 18%, it is necessary to explore the effect of different nanoclay contents on the compressibility of NCS

(2) With nanoclay contents of 4% and 8%, the influences of different cement contents on the consolidation characteristics and improvement effect of NCS could be studied

(3) It is of great importance to optimize the compression prediction model of coastal cement soil and to investigate the model parameters of other cement soil

## Data Availability

The data used to support the findings of this study are available from the corresponding author upon request.

## Conflicts of Interest

The authors declare that they have no conflicts of interest.

## Authors' Contributions

W.Y. and M.D. analyzed the study; N.L. and P.J. wrote and edited the review; D.A. investigated the study; B.Q. and W.W. conceptualized the study.

## Acknowledgments

This research was funded by the National Natural Science Foundation of China (Grant no. 41772311), Zhejiang Provincial Natural Science Foundation of China (Grant no. Q20E080042), Open Research Fund of State Key Laboratory of Geomechanics and Geotechnical Engineering, Institute of Rock and Soil Mechanics, Chinese Academy of Science (Grant no. Z017013), and Scientific Research Projects of Zhejiang Department of Housing and Urban and Rural Construction of China (Grant nos. 2017K179 and 2019K171).

## References

[1] Y. Liu, F.-H. Lee, S.-T. Quek, E. J. Chen, and J.-T. Yi, "Effect of spatial variation of strength and modulus on the lateral compression response of cement-admixed clay slab," *Géotechnique*, vol. 65, no. 10, pp. 851–865, 2015.

[2] N. Li, Y. Zhu, F. Zhang, S. M. Lim, W. Wu, and W. Wang, "Unconfined compressive properties of fiber-stabilized coastal cement clay subjected to freeze-thaw cycles," *Journal of Marine Science and Engineering*, vol. 9, no. 2, p. 143, 2021.

[3] M. Chen, S.-L. Shen, A. Arulrajah, H.-N. Wu, D.-W. Hou, and Y.-S. Xu, "Laboratory evaluation on the effectiveness of polypropylene fibers on the strength of fiber-reinforced and cement-stabilized Shanghai soft clay," *Geotextiles and Geomembranes*, vol. 43, no. 6, pp. 515–523, 2015.

[4] Y. Pan, M. A. Hicks, and W. Broere, "An efficient transient-state algorithm for evaluation of leakage through defective cutoff walls," *International Journal for Numerical and Analytical Methods in Geomechanics*, vol. 45, no. 1, pp. 108–131, 2021.

[5] W. Wang, J. Li, and J. Jun Hu, "Unconfined mechanical properties of nanoclay cement compound modified calcareous sand of the South China Sea," *Advances in Civil Engineering*, vol. 2020, Article ID 6623710, 16 pages, 2020.

[6] Y. Liu, L. Q. He, Y. J. Jiang, M. M. Sun, E. J. Chen, and F.-H. Lee, "Effect of in situ water content variation on the spatial variation of strength of deep cement-mixed clay," *Géotechnique*, vol. 69, no. 5, pp. 391–405, 2019.

[7] E. Mengue, H. Mroueh, L. Lancelot, and R. Medjo Eko, "Physicochemical and consolidation properties of compacted lateritic soil treated with cement," *Soils and Foundations*, vol. 57, no. 1, pp. 60–79, 2017.

[8] Y. Li, Y. Z. Tan, J. Jiang, and C. F. Xia, "Experimental study on the compressibility of cement improved laterite soil," *Applied Mechanics and Materials*, vol. 170–173, pp. 371–374, 2012.

[9] R. Khandelwal, J. Senthilnath, S. N. Omkar, and N. Shivanath, "A novel multiobjective optimization for cement stabilized soft soil based on artificial bee colony," *International Journal of Applied Metaheuristic Computing*, vol. 7, no. 4, pp. 1–17, 2016.

[10] D.-F. Lin and M.-C. Tsai, "The effects of nanomaterials on microstructures of sludge ash cement paste," *Journal of the Air & Waste Management Association*, vol. 56, no. 8, pp. 1146–1154, 2012.

[11] H.-M. Kwon, A. T. Le, and N. T. Nguyen, "Influence of soil grading on properties of compressed cement-soil," *KSCE Journal of Civil Engineering*, vol. 14, no. 6, pp. 845–853, 2010.

[12] E. Mengue, H. Mroueh, L. Lancelot, and R. Medjo Eko, "Evaluation of the compressibility and compressive strength of a compacted cement treated laterite soil for road

application," *Geotechnical and Geological Engineering*, vol. 36, no. 6, pp. 3831–3856, 2018.

[13] N. Li, Q. Zhu, W. Wang, F. Song, D. An, and H. Yan, "Compression characteristics and microscopic mechanism of coastal soil modified with cement and fly ash," *Materials*, vol. 12, no. 19, Article ID 3182, 2019.

[14] K. H. Lee and S. Lee, "Mechanical properties of weakly bonded cement stabilized kaolin," *KSCE Journal of Civil Engineering*, vol. 6, no. 4, pp. 389–398, 2002.

[15] S. Çelik, "An experimental investigation of utilizing waste red mud in soil grouting," *KSCE Journal of Civil Engineering*, vol. 21, no. 4, pp. 1191–1200, 2016.

[16] J. Mao, Q. Wu, F. Tao, W. Xu, T. Hong, and Y. Dong, "Facile fabrication of porous $BiVO_4$ hollow spheres with improved visible-light photocatalytic properties," *RSC Advances*, vol. 10, no. 11, pp. 6395–6404, 2020.

[17] B. Funk, D. Göhler, B. Sachsenhauser et al., "Impact of freeze-thaw weathering on integrity, internal structure and particle release from micro- and nanostructured cement composites," *Environmental Science: Nano*, vol. 6, no. 5, pp. 1443–1456, 2019.

[18] W. Wang, C. Zhang, N. Li, F. Tao, and K. Yao, "Characterisation of nano magnesia-cement-reinforced seashore soft soil by direct-shear test," *Marine Georesources & Geotechnology*, vol. 37, no. 8, pp. 989–998, 2019.

[19] K. Yao, D. An, W. Wang, N. Li, C. Zhang, and A. Zhou, "Effect of nano-MgO on mechanical performance of cement stabilized silty clay," *Marine Georesources & Geotechnology*, vol. 38, no. 2, pp. 250–255, 2020.

[20] W. Wang, Y. Li, K. Yao, N. Li, A. Zhou, and C. Zhang, "Strength properties of nano-MgO and cement stabilized coastal silty clay subjected to sulfuric acid attack," *Marine Georesources & Geotechnology*, vol. 38, no. 10, pp. 1177–1186, 2020.

[21] K. Yao, W. Wang, N. Li, C. Zhang, and L. Wang, "Investigation on strength and microstructure characteristics of Nano-MgO admixed with cemented soft soil," *Construction and Building Materials*, vol. 206, pp. 160–168, 2019.

[22] M. A. Langaroudi and M. Yaghoub, "Effect of nano-clay on the freeze–thaw resistance of self-compacting concrete containing mineral admixtures," *European Journal of Environmental and Civil Engineering*, pp. 1–20, 2019.

[23] S. A. Shakrani, A. Ayob, and M. A. Ab Rahim, "A review of nanoclay applications in the pervious concrete pavement," *AIP Conference Proceedings*, vol. 1885, no. 1, Article ID 020049, 2017.

[24] M. H. Niaki, A. Fereidoon, and M. G. Ahangari, "Experimental study on the mechanical and thermal properties of basalt fiber and nanoclay reinforced polymer concrete," *Composite Structures*, vol. 191, pp. 231–238, 2018.

[25] A. J. Choobbasti and S. S. Kutanaei, "Microstructure characteristics of cement-stabilized sandy soil using nanosilica," *Journal of Rock Mechanics and Geotechnical Engineering*, vol. 9, no. 5, pp. 981–988, 2017.

[26] S. Y. Zhang, Y. F. Fan, H. Y. Luan, and Y. Chan, "Effect of disperse condition of nano-clay on behavior of cement paste," *Journal of Building Materials*, vol. 16, no. 2, pp. 197–202, 2013.

[27] GB/T 50123-2019, *Standard for Geotechnical Test Methods*, China Planning Press, Beijing, China, 2019.

[28] K. M. Ewa, "Sem investigations of clay subjected to 200 MPa pressure," *Procedia Earth and Planetary Science*, vol. 15, pp. 791–796, 2015.

[29] X. L. Wang, S. X. Yan, and H. Q. Wen, "Experimental analysis on microstructure and mineral composition of Jurassic soft rock in Shajihai mining area of Xinjiang," *Applied Mechanics and Materials*, vol. 353–356, pp. 24–27, 2013.

[30] L. Z. Zhang, R. L. Hu, X. Q. Li, and Y. B. Zhang, "Soil microstructure quantitative analysis system and its application," *Geological Science and Technology Information*, vol. 27, no. 1, pp. 108–112, 2008.

[31] X. H. Tu, Z. L. Wang, and Z. M. Liang, "Study on application of modified Weibull model to settlement prediction of foundation," *Rock and Soil Mechanics*, vol. 26, no. 4, pp. 621–628, 2005.

[32] Z. Fan, Y. Zhang, H. A. Wu, Y. Kang, and D. Jiang, "Subsidence monitoring and prediction of high-speed railway in Beijing with multitemporal TerraSAR-X data," in *Proceedings of the MIPPR 2017: Multispectral Image Acquisition, Processing, and Analysis*, Xiangyang, China, February 2018.

[33] H. D. Liu, L. D. Li, S. L. Zhao, and S. H. Hu, "Complete stress–strain constitutive model considering crack model of brittle rock," *Environmental Earth Sciences*, vol. 78, p. 629, 2019.

[34] Q. Yang, W.-m. Leng, S. Zhang et al., "Long-term settlement prediction of high-speed railway bridge pile foundation," *Journal of Central South University*, vol. 21, no. 6, pp. 2415–2424, 2014, in Chinese.

[35] G. W. Mang, "Application of exponential curve model in subgrade settlement prediction," *Value Engineering*, no. 50, pp. 81–83, 2014.

[36] T. P. Chang, J. Y. Shih, and K. M. Yang, "Neural network prediction of the high-fill road foundation settlement of highway," *Journal of Engineering Geology*, vol. 12, no. 4, pp. 427–431, 2004.

Hindawi
Advances in Materials Science and Engineering
Volume 2021, Article ID 5585891, 12 pages
https://doi.org/10.1155/2021/5585891

*Research Article*

# Analysis of the Influence of SBS Content and Structure on the Performance of SBS/CR Composite Modified Asphalt

**Yafeng Gong, Yunze Pang, Fayang Li, Weidong Jin, Haipeng Bi, and Yulin Ma**

*College of Transportation, Jilin University, Changchun 130025, China*

Correspondence should be addressed to Weidong Jin; jinwd@jlu.edu.cn

Received 10 February 2021; Revised 1 April 2021; Accepted 15 April 2021; Published 23 April 2021

Academic Editor: Qinglin Guo



The performance of asphalt can be improved by adding styrene-butadiene-styrene (SBS) copolymer and crumb rubber (CR). This paper investigated the influence of the structure and content of styrene-butadiene-styrene (SBS) copolymer on the properties of SBS/CR modified asphalt (SBS/CRMA). These SBS/CRMA were prepared by mixing 90# matrix asphalt, 60 mesh CR powder, and SBS copolymers with two molecular structures, which were tested for penetration, softening point, ductility, and rheology. The complex modulus, phase angle, rutting factor, storage modulus, and dissipation modulus of SBS/CRMA were analyzed with the 64°C frequency sweep tests. The results revealed that the content and structure had significant impacts on the performances of SBS/CRMA, and the advantages of SBS polymer network structure in the modified asphalt system cannot be reflected when the amount of SBS was small. Meanwhile, the high-temperature stability, low-temperature tensile resistance, temperature sensitivity, and viscoelasticity of rubberized asphalt were further improved by adding a moderate amount of SBS copolymer. Furthermore, the properties of SBS/CRMA were better as the contents of SBS increased when the type of SBS doped was the same. The effect of modification improved by star-shaped SBS copolymer addition was more than that improved by linear SBS copolymer addition. As a conclusion, the content of 4 wt% star-shaped SBS and 20 wt% CR powder-modified 90# matrix asphalt has the best modification effect with the comparison of other groups.

## 1. Introduction

Nowadays, the demand for the performances of asphalt with the rapid development of road traffic construction is increasing. At the same time, the number of used tires is increasing with the increase in the number of motor vehicles [1]. As a nondecomposing material, the accumulation of scrap tires has a serious negative impact on the environment [2, 3]. Shredding waste tires to produce crumb rubber (CR) and then blending CR powder with petroleum asphalt can not only improve the performance of the asphalt but also solve the environmental pollution problem caused by the rubber [4].

After the asphalt is modified with CR powder, the swollen CR powder forms a stable network structure in the asphalt, which can increase the consistency of the asphalt and improve the rheology of the asphalt [5, 6]. In addition, the introduction of high molecular weight macromolecules into the matrix asphalt composed of low molecular weight small molecules can greatly improve the high-temperature deformation resistance of the asphalt [7]. In the application of rubber asphalt, the CR powder mesh can also be selected according to different types of asphalt pavements. Meng et al. [8] found that the low mesh CR powder was better for the low-speed driving region, and the high mesh CR powder was suitable for the high-speed driving region. However, there are still some problems with CR powder as asphalt modifier, such as the poor compatibility of CR powder, and asphalt leads to the unstable performance of rubber asphalt and the agglomeration of CR powder when the content is too high. In order to ensure that CR powder and asphalt can be mixed homogeneously, the amount of CR powder must be strictly controlled during the preparation of modified asphalt. Li et al. [9] proposed that the physical performances were optimal when the CR contents were 20–25 wt% for SK 90# matrix asphalt and 22–26 wt% for SK 70# matrix asphalt.

Therefore, there is a great need for additional modifiers to prepare composite modified asphalt to compensate for these limiting factors to enhance the high- and low-temperature performance, temperature sensitivity, and rheology of rubber asphalt [10].

There are many polymers used for asphalt modification. Among them, styrene-butadiene-styrene (SBS) copolymer is the preferred one with the superb properties of elasticity and strength which can improve the high-temperature and low-temperature performance of asphalt at the same time [11, 12]. Kök et al. [13] compared the performance of CR modified asphalt (CRMA) with SBS modified asphalt (SBSMA), and the results showed that CRMA can achieve the same performance as SBSMA when the dosage of CR reaches twice the dosage of SBS. The modified asphalt with the compound of SBS and rubber not only can improve the elasticity and high-temperature performance of asphalt but also has better comprehensive economic benefits due to the fact that the price of SBS is higher, while the price of CR powder is lower [14].

It can be seen from the above literature that the asphalt modified by SBS and CR powder has a superior research foundation, and some researchers have carried out related research on the composite modification of SBS and CR powder. Qian and Fan [7] blended 20 wt% CR powder with various amounts of SBS and two base asphalts to prepare SBS/CRMA; the performance test results of modified asphalt showed that the increase of SBS content can enhance the elastic properties of modified asphalt, thereby improving its rheology. Jiang et al. [15] evaluated the damping performance of SBS/CRMA, the results showed that SBS improved the integrity of the rubber asphalt system, and the cross-linking reaction of CR and SBS further enhanced the integrity of the modified asphalt system, thereby increasing the damping performance of asphalt. Li et al. [16] studied the thermal-oxidative aging of SBS/CRMA, and the results showed that, during the aging process of modified asphalt, SBS and CR modifiers played an antiaging effect, and SBS/CRMA had excellent antiaging properties. Qian et al. [17] studied the influence of CR powder particle size and SBS structure on the performance of SBS/CRMA, and it was found that larger CR particles were more advantageous in antirutting and antifatigue properties of asphalt, while smaller CR particles were more conducive to improve low-temperature cracking resistance and stability. Through the research mentioned above, it can be known that the complex structure of SBS has different degrees of influence on the modified performance of asphalt, and the influence of its content on the modified asphalt is also different. At the same time, the research of SBS/CRMA is practical and novel in a way, but the differences in SBS structure and dosage influencing the performance of SBS/CRMA have not been studied clearly yet. Therefore, in order to solve this problem, this article has conducted an in-depth study on SBS/CRMA with different structures and content of SBS modifiers. In this paper, various contents of SBS with two types of structure and CR powder were used to modify the matrix asphalt by mixing and high-speed shearing. The high-temperature stability, temperature sensitivity, viscoelasticity, and antideformation ability of all asphalt samples were studied by conventional (penetration, ductility, and softening) tests and dynamic shear rheological tests, and then the effects of the structure and content of SBS copolymers on SBS/CRMA were conducted by analyzing the test results.

## 2. Materials and Methods

*2.1. Materials.* In this study, the 90# base asphalt was supplied by the Maoming Branch of China Petroleum and Chemical Corporation. As per JTG F40-2004 of China, the basic properties of base asphalt are shown in Table 1. CR powder of 60-mesh size was purchased from Sichuan Huayi Rubber Factory. The SBS copolymer was selected as a modifier where the linear SBS was YH792 SBS produced by Yueyang Baling Petrochemical and the star-shaped SBS copolymer was SBS4402 SBS produced by Yanshan Petrochemical.

*2.2. Preparation of Samples.* Firstly, the base asphalt was heated until it flowed fully in the vessel. As the temperature rose to 175°C, 20 wt% CR powder (by weight of base asphalt) was gradually added to the base asphalt and stirred at 1200 rpm for 20 minutes. Then, shearing was continued at a speed of 2500 rpm for 20 minutes when the temperature dropped to 170°C, after which rubberized asphalt (CRMA) was obtained. Secondly, keeping the temperature as a constant, amounts of SBS (1 wt%, 2 wt%, 3 wt%, and 4 wt% by the mass of the base asphalt) and furfural extraction oil (8 wt% by the mass of the base asphalt) were added slowly to the CRMA. Then, the asphalt blends were stirred at 1200 rpm for 30 minutes, and shearing was continued at 5000 rpm for 40 minutes. Finally, the blends were stirred for 1 hour at 170°C and 1000 rpm to obtain SBS/CR powder composite modified asphalt (SBS/CRMA). The sample preparation process is shown in Figure 1. Next, the modified asphalt mixed with 1 wt%, 2 wt%, 3 wt%, or 4 wt% star-shaped SBS was coded as SSA1, SSA2, SSA3, and SSA4, respectively; similarly, the modified asphalt mixed with 1 wt %, 2 wt%, 3 wt%, or 4 wt% linear SBS was coded as LSA1, LSA2, LSA3, and LSA4, respectively.

*2.3. Test Methods.* In this paper, the test content mainly includes penetration, softening point, ductility, and dynamic shear rheology (DSR) test. The experimental instruments used to test asphalt performance indexes mainly include DF-6 asphalt penetration meter, DF-10 softening point meter, SY-1.5D asphalt extensometer, and MCR102 dynamic shear rheometer (as shown in Figure 2). Penetration, softening point, and ductility are the basic performance parameters of road asphalt, which are widely applied to evaluate the high- and low-temperature performance and temperature sensitivity of asphalt. Measurements of penetration (15°C, 25°C, 30°C, 100−g, 5−s, and 0.1 mm), softening point (Ring-and-Ball method), and ductility (5°C) were conducted in accordance with the standard JTG E20-2011.

DSR test was utilized to characterize the rheological properties of asphalt as a viscoelastic material [18].

Table 1: Basic performances of neat asphalt.

| Item | Unit | Standard values | Values |
|---|---|---|---|
| Penetration (25°C, 100 g, 5 s) | 0.1 mm | 80~100 | 84 |
| Penetration index | — | −1.5~1.0 | −1.02 |
| Softening point | °C | ≥45 | 46.0 |
| Dynamic viscosity (60°C) | Pa·s | ≥160 | 178 |
| Ductility (10°C) | cm | ≥20 | >100 |
| Ductility (15°C) | cm | ≥100 | >100 |
| *RTFOT residue* | | | |
| Quality change | % | −0.8~0.8 | −0.112 |
| Residual penetration ratio | % | ≥57 | 62.4 |
| Residual ductility (10°C) | cm | ≥8 | 11.9 |


Figure 1: Mixing and shearing of modified asphalt.


Figure 2: Dynamic shear rheometer (DSR).

Table 2: Penetration test results of asphalt binder.

| Asphalt type | Penetration (0.1 mm) 15°C | 25°C | 30°C | Regression equation | $R^2$ | PI |
|---|---|---|---|---|---|---|
| CRMA | 16.83 | 36.37 | 51.67 | $\lg P = 0.0326T + 0.7391$ | 0.999 | 1.41 |
| SSA1 | 28.80 | 55.23 | 76.90 | $\lg P = 0.0284T + 1.0329$ | 0.999 | 2.40 |
| SSA2 | 28.00 | 52.03 | 71.60 | $\lg P = 0.0271T + 1.0394$ | 0.999 | 2.74 |
| SSA3 | 27.67 | 49.47 | 67.33 | $\lg P = 0.0257T + 1.0557$ | 0.999 | 3.13 |
| SSA4 | 25.37 | 45.60 | 59.13 | $\lg P = 0.0246T + 1.0367$ | 0.998 | 3.45 |
| LSA1 | 25.50 | 54.87 | 76.47 | $\lg P = 0.0298T + 0.9920$ | 0.999 | 2.05 |
| LSA2 | 26.60 | 51.07 | 67.60 | $\lg P = 0.0274T + 1.0160$ | 0.998 | 2.66 |
| LSA3 | 26.37 | 48.17 | 65.73 | $\lg P = 0.0264T + 1.0243$ | 0.999 | 2.93 |
| LSA4 | 22.13 | 42.40 | 55.90 | $\lg P = 0.0253T + 0.9910$ | 0.999 | 3.25 |

According to related researches and comprehensive consideration of the AASHTO asphalt evaluation system, 64°C was adopted as the frequency sweep test temperature in this paper [19–21]. In this paper, the frequency sweep tests were carried out with a diameter of 25 mm and a gap of 1 mm at 64°C, and the frequency domain was 0.1–100 rad/s. Moreover, the resin molds with a diameter of 25 mm and a thickness of 2 mm were used to prepare binder samples. The modified asphalt was poured into the mold after heating to a flow state and then waited until the samples cooled down for the preparation of DSR tests. Through the DSR test, the complex shear modulus ($G^*$) and phase angle ($\delta$) can be directly obtained, and the rutting factor ($G^*/\sin\delta$), storage modulus ($G^* \cdot \cos\delta$), and dissipation modulus ($G^* \cdot \sin\delta$) can also be obtained by calculating these two parameters.

## 3. Results and Discussion

*3.1. Penetration.* Penetration is one of the important indicators of asphalt, which is used to indicate the hardness and consistency of asphalt. The penetration test results of each kind of asphalt binder are listed in Table 2. In the table, the penetrations of 15°C, 25°C, and 30°C were treated by semilogarithm and linearly fitted with the temperature. The obtained linear regression correlation coefficients ($R^2$) are all greater than 0.997, indicating that the fitting results are accurate. The penetration index (PI) was calculated according to the fitting result as in the two following equations:

$$\lg P = AT + K, \tag{1}$$

$$\mathrm{PI} = \frac{20 - 500A}{1 + 50A}, \tag{2}$$

where $\lg P$ is the logarithm of the penetration value measured under different temperature conditions; $T$ is the test temperature (°C); $K$ is the constant term of the regression equation; $A$ is the regression equation coefficient; and PI is the penetration index.

The penetration values of all asphalt samples at 25°C are plotted in Figure 3. It can be seen from the figure that, compared to the CRMA, the penetration of the asphalt was significantly improved after adding SBS to the CRMA. But, comparing the penetration of SBS/CRMA, it can be found

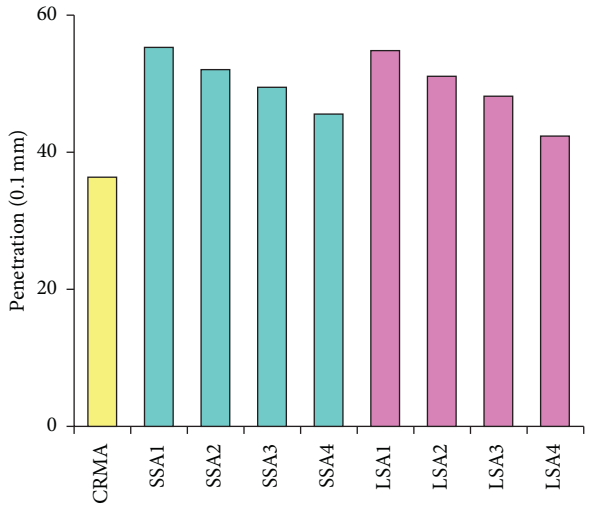


Figure 3: Penetration for each asphalt binder.

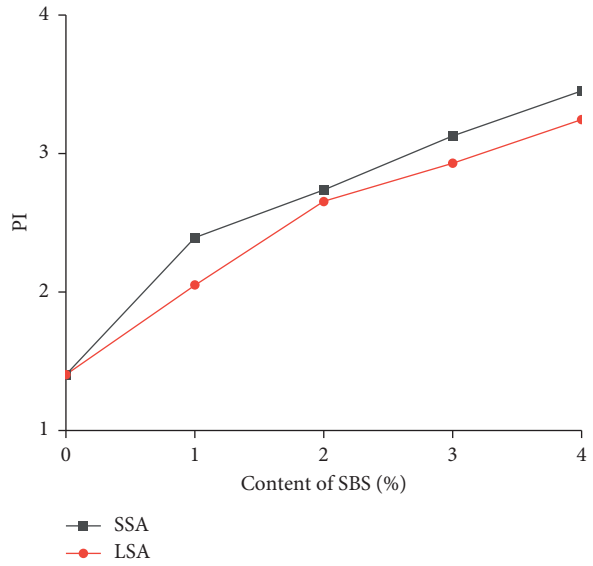


Figure 4: Variation of penetration index (PI) with the SBS contents for modified asphalts.

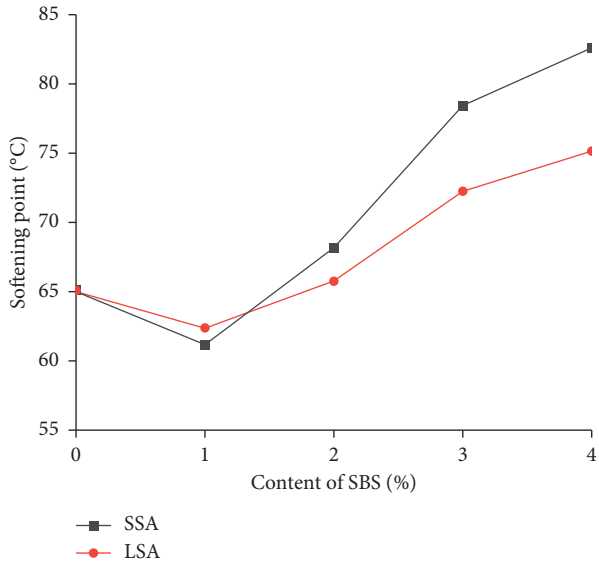


Figure 5: Variation of softening point with the SBS contents for modified asphalts.

that the penetration of SBS/CRMA shows a downward trend with the increase of the amount of SBS. The reason is that SBS is evenly dispersed under the action of high-speed shearing, forming an interconnected network structure. As the content of SBS increases, the viscosity of the asphalt increases and the permeability decreases. In addition, the permeability of SSA was higher than that of LSA when the content of SBS is the same, and the difference in permeability increases with the increase of SBS content.

The variations in PI of modified asphalts with the increase of SBS content for modified asphalts are shown in Figure 4. In the figure, all asphalt samples were divided into two groups of LSA and SSA according to the different types of SBS, which were added into matrix asphalt. The PI of CRMA was the point where the SBS content was 0 wt%. It can be seen in Figure 3 that the PI of SSA and LSA increases with the increase of the amount of modifier. The PI of the two modified asphalts increases significantly when the content of SBS is 0-1 wt%, indicating that the addition of SBS can reduce the temperature sensitivity of the asphalt. Moreover, the penetration index of SSA is generally higher than that of LSA, and this shows that the temperature sensitivity of modified asphalt mixed with star-shaped SBS is lower than that of modified asphalt mixed with linear SBS.

*3.2. Softening Point.* The softening point can reflect the high temperature stability and viscosity of asphalt. The relationship between the softening point of SBS/CRMA and the SBS content is shown in Figure 5. The softening points of the two modified asphalts show a downward trend when the SBS content is 0 wt%-1 wt%. The main reason is that the SBS copolymer and the asphalt cannot be completely miscible. The compatibility of the two is essentially a physical blend; that is, the SBS is fully sheared and stirred evenly in the asphalt with the help of a high-speed shearing machine. Therefore, the SBS is more fully sheared and broken into smaller particles to be dispersed in the asphalt when the blending amount of SBS is 1 wt%. The further reduction in the particle size of SBS leads to a lower softening point of SSA1 and LSA1 than CRMA.

Meanwhile, the softening point of LSA is higher than that of SSA when the amount of SBS is small. From the perspective of SBS structure, it is because linear SBS has better compatibility with asphalt, and linear SBS is easier to form a stable system than star-shaped SBS when the amount of SBS is lower. As the content of SBS continues to increase, the softening point of SBS/CRMA shows an overall upward trend, and the softening point of SSA is higher. It can be concluded that the star-shaped SBS can form a stronger network structure with the asphalt, which helps to stabilize

the asphalt in the high-temperature flow state, so the effect of improving the high-temperature stability of the asphalt is more significant.

*3.3. Ductility.* Ductility is an important index to characterize the plasticity of asphalt, where temperature has a great influence on it [22, 23]. In this paper, the ductility of 5°C was used to evaluate the low-temperature crack resistance of asphalt under external force. Figure 6 shows the relationship between the ductility of SBS/CRMA and the amount of SBS. It can be found that the ductility of asphalt binders increases when the amount of SBS increases whatever the type of SBS was chosen. Meanwhile, LSA outperforms SSA in the ductility. The reason is that SBS and CR powder adsorb the surrounding asphalt to form a cross-linked network, which increases the intermolecular force, thereby effectively offsetting and dispersing the stress and improving the ductility of the asphalt.

*3.4. Frequency Sweep Test.* In this paper, the high-temperature rheological properties of modified asphalt were evaluated by analyzing the results of DSR frequency sweep test. The temperature condition of the test was 64°C, and the frequency domain was 0.1–100 rad/s. Through this test, the complex shear modulus ($G^*$) and the phase angle ($\delta$) of all asphalt binders can be directly obtained. Between them, $G^*$ measures the overall ability to resist deformation under dynamic shear loading, and the variation curves of $G^*$ in the frequency domain of 0.1–100 rad/s are shown in Figure 7. From the longitudinal comparison in the figure, it can be found that the complex modulus of LSA1 and SSA1 is lower than that of CRMA. This is mainly due to the SBS content at a low stage that affects the softening point of asphalt binders negatively, and the results of these two asphalt samples are softer than CRMA at 64°C. The lower softening point of LSA1 and SSA1 indicates that the cohesion between internal components was weaker than CRMA; thus, as for LSA1 and SSA1, the ability to resist external deformation was weaker then. As the SBS content continues to increase, the $G^*$ value of the asphalt binder increases, indicating that a certain amount of SBS can effectively improve the antideformation ability of the asphalt.

$\delta$ is the ratio of the elastic component to the viscous component in the asphalt. The greater $\delta$, the more the viscous component in the asphalt, that is, the more the unrecoverable part of the deformation and the easier the asphalt will be deformed [24]. The variation curves of $\delta$ in the frequency range of 1–10 rad/s for each asphalt sample are shown in Figure 8. The loading frequency of 10 rad/s is equivalent to the simulated high-speed driving speed of 60 km/h. It can be found in Figure 8 that as the loading frequency increases, $\delta$ of all asphalt samples shows a downward trend, indicating that, under the action of high-speed vehicle load, each asphalt binder has more elastic components and stronger resistance to permanent deformation.

Meanwhile, $\delta$ of the LSA and SSA asphalt samples gradually decreased with the increase of the SBS content.

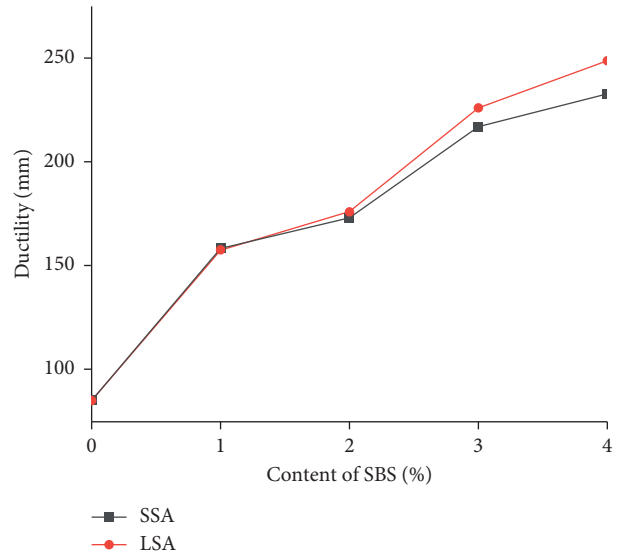


Figure 6: Variation of ductility with the SBS contents for modified asphalts.

The main reason for this change is that the increase of the SBS content increases the elastic component of the modified asphalt, and $\delta$ decreases accordingly. Furthermore, the phase angle of SSA is smaller than the phase angle of LSA when the SBS content is the same. This is mainly due to the internal cross-linking of the star-shaped SBS to form a dense three-dimensional network structure with greater strength, which is more effective to improve the elasticity of the modified asphalt. From comprehensive analysis of Figures 7 and 8, SSA4 shows the maximum complex modulus value and the minimum phase angle value among all asphalt samples, indicating that its antideformation ability and antirutting ability are the best.

The rutting factor ($G^*/\sin\delta$) is an important index to evaluate the high-temperature performance of asphalt, and the larger the rutting factor, the stronger the resistance of asphalt to rutting [25, 26]. The change curves of $G^*/\sin\delta$ with frequency for all asphalt samples are shown in Figure 9. In the figure, it can be seen that the change trend of $G^*/\sin\delta$ is similar to that of $G^*$. By intragroup comparison of the change curves of LSA and SSA, it can be found that $G^*/\sin\delta$ of LSA and SSA increased with the increase of the content of SBS in the range of 0.1–100 rad/s. The $G^*/\sin\delta$ curves of LSA1 and SSA1 in the figure are slightly lower than CRMA, indicating that $G^*/\sin\delta$ of asphalt binders have not been improved when the SBS content was 1 wt%. This result should be attributed to the fact that when the SBS content is low, the new phase composed of a small amount of SBS and CR powder prevented the degradation and dispersion of the CR powder in the asphalt, reducing the effect of CR on improving the elasticity of modified asphalt. Therefore, although SBS can increase the stiffness of asphalt, the increase of asphalt stiffness caused by SBS cannot make up for the decrease of rubber asphalt elasticity when the SBS content is low. When the SBS content exceeds 2 wt%, the $G^*/\sin\delta$ curves of LSA and SSA are higher than CRMA, indicating

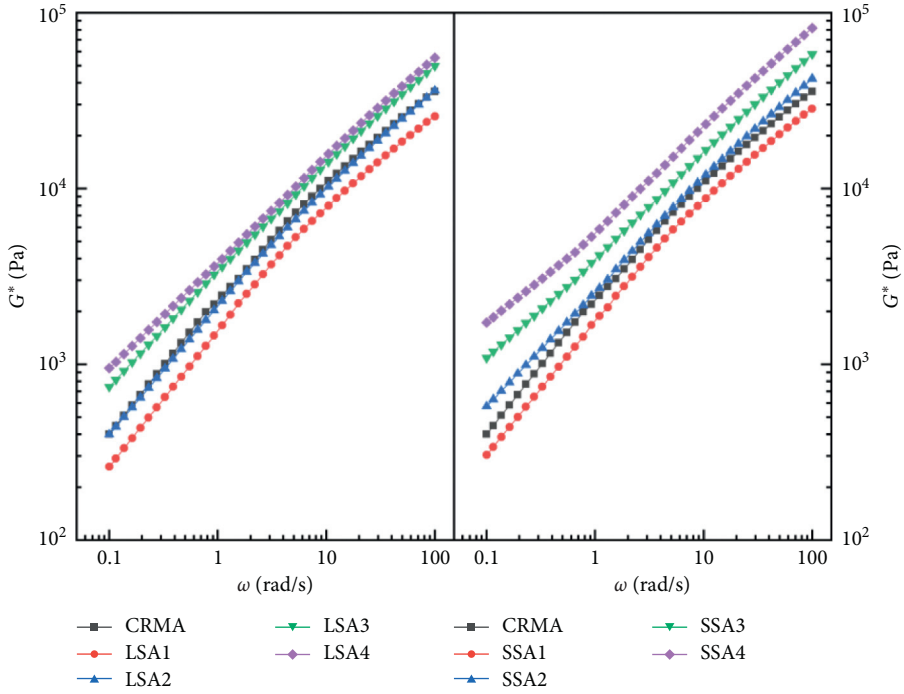


Figure 7: Variation of $G^*$ with the SBS contents for modified asphalts.

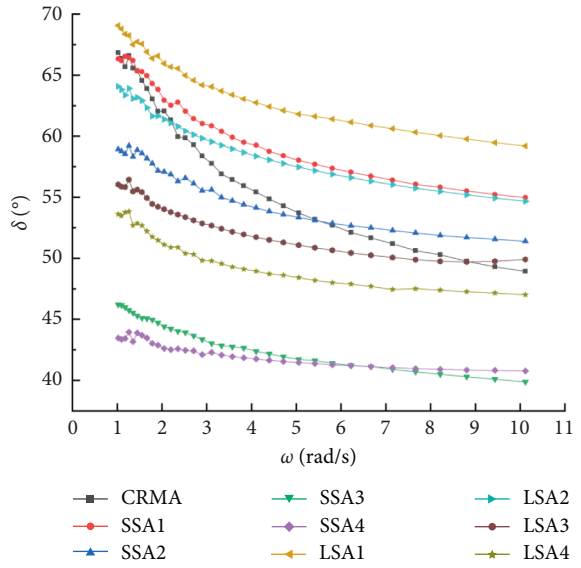


Figure 8: Variation of $\delta$ with the SBS contents for modified asphalts.

that only when the SBS content reaches a certain value can the beneficial modification effect on asphalt be achieved.

Comparing the two sets of asphalt samples of LSA and SSA, it can be found that $G^*/\sin\delta$ of SSA at the same SBS content is higher. Mainly because the star-shaped SBS structure is similar to the polymer cross-linked structure and has greater rigidity, after being dispersed in the asphalt, the modification effect of the asphalt is more obvious. SSA4 has highest $G^*/\sin\delta$ among all asphalt samples, indicating that it has the best high-temperature performance and antirutting ability. It can be concluded that the 4 wt% content of star-shaped SBS has the best effect on CRMA modification in this study.

In order to analyze the elastic and viscous behavior of asphalt at different frequencies, $G^*$ was further divided into storage modulus ($G' = G^* \times \cos\delta$) and loss modulus ($G'' = G^* \times \sin\delta$), as shown in Figure 10, where $G'$ characterized the elastic component in asphalt, and $G''$ characterized the viscous component in asphalt.

As shown in Figures 11 and 12, in the frequency domain of 0.1–100 rad/s, $G'$ and $G''$ show an upward trend as the frequency increases. It can be found in Figure 11 that the $G'$

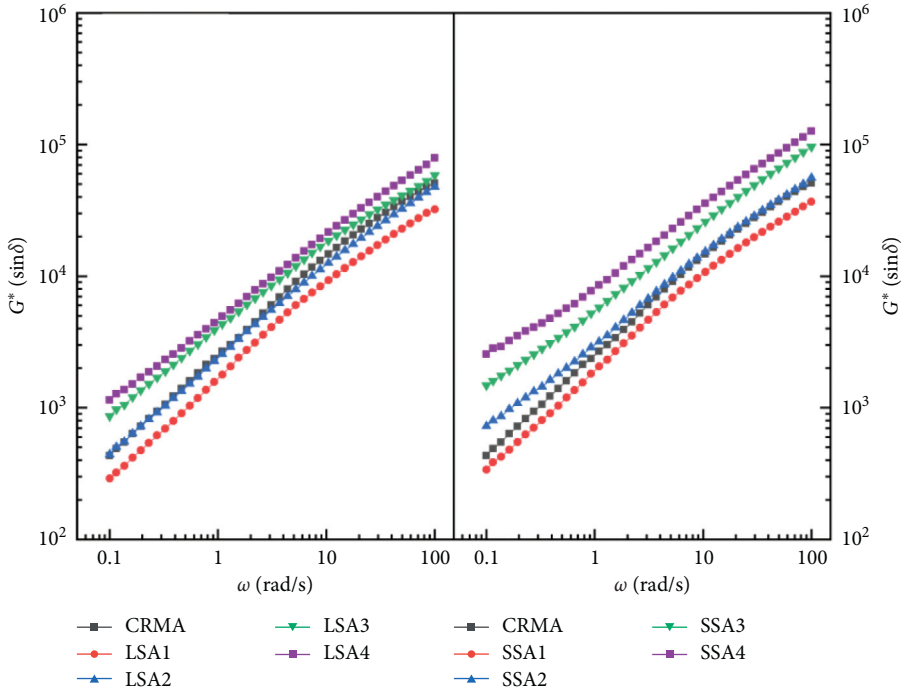


Figure 9: Variation of $G^*/\sin\delta$ with the SBS contents for modified asphalts.

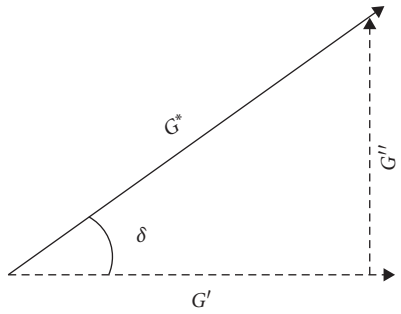


Figure 10: Modulus parameter relationship.

values of LSA1 and SSA1 are lower than CRMA when the SBS content is 1 wt%, and there is an intersection point between LSA2 and CRMA, which indicates that the elastic component of CRMA gradually becomes higher than the elastic component of LSA2 with the frequency increases. Moreover, the $G'$ value of the two modified asphalts continued to rise with the further increase of the SBS content, and the SSA increase was more significant, of which the $G'$ value of SSA4 was one order of magnitude higher than that of SSA1. The $G'$ value of SSA under the same SBS content is higher than that of LSA, indicating that the addition of star-shaped SBS has a better effect on improving the elastic properties of asphalt [27].

Comparing the $G''$ change curves of the two groups of asphalt binders in Figure 12, it can be found that, in the same frequency domain [28], the growth of $G''$ is not obvious with the increase of the SBS content. Among them, the $G''$ curves of LSA3 and LSA4 are almost the same. Similar to the $G'$ curve, the $G''$ value of SSA under the same SBS content is higher than that of LSA, indicating that the star-shaped SBS has a more obvious improvement effect on asphalt viscosity. Overall, the viscoelasticity of asphalt can be enhanced by adding SBS modifiers, and the degree of enhancement is inseparable from the content and structure of SBS.

Moreover, comparing the values of $G'$ and $G''$ in the test frequency range, it can be found that, in the low-frequency range, the rheological behavior of modified asphalt is dominated by viscous components. Then, the $G'$ value of each asphalt binder is higher than the $G''$ value after the frequency increases, and the elastic deformation is greater than the irreversible deformation in the modified asphalt. In addition to being affected by frequency changes, $G'$ and $G''$ of LSA and SSA all increase with the increase of SBS content. Among them, the growth of $G'$ can reach an order of magnitude, which is significantly higher than the growth of $G''$. This result reveals that the addition of SBS modifiers to CRMA mainly enhanced the elastic ability of asphalt to improve the rheological properties of asphalt.

*3.5. Three-Parameter Solid Model.* Since a single elastic element or viscous element cannot satisfy the description of the mechanical behavior of a viscoelastic material, the elastic element and the viscous element are usually combined to characterize the mechanical behavior of the viscoelastic material. The model composed of the Kelvin model and a spring in series is called a three-parameter solid model, in which the Kelvin model is composed of a spring and a dashpot in parallel, as shown in Figure 13 [29].

The three-parameter solid model of viscoelastic materials gives the constitutive equation as follows:

$$\sigma(t) * (E_0 + E) + \eta\dot{\sigma}(t) = EE_0\varepsilon(t) + E_0\eta\dot{\varepsilon}(t). \quad (3)$$

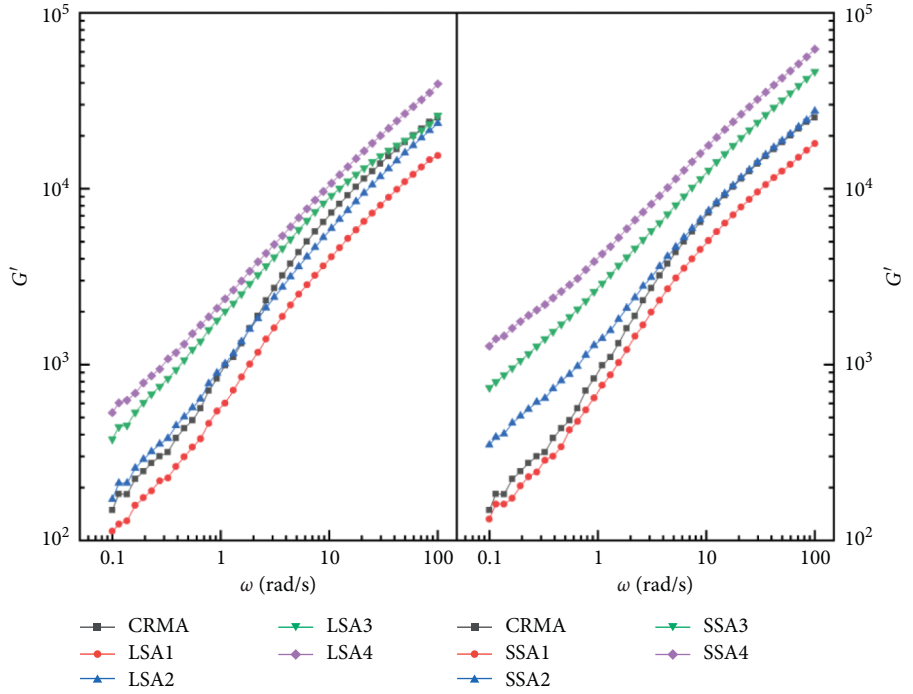


Figure 11: Variation of $G'$ with the SBS contents for modified asphalts.

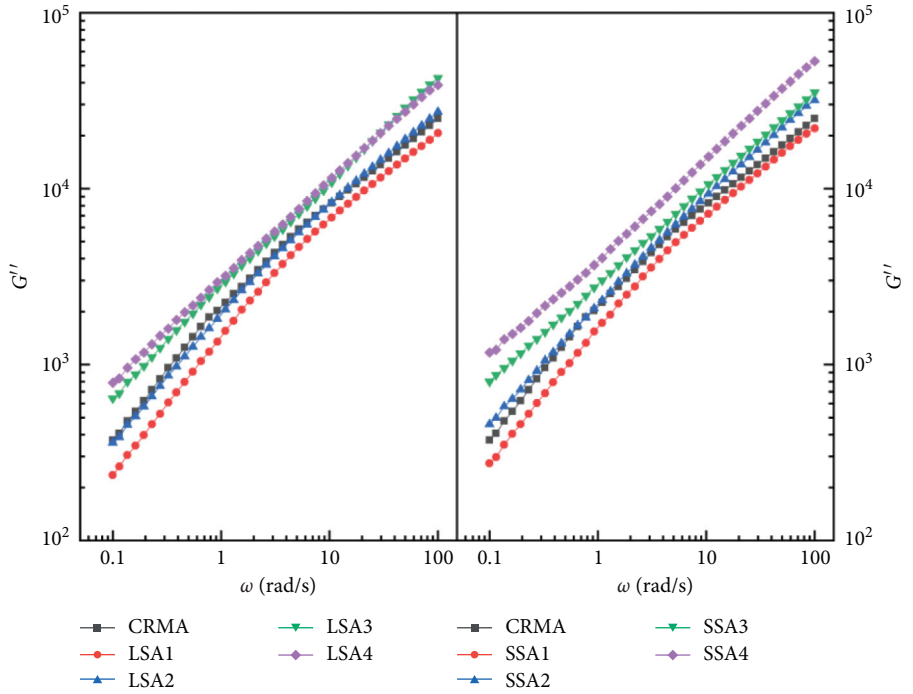


Figure 12: Variation of $G''$ with the SBS contents for modified asphalts.

The three-parameter solid complex modulus formula gives the constitutive equation as follows:

$$G^*(i\omega) = \frac{EE_0(E+E_0)+E_0\eta^2\omega^2}{(E+E_0)^2+\eta^2\omega^2} + \frac{E_0^2\eta\omega}{(E+E_0)^2+\eta^2\omega^2}i, \tag{4}$$

where $E$ (Pa) and $E_0$ (Pa) are unknown modulus parameters, $\eta$ (Pa · s) is the unknown viscosity parameter, and $\omega$ (rad/s) is the angular frequency.

According to the complex modulus expression $G^* = G' + G''i$, the storage modulus and loss modulus are given by the two following equations:

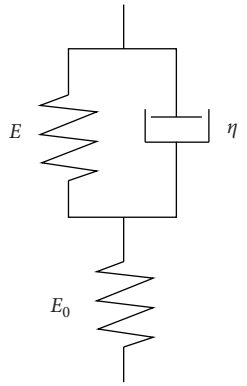


Figure 13: Three-parameter solid model.

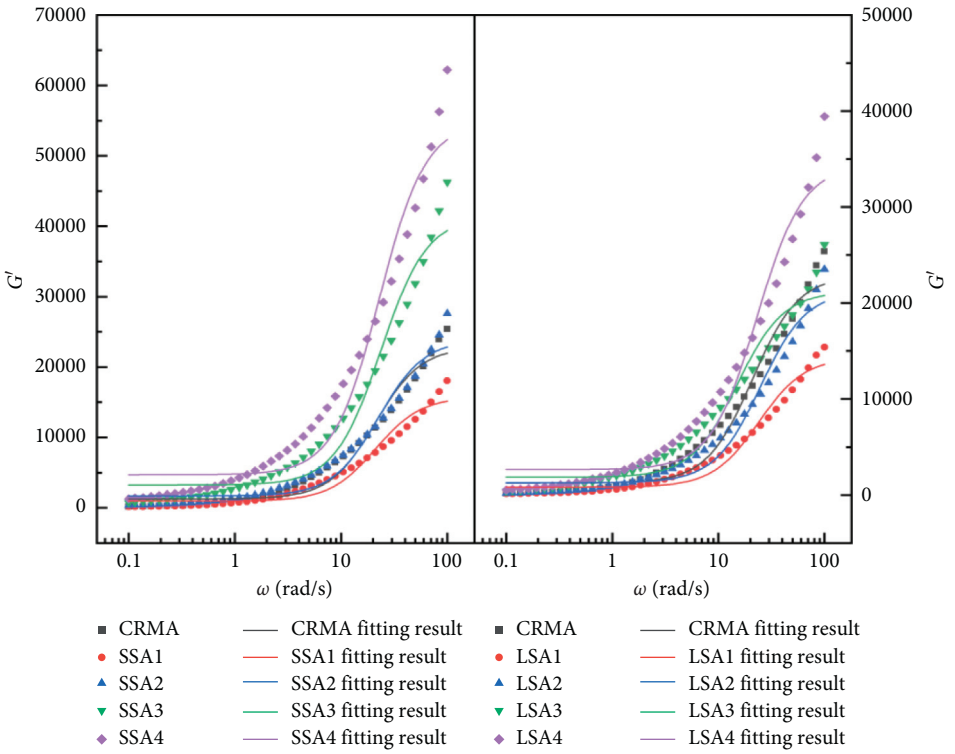


Figure 14: Storage modulus fitting curve.

$$G'(\omega) = \frac{EE_0(E+E_0) + E_0\eta^2\omega^2}{(E+E_0)^2 + \eta^2\omega^2}, \quad (5)$$

$$G''(\omega) = \frac{E_0^2\eta\omega}{(E+E_0)^2 + \eta^2\omega^2}. \quad (6)$$

According to equation (5), the storage modulus results in the test frequency range are nonlinearly fitted, and the fitting results are shown in Figure 14. It can be seen from Figure 14 that the trend of the fitted curves is basically consistent with the trend of the experimental data. Therefore, this paper mainly uses a three-parameter solid constitutive model to obtain $E_0$, $E$, and $\eta$ parameter values and characterizes the influence of SBS structure and content changes on the mechanical properties of modified asphalt through the changing trend of each parameter [30, 31].

The parameter values of $E_0$, $E$, and $\eta$ in equation (5) are obtained by nonlinear fitting, and the fitting results are shown in Table 3.

According to the correlation coefficient $R^2$ in Table 3, it can be found that the three-parameter solid model has a better fit for the storage modulus in the frequency range of 0.1–100 rad/s at 64°C. The variation curves of the fitting parameters $E_0$, $E$, and $\eta$ of SSA and LSA with SBS content are depicted in Figure 15.

Table 3: Storage modulus fitting parameter results.

| Asphalt type | $E$ (Pa) | $E_0$ (Pa) | $\eta$ (Pa·s) | $R^2$ |
|---|---|---|---|---|
| CRMA | 1333.071 | 22885.376 | 1154.752 | 0.968 |
| SSA1 | 1007.848 | 15781.925 | 796.865 | 0.966 |
| SSA2 | 1807.533 | 23904.749 | 1147.557 | 0.966 |
| SSA3 | 3515.963 | 41394.054 | 1898.089 | 0.965 |
| SSA4 | 5150.446 | 54793.403 | 2613.331 | 0.963 |
| LSA1 | 875.173 | 14338.687 | 634.908 | 0.968 |
| LSA2 | 1364.140 | 21280.397 | 909.758 | 0.968 |
| LSA3 | 2020.156 | 21208.892 | 1541.044 | 0.962 |
| LSA4 | 2870.786 | 34399.861 | 1614.797 | 0.963 |

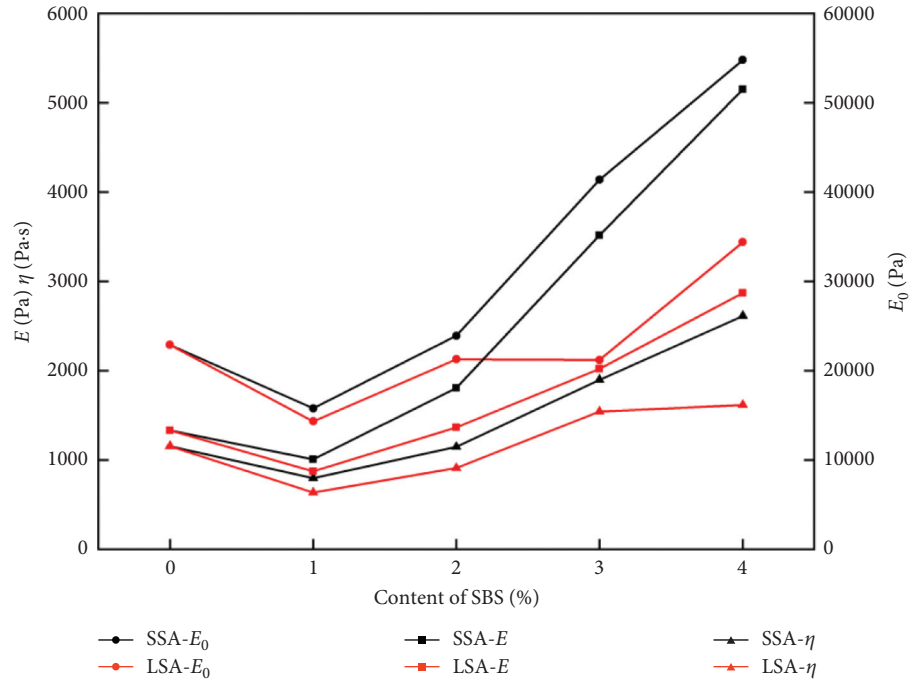


Figure 15: Variation of $E$, $E_0$, and $\eta$ with the SBS contents.

The parameters in the three-parameter solid model have relatively clear mechanical meanings. $E$ and $\eta$, respectively, represent the elastic part and the viscous part of delayed deformation, and $E_0$ represents the instantaneous deformation part. It can be seen from Figure 15 that, with the increase of SBS content, the change curves of $E$, $E_0$, and $\eta$ all show an upward trend, indicating that the instantaneous deformation of modified asphalt decreases with the increase of SBS content. The parameters increase of the modified asphalt with star-shaped SBS is higher than that with linear SBS, and $E_0$ does not change significantly when the content of SBS in the modified asphalt with linear SBS increases from 2 wt% to 3 wt%.

## 4. Conclusions

In this study, two types of SBS were selected to modify CRMA, and the high-temperature performance, temperature sensitivity, low-temperature tensile performance, and rheological performance of SBS/CRMA of different SBS structures and SBS content were systematically studied. Analysis of the test results can draw the following conclusions:

(1) Compared with the performance indicators of CRMA, after adding SBS, the ductility at 5°C and the penetration at 25°C of LSA and SSA were increased, and the softening point first decreased and then increased. With the increase of SBS content, the ductility and softening point of SBS/CRMA at 5°C show an upward trend, while the penetration degree shows a downward trend. The star-shaped SBS modified asphalt has a higher softening point and better temperature sensitivity, while the linear SBS modified asphalt has higher ductility at 5°C and better low-temperature tensile property.

(2) The addition of SBS copolymers can increase the complex modulus $G^*$, rutting factor $G^*/\sin\delta$, storage modulus $G'$, and dissipation modulus $G''$ of CRMA and reduce the phase angle $\delta$. Among the

four SBS contents of 1 wt%, 2 wt%, 3 wt%, and 4 wt%, the higher the SBS content, the stronger the rutting resistance and deformation resistance of LSA and SSA. Furthermore, SBS mainly improves the rheological properties of asphalt by enhancing the elasticity of asphalt, and the proportion of elastic components in asphalt is the highest when the SBS content is 4 wt%.

(3) The antideformation ability of asphalt binders is affected by the loading frequency. The higher the loading frequency in the frequency range of 0.1–100 rad/s, the more elastic components in the asphalt, and the more deformable parts it can recover. Besides, in the frequency domain of 1–10 rad/s, the higher the loading frequency, the smaller $\delta$ of the modified asphalt. According to the angular frequency of 10 rad/s to characterize the vehicle speed of 60 km/h, it can be concluded that the viscous components in the asphalt are smaller under a load of high-speed vehicles, and it is less prone to permanent deformation.

(4) Compared with linear SBS, star-shaped SBS improves the performances of asphalt binders more significantly. The star-shaped SBS has high rigidity and can form a denser and more stable cross-linked network with CR powder in the asphalt, which has a greater degree of improvement in the viscoelasticity, rutting resistance, high-temperature stability, and temperature sensitivity of the asphalt. The linear SBS has better flexibility and has advantages in optimizing the low-temperature tensile properties of the asphalt binders.

CR powder modified asphalt can meet the requirements of road construction for asphalt's high-temperature performance, temperature sensitivity, and antideformation ability. However, due to the limited improvement of CR powder on the viscoelasticity of asphalt and the fact that it is easy to agglomerate when the content is too high, considering the preparation cost and modifier performance, SBS polymer can be added to prepare composite modified asphalt to make up for the deficiencies of the above limiting factors. In this paper, through the analysis of the test results of each asphalt binder with different types and different dosages of SBS, it is concluded that it is recommended that 4 wt% star-shaped SBS be added when the CR powder content is 20 wt%. Under this dosage, SBS/CRMA has the best modification effect, and the performance of modified asphalt is the best.

## Data Availability

The experimental data used to support the findings of this study are included within the article.

## Conflicts of Interest

The authors declare that there are no conflicts of interest regarding the publication of this paper.

## Acknowledgments

This work was funded by the National Natural Science Foundation of China (Project no. 51978309), the Transportation Technology Program of Jilin Province of China (Grant no. 2021-1-1), the Special Funding for Basic Scientific Research Operation Fees of Central Universities, the Scientific and Technological Developing Scheme Program of Jilin Province (Grant no. 20200403157SF), and the Scientific Research Project of the Education Department of Jilin Province (Grant no. JJKH20211113KJ).

## References

[1] L. G. Picado-Santos, S. D. Capitão, and J. M. C. Neves, "Crumb rubber asphalt mixtures: a literature review," *Construction & Building Materials*, vol. 247, no. 2020, pp. 1–13, 2020.

[2] P. Cong, P. Xun, M. Xing, and S. Chen, "Investigation of asphalt binder containing various crumb rubbers and asphalts," *Construction and Building Materials*, vol. 40, no. 2013, pp. 632–641, 2013.

[3] A. Ghavibazoo and M. Abdelrahman, "Composition analysis of crumb rubber during interaction with asphalt and effect on properties of binder," *International Journal of Pavement Engineering*, vol. 14, no. 5, pp. 517–530, 2013.

[4] H. Wang, Z. You, J. Mills-Beale, and P. Hao, "Laboratory evaluation on high temperature viscosity and low temperature stiffness of asphalt binder with high percent scrap tire rubber," *Construction and Building Materials*, vol. 26, no. 1, pp. 583–590, 2012.

[5] X. F. Wang, "Study of rubber asphalt modification mechanism," *Advanced Materials Research*, vol. 194–196, no. 2011, pp. 844–847, 2011.

[6] Y. Jiao, S. Liu, L. Fu, and W. Shan, "Fracture monitoring of SBS and crumb rubber modified porous asphalt mixtures under compression and splitting testing using acoustic emission technique," *Journal of Materials in Civil Engineering*, vol. 31, no. 6, pp. 1–13, 2019.

[7] C. Qian and W. Fan, "Evaluation and characterization of properties of crumb rubber/SBS modified asphalt," *Materials Chemistry and Physics*, vol. 253, no. 2020, pp. 1–12, 2020.

[8] Y. J. Meng, Y. T. Jiang, Y. Y. Wang, Y. Q. Shi, and M. F. Huang, "Discussion the rheological properties of asphalt rubber," *Applied Mechanics and Materials*, vol. 665, no. 2014, pp. 183–187, 2014.

[9] H. Li, W. Li, A. A. Temitope et al., "Analysis of the influence of production method, crumb rubber content and stabilizer on the performance of asphalt rubber," *Applied Sciences-Basel*, vol. 10, no. 16, pp. 1–18, 2020.

[10] C. Qian, W. Fan, M. Liang et al., "Rheological properties, storage stability and morphology of CR/SBS composite modified asphalt by high-cured method," *Construction and Building Materials*, vol. 193, no. 2018, pp. 312–322, 2018.

[11] M. Liang, P. Liang, W. Fan et al., "Thermo-rheological behavior and compatibility of modified asphalt with various styrene-butadiene structures in SBS copolymers," *Materials & Design*, vol. 88, no. 2015, pp. 177–185, 2015.

[12] F. Dong, W. Zhao, Y. Zhang et al., "Influence of SBS and asphalt on SBS dispersion and the performance of modified asphalt," *Construction and Building Materials*, vol. 62, no. 2014, pp. 1–7, 2014.

[13] B. V. Kök, M. Yilmaz, and A. Geçkil, "Evaluation of low-temperature and elastic properties of crumb rubber- and SBS-modified bitumen and mixtures," *Journal of Materials in Civil Engineering*, vol. 25, no. 2, pp. 257–265, 2013.

[14] L. Liu, Z. H. Liu, and S. Li, "The preparation technology and performance study of SBS and rubber powder composite modified asphalt," *Applied Mechanics and Materials*, vol. 361–363, no. 2013, pp. 1617–1620, 2013.

[15] Z. Jiang, S. M. Easa, C. Hu, and X. Zheng, "Understanding damping performance and mechanism of crumb rubber and styrene-butadiene-styrene compound modified asphalts," *Construction and Building Materials*, vol. 206, no. 2019, pp. 151–159, 2019.

[16] X. Li, J. Cheng, and S. Kang, "Thermal oxidative aging mechanism of crumb rubber/SBS composite modified asphalt," *Construction and Building Materials*, vol. 75, no. 2015, pp. 169–175, 2015.

[17] C. Qian, W. Fan, G. Yang et al., "Influence of crumb rubber particle size and SBS structure on properties of CR/SBS composite modified asphalt," *Construction and Building Materials*, vol. 235, no. 2020, pp. 1–13, 2020.

[18] M. Guo, H. Liu, Y. Jiao et al., "Effect of WMA-RAP technology on pavement performance of asphalt mixture: a state-of-the-art review," *Journal of Cleaner Production*, vol. 266, no. 2020, pp. 1–33, 2020.

[19] L. F. Walubita, E. Mahmoud, L. Fuentes et al., "Correlating the asphalt-binder high-temperature properties (DSR) to HMA permanent deformation (RLPD) and field rutting: a laboratory-field study," *Construction & Building Materials*, vol. 262, no. 2020, pp. 1–11, 2020.

[20] G. G. Al-Khateeb and K. Z. Ramadan, "Investigation of the effect of rubber on rheological properties of asphalt binders using superpave DSR," *KSCE Journal of Civil Engineering*, vol. 19, no. 1, pp. 127–135, 2014.

[21] Y. Qian, F. Guo, Z. Leng, Y. Zhang, and H. Yu, "Simulation of the field aging of asphalt binders in different reclaimed asphalt pavement (RAP) materials in Hong Kong through laboratory tests," *Construction and Building Materials*, vol. 265, no. 2020, pp. 1–11, 2020.

[22] Q. Guo, Z. Chen, P. Liu et al., "Influence of basalt fiber on mode I and II fracture properties of asphalt mixture at medium and low temperatures," *Theoretical and Applied Fracture Mechanics*, vol. 112, no. 2021, pp. 1–13, 2021.

[23] Q. Guo, L. Li, Y. Cheng, Y. Jiao, and C. Xu, "Laboratory evaluation on performance of diatomite and glass fiber compound modified asphalt mixture," *Materials & Design (1980–2015)*, vol. 66, no. 2015, pp. 51–59, 2015.

[24] L. Yao, W. Gao, X. Ma, and H. Fu, "Properties analysis of asphalt binders containing bayer red mud," *Materials*, vol. 13, no. 5, pp. 1–14, 2020.

[25] F. Xiao, S. Amirkhanian, H. Wang, and P. Hao, "Rheological property investigations for polymer and polyphosphoric acid modified asphalt binders at high temperatures," *Construction and Building Materials*, vol. 64, no. 2014, pp. 316–323, 2014.

[26] M. Guo, M. Liang, Y. Jiao et al., "A review of phase change materials in asphalt binder and asphalt mixture," *Construction & Building Materials*, vol. 258, no. 2020, pp. 1–9, 2020.

[27] F. Dong, X. Yu, S. Liu, and J. Wei, "Rheological behaviors and microstructure of SBS/CR composite modified hard asphalt," *Construction and Building Materials*, vol. 115, no. 2016, pp. 285–293, 2016.

[28] S. Ren, X. Liu, M. Li, W. Fan, J. Xu, and S. Erkens, "Experimental characterization of viscoelastic behaviors, microstructure and thermal stability of CR/SBS modified asphalt with TOR," *Construction and Building Materials*, vol. 261, no. 2020, Article ID 120524, 2020.

[29] H. Yin, Y. Li, and N. Z. Wang, "Research on fractional derivative viscoelastic constitutive relation of asphalt mixture," *Advanced Materials Research*, vol. 446–449, no. 2012, pp. 2560–2566, 2012.

[30] J. Zhao, *Cement Asphalt Mastic Constitutive Model and Microstructure Research*, Harbin Institute of Technology, Harbin, China, 2014.

[31] X. Ma, H. Chen, X. Zhang, M. Xing, and P. Yang, "Effect of asphalt binder characteristics on filler-asphalt interactions and asphalt mastic creep properties (article)," *Journal of Materials in Civil Engineering*, vol. 31, no. 8, pp. 1–11, 2019.

Hindawi
Advances in Materials Science and Engineering
Volume 2021, Article ID 5597275, 15 pages
https://doi.org/10.1155/2021/5597275

*Research Article*

# The Time Effect and Micromechanism of the Unconfined Compressive Strength of Cement Modified Slurries

**Ping Jiang**,[1,2] **Yewen Chen**,[1] **Lin Zhou**,[1] **Tianhao Mao**,[1] **Wei Wang**,[1] **Junping Yuan**,[2] **and Na Li**[1]

[1]*School of Civil Engineering, Shaoxing University, Shaoxing 312000, China*
[2]*Key Laboratory of Ministry of Education for Geomechanics and Embankment Engineering, Hohai University, Nanjing 210098, China*

Correspondence should be addressed to Na Li; lina@usx.edu.cn

Received 18 January 2021; Revised 11 March 2021; Accepted 3 April 2021; Published 19 April 2021

Academic Editor: Qinglin Guo



This study investigated the unconfined compressive strength change law of cement modified slurries (CMS) under different curing ages. We conducted unconfined compressive strength tests using slurry and cement as raw materials. The cement contents were 5%, 10%, 15%, 20%, and 25%. The curing ages were 7, 14, 28, 56, 90, 120, 150, and 180 d. A time effect model of CMS strength was established based on the measured UCS strength-curing age and the strength-cement content curves. The test results proved that the UCS of the CMS increased significantly with an increase in the curing age, and after 90 days, the UCS gradually increased to a fixed value. The time effect model better characterized the relationship between the UCS of the CMS and the curing age and the cement content, as the predicted value had a high correlation with the measured value. We conducted scanning electron microscopy (SEM), energy dispersive X-ray (EDX), and X-ray diffraction (XRD) tests to analyze the microstructure and chemical composition of the CMS. The microscopic test results demonstrated that the increase of cement content and curing age increased the amount of gelling substances in the CMS and made the overall structure more compact, thereby increasing its macro strength.

## 1. Introduction

Slurry is a type of turbid suspension system composed of water, bentonite particles, clay particles, and admixtures. Generally, in slurry preparation, water accounts for 70% to 80%, and solid particles account for 20% to 30%, by volume ratio. As an engineering auxiliary construction material, slurries are widely used in bored pile construction, shield tunnel construction, and underground diaphragm wall construction. An unreasonable discharge of construction slurry will cause environmental pollution, water pollution, vegetation destruction, and soil consolidation, thereby destroying the ecological environment. Thus, there is an urgent need for social development to find an economical and environmentally friendly treatment method to deal with the waste slurry.

A large amount of earth rock materials is used in highway engineering construction. This is an effective method of resource utilization through curing and modifying the slurry to meet the requirements of highway engineering. Many studies have been carried out on the methods of slurry curing [1–3]. However, the study of slurry curing with high-moisture content requires further discussion [4].

Cement, as a kind of commonly used soft soil curing material, has been well researched [5–10]. Pu [11] performed unconfined compression tests on silt samples and SEU-2 binder-cured silt samples. The brittleness index was introduced to quantitatively evaluate the softening and hardening effects of curing silt. The test results demonstrated that the addition of cement improved the deformation characteristics of silt. With the increase of cement content, the initial porosity and compression index decreased. The unconfined compressive strength (UCS) increased with increasing curing age and cement content, while the failure strain decreased. There are also some studies on the incorporation

of waste materials into soft soil, which not only recycled the waste, but also modified the soft soil. Yoobanpot [12] added cement kiln ash and fly ash into soft soil to improve its compressive strength. The strength of the soft soil was significantly improved early on and slowly increased with an increase in the curing age.

Cement can improve the engineering properties of soft soil, and the UCS of cement soil increases with the increase in curing age. So, cement soil is widely used in many engineering fields, just as bored pile construction, shield tunnel construction, and underground diaphragm wall construction [13–21]. Many studies on the mathematical model of strength growth were conducted. Horpibulsuk studied the strength growth law of high-moisture cement soil based on Abrams' method and put forward the prediction of cement soil strength with the water-cement ratio as the basic parameter [22]. Lee proposed that the strength of the cement soil was related to the cement content and water-cement ratio and thus established a mathematical model [23]. Based on Lee's research, Xiao and Liu proposed a generalized hyperbolic fitting mathematical model for the time effect of cement soil [24, 25]. The above results demonstrated that the UCS of cement soil is related to the cement content and curing age. As slurries and soft soils have similar engineering characteristics, it is feasible to establish a time effect model of cement modified slurries (CMS).

The analysis of micromechanisms has important guidance for macro-mechanical research. At present, the microtests of cement soil mainly use scanning electron microscopy (SEM), energy dispersive X-ray (EDX), and X-ray diffraction (XRD). The SEM analysis of cement stabilized soil conducted by Mousavi [26] demonstrated that cement could improve the strength of soil due to the hydration reaction. During the reaction process, cement filled the smaller pores in the soil and produced gel crystals with the increasing curing age. The space of the large pores gradually decreased. Mola-Abasi [27] incorporated zeolite into the cement sand, and the SEM tests showed that zeolite changed the microstructure of the cement sand. The reaction products of pozzolan filled the porous cement sand, thereby, increasing its strength.

Ghasabkolaei [28] performed SEM image analysis on the cemented soil mixed with and without nanosilicon powder, and the results demonstrated that the cemented soil mixed with nanosilicon power was more uniform and denser than the ordinary cemented soil. Moreover, the UCS of uniformly dense cement soil mixed with nanosilicon powder is high. Homidy [29] studied the microstructure of cement soil. SEM image analysis showed that the schistose structure in the cement soil was caused by the hydration reaction of the cement. XRD diffraction analysis showed that the C–S–H gel formed by the hydration reaction results in the highest proportion of calcium and silicon among all the elements.

The above studies demonstrated that the mechanical properties of slurry can be effectively improved by adding modified materials. Cement is a commonly used modification material due to the advantages of low cost and good modification effects. Using cement is feasible for modifications of slurries. Through studying the changes of the mechanical properties of CMS over extended curing ages, relevant mathematical models were established to effectively predict the key indexes. Through the microtests of CMS, the strength variation mechanism can be explained from the micromechanism aspect, which can provide a reference for the engineering applications of modified slurries.

## 2. Test Preparation

*2.1. Experimental Materials and Program.* The raw materials used in this study are slurry and cement, and the moisture content of the slurry is 100%. The slurry used throughout the experimental test was collected from a construction site in Shaoxing city, China, as shown in Figure 1. The physical and mechanical properties of the slurry are presented in Table 1. SEM, EDX, and XRD tests were performed on the dried slurry, and the microstructure, elemental composition, and compound composition were obtained as shown in Figures 2–4 , respectively.

As demonstrated in Figures 2–4, the slurry was mainly composed of schistose particles, whose main element components were Si, O, Al, Mg, and Ca, whose main compounds were $SiO_2$, $Al_2O_3$, and $CaCO_3$.

The cement used in this test belongs to class PO32.5, ordinary Portland cement, produced by Shangyu Hailuo Cement Co., Ltd. The cement content and the curing age of CMS are presented in Table 2.

*2.2. Sample Making and Testing.* According to the highway geotechnical test regulations [30], the amount of slurry was calculated based on the proposed test scheme, then placed in a mixer, and stirred for three minutes to ensure uniformity. The cement was added, according to Table 2, as a percentage of the dried slurry weight, and then stirred for 3 to 5 minutes. The mixed CMS was charged into the test mold three times and shaken 50 times each charge. The size of the test mold was a cylinder with a diameter of 39.1 mm and a height of 80 mm. Then, the test mold was sealed with cling film and left vertically in position for 2 hours. After the entire sample was solidified and stabilized, both ends of the sample were wrapped with filter paper and placed into a water tank for curing at 20°C. The curing ages were 7 d, 14 d, 28 d, 56 d, 90 d, 120 d, 150 d, and 180 d. The cured samples were demoulded, and then the UCS tests were conducted. The demoulded samples are shown in Figure 5. In this study, the UCS tests were performed using a fully automatic multifunctional unconfined compressive strength tester produced by Nanjing TKA Technology Co., Ltd., which can realize the automation of the whole process of test operation through computer control.

## 3. UCS Test Results and Analysis

*3.1. UCS Test Results.* The stress-strain data curves of CMS measured by UCS tests with different cement contents and different curing ages are shown in Figure 6, where 6(a)–6(h) represent the stress-strain curves with different cement contents at curing ages of 7 d, 14 d, 28 d, 56 d, 90 d, 120 d, 150 d, and 180 d, respectively.

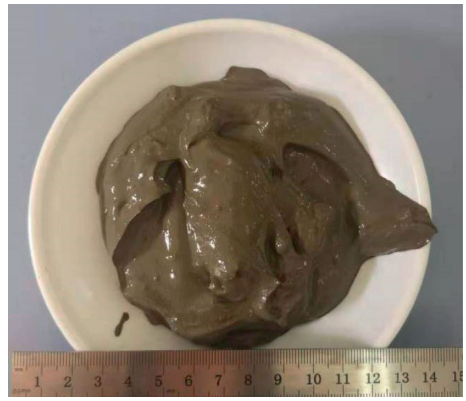

Figure 1: The testing slurry.

Table 1: The physical and mechanical properties of the building slurry.

| Index name | Specific gravity | Liquid limit/(%) | Plastic limit/(%) | Plasticity index/(%) | Moisture content/(%) |
|---|---|---|---|---|---|
| Index value | 2.65 | 43.5 | 23.1 | 20.4 | 100 |

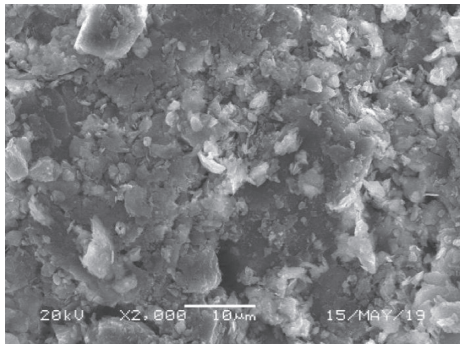


Figure 2: The scanning electron microscopy (SEM) test results of the slurry.

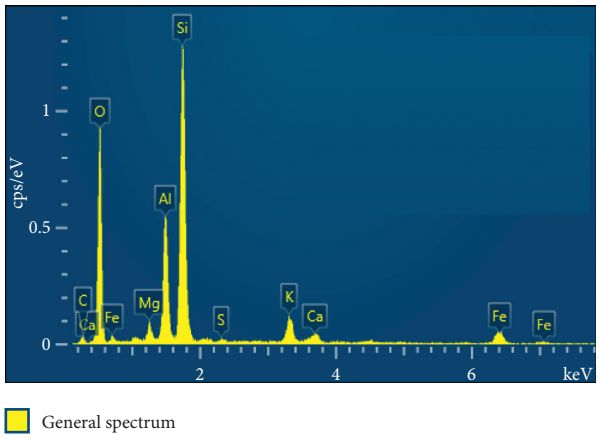


Figure 3: The energy dispersive X-ray (EDX) test results of the slurry.

In Figure 6, there are obvious peaks in the unconfined compressive stress-strain curves of CMS with different cement contents and at different curing ages, which has a softening curve characteristic; that is, when the stress does not reach the peak, the stress increases sharply with the increase of the strain. When the stress reaches its peak value, the stress slowly decreases with increasing strain and finally tends towards a stable value.

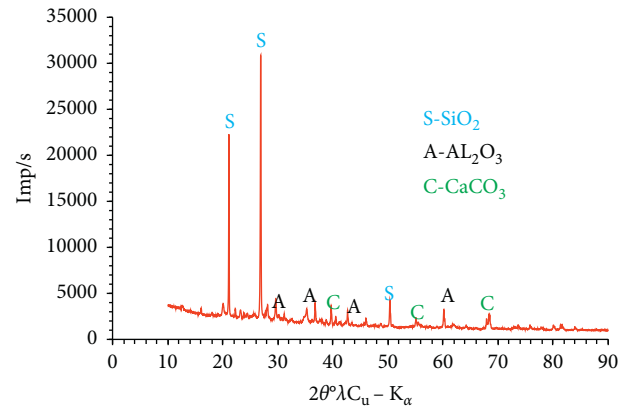


Figure 4: The X-ray diffraction (XRD) test results of the slurry.

Table 2: The unconfined compressive strength (UCS) test scheme.

| Cement content/(%) | Curing age/(d) |
|---|---|
| 5, 10, 15, 20, 25 | 7, 14, 28, 56, 90, 120, 150, 180 |

*3.2. UCS Test Data Analysis.* The peak stress of the unconfined compressive stress-strain curve is taken as the UCS of the CMS. According to the stress-strain curve in Figure 6, the UCS of the CMS with different cement contents at different curing ages can be obtained, as presented in Table 3.

According to Table 3, the comparison of the UCS of the CMS at different curing ages with different cement contents was obtained, as shown in Figure 7.

Figure 7 shows that the UCS of the CMS at each curing age increased with the increase of cement content. In

Figure 5: The demoulded cement modified slurry (CMS) sample.

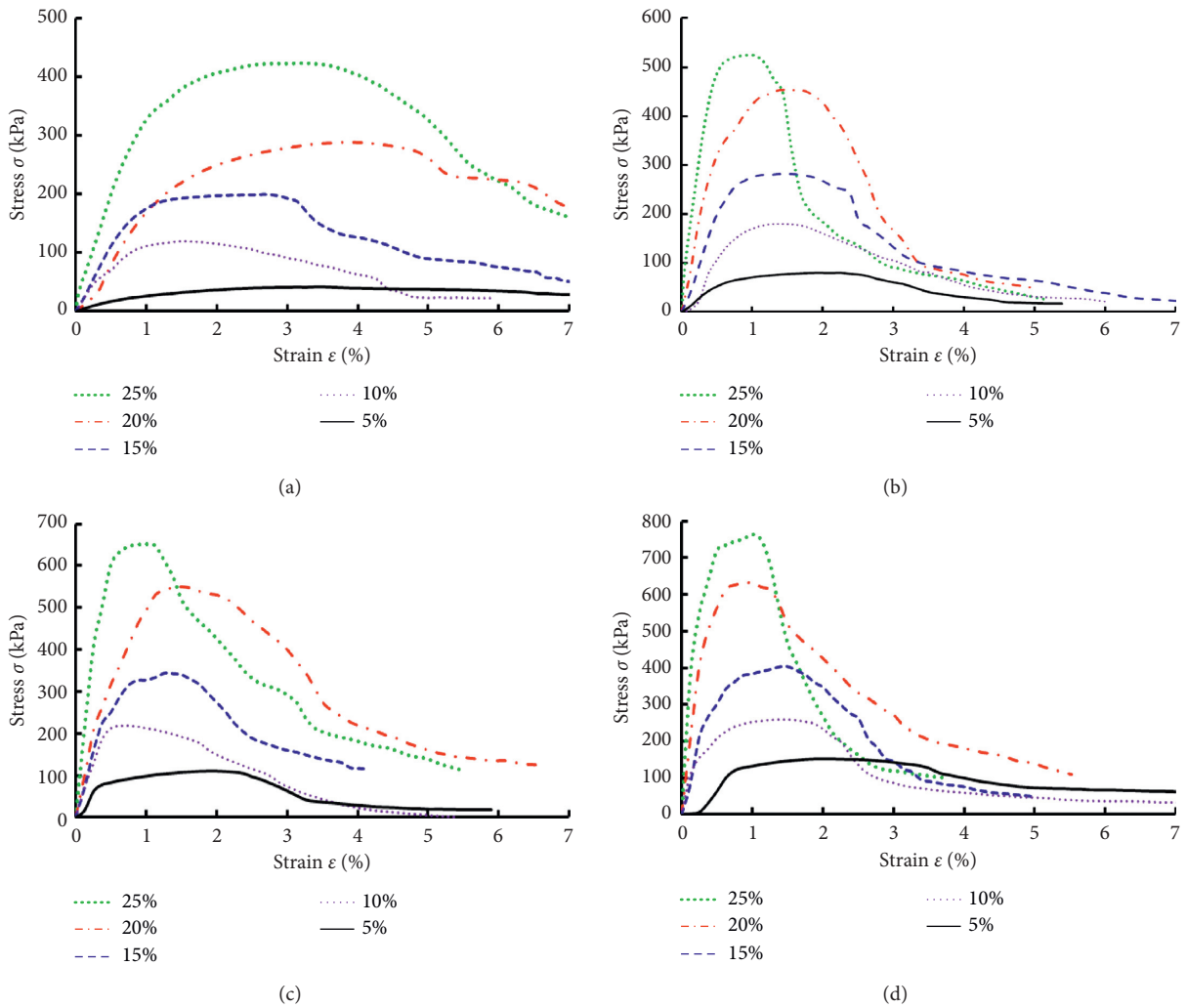


Figure 6: Continued.

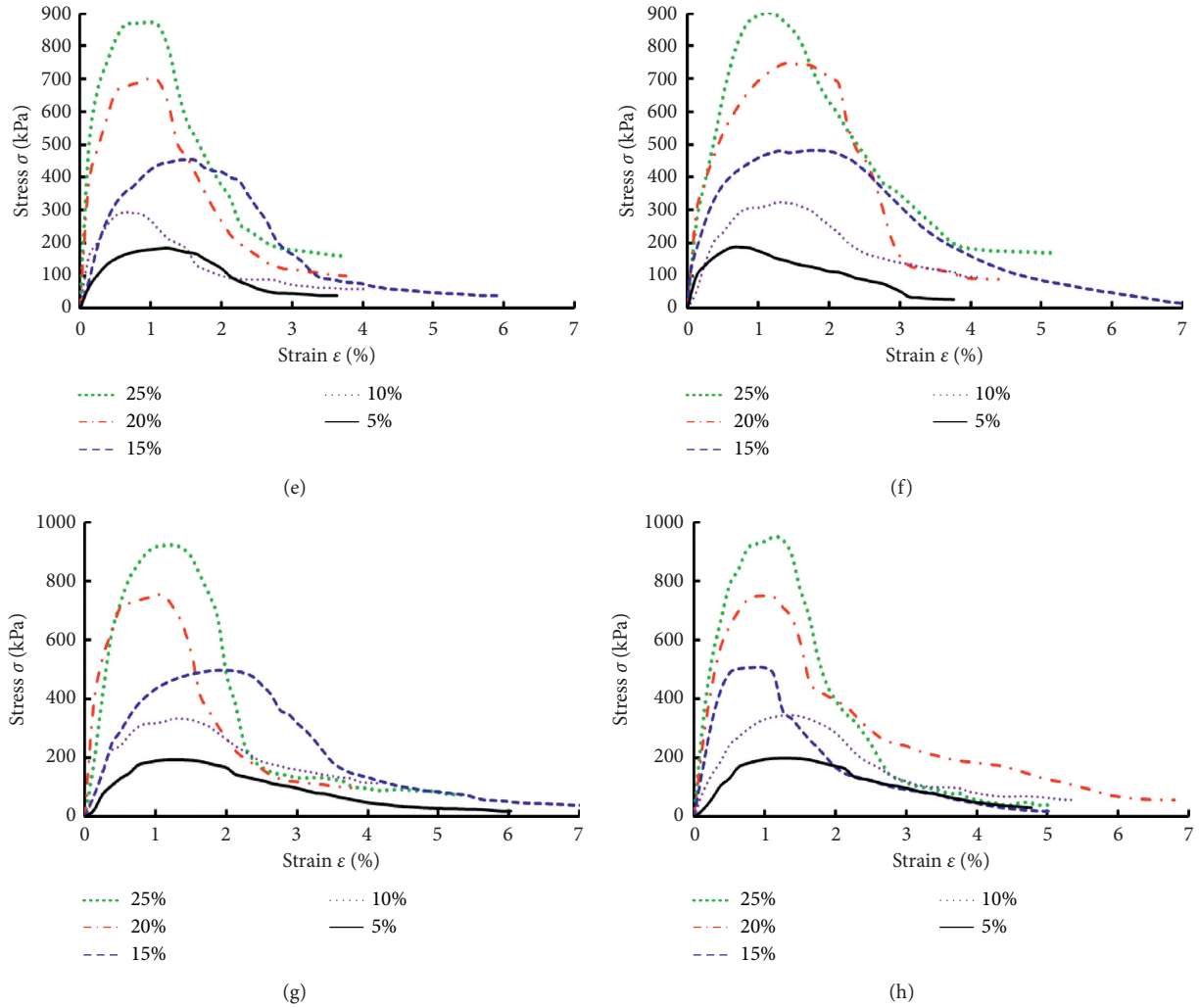


Figure 6: Axial stress and axial strain curves of CMS. (a) 7 d axial stress and axial strain curves. (b) 14 d axial stress and axial strain curves. (c) 28 d axial stress and axial strain curves. (d) 56 d axial stress and axial strain curves. (e) 90 d axial stress and axial strain curves. (f) 120 d axial stress and axial strain curves. (g) 150 d axial stress and axial strain curves. (h) 180 d axial stress and axial strain curves.

Table 3: The UCS of the CMS/kPa.

| Curing age/(d) | Cement content/(%) | | | | |
|---|---|---|---|---|---|
| | 5 | 10 | 15 | 20 | 25 |
| 7 | 43 | 122 | 199 | 298 | 423 |
| 14 | 81 | 179 | 283 | 448 | 518 |
| 28 | 113 | 221 | 339 | 553 | 648 |
| 56 | 151 | 248 | 404 | 625 | 755 |
| 90 | 184 | 288 | 448 | 701 | 867 |
| 120 | 194 | 322 | 478 | 743 | 899 |
| 150 | 195 | 331 | 489 | 752 | 918 |
| 180 | 205 | 338 | 502 | 756 | 953 |

addition, the growth rate of the UCS with a cement content from 20% to 25% clearly decreased. We concluded that the 20% cement content was the optimal content.

In order to further explore the effect of the cement content on the UCS of the CMS, the strength growth multiples of the CMS with different cement contents can be

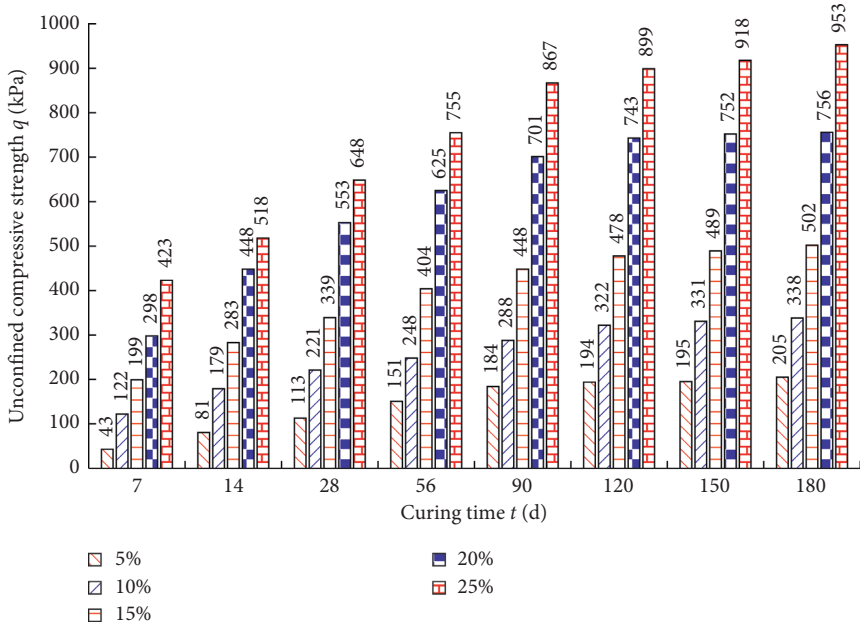


Figure 7: The UCS of the CMS with different cement contents at different curing ages.

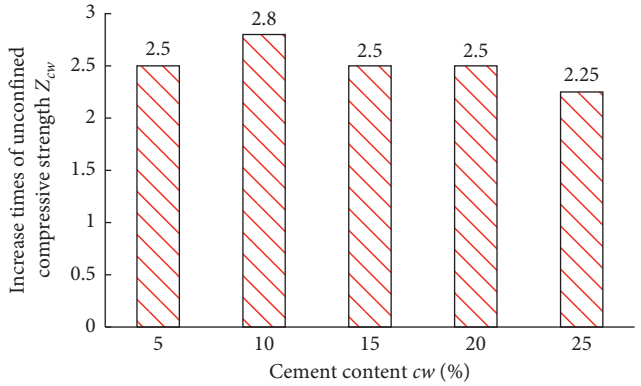


Figure 8: Multiple changes in the strength of CMS with different cement contents during the curing process.

calculated according to formula (1), and the calculated results are shown in Figure 8.

$$Z_{cw} = \frac{q_{180\,d}}{q_{7\,d}}, \tag{1}$$

where $Z_{cw}$ represents the multiple, and $q_{180\,d}$ and $q_{7\,d}$ represents the UCS of the CMS at curing ages of 180 d and 7 d, respectively.

In Figure 8, the UCS of the CMS with each cement content increased by 2.5 times with the increase in curing age.

According to Table 3, the comparison of the UCS of the CMS with different cement contents and different curing ages is shown in Figure 9.

In Figure 9, with the same cement content, the UCS of the CMS increased significantly with the curing age from 7 d to 90 d. During the curing from 120 d to 180 d, the UCS of the CMS did not increase significantly.

In order to further explore the effect of the curing age on the UCS of the CMS, the strength multiples of the CMS at different curing ages were calculated according to formula (2), and the calculated results are shown in Figure 10.

$$Z_d = \frac{\sigma_{25\%}}{\sigma_{5\%}}, \tag{2}$$

where $Z_d$ represents the multiple, $\sigma_{25\%}$ represents the peak strength of the CMS when the cement content is 25%, and $\sigma_{5\%}$represents the peak strength of the CMS when the cement content is 5%.

As can be seen from Figure 10, with the increase in the curing age, the strength increased multiple times, gradually decreased, and finally reached a stable value.

*3.3. Time Effect Model.* In order to comprehensively analyze the improvement effect of the cement content and the curing

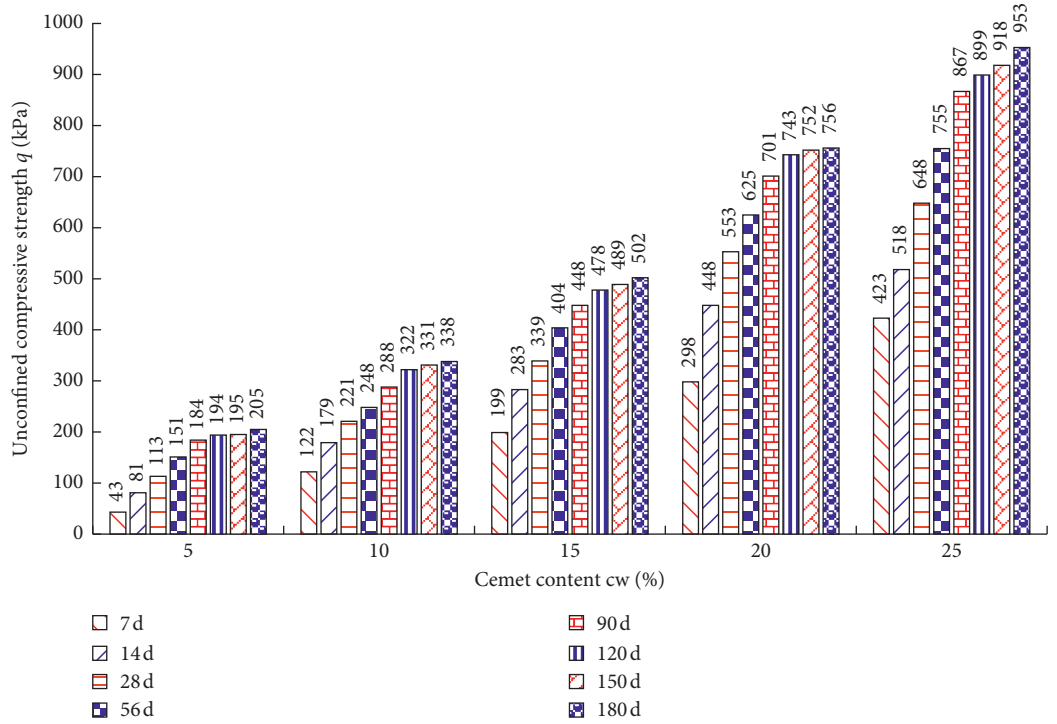


Figure 9: The UCS of the CMS with different cement contents and different curing ages.

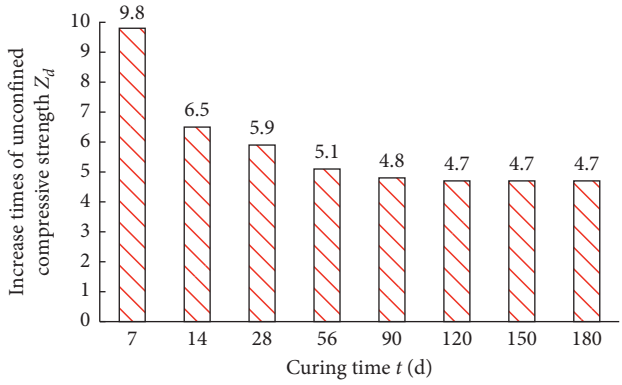


Figure 10: Multiple changes in the strength of the CMS with different cement contents during the curing process.

age on the UCS of the CMS, we obtained from Figures 7 and 8 that, with different cement contents, the UCS of the CMS had a similar change law with the increase in the curing age. The relationship between the UCS and curing age can be described by

$$q = A \ln(t) + B, \tag{3}$$

where $q$ represents the UCS, $t$ represents the curing age, and $A$ and $B$ are functions of the cement content $cw$.

The prediction model of the UCS of the CMS with respect to the curing age can be obtained by fitting calculations:

$$q = \begin{cases} 50.008 \ln(t) - 52.992 & cw = 5\%, \\ 66.735 \ln(t) - 5.3395 & cw = 10\%, \\ 92.745 \ln(t) + 28.09 & cw = 15\%, \\ 138.97 \ln(t) + 63.96 & cw = 20\%, \\ 167.45 \ln(t) + 91.182 & cw = 25\%. \end{cases} \tag{4}$$

The calculated data of formula (4) were compared with the experimental data, as shown in Figure 11.

As can be seen from Figure 11, formula (4) can better predict the UCS of the CMS under different curing ages. In

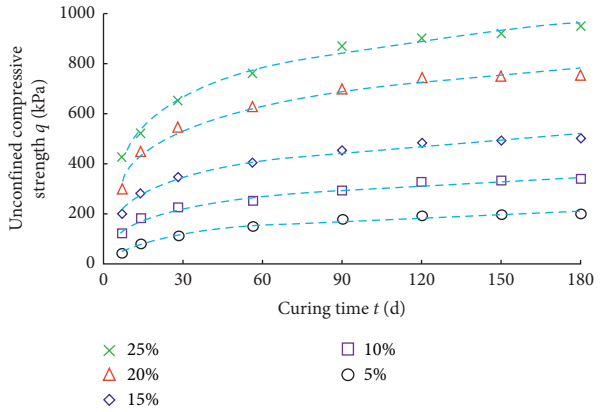


Figure 11: The UCS and curing age curve of the CMS with different cement contents.

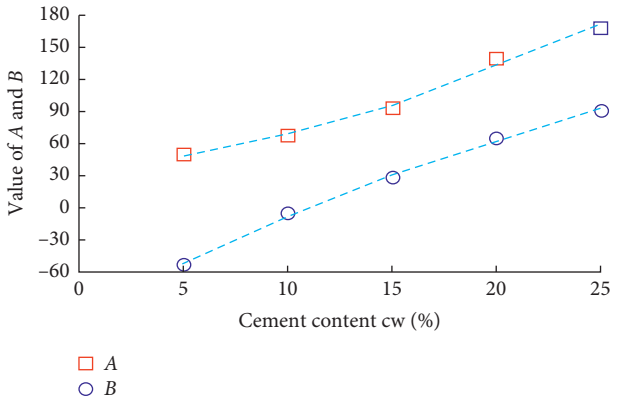


Figure 12: The relationship curves between A, B and the cement content cw.

order to consider the effect of the cement content on the UCS of the CMS, the function relation of A and B in formula (4), on the cement content $cw$, was fitted and calculated. The calculation functions of A and B can be obtained as shown in formulas (5) and (6), respectively.

$$A = 0.1249cw^2 + 2.3949cw + 32.90, \quad (5)$$

$$B = -0.1098cw^2 + 10.446cw - 101.523. \quad (6)$$

The fitting curves of formulas (5) and (6) are shown in Figure 12. Both formulas (5) and (6) have better fitting accuracy.

Formulas (5) and (6) are substituted into formula (3), and the UCS prediction formula for CMS can be obtained:

$$q = \left(0.1249cw^2 + 2.3949cw + 32.906\right)\ln(t) + \left(-0.1098cw^2 + 10.446cw - 101.52\right). \quad (7)$$

The measured UCS value of each group of CMS was compared with the predicted value calculated by formula (7), and the results are presented in Figure 13. We concluded that the correlation coefficient between the predicted value and the measured value was 0.991, indicating that formula (7) can better predict the UCS of the CMS with different cement contents and different curing ages.

Formula (7) fit the measured strength of the CMS with 100% moisture content and had a good correlation. The UCS of the CMS increased linearly with the logarithm of the curing age. According to formula (7), the curve of the UCS of the CMS with different curing ages and different cement contents can be plotted, as shown in Figure 14, which can provide a reference for related engineering designs and practice.

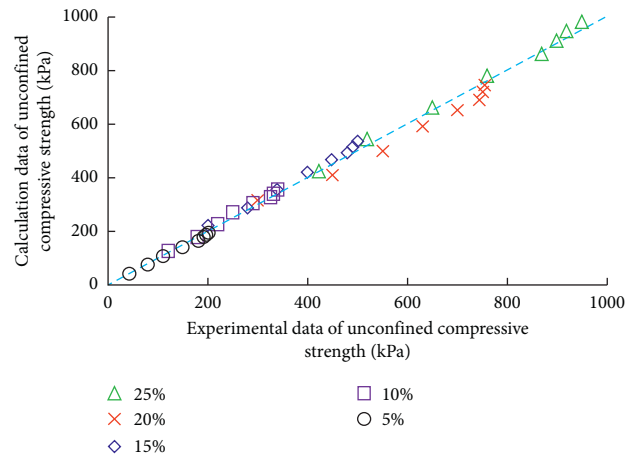


Figure 13: The correlation fitting curve between the prediction data and measured data.

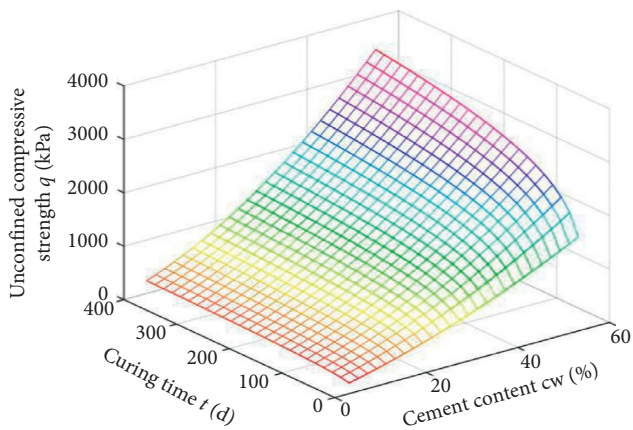


Figure 14: The prediction model of the UCS of the CMS.

## 4. Microscopic Test and Mechanism Analysis

In order to further explore the formation mechanism of the UCS of the CMS by the cement content and curing age, we used SEM, EDX, and XRD testing methods to test the microstructure, element changes, and compound change rules of CMS, so as to study the micromechanism of the time effect of CMS. The test scheme is shown in Table 4.

Table 4: The CMS microtest scheme.

| Cement content/(%) | Curing age/(d) | Test content |
|---|---|---|
| 5 and 20 | 7, 28 and 90 | SEM, EDX, and XRD |

*4.1. SEM Test.* The SEM microtest is a popular microtest method commonly used in civil engineering and geotechnical engineering. SEM is used to enlarge the sample into the specified multiples, and the corresponding multiple microscopic images can be obtained directly. The uneven microstructure on the surface of the sample can be seen intuitively, and the particle distribution, pore distribution, and particle size inside the sample can be clearly observed. A JSM-6360LU tungsten filament high and low vacuum scanning electron microscope instrument produced by Japan Electronics Co., Ltd was used in this test. The SEM test was performed according to the test scheme in Table 4, and the SEM microscopic images of the CMS are shown in Figure 15.

When the curing age is 7 d, the microstructure of CMS with a cement content of 5% is filled with more small particle units, few large particle units, a low degree of internal cementation, and a large number of pores, as shown in Figure 15(a). The microstructure of CMS with a cement content of 20% has larger pores, as shown in Figure 15(b). Compared with Figure 15(a), there are fewer small particle units and more large groups cemented together, forming a large group cemented loose structure at the microscopic scale. The reason is that, with the increasing cement content, after the hydration reaction, more gelling substances will be generated, which will further react to form crystals. In addition, these gelling substances will also wrap the slurry particles to cement them together to form a larger structure, thereby improving the strength of the slurry.

When the curing age was 28 d, there was a small amount of gelling substance inside the CMS sample with a cement content of 5%. However, there were interspaces inside the sample, and the cementation among the units was poor. The overall skeleton was more dispersed, as shown in Figure 15(c). In the microstructure of the CMS with a cement content of 20%, the large particle units became significantly larger, and a small amount of the small particle units is attached to the large particles, as shown in Figure 15(d). Compared with Figure 15(b), the microstructure of the CMS at the 28 d curing age was more compact, which was reflected in the increase of strength, microscopically.

When the curing age was 90 d, compared with the curing age of 7 d and 28 d, the microstructure of the CMS sample with a cement content of 5% had a larger number of large particle units, with only a few small particle units. The degree of cementation between the large particle units was improved, and the pores between the samples decreased. The cementation between units was poor, and the overall skeleton was relatively dispersed, as shown in Figure 15(e). This is because the cement content was too small, resulting in less gelling substances generated by cement hydration, which could not fill the internal pores of the CMS. In the microstructure of the CMS with a cement content of 20%, the overall cementation degree was further deepened, and the structure was more compact, presenting a complete skeleton as shown in Figure 15(f).

We concluded from the above analysis that, with the increase in curing age and cement content, the gelling substances in the microstructure of CMS gradually increased, filling the pores among the soil particles, thereby improving the microstructure compactness of the CMS. Macroscopically, the UCS of the CMS gradually increased with the increase in the curing age and cement content.

*4.2. EDX Test.* By means of high-energy X-ray, the X-ray energy spectrometer recoordinated the atoms in the sample atoms, and the electrons in the outer layer supplemented the vacancy of the electrons in the inner layer, thus releasing the characteristic X-rays, whose wavelength has a certain relationship with the atomic number. Qualitative analysis can be performed according to the wavelength of the spectral line, and the content of the element can also be obtained. The X-ray energy spectrometer used in this test was the British Oxford X-act energy spectrometer produced by the Beijing OBR Scientific Instrument Co., Ltd. The EDX test was performed according to the test scheme in Table 4, and the energy spectrum of the CMS was obtained as shown in Figure 16.

It can be seen from Figure 16 that the main elements in the CMS are Si, O, Al, and Ca. This is because the main minerals, dicalcium silicate and tricalcium silicate, in cement undergo a hydration reaction with water, resulting in the production of gelling substances to improve the strength of the slurries. The chemical components in gelling substances are mainly Si, O, Al, and Ca elements.

*4.3. XRD Test.* The X-ray diffractometer is an analytical instrument for researching and identifying the composition and atomic structure of crystalline substances and materials. The wavelength of X-rays is close to the distance between the atomic surfaces inside the crystal. The crystal can be used as a spatial diffraction grating of X-rays. That is, when an X-ray beam is irradiated on an object, it is scattered by the atoms in the object, and each atom generates a scattered wave. These waves interfere with each other, resulting in diffraction. The superposition of the diffraction waves makes the intensity of the rays strengthen in some directions and weaken in other directions. By analyzing the diffraction results, the crystal structure can be obtained, and its composition can be analyzed. The XRD test was performed according to the test scheme in Table 4, and the X-ray diffraction analysis chart of the CMS is shown in Figure 17.

It can be seen from Figure 17 that the compounds in the CMS are mainly $SiO_2$, $Al_2O_3$, and $CaCO_3$, which are in good agreement with the EDX test results. According to the XRD test results, the mass ratios of $SiO_2$, $CaCO_3$, and $Al_2O_3$ at the curing ages of 7 d, 28 d, and 90 d with a cement content of 5% and 20% can be obtained through statistics, as shown in Figure 18.

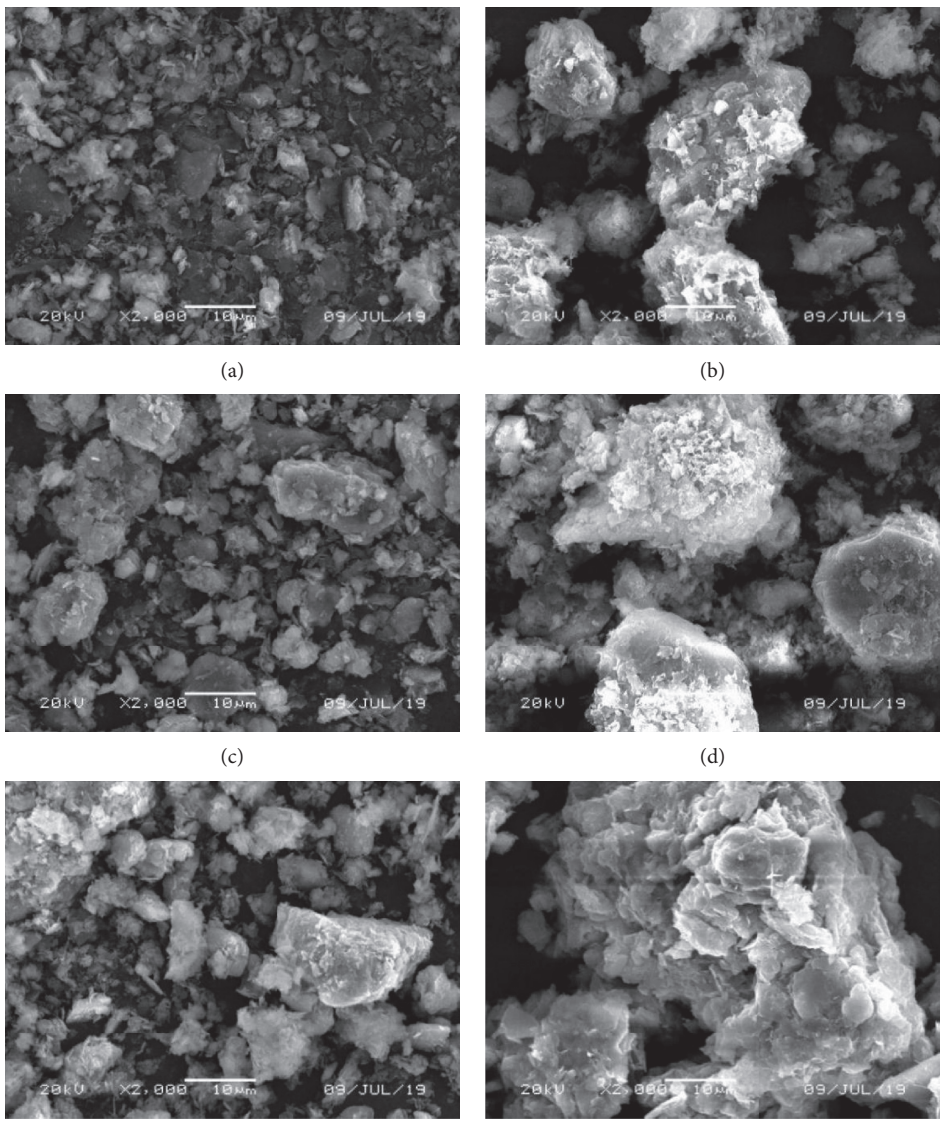


Figure 15: SEM images of CMS with different cement contents and curing ages. (a) Cement content 5% and curing age 7 (d). (b) Cement content 20% and curing age 7 (d). (c) Cement content 5% and curing age 28 (d). (d) Cement content 20% and curing age 28 (d). (e) Cement content 5% and curing age 90 (d). (f) Cement content 20% and curing age 90 d.

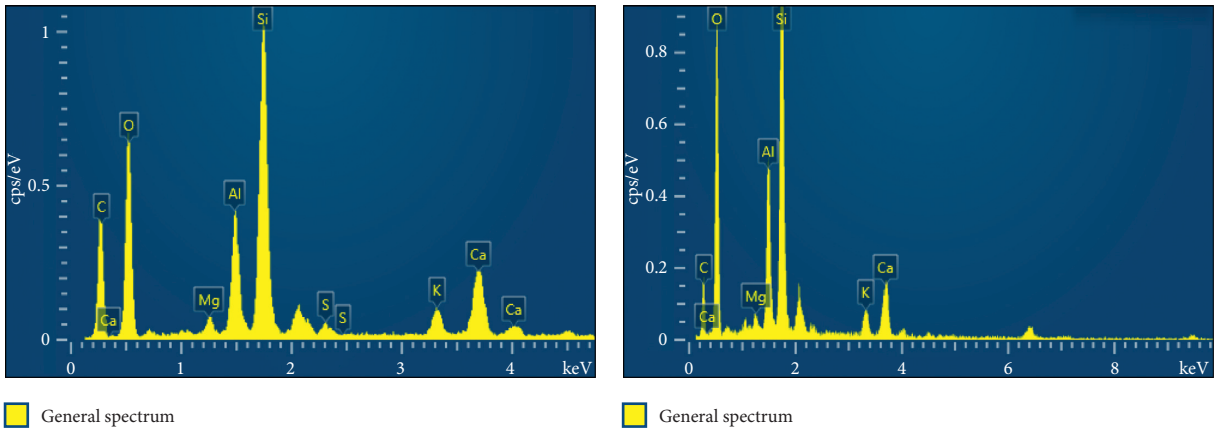


Figure 16: Continued.

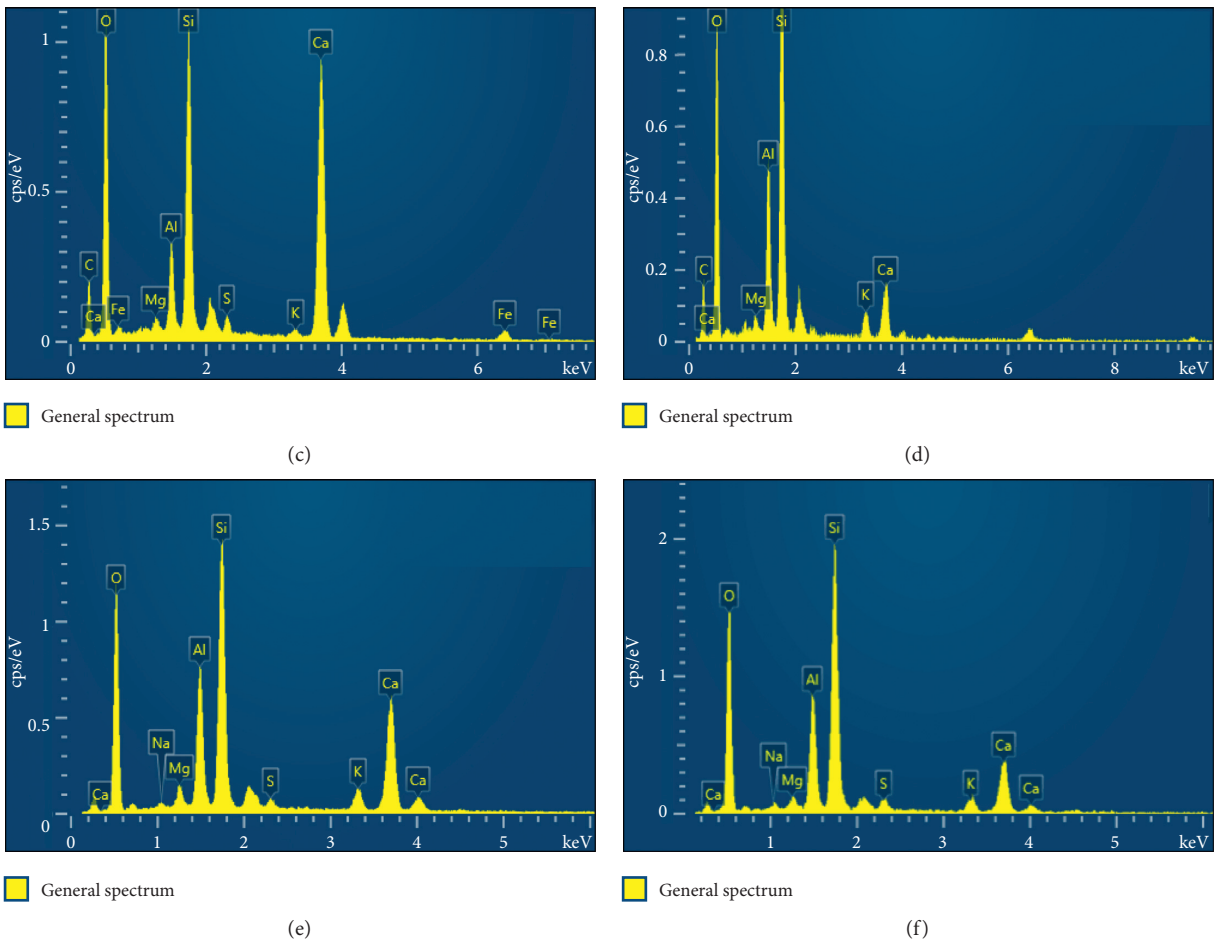


Figure 16: EDX test results under different cement content and curing age. (a) Cement content 5% and curing age 7 (d). (b) Cement content 5% and curing age 28 (d). (c) Cement content 5% and curing age 90 (d). (d) Cement content 20% and curing age 7 (d). (e) Cement content 20% and curing age 28 (d). (f) Cement content 20% and curing age 90 d.

It can be seen from Figure 18 that the mass ratios of $SiO_2$, $Al_2O_3$, and $CaCO_3$ increased with the increasing cement content and curing age.

According to reference [31], the direction index of $SiO_2$ can be calculated. The relative UCS and relative direction index are calculated based on the strength and direction coefficient of the CMS with a cement content of 20% and at a 28 d curing age. The calculated results are shown in Figure 19.

As can be seen from Figure 19, there is a negative linear correlation between the relative UCS and relative direction coefficient. That is, as the UCS increases, the direction coefficient gradually decreases.

*4.4. Micromechanical Analysis.* We concluded through the EDX and XRD tests that, under the same curing age, the mass ratios of Si, Al, and Ca increased with the increase of cement content, due to the chemical reaction between the cement and soil particles and the water inside the slurry. The higher the cement content was, the more the dicalcium silicate, tricalcium silicate, and alumina were produced by the reaction. With the same cement content, the mass ratios of Si, Al, and Ca elements increased with the increase in the curing age. This is because the strength improvement effect of the dicalcium silicate began to play its role after curing for 28 days. As the curing age increased, the hydration reaction of the cement became more and more sufficient, and more hydration products are generated.

As can be seen in Figure 17, the composition and types of the compounds did not change along with the increase of the cement content and curing age. This is because the main components of cement are dicalcium silicate ($C_2S$), tricalcium silicate ($C_3S$), tricalcium aluminate ($C_3A$), tetracalcium iron aluminate ($C_4AF$), and the hydration reaction equations are shown in equations (8)–(11), respectively:

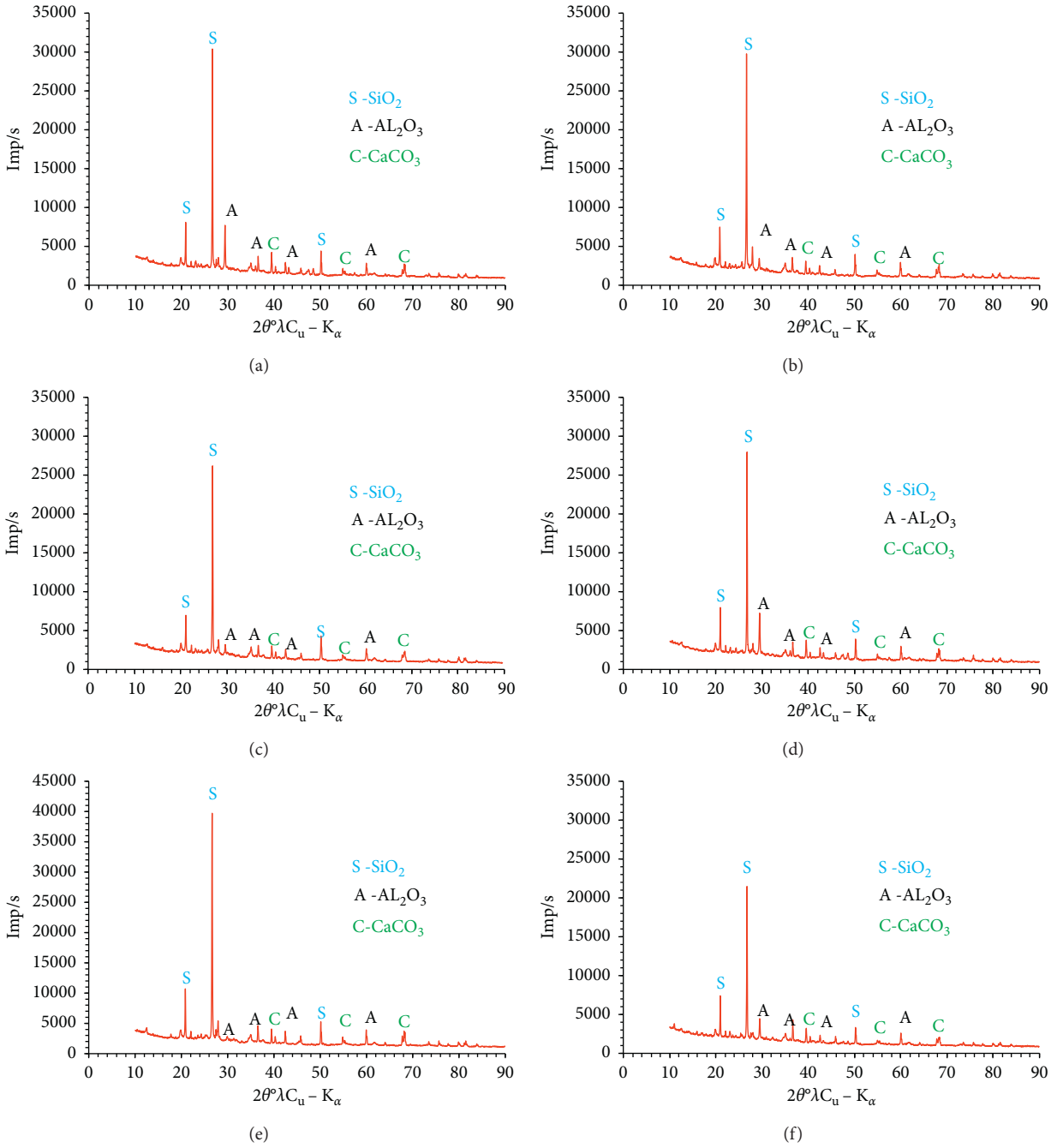


Figure 17: The XRD images of different cement contents and curing ages. (a) Cement content 5% and curing age 7 d. (b) Cement content 20% and curing age 7 d. (c) Cement content 5% and curing age 28 d. (d) Cement content 20% and curing age 28 d. (e) Cement content 5% and curing age 90 d. (f) Cement content 20% and curing age 90 d.

$$x\left(2\mathrm{CaO}\cdot\mathrm{SiO}_2\right)+y\mathrm{H}_2\mathrm{O}=z\mathrm{CaO}\cdot x\mathrm{SiO}_2\left(y-2x+z\right)\mathrm{H}_2\mathrm{O}+(2x-z)\mathrm{Ca}\left(\mathrm{OH}\right)_2, \tag{8}$$

$$m\left(3\mathrm{CaO}\cdot\mathrm{SiO}_2\right)+n\mathrm{H}_2\mathrm{O}=k\mathrm{CaO}\cdot m\mathrm{SiO}_2\left(n-3m+k\right)\mathrm{H}_2\mathrm{O}+(3m-k)\mathrm{Ca}\left(\mathrm{OH}\right)_2, \tag{9}$$

$$3\mathrm{CaO}\cdot\mathrm{Al}_2\mathrm{O}_3+6\mathrm{H}_2\mathrm{O}=3\mathrm{CaO}\cdot\mathrm{Al}_2\mathrm{O}_3 6\mathrm{H}_2\mathrm{O}, \tag{10}$$

$$4\mathrm{CaO}\cdot\mathrm{Al}_2\mathrm{O}_3\cdot\mathrm{Fe}_2\mathrm{O}_3+7\mathrm{H}_2\mathrm{O}=3\mathrm{CaO}\cdot\mathrm{Al}_2\mathrm{O}_3\cdot 6\mathrm{H}_2\mathrm{O}+\mathrm{CaO}\cdot\mathrm{Fe}_2\mathrm{O}_3\cdot\mathrm{H}_2\mathrm{O}. \tag{11}$$

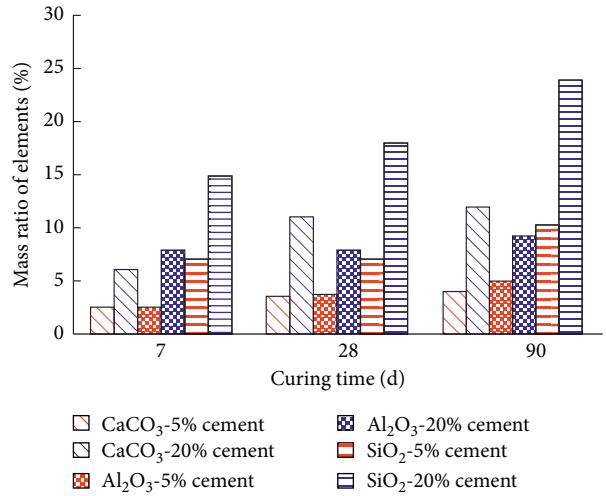


Figure 18: The relationship between mass ratios of various elements with different cement contents.

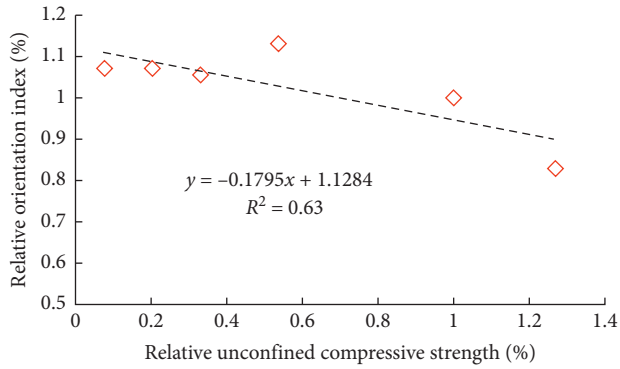


Figure 19: The relationship curve between the relative UCS and relative direction coefficients.

The hydration reaction of C2S and C3S is the main reason for the formation of CMS strength. The action times of the two mineral components are different. C3S generally exerts its improvement effect within 28 days, while C2S begins to exert its effect after 28 days. Therefore, with the increase in curing age, the hydration reaction products increased, and the corresponding Si, O, Al, Ca, and the other elements increased. Therefore, it can be explained from the perspective of the element composition that the UCS of the CMS increased with the increase in curing age.

According to Figure 17, under the same curing age, the $SiO_2$, $CaCO_3$, and $Al_2O_3$ contents of CMS increased with the increase of cement content. As a result, the hydration reaction products in CMS increased to improve its UCS.

## 5. Conclusions and Discussions

*5.1. Conclusions.* By studying the time effect and micromechanisms of the UCS of the CMS, the following conclusions can be obtained:

(1) With the increase of the cement content and curing age, the UCS of the CMS improved significantly. From the curing age of 7 d to 180 d, the UCS of the CMS in each curing age increased with the increase of cement content, and the growth rate of the UCS of the CMS with a cement content from 20% to 25% significantly decreased. Thus, we concluded that the 20% cement content was the optimal content.

(2) With the cement content from 5% to 25%, the UCS of the CMS at each cement content increased first and then tended to be constant with the increase in the curing age. The UCS at the curing age of 180 d was about 2.5 times higher than that at 7 d.

(3) Based on the mathematical characteristics of the strength-age curve and the strength-cement content curve, a time effect model was established, which could better characterize the relationship between the UCS of the CMS and the curing age and the cement content. This can effectively predict and guide the use of CMS in engineering practice.

(4) The strength formation mechanism of CMS mainly includes the following two aspects: on one hand, the hydration reaction of C2S and C3S in cement generated gelling substances, which fill the pores among the particles, thereby improving the strength of CMS. On the other hand, with the increase of the cement

content and curing age, more and more gelling substances were formed, which results in the small particles clumping together to form a larger cement soil mass, thus increasing the strength of the CMS.

*5.2. Discussions.* The strength change law of CMS under different curing ages was obtained by UCS tests and microscopic test. It should be noted that:

(1) This study only discussed the UCS time effect of CMS with 100% moisture content. For other representative moisture contents, such as optimal moisture content, plastic limit and liquid limit, the UCS time effect model of CMS needs to be further studied.

(2) Environmental factors have a certain influence on the UCS of CMS, so it is necessary to study the modification of time effect model of CMS by dry wet cycles and freeze-thaw cycles.

(3) The role of other materials such as nanomaterials [32, 33], polymer materials [34–36], and fibers [37–40] can improve the mechanical properties of building materials, and it is necessary to study the application of these materials in CMS modification.

## Data Availability

The data used to support the findings of this study are available from the corresponding author upon request.

## Conflicts of Interest

The authors declare that they have no conflicts of interest.

## Authors' Contributions

W. W. and J. Y. conceptualized the study L. Z. and T. M. performed investigation; P. J. wrote the original draft; Y. C. and N. L reviewed and edited the article. All authors have read and agreed to the published version of the manuscript.

## Acknowledgments

This research was funded by the National Natural Science Foundation of China (Grant number 41772311), the Zhejiang Provincial Natural Science Foundation of China (Grant number Q20E080042), the Open Research Fund of Key Laboratory of Ministry of Education for Geomechanics and Embankment Engineering of Hohai University (Grant number 2019020), and the Open Research Fund of State Key Laboratory of Geomechanics and Geotechnical Engineering, Institute of Rock and Soil Mechanics, Chinese Academy of Science (Grant number Z017013).

## References

[1] C. Zhang, J. Fu, J. Yang, X. Ou, X. Ye, and Y. Zhang, "Formulation and performance of grouting materials for underwater shield tunnel construction in karst ground," *Construction and Building Materials*, vol. 187, pp. 327–338, 2018.

[2] Y. Chen, S. Gao, L. Chen, G. Chen, and J. Chen, "Laboratory and field test study on the improvement of marine clay slurry by in-situ solidification," *Marine Georesources & Geotechnology*, vol. 37, no. 6, pp. 695–703, 2019.

[3] Y. Cheng, S. Wang, J. Li, X. Huang, C. Li, and J. Wu, "Engineering and mineralogical properties of stabilized expansive soil compositing lime and natural pozzolans," *Construction and Building Materials*, vol. 187, pp. 1031–1038, 2018.

[4] P. Jiang, T. Mao, N. Li, L. Jia, F. Zhang, and W. Wang, "Characterization of short-term strength properties of fiber/cement-modified slurry," *Advances in Civil Engineering*, vol. 20199 pages, 2019.

[5] K. Yao, Q. S. Chen, J. H. Ho, H. W. Xiao, and F. H. Lee, "Strain-dependent shear stiffness of cement-treated marine clay," *Journal of Materials in Civil Engineering*, vol. 30, Article ID 04018255, 2018.

[6] K. Yao, N. Li, D.-H. Chen, and W. Wang, "Generalized hyperbolic formula capturing curing period effect on strength and stiffness of cemented clay," *Construction and Building Materials*, vol. 199, pp. 63–71, 2019.

[7] W. Wang, C. Zhang, N. Li, F. Tao, and K. Yao, "Characterisation of nano magnesia-cement-reinforced seashore soft soil by direct-shear test," *Marine Georesources & Geotechnology*, vol. 37, no. 8, pp. 989–998, 2019.

[8] K. Yao, D. An, W. Wang, N. Li, C. Zhang, and A. Zhou, "Effect of nano-mgo on mechanical performance of cement stabilized silty clay," *Marine Georesources & Geotechnology*, vol. 38, no. 2, pp. 250–255, 2020.

[9] N. Li, S. W. Lv, W. Wang, J. Guo, P. Jiang, and Y. Liu, "Experimental investigations on the mechanical behavior of iron tailings powder with compound admixture of cement and nano-clay," *Construction and Building Materials*, vol. 254, Article ID 119259, 2020.

[10] W. Wang, Y. Li, K. Yao, N. Li, A. Z. Zhou, and C. Zhang, "Strength properties of nano-MgO and cement stabilized coastal silty clay subjected to sulfuric acid attack," *Marine Georesources & Geotechnology*, vol. 3, pp. 1–10, 2019.

[11] S.-Y. Pu, Z.-D. Zhu, W.-L. Song, H.-R. Wang, and R.-J. Wei, "Deformation properties of silt solidified with a new SEU-2 binder," *Construction and Building Materials*, vol. 220, pp. 267–277, 2019.

[12] N. Yoobanpot, P. Jamsawang, and S. Horpibulsuk, "Strength behavior and microstructural characteristics of soft clay stabilized with cement kiln dust and fly ash residue," *Applied Clay Science*, vol. 141, pp. 146–156, 2016.

[13] G. Dai, Y. Sheng, Y. Pan, G. Shi, and S. Li, "Application of a bentonite slurry modified by polyvinyl alcohol in the cutoff of a landfill," *Advances in Civil Engineering*, vol. 2020, pp. 1–9, 2020.

[14] Y. X. Wu, S. L. Shen, Z. Y. Yin, and Y. S. Xu, "Characteristics of groundwater seepage with cut-off wall in gravel aquifer. II: numerical analysis," *Canadian Geotechnical Journal*, vol. 52, Article ID 150223161106004, 2015.

[15] Y. Pan and Y. Fu, "Effect of random geometric imperfections on the water-tightness of diaphragm wall," *Journal of Hydrology*, vol. 580, Article ID 124252, 2019.

[16] Y. Pan, Y. Liu, A. Tyagi, F.-H. Lee, and D.-Q. Li, "Model-independent strength-reduction factor for effect of spatial variability on tunnel with improved soil surrounds," *Géotechnique*, vol. 3, pp. 1–17, 2020.

[17] P. Croce and G. Modoni, "Design of jet-grouting cut-offs," *Ground Improvement*, vol. 10, no. 1, pp. 1–9, 2007.

[18] J. J. Zheng, Y. Liu, Y. T. Pan, and J. Hu, "Statistical evaluation of the load-settlement response of a multicolumn composite

foundation," *International Journal of Geomechanics*, vol. 18, no. 4, Article ID 04018015, 2018.

[19] A. Tyagi, Y. Liu, Y. T. Pan, K. Bte, and M. Ridhwan, "Stability of tunnels in cement-admixed soft soils with spatial variability," *Journal of Geotechnical & Geoenvironmental Engineering*, vol. 144, no. 12, pp. 1–7, 2018.

[20] Y. Liu, F.-H. Lee, S.-T. Quek, E. J. Chen, and J.-T. Yi, "Effect of spatial variation of strength and modulus on the lateral compression response of cement-admixed clay slab," *Géotechnique*, vol. 65, no. 10, pp. 851–865, 2015.

[21] Y. Liu, L. Q. He, Y. J. Jiang, M. M. Sun, E. J. Chen, and F.-H. Lee, "Effect of in situ water content variation on the spatial variation of strength of deep cement-mixed clay," *Géotechnique*, vol. 69, no. 5, pp. 391–405, 2019.

[22] S. Horpibulsuk, N. Miura, and T. S. Nagaraj, "Assessment of strength development in cement-admixed high water content clays with Abrams' law as a basis," *Géotechnique*, vol. 53, no. 4, pp. 439–444, 2003.

[23] F.-H. Lee, Y. Lee, S.-H. Chew, and K.-Y. Yong, "Strength and modulus of marine clay-cement mixes," *Journal of Geotechnical and Geoenvironmental Engineering*, vol. 131, no. 2, pp. 178–186, 2005.

[24] H. Xiao, F. H. Lee, and K. G. Chin, "Yielding of cement-treated marine clay," *Soils and Foundations*, vol. 54, no. 3, pp. 488–501, 2014.

[25] Y. Liu, Y. J. Jiang, H. Xiao, and F. H. Lee, "Determination of representative strength of deep cement-mixed clay from core strength data," *Géotechnique*, vol. 67, no. 4, pp. 1–15, 2017.

[26] S. E. Mousavi, "Stabilization of compacted clay with cement and/or lime containing peat ash," *Road Materials and Pavement*, vol. 18, pp. 1–18, 2017.

[27] H. Mola-Abasi, B. Kordtabar, and A. Kordnaeij, "Effect of natural zeolite and cement additive on the strength of sand," *Geotechnical and Geological Engineering*, vol. 34, no. 5, pp. 1–13, 2016.

[28] N. Ghasabkolaei, A. Janalizadeh, M. Jahanshahi, N. Roshan, and S. E. Ghasemi, "Physical and geotechnical properties of cement-treated clayey soil using silica nanoparticles: an experimental study," *The European Physical Journal Plus*, vol. 131, no. 5, pp. 1–11, 2016.

[29] A. A. Al-Homidy, M. H. Dahim, and A. K. Abd El Aal, "Improvement of geotechnical properties of sabkha soil utilizing cement kiln dust," *Journal of Rock Mechanics and Geotechnical Engineering*, vol. 9, no. 4, pp. 749–760, 2017.

[30] China National Standards JTG/3430-2020, *Test Method of Soils for Highway Engineering*, People's Communications Press, Beijing, China, 2020.

[31] J. Liu, J. Fu, T. Ni, and Y. Yang, "Fracture toughness improvement of multi-wall carbon nanotubes/graphene sheets reinforced cement paste," *Construction and Building Materials*, vol. 200, pp. 530–538, 2019.

[32] W. Wang, J. Li, and J. Hu, "Unconfined mechanical properties of nanoclay cement compound modified calcareous sand of the South China Sea," *Advances in Civil Engineering*, vol. 2020, Article ID 6623710, 16 pages, 2020.

[33] W. Wang, Y. Li, K. Yao, N. Li, A. Zhou, and C. Zhang, "Strength properties of nano-MgO and cement stabilized coastal silty clay subjected to sulfuric acid attack," *Marine Georesources & Geotechnology*, vol. 38, no. 10, pp. 1177–1186, 2020.

[34] M. Guo and Y. Tan, "Interaction between asphalt and mineral fillers and its correlation to mastics' viscoelasticity," *International Journal of Pavement Engineering*, vol. 22, no. 1, p. 1, 2019.

[35] M. Guo, H. Q. Liu, Y. B. Jiao et al., "Effect of WMA-RAP Technology on pavement performance of asphalt mixture: a state-of-the-art review," *Journal of Cleaner Production*, vol. 266, Article ID 121704, 2020.

[36] M. Guo, M. C. Liang, W. Zhao, Y. X. Duan, and H. Q. Liu, "A review of phase change materials in asphalt binder and asphalt mixture," *Construction and Building Materials*, vol. 258, Article ID 119565, 2020.

[37] N. Li, Y. Zhu, F. Zhang, S. M. Lim, W. Wu, and W. Wang, "Unconfined compressive properties of fiber-stabilized coastal cement clay subjected to freeze-thaw cycles," *Journal of Marine Science and Engineering*, vol. 9, no. 2, p. 143, 2021.

[38] Q. Guo, Z. Chen, P. Liu et al., "Influence of basalt fiber on mode I and II fracture properties of asphalt mixture at medium and low temperatures," *Theoretical and Applied Fracture Mechanics*, vol. 112, Article ID 102884, 2021.

[39] P. Jiang, S. L. Lv, Y. Wang, N. Li, and W. Wang, "Investigation on direct shear and energy dissipation characteristics of iron tailings powder reinforced by polypropylene fiber," *Applied Sciences*, vol. 9, pp. 50–98, 2019.

[40] Q. Guo, L. Li, Y. Cheng, Y. Jiao, and C. Xu, "Laboratory evaluation on performance of diatomite and glass fiber compound modified asphalt mixture," *Materials & Design (1980-2015)*, vol. 66, pp. 51–59, 2015.

Hindawi
Advances in Materials Science and Engineering
Volume 2021, Article ID 6614644, 8 pages
https://doi.org/10.1155/2021/6614644

*Research Article*

# Using the Rheological Index to Quantitatively Evaluate the Mechanical Performance of High-Elasticity Modified Asphalt

**Jiani Wang,[1] Zhongjun Xue,[2] Meng Guo ,[3] and Shuaixiang Zhang[3]**

[1]*Beijing University of Civil Engineering and Architecture, Beijing 100044, China*
[2]*The Key Laboratory of Evaluation and Authentication for New Materials and New Technologies of Beijing, Beijing Road Engineering Quality Supervision Station, Beijing 100076, China*
[3]*The Key Laboratory of Urban Security and Disaster Engineering of Ministry of Education, Beijing University of Technology, Beijing 100124, China*

Correspondence should be addressed to Meng Guo; gm@bjut.edu.cn

Received 3 December 2020; Revised 3 February 2021; Accepted 26 March 2021; Published 13 April 2021

Academic Editor: Fuat Kara



High-elasticity modified asphalt is widely used in OGFC and bridge deck paving due to its high viscosity and strong displacement recovery capacity. It can improve the high-temperature deformation resistance and elastic recovery ability of the pavement. Especially in bridge deck pavement, high-elastic modified asphalt can inhibit the formation of reflective cracks and extend the service life. In order to quantitatively evaluate properties of the high-elasticity modified asphalt, rheological properties are studied by using a dynamic shear rheometer (DSR) test. The parameters were fitted with the Burgers model, and the constitutive equation was established. The 3 s elastic recovery rate $E_r$ was proposed to quantitatively evaluate the elastic recovery of high-elasticity modified asphalt. The experimental results show that the instantaneous modulus of elasticity $G_0$ and the delayed modulus of elasticity $G_1$ can be used to evaluate the elastic capacity. $E_r$ can quantitatively evaluate the elastic resilience of high-elasticity modified asphalt. The correlation coefficient between the test results of high-elasticity modified asphalt and those of impact toughness evaluation reached 0.9966, and the 3 s elastic recovery rate $E_r$ could be used to evaluate the elastic recovery ability of high-elasticity modified asphalt.

## 1. Introduction

Asphalt mixtures used for pavements tend to harden and become brittle after prolonged exposure to ultraviolet radiation. Low-temperature cracking and fatigue cracking can be a problem in such environment [1–4]. For some bridge pavement, tunnel road, or airport pavement engineering projects, it is necessary to use modified asphalt with high-elastic recovery ability to solve heavy traffic, cracking, rutting, and other problems [5, 6]. Asphalt mixture is composed of coarse aggregate, fine aggregate, mineral powder, and asphalt, and asphalt is the only deformable component and continuous phase in asphalt mixtures [7, 8]. In this sense, the performance of asphalt binder has a direct impact on the mastics and mixtures [9, 10]. SHRP research results in the United States show that asphalt contributes 29% to high-temperature rut, 52% to fatigue, and 87% to temperature crack [11]. High-elastic asphalt (HEA), also known as high-elasticity modified asphalt, is a modified asphalt based on regular SBS asphalt using additional modifiers such as plasticizers and cross linkers [12, 13]. Compared with ordinary asphalt concrete, high-elasticity modified asphalt concrete performs well in low-temperature anticrack, absorption of diffusion, tensile stress, and good stress absorption capacity. Therefore, in recent years, it has been widely used in cement concrete pavement asphalt layer and cement concrete bridge pavement layer [14]. Hao [15] developed and applied high-elasticity modified asphalt to solve the fatigue cracking problem of asphalt mixture for steel bridge deck pavement. It has been proved by engineering practice that the fatigue life of steel bridge deck asphalt mixture is greatly improved by high-elasticity modified asphalt.

The excellent properties and practical value of high-elastic modified asphalt have also been widely verified in the laboratory. Dennyele [16] indicated through the test results of permeability, softening point, and elastic recovery of asphalt that the elastic properties and production material properties of high-elasticity modified asphalt were improved, which is suitable for application in highway construction. Luo [17] evaluated the rutting resistance, low-temperature performance, and wet-damage resistance of three different types of asphalt through dynamic stability test, three-point beam bending test, and tensile strength ratio test, respectively. It is verified that the HEA mixture containing Mafilon has better road performance and snowmelt performance than ordinary SBS, which also indicates the practical value of HEA. D'angelo [18] pointed out that in the multiple stress creep-recovery test (MSCR) data, there was an obvious relationship between the recovery rate of the creep part and the strain. According to the unrecovered strain at the end of the recovery part of the test divided by the initial stress applied by the creep part, the characteristic called unrecoverable compliance Jnr is defined. Much research expects to find new indices to evaluate the properties of modified asphalt. For instance, $(G^*/(1 - (1/\tan\delta \sin\delta)))$ proposed by Shenoy [19] is one of them, which is used to evaluate the high-temperature performance of polymer-modified asphalt. Qin [20] verified the high accuracy of the Burgers model in simulating the creep process of asphalt and evaluated the high-temperature performance of high-viscosity asphalt with multiple creep-recovery test. Pouria [21] used a generalized fractional viscoelastic model to study the creep and recovery properties of asphalt binders and evaluated the influence of modifier addition on nonlinear viscoelastic parameters of asphalt binders. Indirect tensile tests conducted by Baladi et al. on several modified asphalt mixtures showed that SBS modified asphalt could improve the tensile strength and stiffness of asphalt mixtures [22, 23]. Zhang's study [24] explored the correlation between different rheological indices to better evaluate the properties of asphalt, including complex modulus ($G^*$) and phase angle ($\delta$) master curves, rutting factor ($G^*/\sin\delta$), and zero shear viscosity (ZSV). SHRP also demonstrated a good correlation between the $G^* \times \sin\delta$ of asphalt and the fatigue performance of the mixture [25, 26]. Wang et al. [27] evaluated the antifatigue performance of asphalt and asphalt mixture, respectively, by using $G^* \times \sin\delta$ fatigue factor and four-point bending fatigue test. As a road material used in specific projects, high-elasticity modified asphalt needs more accurate and reliable performance evaluation methods to evaluate its elastic capacity, which is related to the fatigue life of the mixture. In order to guide the selection of materials in engineering, it is necessary to carry out in-depth research in this aspect.

The objective of this research is to define an appropriate parameter to make the high-elasticity modified asphalt binder better distinguishable from other modified asphalt binder based on rheological properties and to compare the performance of different high-elasticity modified asphalt binders more rigorously. In our study, the creep-recovery curves of different asphalt samples were tested by dynamic shear rheometer, and the Burgers model was selected to define the creep and creep-recovery of asphalt materials. Combining speed and safe distance, 3 s elastic recovery rate was defined to characterize the elastic recovery ability of high-elastic modified asphalt. Through this parameter, the branch of high-elasticity modified asphalt could be better distinguished from other functional modified asphalt binders. The reliability of this index was verified by the impact toughness test.

## 2. Materials and Test Methods

*2.1. Experimental Materials.* By adding various polymers, including polyethylene (PE), polypropylene (PP), and styrene–butadiene–styrene (SBS), asphalt can be modified to obtain better mechanical properties and road performance [28–30]. HEA is usually produced by adding a plasticizer and cross-linker to regular SBS modified asphalt. By changing the SBS block ratio, a new SBS modifier was developed and high-viscosity and high-elasticity modified asphalt was prepared. The shear temperature was 170°C, the shear rate was 4000 r/min, the shear time was 50 min, and the development time was 60 min. Five kinds of high-elasticity modified asphalt with different dosages were prepared. They were labeled as HEA1, HEA2, HEA3, HEA4, and HEA5, respectively, and their properties are shown in Table 1.

It can be seen from Table 1 that modified asphalt with different SBS modifier contents has different properties, among which the minimum value of elastic recovery test is 94% and the maximum value is 99%, both of which are far higher than the upper limit of SBS modification documented in "technical specification for construction of asphalt pavement," namely, 75%. However, the elastic recovery ability of those five high-elasticity modified asphalt is not significantly different by using traditional indicators, so its performance cannot be well distinguished. Therefore, a highly discriminative index is urgently needed to evaluate the elastic recovery ability of high-elasticity modified asphalt.

*2.2. Laboratory Testing*

*2.2.1. Repeat Creep Experiment.* In order to compare the creep properties of different high-elasticity modified asphalt binders, five kinds of high-elasticity modified asphalt binders and two kinds of virgin asphalt binders were tested by rheometer under 40°C, 50°C, 60°C, and 70°C. Each cycle includes 1 s loading and 9 s unloading. In order to ensure that the asphalt binder was in the linear viscoelastic range, the stress of 300 Pa was used in the test. The creep-recovery curves under different loading times were obtained by preloading 200 cycles.

*2.2.2. Model Selection.* Asphalt is composed of hydrocarbons and their nonmetallic derivatives with extremely complex chemical constituents. Although the composition is extremely complex, asphalt still has the basic characteristics

Table 1: Performance of different modified asphalt binders with various modifier dosages.

| Test item | | Unit | HEA1 | HEA2 | HEA3 | HEA4 | HEA5 |
|---|---|---|---|---|---|---|---|
| Penetration (25°C, 100 g, 5 s) | | 0.1 mm | 61 | 59 | 58 | 55 | 60 |
| Penetration index | | — | 0.10 | 0.22 | 0.42 | 0.77 | 0.53 |
| Ductility (5°C, 5 cm/min) | | cm | 54 | 53 | 58 | 43 | 45 |
| Softening point (ring and ball method) | | °C | > 90 | > 90 | > 90 | > 90 | > 90 |
| Flash point (opening) | | °C | > 260 | > 260 | > 260 | > 260 | > 260 |
| Storage stability (softening point difference) (165°C, 48 hr) | | °C | 1.5 | 1.5 | 2.0 | 4.5 | 3.0 |
| Elastic recovery (25°C, 10 cm) | | % | 94 | 95 | 99 | 96 | 98 |
| Dynamic viscosity (60°C) | | Pa·s | 169403 | 430521 | 761774 | 440524 | 450535 |
| Kinematic viscosity (135°C) | | Pa·s | 2.3 | 2.5 | 3.1 | 3.8 | 4.0 |
| Residue of RTFOT (163°C, 75 min) | Elastic recovery (25°C, 10 cm) | % | 80 | 85 | 88 | 87 | 86 |
| | Penetration ratio (25°C) | % | 95 | 95 | 98 | 98 | 95 |
| | Ductility (5°C, 5 cm/min) | cm | 28 | 30 | 35 | 35 | 30 |

of amorphous structures. In the macrosense, asphalt is a homogeneous viscoelastic material. In the range of linear viscoelastic behavior, the creep and creep recovery of the Burgers model are shown in Figure 1. The four-unit Burgers model is most widely used in the research of asphalt rheology, as shown in Figure 2.

As shown in Figure 2, the instantaneous deformation is the elastic response of the material, and time-dependent deformation is the viscous part of the material, including viscoelasticity, namely, delayed elastic deformation and viscous flow deformation. After removing the load, the instantaneous elastic deformation immediately recovers. Viscous deformation no longer develops, but it cannot be recovered. The delayed elastic deformation gradually recovers at a decreasing rate. Therefore, the elastic recovery capacity of the asphalt used in the stress-absorbing layer mixture is required to be relatively high, and the size of permanent deformation should be close to 0. The constitutive equation of the Burgers model is shown in the following equation:

$$\gamma = \frac{\tau_0}{G_0} + \frac{\tau_0}{G_1}\left(1 - e^{\left(-tG_1/\eta_1\right)}\right) + \frac{\tau_0}{\eta_0}t = \gamma_e + \gamma_{de} + \gamma_v, \quad (1)$$

where $\gamma$ is the shear strain, $\tau_0$ is constant shear stress (creep load), Pa, $G_0$ is elastic modulus in Maxwell model, Pa, $G_1$is the modulus of elasticity in the Kelvin model, Pa, $\eta_1$ is the coefficient of viscosity in the Kelvin model (viscosity), Pa·s, $\eta_0$ is the viscosity coefficient in Maxwell model (viscosity), Pa·s; $t$ is creep time (loading time).

It can be seen that the strain response of the Burgers model is divided into elastic parts $\gamma_e$, delayed elastic part $\gamma_{de}$ , and the viscous part $\gamma_v$. Compliance is the strain equivalent to unit stress and reflects the deformation property of the material. Corresponding to formula (1), the creep compliance of asphalt consists of three parts: the elastic part $J_0$, the delayed elastic part $J_{de}$ , and the viscous part $J_v$:

$$J(t) = J_0 + J_{de} + J_v = \frac{1}{G_0} + \varphi(t) + \frac{t}{\eta_0}, \quad (2)$$

where $J(t)$ is the creep compliance, $J_0$ is instantaneous/glassy shear compliance, $J_{de}$ is the delayed shear compliance, and $J_v$ is the viscous creep compliance.

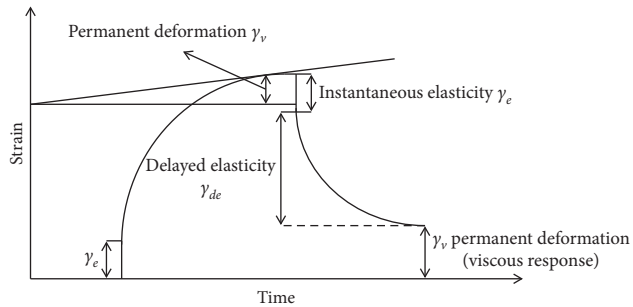


Figure 1: Creep-recovery response of binders.

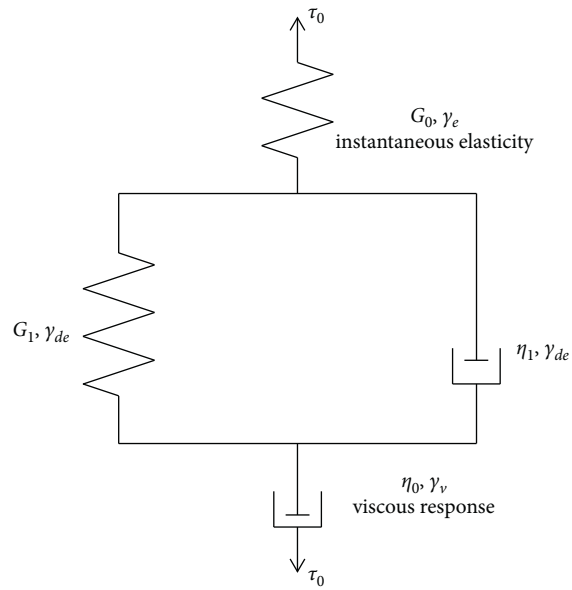


Figure 2: Burgers rheological model.

The Burgers model shows high accuracy in simulating asphalt's creep process [20]. Furthermore, the four-unit burgers model has good convergence. Therefore, this paper selected the Burgers model as the rheological model of fitting parameters.

*2.2.3. Impact Toughness Test.* The five kinds of high-elasticity modified asphalt mentioned above were used respectively, and the same gradation, aggregate, and mineral powder were selected to make the stress-absorbing layer mixture. According to the requirements of "Standard Test Methods of Bitumen and Bituminous Mixtures for Highway Engineering," the 300 mm × 300 mm × 50 mm specimens were made by wheel-grind method.

The formed specimens were cut into prismatic specimens of 250 mm × 35 mm × 35 mm using the double-sided saw cutter made in Finland in the laboratory.

The test procedure is detailed as follows: the prepared asphalt concrete prism was placed in a constant temperature tank at the specified temperature for 2~4 h. The test specimen should be spaced, and the bottom of it should be padded, not less than 5 cm from the bottom of the container. The test was carried out after the water bath, and the loading rate was set at 500 mm/min. The test specimen should be removed from the constant temperature water bath for no more than 1 min at the end of the test, in order to avoid temperature changing of the trabecular beam after it is removed from the water bath.

## 3. Results and Discussion

*3.1. Repeat Creep Experiment.* As can be seen from Figure 3, the strain tends to be stable after loading more than 50 times, and the strain gradually becomes larger and larger with the increase of loading times, but the difference is not significant. Therefore, the number of subsequent tests is selected as 100 cycles, and the 50$^{th}$ cycle is taken for analysis [31].

*3.2. Fitting Based on Burgers Model.* By comparing the viscosity, elasticity, and delayed elasticity parameters of various bitumen, the following can be found:

(1) The instantaneous elastic modulus of HEA3 is 833 times that of matrix asphalt and 14 times that of ordinary modified asphalt

(2) The difference in delayed elastic properties of $G_1$ was also significant, among which the high-elasticity modified asphalt HEA3 was 19 times that of the matrix asphalt

(3) In terms of creep stiffness of viscous component $\eta_0$, HEA3 is 13 times that of matrix asphalt and 3 times that of ordinary modified asphalt, so highly elasticity modified asphalt has the strongest rutting resistance

The rheological properties of asphalt binders can be quantitatively evaluated with Table 2, but its elastic recovery ability cannot be well evaluated. $\varepsilon_L$ is the total strain under creep load, $\varepsilon_P$ is the residual strain after recovery stage, $\varepsilon_P/\varepsilon_L$ is used to characterize the elasticity of asphalt. This index can effectively distinguish general modified asphalt and virgin asphalt, mainly because of their different elastic recovery ability as shown in Figures 4 and 5.

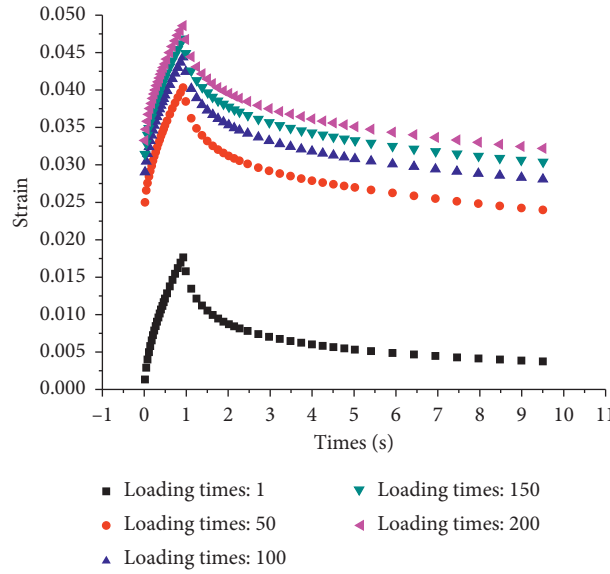


Figure 3: Creep-recovery response of binders.

However, the method mentioned above is not suitable for high-elasticity modified asphalt because the high-elasticity asphalt almost completely recovers its deformation within 9 s. Figure 6 shows the 50$^{th}$ repeated creep-recovery curve of five kinds of high-elasticity asphalt.

As can be seen from Figure 6, although the trend is similar, the elastic recovery of the five kinds of high-elastic modified asphalt is not the same. After 1 s loading, the deformation of the five samples reached the maximum. The deformation of HEA2 was the largest and that of HEA3 was the smallest. Considering the difference of permanent strain, a universal index should be defined. Therefore, in order to better evaluate the flexibility of high-elasticity modified asphalt recovery ability, assume a highway vehicle traffic speed of 120 km/h and a distance of 100 m intervals; then, the car after the time of arrival in the leading position needs 3 s, and the ideal state is the best state road within 3 s. For this reason, we define elastic recovery rate at 3 s to evaluate the elastic recovery capacity. $E_r$ is the percentage of the recovery strain $\varepsilon_{3S}$ at the end of 3 s unloading to the total strain $\varepsilon_L$ at the end of 1 s loading, as shown in formula (3). The index has a good differentiation as we can see from Figures 5 and 6.

$$Er = \frac{\varepsilon_{3S}}{\varepsilon_L} \times 100\%, \tag{3}$$

where $E_r$ is the elastic recovery rate at 3 s, $\varepsilon_{3S}$ is recovery strain at the end of 3 s unloading, and $\varepsilon_L$ is total strain at the end of 1 s loading.

The 3 s elastic recovery rate $E_r$ of five kinds of high-elasticity modified asphalt and ordinary modified asphalt was calculated by formula (3), as shown in Table 3.

From Table 3, the elastic recovery rate $E_r$ can clearly distinguish the elastic recovery capacity of different kinds of asphalt. HEA3 had the most outstanding elastic recovery ability, and the other high-elastic modified asphalt had

Table 2: Fitting parameters of the Burgers rheological model with different high-elasticity modified asphalt.

| Parameters | Virgin asphalt | Ordinary modified asphalt | HEA1 | HEA2 | HEA3 | HEA4 | HEA5 |
|---|---|---|---|---|---|---|---|
| $G_0$ (Pa) | $1.56E+03$ | $9.32E+04$ | $8.27E+05$ | $8.11E+05$ | $1.30E+06$ | $9.37E+05$ | $9.49E+05$ |
| $G_1$ (Pa) | $9.45E+04$ | $3.03E+05$ | $1.03E+06$ | $1.22E+06$ | $1.81E+06$ | $1.45E+06$ | $1.72E+06$ |
| $\eta_1$ (PaS) | $5.88E+05$ | $2.63E+05$ | $1.93E+05$ | $2.23E+05$ | $3.16E+05$ | $2.65E+05$ | $3.13E+05$ |
| $\eta_0$ (PaS) | $8.62E+04$ | $4.26E+05$ | $6.80E+05$ | $9.55E+05$ | $1.14E+06$ | $1.02E+06$ | $1.18E+06$ |
| $J_0$ (1/Pa) | $6.40E-04$ | $1.07E-05$ | $1.21E-06$ | $1.23E-06$ | $7.67E-07$ | $1.07E-06$ | $1.05E-06$ |
| $J_{de}$ (1/Pa) | $1.57\,E-06$ | $2.25\,E-06$ | $9.70\,E-07$ | $8.15\,E-07$ | $5.51\,E-07$ | $6.87\,E-07$ | $5.78\,E-07$ |
| $J_v$ (1/Pa) | $1.16E-05$ | $2.35E-06$ | $1.47E-06$ | $1.05E-06$ | $8.74E-07$ | $9.77E-07$ | $8.46E-07$ |
| $J(60)$ (1/Pa) | $6.53E-04$ | $1.53E-05$ | $3.65E-06$ | $3.10E-06$ | $2.19E-06$ | $2.73E-06$ | $2.48E-06$ |

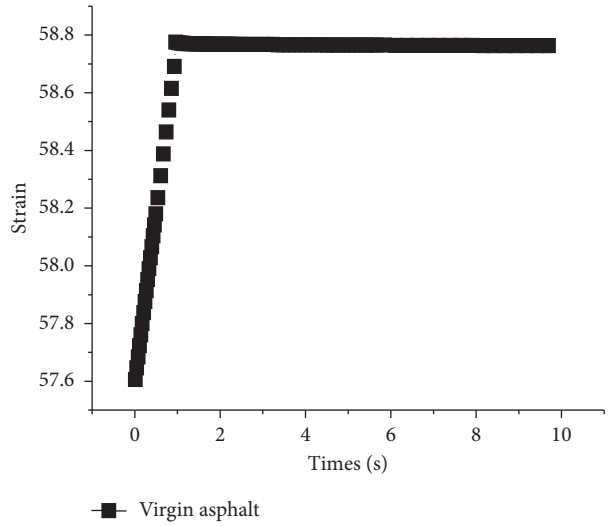


Figure 4: Creep-recovery response of virgin asphalt.

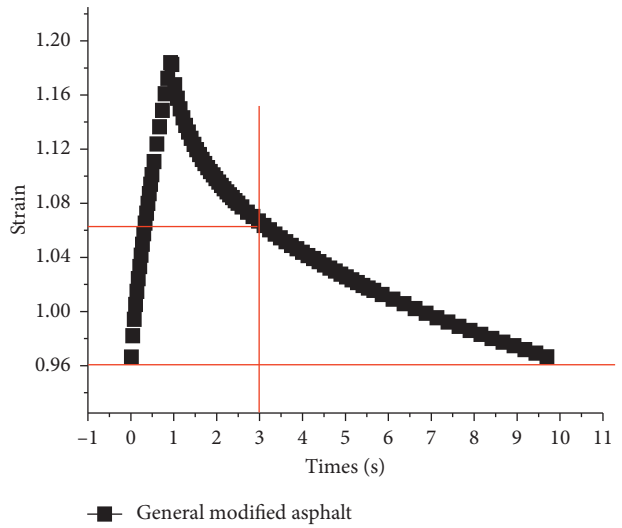


Figure 5: Creep-recovery response of general modified asphalt.

similar properties. Their elastic recovery ability was better than that of ordinary modified asphalt.

*3.3. Performance Verification Based on Impact Toughness Test.* The experimental results of impact toughness of five kinds of high-elasticity modified asphalt are shown in Figure 7.

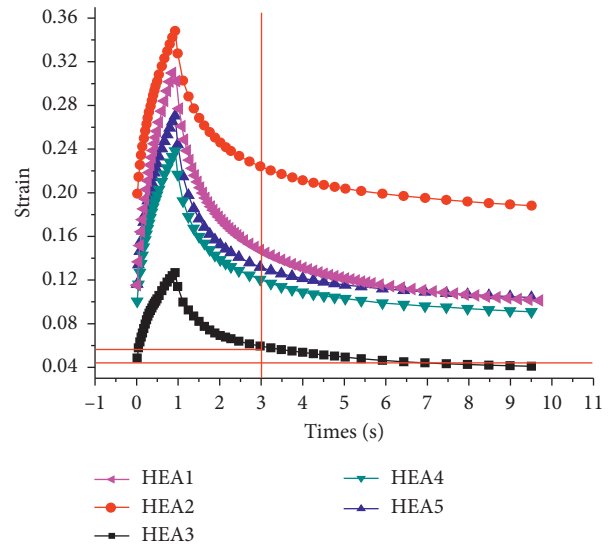


Figure 6: Creep-recovery response of five-type high-elasticity modified asphalt.

It can be seen from Figure 7 that the stress absorption layer produced by different kinds of high-elasticity asphalt has different impact toughness. The impact toughness can be calculated according to the area enclosed by the vertical line when the specimen was broken. When the failure displacement of each specimen was similar, the load applied to HEA3 was the maximum. The five kinds of modified asphalt have obvious differentiation.

The impact toughness test results of stress-absorbing layer asphalt mixture and the elastic recovery test results of 3 s before aging are shown in Table 4.

As can be seen from Table 4, the elastic recovery rate at 3 s and impact toughness show a positive correlation. In order to analyze the test results more intuitively, the relationship between impact toughness and elastic recovery rate at 3 s $E_r$ is drawn in the same diagram, as shown in Figure 8.

It can be seen from Figure 8 that impact toughness has a good correlation with 3 s elastic recovery rate $E_r$, and the correlation coefficient reaches 0.9966. Impact toughness refers to the ability of the material to absorb plastic deformation work and fracture work under impact load. From this, we can infer that the stronger the ability of the asphalt mixture to absorb plastic deformation work is, the more deformation can be recovered after the action of load. This also explains the good positive correlation between elastic recovery and impact

Table 3: Elastic recovery rates of different asphalt binders.

| Types of asphalt | Ordinary modified asphalt | HEA1 | HEA2 | HEA3 | HEA4 | HEA5 |
|---|---|---|---|---|---|---|
| Elastic recovery rate $E_r$ (%) | 56.5 | 82.5 | 83 | 93.3 | 85.7 | 87.5 |

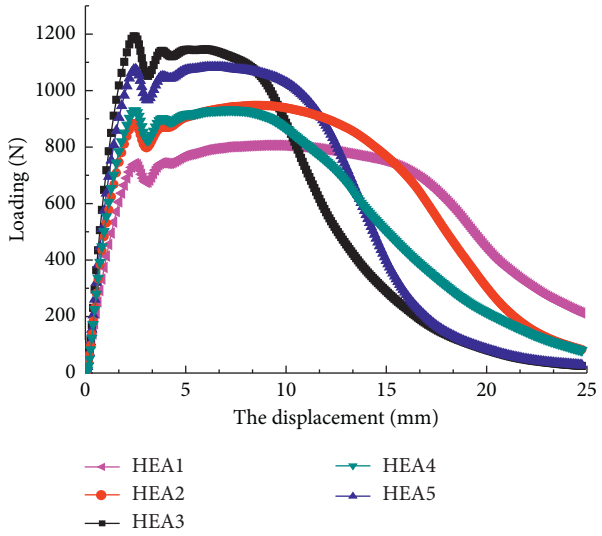


Figure 7: Impact toughness curve of asphalt with different asphalt binders.

Table 4: Elastic recovery and impact toughness OF high-elasticity modified asphalt.

| High-elasticity asphalt species | Elastic recovery rate at 3 s $E_r$ (%) | Impact toughness (N.m) |
|---|---|---|
| HEA3 | 93.3 | 1.95 |
| HEA5 | 87.5 | 1.74 |
| HEA4 | 85.7 | 1.51 |
| HEA2 | 83 | 1.36 |
| HEA1 | 82.5 | 1.26 |

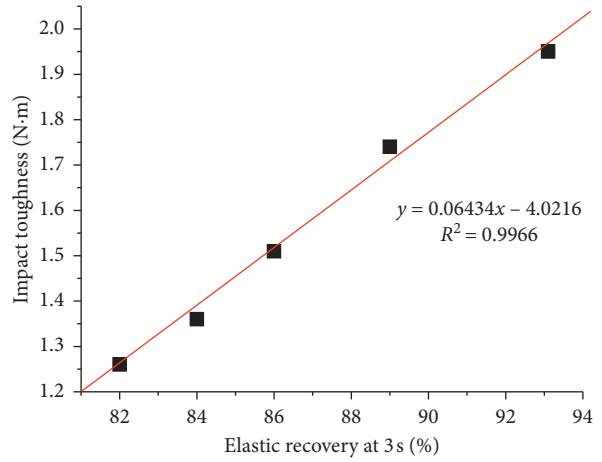


Figure 8: Correlation of impact toughness and elastic recovery at 3 s.

toughness. Experimental analysis shows that 3 s elastic recovery rate $E_r$ is a good indicator to evaluate the anti-impact performance of the stress absorption layer, and because impact toughness has a good correlation with fatigue life, the value of this indicator can indirectly reflect the antifatigue performance of the stress absorption layer [32, 33].

## 4. Conclusion

Through the rheological test, theoretical analysis, and impact performance verification of asphalt mixture, the main test conclusions are as follows:

(1) Burgers model can be used to fit the rheological behavior of high-elastic modified asphalt. The performance of instantaneous elastic modulus $G_0$ and delayed elastic modulus $G_1$ can be used to evaluate its elastic capacity.

(2) In combination with car following behavior on the highway, the percentage of 3 s recovery strain in the total strain at the end of 1 s loading was used to evaluate the elastic recovery ability of high-elasticity modified asphalt, which can be used to distinguish between ordinary modified asphalt and other high-elasticity modified asphalt.

(3) The correlation coefficient between the test results of high-elasticity modified asphalt and the test results of impact toughness evaluation reached 0.9966. The 3 s elastic recovery rate $E_r$ provides a means to predict the impact toughness of asphalt mixture.

## Data Availability

The data used to support the findings of this study are available from the corresponding author upon request.

## Conflicts of Interest

The authors declare that they have no conflicts of interest.

## Acknowledgments

This study was supported by the Beijing University of Civil Engineering and Architecture's Beijing Advanced Innovation Center for Future Urban Design's project "Research on the Technology of Ultra-Thin Anti-Slip Layer of Energy-Saving and Environment-Friendly Cold Mix and Cold Spread Asphalt Mixture" (Grant no. UDC2019032724), Beijing Hundred-Thousand-Ten Thousand Talents Project (Grant no. 2018A43), and Fundamental Research Funds for the Universities in Beijing "Study on Influencing Factors of Ultraviolet Aging of Asphalt Pavement Based on Micro-Analysis" (Grant no. X20072).

## References

[1] D. Zheng, Z.-D. Qian, P. Li, and L.-B. Wang, "Performance evaluation of high-elasticity asphalt mixture containing inorganic nano-titanium dioxide for applications in high altitude regions," *Construction and Building Materials*, vol. 199, pp. 594–600, 2019.

[2] A. Gundla, P. Gudipudi, and B. S. Underwood, "Evaluation of the sensitivity of asphalt concrete modulus to binder oxidation with a multiple length scale study," *Construction and Building Materials*, vol. 152, pp. 954–963, 2017.

[3] H. Zhang, Z. Chen, L. Li, and C. Zhu, "Evaluation of aging behaviors of asphalt with different thermochromic powders," *Construction and Building Materials*, vol. 155, pp. 1198–1205, 2017.

[4] Editorial Department of China Journal of Highway and Transport, "Review on China's pavement engineering research·2020," *China Journal of Highway and Transport*, vol. 33, no. 10, pp. 1–66, 2020.

[5] Q. Yang, Y. Qian, Z. Fan et al., "Exploiting the synergetic effects of graphene and carbon nanotubes on the mechanical properties of bitumen composites," *Carbon*, vol. 172, pp. 402–413, 2021.

[6] D. Wang, Q. Liu, Q. Yang, C. Tovar, Y. Tan, and M. Oeser, "Thermal oxidative and ultraviolet ageing behavior of nano-montmorillonite modified bitumen," *Road Materials and Pavement Design*, vol. 22, pp. 2164–7402, 2021.

[7] A. A. Cuadri, M. García-Morales, F. J. Navarro, and P. Partal, "Enhancing the viscoelastic properties of bituminous binders via thiourea-modification," *Fuel*, vol. 97, pp. 862–868, 2012.

[8] X. Xu, Z. Leng, J. T. Lan et al., "Sustainable practice in pavement engineering through value-added collective recycling of waste plastic and waste tyre rubber," *Engineering*, 2020.

[9] M. Guo and Y. Tan, "Interaction between asphalt and mineral fillers and its correlation to mastics' viscoelasticity," *International Journal of Pavement Engineering*, vol. 22, no. 1, pp. 1–10, 2021.

[10] M. Guo, H. Liu, Y. Jiao et al., "Effect of WMA-RAP technology on pavement performance of asphalt mixture: a state-of-the-art review," *Journal of Cleaner Production*, vol. 266, p. 121704, 2020.

[11] S. Laurent Blvd, "Ottawa, Ontario. Canadian strategic highway research program-C-SHRP," *Transportation Association of Canada*, vol. 2323, pp. 4–6, 2001.

[12] F. Zhang and C. B. Hu, "The research for high-elastic modified asphalt," *Journal of Applied Polymer Science*, vol. 132, no. 25, 2015.

[13] D. Wang, Q. Liu, Q. Yang, C. Tovar, Y. Tan, and M. Oeser, "Thermal oxidative and ultraviolet ageing behaviour of nano-montmorillonite modified bitumen," *Road Materials and Pavement Design*, vol. 22, no. 1, pp. 121–139, 2021.

[14] F. Zhang and C. Hu, "The composition and ageing of high-viscosity and elasticity asphalts," *Polymer Composites*, vol. 38, no. 11, pp. 2509–2517, 2017.

[15] Z. H. Hao and B. Gao, "Properties and mechanism analyse of high-elasticity modified asphalt," *Key Engineering Materials*, vol. 599, pp. 212–217, 2014.

[16] G. A. Dennyele, J. M. Rosa Júnior, T. J. Alves De Melo, and J. K. Guedes Rodrigues, "Rheological studies of asphalt modified with elastomeric polymer," *Construction and Building Materials*, vol. 106, pp. 290–295, 2016.

[17] S. Luo and X. Yang, "Performance evaluation of high-elastic asphalt mixture containing deicing agent Mafilon," *Construction and Building Materials*, vol. 94, pp. 494–501, 2015.

[18] J. D'Angelo, R. Kluttz, and R. Dongré, "Revision of the superpave high temperature binder specification: the multiple stress creep recovery test," *Journal of the Association of Asphalt Paving Technologists*, vol. 76, pp. 123–162, 2007.

[19] A. Shenoy, "Model-fitting the master curves of the dynamic shear rheometer data to extract a rut-controlling term for asphalt pavements," *Journal of Testing and Evaluation*, vol. 30, no. 2, pp. 95–102, 2002.

[20] X. Qin, S. Zhu, X. He, and Y. Jiang, "High temperature properties of high viscosity asphalt based on rheological methods," *Construction and Building Materials*, vol. 186, pp. 476–483, 2018.

[21] H. Pouria, M. N. Fereidoon, and K. Ali, "Introducing a stress-dependent fractional nonlinear viscoelastic model for modified asphalt binders," *Construction and Building Materials*, vol. 183, pp. 102–113, 2018.

[22] G. Y. Baladi and M. J. Khattak, "Engineering properties of polymer modified asphalt mixture," *Transportation Research Board*, vol. 1638, no. 1, pp. 11–15, 1998.

[23] P. S. Pell and I. F. Taylor, "Asphalt road materials in fatigue," in *Proceedings of the-Association of the Asphalt Pavement Technologist*, pp. 577–593, Los Angeles, CA, USA, February 1969.

[24] H. Zhang, Z. Chen, G. Xu, and C. Shi, "Evaluation of aging behaviors of asphalt binders through different rheological indicesfferent rheological indices," *Fuel*, vol. 221, pp. 78–88, 2018.

[25] W. C. Vonk and G. G. Van, "Improvement of paving grade bitumens with SBS polymers," in *Proceedings of the Fourth Eurobitume Symposium*, no. 10, pp. 298–303, Madrid, Spain, October 1989.

[26] SHRP-A-398, *Stage1 Validation of the Relationship Between Asphalt Properties and Asphalt-Aggregate Mix Performance*, Strategic Highway Research Program, Washington, DC, USA, 1994.

[27] D. W. Van, "Practical fatigue characterization of bituminous mixes," in *Proceeding of the Association of Asphalt Paving Technologists*, vol. 44, Phoenix, AZ, USA, February 1975.

[28] A. I. Al-Hadidy and T. Yi-Qiu, "Effect of polyethylene on life of flexible pavements," *Construction and Building Materials*, vol. 23, no. 3, pp. 1456–1464, 2009.

[29] A. I. Al-Hadidy, Y. Q. Tan, and H. Ayman Talib, "Starch as a modifier for asphalt paving materials," *Construction and Building Materials*, vol. 25, no. 1, pp. 14–20, 2011.

[30] M. Guo, M. C. Liang, Y. B. Jiao et al., "A review of phase change materials in asphalt binder and asphalt mixture," *Construction and Building Materials*, vol. 258, p. 199565, 2020.

[31] M. Ameri, M. Seif, M. Abbasi, M. Molayem, and A. KhavandiKhiavi, "Fatigue performance evaluation of modified asphalt binder using of dissipated energy approach," *Construction and Building Materials*, vol. 136, pp. 184–191, 2017.

[32] M. A. Mull, A. Othman, and L. Mohammad, "Fatigue crack propagation analysis of chemically modified crumb rubber-asphalt mixtures," *Journal of Elastomers & Plastics*, vol. 37, no. 1, pp. 73–87, 2005.

[33] M. A. Mull, K. Stuart, and A. Yehia, "Fracture resistance characterization of chemically modified crumb rubber asphalt pavement," *Journal of Materials Science*, vol. 37, no. 3, pp. 557–566, 2002.

Hindawi
Advances in Materials Science and Engineering
Volume 2021, Article ID 5514165, 15 pages
https://doi.org/10.1155/2021/5514165

*Research Article*

# Analysis of Underwater Topographic Survey of Stilling Basin Based on Unmanned Survey System

**Hui Xie,[1] Haoran Wang,[1,2] Yayi Yang,[3] Yongcan Chen,[2,4] Jun Yang,[5] Shuang Wang,[4] and Zhaowei Liu[2]**

[1]*Sichuan Energy Internet Research Institute, Tsinghua University, Chengdu 610042, China*
[2]*State Key Laboratory of Hydroscience and Engineering, Tsinghua University, Beijing 100084, China*
[3]*Sichuan Technology and Business College, Dujiangyan 611830, China*
[4]*Southwest University of Science and Technology, Mianyang 621010, China*
[5]*Sichuan Electic Power Design & Consulting Co., Ltd., Chengdu 610041, China*

Correspondence should be addressed to Haoran Wang; hrwang@mail.tsinghua.edu.cn

Received 27 January 2021; Revised 4 March 2021; Accepted 17 March 2021; Published 2 April 2021

Academic Editor: Yubo Jiao



The combination of Global Positioning System-Real Time Kinematic (GPS-RTK) and depth sounder is an important technical method of modern underwater topographic survey. In this paper, the combined technology was integrated with unmanned surface vehicle (USV) technology to construct an unmanned survey system suitable for underwater topographic survey in stilling basin, and it was applied to survey the underwater topography of the stilling basin of Tingzikou hydrojunction project. Based on the surveying and mapping data and 3D model, the trend of elevation change of the stilling basin including apron, end sill, antiscour section, and river convergence section was analyzed. The results show that, for the surface outlet stilling basin of Tingzikou, after flood, the structure is complete, the boundaries are clear, the water quality is good, and there is little sediment on the surface of apron from overflow dam section to end sill. Furthermore, no obvious sediment or structural abnormality has been found in the still basin. Affected by the bedrock and cofferdam cobble gravel sediment, the elevation of the antiscour section and the downstream convergence section of the surface outlet stilling basin increased significantly. For the bottom outlet stilling basin of Tingzikou, there is large sediment within a range of 20 m~40 m from the bottom sill and the maximum height of it reaches 2.04 m, while there is no obvious sediment or structural abnormality in the remaining region of basin. The critical sedimentation height can effectively judge the safety grade of the sedimentation height in stilling basin and provide a reliable support for assessing the overall safety of stilling basin. The application of unmanned survey technology improves the accuracy and timeliness of underwater topography and sedimentation distribution of stilling basin, which has significant application research value and promotion significance.

## 1. Introduction

As an important energy dissipating facility of hydraulic structure, the safe operation and long-term stability are essential to ensure the power generation and flood discharge of a hydropower station [1–3]. Hyperconcentrated flow, gravels and boulders flowing through the dam into the basin with high-speed flow, and riverbed sandstones flowing into the basin with turbulent flow after the end sill can cause scour damage to the apron and side wall of stilling basin with the certain extent, and it will increase the risk of cavitation damage [4–7]. Therefore, the underwater topographic survey and underwater sedimentation detection of the stilling basin during the operation period are important parts of the routine inspection work for hydraulic structure and are the key to timely grasp the risk and hidden dangers of energy dissipation and to evaluate the safety status of the water discharge stricter of the power station. For the surveying and mapping of the stilling basin, the traditional manual measurement has large workload and low efficiency, and the

implementation of multibeam measurement on the ship is difficult and costly, and both conventional methods need to be measured by the mother ship [8–11] which affect the effectiveness of underwater topographic survey in the stilling basin to a certain extent. Li et al. [12] provided a visual detection method and applied to stilling basin; however, it is necessary for the underwater robot dive to the bottom of the water for detection, which is inefficient.

With the development of information, automation control, and surveying and mapping technology, underwater survey is more and more integrated, refined, and standardized. The combination of GPS-RTK and depth sounder is an important technical method of modern underwater topographic survey. The combined technology was integrated with USV technology to construct an unmanned survey system which can greatly reduce the labor intensity and improve the automation degree and work efficiency of survey. Additionally, it also has the advantages that the traditional survey methods cannot match such as flexibility, rapidity, and applicability [13–15]. In the past five years, unmanned intelligent technology has been adopted in various fields, such as reservoir topographic survey and storage capacity calculation [16–20], bathymetric and underwater topographic surveying and mapping of oceans, rivers, and lakes [21–23], and monitoring and control of water environment pollution [24–26], etc. with remarkable results.

In the analysis and postprocessing stage of survey results, some scholars have done researches on the formation mechanism of sediment in stilling basin. Wang et al. [27], Athat et al. [28], and Zhao et al. [29] used FLUENT to solve the hydraulic factors in the node area and solved the suspended sediment equation and riverbed deformation equation by the water-sand noncoupling method and explored the sediment distribution of suspended load. Madej et al. [30], Wang et al. [31], and Zhang et al. [32] systematically studied the sediment deposition characteristics under different roughness conditions through experimental methods, and found that the sediment was mainly deposited at the boundary between the main flow and the backflow area with a vector velocity of less than 0.1 m/s. Song et al. [33] established the calculation formula of flow resistance and water depth change caused by sediment movement by theoretical analysis method. Gao and Abrahams [34] used dimensionless analysis to get the formula for calculating resistance caused by bed load movement. The numerical simulation method and experimental method have fully explained the deposition phenomenon in the backflow area, and the theoretical calculation formula can be used to analyze the sedimentation principle in special situation. However, the research on the classification of sedimentation height has not been found, and it is impossible to use the sedimentation height to evaluate the overall safety of the stilling basin.

In conclusion, although the application of intelligent undammed survey technology is active, few surveying and mapping practices for draining building such as stilling basin have been found, and unmanned survey systems, process or postprocessing methods for the structure of stilling basin, and the characteristics of regularized measuring areas have not yet been established. The occurrence of sediment in the backflow area has reached consensus in the field of hydraulics, but there is little research on the degree of sediment to determine the safety grade of the stilling basin. This paper has constructed an unmanned underwater topographic survey system based on GPS-RTK combined with depth sounder and has applied it to engineering practice to realize the autonomous underwater surveying and mapping of stilling basin. In this paper, the degree of sediment in stilling basin has been safely classified to provide support for evaluating the overall safety of stilling basin. This research is an application innovation of frontier surveying and mapping technology effectively applied in the field of water conservancy and hydropower engineering. It meets the requirements for hydropower development and puts forward new requirements for digital watersheds, digital hydropower, and "Internet+" smart hydropower stations. It has significant application research value and promotion significance.

## 2. Project Background

The Tingzikou hydrojunction project (Tingzikou) is one of the six key projects for the improvement of the Yangtze River flood control system. It is the only controlling backbone project of Jialing River mainstream. The main functions of Tingzikou are flood discharge, irrigation, and urban and rural water supply and power generation, considering navigation, and sand blocking and sediment reducing. The drainage structure of the Tingzikou consists of eight surface outlets and five bottom outlets, which adopt the form of underflow dissipation. The main task of the surface outlets is flood discharge, and the exit adopts a wide tail design. The surface outlet stilling basin is a tetragonal structure surrounded by the middle guide wall, the right guide wall, the surface sill, and the apron. The top elevation of apron is 355.0 m, the basin length is 135 m, and the basin width is 143.5 m. The end sill of the stilling basin is continuous, and the elevation of the sill is 367 m. The length of the antiscour section of the end sill is 35 m and the elevation is 360.3 m. The main tasks of the bottom outlet are flood discharge and sand discharge, and it also serves as a diversion bottom outlet during construction. The bottom outlet stilling basin is a rectangular structure surrounded by the left guide wall, the middle guide wall, the end sill, and the apron. The top elevation of apron is 354.0 m, the basin length is 187.7 m, and the basin width is 75 m. The end sill of the stilling basin is continuous, and the elevation of the sill is 367 m. The antiscour section of the end sill is 35 m in length and 360.3 m in elevation [35–37]. The plan and the picture of surface outlet stilling basin and bottom outlet stilling basin are shown in Figure 1 and Figure 2, respectively.

With the transition of Tingzikou from capital construction period to production and operation period, the importance of safe and stable operation of the project is increasingly apparent. The peak-volume of Jialing River is relatively large. The design flood peak of Tingzikou is 34500 $m^3$/s. and the design flood recurrence interval of the energy dissipation is 100 years. In July 2018, Sichuan

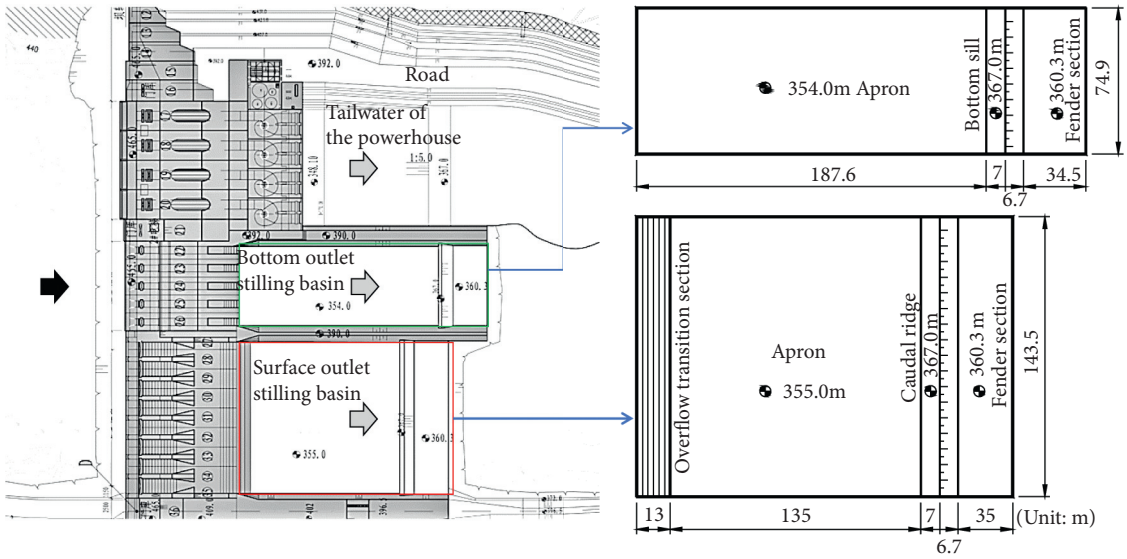


Figure 1: The plan of surface outlet stilling basin and bottom outlet stilling basin.


Figure 2: The picture of surface outlet stilling basin and bottom outlet stilling basin.

experienced severe grievances. The peak discharge of the Tingzikou reached 25130 $m^3/s$, which is the largest one in the last 80 years. It refreshed the largest measured flood since the historical record. After flood season, to patrol and evaluate the underwater structure of stilling basin to determine structural integrity and potential structural risks were urgently needed. The underwater topography and sedimentation measurement of stilling basin can timely reflect the overall shape of the apron and preliminarily obtain the distribution of rubble and sediment deposition and provide guidance for the underwater positioning refinement measurement. In view of the urgent need for underwater sedimentation measurement in the Tingzikou, and the limitations of the existing surveying methods, the intelligent USV system carrying single beam bathymetry is adopted in the research, which can replace the manual measurement without drainage. Through this method, the bottom sedimentation distribution data and monitoring data on the high precision positions are collected. This research method can support the further structural safety assessment and normal operation of the stilling basin.

## 3. Principle of Unmanned Survey System

*3.1. Unmanned Survey System.* Underwater topographic survey includes two parts: positioning and water depth measurement [38]. The unmanned survey system for the underwater topography of the stilling basin, formed by GPS-RTK combined with depth sounder, is a real-time dynamic positioning survey system. It adopted RTK (real-time kinematic) real-time difference method on orientation, and echo sounding technology on water depth survey. This system consists of four parts, base station, mobile station, communication system, and control site (ground site). Figure 3 shows the schematic diagram of the unmanned survey system for the underwater topography of the stilling basin.

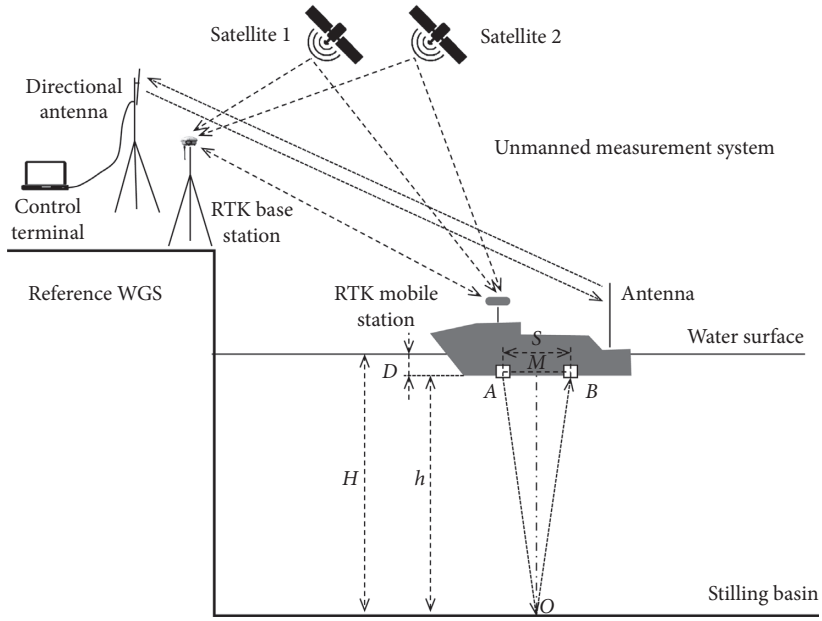


Figure 3: The diagram of unmanned survey system for underwater topography of the stilling basin.

The core function of base station is to determine the geodetic coordinate system. The base station consists of GPS receiver and antenna, and the independent base station including transmitting station and antenna [16, 39], and it needs to be placed in the higher-lying open area near the side wall of stilling basin, to enhance the effect of the communication module and avoid the multipath effect caused by occlusion. The mobile station system uses the base station as the origin coordinate to solve the relative position coordinates of each measuring point. The mobile station includes four parts, the USV module (including hull, electronic compass, propulsion system, energy power system, obstacle avoidance radar, wireless transmission system, and shipborne master control), mobile GPS receiver and antenna, differential antenna, and depth sounder. The detailed parameters of iBoat BS2 USV and senor are shown in Table 1. In addition, the control terminal is an important ground control system. It realizes remote communication, image transmission, and command feedback with the USV and sounding software through the image transmission and communication equipment. The USV and RTK are shown in Figures 4 and 5, respectively.

*3.2. Principle of Depth Sounder.* The single beam bathymetry technology gets the overall data through the water depth survey and data recording of the various discrete monitoring points, and it is widely used in the underwater topographic survey of the river and lake reservoirs because of its simple operation and high cost performance. HD-510 USV-mounted single beam bathymetry is used as the depth sounder of this system. Its working principle is to use the transducer to emit sound waves in the water. The sound waves are reflected and recovered when they touch the obstacles such as apron and sediment. According to the time interval of echo and launch pulse time combined with the wave velocity in the surveyed water, the distance between the bottom of water and the bottom of boat is calculated, that is, the depth of the measuring point [39]. As can be seen from Figure 3, the water depth should be

$$H = D + h, \tag{1}$$

$$\begin{aligned} h = \mathrm{MO} &= \sqrt{(\mathrm{AO})^2 - (\mathrm{AM})^2}, \\ &= \sqrt{\left(\frac{ct}{2}\right)^2 - \left(\frac{S}{2}\right)^2}, \end{aligned} \tag{2}$$

where $H$ is the measured water depth, $D$ is the draft depth, unit, $m$, $h$ is the transducer to the bottom depth, $c$ is the propagation speed of the sound wave in the water, $S$ is the transducer spacing, and $t$ is the time intervals.

For the transceiver transducer, equation (2) can be simplified as

$$h = \frac{ct}{2}. \tag{3}$$

In the echo sounding principle, the propagation speed of ultrasonic waves in water is approximately 1500 m/s. The propagation speed of ultrasonic waves in water is affected by the changes of temperature, salinity, hydrostatic pressure, etc.; among them, temperature has the greatest influence. Therefore, the parameter compensation is performed in HiMAX software.

*3.3. Process of Underwater Topographic Survey.* The standardized underwater survey process of stilling basin is the key to ensure the measurement results. In view of the structural characteristics and surveying and mapping requirements of stilling basin, the research process is as follows:

Table 1: The main parameters of USV and depth sounder.

| USV | Technical parameters | Depth sounder | Technical parameters |
|---|---|---|---|
| Hull weight | 14.00 kg | Working frequency | 200 kHz |
| Size | 1.05 m × 0.56 m × 0.27 m | Sound speed adjustment range | 1370 ~ 1700 m/s |
| Wind and wave resistance level | Level 3 wind and level 2 wave | Precision | ±10 mm |
| Endurance | 4 h | Resolution | 0.01 m |
| Maximum speed | 4.5 m/s | Transducer open angle | 5 ± 0.5° |
| Waterproof level | IP65 | Draught adjustment | 0 ~ 15 m |
| Remote control distance | 2 km | Weight | 0.50 kg |
| Draught | 0.2 m | Waterproof level | IP 66 |
| Software | HiMAX | Power supply | 12V DC |

Figure 4: The unmanned surface vehicle (USV).

Figure 5: The real-time kinematic (RTK).

(1) To select the appropriate launch point after comprehensively examining the terrain around the survey area.

(2) To turn on the directional antenna and configure the RTK base station, connect the antenna to the PC, turn on the remote control, turn on the USV power supply, and test the communication to check if it is normal.

(3) To turn on the visual serial port, and test the antenna to receive the USV data normally.

(4) To plan the route in the satellite map area to be measured, and load generated route point files, to ensure the software is connected. In this research, a total of 44 routes parallel to the guide wall were planned along the discharge direction of the surface outlet stilling basin, with a single route of about 230 m and a row spacing of 3 m. On a single route, measurements were taken every 0.2 m apart. A total of 27 routes parallel to the guide wall are planned for the bottom outlet stilling basin, and a single outlet is about 260 m with a row spacing of 4 m. On a single route, a measurement was collected every 0.2 m, as shown in Figure 6.

(5) To turn on the sounder software, connect GPS set as fixed solution or RTK solution, collocate geographic coordinates, meridian, receive data packet format, serial communication format, and connect the serial port to ensure normal communication.

(6) To set the antenna height of USV mobile station, draught, local underwater sound speed, and measure the depth by distance. The data recording will be synchronous with the sounding survey start. The automatic route survey starts when clicking the automatic navigation control of USV control software.

(7) To take over the USV manually when all the routes are completed, stop sounding recording, save the collected data, and take the USV back.

When using USV for underwater topographic surveying, the time synchronization between the systems and the attitude control of the hull should be ensured as much as possible to reduce the time error and measurement error [8]. Through the system coordination control, time synchronization processing, and measurement point control, to ensure the time synchronization between the GPS and depth sounder. According to the variation of water level in stilling basin, the measured data of initial hull attitude instability are selected to reduce the measurement error. The field working is shown in Figures 7 and 8.

## 4. Results and Analysis of the Survey

*4.1. Results of Underwater Topographic Survey of the Stilling Basin.* The data processing after the survey of stilling basin is completed, and the sounding data is filtered, sampled, previewed, and exported by the sounder software. The surface outlet stilling basin survey operation totaled 2.5 hours, and a total of 54202 sets of effective measurement data were generated. And the bottom outlet stilling basin survey operation totaled 1.5 hours, and a total of 10925 sets of effective measurement data were generated. The coordinates of the collected data are WGS84 geodetic coordinates

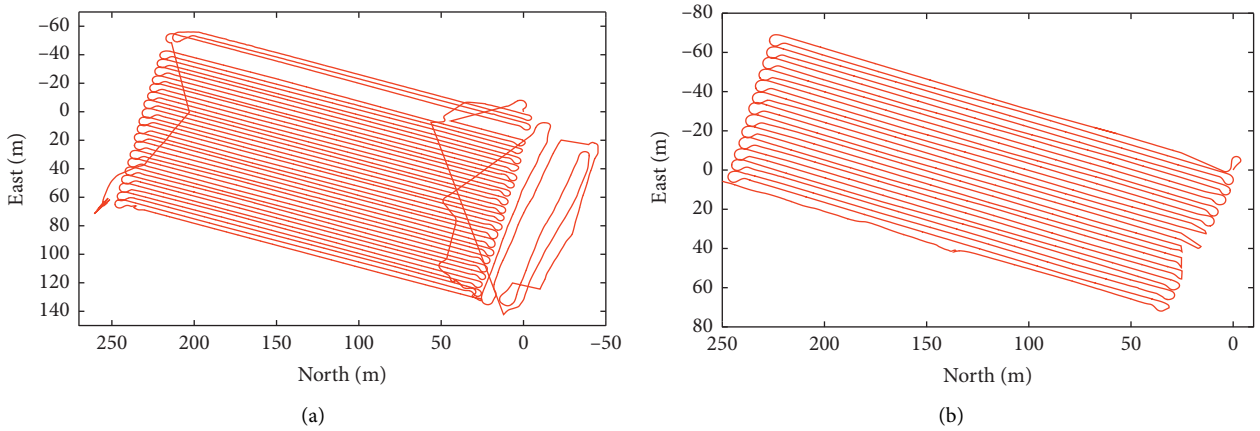


Figure 6: The path planning of USV. (a) Surface outlet stilling basin. (b) Bottom outlet stilling basin.

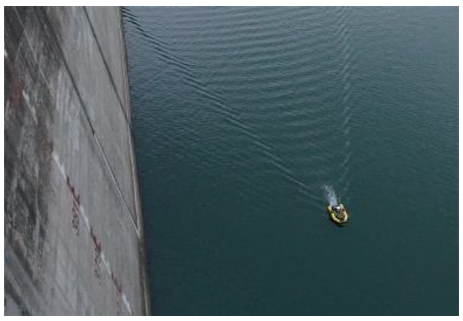

Figure 7: The field working picture of USV.

Figure 8: The field working picture of surveyors.

system, in which the north coordinate, east coordinate, underwater elevation, measured water depth, and surface elevation data are used for later MATLAB data processing. Under the influence of the peaking power generation tail water in the day, the water depth of the surface outlet stilling basin is decreasing. The maximum water level variation intervals are 0.5 m. The water depth in the bottom outlet stilling basin shows an upward trend, and the maximum water level fluctuation range is about 0.6 m. Some data anomalies are caused by the hull tilting or near the side wall of the stilling basin. The water depth time series data collected by the ship-borne depth sounder is well coupled with the 0.5 h interval water depth measurement data provided by the power station management department, indicating that the sounder is well calibrated and the measurement process is standardized and effective. The surface outlet stilling basin and bottom outlet stilling basin water level elevation process is shown in Figure 9.

The bottom elevation data of the stilling basin is filled and rendered according to different colors, and finally the underwater topographic data of the reservoir area is obtained. Figure 10 shows the contour distribution of the surface outlet and bottom outlet of the stilling basin. From Figure 10(a), in the regular rectangular area between the inflow surface and the end tail of surface outlet stilling basin, the depth of water is deeper than other areas; the underwater height is the lowest; and the end tail is clearly visible. In the figure, we can see it is the highest on underwater height in the whole survey area. After the end tail, the underwater topography is complex; the siltation is obvious. The sediment presents a trend of increasing gradually towards the downstream river. It can be seen from Figure 10(b) that the water depth in the apron zone between bottom outlet stilling basin and end sill is deep, and the change in underwater elevation is clearly visible. There is a large sediment in the range of 20 ~ 40 m from the drop-step. There is no obvious change in elevation between the sediment and the end sill, and the end sill is clearly visible. After the end sill, like the surface outlet stilling basin, the underwater topography distribution is complicated, and the sedimentation is obvious. The sediment gradually increases to the downstream channel.

*4.2. Analysis of the Results.* In order to quantitatively analyze the underwater siltation distribution and topographic change of the stilling basin, the transition section between overflow dam and the apron is used as the initial characteristic section, and seven characteristic sections are selected along the discharge direction of stilling basin for the comparison of relative elevations. The measured values of each characteristic section of surface outlet stilling basin are shown in Table 2. Similarly, starting from the drop-step of the bottom outlet stilling basin, 12 characteristic sections are selected along the discharge direction of stilling basin for the

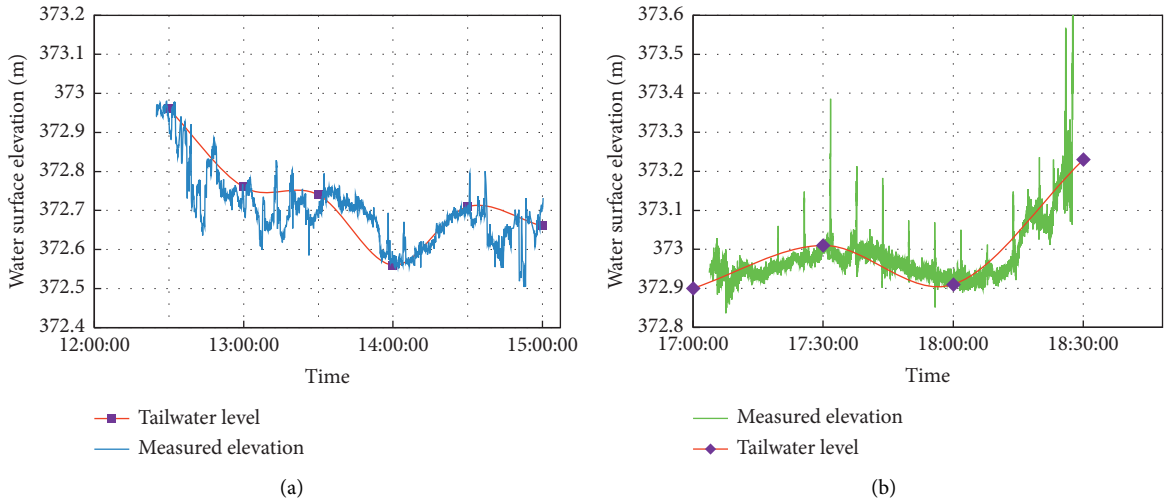


Figure 9: Diagram of water surface elevation variation. (a) Surface outlet stilling basin. (b) Bottom outlet stilling basin.

comparison of relative elevations. The measured values of each characteristic section of bottom outlet stilling basin are shown in Table 3. The sedimentation height should be

$$h_s = H - h_r, \tag{4}$$

where $h_s$ is the sedimentation height, $H$ is the measured height, and $h_s$ is reference value.

The data of Table 2 shows that the average elevation of section 1 (the transition section) is higher than that of the apron sections, and the difference between the average elevation of apron and the reference value can be used to characterize the average sediment thickness of apron. The water in surface outlet basin is clear, and there is no large sediment such as gravels. The stilling basin apron is characterized by small siltation and high homogeneity. The average elevation and elevation standard deviation increase with the direction of discharge from section 2 to section 4. At the left hand of apron the underwater sediment of about 30 m strip width can be seen clearly, and the sediment is much more than the other areas of apron. The structure of end sill is complete and the boundaries of the upstream apron and the downstream antiscour section are clear. There is a little sediment at the top of the end sill, and the average sediment thickness of section 5 is only 0.04 m. The average sedimentation height of the 35 m long antiscour section after the end sill is 0.38 m and the homogeneity is high. Due to the influence of bedrock and gravel sediments, the underwater elevation of the antiscour section and the downstream river convergence section is significantly increased and the closer it is to the downstream, the higher the underwater elevation is. The average elevation can be up to 364.03 m, and the standard deviation is 3.11 m.

The data in Table 3 shows that the average elevation of the stilling basin apron in section 1 immediately adjacent to the drop-step is only 0.09 m higher than the reference elevation, and there is a little sediment in section 1. The sediment in section 2, section 3, and section 4 is obvious, the maximum sedimentation height can reach 2.04 m, and the sediment is mainly distributed in the range of 20 m~40 m after drop-step. There is a little difference between the average elevations of section 5~section 8 and the reference elevation. Within this range, the stilling basin apron as a whole has the characteristics of small sedimentation and high homogeneity. The structure of the end sill is complete, the boundaries of the upstream apron and the downstream antiscour section are clear, the siltation at the top of the end sill is less, and the average sediment thickness of the section 9 is only 0.02 m. Due to the influence of bedrock and gravel sediment, the underwater elevation of the antiscour section and the downstream river convergence section is significantly increased and the closer it is to the downstream, the higher the underwater elevation is.

From the data in Table 2, the section elevation comparison chart of surface outlet stilling basin is shown in Figure 11. It can be found that the difference in elevation in section 1 is not significant, while the difference in elevation between section 2 and section 4 gradually increased that the thickness of sedimentation in apron is increasing along the flow direction. Section 6 is the antiscour section behind the apron. There is a little difference in elevation of this section and the standard deviation of elevation is 0.4 m. It is significantly affected by the flow velocity and riverbed cobbles after the antiscour section and the elevation difference is particularly obvious. The maximum height difference of the section is 7.82 m and the standard deviation is 3.11 m.

From the data in Table 3, the section elevation comparison chart of the bottom outlet stilling basin is shown in Figure 12. It can be found that the difference in elevation of section 1 in the bottom outlet stilling basin is not significant, and the difference in elevation among section 2~section 4 is obvious, indicating that there is an obvious sediment in stilling basin apron. The sediment is distributed within the range of 20 m~40 m from the drop-step and it gradually decreases along the direction of flow. Within section 5~section 8, the elevation difference is not apparent and the sediment in apron is small. It is significantly affected by the flow velocity and riverbed cobbles in antiscour (section 10 and section 11) and antiscour transition (section 12) section

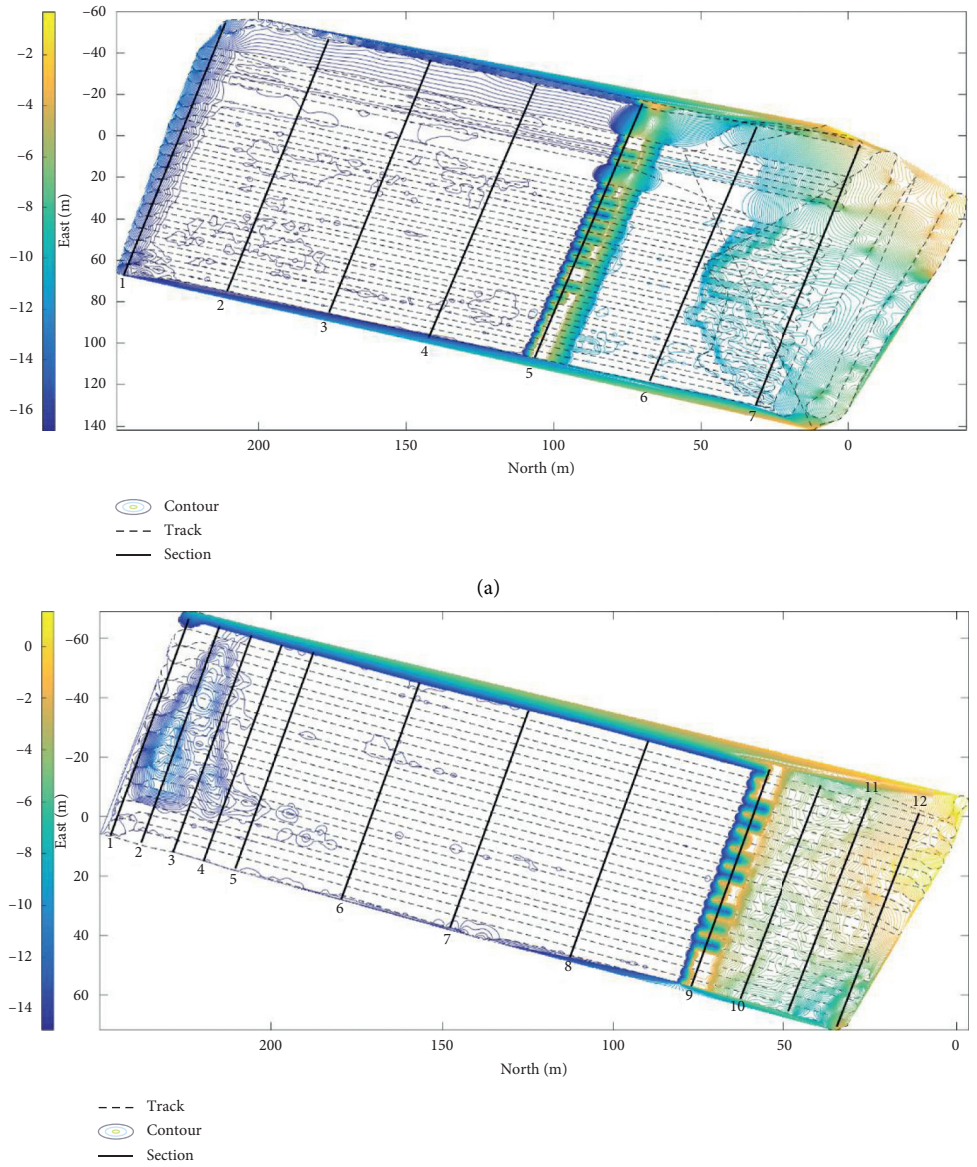


Figure 10: Underwater topographic contour lines and selected sections of the stilling basin. (a) Surface outlet stilling basin. (b) Bottom outlet stilling basin.

Table 2: Comparison table of elevation parameters among selected sections of the surface outlet stilling basin (unit: m).

| Section no. | Location | Maximum height | Minimum height | Average height | Standard deviation | Reference value |
|---|---|---|---|---|---|---|
| 1 | Overflow transition section | 357.15 | 356.54 | 356.73 | 0.26 | — |
| 2 | Apron | 355.42 | 355.23 | 355.29 | 0.08 | 355.00 |
| 3 | Apron | 356.02 | 355.23 | 355.44 | 0.33 | 355.00 |
| 4 | Apron | 356.59 | 355.22 | 355.54 | 0.59 | 355.00 |
| 5 | End sill | 367.08 | 367.00 | 367.04 | 0.03 | 367.00 |
| 6 | Antiscour section | 361.39 | 360.48 | 360.68 | 0.40 | 360.30 |
| 7 | Antiscour transition section | 368.58 | 360.76 | 364.03 | 3.11 | — |

*Note*. The data in the table is based on the statistical calculation of multiple corresponding measurement points on each section.

Table 3: Comparison table of elevation parameters among selected sections of the bottom outlet stilling basin (unit: m).

| Section no. | Location | Maximum height | Minimum height | Average height | Standard deviation | Reference value |
|---|---|---|---|---|---|---|
| 1 | Apron | 354.33 | 354.12 | 354.20 | 0.09 | 354.00 |
| 2 | Apron | 356.04 | 354.08 | 355.15 | 0.86 | 354.00 |
| 3 | Apron | 354.88 | 354.06 | 354.45 | 0.38 | 354.00 |
| 4 | Apron | 354.84 | 354.09 | 354.26 | 0.33 | 354.00 |
| 5 | Apron | 354.47 | 354.09 | 354.19 | 0.16 | 354.00 |
| 6 | Apron | 354.16 | 354.05 | 354.13 | 0.05 | 354.00 |
| 7 | Apron | 354.20 | 354.10 | 354.14 | 0.04 | 354.00 |
| 8 | Apron | 354.15 | 354.11 | 354.13 | 0.02 | 354.00 |
| 9 | End sill | 366.93 | 366.89 | 366.91 | 0.02 | 367.00 |
| 10 | Antiscour section | 364.59 | 363.01 | 363.80 | 0.68 | 360.30 |
| 11 | Antiscour section | 365.26 | 362.19 | 364.26 | 1.23 | 360.30 |
| 12 | Antiscour transition section | 367.47 | 362.72 | 365.45 | 2.06 | — |

*Note*. The data in the table is based on the statistical calculation of multiple corresponding measurement points on each section.

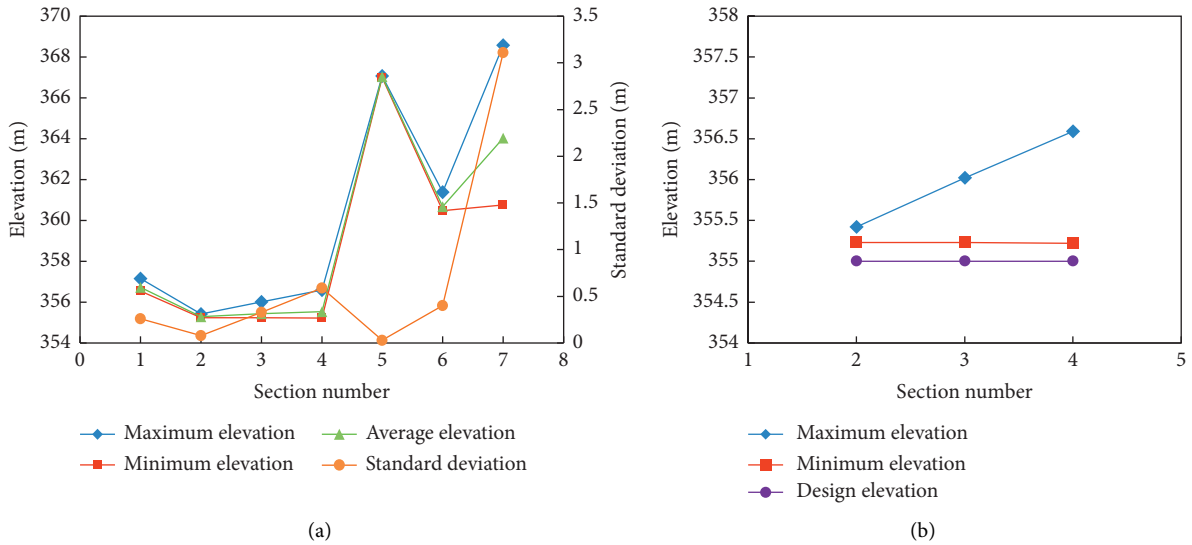


Figure 11: Comparison diagram of section elevation of the surface outlet stilling basin. (a) Diagram of section elevation and standard deviation. (b) Section elevation change of stilling basin apron.

and the elevation difference is particularly obvious. The maximum elevation difference can reach 4.96 m, and the standard deviation is 2.06 m.

*4.3. Three-Dimensional Underwater Topography.* Through the mesh and surf functions in MATLAB, the three-dimensional (3D) model of the underwater topography of stilling basin is constructed. As is shown in Figure 13, it comprehensively presents the elevation change trend of overflow dam section, apron, end sill, antiscour section, and the river convergence section. The 3D model can directly and vividly reflect the fluctuation in the height of the stilling basin measurement area, and make the underwater morphology and sedimentation situation clear at a glance. It can be seen that no obvious sediment or structural abnormality has been found in the basin area of surface outlet stilling basin, while the elevation difference of underwater topography between the antiscour section and the downstream convergence section is obvious. However, obvious sediment has been found near the drop-step in bottom outlet stilling basin, and no structural abnormalities have been found. Meanwhile, the elevation difference of underwater topography between the antiscour section and the downstream convergence section of bottom outlet stilling basin is obvious. The irregularity of the end sill area is caused by missing data.

## 5. Discussions

*5.1. Analysis of Sediment Disciplines.* According to the results of the unmanned survey system, there is no obvious sediment in the apron of surface outlet stilling basin while there is a large amount of sediment in the bottom outlet stilling basin. For the function of the surface outlet stilling basin is to release flood, almost no upstream sand stone is discharged into it, while the function of the bottom outlet stilling basin is to release flood and discharge sand and the sediment in it mainly comes from the silted sand stone in the reservoir area. The sedimentation difference between surface outlet stilling basin and bottom outlet stilling basin can be directly shown in Figure 14.

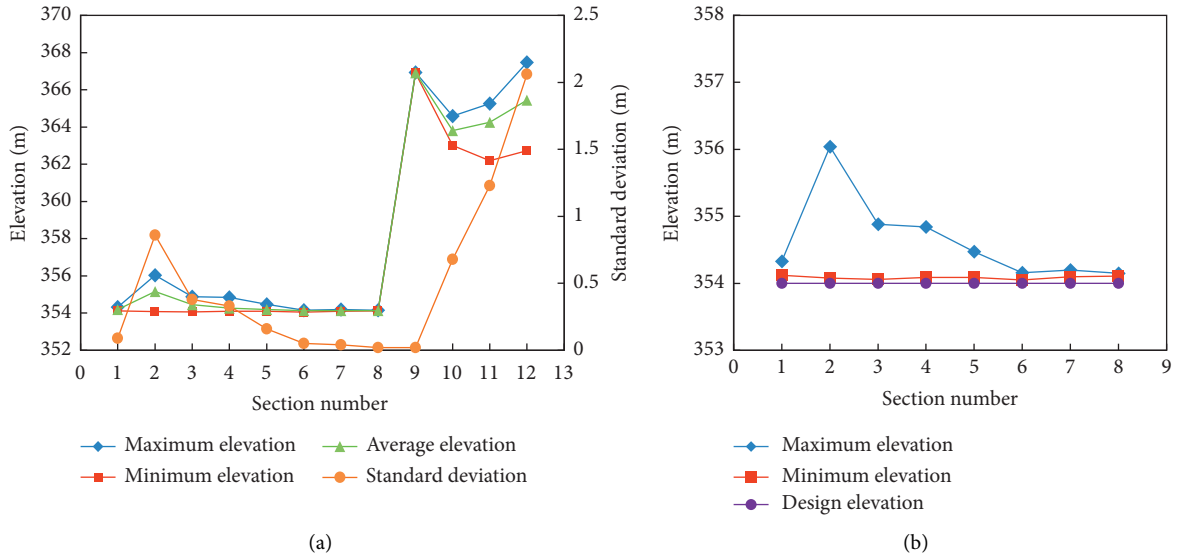


Figure 12: Comparison diagram of section elevation of the bottom outlet stilling basin. (a) Diagram of section elevation and standard deviation. (b) Section elevation change of stilling basin apron.

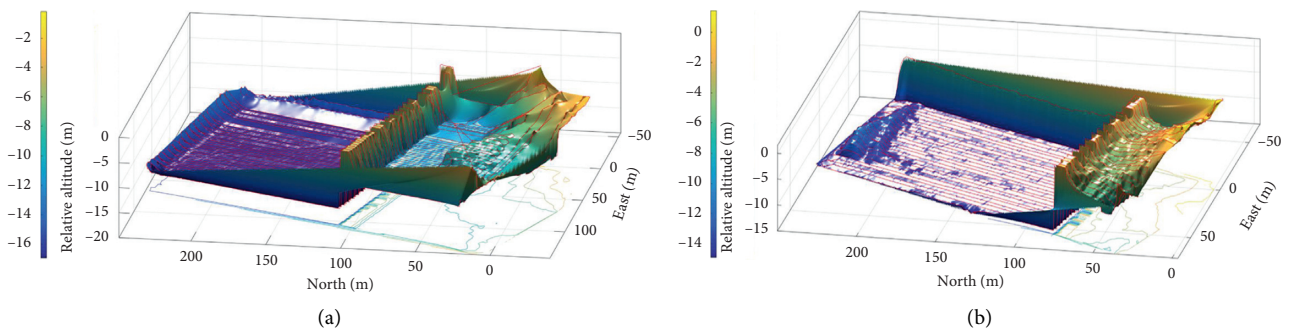


Figure 13: Three-dimensional underwater topography of stilling basin. (a) Surface outlet stilling basin. (b) Bottom outlet stilling basin.

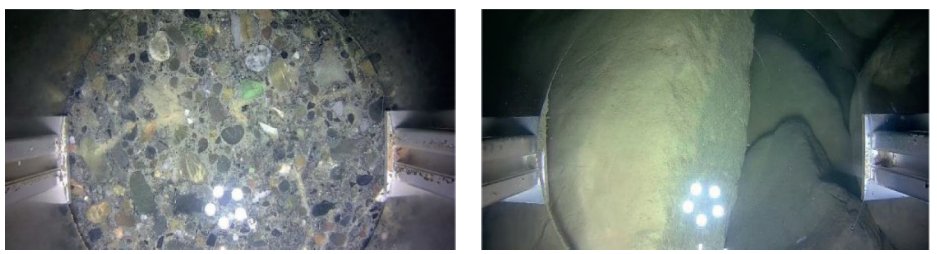


Figure 14: HD underwater pictures of the stilling basins. (a) Surface outlet stilling basin (no sediment). (b) Bottom outlet stilling basin (obvious sediment).

It can be seen from the results of section division that the sand stone sediment in the bottom outlet stilling basin is within a fixed range of 20 m~40 m near the drop-step, just in the longitudinal backflow area of flood discharge, for the sand stone in the upstream reservoir area cannot be carried further downstream by the flow and it begins to sediment under the influence of gravity. Meanwhile, the main sediment is located more than 20 m away because the sand stone has certain velocity and inertia after being impacted by the flow.

As we know, when the sectional depth is less than the critical depth, the flow is supercritical flow, while the

downstream is subcritical flow, and the hydraulic jump, as shown in Figure 15, is an inevitable result from supercritical flow to subcritical flow. Small water depth and high velocity are characteristics of the contraction section before the hydraulic jump. The pressure in the hydraulic jump section changes obviously with the water depth of the section, with high fluctuating pressure and violent turbulence.

In the hydraulic jump section, the velocity changes greatly, the flow morphology is complex, the velocity distribution is extremely uneven, and the flow movement intensity varies greatly, which will lead to the negative velocity vector and that is the backflow. In the bottom outlet stilling basin, the sediment is in the backflow area of hydraulic jump. It can be seen from Figure 15 that the hydraulic jump divides the flow into two areas, the surface rolling area above and the main flow area below. There is sediment in the hydraulic jump and that is in the backflow area.

The sediment concentration in water changes with the difference of velocity and depth of water, and at the same time, with the change of relevant hydraulic factors, it will cause scour and sediment. The formula of the relationship between sediment carrying capacity and velocity [40] is

$$S = k\frac{v^3}{ghw} + S_0, \tag{5}$$

where $S$ is the sediment carrying capacity, $k$ is the coefficient, $v$ is the average velocity, $g$ is the acceleration of gravity, $h$ is the depth of water, $w$ is the sedimentation speed, and $S_0$ is the initial sediment concentration.

It can be known from the formula above that the larger the flow velocity is, the stronger the sediment carrying capacity is. Only when the velocity is low, the sand would be deposited and the sediment will appear. The backflow area can be divided into two parts: positive and negative. In these two parts, there is flow exchange and the flow velocity can be expressed as follows:

$$U^2 = u^2 + v^2, \tag{6}$$

where $u$ is the lateral velocity, $v$ is the longitudinal velocity, and $U$ is the magnitude of the vector velocity. Studies have shown that sediment is mainly deposited at the junction of main flow and backflow, and usually its scalar velocity is less than 0.1 m/s [31].

According to the formula of sedimentation rate,

$$G_S = 0.0235U_\infty bh\left(S_\infty - S_r\right), \tag{7}$$

where $Gs$ represents the sedimentation rate, $U_\infty$ represents the velocity of main flow, $b$ and $h$ are geometric parameters of the section, $S_\infty$ is the sediment concentration of main flow, and $Sr$ is the sediment concentration of backflow area.

When the suspended sediment concentration in backflow area is lower than that in mainstream area, the sedimentation rate will always be nonzero, and the sedimentation phenomenon in the backflow area will inevitably occur until there is no difference in sediment concentration between the two areas.

To sum up, the backflow area is located in the hydraulic jump section with large velocity gradient, full turbulence, and high shear stress, and as the decrease of vector velocity in backflow area is greater than the increase of turbulence intensity, the sediment carrying capacity of the flow is reduced, the sediment carrying capacity in main flow area is greater than that in backflow area, and the sedimentation rate is nonzero. The sediment begins to appear, and it will continue to deposit in the backflow area until the sedimentation rate is zero. At the same time, when the high-speed flow falls into the bottom outlet stilling basin, under the influence of drop-step, the surface of the flow forms a backflow area, and the water in backflow area meets the water in main flow area, which presents a relatively static state, so a large number of sediment stay near the drop-step.

*5.2. Classification of Sedimentation Height.* According to the results above, the sediment in the apron of bottom outlet stilling basin is big. With the high-speed flow of the next flood discharge, the cobbles in the bottom sediment may have a risk to cause cavitation damage to apron and side wall of stilling basin. In addition, the sediment height has a great influence on the flow pattern. As is shown is [41], the water tank test shows that as the sediment height increases, the flow pattern changes from a uniform flow to an antislope hydraulic jump, and as the sediment height decreases, the flow pattern changes from antislope hydraulic jump or a locally backflow to a uniform flow. When the sediment height is low, the water flows uniformly along the sediment in the form of supercritical flow. When the sediment height increases to a certain extent, the flow will suddenly form an antislope hydraulic jump at the upstream face of sediment, and the water level in front of the sediment increases sharply. Once the sediment in apron of the stilling basin caused the antislope hydraulic jump, the stilling basin will operate at a high water level. Moreover, the corrosion on the rest of the apron caused by cobbles may lead to cavitation damage, which is harmful to the safety of stilling basin.

In order to analyze the influence of sediment in apron of the stilling basin on flow and structural safety, and to judge the magnitude of the impact of different sedimentation heights on structure safety of stilling basin, different security levels of the stilling basin can be correspondingly classified by different heights of sediment. By introducing the research results of [41], as is shown in Figure 16, the sudden increase of water level caused by the increase of sedimentation height is the *A-B-C* trend line; the steep decrease of water level caused by the decrease of the sedimentation height is the *C-D-A* trend line; the height of sediment causing a sudden increase of the water level is the upper critical sedimentation height $h_{s1;}$ and the height of the sediment causing a steep drop in water level is the lower critical sedimentation height $h_{s2}$.

$$h_{S1} = h_k^{28\times i_1 - 3.5\times i_2 + 0.065\times F_r + 1.42}, \tag{8}$$

$$h_{S2} = h_k^{25.7\times i_1 - 4.6\times i_2 + 0.11\times F_r + 1.1}, \tag{9}$$

where $h_{s1}$ is the upper critical sedimentation height, $h_{s2}$ is the lower critical sedimentation height, $h_k$ is the critical depth, $i_1$

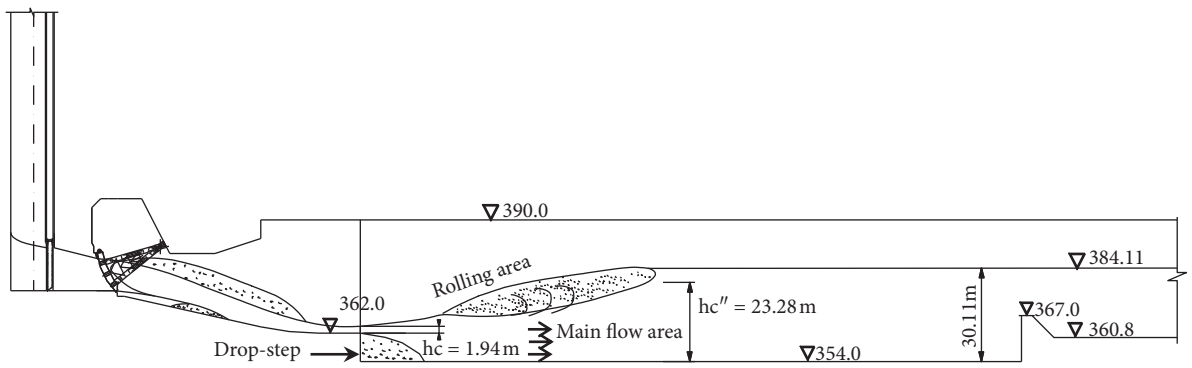


Figure 15: Diagram of hydraulic jump (unit: m).

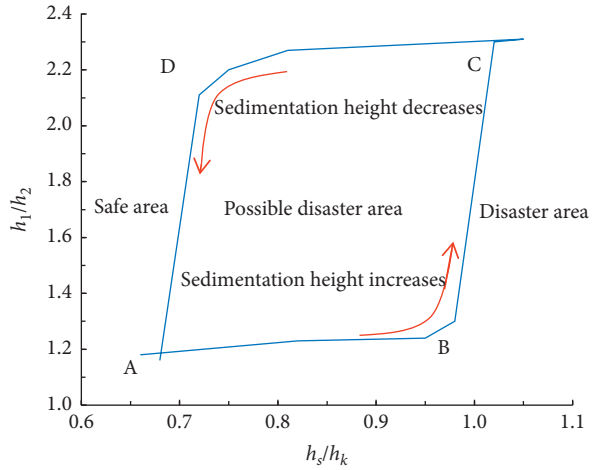


Figure 16: Division of disaster areas.

is the slope of apron, $i_2$ is the slope at upstream face of the sediment, and $F_r$ is the Froude number of the flow.

$$h_k = \sqrt[3]{\frac{\alpha q^2}{g}}, \tag{10}$$

where $\alpha$ is the kinetic energy correction factor, usually $\alpha \approx 1$, $q$ is the unit width discharge, and $g = 9.8\ \text{m/s}^2$.

According to the data from Tingzikou, when the flood was discharged in July 2018, the maximum flow discharge of the bottom outlet was $5607\ \text{m}^3/\text{s}$, and the unit width discharge was $74.76\ \text{m}^3/\text{s}$. The critical water depth of the bottom outlet stilling basin was 8.293 m. The calculation process is shown in Table 4.

When $h_s < 0.418$ m, the sediment has no obvious impact on the safety of the stilling basin.

When $0.418\ \text{m} \le h_s \le 1.246$ m, the sediment has great impact on the safety of the stilling basin.

When $h_s > 1.246$ m, the sediment has significant impact on the safety of the stilling basin.

During the formal safety assessment (FSA) of hydraulic structures, the safety status is often divided into five grades including normal, basically normal, mildly abnormal, abnormal, and dangerous, and it is necessary to comprehensively consider the relevant characteristic indicators such as deformation, seepage, and stress [42]. However, in the FSA of stilling basin, monitoring indicators (such as uplift and seepage discharge), measurement indicators (such as sedimentation height and rock mass quality), inspection indicators (such as corrasion and flatness), and numerical simulation indicators (such as velocity, pressure, and turbulent kinetic energy), etc. are often considered. In order to correspond to the grading standards of the overall safety evaluation, the sedimentation height is used as one of the FSA indexes for stilling basin, and it is also recommended to be divided into five grades. Based on the calculations of the upper and lower critical sedimentation heights, and the division of the sedimentation height on the safety of the stilling basin, using the method of equalization interpolation, the sedimentation height classification of the bottom outlet stilling basin is shown in Table 5.

According to the underwater topographic survey results of bottom outlet stilling basin, the safety grade of sedimentation height of stilling basin floor is evaluated by the methods above. It can be found that the maximum sedimentation height of the apron in bottom outlet stilling basin is 2.04 m, and the average sedimentation height in the sedimentation area is more than 1 m; that means the safety

Table 4: The main calculation parameters of critical sedimentation height of bottom outlet stilling basin.

| Parameters involved in calculation | Value |
|---|---|
| Bottom outlet flow | 5607 $m^3/s$ |
| Bottom outlet stilling basin width | 75 m |
| Single-width flow | 74.76 $m^3/s$ |
| Critical water depth | 8.293 m |
| $Fr$ | 8.83 |
| $i_1$ | 0 |
| $i_2$ | 0.54 |
| $h_{s1}$ | 1.246 m |
| $h_{s2}$ | 0.418 m |

Therefore, the judgment of the impact of the sedimentation height on the safety of the stilling basin is as follows.

Table 5: The safety grade classification of sedimentation height of bottom outlet stilling basin.

| $j$ | Safety grade | Minimum (m) | Maximum (m) |
|---|---|---|---|
| 1 | Normal | 0 | 0.209 |
| 2 | Basically normal | 0.209 | 0.418 |
| 3 | Mildly abnormal | 0.418 | 0.832 |
| 4 | Abnormal | 0.832 | 1.246 |
| 5 | Dangerous | 1.246 | + |

grade of sedimentation in this area has reached the abnormal grade~dangerous grade, and it is necessary to take engineering measures to clean up the sedimentation. However, in the remaining areas of the bottom outlet stilling basin, the sedimentation height is generally not more than 0.4 m, which belongs to the normal grade~basically normal grade. The table above is the safety grade classification of sedimentation height for bottom outlet stilling basin of Tingzikou. As different engineering has different characteristic parameters, which may result in different classification tables, in order to obtain the sedimentation height classification table applicable to different engineering conditions, more engineering cases are needed for further research.

## 6. Conclusions

Based on the combination of GPS-RTK and depth sounder, the unmanned underwater topographic survey system has the advantages of flexibility, high efficiency, safety, high precision, and low cost compared with traditional survey methods. This paper elaborated the system design, standardized operation process, and tree-dimensional model construction method of underwater topographic survey of the typical survey scene of stilling basin and they have been successfully applied to the underwater topographic survey of Tingzikou stilling basin after flood season. The underwater topographic survey of stilling basin is an application innovation of frontier survey technology effectively applied in the field of water conservancy and hydropower engineering, with significant application research value and promotion significance. The main conclusions are as follows:

(1) For the surface outlet stilling basin of Tingzikou, the structures are complete after flood season, the boundaries are clear, and the water quality in it is clear. No apparent sediment or anomalous structure change of stilling basin has been found. Affected by the bedrock and cofferdam cobble and gravel sediment, the elevation of antiscour section and downstream convergence section increased significantly. For the bottom outlet stilling basin of Tingzikou, the sediment within the range of 20 m~40 m away from the bottom sill is large, and the maximum height of it reaches 2.04 m, while there is no obvious sediment or structural abnormality in the remaining region of basin. Affected by the bedrock and cofferdam cobble gravel sediments, the elevation of the antiscour section and the downstream convergence section of the bottom outlet stilling basin increased significantly.

(2) The bottom outlet stilling basin has both the functions of flood discharge and sand discharge. Affected by the backflow, the sediment carrying capacity of the flow is reduced in the process of dissipation and large sediment is formed at a distance of 20 m~40 m from the bottom sill. The height of the sediment has different effects on the safety of stilling basin. Based on the critical sediment height, five safety grades of sedimentation and their division intervals are determined, which provide a reliable support for the overall safety evaluation of the stilling basin.

(3) The surveying and mapping data and 3D model of the unmanned survey system show the elevation trend of the overflow dam section, the apron, the end sill, the antiscour section, and the river convergence section, which can be effectively combined with the building reference value to describe the degree and distribution of underwater sediment. In further research and application, including but not limited to, the side wall effect in inspection route planning and the wave effect should be focused. In order to improve the coverage integrity and accuracy of the survey area, in addition to grasping the ideal survey time, we should explore some technical methods, such as manual mode compensation, hull attitude control, data correction, etc.

## Data Availability

The data used to support the findings of this study are available from the corresponding author upon request.

## Conflicts of Interest

The authors declare that there are no conflicts of interest regarding the publication of this paper.

## Acknowledgments

This work was supported by the National Key R&D Program of China (Nos. 2019YFB1310505, 2019YFB1310504), Open

Research Fund Program of State Key Laboratory of Hydroscience and Engineering (sklhse-2019-B-06), and Sichuan Science and Technology Program (Nos. 2021YFG0100, 2020JDRC0130, 2019YFG0143).

## References


[1] T. Honar, N. Khoramshokooh, and M. R. Nikoo, "Hydraulic optimization of corrugated stilling basin with adverse slope," *Water Supply*, vol. 19, no. 1, pp. 313–322, 2019.

[2] J. Guo and J. Z. Gao, "Discussions on operation safety of discharge facilities with high head and large discharge flow," *Journal of Hydroelectric Engineering*, vol. 32, no. 5, pp. 169–173, 2013, in Chinese.

[3] L. J. Wang, H. F. Qin, and T. Li, "Experimental study on hydraulic characteristics of stilling pool with contraction pier and falling sill," *Water Resources and Hydropower Engineering*, vol. 47, no. 10, pp. 40–44, 2016, in Chinese.

[4] L. M. Limantara, D. Priyantoro, and L. Prasetyorini, "Design of stilling basin for decreasing back water in the dam foot," *International Journal of Geomate*, vol. 15, no. 51, pp. 98–105, 2018.

[5] F. Naseri, H. Sarkardeh, and E. Jabbari, "Effect of inlet flow condition on hydrodynamic parameters of stilling basins," *ACTA Mechanica*, vol. 229, no. 3, pp. 1415–1428, 2018.

[6] Z. Zhou and J. X. Wang, "Hydraulic study of combined stilling basin between overflowing orifice and bottom outlet in Lianhuasi Hydropower Station," *Engineering Journal of Wuhan University*, vol. 52, no. 3, pp. 201–206, 2019, in Chinese.

[7] A. M. Hayder, "A laboratory study on stilling basin with semicircular rough bed elements," *Jordan Journal of Civil Engineering*, vol. 11, no. 2, pp. 198–205, 2017.

[8] T. X. Chen, R. H. Wei, and J. Zhang, "Application of the 5th generation multi-beam depth-sounding system in reservoir storage survey," *Yangtze River*, vol. 47, no. 9, pp. 29–32, 2016, in Chinese.

[9] R.-J. Yan, S. Pang, H.-B. Sun, and Y.-J. Pang, "Development and missions of unmanned surface vehicle," *Journal of Marine Science and Application*, vol. 9, no. 4, pp. 451–457, 2010.

[10] R. B. Rubén, A. G. Miguel, and E. Cecilia, "Experimental evaluation of an autonomous surface craft for shallow-water bathymetry," *Marine Technology Society Journal*, vol. 51, no. 4, pp. 59–67, 2017.

[11] X. Y. Liu and X. P. Mao, "Application of multi-beam sounding system in review of reservoir capacity and sediment," *Dam and Safety*, vol. 6, pp. 24–26, 2013, in Chinese.

[12] Y. Li, X. Li, H. Wang, S. Wang, S. Gu, and H. Zhang, "Exposed aggregate detection of stilling basin slabs using attention U-net network," *KSCE Journal of Civil Engineering*, vol. 24, p. 17406, 2020.

[13] I. M. Konstantin, I. P. Nicholaus, and W. M. Alexander, "Development of a remotely controlled testing platform with low-drag air-ventilated hull," *Journal of Marine Science and Application*, vol. 14, no. 1, pp. 25–29, 2015.

[14] J. M. Peschel and R. R. Murphy, "On the human-machine interaction of unmanned aerial system mission specialists," *IEEE Transactions on Human-Machine Systems*, vol. 43, no. 1, pp. 53–62, 2013.

[15] Z. B. Gao, X. J. Li, and P. An, "Application of GPS-RTK cooperating with depth sounder in river cross section measurement," *Yellow River*, vol. 33, no. 12, pp. 24–26, 2011, in Chinese.

[16] C. Zhang, N. X. Mou, and X. Zhou, "Application of unmanned intelligent technology in topographic surveying and capacity calculation of reservoir," *Bulletin of Surveying and Mapping*, vol. 11, pp. 72–76, 2017.

[17] H. Yang, J. B. Xu, and H. Huang, "Underwater terrain surveying and mapping of daning reservoir by unmanned boat surveying and mapping system," *Beijing Surveying and Mapping*, vol. S2, pp. 51–54, 2017, in Chinese.

[18] A. Ajith, R. Rajkumar, and R. M. Shibu, "Design and development of novel system for increasing range of an unmanned underwater vehicle," in *Proceedings of the 2019 IEEE Underwater Technology (UT)*, Kaohsiung, China, April 2019.

[19] Z. Y. Liang, "Application of unmanned surface vehicle surveying system in reservoir topographic survey," *Urban Geotechnical Investigation and Surveying*, vol. 1, pp. 132–135, 2018, in Chinese.

[20] Y. F. Cao and H. Gao, "Application of ship-borne mobile mapping system in acquiring reservoir topography information," *Geomatics and Spatial Information Technology*, vol. 41, no. 3, pp. 57–64, 2018, in Chinese.

[21] J. C. Jin, J. Zhang, and Y. Ma, "An unmanned surface vehicle for bathymetry," *Hydrographic Surveying and Charting*, vol. 33, no. 2, pp. 53–56, 2013, in Chinese.

[22] C. Powers, R. Hanlon, and D. G. Schmale, "Remote collection of microorganisms at two depths in a freshwater lake using an unmanned surface vehicle (USV)," *Peer Journal*, vol. 6, no. 5, pp. 1–16, 2018.

[23] B. R. Dzikowicz, B. T. Hefner, and R. A. Leasko, "Underwater acoustic navigation using a beacon with a spiral wave front," *IEEE Journal of Oceanic Engineering*, vol. 40, no. 1, pp. 177–186, 2015.

[24] D. P. Eickstedt, M. R. Benjamin, and H. Schmidt, "Adaptive control of heterogeneous marine sensor platforms in an autonomous sensor network," in *Proceedings of the International Conference on Intelligent Robots and Systems*, pp. 5514–5521, IEEE, Beijing, China, October 2016.

[25] J. C. Jin, J. Zhang, and F. Shao, "An unmanned surface vehicle for ocean environment monitoring and its oceanic application," *Coastal Engineering*, vol. 34, no. 3, pp. 87–92, 2015, in Chinese.

[26] Y. Sierra, P. Joshua, and P. Gopal, "Robot-assisted measurement for hydrologic understanding in data sparse regions," *Water*, vol. 9, no. 7, p. 494, 2017.

[27] Y. Z. Wang and Y. Z. Zhang, "Numerical simulation of distribution of sediment deposition on the joints in canal systems," *Journal of Irrigation and Drainage*, vol. 37, no. 5, pp. 81–85, 2018.

[28] M. Athat, U. C. Kothyari, and R. J. Garde, "Distribution of sediment concentration in the vortex chamber type sediment extractor," *Journal of Hydrological Research*, vol. 41, no. 4, pp. 427–438, 2003.

[29] Z. P. Zhao, X. S. Xie, and K. F. Lin, "Numerical simulation of characteristics of flow field and sediment movement," *Yellow River*, vol. 40, no. 2, pp. 105–134, 2018.

[30] M. A. Madej, D. G. Sutherland, T. E. Lisle, and B. Pryor, "Channel responses to varying sediment input: a flume experiment modeled after Redwood Creek, California," *Geomorphology*, vol. 103, no. 4, pp. 507–519, 2009.

[31] X. K. Wang, M. Asim, and L. Wang, "Experimental study on sediment deposition in circulation zone of shallow water flows," *Journal of Hydroelectric Engineering*, vol. 28, no. 4, pp. 149–153, 2009.

[32] C. L. Zhang, J. C. Guan, and C. M. Fang, "Experimental study on the response of river to water and sediment supply processes," *Journal of Sediment Research*, vol. 2, pp. 15–20, 2018.
[33] T. Song, Y. M. Chiew, and C. O. Chin, "Effect of bed-load movement on flow friction factor," *Journal of Hydraulic Engineering*, vol. 124, no. 2, pp. 165–175, 1998.
[34] P. Gao and A. D. Abrahams, "Bedload transport resistance in rough open-channel flows," *Earth Surface Processes and Landforms*, vol. 29, no. 4, pp. 423–435, 2004.
[35] Q. Y. Wang, C. H. Lei, and L. H. Zeng, "Design of Tingzikou water control project," *Water Power*, vol. 35, no. 10, pp. 26–28, 2009, in Chinese.
[36] H. R. Wang, S. Wang, and Y. C. Chen, "Application of unmanned intelligent technologies in underwater topographic survey of stilling basins," *Journal of Hydroelectric Engineering*, vol. 38, no. 12, pp. 11–18, 2019, in Chinese.
[37] Y. Li, H. Zhang, S. Wang, H. Wang, and J. Li, "Image-based underwater inspection system for abrasion of stilling basin slabs of dam," *Advances in Civil Engineering*, vol. 2019, pp. 1–13, Article ID 6924976, 2019.
[38] L. H. Zhu and Q. Hu, "The Application of GPS-RTK and bathymetric technologies in underwater topographic survey," *Geomatics and Spatial Information Technology*, vol. 34, no. 5, pp. 162–164, 2011, in Chinese.
[39] Y. H. Yan, J. X. Xu, and W. Q. Wu, "Application of GPS-PPK connecting depth sounder in underwater topographic survey," *Yellow River*, vol. 35, no. 5, pp. 128–130, 2013, in Chinese.
[40] J. Yang, Y. Y. Zhang, and J. C. Feng, "Sediment carrying capacity downstream of the spur dike in open channel flow," *Journal of MUC (National Sciences Edition)*, vol. 25, no. 2, pp. 53–57, 2016, in Chinese.
[41] Y. H. Zhong, X. D. Ma, and R. H. Nie, "Experimental study on the effect of siltation height on water level chang in steep slope channel," *Advanced Engineering Sciences*, vol. 51, no. 6, pp. 134–138, 2019, in Chinese.
[42] Z. R. Wu, C. S. Gu, and D. J. Zheng, "Theory and method on life diagnosis in important hydraulic engineerings," *Chinese Journal of Rock Mechanics and Engineering*, vol. 24, no. 17, pp. 3017–3022, 2005, in Chinese.

Hindawi
Advances in Materials Science and Engineering
Volume 2021, Article ID 5555535, 12 pages
https://doi.org/10.1155/2021/5555535

*Research Article*

# Performance Evaluation and Optimization of Waterproof Adhesive Layer for Concrete Bridge Deck in Seasonal Frozen Region Using AHP

**Weidong Jin, Yu Zhao, Wensheng Wang, and Feng He**

*College of Transportation, Jilin University, Changchun 130025, China*

Correspondence should be addressed to Wensheng Wang; wangws@jlu.edu.cn and Feng He; hefjlu@126.com

Received 17 February 2021; Revised 19 March 2021; Accepted 20 March 2021; Published 31 March 2021

Academic Editor: Yubo Jiao



The weak connection performances between the waterproof adhesive layer, the bridge deck, and asphalt pavement are important factors that cause the bridge deck slippage and upheaval and affect the safety and durability of the bridge. In this paper, styrene-butadiene-styrene- (SBS-) modified asphalt, SBS-emulsified asphalt, rubber-modified asphalt, and AMP-100 waterproof materials are selected to study the performance of the bridge deck waterproof adhesive layer in the seasonal frozen region. The shear strength and bond strength of the four waterproof adhesive materials were obtained through the shear test and pull-out test of the composite specimens composed of four kinds of adhesive materials, diatomite rubber-particle asphalt mixture, and concrete bridge deck at different dosages and temperatures. According to the priority analysis of the factors including cost, construction difficulty, and environmental protection for the four kinds of materials by using analytic hierarchy process (AHP), SBS-modified asphalt is obtained as the most suitable waterproof adhesive layer of diatomite rubber particle asphalt mixture bridge deck in seasonal frozen region.

## 1. Introduction

With the development of highway traffic in China and the quantity of bridges increasing, the bridge deck pavement has become an important part of the bridge traffic system [1–4]. Among them, the waterproof adhesive layer between asphalt pavement and cement concrete bridge deck cannot only prevent rainwater from penetrating into the bridge deck but also improve the stress condition between the two structures [5]. The weak connection performance between the waterproof adhesive layer, bridge deck, and asphalt pavement layer is an important factor affecting the safety and durability of bridges, which causes bridge deck slippage and upheaval. So more and more attention is paid to the performance of the bridge deck waterproof adhesive layer [6].

In the mid-1970s, Manning D G of the United States systematically studied more than 100 kinds of waterproof adhesive layers at that time and selected 5 kinds of materials as more promising waterproof materials [7]. The study of the waterproof adhesive layer was carried out in China from 1980s to 1990s [8]. Moisture content in the waterproof adhesive layer is an important factor affecting its performance. Feng et al. studied the effect of moisture content on the strength of the waterproof adhesive layer. The results showed that the shear strength of the waterproof bonding layer increased with the decrease of moisture content [9, 10]. In addition, the performance of the waterproof adhesive layer is not only related to itself but also related to the cement concrete layer and asphalt mixture layer bonded with it. In this regard, Qian et al. studied the influence of the replacement of aggregate in the asphalt mixture with phosphorus slag on the performance of the waterproof adhesive layer and found that phosphorus slag can improve the interlayer bond strength of the waterproof adhesive layer [11]. Wu et al. studied the influence of roughness of the cement concrete bridge deck connected with the adhesive layer and loading speed of the adhesive layer on the performance of the adhesive layer and concluded that the rougher the

concrete bridge deck and the greater the loading speed of the adhesive layer, the greater the adhesive layer performance strength [12]. However, these scholars generally consider the influence of internal factors, without considering the influence of external environment and temperature on the performance of the waterproof adhesive layer in actual laying. Xu et al. studied the bond strength under vehicle load [13]. Liu et al. studied the bond strength under the combined action of load and temperature and obtained that, with the increase of temperature, the performance of the adhesive layer decreased significantly [14]. These scholars considered the influence of vehicles and external temperature on the waterproof adhesive layer, but did not take into account the other structures of bridge deck pavement and asphalt mixture pavement which were paved by them are just common asphalt mixture.

In recent years, to study the performance of different waterproof adhesive layers, Guo et al. selected three different waterproof adhesive layers to do waterproof and shear strength tests, and the results showed that SBS-modified asphalt was better [15, 16]. Wang et al. studied the steel bridge pavement under vehicle load by the pull-out test and direct shear test and studied the effects of temperature, spraying quantity, and environmental conditions. It was concluded that rubber asphalt as the waterproof adhesive layer had good performance [17]. Zhang analyzed the influence of impermeability and aging resistance on the properties of materials through the shear test and pull-out test under different conditions. And, on comparing several adhesive layers, the epoxy asphalt has significant advantages [18]. Liu et al. found that waterborne epoxy-resin emulsified asphalt had good adhesion and waterproof performance through theoretical analysis on cohesion and simulation failure tests of cohesion and waterproof, which could effectively prevent the passage of bridge deck pavement [19]. Some scholars considered other properties of the waterproof adhesive layer. Chen et al. tested the effects of different bond surfaces on shear properties, measured the shear strength of specimens at different temperatures, and carried out fatigue life tests [20]. Fang et al. determined the influence of shear stress and temperature on the fatigue life of the waterproof adhesive layer by the shear fatigue test and discussed the design method and design index of the bridge deck considering the shear fatigue damage of the waterproof adhesive layer [21]. Qiu et al. used five performance indexes, such as tensile strength, direct shear strength, oblique shear strength, fatigue life, and project cost, to evaluate. A suitable waterproof adhesive system was recommended by using the multiobjective grey target decision method as the optimization method [22]. Some scholars considered the relationship between adhesive layer and bridge deck damage. Liu et al. studied two different types of asphalt mixtures and three different types of asphalt waterproof adhesive materials and obtained that the air void and test temperature of the asphalt mixture have different effects on the blister damage performance [23].

Based on the change of temperature difference in the seasonal frozen region, the research group developed a new type of asphalt mixture called diatomite rubber-particle asphalt mixture [24, 25]. This kind of bridge deck pavement material not only has green ecology but also has strong noise reduction ability and can solve the safety hidden danger of ice and snow pavement. In the seasonal frozen region where the temperature difference between winter and summer is large, laying this new asphalt mixture needs to consider the selection of the waterproof adhesive layer to make the performance of bridge deck pavement more excellent. This paper selects several high-quality waterproof adhesive materials commonly used in seasonal frozen area engineering such as SBS-modified asphalt, SBS emulsified asphalt, rubber-modified asphalt, and AMP-100 waterproof material. It is bonded with this new type of asphalt mixture and cement board to study its shear performance and bond performance at different temperatures. Through comparison combined with some other conditions such as environmental protection and cost, a waterproof adhesive layer material with better bond performance with the diatomite rubber-particle asphalt mixture which is suitable for the environment of the seasonal freezing region is selected.

## 2. Experimental Materials and Methods

*2.1. Experimental Materials.* In this study, the composite bridge deck structure of cement concrete-waterproof adhesive layer-asphalt mixture was used as the experimental object. Cement concrete specimens were made using a common mix proportion provided on-site, i.e., cement : water : river sand : gravel (by quality) is 10 : 3.8 : 15 : 20 [26–28]. C50 concrete was used for cement concrete specimens, and a high-efficiency water reducing agent was added. Four types of waterproof adhesive layers were selected as the waterproof adhesive layer in this paper, including SBS-modified asphalt waterproof adhesive layer, SBS emulsified asphalt waterproof adhesive layer, rubber asphalt waterproof adhesive layer, and AMP-100 waterproof adhesive material. And, the corresponding basic performances are shown in Tables 1–3 following JTG F40-2004, GB/T16777-2008, and JC/T975-2005 [29–31]. The new type of asphalt mixture modified by diatomite and rubber crumb was adopted as asphalt pavement on the bridge deck. According to the Chinese specification JTG F40-2004 "Technical Specifications for Construction of Highway Asphalt Pavements" [29], the median aggregate gradation of stone matrix asphalt (SMA)-13 was used in this paper. The AH-90 # asphalt from Panjin City was also used, and the asphalt-aggregate ratio was designed to be 6.3% in this study. The high-quality diatomite from Changbai Mountain area of Jilin Province was used to replace the mineral powder by equal volume replacement, whose content is 15% of asphalt by quality. The content of rubber crumb is 3% of aggregate by dry weight, and the particle size of rubber crumb is 1–3 mm [24, 25].

*2.2. Specimen Preparation.* According to the requirements of the Chinese specification JTG 3420-2020 "Testing Methods of Cement and Concrete for Highway Engineering" [32], the cement concrete specimens of $\varphi 101.6\,\text{mm} \times 50\,\text{mm}$ were

Table 1: Basic properties of SBS-modified asphalt and rubber-modified asphalt.

| Properties | SBS-asphalt | Rubber-asphalt | Standard | Method |
|---|---|---|---|---|
| Penetration at 25°C, 100 g, 5 s (0.1 mm) | 69 | 65 | 60–80 | T 0604 |
| Ductility at 5°C, 5 cm/min (cm) | 31 | 33 | ≥30 | T 0605 |
| Softening point (°C) | 75 | 71 | ≥55 | T 0606 |
| Brookfield viscosity at 135°C (Pa·s) | 1.912 | 2.032 | ≤3 | T 0625 |

Table 2: Basic properties of SBS-modified emulsified asphalt.

| Properties | | Test value | Standard | Method |
|---|---|---|---|---|
| Ion charge | | + | + | T 0653 |
| Residue on sieve (%) | | 0.05 | ≤0.1 | T 0652 |
| Enguera viscosity at 25°C | | 18 | 2–30 | T 0622 |
| Storage stability (%) | | 0.64 | ≤1 | T 0655 |
| Evaporation residue | Solid content (%) | 57 | ≥55 | T 0651 |
| | Penetration (0.1 mm) | 55 | 45–150 | T 0604 |
| | Ductility at 5°C (cm) | 26 | ≥20 | T 0605 |
| | Softening point (°C) | 58 | ≥50 | T 0606 |

Table 3: Basic properties of the AMP-100 waterproof adhesive material.

| Properties | Test value | | Standard |
|---|---|---|---|
| Appearance (before curing) | Black liquid | | — |
| Moisture content (%) | 2.2 | | ≤3 |
| Extensibility (mm) | 850 | | ≥600 |
| Water tightness at 0.3 MPa, 30 min | No seepage | | No seepage |
| Heat resistance at 160 ± 2°C | No flowing and sliding | | No flowing and sliding |
| Frost resistance at −25°C | No cracks after 20 times | | No cracks after 20 times |
| Dryness at 25°C | Surface dry | 1.5 h | ≤2 |
| | Hard dry | 2.8 h | ≤4 |

prepared using the vibration compaction method, in which the specimen mold was made separately. After demolding, the specimens were made to undergo shot blasting, and their surfaces were chiseled, cleaned, and dried. The specimens were then subjected to the standard curing preservation for 28 days to achieve a good strength. Subsequently, the waterproof bonding layer was spread twice, and each spreading requires about 4 h natural drying. This is because the amounts of waterproof adhesive materials were relatively large. It is easy to flow when spraying too much on Marshall specimens once, which would make the amount of waterproof adhesive layer materials inaccurate. Two small spreading of waterproof adhesive layer materials makes the amount of material more accurate and the coating more uniform [26]. According to the Chinese specification JTG E20-2011 "Standard Test Methods of Bitumen and Bituminous Mixtures for Highway Engineering" [33], the SMA-13 asphalt mixture Marshall specimen was formed by the compaction method [34]. Then, put the prepared asphalt mixture specimen on the surface of the cement concrete specimen which has been sprinkled with the waterproof adhesive layer. The specimen was compacted on the compaction instrument by the compaction method so that the waterproof adhesive layer can be fully bonded. Due to the high density of asphalt concrete containing rubber particles, the porosity of the specimen prepared by the compaction method was smaller than that prepared by the wheel pressure method, leading to a better performance; then, the compaction method was used here [35]. Finally, the composite specimen of the cement concrete-waterproof adhesive layer-asphalt mixture structure would be prepared in Figure 1. There are four different types of waterproof adhesive layers, and the corresponding amount of each adhesive layer was in their respective optimal dosage range [14, 36, 37]. In the study, four dosage gradients for each type of waterproof adhesive layer were set, as listed in Table 4.

### 2.3. Experimental Methods

*2.3.1. Shear Test.* In order to study the influence of waterproof adhesive layer types on the shear performance between the cement concrete layer and asphalt mixture layer on bridge decks, the laboratory shear test was carried out by using the indoor-formed composite shear specimen. Refer to the Chinese specification CJJ 139-2010 "Technical Specification for Waterproof of City Bridge Decks" [38], the shear strength test method was adopted. The test instrument adopted YAW series microcomputer-controlled electro-hydraulic servo pressure testing machine for shear tests. The specimen was placed in the premade test mold, and the test

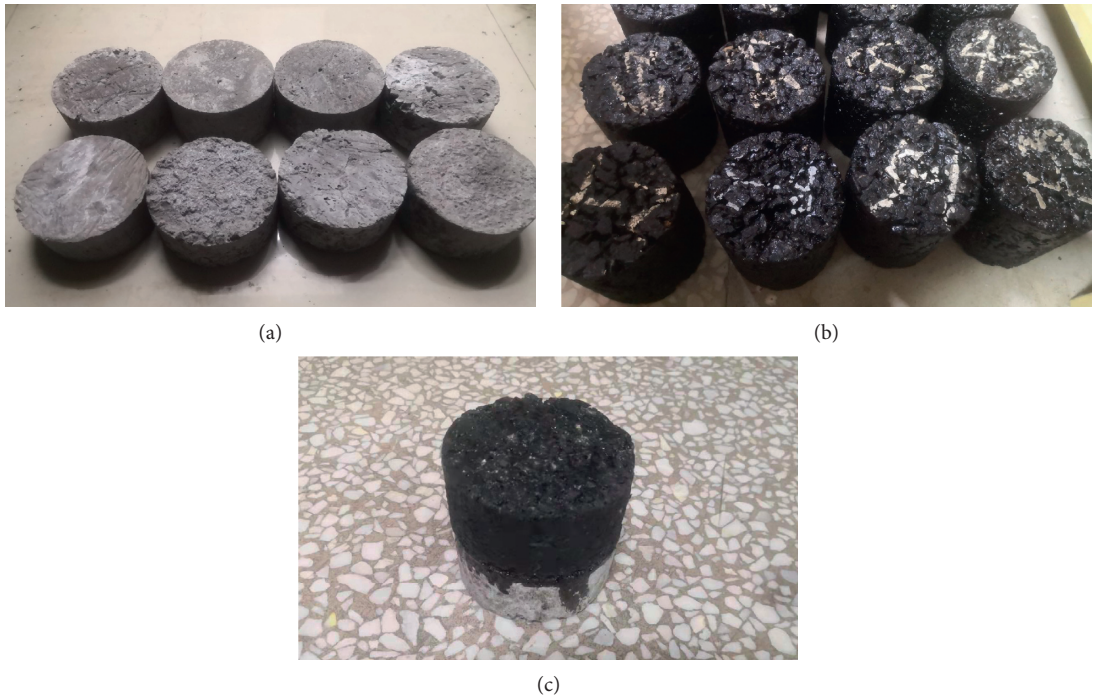

(a) (b)

(c)

Figure 1: Preparation of the composite specimen. (a) Cement concrete specimens. (b) Asphalt mixture specimens. (c) Composite specimen of the cement concrete-waterproof adhesive layer-asphalt mixture.

Table 4: Design of the waterproof adhesive layer for shear and pull-out tests.

| Waterproof adhesive layer types | The dosage gradient design (kg/m$^2$) | | | |
|---|---|---|---|---|
| Rubber-modified asphalt [36] | 2.0 | 2.2 | 2.4 | 2.6 |
| SBS-modified asphalt [14] | 1.6 | 1.8 | 2.0 | 2.2 |
| SBS emulsified asphalt [36] | 0.4 | 0.6 | 0.8 | 1.0 |
| AMP-100 waterproof materials [37] | 0.6 | 0.8 | 1.0 | 1.2 |

mold was placed in the center of the instrument. During the test, the prepared composite specimen was placed in the iron mold in the order of the concrete layer below and asphalt mixture layer above. The position of the specimen was adjusted to make the adhesive layer exactly located in the shear plane, and the press was dropped to the upper surface of the iron mold. The shear rate was controlled at 45 mm/min. After starting the instrument, record the pressure curve over time. When the specimen was destroyed, stop the shear test and record the maximum pressure value as well as the displacement value.

The shear test specimens were divided into two groups: (1) the first group of specimens was tested for four types of waterproof adhesive layers with different dosages in Table 4 at room temperature of 25°C. (2) The second group of specimens with the optimum dosage was tested at four temperature gradients of −5°C, 10°C, 25°C, and 40°C, simulating the temperature variation range of pavement in the northern region during cold and summer. The specimens at −5°C were placed in the refrigerator for 4 h to control the temperature, and the specimens at 10°C, 25°C, and 40°C were placed in the constant-temperature water bath pot for 4 h to control the temperature. The shear tests were carried out, respectively, and the pressure was converted to shear force after the test. The shear strength of each waterproof adhesive layer at different temperatures can be also obtained. There are three parallel specimens under each different parallel condition. Finally, the specimen failure was taken as the test termination condition. The shear test is shown in Figure 2.

The principle of the shear test in this paper is that the pressure plate of the test machine is applied from above to the test mold, and the test mold transmits the pressure to asphalt concrete and divides the pressure into a pressure normal and a shear force. The shear force provides a downward sliding effect on the asphalt mixture, in which the effect of pressure normal is ignored so that the waterproof adhesive layer is subjected to shear force. Finally, the shear force at failure is obtained, and the shear force is divided by the area of the waterproof adhesive layer, which is the shear strength.

In general, the shear strength is calculated by $\tau = (L/A)$, $\tau$ = shear strength (kPa), $L$ = applied load (kN), and $A$ = applied area (m$^2$). In this study, the shear strength of the waterproof adhesive layer measured as in Figure 1 can be calculated by

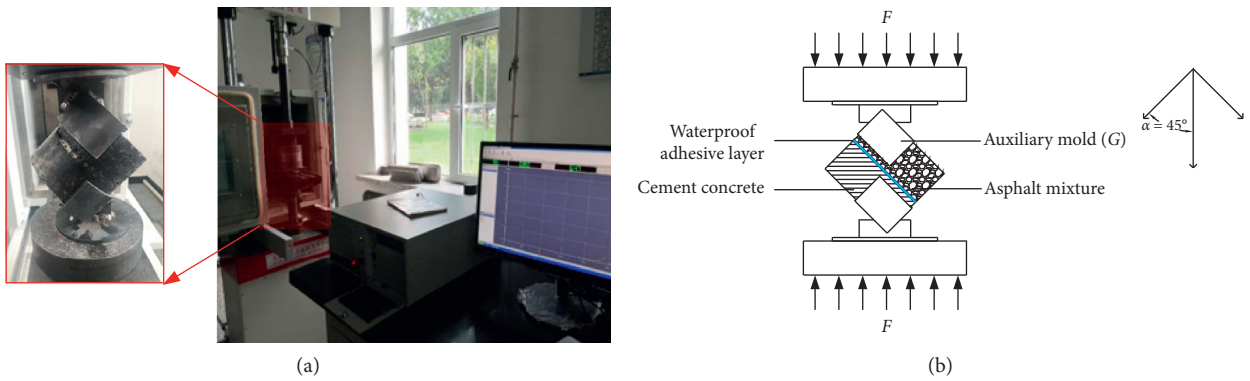


Figure 2: Shear test of the composite bridge deck structure. (a) Shear test in this paper. (b) The diagram of the shear test.

$$\tau = \frac{(F_S + G)\sin\alpha}{A_S}, \quad (1)$$

where $\tau$ = shear strength of the waterproof adhesive layer (kPa), $F_S$ = external load applied by the testing machine (kN), $G$ = weight of the auxiliary test mold (kN), $\alpha$ = angle between load and specimen (here, it is 45°), and $A_S$ = area of the waterproof adhesive layer on the cement concrete slab ($m^2$).

*2.3.2. Pull-Out Test.* Similar to the shear test, the bond strength of the waterproof adhesive layer is also an important evaluation index of the adhesive layer. Referring to CJJ 139-2010 "Technical Specification for Waterproof Engineering of Urban Bridge Deck" [38], pull-out tests were conducted for evaluating the bond strength. In order to determine the bond strength of the waterproof adhesive layer, the CMT-100 electronic universal testing machine was used in this paper to conduct the pull-out test of the composite specimen with a specially fabricated mold. During the pull-out test, the epoxy AB adhesive was used to bond the iron mold to the surface of the composite specimen, and the mechanical clamping specimen was connected to the mold, which was placed without pressure for 12 h to wait for the glue to provide enough strength. The drawing rate was controlled at 10 mm/min. When the test value would no longer increase, stop the test and record the final maximum value.

The pull-out test specimens were also divided into two groups. The first group of specimens was tested for four types of waterproof adhesive layers with different dosages in Table 4 at room temperature of 25°C. As for the second group, the specimens with the optimum dosage were tested at −5°C, 10°C, 25°C, and 40°C. The condition treatments of specimens were the same as those of the shear test specimens [26]. Then, pull-out tests were carried out to record the test data. There are three parallel specimens under each different parallel condition. Finally, the specimen failure is taken as the test termination condition. The pull-out test is shown in Figure 3.

The principle of the pull-out test is that the testing machine applies a pull upward to the test mold, the test mold transmits tension to asphalt concrete, and asphalt concrete transmits tensile force to the waterproof adhesive layer so that it is subjected to tensile force. Finally, the tensile force at failure is obtained. The required bond strength is divided by tensile force by the area of the waterproof adhesive layer. According to the specification, the bond strength can be calculated by

$$p = \frac{F_T}{A_T}, \quad (2)$$

where $p$ = bond strength (kPa), $F_T$ = tensile force (kN), and $A_T$ = tension area ($m^2$).

*2.3.3. Analytic Hierarchy Process (AHP) Method.* Analytic hierarchy process (AHP) [39, 40] is a method to solve complex multicriteria decision-making problems, which has the advantage of systematic analysis. It takes the research object as a system and makes decisions according to the way of decomposition, comparative judgment and comprehensive thinking. AHP requires decision-makers to judge the relative importance of each standard and use each standard to make the preference of each decision scheme. Finally, a list of schemes based on overall evaluation is formed. The specific steps are as follows:

(1) Building hierarchical structure model

(2) Constructing importance judgment matrix of hierarchy

(3) Hierarchical consistency analysis

(4) Final hierarchical ranking

After the hierarchical structure model is established, its judgment matrix is constructed. The judgment matrix is used to describe the importance between the two factors. In order to accurately describe the proportion of importance among different factors, the scale method is introduced in the analytic hierarchy process in Table 5.

The priority tables of the various influencing factors are obtained through Table 5. Then, the influence factors in the table are normalized so that the sum of each column element is 1:

$$b_{ij} = \frac{\sum_i d_{ij}}{n} d_{ij}, \quad (3)$$

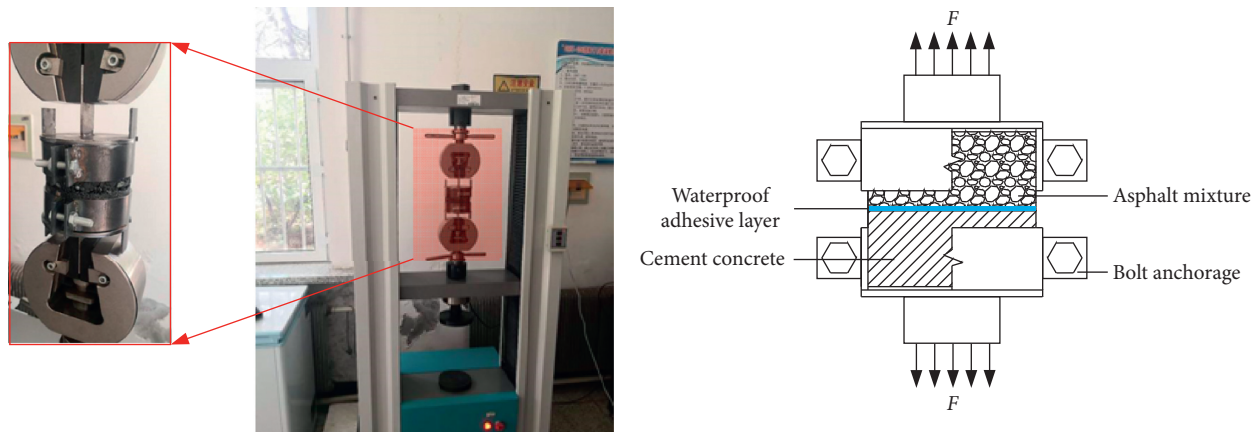


Figure 3: Pull-out test of the composite bridge deck structure. (a) Pull-out test in this paper. (b) The diagram of the pull-out test.

Table 5: Definition of the judgment matrix scale.

| Scale | Meaning |
|---|---|
| 1 | Comparing the two factors, two factors are equally important |
| 3 | Compared with the two factors, the former is slightly important |
| 5 | Compared with the two factors, the former is obviously important |
| 7 | Compared with the two factors, the former is very important |
| 9 | Comparing the two factors, the former is extremely important |
| 2, 4, 6, and 8 | Median of adjacent scales |

where $d_{ij}$ = the $i$th row and $j$th column elements in the influence factor priority table, $b_{ij}$ = the $j$th column element of the $i$th row in the priority normalization table, and $n$ = the number of influencing factors of the waterproof adhesive layer.

Then, the average value of each row of the priority normalization table is taken to calculate the priority $\alpha$:

$$\alpha_i = \frac{\sum_j b_{ij}}{n}. \tag{4}$$

Consistency analysis is performed after the judgment matrix is constructed. Consistency analysis is used to measure whether the judgment matrix obtained before is consistent. If the final value is less than 0.1, it would indicate that the consistency of the judgment matrix is acceptable. If not, it proves that the judgment matrix is unreasonable. The consistency ratio can be calculated by

$$\mathrm{CI} = \frac{\lambda_{\max} - n}{n-1}, \tag{5}$$

where $\lambda_{\max}$ = the maximum eigenvalue of the judgment matrix and CI = the consistency ratio:

$$\lambda_{\max} = \frac{\sum_i \sum_j \alpha_i a_{ij} / \alpha_i}{n}, \tag{6}$$

where $\alpha_i$ = the elements of the $i$th line in the judgment matrix and $a_{ij}$ = the elements of the $i$th row and $j$th column in the judgment matrix.

The revised consistency ratio can be calculated by

$$\mathrm{CR} = \frac{\mathrm{CI}}{\mathrm{RI}}, \tag{7}$$

where CR = the revised consistency ratio and RI = correction factor.

Finally, the final ranking of the hierarchy is obtained by the judgment matrix.

## 3. Results and Discussion

*3.1. Comparative Analysis of Shear Properties of Four Types of Waterproof Adhesive Layers.* The interlayer shear strength curves of different types of waterproof adhesive layers at 25°C are shown in Figure 4. From Figure 4, the shear strength values at room temperature 25°C of four types of waterproof adhesive layers increase first and then decrease with the increase of dosage, and there is maximum shear strength. Because the amount of the waterproof adhesive layer is less, there is not enough bond strength to resist the effect of external force. With the increase of the amount of the adhesive layer, the shear strength increases gradually. After reaching a limit, as the amount of the adhesive layer continues to increase, the waterproof adhesive layer will accumulate between the cement concrete layer and asphalt mixture layer, which cannot play a good bonding role, and the shear strength between the layers decreases gradually. Therefore, it can be considered that there is an optimal amount of the waterproof adhesive layer. And, with the increase of the amount of the adhesive layer, the shear strength gradually tends to a constant value. It indicates that the shear strength between layers is completely provided by

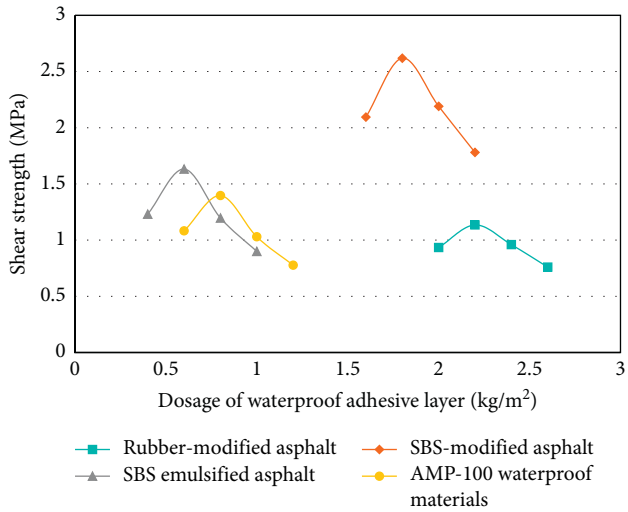


Figure 4: Shear strength of four types of waterproof adhesive layers with different dosages.

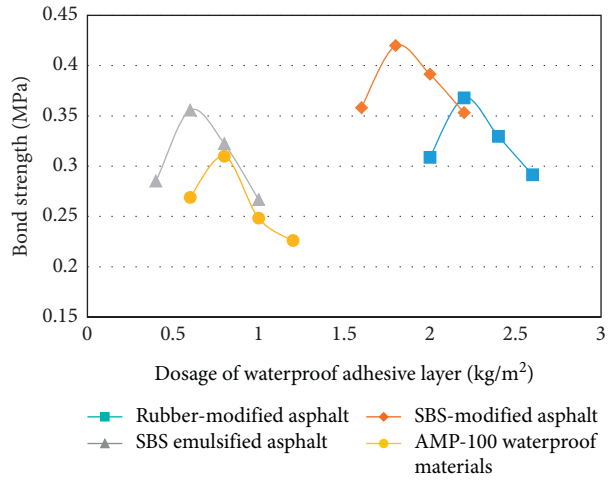


Figure 5: Bond strength of four types of waterproof adhesive layers with different dosages.

the shear strength of the adhesive layer itself, and it is not attached to concrete and asphalt mixture.

SBS-modified asphalt has a two-phase separation structure so that it can form a spatial three-dimensional network structure with the asphalt matrix and has a strong cohesion. It can be well adsorbed on the diatomite rubber-particle asphalt mixture, so the shear strength is larger [41]. When the rubber asphalt is bonded with the asphalt mixture, there are rubber particles added on the surface of the asphalt mixture, which accumulates with the rubber powder of the rubber asphalt itself. Too many rubber powders cannot be well compatible with the asphalt matrix, and the intermolecular force is weakened. And, rubber asphalt is not easy to combine with the dense cement concrete layer, the interface friction resistance is small, and the bond effect is poor, so the shear strength is small [42–45]. SBS emulsified asphalt has good fluidity, which can fully contact with the adhesive surface. Because of its own modifier and emulsifier, the relative bonding ability is weak, so the shear strength is small [45–47]. AMP-100 materials can accelerate construction due to second-order reactions and high fluidity. But because asphalt content is not high, its own bond performance is general [37].

When the amount of rubber asphalt is 2.2 kg/m$^2$, the shear strength is the largest. When the dosage of SBS-modified asphalt is 1.8 kg/m$^2$, the shear strength is the highest. When the dosage of SBS emulsified asphalt is 0.6 kg/m$^2$, the shear strength is the highest. The maximum shear strength was obtained when AMP-100 waterproof materials' content was 0.8 kg/m$^2$. Among them, the maximum shear strength of SBS-modified asphalt is 2.61 MPa, which is higher than the other three kinds of adhesive layers, and its shear resistance is better than the other three adhesive layers.

*3.2. Comparative Analysis of Pull-Out Properties of Four Types of Waterproof Adhesive Layers.* Figure 5 is the bond strength curve of different types of waterproof adhesive layers at 25°C.

It can be seen from Figure 5 that, at room temperature of 25°C, with the increase of the amount of the four waterproof adhesive layers, the bond strength increases first and then decreases, and there is maximum bond strength. This is due to the less amount of the adhesive layer and the weaker bond capacity of the adhesive layer with cement concrete and asphalt mixture. With the increase of the amount of the adhesive layer, the bond ability gradually increases and reaches a peak value. At this point, the waterproof bonding layer obtains the optimal amount of the material when the bond strength is maximum. The waterproof bonding layer not only has the bonding effect between layers but also can repair the cracks on the surface of the upper and lower structural layers. Thus, the friction and meshing between layers are increased, and the bond ability between layers is increased [48]. When the amount of the waterproof bonding layer exceeds the optimal amount, too much bonding layer material makes the overall thickness of the bonding layer larger, reducing the friction and meshing between cement concrete and asphalt mixture. At this time, only the bonding effect of the waterproof bonding layer material is left, so the overall bonding strength is reduced.

The shear strength and bond strength of the waterproof bonding layer are from the bonding ability of the adhesive layer itself and the bond effect between the layers. In addition, the shear strength partly comes from the friction resistance of the interface, and the bond strength has little correlation with it. So the range dosage and optimum dosage of shear strength and bond strength are the same, and shear strength is greater than bond strength [37]. Rubber asphalt mainly enhances its bond performance by adding the rubber powder and modifier. An appropriate amount of the rubber powder can adsorb asphalt molecules and have a large cohesive force. Because the interface friction resistance is small and the bond effect is poor, the bonding performance of rubber asphalt is small. But the bond ability is large, so the bond performance is large [37]. The bond strength principle of other adhesive layers is the same as the shear strength principle.

When the rubber asphalt content is 2.2 kg/m$^2$, the bond strength is the highest. When the dosage of SBS-modified asphalt is 1.8 kg/m$^2$, the bond strength is maximum. The maximum bond strength was obtained when SBS emulsified asphalt content was 0.6 kg/m$^2$. When AMP-100 material dosage was 0.8 kg/m$^2$, the bond strength was the highest. The maximum bond strength of SBS-modified asphalt is 0.42 MPa, and its bond performance is better than the other three adhesive layers. The bond ability of SBS emulsified asphalt is similar to rubber asphalt.

*3.3. Influences of Temperature on the Shear and Pull-Out Properties of the Waterproof Adhesive Layer.* Generally, the waterproof adhesive layer is mostly asphalt mixture, with a certain temperature sensitivity. Therefore, in the seasonal frozen region, the influence of temperature on the waterproof adhesive layer should be considered. Figure 6 shows the interlaminar shear strength curves of different waterproof adhesive layers at different temperatures under the optimum dosage.

It can be seen from Figure 6 that, with the increase of temperature, the shear strength of the four adhesive layers decreases by varying degrees, which indicates that the waterproof adhesive layer is temperature sensitive. As the temperature rises, the internal structure of the adhesive layers becomes unstable and the shear strength decreases. At low temperature, the shear strength is large, indicating that the low-temperature performance of these waterproof adhesive layers is excellent, and the internal stability is very stable. At high temperature, the shear strength is very low, indicating that the internal shear layer has been very unstable and lost its proper strength.

Physical entanglement or chemical cementation of SBS-modified asphalt due to continuous polymerization of SBS modifier particles with increasing temperature reduces the temperature sensitivity of materials. And, energy is needed to destroy the three-dimensional network structure of SBS-modified asphalt. SBS-modified asphalt has better temperature performance [49]. The rubber powder of rubber asphalt is added to the matrix asphalt, changing the asphalt colloid structure. Under the change of temperature, a uniform and insoluble phase solution system was formed. Therefore, the temperature sensitivity is also low, and the temperature performance is good [42, 45, 50]. SBS emulsified asphalt has high temperature sensitivity because the emulsifier has high temperature sensitivity. With the increase of temperature, the internal particles are more active, so the temperature performance is low [45, 46]. The AMP-100 material can adsorb asphalt molecules because of its internal macromolecular structure when temperature changes, so the temperature sensitivity is low. But because its shear strength is low, the overall strength is low [37].

At different temperatures, the shear properties of the four materials are greatly different. The maximum shear strength of SBS-modified asphalt is 5.41 MPa at −5°C higher than other adhesive layers, and the minimum shear strength of SBS emulsified asphalt is 0.27 MPa at 40°C lower than other adhesive layers. The shear strength of the AMP-100 material decreased least at different temperatures. In the seasonal frozen region, the temperature of bridge deck pavement varies from 0°C to 30°C. In this range, rubber asphalt and AMP-100 materials have low shear strength. Although the shear strength of SBS emulsified asphalt is high, the strength decreases greatly with the increase of temperature. The shear strength of SBS-modified asphalt is relatively high, and the strength changes little with the increase of temperature. Therefore, the overall performance of SBS-modified asphalt is better.

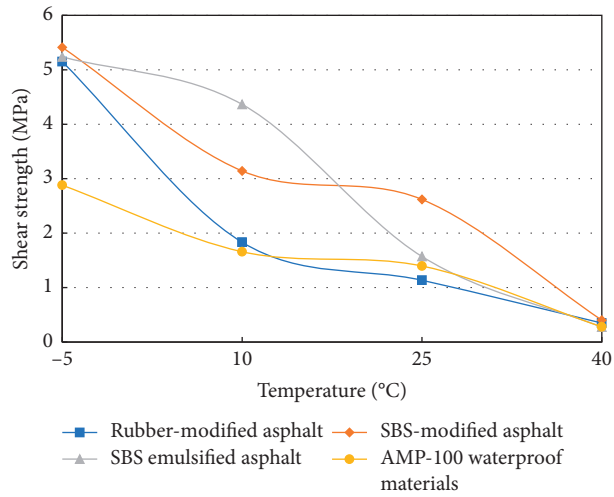


Figure 6: Shear strength of four types of waterproof adhesive layers at different temperatures.

Figure 7 is the bond strength curve of different kinds of waterproof adhesive layers at different temperatures under the optimal dosage. It can be seen from Figure 7 that the bond strength of the waterproof adhesive layer gradually decreases with the increase of temperature. The adhesive layer is larger at low temperature than at high temperature, indicating that the adhesive layer is temperature sensitive. And, it is not active at low temperature, so the bond strength is higher. With the increase of temperature, the internal adhesive layer is becoming more and more unstable, so the bond strength decreases. And, with temperature to rise, the adhesive layer is melting, which would destroy its bond performance.

Shear performance and bond performance principles are similar, determined by their own bonding ability and interlayer bond effect. SBS-modified asphalt has good bond property because SBS modifier particles have good adsorption property [49]. The AMP-100 material has low overall bond strength because of low asphalt content. The bond strength of rubber asphalt and SBS emulsified asphalt is basically the same. However, because rubber asphalt contains rubber, whose low-temperature stability is greater and adsorption capacity is stronger, its low-temperature bond strength is greater [50].

At different temperatures, the bond strength of the waterproof adhesive layer is very different. The maximum bond strength of rubber asphalt is 0.81 MPa at −5°C, and the minimum bond strength of the AMP-100 material is

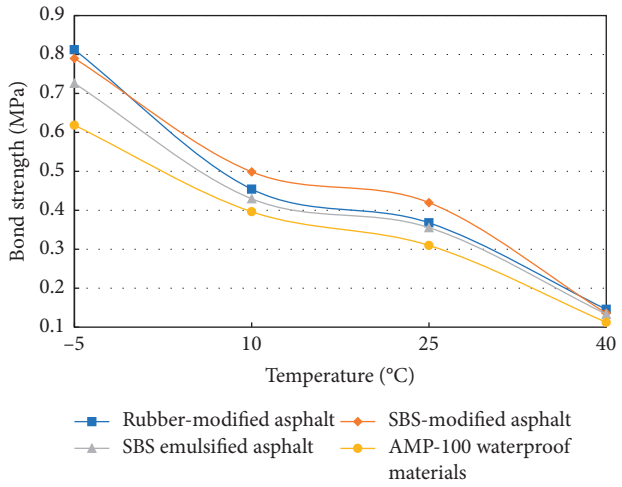


Figure 7: Bond strength of four types of waterproof adhesive layers at different temperatures.

0.11 MPa at 40°C. The bond strength of the AMP-100 material is little low, and the bond strength of SBS-modified asphalt is excellent.

*3.4. Evaluation Analysis and Optimization Based on Comprehensive Performances of the Waterproof Adhesive Layer Using AHP.* According to the previous strength test and temperature test of the waterproof adhesive layer, it is not enough to give a waterproof adhesive layer which has enough advantages to bond with the diatomite rubber-particle asphalt mixture. There are many external factors to be considered in the practical projects, such as the cost of each waterproof adhesive layer, the construction difficulty during the construction, and the time taken to block public transportation, which is the problem that should be considered when paving the bridge deck. Therefore, to get a better waterproof adhesive layer, the performance value obtained above and external factors such as the cost of waterproof adhesive layer, construction difficulty, environmental protection, and energy saving are considered for analysis.

According to the research and analysis of multi-objective grey target decision theory, some scholars have obtained the priority relationship among shear performance, bond performance, and cost. According to priority size, shear performance ≥ bonding performance ≥ cost [51]. For temperature, some scholars believe that the waterproof bonding layer has been under the influence of high temperature from the beginning of laying, which is the main reason affecting the bond performance [14, 17]. So the temperature should be the highest priority, which is higher than the bond performance and shear performance. Construction difficulty and environmental protection are not factors affecting the overall performance of the waterproof bonding layer, so their priority is low. And, in the construction, some defects of construction difference may be caused by the long and difficult construction process, so the priority of construction difficulty is higher than environmental protection [52]. Here, the analytic hierarchy process (AHP) [39, 40] was used to process the data. First, the priority of each factor is determined in Table 6.

Then, carry out normalized processing and calculate the priority. The priority here is the proportion of each influencing factor for the waterproof adhesive layer, as listed in Table 7.

Next, calculate the priority consistency to determine whether the previous comparison between any two means is consistent:

$$\sum \alpha_i A_i = \sum \left( \alpha_i \begin{bmatrix} a_{i1} \\ a_{i2} \\ a_{i3} \\ a_{i4} \\ a_{i5} \\ a_{i6} \end{bmatrix} \right) = \begin{bmatrix} 0.528 \\ 0.290 \\ 0.190 \\ 0.986 \\ 1.593 \\ 2.523 \end{bmatrix}, \quad (8)$$

where $A_i$ = normalized matrix of influencing factors in Table 7, and $a_{i1}$ = normalized values of each influencing factor in Table 7. Therefore, the consistency ratio can be calculated by equation (5), i.e., $\mathrm{CI} = ((\lambda_{\max} - n)/(n-1))$, where $\lambda_{\max} = 6.073$.

The revised consistency ratio calculated by equation (7) is $\mathrm{CR} = \mathrm{CI}/\mathrm{RI} = 0.012 \le 0.1$. Here, the value of RI is 1.24. So the consistency ratio meets the requirements. Therefore, the priority of the waterproof adhesive layer under various influencing factors is shown in Table 8.

Priority of the waterproof adhesive layer can be calculated by

$$\mu = \sum_i \alpha_i b_{ij}, \quad (9)$$

where $b_{ij}$ = normalized values of each waterproof adhesive layer under different factors in Table 8. So the priority of rubber-modified asphalt $\mu = 0.131$, the priority of SBS-modified asphalt $\mu = 0.376$, the priority of SBS emulsified asphalt $\mu = 0.210$, and the priority of SBS AMP-100 waterproof materials $\mu = 0.282$.

Therefore, considering the cost, bond strength, shear strength, construction difficulty, environmental protection, energy saving, and temperature performance of the waterproof adhesive layer, according to the priority order of performance analysis, SBS-modified asphalt has the best comprehensive performance, and its bond properties and shear properties are better; the second is AMP-100, which has better temperature performance than other materials; the third is the performance of SBS emulsified asphalt, and the overall performance is more common; and, the last is the rubber asphalt performance, and its temperature performance is poor. So the SBS-modified asphalt waterproof adhesive layer is the most suitable for laying on diatomite rubber-particle asphalt mixture pavement.

Table 6: Priority determination of influencing factors of the waterproof adhesive layer.

| Priority | Cost | Construction difficulty | Environmental protection | Bond property | Shear property | Temperature |
|---|---|---|---|---|---|---|
| Cost | 1 | 2 | 3 | 1/2 | 1/3 | 1/5 |
| Construction difficulty | 1/2 | 1 | 2 | 1/4 | 1/6 | 1/8 |
| Environmental protection | 1/3 | 1/2 | 1 | 1/6 | 1/8 | 1/9 |
| Bond property | 2 | 4 | 6 | 1 | 1/2 | 1/3 |
| Shear property | 3 | 6 | 8 | 2 | 1 | 1/2 |
| Temperature | 5 | 8 | 9 | 3 | 2 | 1 |

Table 7: Priority normalization of influencing factors of the waterproof adhesive layer.

| Priority | Normalization | | | | | | |
|---|---|---|---|---|---|---|---|
| Average | Cost | Construction difficulty | Environmental protection | Bond property | Shear property | Temperature | Priority $\alpha$ |
| Cost | 0.085 | 0.093 | 0.103 | 0.072 | 0.081 | 0.088 | 0.087 |
| Construction difficulty | 0.042 | 0.047 | 0.069 | 0.036 | 0.040 | 0.055 | 0.048 |
| Environmental protection | 0.028 | 0.023 | 0.034 | 0.024 | 0.030 | 0.049 | 0.032 |
| Bond property | 0.169 | 0.186 | 0.207 | 0.145 | 0.121 | 0.147 | 0.162 |
| Shear property | 0.254 | 0.279 | 0.276 | 0.289 | 0.242 | 0.220 | 0.260 |
| Temperature | 0.423 | 0.372 | 0.310 | 0.434 | 0.485 | 0.441 | 0.411 |

Table 8: Priority normalization of the waterproof adhesive layer under various influencing factors.

| | Cost | Construction difficulty | Environmental protection | Bond property | Shear property | Temperature |
|---|---|---|---|---|---|---|
| Rubber-asphalt | 0.167 | 0.167 | 0.423 | 0.227 | 0.074 | 0.096 |
| SBS-asphalt | 0.333 | 0.167 | 0.123 | 0.423 | 0.586 | 0.277 |
| SBS-emulsified asphalt | 0.333 | 0.333 | 0.227 | 0.227 | 0.212 | 0.161 |
| AMP-100 materials | 0.167 | 0.333 | 0.227 | 0.123 | 0.128 | 0.466 |

## 4. Conclusions

Some conclusions are obtained by testing the properties of these four waterproof adhesive layers bonded with diatomite rubber-particle asphalt mixture and cement concrete.

(1) At 25°C, the maximum shear strength of SBS-modified asphalt is 2.61 MPa at 1.8 kg/m$^2$, whose shear resistance is better than the other three adhesive layers, and the maximum adhesive strength is 0.42 MPa at 1.8 kg/m$^2$, which is better than the other three adhesive layers. For shear and bond properties, the optimum dosage of rubber asphalt is 2.2 kg/m$^2$, and the optimum dosage of SBS-modified asphalt is 1.8 kg/m$^2$. The optimum dosage of SBS emulsified asphalt is 0.6 kg/m$^2$, and the optimum dosage of AMP-100 materials was 0.8 kg/m$^2$.

(2) At the same temperature, with the increase of the amount of the waterproof adhesive layer, the bond strength and shear strength both increased first, then decreased, and gradually stabilized.

(3) At different temperatures, the shear strength of AMP-100 materials has the least reduction. The shear strength of rubber asphalt and SBS-modified asphalt is very high, but the overall performance of SBS-modified asphalt is better. The bond strength of the AMP-100 material is low, and the bond strength of SBS-modified asphalt is excellent as a whole.

(4) Compared with other adhesive layer materials, SBS-modified asphalt has the best comprehensive performance, which is more suitable for the climate with large temperature difference in winter and summer in the seasonal frozen region and has a better bond effect in the seasonal frozen region. Therefore, this paper selects the SBS-modified asphalt material as the most suitable waterproof adhesive layer bonded with diatomite rubber-particle asphalt mixture.

## Data Availability

The data used to support the findings of this study are available from the corresponding author upon request.

## Conflicts of Interest

The authors declare that they have no conflicts of interest.

## Acknowledgments

This research was funded by Scientific and Technological Project of Science and Technology Department of Jilin Province (Grant no. 20190303052SF).

## References


[1] C. Raab and M. N. Partl, "Mechanical evaluation of concrete bridge deck pavement systems," *Journal of Testing and Evaluation*, vol. 48, no. 1, pp. 211–222, 2020.

[2] L. Chen, Z. Qian, D. Chen, and Y. Wei, "Feasibility evaluation of a long-life asphalt pavement for steel bridge deck," *Advances in Civil Engineering*, vol. 2020, Article ID 5890945, 8 pages, 2020.

[3] L. Chen, G. Liu, Z. Qian, and X. Zhang, "Determination of allowable rutting depth based on driving safety analysis," *Journal of Transportation Engineering, Part B: Pavements*, vol. 146, no. 2, 2020.

[4] L. Chen, Z. Qian, and Q. Lu, "Crack initiation and propagation in epoxy asphalt concrete in the three-point bending test," *Road Materials and Pavement Design*, vol. 15, no. 3, pp. 507–520, 2014.

[5] H. Zhang, P. Gao, Z. Zhang, and Y. Pan, "Experimental study of the performance of a stress-absorbing waterproof layer for use in asphalt pavements on bridge decks," *Construction and Building Materials*, vol. 254, Article ID 119290, 2020.

[6] Y. Guan, C. Han, M. Li, and L. Yan, "Performance of modified epoxy resin waterproof adhesive layer on cement concrete bridge surface," *Journal of Building Materials*, vol. 16, no. 5, pp. 894–902, 2013.

[7] F. Mazzotta, C. Lantieri, V. Vignali, A. Simone, G. Dondi, and C. Sangiorgi, "Performance evaluation of recycled rubber waterproofing bituminous membranes for concrete bridge decks and other surfaces," *Construction and Building Materials*, vol. 136, pp. 524–532, 2017.

[8] J. S. Gong, H. L. Zhou, and H. L. Zhang, "Development and application of modified asphalt," *Petroleum Engineering Construction*, vol. 51987, in Chinese.

[9] D.-c. Feng, M. Xu, and W.-d. Wei, "Analysis of the influence of cement concrete deck moisture content on the bonding performance of waterproof adhesion layer," *Journal of Highway and Transportation Research and Development (English Edition)*, vol. 8, no. 2, pp. 31–36, 2014.

[10] M. Guo, M. Liang, Y. Jiao, W. Zhao, Y. Duan, and H. Liu, "A review of phase change materials in asphalt binder and asphalt mixture," *Construction and Building Materials*, vol. 258, Article ID 119565, 2020.

[11] G. P. Qian, S. J. Li, H. N. Yu et al., "Interlaminar bonding properties on cement concrete deck and phosphorous slag asphalt pavement," *Materials*, vol. 12, no. 9, 2019.

[12] S. P. Wu, H. Wang, J. Han, and J. T. Lin, "Research on waterproof-adhesive layer's shearing strength in cement concrete bridge pavement," *Key Engineering Materials*, vol. 417-418, pp. 849–852, 2009.

[13] Q. Xu, Q. Zhou, C. Medina, G. K. Chang, and D. K. Rozycki, "Experimental and numerical analysis of a waterproofing adhesive layer used on concrete-bridge decks," *International Journal of Adhesion and Adhesives*, vol. 29, no. 5, pp. 525–534, 2009.

[14] Y. Liu, J. Wu, and J. Chen, "Mechanical properties of a waterproofing adhesive layer used on concrete bridges under heavy traffic and temperature loading," *International Journal of Adhesion and Adhesives*, vol. 48, pp. 102–109, 2014.

[15] M. Guo, Y. Tan, L. Wang et al., "Study on water permeability, shear and pull-off performance of waterproof bonding layer for highway bridge," *International Journal of Pavement Research and Technology*, vol. 11, no. 4, pp. 396–400, 2018.

[16] Y. Jiao, Y. Zhang, L. Fu, M. Guo, and L. Zhang, "Influence of crumb rubber and tafpack super on performances of SBS modified porous asphalt mixtures," *Road Materials and Pavement Design*, vol. 20, 2019.

[17] H. Wang, C. Jin, H. Liu, and Z. Xue, "Rubber asphalt waterproof adhesive layer for steel bridge gussasphalt pavement," *International Journal of Structural Integrity*, vol. 12, no. 2, 2020.

[18] K. Zhang, "Interlaminar performance of waterproof and cohesive materials for concrete bridge deck under specific test conditions," *Journal of Materials in Civil Engineering*, vol. 30, no. 8, 2018.

[19] M. Liu, S. Han, J. Pan, and W. Ren, "Study on cohesion performance of waterborne epoxy resin emulsified asphalt as interlayer materials," *Construction and Building Materials*, vol. 177, pp. 72–82, 2018.

[20] J. Chen, C. Yao, H. Wang, W. Huang, X. Ma, and J. Qian, "Interface shear performance between porous polyurethane mixture and asphalt sublayer," *Applied Sciences*, vol. 8, no. 4, p. 623, 2018.

[21] N. Fang, X. Wang, H. Ye et al., "Study on fatigue characteristics and interlayer design method of waterproof cohesive bridge deck layer," *Applied Sciences*, vol. 9, no. 10, 2019.

[22] Y. Qiu, S. An, A. Rahman, and C. Ai, "Evaluation and optimization of bridge deck waterproof bonding system using multi-objective grey target decision method," *Road Materials and Pavement Design*, vol. 21, no. 7, pp. 1844–1858, 2020.

[23] H. Liu, G. Yuan, Q. Zhang, P. Hao, S. Dong, and H. Zhang, "Study on influence factors of asphalt mixtures pavement blistering on portland cement concrete bridge deck," *International Journal of Pavement Engineering*, vol. 22, no. 2, pp. 249–256, 2021.

[24] M. Z. Pei, *Research on the Optimized Preparation Process and Anti-aging Property of Diatomite-Crumb Rubber Compound Modified Asphalt*, Jilin University, Changchun, China, 2016, in Chinese.

[25] Y. Q. Zhao, H. D. Kuai, F. Chen et al., "Study on factors influencing the viscosity of diatomite + rubber powder modified bitumen," *Technology of Highway and Transport*, vol. 3, no. 1, pp. 37–40, 2018, in Chinese.

[26] F. Zhang and M. Li, "Performance of composite waterproof cohesive layer on cement concrete bridge," *Journal of Harbin Institute of Technology*, vol. 52, no. 3, pp. 26–32, 2020, in Chinese.

[27] Y. Jiao, Y. Zhang, M. Guo, L. Zhang, H. Ning, and S. Liu, "Mechanical and fracture properties of ultra-high performance concrete (UHPC) containing waste glass sand as partial replacement material," *Journal of Cleaner Production*, vol. 277, Article ID 123501, 2020.

[28] G. Tan, Z. Zhu, W. Wang et al., "Flexural ductility and crack-controlling capacity of polypropylene fiber reinforced ECC thin sheet with waste superfine river sand based on acoustic emission analysis," *Construction and Building Materials*, vol. 277, Article ID 122321, 2021.

[29] JTG F40-2004, *Technical Specifications for Construction of Highway Asphalt Pavements (Explanation)*, China Communications Press, Beijing, China, 2004, in Chinese.

[30] GB/T16777-2008, *Test Methods for Building Waterproofing Coatings*, Standardization Administration of China, Beijing, China, 2008, in Chinese.

[31] JC/T975-2005, *Waterproofing Coating for Concrete Bridge and Road Surface*, National Development and Reform Commission of the PRC, Beijing, China, 2005, in Chinese.

[32] JTG 3420-2020, *Testing Methods of Cement and Concrete for Highway Engineering*, Ministry of Communications of the PRC, Beijing, China, 2020, in Chinese.

[33] JTG E20-2011, *Standard Test Methods of Bitumen and Bituminous Mixtures for Highway Engineering*, China Communications Press, Beijing, China, 2011, in Chinese.
[34] J. Yubo, L. Zhang, G. Qinglin et al., "Acoustic emission-based reinforcement evaluation of basalt and steel fibers on low-temperature fracture resistance of asphalt concrete," *Journal of Materials in Civil Engineering*, vol. 32, no. 5, Article ID 04020104, 2020.
[35] P. Li, M. Z. Lu, and H. R. Wu, "Influence analysis of Marshall molding method and rolling molding method on the volume parameters of asphalt mixture," *Science Technology and Engineering*, vol. 11, pp. 3049–3051, 2008, in Chinese.
[36] DB11/T 1680-2019, *Technical Specification for Rapid Construction of Waterproof-Bonding Layer on Concrete Bridge Deck*, Beijing Municipal Bureau of Market Supervision, Beijing, China, 2019, in Chinese.
[37] W. H. Zhang, *Study on Waterproof and Cohesive Layer of Asphalt Concrete Pavement for Cement Concrete Bridge under the Condition of Warm-Wet and Heavy Load*, Guangzhou University, Guangzhou, China, 2017, in Chinese.
[38] CJJ 139-2010, *Technical Specification for Waterproofing of City Bridge Decks*, Ministry of Housing and Urban-Rural Construction of the PRC, Beijing, China, 2010, in Chinese.
[39] D. Wu, Z. Yang, N. Wang, C. Li, and Y. Yang, "An integrated multi-criteria decision making model and AHP weighting uncertainty analysis for sustainability assessment of coal-fired power units," *Sustainability*, vol. 10, no. 6, p. 1700, 2018.
[40] W. Xiang, S. Xue, S. Qin, L. Xiao, F. Liu, and Z. Yi, "Development of a multi-criteria decision making model for evaluating the energy potential of Miscanthus germplasms for bioenergy production," *Industrial Crops and Products*, vol. 125, pp. 602–615, 2018.
[41] X. Gao, *Research on Asphalt Deck of Binzhou Three-Cable-Stayed Bridge over Yellow River*, Southeast University, Nanjing, China, 2006, in Chinese.
[42] S. Liu, "Analysis of the performance and mechanism of desulfurized rubber and low-density polyethylene compound-modified asphalt," *Journal of Applied Polymer Science*, vol. 136, no. 45, 2019.
[43] H. Liu, Z. Chen, W. Wang, H. Wang, and P. Hao, "Investigation of the rheological modification mechanism of crumb rubber modified asphalt (CRMA) containing TOR additive," *Construction and Building Materials*, vol. 67, pp. 225–233, 2014.
[44] X. F. Wang, "Study of rubber asphalt modification mechanism," *Advanced Materials Research*, vol. 194–196, pp. 844–847, 2011.
[45] Y. Li, S. Li, R. Lv et al., "Research on failure mode and mechanism of different types of waterproof adhesive materials for bridge deck," *International Journal of Pavement Engineering*, vol. 16, no. 7, pp. 602–608, 2015.
[46] R. Gong, "The influence of SBS modifier on the performance of modified emulsified asphalt," *Petroleum Asphalt*, vol. 15, no. 529, pp. 4–6, 2017, in Chinese.
[47] L. Xu, "Chemical, morphological and rheological investigations of SBR/SBS modified asphalt emulsions with waterborne acrylate and polyurethane," *Construction and Building Materials*, vol. 272, 2021.
[48] C. H. Liu, *Research on Properties of Several Waterproof and Cohesive Layers for Concrete Bridge Deck*, Wuhan University of Technology, Wuhan, China, 2009, in Chinese.
[49] C. Yang, "The mechanism analysis of SBS modified asphalt by GPC method," *Urban Construction Theory Research*, vol. 10, pp. 1–8, 2012, in Chinese.
[50] J. Lu, *Performance Influence Factors and Mechanism of Rubber Asphalt*, Chang'an University, Xi'an, China, 2010, in Chinese.
[51] Y. Qiu, S. An, R. Ali, and C. Ai, "Evaluation and optimization of bridge deck waterproof bonding system using multi-objective grey target decision method," *Road Materials and Pavement Design*, vol. 21, no. 7, 2020.
[52] H. Fan, *Selection and Application of Waterproof Adhesive Layer for Cement Concrete Bridge Deck*, Beijing University of Technology, Beijing, China, 2019, in Chinese.

Hindawi
Advances in Materials Science and Engineering
Volume 2021, Article ID 5586615, 11 pages
https://doi.org/10.1155/2021/5586615

*Research Article*

# Pixel-Level Recognition of Pavement Distresses Based on U-Net

**Deru Li**,[1] **Zhongdong Duan**,[1] **Xiaoyang Hu**,[2] **and Dongchang Zhang**[2]

[1]*School of Civil and Environmental Engineering, Harbin Institute of Technology, Shenzhen 518055, China*
[2]*China Merchants Roadway Information Technology (Chongqing) Co., Ltd., Chongqing 400067, China*

Correspondence should be addressed to Zhongdong Duan; duanzd@hit.edu.cn

Received 28 January 2021; Revised 22 February 2021; Accepted 26 February 2021; Published 15 March 2021

Academic Editor: Yubo Jiao



This study develops and tests an automatic pixel-level image recognition model to reduce the amount of manual labor required to collect data for road maintenance. Firstly, images of six kinds of pavement distresses, namely, transverse cracks, longitudinal cracks, alligator cracks, block cracks, potholes, and patches, are collected from four asphalt highways in three provinces in China to build a labeled pixel-level dataset containing 10,097 images. Secondly, the U-net model, one of the most advanced deep neural networks for image segmentation, is combined with the ResNet neural network as the basic classification network to recognize distressed areas in the images. Data augmentation, batch normalization, momentum, transfer learning, and discriminative learning rates are used to train the model. Thirdly, the trained models are validated on the test dataset, and the results of experiments show the following: if the types of pavement distresses are not distinguished, the pixel accuracy (PA) values of the recognition models using ResNet-34 and ResNet-50 as basic classification networks are 97.336% and 95.772%, respectively, on the validation set. When the types of distresses are distinguished, the PA values of models using the two classification networks are 66.103% and 44.953%, respectively. For the model using ResNet-34, the category pixel accuracy (CPA) and intersection over union (IoU) of the identification of areas with no distress are 99.276% and 99.059%, respectively. For areas featuring distresses in the images, the CPA and IoU of the model are the highest for the identification of patches, at 82.774% and 73.778%, and are the lowest for alligator cracks, at 14.077% and 12.581%, respectively.

## 1. Introduction

The traditional way of pavements distress evaluation involves manual visual inspection and measurement. This is labor intensive, hinders traffic, and poses risk to workers' safety. It is also inefficient and inaccurate and makes it difficult to objectively assess the pavement condition. To improve the situation, cameras [1] and intelligent vehicles [2] have been used to capture images of the surfaces of pavements to obtain a large amount of data that are then analyzed manually. Such semiautomatic (in terms of image acquisition) and semimanual (in terms of distress identification) methods still require a large amount of labor. To address this issue, researchers have proposed methods for the automatic identification of pavement distresses using image analysis.

Li [3] and Li et al. [4] used an eight-directional Sobel operator and the maximum intercluster variance algorithm to develop an edge detection method suitable for processing images showing damage to pavements. Li et al. [5] proposed a method to detect pavement cracks based on the minimal-cost path search for strong speckle noise and low-contrast and poor continuity of pavement cracks. These image segmentation methods are complex and difficult to achieve rapid batch detection. Lin and Liu [6] used a nonlinear support vector machine (SVM) to identify potholes, and Shen et al. [7] used the SVM to recognize damage on pavement images. Acosta [8] proposed a horizontal and vertical segmentation algorithm, which divides the road damage image pixels into background, foreground, and possible foreground. The road crack image is obtained through the connection of the adjacent foreground and the possible foreground area. Chu et al. [9] used the optimal threshold algorithm to remove noise pixels in the road image and realized image binarization through online learning. Wu et al. [10] used the CCOI algorithm to realize the connection

of the cracks according to the degree of connectivity between the binary image and the surrounding objects. The algorithm improves the accuracy and efficiency of the pavement distress recognition but cannot distinguish among the types of distresses or meets the requirements for real-time detection.

With the rapid development of artificial intelligence, in particular the image classification and object segmentation technology based on the convolutional neural network (CNN) in recent years, researchers have applied computer vision and machine learning technology to achieve automatic detection of pavements distresses [11–16]. Maeda et al. [12] proposed an object classification method based on the CNN. The authors used images captured by a smartphone mounted on a car and classified eight categories of pavement damage with an image dataset containing 9,053 images showing damage to pavements and 15,435 instances of such damage. Zhang et al. [13] proposed a model that contains four convolutional layers, a maximum pooling layer, and two fully connected layers for pavement crack detection. Sha et al. [14] introduced the CNN to the image analysis based on pavement distress recognition and measurement and proposed models to extract crack and pothole features. Their experiments showed that CNN can achieve accurate results for the identification and measurement of pavement cracks and potholes. Shi et al. [15] detected bare surface distress on concrete pavements using deep learning and achieved an accuracy of 90.2%. Tang et al. [16] cut the pavement images into subblocks of 128 pixels × 128 pixels, manually labeled them as crack and noncrack images, and used a variety of deep learning models to identify the subblocks, showing cracks with recognition accuracy of 92%.

Existing methods that use deep neural networks to process images to identify pavement distresses have the following problems: (1) There is a lack of high-quality, large-scale, multidistress pavement datasets for model training. Most of current researches on pavement distress recognition have been on a single type of distress, such as cracks [17–20]. (2) When the deep neural networks are used to analyze images of pavement distress, the images need to be manually divided into subblocks to reduce their size while maintaining high pixel. It helps to improve the distress images recognition accuracy, but it is labor intensive as it is done manually. (3) Advanced technologies for image segmentation, such as the U-net, can significantly improve the efficiency of image detection while maintaining a high accuracy, and it has been used for crack detection in concrete structures [21] and pavements [22–24]. Ji et al. [21] achieved an accuracy of 99.56% on their test set, and Chen et al. [22] obtained an accuracy of 89.92% in their asphalt pavement dataset. However, this model has not been applied to the identification of multiple distresses of pavements.

For multidistress identification of pavement images, a large number of pavement images from four asphalt highways in three provinces and cities in China were collected and labeled on pixel level. Six types of distresses are considered in this study, namely, alligator cracks, longitudinal cracks, transverse cracks, block cracks, potholes, and patches. The U-net model is combined with the ResNet, a deep convolutional neural network (CNN), to train the pavement image recognition model. Techniques such as data augmentation, batch normalization, momentum learning, and other regularization techniques are used to enhance the model training. The developed model does not require manual preprocessing of the pavement images and delivers pixel-level distress location, shape, and size in the images, which could automate the distress detection procedure and improve the distress identification accuracy.

This paper trained a new model to identify the distress area and classify the distress types for multidistress pavement images. In Section 2, a pixel-level dataset of six types of distresses is built. In Section 3, a U-net model combined with the ResNet is introduced. Section 4 demonstrates the training and verification of pixel-level pavement distress recognition model. Section 5 summarizes the outcomes and concludes the paper.

## 2. Dataset of Pavement Distresses

The images of pavement distress used in this article were collected by the Intelligent Road Measuring Vehicle (Luxin-CT616, see Figure 1), manufactured by the China Merchants Roadway Information Technology (Chongqing) Co., Ltd. The vehicle was equipped with one CCD (charge coupled device) camera at a right angle to cover the pavement surface. A 3,662 × 2,032-pixel pavement image was captured every 2 m along the driving direction. Each image covered a pavement patch of 3.5 m × 2 m at a resolution of 0.96 mm/px × 1 mm/px. The frame rate changed with vehicle speed.

A total of 10,097 pavement images featuring six types of distresses, alligator cracks, longitudinal cracks, transverse cracks, block cracks, potholes, and patches, were collected on four asphalt expressways in three provinces and cities in China (G15 Yueqing section and Ounan section in Zhejiang Province, G243 Meitan-to-Yuqing highway in Guizhou, Chongqing Inner Ring Expressway, and Chongqing Yuchang Expressway. The images were captured over 567.33 km).

Each image might have contained no, one, or more than one type of distress. Each type of distress was labeled at pixel level as shown in Figure 2. A total of 5,427 images contain one type of distress, accounting for 53.75% of all images, and 4,670 images contain two or more types of distresses, accounting for 46.25%.

The 10,097 images of the pavement distress dataset feature 14,697 cases of distress. The number of occurrences of each type of distress is shown in Table 1. Patches accounts for the largest portion of the dataset, and block cracks is the smallest.

## 3. Deep Neural Network for Pixel-Level Pavement Distress Recognition

In traditional methods of image recognition, such as feature engineering tasks, the extraction of image features and tags needs to be carried out manually. Recent years have witnessed the rapid development of convolutional neural network (CNN) [25] that can automatically extract image features. The deep CNN contains multiple CNNs, which

Figure 1: Intelligent road measuring vehicle (luxin-CT616).

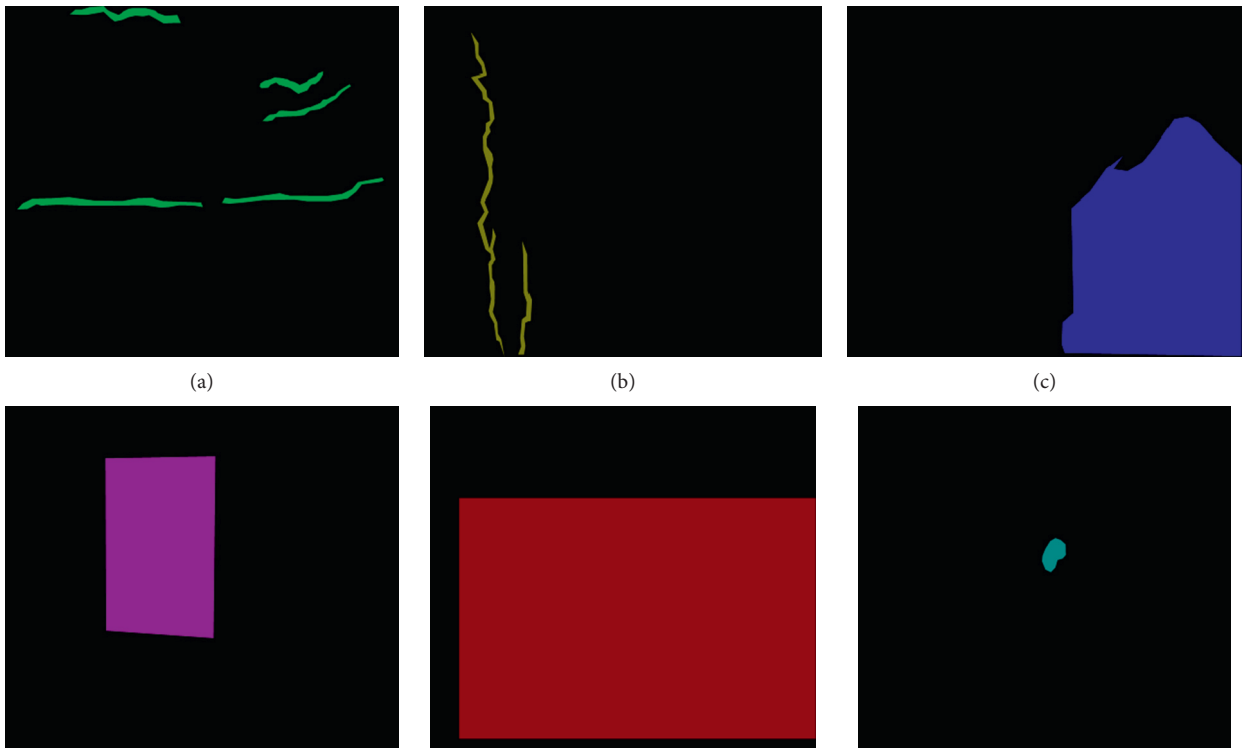


Figure 2: Six types of pavement distress. (a) Transverse crack. (b) Longitudinal crack. (c) Alligator crack. (d) Patch. (e) Block crack. (f) Pothole.

enables the extraction of local and global features from images in one model. Through the automatic feature extraction of images by a low-level CNN, some basic edge-related features, such as points and lines, can be constructed and converted into higher-level features through a high-level CNN for the accurate recognition of images. Therefore, when a deep CNN is used to train a model to detect damage to pavements, the images are input to the model for automatic distress identification without the need of manual feature extraction. To improve the identification accuracy, the semantic segmentation of images is used, and the pavement distresses are identified at pixel level. Specifically, the U-net network is employed as the main algorithmic architecture of the model and ResNet as its basic classification network.

*3.1. ResNet.* There is a consensus in image recognition that the greater the number of layers used for image recognition with deep CNN networks, the higher the recognition

Table 1: The numbers of all distress types.

| Distress | Number | Percent (%) |
|---|---|---|
| Transverse crack | 1786 | 12.09 |
| Longitudinal crack | 2348 | 15.90 |
| Alligator crack | 1662 | 11.31 |
| Block crack | 126 | 0.86 |
| Patch | 6924 | 47.11 |
| Pothole | 1919 | 13.06 |

accuracy. However, when the network reaches a certain depth in image recognition experiments, further increasing network depth degrades its performance [26]. Simply increasing the number of layers does not yield an improvement in recognition performance but reduces the speed of convergence and the classification accuracy of the network.

To solve this problem, He et al. [26] proposed a residual network (namely, ResNet) that uses residual blocks by adding an identity mapping to the usual deep CNN, as shown in Figure 3. Take a deep CNN network with output $x$ for an example. ResNet is to add a residual block as shown in Figure 3 after the last layer of the deep CNN network. The input to the residual block is the output $x$ of the original deep CNN, its learning feature is the output $F(x)$ of the two middle CNN layers, and the final output $H(x)$ of the residual block is $H(x) = F(x) + x$. When $F(x)$ is zero, the residual block is subjected to only identity mapping, and the two convolutional layers in it have no effect on the output of the original depth of the CNN. Thus, the performance of the CNN network does not suffer if the depth of the residual block is increased. When $F(x)$ is not zero, the residual block learns a new feature $F(x)$, and the entire deep CNN network can learn $F(x)$ based on the input feature $x$, which improves the classification performance. In this paper, ResNet is used as the classification network of the semantic segmentation model for pavement distress identification.

Table 2 shows the network structures of ResNet-34 and ResNet-50. Both contained 16 residual blocks. ResNet-34 has 36 convolution layers, a max pooling layer, two average pooling layers, and a fully connected layer. The total number of parameters is 21,813,570. ResNet-50 has 53 convolution layers, a max pooling layer, two average pooling layers, and a fully connected layer, and its total number of parameters is 30,682,729.

*3.2. U-Net Neural Network.* The probability of occurrence of different distresses in asphalt pavements varies. For example, a patch has a higher incidence probability than that of block cracks. The imbalance in the dataset can cause the deep CNN algorithm to attend more to the distresses with more instances and ignore those with fewer exemplars when recognizing image features. The consequence is to lower the recognition accuracy of the latter. The U-net model [27] could help solve this problem by a symmetrical U-shaped structure.

ResNet-34 is shown to have high accuracy in image classification, and it is used as the backbone of the U-net network, which is shown in Figure 4. It is a fully convolutional semantic segmentation network that has a symmetrical U-shaped structure containing a compression path and an expansion path. The left side of Figure 4 shows the path of contraction and the right side shows that of expansion. The contraction path consists of a ResNet-34 with repeated applications of residual blocks. Some residual blocks are followed by maximum pooling layers for downsampling, and a skip connection is used to splice the feature map in the expansion path. In the expansion path, each repeated step involves firstly upsampling the feature map and then performing a $2 \times 2$ deconvolution to halve the number of feature channels and double the size of the feature map. This feature map is spliced using the corresponding feature map in the contraction path. After stitching, two $3 \times 3$ convolutions are performed, and each convolution layer is followed by a ReLU activation function. In the last layer of the network, a $1 \times 1$ convolution is used to map each 64-channel feature map to the required number of categories. The blue arrow in Figure 4 indicates the feature splicing operation.

The network structure of U-net based on ResNet-34 is shown in Table 3. It contains 54 convolutional layers, and the total number of parameters is 41,132,518. The U-net network structure based on ResNet-50 is similar, with 71 convolutional layers and 338,306,566 parameters.

Before the pavement distress images are input to the model in the form of a pixel matrix, the value of each pixel in the image is converted. Pixel values of the no-distress areas (the remaining part of the image except the distress) are all set to zero, and those of block cracks, longitudinal cracks, transverse cracks, alligator cracks, potholes, and patches are set to 1, 2, 3, 4, 5, and 6, respectively. Hence, each pixel in the images is an integer value between 0 and 6. The converted image set is then input to the U-net model for training and validation.

## 4. Level Pavement Distress Recognition Model

*4.1. Techniques for Training.* To improve the model's pixel-level recognition accuracy of pavement distresses and speed-up training, techniques such as data augmentation [28], batch normalization [28], momentum learning [29], fine-tuning [30], and a discriminative learning rate [31] are used.

Data augmentation [28] enables a limited amount of data to produce value equivalent to larger amounts of data without substantially increasing data. It is an important regularization technique in computer vision which applies geometric transformations (such as flipping, rotation, cropping, deformation, and scaling) and color transformations (such as pertaining to noise, blur, erasure, and filling) to images. Because the pavement distress images are captured vertically and longitudinal cracks and transverse cracks have obvious directionality, geometric transformations such as rotation and deformation cannot be used for data augmentation. In this paper, each image is randomly flipped vertically with a probability of 0.75. Figure 5 compares the longitudinal cracks after flipping with the original image.

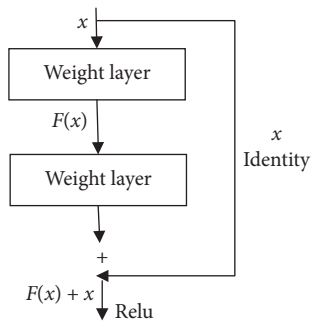


Figure 3: Residual model: a building block.

Table 2: The architecture of ResNet-34 and ResNet-50.

| Layer name | 34-layer | 50-layer |
|---|---|---|
| Conv1 | $[7\times7, 64]$[a], stride 2 | |
| Max pool | $[3\times3]$, stride 2 | |
| Conv2_x | $\begin{bmatrix} 3\times3, 64 \\ 3\times3, 64 \end{bmatrix}\times3$ | $\begin{bmatrix} 1\times1, 64 \\ 3\times3, 64 \\ 1\times1, 256 \end{bmatrix}\times3$ |
| Conv3_x | $\begin{bmatrix} 3\times3, 128 \\ 3\times3, 128 \end{bmatrix}\times4$ | $\begin{bmatrix} 1\times1, 128 \\ 3\times3, 128 \\ 1\times1, 512 \end{bmatrix}\times4$ |
| Conv4_x | $\begin{bmatrix} 3\times3, 256 \\ 3\times3, 256 \end{bmatrix}\times6$ | $\begin{bmatrix} 1\times1, 256 \\ 3\times3, 256 \\ 1\times1, 1024 \end{bmatrix}\times6$ |
| Conv5_x | $\begin{bmatrix} 3\times512 \\ 3\times512 \end{bmatrix}\times3$ | $\begin{bmatrix} 1\times1, 512 \\ 3\times3, 512 \\ 1\times1, 2048 \end{bmatrix}\times3$ |
| Adaptive average pool | Output_size = 1 | |
| Adaptive max pool | Output_size = 1 | |
| Fully connected layer | Dimensionality = 7 | |

[a]The number of the convolutional filters is 64, each of size $7\times7$.

Batch normalization [28] uses normalization and linear transformation to constrain the mean and variance of the input data of each layer to within a certain order of magnitude, which could avoid the mean and variance being too large or too small, so that subsequent layers of the network do not need to adapt to changes in the input to the previous network, and each layer can independently learn the data. This improves the learning speed of the entire neural network. Batch normalization after each convolutional layer is used.

When applying the gradient descent method, if the absolute value of the slope of the objective optimization function in the vertical direction is greater than that in the horizontal direction at a certain position, the gradient descent causes the variable to move to a greater extent along the vertical direction than the horizontal direction at a given learning rate. Therefore, a lower learning rate needs to be set to prevent the independent variable from crossing the optimal solution of the objective function in the vertical direction. However, this causes the independent variable to move slowly in the horizontal direction and prolonged the time needed for convergence. In order to solve this problem, the momentum method uses the weighted average of the gradient of the past time step, where the weight decays exponentially according to the time step, so that the independent variable updates of adjacent time steps are more consistent in direction. Therefore, a higher learning rate is used to enable the independent variable to move more quickly to the optimal solution and accelerate convergence. According to Smith's experiments [29], a cyclical momentum of 0.95–0.85 provides better performance than a constant momentum. Therefore, the momenta used in this paper are (0.95, 0.85).

When recognizing an image, the system first learns low-level features, such as lines, and then learns specific abstract features. Model parameters that have been trained on large image sets are well-learned low-level features. Hence, they can be migrated to other, smaller image sets to speed up the training of the model. This paper uses the transfer learning method [30] to transfer parameters of the ResNet-34 and ResNet-50 models, which have been trained on ImageNet (containing 14,197,122 images in 21,841 categories), to the model for the semantic segmentation of images of pavement distress. The parameters are retrained by fine-tuning and using a discriminative learning rate [31] to obtain values suitable for images of pavement distress. Fine-tuning is used to lock parameters of part of the network layer in the model and to train only the last layer or few layers of parameters; the discriminative learning rate is used to divide the parameters in the model into three parts according to the depth of the CNN model (each part is assigned a different learning rate). The changes in the parameters decrease with decreasing distance to the bottom of the model, where the learning rate is lower. Thus, it becomes easier for the model parameters to reach a stable state, which speeds up the training process.

*4.2. Measures of Model Performance.* Pixel accuracy (PA), category pixel accuracy (CPA), intersection over union (IoU), and mean intersection over union (MIoU) are commonly used as measures of semantic segmentation. They are defined as follows.

Suppose that there are $k+1$ categories $(0 \sim k)$ in a dataset, and "0" usually represents the background. $P_{ii}$ represents the number of pixels that are originally $i$ type and are predicted to be so, $P_{ij}$ represents the number of pixels that are originally $i$ type but predicted to be $j$ type, and $P_{ji}$ is the number of pixels that are originally $j$ type but predicted to be $i$ type.

PA is defined as the ratio of the number of pixels correctly predicted to the total number of pixels defined in the following:

$$\mathrm{PA} = \frac{\sum_{i=0}^{k} p_{ii}}{\sum_{i=0}^{k}\sum_{j=0}^{k} p_{ij}}. \tag{1}$$

The larger PA is, the greater the number of pixels that the model has predicted correctly is, and the stronger the classification ability is for the model.

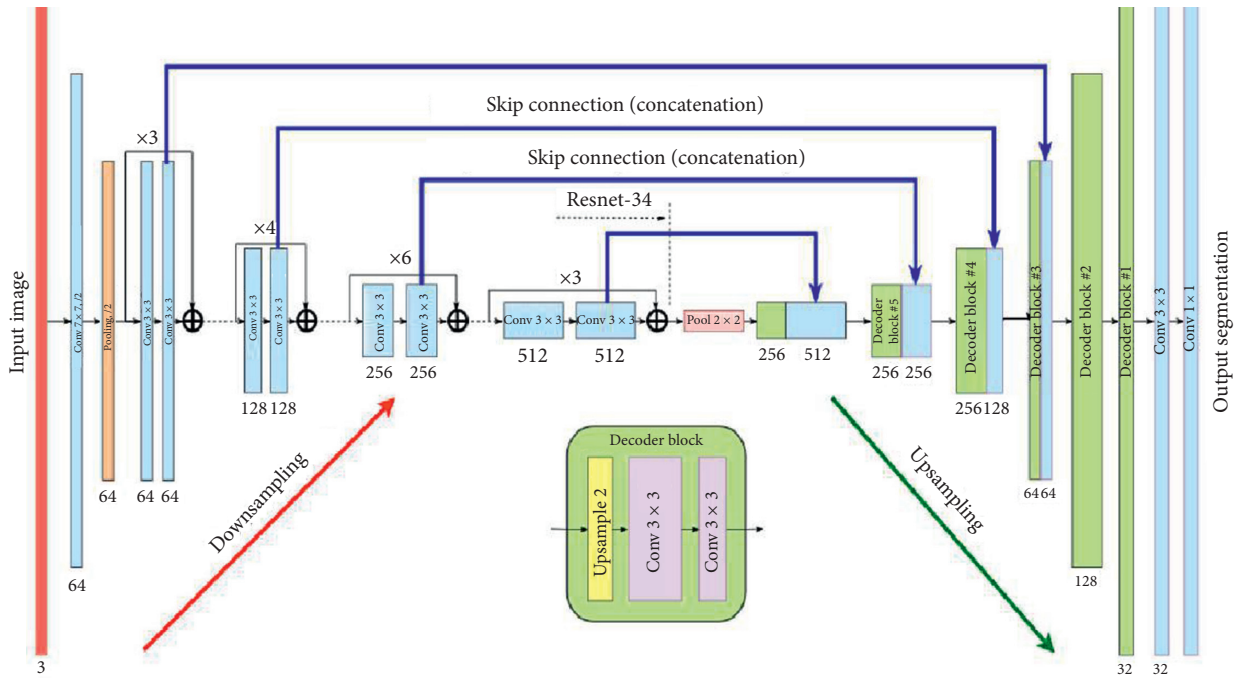


Figure 4: U-net architecture based on ResNet-34.

Table 3: The architecture of U-net based on ResNet-34.

| The contraction path | Layers | The expansion path | Layers |
|---|---|---|---|
| Conv2d | $[7\times7,\ 64]$, stride = 2 | Pixel shuffle | $[1\times1,\ 1024]$ |
| Max pool | $[3\times3]$, stride = 2 | Average pool | $[2\times2]$ |
| Conv2d | $\begin{bmatrix}3\times3, 64\\3\times3, 64\end{bmatrix}\times3$ | Conv2d | $\begin{bmatrix}3\times3, 512\\3\times3, 512\end{bmatrix}\times2$ |
| Conv2d | $\begin{bmatrix}3\times3, 128\\3\times3, 128\end{bmatrix}\times2$ | Pixel shuffle | $[1\times1,\ 512]$ |
| Downsample | $[1\times1,\ 128]$ | Average pool | $[2\times2]$ |
| Conv2d | $\begin{bmatrix}3\times3, 128\\3\times3, 128\end{bmatrix}\times3$ | Conv2d | $\begin{bmatrix}3\times3, 384\\3\times3, 384\end{bmatrix}\times2$ |
| Conv2d | $\begin{bmatrix}3\times3, 256\\3\times3, 256\end{bmatrix}\times2$ | Pixel shuffle | $[1\times1,\ 768]$ |
| Downsample | $[1\times1,\ 256]$, stride = 2 | Average pool | $[2\times2]$ |
| Conv2d | $\begin{bmatrix}3\times3, 256\\3\times3, 256\end{bmatrix}\times5$ | Conv2d | $\begin{bmatrix}3\times3, 256\\3\times3, 256\end{bmatrix}\times2$ |
| Conv2d | $\begin{bmatrix}3\times3, 512\\3\times3, 512\end{bmatrix}\times2$ | Pixel shuffle | $[1\times1,\ 512]$ |
| Downsample | $[1\times1,\ 512]$, stride = 2 | Average pool | $[2\times2]$ |
| Conv2d | $\begin{bmatrix}3\times3, 512\\3\times3, 512\end{bmatrix}\times2$ | Conv2d | $\begin{bmatrix}3\times3, 96\\3\times3, 96\end{bmatrix}\times2$ |
| Conv2d | $[3\times3,\ 1024]$ | Pixel shuffle | $[1\times1,\ 384]$ |
| Conv2d | $[3\times3,\ 512\ ]$ | Average pool<br>Conv2d<br>Conv2d<br>Conv2d | $[2\times2]$<br>$[3\times3,\ 49]$<br>$[3\times3,\ 99]$<br>$[1\times1,\ 7\ ]$ |

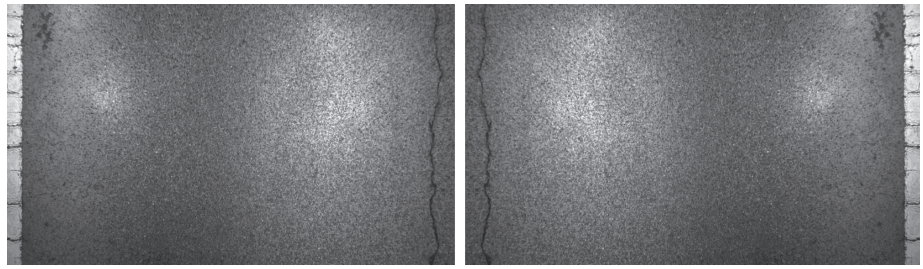

Figure 5: Images of longitudinal crack using flip. (a) Original image. (b) Flipped image.

Table 4: PA values of different models using images of different sizes.

| Model | Input image size (pixel) | PA | |
|---|---|---|---|
| | | Detecting distress with six types | Detecting with or without distress |
| ResNet-34 | $256 \times 256$ | **0.66103** | **0.97336** |
| | $512 \times 512$ | 0.62716 | 0.97113 |
| ResNet-50 | $256 \times 256$ | 0.44953 | 0.95772 |

CPA is defined as the ratio of pixels predicted to be correct in one category defined in the following:

$$\text{CPA} = \frac{p_{ii}}{\sum_{j=0}^{k} p_{ji}}. \tag{2}$$

The larger CPA is, the less likely it is that the model predicts pixels of other categories as belonging to the given category, and the stronger the model's classification ability is.

IoU is defined as the ratio of the intersection and union of the ground truth and the predicted value of one category, as defined in the following:

$$\text{IoU} = \frac{p_{ii}}{\sum_{j=0}^{k} p_{ij} + \sum_{j=0}^{k} p_{ji} - p_{ii}}. \tag{3}$$

The closer the IoU is to one, the more consistent the model's predicted position for the category is with the true position, and the stronger the model's ability is to locate the category.

MIoU is the average of the IoU of all classes defined by

$$\text{MIoU} = \frac{1}{k+1} \sum_{i=0}^{k} \frac{p_{ii}}{\sum_{j=0}^{k} p_{ij} + \sum_{j=0}^{k} p_{ji} - p_{ii}}. \tag{4}$$

The closer the MIoU is to one, the stronger the model's ability to locate all classes is.

### 4.3. Analysis of Results

*4.3.1. Training Process.* A total of 80% of images in the dataset are used to train the models and the remaining 20% are used for validation. Cross-entropy loss is used as loss function for the training process. The image sizes are set to $256 \times 256$-pixel and $512 \times 512$-pixel, respectively. Using the above training techniques, the pixel-level recognition model of pavement distresses is trained based on ResNet-34 and ResNet-50. All code is implemented on Fast.ai with a PyTorch backbone on an NVIDIA RTX 2080Ti GPU. The training of the model includes the three following steps.

Table 5: CPA values of different labels using ResNet-34.

| Distress | CPA |
|---|---|
| No distress | 0.99276 |
| Patch | 0.82774 |
| Pothole | 0.31902 |
| Transverse crack | 0.19139 |
| Block crack | 0.25135 |
| Alligator crack | 0.14077 |
| Longitudinal crack | 0.27439 |

Table 6: IoU of different labels using ResNet-34.

| Distress | IoU |
|---|---|
| No distress | 0.99059 |
| Patch | 0.73778 |
| Pothole | 0.28436 |
| Transverse crack | 0.21429 |
| Block crack | 0.19445 |
| Alligator crack | 0.23038 |
| Longitudinal crack | 0.12581 |
| Average (MIoU) | 0.3968 |

The first step is to randomly flip the pavement images for data augmentation and set the original image size to $256 \times 256$-pixel and $512 \times 512$-pixel, respectively.

The second step is to load the U-net model with ResNet-34 and ResNet-50, where the parameters have been pre-trained on a large dataset [32] and [33] input the images of step 1 into the model and specify the evaluation index of the model.

The last step is to train the model using fine-tuning and discriminating the learning rate. Firstly, the parameters of the network layer in the model except the last layer or a few layers are locked using fine-tuning method, and only the

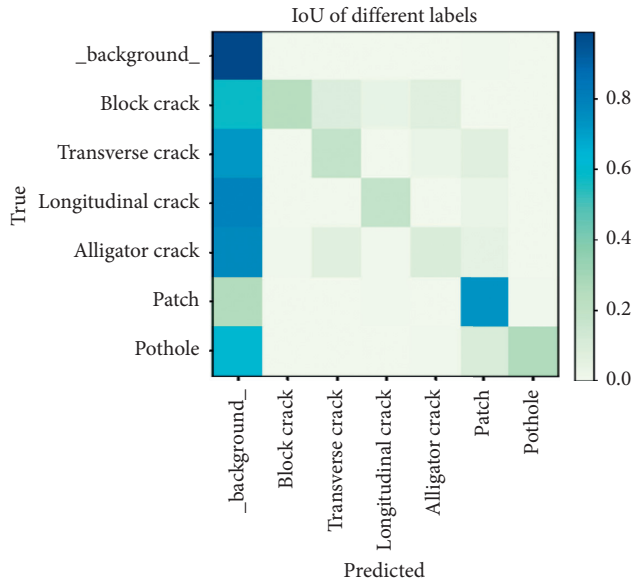


Figure 6: Confusion matrix of IoU values of different labels.

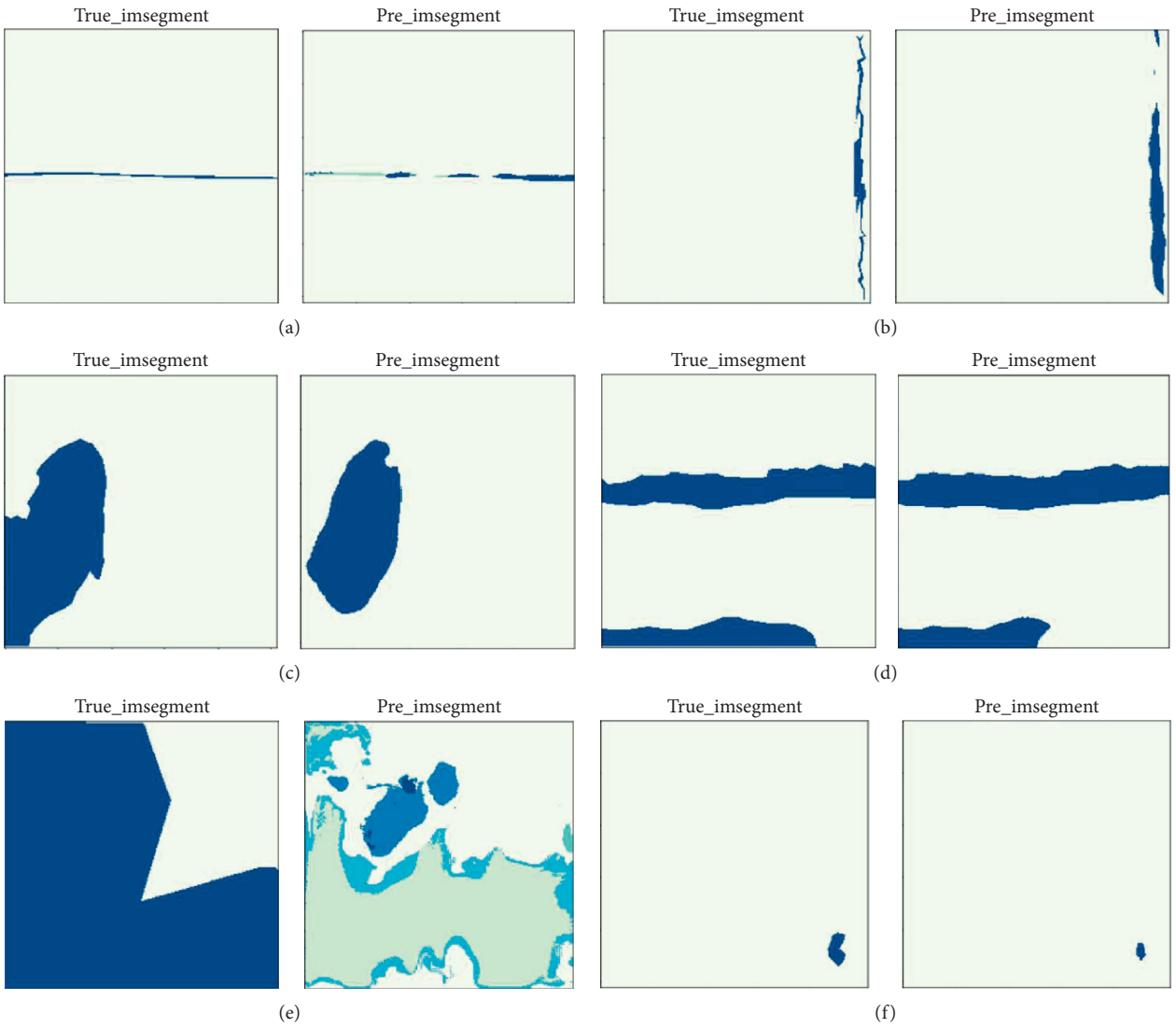


Figure 7: Examples of empirically determined and predicted labels. (a) Transverse crack. (b) Longitudinal crack. (c) Alligator crack. (d) Patch. (e) Block crack. (f) Pothole.

unlocked layers parameters are trained. Then the parameters of the model are divided into three parts by discriminating the learning rate, and the model is trained with each part assigned a different learning rate.

*4.3.2. Test of the U-Net Model.* Table 4 shows the PA values of the pavement distress pixel-level recognition model using ResNet-34 and ResNet-50 by inputting images with different sizes. When only the distressed or nondistressed areas in an image are to be distinguished, the PA values obtained on the verification set of the two models are 97.336% and 95.772%, respectively. This is higher than the single-category model (89.92%) for crack recognition on an asphalt pavement in Chen et al.'s work [22] and the single-category model (92.12%) for crack recognition of Fitchburg Municipal Airport runways as reported in Cheng et al.'s work [23].

When the distress types detection are concerned, for example, in our case, six types of distresses are to be categorized, the PA of ResNet-34 is evaluated to be 66.103%, higher than the PA of ResNet-50 (44.953%) on the $256 \times 256$-pixel image size dataset. However, when $512 \times 512$-pixel image size is used, the PA of the model based on ResNet-34 is 62.716%, lower than that on $256 \times 256$-pixel image size.

For the six types of distresses detection, the CPA and IoU of each distress obtained by the ResNet-34 model on the validation set with $256 \times 256$-pixel image size are shown in Tables 5 and 6, respectively. Compared with distress detection model based on SSD (Single-Shot MultiBox Detector) [34] using the same distress images dataset, where the distressed areas are labeled with rectangle bounding boxes, the IoU is set to 0.5 (the common value in object detection), the average precision (AP) of patches, potholes, transverse cracks, block cracks, alligator cracks and longitudinal cracks is 0.53061, 0.00263, 0.30748, 0.28322, 0.41175, and 0.09820, respectively [35]. The U-net model has great improvement on patches (0.82774 versus 0.53061), potholes (0.31902 versus 0.00263), and longitudinal cracks (0.27439 versus 0.09820) detection over the SSD model but poorly performs on transverse cracks (0.19139 versus 0.30748), block cracks (0.25135 versus 0.28322), and alligator cracks (0.14077 versus 0.28322). The poor performance of the U-net model on the three types of distresses may be due to the fact that some image pixels within the distress outline have the same features as the no-distress pixels outside the outline on the distress images.

Table 6 shows the IoU of different categories (including no-distress areas, that is, the background) on the verification set. The IoU of the no-distress area is 99.059%, and the average is 39.68% (MIoU). Compared with the IoU value of 0.6 for pavement cracks obtained by Jiang et al. [24] with a single-class model, the IoUs of various cracks achieved in this study are low, showing that the detection of location, shape, and size of distressed area of images is still a challenge for multiple classifiers.

Figure 6 shows the IoU confusion matrix diagram of different categories (including the no-distress areas, that is, the background) on the validation set. The horizontal axis in the figure represents the predicted category and the vertical axis represents the true category. The darker the color is, the closer the IoU is to one. In the confusion matrix, the darker the diagonal block is, the higher the accuracy of the model is, and the darker the nondiagonal block is, and there is a greater probability of being incorrectly recognized. Pixels with various distresses have a significant probability of being recognized as no-distress pixels (background pixels). In addition, block cracks are more likely to be mistaken for transverse and alligator cracks, while patches and potholes are rarely mistaken for other types of distresses.

Figure 7 shows a comparison between the manually determined area of pavement distress and the predicted area by the trained model for various types of distresses. It shows that the developed model could recognize multiple distress labels in the images but incur certain errors in identifying the specific type and location of the distresses. This might have occurred for a number of reasons. Firstly, the size of certain pavements distresses occupied a relatively small part of an image. When the image of the pavement distress is reduced, the distress characteristics become less prominent, which might have affected the recognition performance of the model. Secondly, for such distresses as alligator and block cracks, some image pixels within the distress outline have the same features as the no-distress pixels, which might have reduced the recognition accuracy of the model.

## 5. Conclusions

The development of pavement distress inspection technology and AI, especially convolutional neural networks (CNN), makes it possible to automate the road inspection and evaluation process from road image collection, distress detection, and road condition assessment. To achieve this goal, an efficient and high-precision pavement distress classification and detection model is needed. Toward this purpose, road distress image detection models based on U-net are trained and tested with a road distress image dataset built by road images collected from 567.33 km asphalt expressways in China. The major conclusions of this study are drawn in the following:

(1) A total of 10,097 images of six common distresses captured from four asphalt expressways in three provinces in China are labeled in pixel level to construct a pavement distress image dataset.

(2) Using the U-net model and ResNet, an advanced semantic segmentation model for road distress detection is trained for pixel-level pavement distress recognition. The developed model does not require manual preprocessing of the pavement images and delivers pixel-level distress location, shape, and size in the images, which could automate the distress detection procedure and improve the distress identification accuracy.

(3) For binary classification, which classifies an image pixel as distressed or not distressed, the PA values are evaluated to be 97.336% for the ResNet-34 model using the test dataset. When the six types of common road distresses are to be classified, the trained

multiple feature classifier performs differently on the six types of distresses. It achieves an accuracy of 82.774% for patches but incurs fairly large errors in predicting the shape and location of other types of distresses.

(4) The U-net network structure used in this article contains 4 downsampling processes and 4 upsampling processes, and the image has undergone multilayer convolution before the first downsampling, which makes it extract a smaller number of the feature maps of small size distress such as pothole. On the other hand, cracks have more point and line characteristics, and shallow convolution layers will be helpful to extract the characteristics of cracks and potholes. Thus, changing the number of downsampling processes or upsampling processes, converting long skip connection in the U-Net structure into short skip connection, and integrating multilayer feature maps may help to improve the recognition accuracy.

## Data Availability

Some or all data, models, or code supporting the findings of this study are available from the corresponding author upon reasonable request.

## Conflicts of Interest

The authors declare that there are no conflicts of interest regarding the publication of this paper.

## Acknowledgments

The authors are grateful to Weixiang Liu, Ruibo Zhang, and Guocai Zheng for their labeling work for the dataset used in this study.

## References

[1] H. D. Cheng and M. Miyojim, "Automatic pavement distress detection system," *Information Sciences*, vol. 108, no. 1–4, pp. 219–240, 1998.

[2] A. Zhang, K. C. Wang, Y. Fei et al., "Deep learning–based fully automated pavement crack detection on 3D asphalt surfaces with an improved cracknet," *Journal of Computing in Civil Engineering*, vol. 32, no. 5, Article ID 04018041, 2018.

[3] J. H. Li, "Pavement crack diseases detecting by image processing algorithm," *Journal of Chang'an University (Natural Science Edition)*, vol. 24, no. 3, pp. 24–29, 2004, in Chinese.

[4] L. Li, L. J. Sun, and C. Chen, "An edge detection method designed for pavement distress images," *Journal of Tongji University (Natural Science)*, vol. 39, no. 5, pp. 688–692, 2010, in Chinsese.

[5] Q. Q. Li, Q. Zou, and Q. Z. Mao, "Pavement crack detection based on minimum cost path searching," *China Journal of Highway and Transport*, vol. 23, no. 6, pp. 28–33, 2010, in Chinese.

[6] J. Lin and Y. Liu, "Potholes detection based on SVM in the pavement distress image," in *Proceedings of the 2010 Ninth International Symposium on Distributed Computing and Applications to Business, Engineering and Science*, pp. 544–547, Hong Kong, China, August 2010.

[7] Z. Q. Shen, Y. H. Peng, and N. Shu, "Road damage identification method based on scale-span image and SVM," *Geomatics and Information Science of Wuhan University*, vol. 38, no. 8, pp. 993–997, 2013, in Chinese.

[8] J. A. Acosta, *Pavement Surface Distress Evaluation Using Video Image Analysis*, Case Western Reserve University, Cleveland, OH, USA, 1994.

[9] X. Chu, X. Yan, and M. Long, "The automatic search of pavement surface distress image based on on-line learning," in *Proceedings of the International Conference on Transportation Engineering 2007*, pp. 3282–3287, Chengdu, China, July 2007.

[10] M. Wu, X. Chen, and C. R. Liu, "Smart structures and materials 2002: smart systems for bridges, structures, and highways," *International Society for Optics and Photonics*, vol. 4696, pp. 293–300, 2002.

[11] S. Gao, Z. Jie, Z. Pan et al., "Automatic recognition of pavement crack via convolutional neural network," *Transactions on Edutainment XIV*, pp. 82–89, Springer, Berlin, Heidelberg, 2018.

[12] H. Maeda, Y. Sekimoto, T. Seto, and H. Omata, "Road damage detection and classification using deep neural networks with smartphone images," *Computer-Aided Civil and Infrastructure Engineering*, vol. 33, no. 12, pp. 1127–1141, 2018.

[13] L. Zhang, F. Yang, D. Zhang et al., "Road crack detection using deep convolutional neural network," in *Proceedings of the IEEE International Conference on Image Processing (ICIP 2016)*, pp. 3708–3712, IEEE, Phoenix, AZ, USA, September 2016.

[14] A. M. Sha, Z. Tong, and J. Gao, "Recognition and measurement of pavement disasters based on convolutional neural networks," *China Journal of Highway and Transport*, vol. 31, no. 1, pp. 1–10, 2018, in Chinese.

[15] L. Shi, J. J. Hu, W. Li et al., "Automatic detection method of road surface distress based on deep learning," in *Proceedings of the 10th Annual Conference of the Maintenance and Management Branch of China Highway Society*, pp. 164–170, 2020, in Chinese.

[16] J. Tang, B. Peng, and Y. Zhang, "Automatic pavement crack detection based on deep learning," in *Proceedings of the 14th China Intelligent Transportation Conference*, pp. 458–468, 2019, in Chinese.

[17] W. Liu, Y. Huang, Y. Li et al., "FPCNet: fast pavement crack detection network based on encoder-decoder architecture," 2019, https://arxiv.org/abs/1907.02248.

[18] W. Song, G. Jia, H. Zhu, D. Jia, and L. Gao, "Automated pavement crack damage detection using deep multiscale convolutional features," *Journal of Advanced Transportation*, vol. 2020, Article ID 6412562, 11 pages, 2020.

[19] Z. Fan, C. Li, Y. Chen et al., "Ensemble of deep convolutional neural networks for automatic pavement crack detection and measurement," 2020, https://arxiv.org/abs/2002.03241.

[20] B. Li, K. C. P. Wang, A. Zhang, E. Yang, and G. Wang, "Automatic classification of pavement crack using deep convolutional neural network," *International Journal of Pavement Engineering*, vol. 21, no. 4, pp. 457–463, 2020.

[21] J. Ji, L. Wu, Z. Chen et al., "Automated pixel-level surface crack detection using U-net," in *Proceedings of the International Conference on Multi-Disciplinary Trends in Artificial Intelligence*, Springer, Hanoi, Vietnam, November 2018.

[22] Z. B. Chen, W. T. Luo, and L. Li, "Automatic identification of pavement crack using improved U-net model," *Journal of*

*Data Acquisition and Processing*, vol. 35, no. 2, pp. 260–269, 2020, in Chinese.

[23] J. Cheng, W. Xiong, W. Chen et al., "Pixel-level crack detection using U-net," in *Proceedings of the TENCON 2018-2018 IEEE Region 10 Conference*, IEEE, Jeju, South Korea, October 2018.

[24] L. Jiang, Y. Xie, and T. Ren, "A deep neural networks approach for pixel-level runway pavement crack segmentation using drone-captured images," 2020, https://arxiv.org/abs/2001.03257.

[25] Y. Lecun, Y. Bengio, and G. Hinton, "Deep learning," *Nature*, vol. 521, no. 7553, p. 436, 2015.

[26] K. He, X. Zhang, S. Q. Ren et al., "Deep residual learning for image recognition," in *Proceedings of the IEEE Conference on Computer Vision and Pattern Recognition*, pp. 770–778, Las Vegas, NV, USA, June 2016.

[27] O. Ronneberger, P. Fisher, and T. Brox, "U-Net: convolutional networks for biomedical image segmentation," in *International Conference on Medical Image Computing and Computer-Assisted Intervention*, Springer, Munich, Germany, October 2015.

[28] I. Sergey and S. Christian, "Batch normalization: accelerating deep network training by reducing internal covariate shift," in *Proceedings of the International Conference on International Conference on Machine Learning*, Lille, France, 2015.

[29] L. N. A. Smith, "Disciplined approach to neural network hyper-parameters: part 1-learning rate, batch size, momentum, and weight decay," 2018, https://arxiv.org/abs/1803.09820.

[30] J. Lu, V. Behbood, P. Hao, H. Zuo, S. Xue, and G. Zhang, "Transfer learning using computational intelligence: a survey," *Knowledge-Based Systems*, vol. 80, pp. 14–23, 2015.

[31] J. Howard and S. Ruder, "Universal language model fine-tuning for text classification," 2018, https://arxiv.org/abs/1801.06146.

[32] J. Deng, W. Dong, R. Socher et al., "Imagenet: a large-scale hierarchical image database," in *Proceedings of the IEEE Computer Society Conference on Computer Vision and Pattern Recognition*, Miami, FL, USA, June 2009.

[33] M. Everingham, S. M. A. Eslami, L. Van Gool, C. K. I. Williams, J. Winn, and A. Zisserman, "The pascal visual object classes challenge: a retrospective," *International Journal of Computer Vision*, vol. 111, no. 1, pp. 98–136, 2015.

[34] W. Liu, D. Anguelov, D. Erhan et al., "Single shot multibox detector," in *Proceedings of the European Conference on Computer Vision*, pp. 21–37, Amsterdam, Netherlands, October 2016.

[35] D. R. Li, Z. D. Duan, X. Y. Hu, D. C. Zhang, and Y. Y. Zhang, "Automated classification and detection of multiply pavement distress images based on deep learning," *Journal of Traffic and Transportation Engineering (English Edition)*, 2020.

Hindawi
Advances in Materials Science and Engineering
Volume 2021, Article ID 6637200, 13 pages
https://doi.org/10.1155/2021/6637200

*Research Article*

# Experimental Study on Acoustic Emission and Resistivity Response of Sandstone under Constant Amplitude Cyclic Loading

**Kui Wang**[1], **Xue Li**[2], **Zheng Huang**[1,2] **and Mingjie Zhao**[1]

[1]*Engineering Research Center of Diagnosis Technology of Hydro-Construction, Chongqing Jiaotong University, Chongqing 400074, China*
[2]*Chongqing Surveying and Design Institute of Water Resources, Electric Power and Architecture, Chongqing 400020, China*

Correspondence should be addressed to Kui Wang; anhuiwk@163.com

Received 23 November 2020; Revised 5 February 2021; Accepted 22 February 2021; Published 9 March 2021

Academic Editor: Xiangxiong Kong



A lot of engineering practice shows that, during the construction and operation of rock mass projects, in addition to the static load, the rock is more subjected to cyclic load. Constant amplitude cyclic load is one of the simpler cyclic loading methods. The damage of rocks gradually accumulates under the action of periodic cyclic load, and finally, fatigue damage occurs, which affects the stability of the project. Therefore, it is necessary to study the mechanical properties of the rock under the action of constant amplitude cyclic load. Acoustic emission (AE) parameters and resistivity are both sensitive to the damage process of the rock and can well describe the damage evolution law of the rock. Under the action of constant amplitude cyclic loading, different loading conditions, different state specimens, and so on, factors will make a big difference to the AE signal and resistivity, such as the difference in stress amplitude, loading rate, and saturation. Therefore, in this paper, the typical sandstone in the Chongqing area is taken as the research object, the AE characteristics and resistivity characteristics of sandstone under different test conditions such as different stress amplitude, different loading frequency, and different saturation are tested, and the evolution of AE is found. It also has a three-stage rule: in the initial stage, the deformation is faster and the AE signal is strong; in the constant velocity stage, the deformation develops slowly and the AE signal is also stable; in the acceleration stage, the deformation develops sharply and the AE signal also becomes more intense. With the increase of cyclic loading stress amplitude, or the decrease of cyclic loading frequency, or the decrease of rock sample saturation, the acoustic emission signal generated in each cycle will be stronger. The resistivity as a whole shows a rapid decline in the loading phase and a rapid rebound in the unloading phase. The changes in resistivity at different stress amplitudes show differences in the first few cycles; the overall change trend of resistivity at different frequencies is consistent, but the rate of change increases with decreasing frequency, and the variation trend of resistivity is very different under different saturation.

## 1. Introduction

In practice, rock mass is often subjected to cyclic loading. As one of the relatively simple cyclic loading modes, the damage of rock under cyclic loading gradually accumulates until fatigue failure occurs, which affects the stability of the project. Therefore, it is of great practical value to study the damage law of rock under constant amplitude cyclic load to judge the stability of engineering rock mass.

As early as the 1930s, Obert and Duvall first discovered that there is acoustic emission (AE) activity in the process of rock compression, and then many scholars continue to study the AE characteristics in the process of rock failure [1]. For example, Ganne [2] carried out experimental research on AE characteristics of brittle rock in the process of failure and analyzed the accumulation of AE energy of rock. Shkuratnik et al. [3] studied the memory effect of AE of coal rock under triaxial cyclic loading. Rodríguez and Celestino [4] studied the crack propagation of granite and marble in combination with AE parameters and time-frequency characteristics. Wang et al. [5] made a detailed analysis of the AE characteristics of granite and sandstone during uniaxial compression. Jiang et al. [6] analyzed the AE characteristics of red sandstone during fatigue damage and discussed that the

rationality of damage varies based on axial strain. Wang [7] studied the AE characteristics of conglomerate, sandstone, and mudstone under different stress conditions. Song [8] studied the AE characteristics corresponding to the evolution, stretching, and dislocation of rock deformation process in the deformation localization zone. The results show that the damage and failure process of rock must be accompanied by the generation of AE signal, which can characterize the damage evolution law of rock.

As an important electrical parameter of rock, the resistivity indicates the strength of rock conductivity. In 1942, Archie, an American logging engineer, obtained the relationship between resistivity and porosity of saturated sandstone samples using double logarithmic coordinates, which is the famous Archie formula. Since then, the research on rock resistivity characteristics has gradually developed, and the application of resistivity testing has developed from the interpretation of formation logging data to the study of rock deformation characteristics under loading [9–12]. For example, brace and orange [13] measured the resistivity changes of a variety of rocks under different constant amplitude and fracture water pressures through the bipolar method and studied the correlation between resistivity and deformation of loaded rocks; Chen and Lin [12] studied the electrical effect of rock under load through experiments and put forward the state equation of rock failure law. Kahtaman et al. [14] conducted uniaxial compression tests and tensile tests on igneous rocks and found that both compressive strength and tensile strength are linearly related to resistivity. Ji et al. [15] analyzed resistivity changes during rock deformation and failure based on the test results of resistivity testing under cyclic loading conditions and indirectly linked the resistivity and damage variables through the secant modulus. Song et al. [16] conducted constant amplitude cyclic loading and graded cyclic loading experiments on limestone and found that the change of resistivity can better reflect the development of microcracks in the rock sample under this state. Tu et al. [17] derived the expression of the ratio of the stress to the peak stress of the rock corresponding to the sudden change of the resistivity before the rock rupture under the load based on the evolution law of the resistivity during the deformation and failure of the rock under load. The above studies show that the closure of rock pores and the expansion of microcracks will affect the electrical conductivity of the rock. Therefore, the damage state of the rock can be judged through the change of resistivity, and the mechanical properties of the rock can be inverted.

In summary, AE parameters and resistivity are both sensitive parameters in the process of rock deterioration and damage. At present, although certain studies have been carried out on the AE characteristics and resistivity of rocks, there is still a lack of research on the correlation between rock wave electrical characteristic parameters and stress and the comprehensive use of wave electrical testing techniques to study rock damage evolution. In view of this, this paper has studied the change law of sandstone AE parameters and resistivity under constant amplitude cyclic loading and provides a basic foundation for further analysis of rock damage evolution under cyclic loading through wave-electric combined testing technology.

## 2. Experimental Device Design and Testing

*2.1. Experimental Device Design.* This test mainly studied the AE characteristics and resistivity characteristics of sandstone under constant amplitude cyclic loading. AE test system and resistivity test system were used in conjunction with rock pressure testing machine to carry out AE-resistivity-stress simultaneous test. As shown in Figure 1, the RMT-301 rock mechanics test system was used as the loading system, SAEU2S AE system was used for AE testing, and M300 data acquisition system was used for resistivity testing. By designing a fixing device, the AE probe and electrode sheet were fixed in the experimental device, so as to achieve the purpose of the AE-resistivity-stress synchronous test.

*2.2. Sample Preparation and Screening.* The sandstone specimens this time were taken from the same sandstone rock mass in the Chongqing area. The drilled sandstone specimens were processed into standard cylindrical specimens of $\Phi 50\ \text{mm} \times 100\ \text{mm}$ by the wet processing method. As shown in Figure 2, the two end faces are flat. The degree error is less than 0.02 mm. In order to minimize the discreteness of the test results caused by the individual differences of the specimens, the diameter, height, mass, and wave velocity of the specimens were measured, and the sandstone specimens with the closest parameters such as density, geometric size, and wave velocity were selected for grouping and numbering, as shown in Table 1. The first group of samples (DZ01–DZ 06) was used for static uniaxial compression test, the second group of samples (SX01, SX 01–1, SX 01-2- SX 03, SX 03–1, and SX 03–2) was used for constant amplitude cyclic loading test with different stress amplitude, the third group of samples (PL01, PL01-1, PL01-2-PL03, PL03-1, and PL03-2) was used for constant amplitude cyclic loading test with different frequency, and the fourth group of samples (BH01, BH01-1, BH01-2-BH03, BH03-1, and BH03-2) was used for cyclic loading test of different water saturation states (saturated state, natural state, and drying state).

*2.3. Experimental Process.* First, a uniaxial compression test was performed to obtain the uniaxial compressive strength of the specimen. Since the upper limit and lower limit of the load in the constant amplitude cyclic loading test are determined based on the stress, the axial force is used as the control parameter during the uniaxial compression test, which can maintain the consistency before and after the experiment. The average loading rate is set. It is 0.5 kN/s.

The constant amplitude cyclic loading and unloading test adopted the axial force to control, and the loading was carried out in two stages: the first stage was the linear loading stage, and the axial stress was loaded from zero to the average stress $(\sigma\ \text{MAX} + \sigma\ \text{min})/2$ at the rate of 0.5 kN/s; the second stage was the cyclic loading stage, in which the cyclic load was applied from the average stress until the fatigue

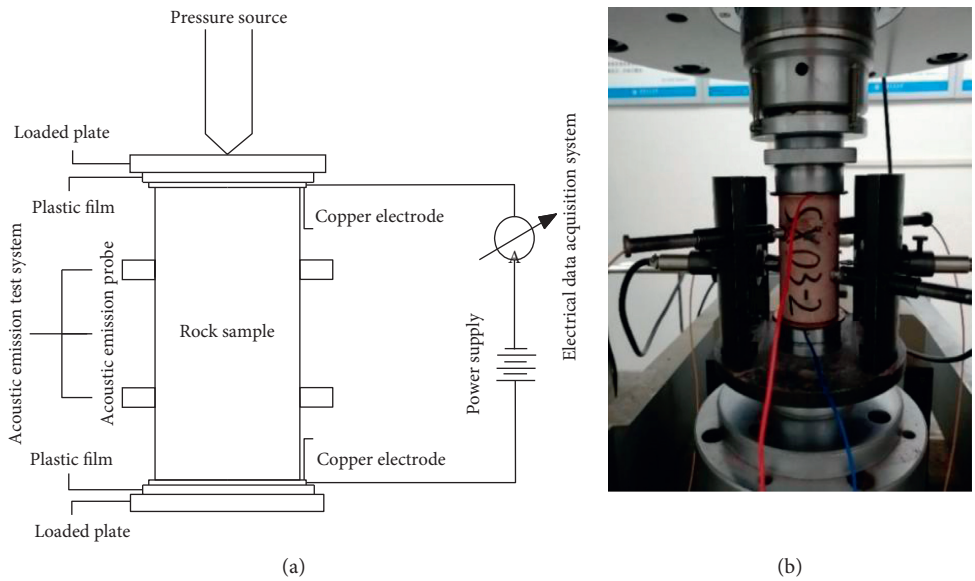


Figure 1: Experimental device. (a) Design of test system. (b) Acoustic emission-resistivity-stress synchronous test.

Figure 2: Sandstone specimen.

failure of the specimen occurs, and the loading waveform was a sine wave, as shown in Figure 3.

In order to reduce the influence caused by the discreteness of the samples, parallel tests of three samples were carried out under each test condition. The specific experimental conditions are as follows:

(1) Study on the influence of stress amplitude: the stress amplitude is changed by using the same lower limit stress ratio (i.e., the ratio of the lower limit stress value $\sigma$_min to the compressive strength value $\sigma$_c) and the different upper limit stress ratio. This experiment uses three different stress amplitude ratios: 20%–80%, 20%–85%, and 20%–90%. Three specimens were used for each group of stress ratio, and the average loading and unloading frequency was set to 0.2 HZ.

(2) Research on the influence of loading frequency: this cyclic loading test used three different frequencies (0.1 Hz, 0.2 HZ, and 0.5 HZ), the upper limit stress ratio was 80%, and the lower limit stress ratio was 20%.

(3) Research on the influence of saturated sandstone: three different saturated sandstone samples (saturated, natural, and dried) were used for the constant amplitude cyclic loading test. The loading frequency is 0.2 HZ. The upper limit stress ratio was 80%. The lower limit stress ratio was 20%. The sample was saturated with water for 24 hours with a vacuum saturated machine to make a saturated test piece, and the sample was placed in an oven at a constant temperature of 105°C for 48 hours to make a dry test piece.

## 3. Analysis of Acoustic Emission Response Characteristics of Sandstone under Constant Amplitude Cyclic Loading

The number of ringing counts generated inside the rock per unit time can reflect the damage state of the internal structure of the rock. The more the counts, the more serious the rock damage, and the opposite, the lighter the rock damage. Therefore, this paper mainly used AE ringing counting to explore the AE characteristics of sandstone.

*3.1. Acoustic Emission Characteristics of Sandstone under Different Stress Amplitudes.* According to the test results, the axial force-time-ringing count relationship curve of typical sandstone samples under different stress amplitude conditions was drawn, as shown in Figure 4. In the initial stage of cyclic loading, the sandstone deformed quickly, the AE activity was strong, and the AE ringing count was large; in the isokinetic development stage, the AE signals of almost the same size were generated in each cycle, but the AE activity weakened and the ringing count reduced, which indicated that the upper limit stress reaches the yield strength of rock, and a small amount of plastic damage was produced in each cycle; during the accelerated failure stage,

Table 1: Grouping of test pieces.

| Grouping | Specimen number | Diameter (mm) | Height (mm) | Duality (g) | Density (g/cm$^3$) | Velocity (km/s) |
|---|---|---|---|---|---|---|
| No. 1 | DZ01 | 49.29 | 100.30 | 451.6 | 2.36 | 2.564 |
| | DZ02 | 49.40 | 100.22 | 455.5 | 2.37 | 2.525 |
| | DZ03 | 49.45 | 100.01 | 454.8 | 2.37 | 2.564 |
| | DZ04 | 49.43 | 99.86 | 456.2 | 2.38 | 2.538 |
| | DZ05 | 49.38 | 100.53 | 456.1 | 2.37 | 2.584 |
| | DZ06 | 49.44 | 99.70 | 449.8 | 2.35 | 2.532 |
| No. 2 | SX01 | 49.38 | 99.18 | 452.1 | 2.38 | 2.571 |
| | SX01-1 | 49.30 | 99.76 | 453.4 | 2.38 | 2.500 |
| | SX01-2 | 50.36 | 100.03 | 468.4 | 2.35 | 2.513 |
| | SX02 | 49.40 | 99.14 | 453.3 | 2.39 | 2.598 |
| | SX02-1 | 49.50 | 99.67 | 451.8 | 2.36 | 2.538 |
| | SX02-2 | 50.21 | 99.96 | 469.8 | 2.37 | 2.525 |
| | SX03 | 49.41 | 99.59 | 454.2 | 2.38 | 2.538 |
| | SX03-1 | 49.26 | 99.94 | 452.5 | 2.38 | 2.506 |
| | SX03-2 | 49.35 | 99.17 | 452.8 | 2.39 | 2.604 |
| No. 3 | PL01 | 49.40 | 100.06 | 451.3 | 2.35 | 2.500 |
| | PL01-1 | 49.50 | 100.16 | 457.7 | 2.38 | 2.525 |
| | PL01-2 | 49.42 | 98.89 | 451.2 | 2.38 | 2.591 |
| | PL02 | 49.38 | 99.18 | 452.1 | 2.38 | 2.571 |
| | PL02-1 | 49.30 | 99.76 | 453.4 | 2.38 | 2.500 |
| | PL02-2 | 50.36 | 100.03 | 468.4 | 2.35 | 2.513 |
| | PL03 | 49.22 | 99.98 | 449.6 | 2.36 | 2.538 |
| | PL03-1 | 49.48 | 100.01 | 456.1 | 2.37 | 2.577 |
| | PL03-2 | 50.34 | 100.13 | 472.6 | 2.37 | 2.525 |
| No. 4 | BH01 | 49.38 | 99.18 | 452.1 | 2.38 | 2.571 |
| | BH01-1 | 49.30 | 99.76 | 453.4 | 2.38 | 2.500 |
| | BH01-2 | 50.36 | 100.03 | 468.4 | 2.35 | 2.513 |
| | BH02 | 49.45 | 99.92 | 456.5 | 2.38 | 2.551 |
| | BH02-1 | 49.43 | 100.23 | 456.2 | 2.37 | 2.625 |
| | BH02-2 | 49.35 | 99.89 | 453.1 | 2.37 | 2.551 |
| | BH03 | 50.34 | 100.19 | 471 | 2.36 | 2.532 |
| | BH03-1 | 50.25 | 99.17 | 461.8 | 2.35 | 2.494 |
| | BH03-2 | 49.51 | 99.78 | 451 | 2.35 | 2.475 |

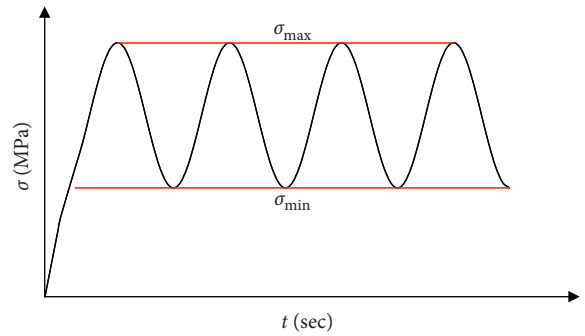


Figure 3: Cyclic loading path.

the rock deformation suddenly increased, the AE activity suddenly increased, and the ringing count increased exponentially until the rock failed.

At the same time, the test results also showed that the activity of AE is related to the stress level. With the increase of stress amplitude, the activity of AE increases, and the ringing count of AE is increased. At the same time, the test results also showed that the activity of AE is related to the stress level. With the increase of stress amplitude, the activity of AE increases, and the ringing count of AE is increased. This is because with the increase of stress amplitude, the deformation of sandstone increases in each cycle, so the strain energy has a positive correlation with the stress amplitude. The generation of AE is actually the process that the accumulated strain energy is released to the outside in the form of a transient elastic wave. If the energy of AE is increased indirectly, the activity of AE is more obvious. In addition, the AE signals almost appear near the upper limit stress, which indicates that the upper limit stress is more sensitive to the generation of AE signals.

*3.2. Acoustic Emission Characteristics of Sandstone under Different Loading Frequencies.* According to the test results, the axial force-time-AE ringing count relationship curve of typical sandstone specimens under different loading frequency conditions was drawn, as shown in Figure 5. Under different loading frequencies, the AE response characteristics of sandstone are basically similar. In the initial cycle stage, the primary cracks and weak structural planes in the specimen produce damage and failure, the deformation of sandstone is large, the plastic damage is large, and the AE ringing count is large; after entering the fatigue stable period, the deformation is small, and the plastic damage produced

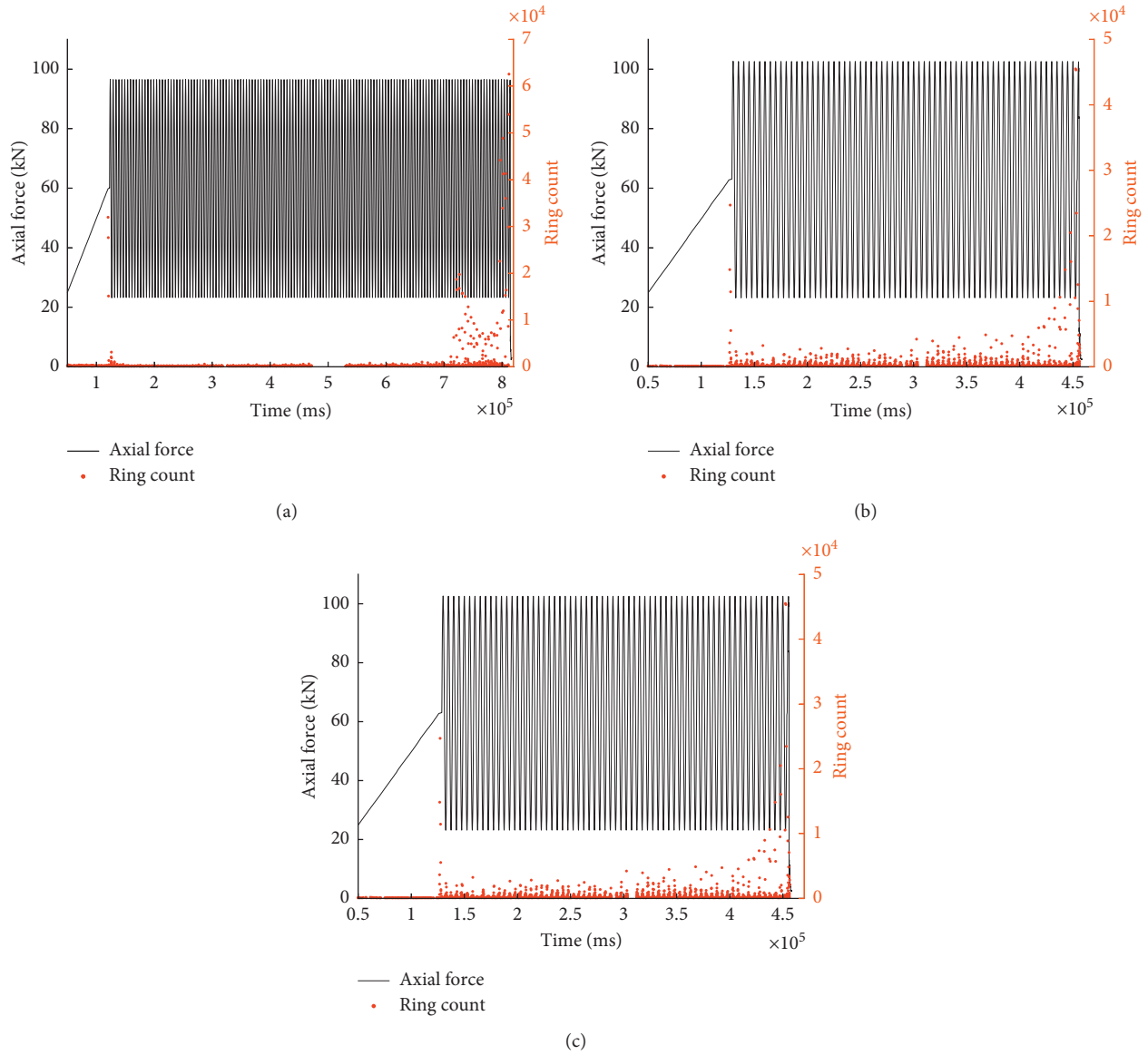


Figure 4: Evolution Law of acoustic emission of sandstone under different stress amplitudes. (a) Acoustic emission law of 20%–80% stress level. (b) Acoustic emission law of 20%–85% stress level. (c) Acoustic emission law of 20%–90% stress level.

by each cycle is small, so the AE ringing count is small, which lasts for a long time. Near the last few cycles of failure, that is, when the damage of rock has accumulated to a certain extent, the deformation of rock develops rapidly. In a few cycles, the strain reaches the limit deformation of rock. The macrocracks are connected and the rock is destroyed. At this stage, the AE activity increases sharply and the ringing count increases suddenly. These well reflect the failure process of the rock cycle.

The test results also showed that the higher the loading frequency, the weaker the AE signal generated in each cycle. This is because as the loading frequency increases, the cycle life of the rock is longer, and the strength of the rock will increase. However, the loading stress value was selected by the same standard, so this indirectly reduced the loading stress, resulting in the fact that the smaller the damage and deformation of the rock during each loading cycle, the longer the cycle period. The strength of the AE signal is directly related to the degree of damage inside the material. The more severe the material damage, the stronger the AE activity, and vice versa. Therefore, as the loading frequency increases, that is, while the cycle life of the rock increases, the AE activity during the cyclic loading process is correspondingly weakened.

*3.3. Acoustic Emission Characteristics of Sandstone under Different Saturations.* According to the test results, the axial force-time-AE ringing count relationship curve of three typical sandstone specimens under different water saturation was drawn, as shown in Figure 6. The AE signals of sandstone under different water saturation conditions are

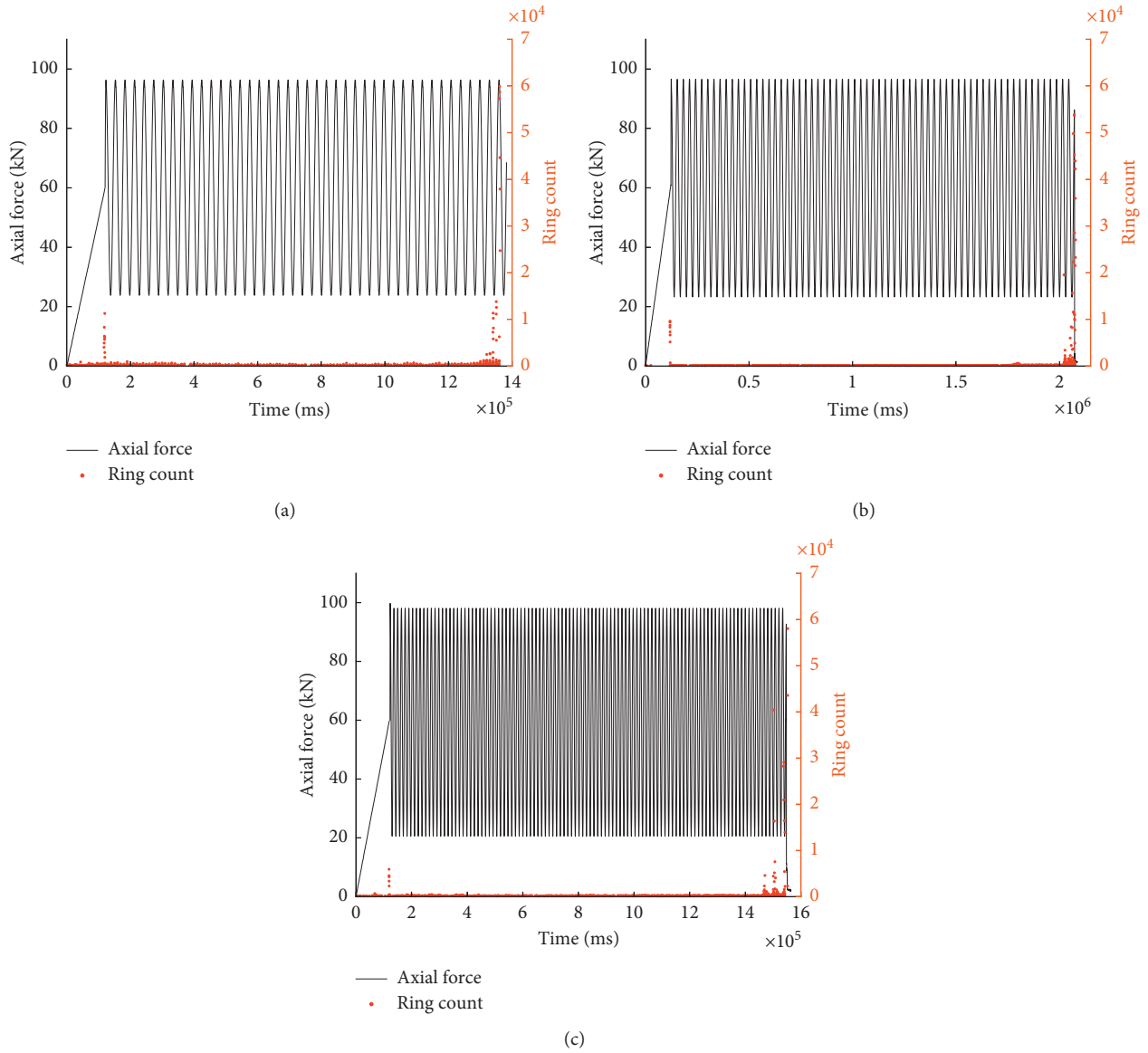


Figure 5: Acoustic emission evolution of sandstone under different loading frequencies. (a) Evolution of acoustic emission at 0.1 Hz frequency. (b) Evolution of acoustic emission at 0.2 Hz frequency. (c) Evolution of acoustic emission at 0.5 Hz frequency.

obviously different. The AE signals of sandstone under water saturation conditions were relatively sparse, which was obviously weaker than those under dry state and natural state. Under natural conditions, the water content of sandstone was relatively low, which was similar to that of sandstone after drying treatment. Therefore, the AE characteristics under natural conditions were basically similar to those under dry conditions. However, it can be seen that the AE activity of sandstone under dry conditions is stronger than that of sandstone under natural conditions. In addition, it can be seen from the sound produced by the failure of sandstone in three different water-saturated states that the dry and natural specimens emit strong noise, while the sound of saturated specimens is relatively weak. These phenomena showed that the water content has a great influence on the activity of AE: high water content reduces the brittleness of the specimen, which weakens the activity of AE; low water content increases the brittleness of the specimen and enhances the activity of AE; that is, water content greatly affects the activity of AE. The reason is that the rock fracture is mainly transgranular fracture and intergranular fracture. The moisture can soften and lubricate the specimen and reduce the connection between the rock-forming grains and the mechanical strength of the grains, so that the energy needed to be injected into the rock during fracture is reduced. The more the water is, the more obvious this phenomenon is, and the AE activity of sandstone is obviously weakened.

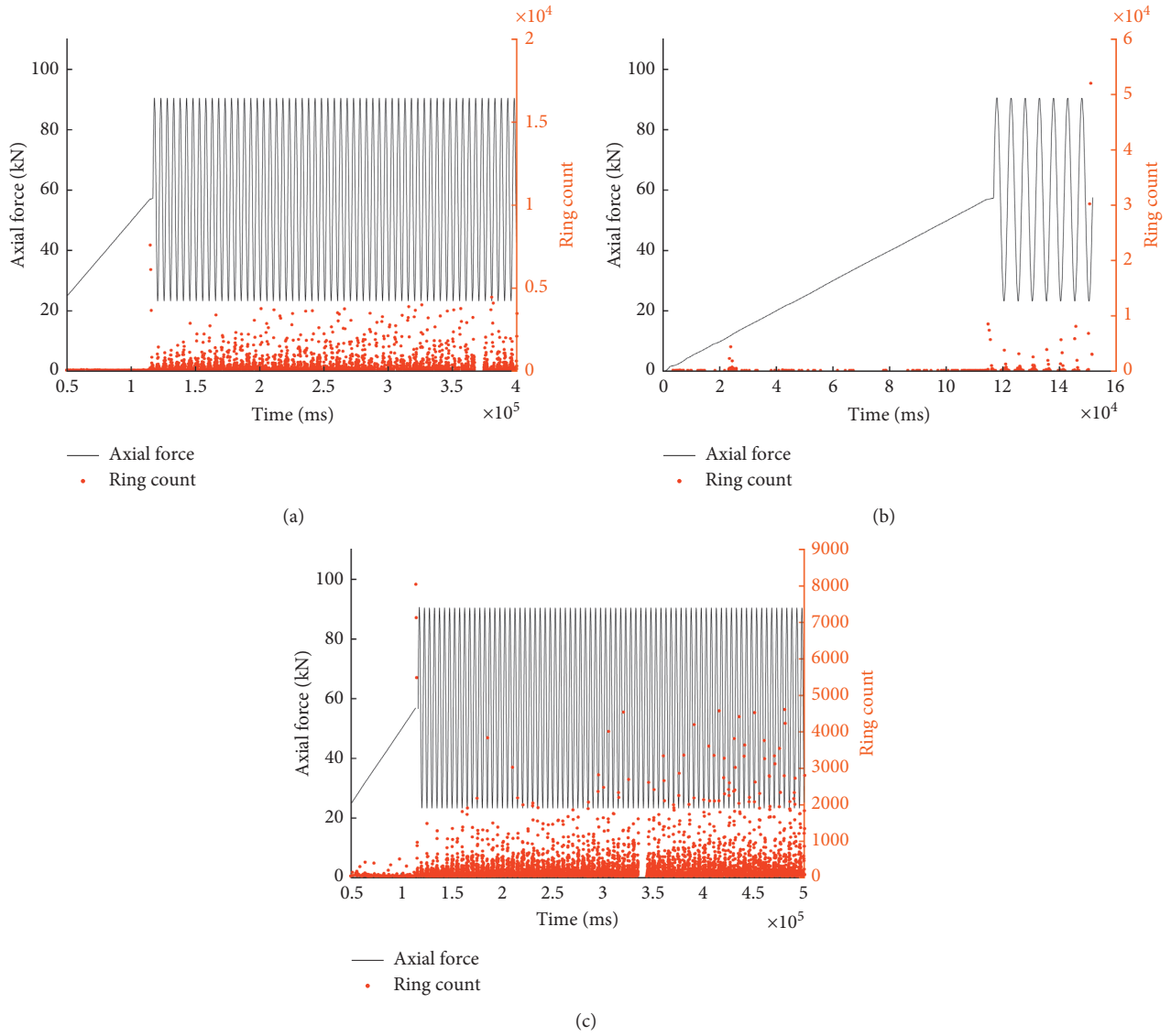


Figure 6: Acoustic emission evolution law of sandstone under different saturation conditions. (a) Evolution of acoustic emission in natural state. (b) Evolution of acoustic emission in saturated state. (c) Evolution of acoustic emission in dry state.

## 4. Analysis of Resistivity Response Characteristics of Sandstone under Constant Amplitude Cyclic Loading

*4.1. Resistivity Characteristics of Sandstone under Different Stress Amplitudes.* According to the test results, the axial force-time-resistivity curve of typical sandstone samples under different stress amplitude conditions is drawn, as shown in Figure 7. Under different stress amplitude loading conditions, the variation law of resistivity of sandstone specimen is basically the same as that of loading way. The specific performance was as follows: in the loading stage, the rock specimen was heterogeneous, and there were many microcracks and pores inside, which made the stress increase, the pores closed quickly, and the resistivity decreased rapidly; in the unloading stage, due to the decrease of stress, the compacted pores and microcracks gradually opened, and the resistivity increased. Generally speaking, the residual plastic deformation of the specimen occurred due to yield after each cycle of loading and unloading. The contact between mineral particles, the contact between skeleton and pore water, and the connectivity of water passage would be better than those of the previous cyclic loading. Therefore, with the development of cyclic loading, the resistivity of rock samples presented a gradual decline trend. But in the last few cycles, the specimen was on the verge of failure, the internal cracks accelerated to expand, the contact between skeleton particles became worse, and the rock resistivity presented a gradual increase process. When the fatigue life of the specimen was reached, the microcracks had penetrated into a large macrocrack, and the electrical resistivity increased suddenly when the specimen was destroyed.

At the same time, the test results also showed that the evolution characteristics of resistivity of different samples

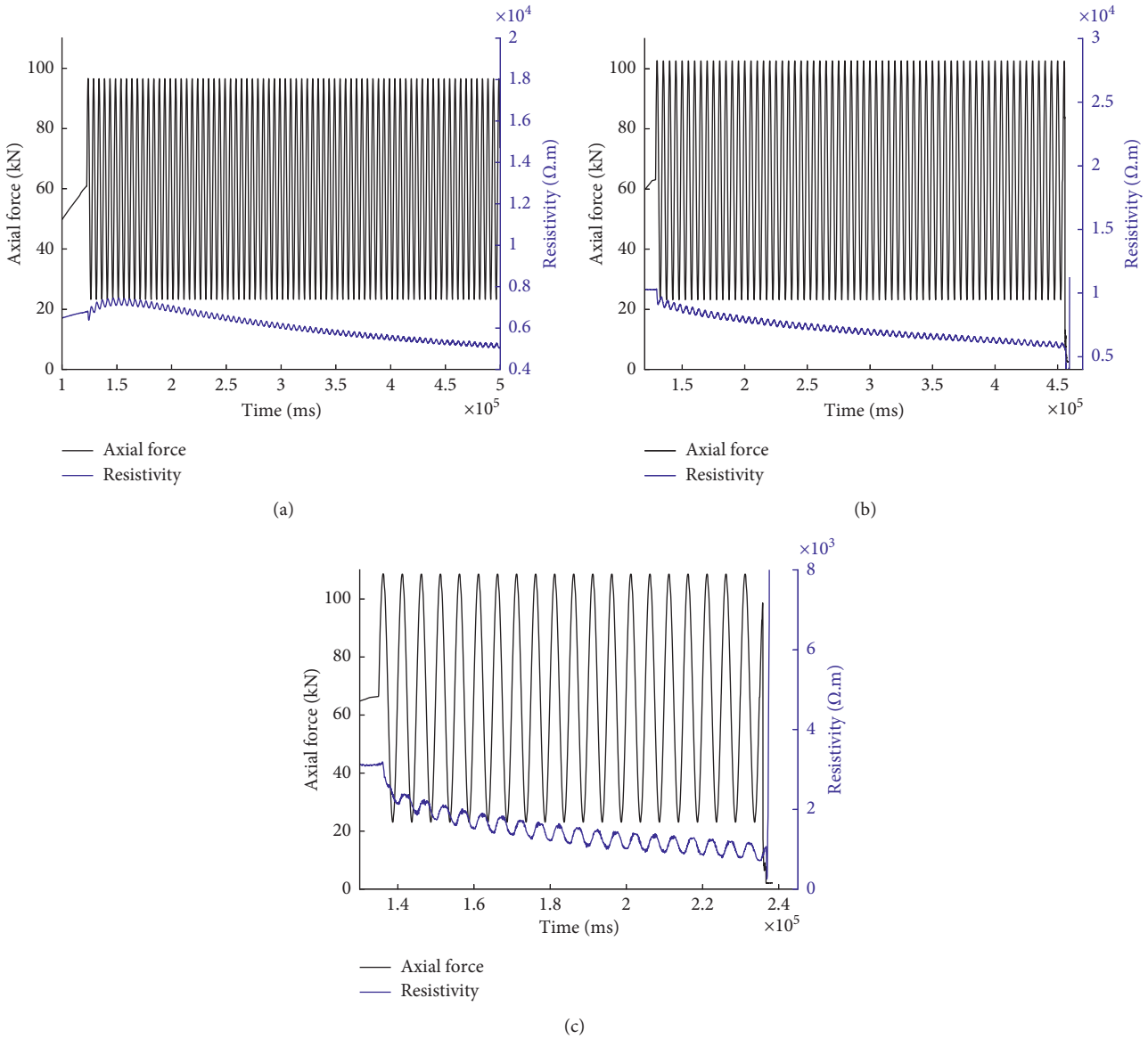


Figure 7: The resistivity evolution law of sandstone under different stress amplitude conditions. (a) Evolution of resistivity at 20%–80% stress level. (b) Evolution of resistivity at 20%–85% stress level. (c) Evolution of resistivity at 20%–90% stress level.

were different under different stress amplitude loading conditions. In the case of high-stress amplitude (when the stress level was 20%–85% and 20%–90%), it can be seen that the resistivity decreased gradually from the beginning to the end of the cycle and then increased suddenly until the failure. However, when the stress level was between 20% and 80%, the change of resistivity was different. The specific performance was as follows: within the initial several cycles, the resistivity increased gradually and then decreased gradually until the end of the cycle. The reason for this phenomenon is that when the stress level is 20%–80%, the stress level is low and the yield strength of rock is not reached. At the initial cycle, the microcracks have begun to expand. During the whole loading and unloading process, the closing effect of microcracks is less than the crack propagation effect. The closing of microcracks leads to the decrease of resistivity, and the propagation of microcracks leads to the increase of resistivity. Therefore, the resistance first increases gradually and then decreases gradually after plastic residual deformation occurs for a certain number of cycles. When the stress amplitude continues to increase, the upper limit stress has exceeded the yield strength of rock, and each cycle will produce a certain amount of plastic residual deformation, which makes the resistivity continue to decrease.

In order to reflect the change rate of resistivity under different stress ratios, the change of resistivity is represented by the ratio $((\rho - \rho_0)/\rho_0)$ of the difference of resistivity $(\rho - \rho_0)$ and initial resistivity $(\rho_0)$, and the resistivity change rate cycle number curve of the specimen was obtained, as shown in Figure 8. It can be seen that the change trend of resistivity analyzed above is well corresponding to this

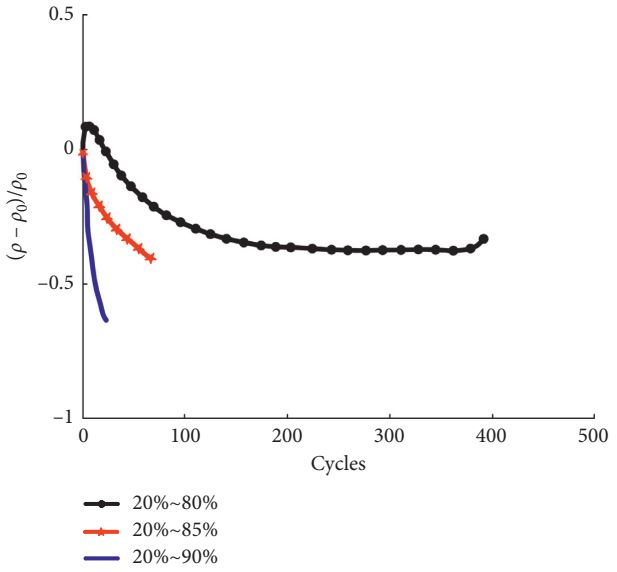


Figure 8: Resistivity evolution law of sandstone under different stress amplitudes.

diagram. If the previous several cycles are ignored, the variation trend of resistivity also conforms to the three-stage variation rule, which can be divided into initial stage, constant velocity stage, and acceleration stage. The resistivity decreases sharply at the beginning, then decreases gently at the constant speed stage, and increases gradually at the final acceleration stage. With the difference of stress amplitude, the proportion of each stage is different, which is consistent with the deformation law of sandstone. It can also be seen that the curve with high loading stress amplitude is always below the curve with low loading stress amplitude, which indicates that the resistivity change rate with high loading stress amplitude is higher than that with low loading stress amplitude in the same cycle times.

*4.2. Resistivity Characteristics of Sandstone under Different Loading Frequencies.* According to the test results, the axial force-time-resistivity curves of typical sandstone samples under different frequency loading conditions were drawn, as shown in Figure 9. The basic change trend of resistivity with stress was not changed under different frequency. In the loading stage, the internal porosity of the specimen decreased and the rock resistivity decreased; in the unloading stage, the internal closed cracks opened and the resistivity increased. However, the cyclic loading of specimens at different frequencies is at the same stress level, and the stress is the same, so the overall change trend of resistivity is different from that under different stress amplitude. Under different frequencies, the variation trend of the resistivity of sandstone specimens is basically the same from the beginning of the cycle to the failure stage. The resistivity gradually rises from the beginning of several cycles and then decreases after a few cycles. Finally, the resistivity suddenly increases when the specimen is damaged. Therefore, the different loading frequency has no effect on the overall change trend of resistivity at the same stress level.

The change of resistivity is still represented by the ratio $(((\rho-\rho\_0)/\rho\_0)$ of the difference of resistivity $(\rho-\rho\_0)$ and initial resistivity $(\rho\_0)$. The resistivity change rate cycle number curve was obtained, as shown in Figure 10. It can be seen that the curve with low frequency is always under the curve with high frequency. In the same cycle times, the resistivity with low frequency changes greatly, which indicates that the damage caused by the low loading frequency of each cycle is larger than that of the high loading frequency. This also explains why the lower the loading frequency is, the longer the cycle of the sample is.

*4.3. Resistivity Characteristics of Sandstone under Different Saturations.* According to the test results, the axial force-time-resistivity relationship curves of typical sandstone samples under different saturation conditions were drawn, as shown in Figure 11. The water content had a great influence on the resistivity of sandstone specimens. It can be seen that the resistivity of sandstone in saturated state was only a few hundred Ω·m, but the resistivity of natural state specimen was relatively high due to its small water content, which could reach several thousand Ω·m. After drying, the resistivity of the dry specimen had reached tens of thousands Ω·m, which was mainly because the dry specimen has almost no moisture, and the current could only be conducted through the rock skeleton particles with weak conductivity, so that the resistivity of the dry specimen was relatively high. With the increase of saturation, the water content of the specimen was also increasing. Water is very easy to conduct electricity, which greatly improves the conductivity of the whole specimen, so the resistivity of the specimen decreases rapidly with the increase of saturation. Therefore, the moisture content is a very important factor affecting the resistivity of the specimen.

It can be seen that the evolution trend of resistivity of saturated samples under load is as follows: in the initial linear loading stage, the resistivity gradually decreases, which may be because the saturated samples are not really saturated but still have certain voids. With the increase of loading stress, the pores are closed, so the resistivity tends to decrease. Then the resistivity increases gradually, which may be due to the gradual seepage of mineralized water in the pores after the pores are compacted. When the stress reaches a certain value, microcracks and fracture surfaces are produced in different degrees, and air entry leads to an increase in resistivity. After entering the cyclic loading process, due to the sharp increase of stress, the initial cyclic loading resistivity changes greatly, and then the resistivity presents an increasing process with the increase of the number of cycles. This is because the strength of the rock will decrease sharply after the specimen is saturated with water, and the upper limit stress ratio of 75% is determined by the compressive strength of the rock under natural state. For water-saturated specimens, the upper limit stress ratio has exceeded the yield strength or even close to the peak strength, which makes more fractures and fracture surfaces appear in each cycle, so the resistivity of sandstone shows a trend of gradual increase. However, the specimen in the natural state will produce a certain plastic residual deformation after each cycle. The contact

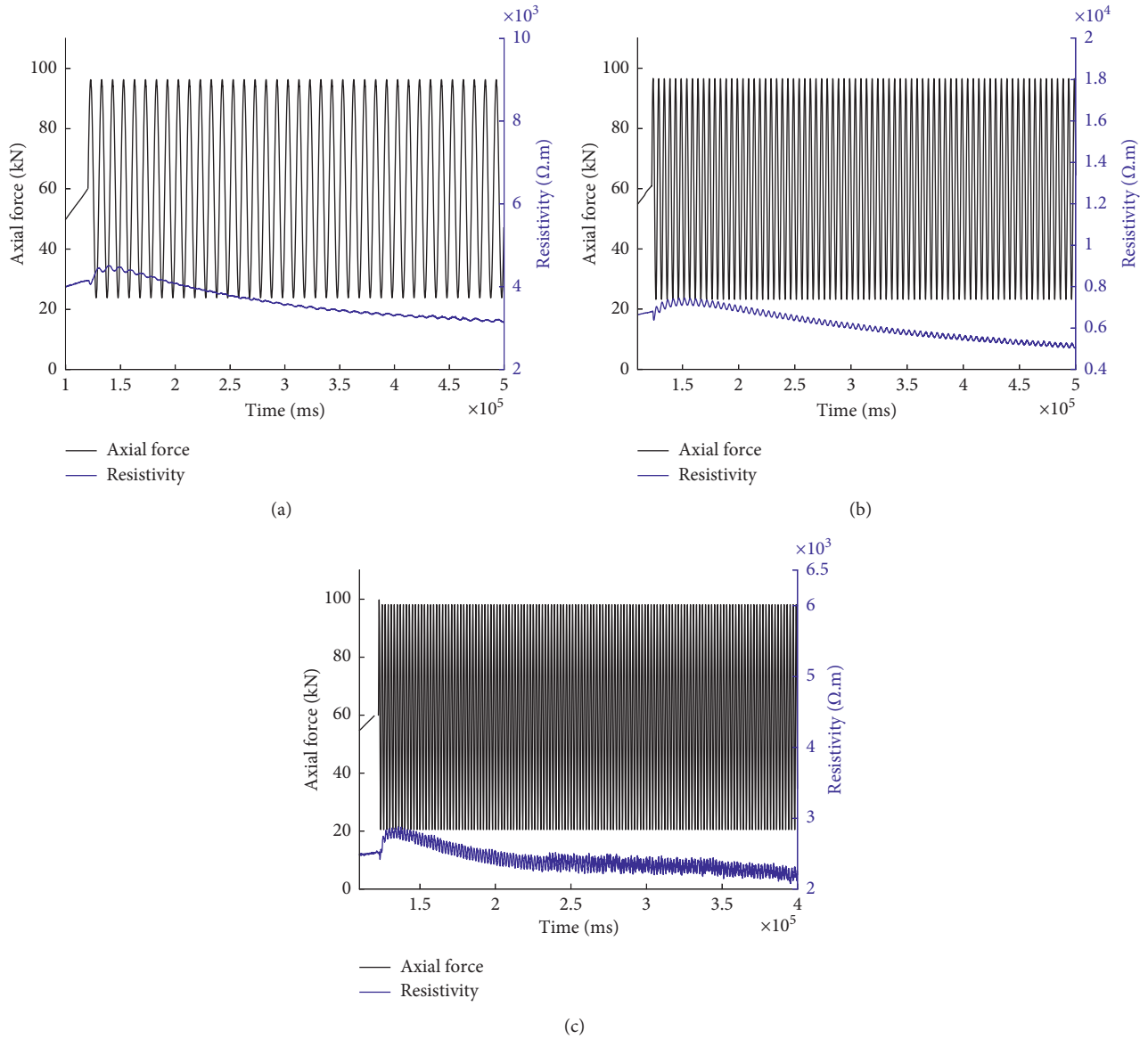


Figure 9: Resistivity evolution of sandstone under different loading frequencies. (a) Resistivity evolution law of frequency at 0.1 Hz. (b) Resistivity evolution law of frequency at 0.2 Hz. (c) Resistivity evolution law of frequency at 0.5 Hz.

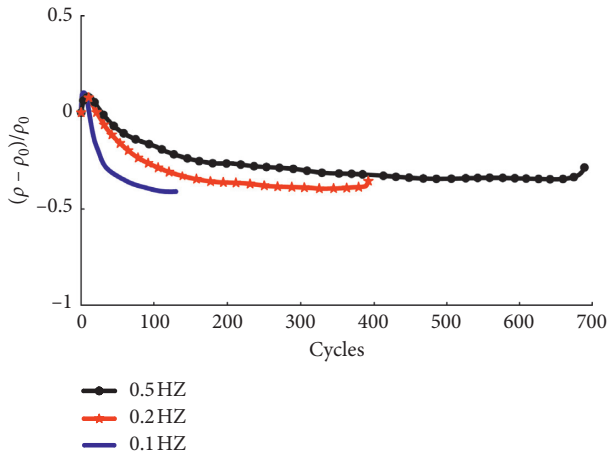


Figure 10: Variation of resistivity at different frequencies.

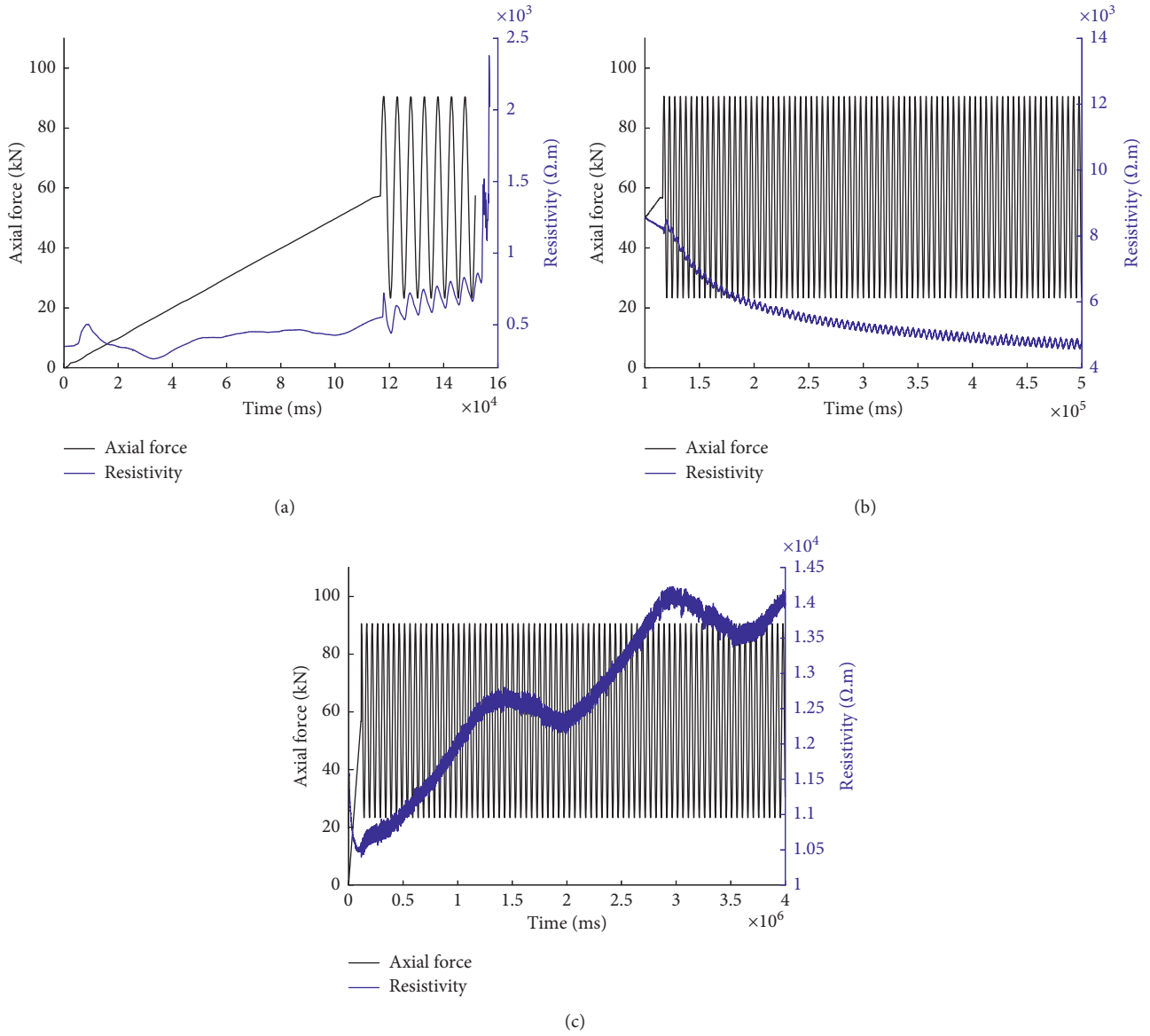


Figure 11: Resistivity evolution of sandstone under different saturation conditions. (a) In saturated state. (b) In natural state. (c) In dry condition.

between the mineral particles and the contact between the skeleton and the pore water will be better than the previous cycle loading. As the loading progresses, the resistivity of the rock specimen shows a gradual decline in evolution trend. In the dry state, the water content of the specimen is almost zero, and the strength is greatly increased, so it has not been damaged even after 2,000 cycles. At the same time, the changing law of resistivity is also quite different. After the initial decline in resistivity, it shows periodic changes (rising-falling-rising-falling) as the number of cycles increases. This may be due to the periodic expansion and closure of microcracks. Due to the time, this test failed to compress the dry specimen to failure. The change trend of the resistivity later is unknown. It is inconvenient to analyze the specific reason. It is hoped that the follow-up researchers can press it to destruction and then analyze the specific reasons in detail through the change trend of resistivity in the whole destruction process.

## 5. Conclusion

In this paper, the AE-resistivity-stress synchronous test experiment of sandstone is carried out to analyze the evolution of AE and resistivity of sandstone under constant amplitude cyclic loading. The main conclusions are as follows:

(1) Under the condition of constant amplitude cyclic loading, the evolution law of AE of sandstone corresponds to the three stages of rock fatigue deformation, and the change law of resistivity is basically the same as the way of loading. The magnitude of the stress

amplitude has a significant impact on the AE and resistivity evolution law of sandstone. Specifically, as the stress amplitude increases, the AE activity increases, and the AE ringing count generated increases. When the stress amplitude is relatively high, the resistivity will gradually decrease from the beginning of the cycle to the end of the cycle, until the resistivity suddenly increases when the stress is broken, and when the stress amplitude is relatively low, the resistivity first gradually increases, and then the resistivity gradually decreases as a whole. Generally, the resistivity evolution rate of the specimen with high loading stress amplitude is higher than that of the specimen with low loading stress amplitude.

(2) The loading frequency has a greater impact on the AE activity of sandstone. The higher the loading frequency, the smaller the rock damage caused by each cycle, the weaker the AE signal produced, and the less the ringing count per unit time. However, the different loading frequency has no effect on the overall variation trend of resistivity under the same stress level. The resistivity increases gradually from the beginning of several cycles, then decreases gradually after a few cycles, and finally increases suddenly when the failure occurs. And the lower the loading frequency, the faster the resistivity change rate.

(3) Saturation has a significant influence on AE activity and electrical resistivity of rocks. Saturation represents the level of water content. The higher the water content, the weaker the AE activity; otherwise, the stronger the AE activity. After entering the cyclic loading process, the resistivity of water-saturated specimens changes greatly in the initial stage, and the resistivity increases with the increase of the number of cycles. However, the resistivity of the specimens in natural state decreases gradually. In the dry state, after the initial decline in resistivity, the later period showed a periodic change (up-down-up-down) as the number of cycles increased.

## Data Availability

The data used to support the findings of this study are available from the corresponding author upon request.

## Conflicts of Interest

The authors declare that they have no conflicts of interest.

## Acknowledgments

The authors gratefully acknowledge the financial supports from the Natural Science Foundation Project of China (Grant no. 51609027), and Innovative Research Program of Chongqing Jiaotong University (Grant no. 2020S0024), and Science and Technology Projects of Department of Transportation of Jiangxi Province (Grant no. 2019Q0027).

## References

[1] L. Obert and W. I. Duvall, *Micro-seismic Method of Determining the Stability of Underground openings[R]*, United States Department of the Interior, Washington, DC, USA, 1957.

[2] P. Ganne, A. Vervoort, and M. Wevers, "Quantification of pre-peak brittle damage: correlation between acoustic emission and observed micro-fracturing," *International Journal of Rock Mechanics and Mining Sciences*, vol. 44, no. 5, pp. 720–729, 2007.

[3] V. L. Shkuratnik, Y. L. Filimonov, and S. V. Kuchurin, "Regularities of acoustic emission in coal samples under triaxial compression," *Journal of Mining Science*, vol. 41, no. 1, pp. 44–52, 2005.

[4] P. Rodríguez and T. B. Celestino, "Application of acoustic emission monitoring and signal analysis to the qualitative and quantitative characterization of the fracturing process in rocks," *Engineering Fracture Mechanics*, vol. 210, pp. 54–69, 2019.

[5] L. J. Wang, B. Zhang, Z. K. Qian et al., "Experimental investigation of the acoustics emission Characteristics of two types of brittle rocks under uniaxial compression," *Journal of Engineering Geology*, vol. 27, no. 4, pp. 699–705, 2019.

[6] Y. Jiang, X. Ge, and J. Ren, "Deformation law and acoustic emission characteristics of rock during fatigue failure," *Journal of Rock Mechanics and Engineering*, vol. 23, no. 11, pp. 1810–1814, 2004.

[7] X. Wang, H. Ge, L. song, hetaiming, and X. Wei, "Experimental study on two types of rock acoustic emission events and Kaiser effect point identification method," *Chinese Journal of Rock Mechanics and Engineering*, vol. 30, no. 3, pp. 580–588, 2011.

[8] Y. Song, T. Xing, T. Zhao, Z. Zhao, and P. Gao, "Study on acoustic emission characteristics of rock uniaxial compression deformation field evolution," *Journal of Rock Mechanics and Engineering*, vol. 36, no. 03, pp. 534–542, 2017.

[9] G. E. Archie, "The electrical resistivity log as an aid in determining some reservoir characteristics," *Transactions of the AIME*, vol. 146, no. 1, pp. 54–62, 1942.

[10] O. A. L. Lima, B. C. Michael, G. N. Geraldo et al., "A volumetric approach for the resistivity response of freshwater shaly sandstones," *Geophysics*, vol. 70, no. 1, pp. F1–F10, 2005.

[11] T. Masao, Y. Isao, and F. Yoshio, "Anomalous electrical resistivity of almost dry marble and granite under axial compression," *Journal of Physics of the Earth*, vol. 41, no. 6, pp. 337–346, 1993.

[12] G. Chen and Y. Lin, "Stress-strain-electrical resistance effects and associated state equations for uniaxial rock compression," *International Journal of Rock Mechanics and Mining Sciences*, vol. 41, no. 2, pp. 223–236, 2004.

[13] W. F. Brace and A. S. Orange, "Electrical resistivity changes in saturated rock under stress," *Science*, vol. 153, no. 3743, pp. 1525-1526, 1966.

[14] S. Kahraman and T. Yeken, "Electrical resistivity measurement to predict uniaxial compressive and tensile strength of

igneous rocks," *Bulletin of Materials Science*, vol. 33, no. 6, pp. 731–735, 2010.

[15] H. Ji, P. Xiang, L. Zhang et al., "Experimental study and detection analysis of mechanical property variation of mining disturbed rock mass," *Journal of Rock Mechanics and Engineering*, vol. 30, no. 11, pp. 2 352–2 359, 2011.

[16] J. Song, Z. Li, B. Liu et al., "Study on resistivity response law of limestone samples during constant amplitude and graded cyclic loading and unloading," *Journal of Rock Mechanics and Engineering*, vol. 34, no. S2, pp. 3880–3887, 2015.

[17] J. Tu, Q. sun, Z. Jiang et al., "Apparent resistivity change and stress ratio of brittle critical failure of rock," *Acta Sinica Sinica*, vol. 38, no. 2, pp. 221–225, 2013.

Hindawi
Advances in Materials Science and Engineering
Volume 2021, Article ID 5574013, 13 pages
https://doi.org/10.1155/2021/5574013

*Research Article*

# Laboratory Study on Performance Evaluation and Automobile Exhaust Degradation of Nano-$TiO_2$ Particles-Modified Asphalt Materials

**Yaozong Ma**,[1,2] **Lilin Li**,[3] **Hua Wang**,[3,4] **Wensheng Wang**,[1] **and Kunkun Zheng**[5]

[1]*College of Transportation, Jilin University, Changchun 130025, China*
[2]*Guangxi Liyu Expressway Co. Ltd., Nanning 530005, China*
[3]*Guangxi Transportation Science and Technology Group Co. Ltd., Nanning 530007, China*
[4]*Guangxi Beibu Gulf Investment Group Co. Ltd., Nanning 530029, China*
[5]*Guangdong Aohong Technology Co. Ltd., Zhongshan 528437, China*

Correspondence should be addressed to Hua Wang; wanghua15@mails.jlu.edu.cn and Wensheng Wang; wangws@jlu.edu.cn

Received 9 January 2021; Revised 5 February 2021; Accepted 9 February 2021; Published 23 February 2021

Academic Editor: Qinglin Guo



Automobile exhaust pollution is a serious problem that restricts urban development, and it poses a serious threat to people's lives and health and even the climate. At present, the treatment of automobile exhaust has attracted people's attention, and numerous works have been focused on it thereafter. The purpose of the present study is to drive $TiO_2$ nanoparticles application into pavement, and the study present an experimental investigation of performances and automobile exhaust purification of asphalt and its mixture modified by nano-$TiO_2$. In this work, a series of rheometer properties and pavement performances were studied, including penetration, softening point, ductility, DSR and BBR for asphalt binder, conventional pavement performances, and creep test for asphalt mixture. Moreover, the photocatalytic degradation test of automobile exhaust was conducted to assess degradation of $TiO_2$ nanoparticles in the asphalt mixture on automobile exhaust. Results indicate that the $TiO_2$ nanoparticle was beneficial to increase the viscosity and reduce the temperature sensitivity, which would enhance its high-temperature stabilization capability of asphalt. Meanwhile, nano-$TiO_2$ can significantly enhance the rheometer properties of asphalt and its capacity of high-temperature antirutting, and its low-temperature performance could also comply with the specification. Besides, the incorporation of nano-$TiO_2$ in mixtures could effectively enhance the antirutting and anticracking as well as water stabilization. Moreover, the nano-$TiO_2$-modified asphalt mixture possesses a positive impact on photocatalytic degradation of CH and $NO_x$, which could provide a reference for the treatment of automobile exhaust. The photocatalytic degradation effect of asphalt mixtures modified by nano-$TiO_2$ on $NO_x$ is significantly better than that of CH.

## 1. Introduction

With the global civilization process and the construction level development of road engineering, the functional requirements of roads are increasing, and the requirements for road service functions, green construction, and safety protection are more urgent [1–9]. With the rapid development of nanotechnology, more and more researchers are getting committed to introducing nanomaterials into the road pavement [10–12]. Nanomaterials refer to materials in the range of 1~100 nanometers in at least one dimension. It is worth noting that nanomaterials usually have the advantages of significant temperature susceptibility, better extendability, and larger specific surface area (SSA). Besides, the physical, chemical, and other properties of nanomaterials have great differences with the original raw materials [13]. Therefore, on the above basis, researchers introduced nanomaterials into road and construction fields.

Nowadays, the asphalt pavement has become the largest pavement type in China's high-level pavements [14–22]. However, it is worth noting that there are yet many problems in the field of flexible pavement that need to be solved

urgently. The resulting damage will reduce the service performance of the asphalt flexible pavement, such as rutting, cracks, and other damage phenomena [15, 23–25]. A lot of related research work has been done, including modifying asphalt materials [26–28] and optimizing the asphalt flexible pavement structure [29]. Jahromi et al. employed two kinds of nanoclay to improve the performances of asphalt materials. According to X-ray diffraction along with DSR, nanoclay-modified asphalt increased stiffness and decreased the phase angle [30]. Abdelrahman et al. assessed the physical performances of asphalt through adding the modified nanoclay using dynamic mechanical analysis and showed that the incorporation of modified nanoclay materials into asphalt materials enhanced their physical properties. Also, they investigated the modification mechanism of nanoclay, which was considered to be the interactivity of the modified nanosilox tetrahedron in asphalt using the FTIR test [31]. You et al. used nanoclay to modify asphalt and compared two kinds of nanoclay. The results indicated that nanoclay could effectively boost the comprehensive performances of asphalt materials. Furthermore, the blending procedure was considered as the key to achieving a well-distributed nanoclay-modified asphalt [32]. Khattak et al. employed different dosages of carbon nanofibers to modify three types of asphalt cements based on two asphalt mixing procedures, i.e., dry and wet procedures. Due to the larger SSA, better interface combination effect, as well as higher modulus values of carbon nanofiber, the test results showed that carbon nanofiber-modified asphalt exhibited good viscoelastic response and fatigue performances [33].

On the contrary, the world has witnessed a rapid development of social urbanization, which has also resulted in increasing energy consumption and car ownership, bringing about many environmental problems [34, 35]. Among them, atmospheric pollution and the decline of air quality have a huge negative effect on people's health and the ecology of the Earth, such as smoggy weather and respiratory diseases [36, 37]. Currently, catalytic materials are widely used for automobile exhaust gas cleaning, which are mostly semiconductor materials and have their own catalytic function [38]. Semiconductor catalytic materials (such as $Fe_2O_3$, ZnO, $TiO_2$, and CdS) can be used to a greater extent to generate free electrons and holes from visible solar light sources, of which $TiO_2$ is the most widely used catalytic material, with good stability, catalytic properties, and low prices [39–41]. Chen et al. utilized nano-$TiO_2$ to modify asphalt through permeability technology and evaluated the penetration effect using the scanning electron microscope. Because of the large surface area and advanced oxidation technology of nano-$TiO_2$, nano-$TiO_2$-modified asphalt produced good performances of asphalt and also had a good environment purification function [42]. Hashimoto et al. applied $TiO_2$ to a highway to achieve photocatalytic vehicle exhaust [43]. Loftness et al. studied the effect of photocatalytic automobile exhaust by applying $TiO_2$ as a coating to the test road [44]. Jin et al. prepared composite nanomaterials by adding anatase-type nano-$TiO_2$ to montmorillonite, which significantly reduced the agglomeration problem of $TiO_2$ and studied the road performance and photocatalytic degradation of automobile exhaust when containing the composite nanomaterial [45]. Qian et al. tested aging for SBS asphalt containing nano-$TiO_2$. In addition, a photocatalytic reaction system was developed to study the photocatalytic degradation analysis of nano-$TiO_2$ on $NO_x$ [46].

Through the abovementioned literature analysis, it can be found that nanomaterials have been widely utilized in pavement engineering. But the research of nano-$TiO_2$ in flexible roads is yet not systematic, and its application still needs to be improved. Therefore, this research designs for nano-$TiO_2$ nanoparticles applied in asphalt road. The impacts of nano-$TiO_2$ are evaluated mainly based on several indexes of conventional tests, and its rheological properties are evaluated through DSR and BBR. In addition, the influences of nano-$TiO_2$ on asphalt road and creep characteristics of mixtures were also studied. Finally, the automobile exhaust purification is performed by simulating the actual environment to assess the degradation of nano-$TiO_2$ in the asphalt mixture on automobile exhaust.

## 2. Materials and Methods

### 2.1. Materials and Samples

#### 2.1.1. Materials

*(1) Asphalt*. AH-90 was used, obtained from Panjin Petroleum Asphalt Co., Ltd. Table 1 presents the main technical indicators.

*(2) Nano-$TiO_2$*. The nanomaterial used in this paper is titanium dioxide, anatase crystal structure with the formula of $TiO_2$. Its detailed technical characteristics are presented in Table 2.

*(3) Coarse and Fine Aggregates and Mineral Powder*. In this paper, stones are acquired from the local area, and the powder in the asphalt mixture is the limestone powder from Antu, Jilin Province. Referring to the requirements of JTG F40-2004, Tables 3–5 show the main technical properties of aggregates and limestone powder.

*2.1.2. Sample Preparation Procedure.* According to previous studies, it has been noted that the reasonable dosage of nano-$TiO_2$ is 5% in weight of asphalt [47]. During the preparatory stage of nano-$TiO_2$-modified asphalt, original asphalt materials were preheated to 160°C, and next, they were blended with weighted nano-$TiO_2$ by manually stirring for 5~8 min. The corresponding temperature increased to 170°C in a short time. Finally, apply the high-speed shearing at 6000 r/min and 170°C for $(40 \pm 5)$ min. When used, heat the asphalt sample again to 170°C, control the shearing speed at 450~600 r/min, and stir continuously for about 20 min.

As for the preparation of the AC mixture, CAVF is selected to design asphalt mixture gradation including base asphalt and nano-$TiO_2$-modified asphalt, as shown in Figure 1 [48]. Following the JTG E20-2011 specification, the optimum asphalt-aggregate ratios of the base original asphalt mixture as well as the nano-$TiO_2$-modified asphalt mixture were obtained by the Marshall design method. Marshall stability, flow, air voids, etc.,

Table 1: Technical indicators of AH-90.

| Technical indicators | Tested |
|---|---|
| Penetration | 88.9 |
| Ductility | >100 |
| Softening point | 43.2 |
| Density | 1.017 |
| Dynamic viscosity | 0.295 |
| *RTFOT* | |
| Weight loss | −0.191 |
| Residual penetration ratio | 84.9 |

Table 2: Technical indicators of nano-$TiO_2$.

| Technical indicators | | Values |
|---|---|---|
| Appearance | — | White powder |
| Structure | — | Anatase |
| Diameter | nm | 25 |
| Density | $g/cm^3$ | 3.8 |
| Specific surface area | $m^2/g$ | 60 |
| Purity | % | 99.5 |

Table 3: Technical indicators of coarse aggregate in this paper.

| Technical indicators | | Units | Values |
|---|---|---|---|
| Los Angeles abrasion value | | % | 16.9 |
| Crushing value | | % | 13.3 |
| Apparent specific gravity | 13.2 mm | — | 2.827 |
| | 9.5 mm | | 2.802 |
| | 4.75 mm | | 2.845 |
| Water absorption | 13.2 mm | % | 0.64 |
| | 9.5 mm | | 0.37 |
| | 4.75 mm | | 0.89 |
| Flat and elongated particle content | | % | 8.7 |

Table 4: Technical properties of fine aggregate in this paper.

| Technical properties | Units | Values |
|---|---|---|
| Apparent specific gravity | — | 2.762 |
| Sand equivalent | % | 76 |

Table 5: Technical properties of the mineral powder in this paper.

| Technical properties | | Units | Values |
|---|---|---|---|
| Apparent density | | $kg/m^3$ | $2.746 \times 10^{-3}$ |
| Hydrophilic coefficient | | — | 0.88 |
| Water content | | % | 0.88 |
| Plastic index | | % | 2 |
| Granular composition | <0.6 mm | % | 100 |
| | <0.15 mm | | 98.5 |
| | <0.075 mm | | 78.6 |

have been comprehensively considered [29, 49]. The detailed preparation procedure of nano-$TiO_2$-modified asphalt and mixture is shown in Figure 2.

### 2.2. Laboratory Experiments

#### 2.2.1. Conventional Tests and Rheometer Tests of Asphalt

*(1) Conventional Tests.* The penetration test has been performed to analyze consistency of asphalt, which is carried out at 25°C following JTG E20-2011 T 0604. The softening point (SP) test is adopted for asphalt materials, which is determined by a ring and ball apparatus following the JTG E20-2011 T 0606 (ASTM D36) specification. The ductility property of asphalt materials is measured by the ductility test following the JTG E20-2011 T 0605 specification. The asphalt samples with standard size are stretched until broken. Then, the ductility value is defined as the stretched distance at breaking.

*(2) Dynamic Shear Rheometer Test.* DSR developed by SHRP has been employed for dynamic characteristics and evaluating the viscoelastic behavior of asphalt materials [50–52]. Compared to static experiments (penetration and softening point), the DSR test has more intuitive and real advantages to assess the properties of asphalt materials. According to the ASTM D7175 (AASHTO T31509) specification, the rheological parameters of asphalt materials are determined. By using two parallel plates at this temperature, the DSR test is carried out under temperature and frequency sweep modes, respectively.

In the DSR test, the dynamic viscoelastic characteristics of asphalt can be divided into two parts. $G^*$ is generally calculated by applying dynamic shear stress ($\tau_{max}$) to the asphalt sample and the corresponding measured shear strain ($\gamma_{max}$), defined in equation (1). The characteristics ($\delta$) reflect the ratio of viscoelasticity in asphalt. When at higher temperature or lower frequency loading, asphalt is more prone to the viscous flow, so the phase angle is larger. While, at lower temperature or higher frequency loading, asphalt exhibits more elastic properties, and the phase angle is smaller.

$$G^* = \frac{\tau_{max}}{\gamma_{max}}. \quad (1)$$

*(3) Beam Bending Rheometer Test.* BBR was used to measure hardness of the asphalt beam with a dimension of $6.25 \times 12.5 \times 127$ mm under creep loading based on the theory of engineering beam [51]. In the BBR test, according to the ASTM D6648 specification, the small asphalt binder beam is prepared and kept in the bath. Then, the asphalt binder beam is tested at −18°C. A load of 100 g is imposed to the asphalt beam, and the corresponding deformations are obtained. Therefore, two parameters can be obtained from the deflection curves versus time, i.e., $S(t)$ and $m$ value. Their equations are expressed as follows:

$$S(t) = \frac{Pl^3}{4bh^3 u(t)}, \quad (2)$$

$$\log S(t) = A + B\lg t + C(\lg t)^2, \quad (3)$$

$$m(t) = |B + 2C\lg t|, \quad (4)$$

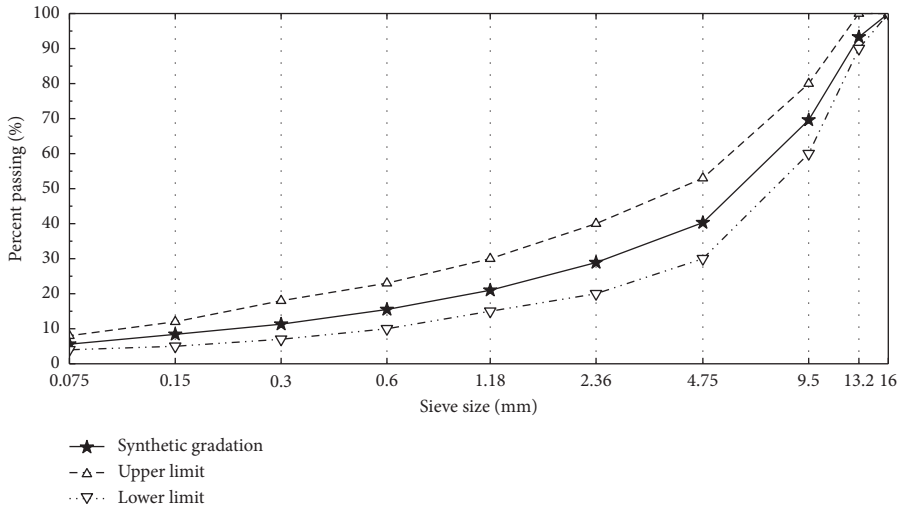


Figure 1: Asphalt mixture gradation curve in this paper.

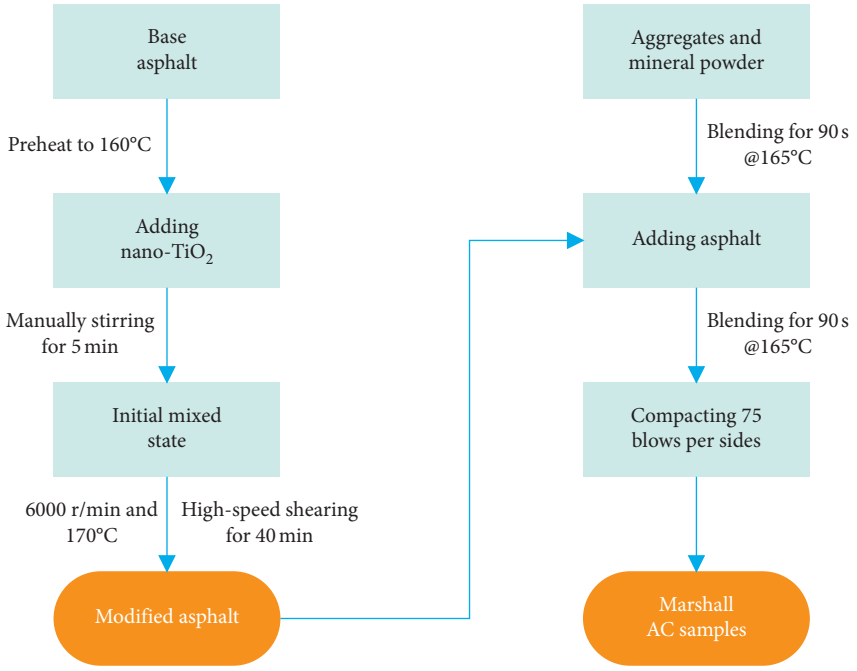


Figure 2: Sample preparation steps.

in which $P$ represents an imposed force, $l$, $b$, and $h$ are the beam dimensions, and $A$, $B$, and $C$ are empirically determined constants.

*2.2.2. Pavement Performances and Viscoelastic Properties Tests of the Asphalt Mixture*

*(1) Pavement Performance Tests.* This paper investigated and assessed the pavement performances of the asphalt mixture by using rutting test, flexural experiment, and freeze-thaw (F-T) splitting. Referring to JTG E20-2011 T 0719, firstly, square slab samples of asphalt mixtures (300 × 300 × 50 mm) were prepared, and perform the high-temperature rutting test at a rolling speed $N = (42 \pm 1)$ cycles/min. Then, the high-temperature performance could be evaluated by the index of dynamic stability (DS), which is calculated through the deflections $d_{45}$ and $d_{60}$:

$$\mathrm{DS} = \frac{15 \times N}{d_{60} - d_{45}}. \tag{5}$$

The flexural experiment is conducted to assess the low-temperature mechanical performance of the asphalt mixture. Referring to JTG E20-2011 T 0715, the prism samples (250 × 30 × 35 mm) were loaded by a pressure. Through the obtained deflection as well as load, $R_B$ and $\varepsilon_B$

as well as $S_B$ could be calculated according to the following:

$$R_B = \frac{3 \times L \times P_B}{2 \times b \times h^2}, \quad (6)$$

$$\varepsilon_B = \frac{6 \times h \times d}{L^2}, \quad (7)$$

$$S_B = \frac{R_B}{\varepsilon_B}. \quad (8)$$

Referring to JTG E20-2011 T 0729, F-T splitting was selected to analyze water sensitivity. Marshall specimens were prepared by one freeze-thaw cycle and without the freeze-thaw cycle, respectively. Then, these specimens were loaded. Through obtained results ($R_{T1}$ for the Marshall specimen without the freeze-thaw cycle and $R_{T2}$ for the Marshall specimen under one cycle), TSR is defined as follows:

$$\text{TSR} = \frac{R_{T2}}{R_{T1}} \times 100. \quad (9)$$

*(2) Uniaxial Static Compression Creep Test.* The creep test methods mainly include uniaxial static compression creep, bending creep and splitting creep, and dynamic triaxial compression creep. At present, the commonly used creep test methods in the world for the asphalt mixture are mainly uniaxial static compression creep and bending creep. A major advantage of the uniaxial static compression creep test is that the test equipment is relatively simple; therefore, this creep test method has been widely used [53, 54].

The experiment has been performed for base original asphalt mixture and nano-$TiO_2$-modified asphalt mixture specimens using a NU-14 tester, whose sensor measurement accuracy is 0.001%. Before the test, a smooth polytetrafluoroethylene (PTFE) plastic film was placed on the upper and lower surfaces of the asphalt mixture sample to eliminate or reduce the influence of friction on contact surfaces. Meanwhile, asphalt mixture samples should be kept to make inside samples uniform. During the uniaxial static compression creep test, both sides of test samples are required to be flat to prevent local stress concentration from affecting the deformation response. At the beginning of the creep test, a loading of 0.002 MPa was preloaded first, and then, the loading for 2700 s as well as unloading for 1800 s were carried out. During the creep test, the deformation data of samples were collected by linear variable differential transformer (LVDT) sensors.

*2.2.3. Photocatalytic Degradation Test.* Photocatalytic degradation test was conducted by the MQW-50A exhaust gas analyzer, as illustrated in Figure 3. The square slab sample ($300 \times 300 \times 50$ mm) was also used and placed at the bottom of the reaction box. Then, the position of the ultraviolet lamp was adjusted at 135 mm from the test slab sample [41]. The automobile exhaust pipe was regarded as the exhaust supply, which was connected with the air inlet of the reaction box. Cover the reaction box with a light-shielding cloth, turn on the ultraviolet light, and monitor the contents of CH and $NO_x$ in real time through the automobile exhaust gas analyzer. The photocatalytic degradation test of automobile exhaust would last 60 min, and the contents of CH and $NO_x$ were checked every 10 min. The photocatalytic degradation rate (PDR) and concentration variation (CV) of automobile exhaust can be calculated as follows:

$$\text{PDR}_i = \frac{\text{Gas}_{i-1} - \text{Gas}_i}{\text{Duration}} \times 100, \quad (10)$$

$$\text{CV} = \frac{\text{Gas}_0 - \text{Gas}_i}{\text{Gas}_0}, \quad (11)$$

where $\text{Gas}_{i-1}$ and $\text{Gas}_i$ are the initial and tested concentration of automobile exhaust (i.e., CH and $NO_x$) for each duration ($i = 1, 2, 3,,4, 5, 6$), respectively. Duration is the reaction time between two photocatalytic degradation tests, and duration = 10 min. $\text{Gas}_0$ is the initial concentration of automobile exhaust (i.e., CH and $NO_x$).

## 3. Results and Discussion

### 3.1. Analysis of Conventional and Rheometer Properties of Asphalt

*3.1.1. Conventional Tests Analysis.* The experimental results of conventional physical performances of asphalt with and without nano-$TiO_2$ are plotted in Figure 4. It is observed that the penetration at 25°C containing nano-$TiO_2$ decreases significantly compared with base asphalt, which shows that adding nano-$TiO_2$ reduced the sensitivity of asphalt to temperature. Besides, the softening point increases slightly through the addition of nano-$TiO_2$. It shows that the stabilization capability of asphalt could be enhanced by nano-$TiO_2$. On the contrary, the ductility at 10°C of both base asphalt and nano-$TiO_2$-modified asphalt are higher than 100 cm, which could conform to JTG F40-2004. The above changing trend indicates that adding 5% nano-$TiO_2$ would decrease the sensitivity of asphalt to temperature and increase its high-temperature properties.

*3.1.2. Dynamic Shear Rheometer Test Analysis*

*(1) Temperature Sweep Test.* Asphalt has significant temperature sensitivity and has different mechanical properties at different temperatures. To explore the rheological characteristics of the asphalt binder in medium- and high-temperature ranges, the DSR test was conducted at 10 rad/s from 40°C to 80°C, and the strain controlled at 12%. The measured $G^*$ and $\delta$ results versus temperature are plotted in Figure 5.

$G^*$ values decrease with the increasing of test temperature in Figure 5(a). This is because the fluidity of asphalt increases as the temperature increases, and it is prone to emerge in more significant deformation at the same stress level. Clearly, a higher complex shear modulus is generally required to ensure that the asphalt pavement still has a good resistance to

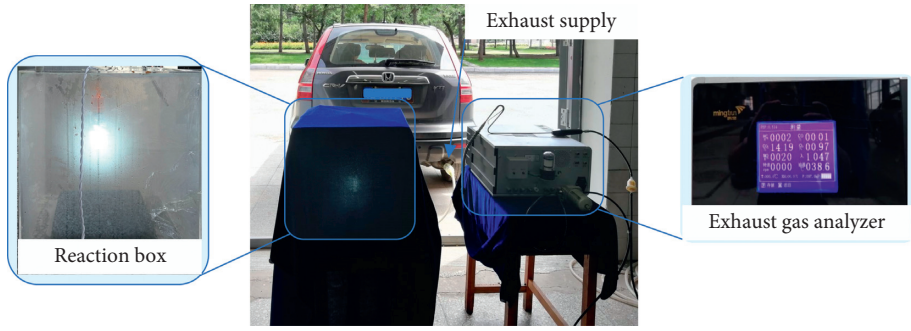


Figure 3: The photocatalytic degradation test.

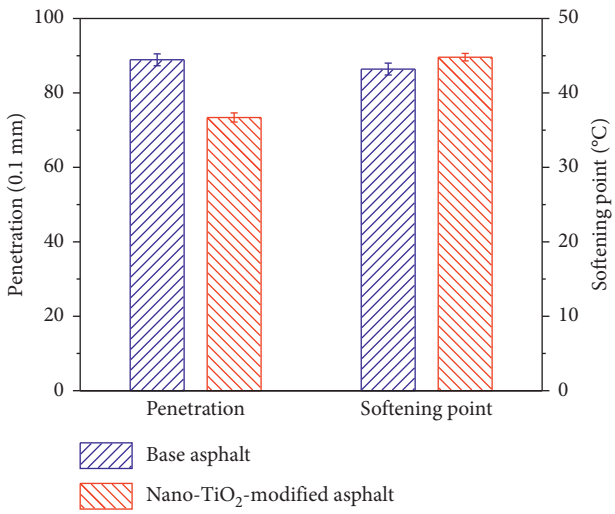


Figure 4: Penetration and softening point results of asphalt samples with and without nano-$TiO_2$.

high-temperature deformation. Furthermore, while by comparison, the increase of $G^*$ value of nano-$TiO_2$-modified asphalt is lower at 40°C, and the corresponding increase in value is much higher at 80°C. This indicates that the asphalt modified by nano-$TiO_2$ has a higher temperature stability than original asphalt due to the higher complex shear modulus.

The characteristics ($\delta$) is the relative indicatrix between recoverable and unrecoverable deformation, in which $\delta = 0°$ for elastic solids and $\delta = 90°$ for viscous fluids. In Figure 5(b), $\delta$ values increase as test temperature increases, which fully reflects the characteristics of a viscous fluid for asphalt as a typical viscoelastic material. With test temperature varying in the range of 40~80°C, $\delta$ values of base asphalt change about 27°, and $\delta$ values of the modified one change about 26°. This implies that asphalt modified by nano-$TiO_2$ has a lower temperature sensitivity. Moreover, since the flow deformation of nano-$TiO_2$-modified asphalt at high temperature is smaller, nano-$TiO_2$ is beneficial for the asphalt pavement to resist high-temperature deformation.

However, it generally needs to use different indicators to evaluate the performances of asphalt for various performances at different test conditions by $G^*$ and $\delta$ values. Many studies have shown that $G^*/\sin\delta$ represents the rutting factor [55]. The larger the value of $G^*/\sin\delta$, the better the ability to resist deformation. Therefore, compared to static tests (such as penetration and softening point), dynamic tests have more intuitive and real advantages to evaluate the performances of asphalt binders. In general, the high-temperature range of the asphalt pavement is generally taken as 40°C ~ 80°C, and the rutting factor results of base and modified asphalt by nano-$TiO_2$ are plotted in Figure 6. As seen, the rutting factor of nano-$TiO_2$-modified asphalt is larger by comparison at the same test temperature, which means asphalt modified by nano-$TiO_2$ has a better high-temperature antirutting ability. Moreover, the growth rate of the rutting factor for nano-$TiO_2$-modified asphalt changes from 5% to 13% when the test temperature increases from 40°C to 80°C. This also implies that asphalt modified by nano-$TiO_2$ possesses a good rutting resistance.

*(2) Frequency Sweep Test.* The frequency sweep test is currently the most popular method for investigating viscoelastic mechanical parameters of asphalt. The dynamic shear modulus mechanical response of asphalt in the linear viscoelastic range can be obtained using the DSR test with the small-strain level under different loading frequencies at the test temperature. To explore the viscoelastic properties of nano-$TiO_2$-modified asphalt at higher temperature, the frequency sweep experiment was conducted based on the DSR test from 40 to 80°C with an interval temperature of 10°C for base and modified asphalt by nano-$TiO_2$. Before the frequency sweep test, asphalt needs to be kept at test temperature for at least 15 min. Figure 7 illustrates the measured $G^*$ varying with frequency.

As loading frequency rises, complex shear modulus of both base asphalt and nano-$TiO_2$-modified asphalt increases and shows a linear growth trend in the logarithmic coordinate. Simultaneously, from the perspective of slope, modified asphalt possesses a high growth speed, meaning nano-$TiO_2$-modified asphalt has a larger complex shear modulus than base asphalt.

*3.1.3. Beam-Bending Rheometer Test Analysis.* The creep deformations versus loading time at −18°C have been measured, and the deflection-time curve reflects the typical viscoelastic behavior of asphalt. Although the creep characteristics of base asphalt and nano-$TiO_2$-modified asphalt are not essentially different, their proportion of viscoelastic

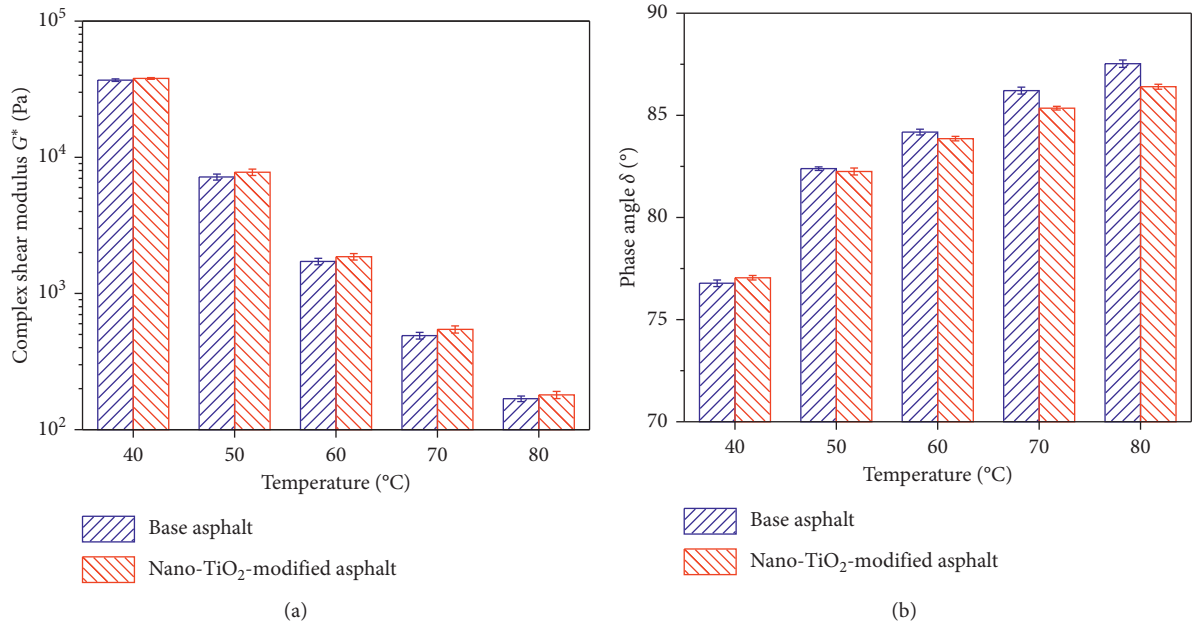


Figure 5: Temperature sweep test of asphalt with and without nano-$TiO_2$. (a) $G*$. (b) $\delta$.

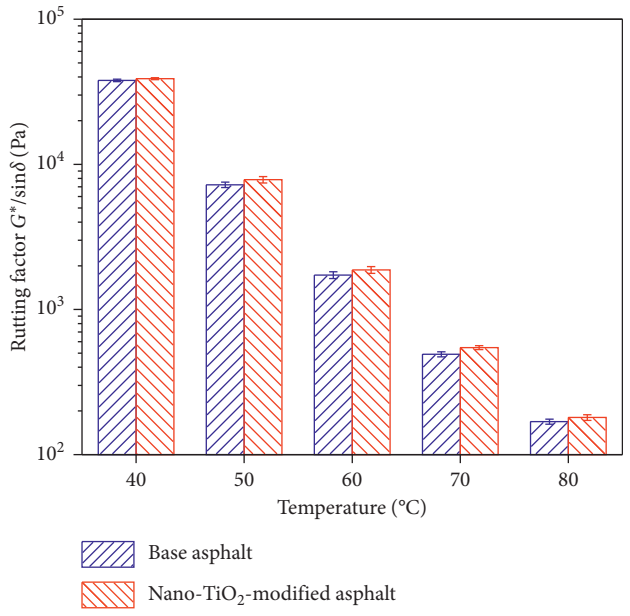


Figure 6: $G*/\sin\delta$ comparison results.

components have been changed. Under the same constant load, the deformation of nano-$TiO_2$-modified asphalt is smaller by comparison, which means that incorporating nano-$TiO_2$ improves the elastic component of asphalt, but decreases the viscosity component.

In the specifications of SHRP, the stiffness modulus result and its changing $m$ value are recommended as the basis for PG performance classification. The $m$ value reflects the sensitivity of stiffness to time and stress relaxation ability. However, with a corresponding higher modulus or lower deflection, the greater the stress required to produce unit strain, indicating that the asphalt material is harder. Figure 8 plots the test results for base and modified asphalt by nano-$TiO_2$. As seen, the modulus of base and modified asphalt by nano-$TiO_2$ decreases with time. However, the modulus of nano-$TiO_2$-modified asphalt is larger by comparison and not more than 300 MPa, which meets the specification requirements. In Figure 8(b), the $m$ value of base asphalt and nano-$TiO_2$-modified asphalt becomes larger as time goes on. The $m$ value at 60 s of nano-$TiO_2$-modified asphalt is smaller, and the $m$ value is larger than or equal to 0.3, meeting the specification requirements. Compared with base asphalt, nano-$TiO_2$-modified asphalt has a larger modulus as well as a smaller $m$ value, representing that the anticrack of asphalt containing nano-$TiO_2$ has been reduced slightly, but it can also meet the Superpave specification requirements, that is, the $m$ value is not less than 0.3.

### 3.2. Analysis of Pavement Performances and Viscoelastic Properties of the Asphalt Mixture

*3.2.1. Pavement Performances Analysis.* Figure 9 summarizes the pavement performances of the asphalt mixture, DS, $\varepsilon_B$, $S_B$, and TSR. From Figure 9, it is observed that nano-$TiO_2$ asphalt mixture has higher DS, which shows that the addition of nano-$TiO_2$ would enhance antirutting ability. Nano-$TiO_2$ can absorb the light components, then affecting the temperature sensitivity of modified asphalt. Nano-$TiO_2$ have a certain surface activity, thereby enhancing antirutting of the modified asphalt mixture.

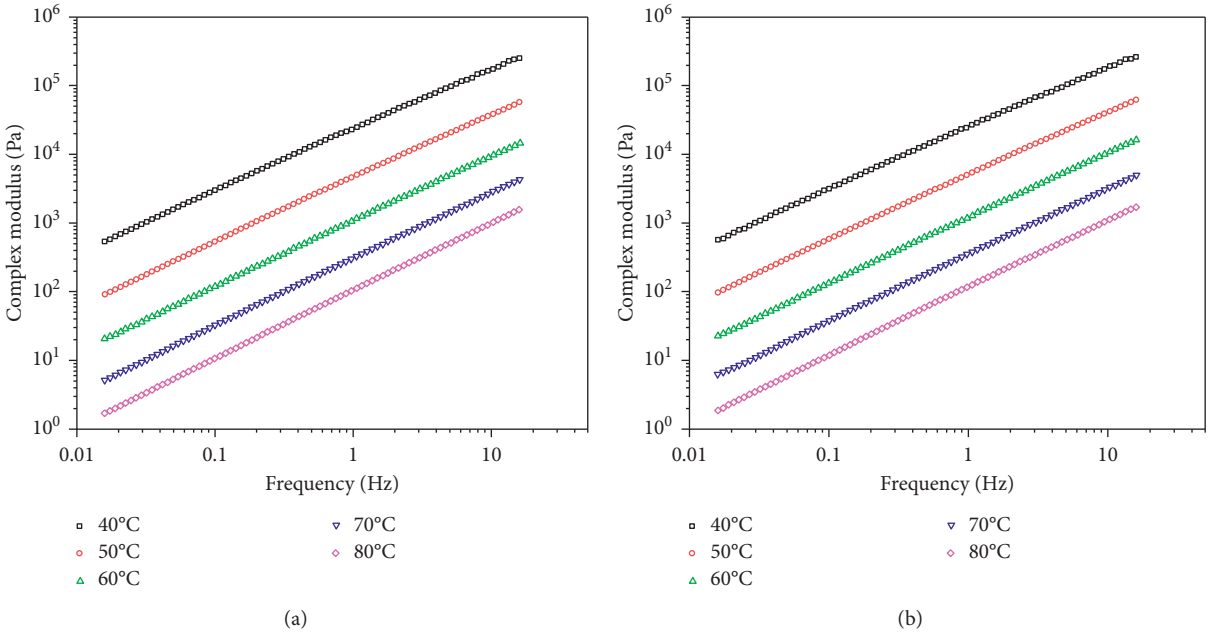


Figure 7: $G*$ results versus frequencies and temperatures of asphalt with and without nano-$TiO_2$. (a) Base asphalt. (b) Nano-$TiO_2$-modified asphalt.

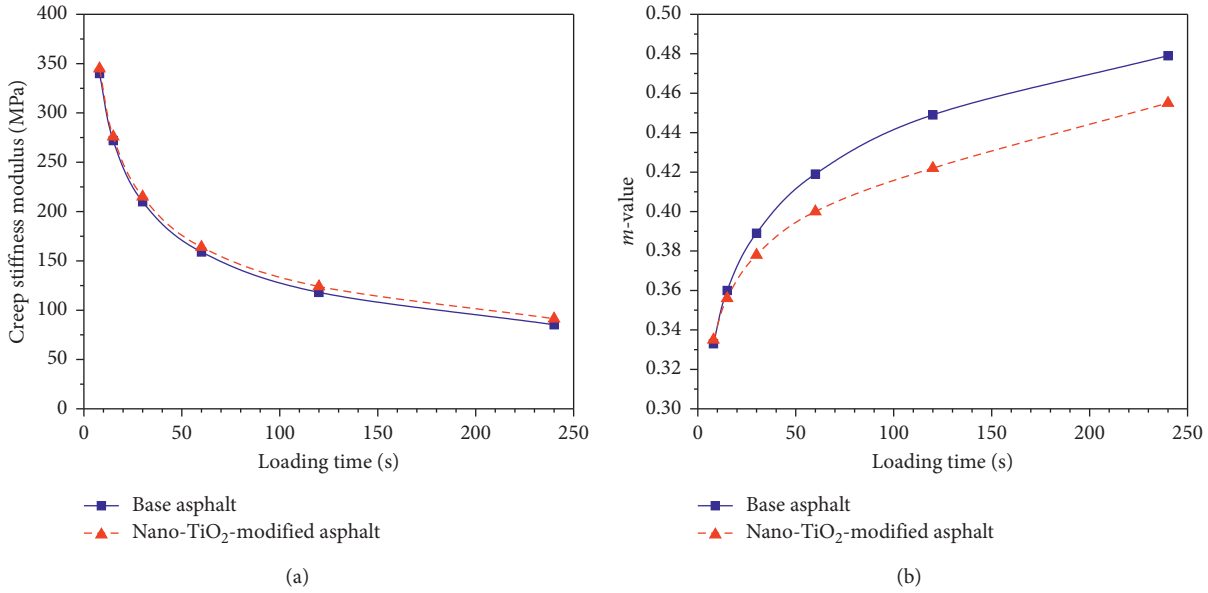


Figure 8: BBR comparison. (a) Modulus. (b) $m$ value.

Besides, the nano-$TiO_2$ mixture possesses higher $\varepsilon_B$ and lower $S_B$. It could be considered that adding nano-$TiO_2$ can improve $\varepsilon_B$ value and then reduce corresponding flexural-tensile stiffness modulus ($S_B$). Thus, the nano-$TiO_2$-modified mixture has a better anticracking ability at low temperature.

From the perspective of moisture stability, the nano-$TiO_2$ mixture possesses large TSR, which conforms to JTG F40-2004. This is because nano-$TiO_2$ has a larger specific surface area, and it can improve the structural asphalt content, thereby improving the moisture stability of the modified mixture.

*3.2.2. Static Creep Test Analysis.* Generally, the viscous and elastic elements are generally combined in series or in parallel to represent the viscoelastic mechanical performances of asphalt mixtures, and the Burgers' model as well as its modified model are widely used and have good

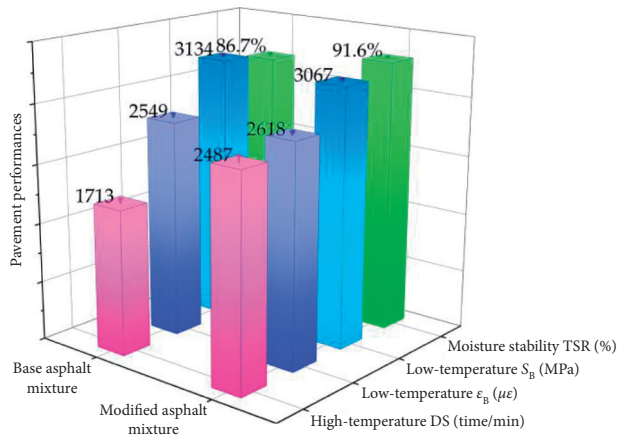


Figure 9: Pavement performances' comparison results.

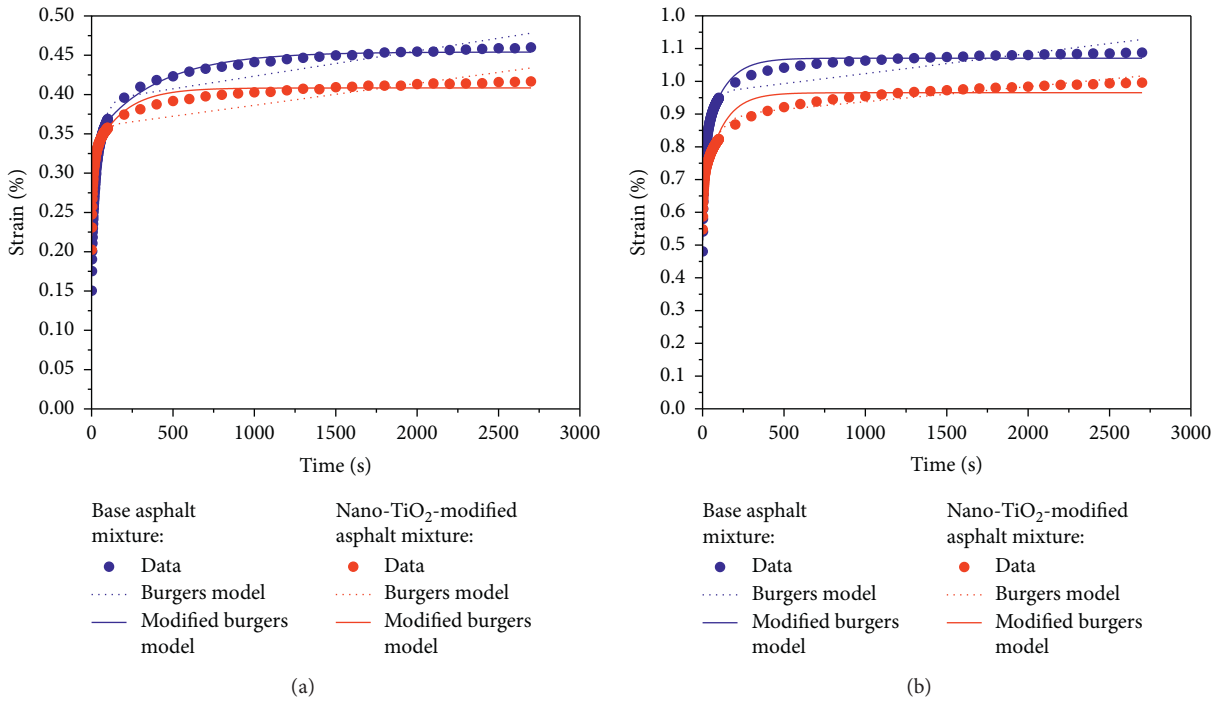


Figure 10: Comparative results of the Burgers' model and modified Burgers' model for asphalt mixtures versus time. (a) 20°C. (b) 50°C.

application effects [53, 54]. The creep functions of these two models are given as follows:

$$\varepsilon(t) = \sigma_0 \left[ \frac{1}{E_1} + \frac{t}{\eta_1} + \frac{1}{E_2}\left(1 - e^{\left(-E_2 t/\eta_2\right)}\right) \right], \quad (12)$$

for the Burgers' model,

$$\varepsilon(t) = \sigma_0 \left[ \frac{1}{E_1} + \frac{\left(1 - e^{-Bt}\right)}{AB} + \frac{1}{E_2}\left(1 - e^{\left(-E_2 t/\eta_2\right)}\right) \right], \quad (13)$$

for the modified Burgers' model.

The uniaxial static compression creep tests at 20°C and 50°C were conducted on base and modified asphalt by nano-$TiO_2$. Figure 10 illustrates the creep deformation results versus time. Both asphalt mixtures have similar creep deformation curves. At the loading stage, the creep deformation includes instant and delayed elastic as well as viscous flow deformations. Although incorporating nano-$TiO_2$ will not change the creep deformation law of the asphalt mixture, nano-$TiO_2$ could affect the creep deformation rate, cumulative deformation, and residual permanent deformation.

Figure 10 also plots the fitting curves of creep deformation for the base original asphalt mixture as well as the nano-$TiO_2$ mixture. As seen, the modified Burgers' model is closer to actual measured creep deformation data, and the fitting accuracy is higher. The modified Burgers' model could consider the consolidation effect of the asphalt mixture, that is, the creep growth rate of the asphalt mixture gradually

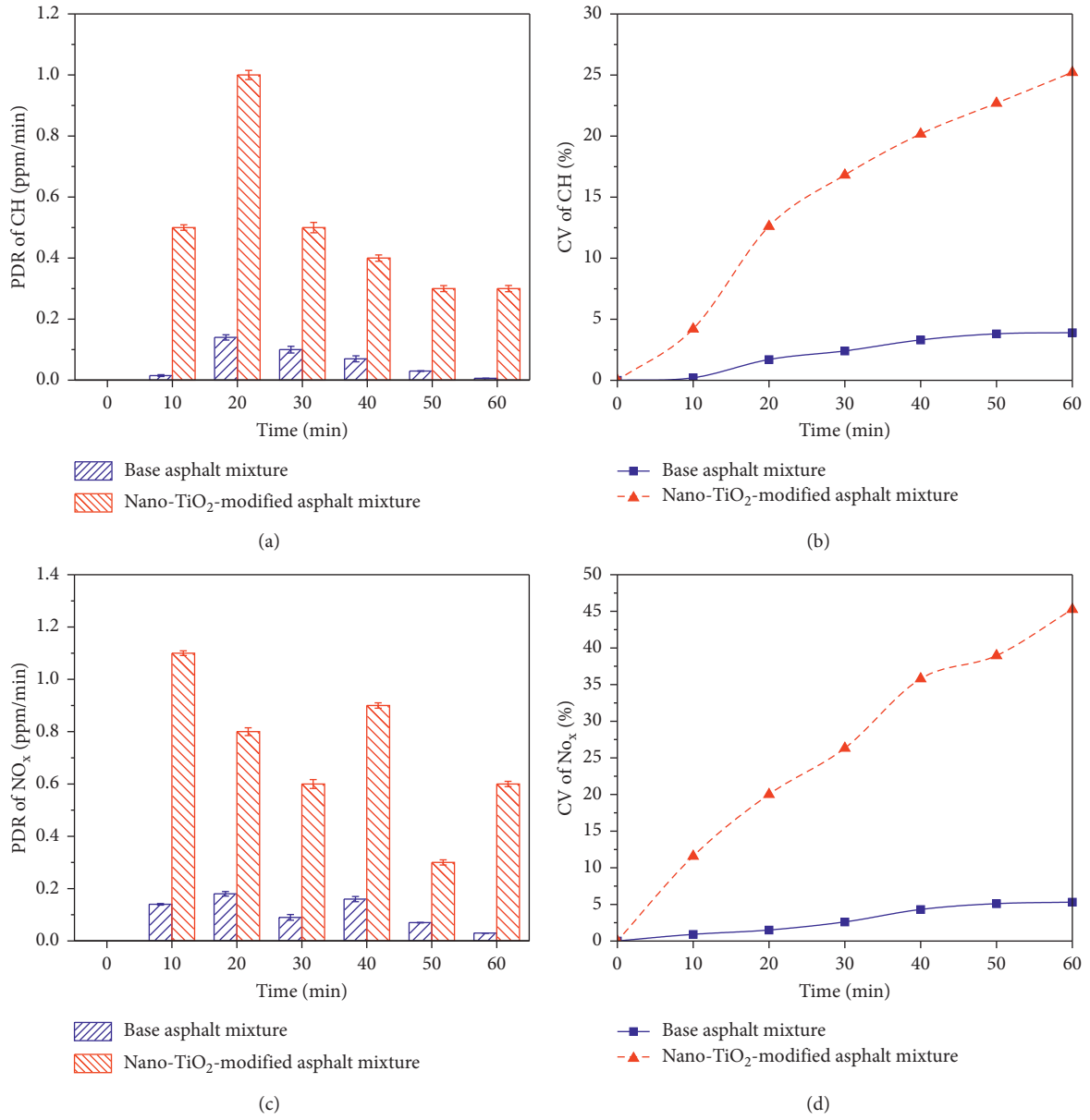


Figure 11: Photocatalytic degradation test results of automobile exhaust for asphalt mixtures with and without nano-$TiO_2$. (a) PDR of CH. (b) CV of CH. (c) PDR of $NO_x$. (d) CV of $NO_x$.

decreases in the actual creep process. However, the Burgers' model has good fitting results at the early stage of creep, but the creep deformation is gradually different from the actual deformation after the creep migration period. Therefore, the Burgers' model is more ideal, and the modified Burgers' model is closer to reality.

*3.3. Analysis of the Photocatalytic Degradation Test of Automobile Exhaust.* The photocatalytic degradation test was carried out for the asphalt mixture with and without $TiO_2$ nanoparticles to monitor CH and $NO_x$ contents using the automobile exhaust gas analyzer. The initial concentrations of CH for the base original asphalt mixture as well as the nano-$TiO_2$-modified asphalt mixture are 115 ppm and 119 ppm, respectively. The initial concentrations of $NO_x$ for the base original asphalt mixture as well as the nano-$TiO_2$-modified asphalt mixture are 112 ppm and 95 ppm, respectively. Figures 11(a) and 11(b) present the PDR and CV of CH for the base original asphalt mixture as well as the nano-$TiO_2$-modified asphalt mixture. It is observed intuitively in Figure 11(a) that the PDR value of CH for both asphalt mixtures increase first and then decrease with time. In Figure 11(b), CH is continuously decreasing with time, which shows that the photocatalytic degradation rate of nano-$TiO_2$ for CH in mixtures will gradually decrease with the reaction time. When the reaction time is about 20 min, the PDR of nano-$TiO_2$ for CH reaches the maximum, and the PDR value is about 1.0 ppm/min.

Figures 11(c) and 11(d) present the PDR and CV of $NO_x$ for the base original asphalt mixture and nano-$TiO_2$-modified mixture. From Figure 11(c), the photocatalytic degradation rate of nano-$TiO_2$ for $NO_x$ has certain fluctuation and generally shows a slight downward trend with the reaction time. In Figure 11(d), it can be seen that the concentration of $NO_x$ is continuously decreasing with the reaction time, which shows that the PDR of nano-$TiO_2$ for $NO_x$ in mixtures only decreases slightly with the reaction time.

The nano-$TiO_2$-modified asphalt mixture has a very positive influence for purification of CH and $NO_x$. Due to the PDR above 0.4 ppm/min, purification of CH by the modified asphalt mixture can be considered to occur mainly within 40 minutes during the reaction time, and the photocatalytic degradation efficiency is relatively high. While, the photocatalytic degradation of $NO_x$ by the nano-$TiO_2$-modified asphalt mixture has a good degradation efficiency within 1 hour of the reaction time, although the degradation rate fluctuates. Theoretically, the PDR and CV of the base asphalt mixture will not change at all. However, the asphalt mixture is a kind of porous structure material, which may have a certain adsorption on CH and $NO_x$, resulting in its change. In general, adding nano-$TiO_2$ can greatly improve the photocatalytic degradation treatment of automobile exhaust from asphalt mixtures. Meanwhile, the photocatalytic degradation effect of nano-$TiO_2$-modified mixtures on $NO_x$ is significantly better than that of CH.

## 4. Conclusions

In this work, nanomaterial (nano-$TiO_2$) was used for asphalt, and then, nano-$TiO_2$-modified asphalt was also added into the asphalt mixture. In addition, the conventional and rheological indicators of base and nano-$TiO_2$-modified asphalt, as well as pavement performances and photocatalytic degradation of automobile exhaust of base and nano-$TiO_2$-modified asphalt mixtures have been tested and analyzed. The following conclusions are drawn:

(1) Nano-$TiO_2$ can enhance the mechanical performances of asphalt. According to penetration and softening point tests, adding nano-$TiO_2$ was beneficial to increase the viscosity and reduce the temperature sensitivity, which would enhance its high-temperature stabilization capability of asphalt.

(2) Rheological properties of asphalt can be improved by $TiO_2$ nanoparticles significantly. Compared to base asphalt, nano-$TiO_2$-modified asphalt has higher $G^*$ and lower $\delta$. Addition of nano-$TiO_2$ was beneficial to enhance the capacity of high-temperature antirutting of asphalt due to its larger rutting factor. The growth rate of the rutting factor for nano-$TiO_2$-modified asphalt changes from 5% to 13% when the temperature range is 40°C~80°C.

(3) Due to the larger creep stiffness modulus (not more than 300 MPa) and smaller $m$ value (not less than 0.3), the low-temperature anticracking property of nano-$TiO_2$-modified asphalt is weaker. According to ductility results at 10°C and $m$ values of the BBR test, the low-temperature performance of nano-$TiO_2$-asphalt could also comply with the Superpave specification.

(4) According to the analysis of pavement performances, adding nano-$TiO_2$ can effectively enhance the antirutting and anticracking performances and water stabilization. Besides, the cumulative strain of asphalt mixtures can be accurately characterized by the modified Burgers' model.

(5) The nano-$TiO_2$-modified asphalt mixture has a positive influence on the photocatalytic degradation of CH and $NO_x$, which could provide a reference for the treatment of automobile exhaust. Meanwhile, the photocatalytic degradation effect of nano-$TiO_2$-modified asphalt mixtures on $NO_x$ is significantly better than that of CH. The photocatalytic degradation of CH and $NO_x$ by the nano-$TiO_2$-modified asphalt mixture can be considered to occur mainly within 40 minutes and 1 hour, respectively, during the reaction time.

## Data Availability

The data used to support the findings of this study are available from the corresponding author upon request.

## Conflicts of Interest

The authors declare that they have no conflicts of interest.

## Acknowledgments

This work was funded by the Nanning Excellent Young Scientist Program (Grant no. RC20180108), Nanning Excellent Young Scientist Program and Guangxi Beibu Gulf Economic Zone Major Talent Program (Grant no. RC20190206), Science and Technology Base and Talent Special Project of Guangxi Province (Grant no. AD19245152), "Yongjiang Plan" of Nanning Leading Talents in Innovation and Entrepreneurship (Grant no. 2018-01-04), Scientific and Technological Project of Science and Technology Department of Jilin Province (Grant no. 20190303052SF), and the Innovation Special Project of Zhongshan Science and Technology Bureau (Grant no. 2019AG001).

## References

[1] S. Mondal and K. P. Biligiri, "Crumb rubber and silica fume inclusions in pervious concrete pavement systems: evaluation of hydrological, functional, and structural properties," *Journal of Testing and Evaluation*, vol. 46, no. 3, pp. 892–905, 2018.

[2] Y. Gao, B. He, M. Xiao, Z. Fang, and K. Dai, "Study on properties and mechanisms of luminescent cement-based pavement materials with super-hydrophobic function," *Construction and Building Materials*, vol. 165, pp. 548–559, 2018.

[3] F. L. Tang, T. Ma, and Y. S. Guan, "Parametric modeling and structure verification of asphalt pavement based on bim-abaqus," *Automation in Construction*, vol. 111, 2020.

[4] F. L. Tang, T. Ma, and J. H. Zhang, "Integrating three-dimensional road design and pavement structure analysis based on bim," *Automation in Construction*, vol. 113, 2020.

[5] Q. Guo, L. Li, Y. Cheng, Y. Jiao, and C. Xu, "Laboratory evaluation on performance of diatomite and glass fiber compound modified asphalt mixture," *Materials & Design (1980-2015)*, vol. 66, pp. 51–59, 2015.

[6] Q. L. Guo, H. Y. Wang, and Y. Gao, "Investigation of the low-temperature properties and cracking resistance of fiber-reinforced asphalt concrete using the dic technique," *Engineering Fracture Mechanics*, vol. 229, 2020.

[7] M. Guo, M. C. Liang, and Y. B. Jiao, "A review of phase change materials in asphalt binder and asphalt mixture," *Construction and Building Materials*, vol. 258, 2020.

[8] M. Guo, H. Q. Liu, and Y. B. Jiao, "Effect of wma-rap technology on pavement performance of asphalt mixture: a state-of-the-art review," *Journal of Cleaner Production*, vol. 266, 2020.

[9] H. B. Liu, G. B. Luo, and X. Q. Wang, "Laboratory evaluation of the pavement performance of a rubber-modified asphalt mixture," *Emerging Materials Research*, vol. 9, no. 1, pp. 99–103, 2020.

[10] Z. B. Ren, Y. Q. Zhu, and Q. Wu, "Enhanced storage stability of different polymer modified asphalt binders through nano-montmorillonite modification," *Nanomaterials*, vol. 10, no. 4, 2020.

[11] M. L. Zheng, Y. J. Tian, and L. T. He, "Analysis on environmental thermal effect of functionally graded nano-composite heat reflective coatings for asphalt pavement," *Coatings*, vol. 9, no. 3, 2019.

[12] G. Tan, Z. Zhu, and W. Wang, "Flexural ductility and crack-controlling capacity of polypropylene fiber reinforced ecc thin sheet with waste superfine river sand based on acoustic emission analysis," *Construction and Building Materials*, vol. 277, 2021.

[13] H. N. Yu, W. Dai, and G. P. Qian, "The $NO_x$ degradation performance of nano-$TiO_2$ coating for asphalt pavement," *Nanomaterials*, vol. 10, no. 5, 2020.

[14] T. Chen, Y. C. Luan, and T. Ma, "Mechanical and microstructural characteristics of different interfaces in cold recycled mixture containing cement and asphalt emulsion," *Journal of Cleaner Production*, vol. 258, 2020.

[15] J. P. Bilodeau, J. Y. Yi, and P. M. Thiam, "Surface deflection analysis of flexible pavement with respect to frost penetration," *Journal of Cold Regions Engineering*, vol. 33, no. 4, 2019.

[16] J. Q. Zhu, T. Ma, and J. W. Fan, "Experimental study of high modulus asphalt mixture containing reclaimed asphalt pavement," *Journal of Cleaner Production*, vol. 263, 2020.

[17] Q. L. Guo, Q. Liu, and P. Zhang, "Temperature and pressure dependent behaviors of moisture diffusion in dense asphalt mixture," *Construction and Building Materials*, vol. 246, 2020.

[18] Q. Guo, G. Li, Y. Gao et al., "Experimental investigation on bonding property of asphalt-aggregate interface under the actions of salt immersion and freeze-thaw cycles," *Construction and Building Materials*, vol. 206, pp. 590–599, 2019.

[19] Y. B. Jiao, L. D. Zhang, and Q. L. Guo, "Acoustic emission-based reinforcement evaluation of basalt and steel fibers on low-temperature fracture resistance of asphalt concrete," *Journal of Materials in Civil Engineering*, vol. 32, no. 5, 2020.

[20] Y. B. Jiao, S. Q. Liu, and L. X. Fu, "Fracture monitoring of sbs and crumb rubber modified porous asphalt mixtures under compression and splitting testing using acoustic emission technique," *Journal of Materials in Civil Engineering*, vol. 31, no. 6, 2019.

[21] X. Y. Zhang, L. Xu, and J. X. Lv, "Investigation on the flexural-tensile rheological behavior and its influence factors of fiber-reinforced asphalt mortar," *Polymers*, vol. 12, no. 9, 2020.

[22] C. Liang, X. Xu, and H. Chen, "Machine learning approach to develop a novel multi-objective optimization method for pavement material proportion," *Applied Sciences*, vol. 11, no. 2, 2021.

[23] X. H. Ding, T. Ma, and L. H. Gu, "Investigation of surface micro-crack growth behavior of asphalt mortar based on the designed innovative mesoscopic test," *Materials & Design*, vol. 185, 2020.

[24] L. Garcia-Gil, R. Miró, and F. E. Pérez-Jiménez, "New approach to characterize cracking resistance of asphalt binders," *Construction and Building Materials*, vol. 166, pp. 50–58, 2018.

[25] X. Zhang, X. Gu, and J. Lv, "Effect of basalt fiber distribution on the flexural-tensile rheological performance of asphalt mortar," *Construction and Building Materials*, vol. 179, pp. 307–314, 2018.

[26] L. Brasileiro, F. Moreno-Navarro, and R. Tauste-Martinez, "Reclaimed polymers as asphalt binder modifiers for more sustainable roads: a review," *Sustainability*, vol. 11, no. 3, 2019.

[27] W. S. Wang, Y. C. Cheng, and H. P. Chen, "Study on the performances of waste crumb rubber modified asphalt mixture with eco-friendly diatomite and basalt fiber," *Sustainability*, vol. 11, no. 19, 2019.

[28] X. Zhang, X. Gu, J. Lv, Z. Zhu, and F. Ni, "Mechanism and behavior of fiber-reinforced asphalt mastic at high temperature," *International Journal of Pavement Engineering*, vol. 19, no. 5, pp. 407–415, 2018.

[29] W. S. Wang, Y. C. Cheng, and G. J. Tan, "Design optimization of sbs-modified asphalt mixture reinforced with eco-friendly basalt fiber based on response surface methodology," *Materials*, vol. 11, no. 8, 2018.

[30] S. G. Jahromi and A. Khodaii, "Effects of nanoclay on rheological properties of bitumen binder," *Construction and Building Materials*, vol. 23, no. 8, pp. 2894–2904, 2009.

[31] M. Abdelrahman, D. R. Katti, and A. Ghavibazoo, "Engineering physical properties of asphalt binders through nanoclay-asphalt interactions," *Journal of Materials in Civil Engineering*, vol. 26, no. 12, 2014.

[32] Z. You, J. Mills-Beale, J. M. Foley et al., "Nanoclay-modified asphalt materials: preparation and characterization," *Construction and Building Materials*, vol. 25, no. 2, pp. 1072–1078, 2011.

[33] M. J. Khattak, A. Khattab, H. R. Rizvi, and P. Zhang, "The impact of carbon nano-fiber modification on asphalt binder rheology," *Construction and Building Materials*, vol. 30, pp. 257–264, 2012.

[34] I. R. Segundo, C. Ferreira, and E. F. Freitas, "Assessment of photocatalytic, superhydrophobic and self-cleaning properties on hot mix asphalts coated with $TiO_2$ and/or ZNO aqueous solutions," *Construction and Building Materials*, vol. 166, pp. 500–509, 2018.

[35] Y. Shu, J. Ji, Y. Xu et al., "Promotional role of mn doping on catalytic oxidation of vocs over mesoporous $TiO_2$ under vacuum ultraviolet (vuv) irradiation," *Applied Catalysis B: Environmental*, vol. 220, pp. 78–87, 2018.

[36] M. M. Hassan, H. Dylla, S. Asadi, L. N. Mohammad, and S. Cooper, "Laboratory evaluation of environmental performance of photocatalytic titanium dioxide warm-mix asphalt pavements," *Journal of Materials in Civil Engineering*, vol. 24, no. 5, pp. 599–605, 2012.

[37] J. V. S. de Melo and G. Trichês, "Evaluation of the influence of environmental conditions on the efficiency of photocatalytic

coatings in the degradation of nitrogen oxides (NOx)," *Building and Environment*, vol. 49, pp. 117–123, 2012.

[38] R. Ahmad, Z. Ahmad, A. U. Khan, N. R. Mastoi, M. Aslam, and J. Kim, "Photocatalytic systems as an advanced environmental remediation: recent developments, limitations and new avenues for applications," *Journal of Environmental Chemical Engineering*, vol. 4, no. 4, pp. 4143–4164, 2016.

[39] I. Kitsou, P. Panagopoulos, T. Maggos, and A. Tsetsekou, "ZNO-coated $SiO_2$ nanocatalyst preparation and its photocatalytic activity over nitric oxides as an alternative material to pure ZNO," *Applied Surface Science*, vol. 473, pp. 40–48, 2019.

[40] A. A. Nada, W. M. A. El Rouby, and M. F. Bekheet, "Highly textured boron/nitrogen co-doped $TiO_2$ with honeycomb structure showing enhanced visible-light photoelectrocatalytic activity," *Applied Surface Science*, vol. 505, 2020.

[41] G. B. Luo, H. B. Liu, and W. J. Li, "Automobile exhaust removal performance of pervious concrete with nano $TiO_2$ under photocatalysis," *Nanomaterials*, vol. 10, no. 10, 2020.

[42] M. Chen and Y. Liu, "NOx removal from vehicle emissions by functionality surface of asphalt road," *Journal of Hazardous Materials*, vol. 174, no. 1-3, pp. 375–379, 2010.

[43] K. Hashimoto, H. Irie, and A. Fujishima, "$TiO_2$ photocatalysis: a historical overview and future prospects," *Japanese Journal of Applied Physics*, vol. 44, no. 12, pp. 8269–8285, 2005.

[44] V. Loftness, B. Hakkinen, O. Adan, and A. Nevalainen, "Elements that contribute to healthy building design," *Environmental Health Perspectives*, vol. 115, no. 6, pp. 965–970, 2007.

[45] J. Jin, T. Xiao, Y. Tan et al., "Effects of TiO2 pillared montmorillonite nanocomposites on the properties of asphalt with exhaust catalytic capacity," *Journal of Cleaner Production*, vol. 205, pp. 339–349, 2018.

[46] G. Qian, H. Yu, X. Gong, and L. Zhao, "Impact of Nano-TiO2 on the NO2 degradation and rheological performance of asphalt pavement," *Construction and Building Materials*, vol. 218, pp. 53–63, 2019.

[47] Y. Gong, H. Bi, Z. Tian, and G. Tan, "Pavement performance investigation of nano-TiO2/CaCO3 and basalt fiber composite modified asphalt mixture under freeze–thaw cycles," *Applied Sciences*, vol. 8, no. 12, p. 2581, 2018.

[48] J. M. Yu, F. D. Chen, and W. Deng, "Design and performance of high-toughness ultra-thin friction course in South China," *Construction and Building Materials*, vol. 246, 2020.

[49] W. Wang, Y. Cheng, G. Tan, and C. Shi, "Pavement performance evaluation of asphalt mixtures containing oil shale waste," *Road Materials and Pavement Design*, vol. 21, no. 1, pp. 179–200, 2020.

[50] Y. C. Cheng, W. S. Wang, and G. J. Tan, "Assessing high- and low-temperature properties of asphalt pavements incorporating waste oil shale as an alternative material in Jilin province, China," *Sustainability*, vol. 10, no. 7, 2018.

[51] W. Wang, Y. Cheng, G. Tan, Z. Liu, and C. Shi, "Laboratory investigation on high- and low-temperature performances of asphalt mastics modified by waste oil shale ash," *Journal of Material Cycles and Waste Management*, vol. 20, no. 3, pp. 1710–1723, 2018.

[52] Y. Zhang, T. Ma, and M. Ling, "Predicting dynamic shear modulus of asphalt mastics using discretized-element simulation and reinforcement mechanisms," *Journal of Materials in Civil Engineering*, vol. 31, no. 8, 2019.

[53] W. S. Wang, G. J. Tan, and C. Y. Liang, "Study on viscoelastic properties of asphalt mixtures incorporating sbs polymer and basalt fiber under freeze-thaw cycles," *Polymers*, vol. 12, no. 8, 2020.

[54] W. S. Wang, Y. C. Cheng, and P. L. Zhou, "Performance evaluation of styrene-butadiene-styrene-modified stone mastic asphalt with basalt fiber using different compaction methods," *Polymers*, vol. 11, no. 6, 2019.

[55] C. Wu, L. Li, and W. Wang, "Experimental characterization of viscoelastic behaviors of nano $TiO_2/CaCO_3$ modified asphalt and asphalt mixture," *Nanomaterials (Basel)*, vol. 11, no. 1, 2021.

Hindawi
Advances in Materials Science and Engineering
Volume 2021, Article ID 6667853, 13 pages
https://doi.org/10.1155/2021/6667853

*Research Article*

# Dynamic Response of Multitower Suspension Bridge Deck Pavement under Random Vehicle Load

**Chenchen Zhang,[1,2] Leilei Chen ,[1,3] Gang Liu,[3] and Zhendong Qian[1,3]**

[1]*Key Laboratory of Safety and Risk Management on Transport Infrastructures, Ministry of Transport, Southeast University, Nanjing 210096, Jiangsu Province, China*
[2]*China Iconic Technology Company Limited, Hefei 230000, Anhui Province, China*
[3]*Intelligent Transportation System Research Center, Southeast University, Nanjing 210096, Jiangsu Province, China*

Correspondence should be addressed to Leilei Chen; chenleilei@seu.edu.cn

Received 27 December 2020; Revised 25 January 2021; Accepted 1 February 2021; Published 12 February 2021

Academic Editor: Qinglin Guo



Recently, the multitower suspension bridge has been widely used in long-span bridge construction. However, the dynamic response of the deck and pavement system of the multitower suspension bridge under random vehicle load is still not clear, which is of great significance to steel-bridge deck pavement (SBDP) design and construction. To reveal the mechanical mechanism of the steel-bridge deck pavement of the multitower suspension bridge under traffic load, this paper analyzed the mechanical response of the pavement based on case study through the multiscale numerical approach and experimental program. Firstly, considering the full-bridge effect of the multitower suspension bridge, the finite element model (FEM) of the SBDP composite structure was established to obtain key girder segments. Secondly, the influences of pavement layer, bending moment and torque, random traffic flow, and bridge structure on the stress of the girder segment were analyzed. Thirdly, the mechanical response of the pavement layer to the orthotropic plate under random vehicle load was studied. Finally, a full-scale model of the experimental program was established to verify the numerical results. Results show that (1) the pavement layer reduced the stress of the steel-box girder roof by about 10%. In the case of adverse bending moment and torque, the longitudinal and transverse stresses of the pavement layer were mainly concentrated in the stress concentration area near the suspender. Under the action of the random vehicle flow, the stress response of the pavement layer was increased by 40% compared with that under standard load. (2) Three-tower and two-span bridge structures have a great influence on the vertical deformation of the pavement layer under the action of vehicle load. Thus, the pavement material needs to have great deformation capacity. (3) The full-bridge effect has a significant influence on the longitudinal stress of the local orthotropic plate, but a small influence on the transverse stress. (4) There is a good correlation between the experimental measurement results of the full-size model and that of the numerical model. The research results can provide guidance for SBDP design and construction of the multitower suspension bridge.

## 1. Introduction

Multitower suspension bridge is a new type of bridge structure which has been widely used in recent years [1]. The continuous layout of multiple main spans is achieved by adding one or more main towers. The technical difficulty of scheme implementation and the overall project cost can be reduced [2]. However, the structure of a multitower suspension bridge is quite different from that of a traditional two-tower suspension bridge. The mechanical behavior of the multitower suspension bridge is more complicated. In addition, the steel-bridge deck pavement (SBDP) is placed directly above the bridge deck to protect the steel-bridge deck and share load, providing a riding surface that meets the driving requirements of the vehicle [3, 4]. In recent years, with the continuous progress of deck pavement technology, design theory and construction technique of SBDP have increasingly matured. However, mechanical features are closely related to the steel-bridge deck system and are greatly influenced by the type of the bridge structure. The

mechanical behavior of multitower suspension bridge SBDP still remains to be clarified.

Vehicle load is a critical external factor in the analysis of SBDP mechanical performance. Vehicle load is actually a fleet of vehicles distributed randomly in time and space. In addition, vehicle weight, speed, distance, axle weight, tire pressure, and other parameters have great randomness. Therefore, the concept of random vehicle load was proposed to study the fatigue damage of the bridge and its attached pavement. Early research studies focused on the statistical analysis of the random vehicle load spectrum [5]. At present, simulation of the random traffic flow is the main research direction [6, 7]. The structural safety and the antifatigue performance of the bridge were verified by random vehicle load. However, there are few studies on the dynamic response of the deck and pavement system of the multitower suspension bridge under random vehicle load.

A lot of research has been done on the mechanical properties of asphalt concrete and SBDP [8–13]. At present, the research of SBDP mainly focuses on its mechanical properties. Zhao regarded the steel box girder for the long-span suspension bridge as the research object and then studied the calculation method of the load effect, fatigue-damage pavement failure mode, index system, calculation method, and reliability of the deck pavement design. Taking the steel box girder of the long-span suspension bridge as the research object, the calculation method of load effect, failure mode of the fatigue damage pavement, index system, calculation method, and reliability of the bridge deck pavement design were studied [14]. Wu et al. pointed out that with the increase of temperature, the stiffness of asphalt mixture SBDP decreased rapidly, which would lead to the rapid increase of stress on the orthogonal orthotropic steel-bridge deck [15]. Kainuma et al. used 3D FEM to analyze the stress and strain of orthotropic steel deck reinforced by bulb ribs [16]. A small-scale model of steel-bridge deck was established under static load to monitor the health of the bridge structure [17]. Taking Grota-Roweckiego Bridge as the example, the estimation of the residual fatigue life of the orthotropic bridge deck was studied [18]. Other experts have also studied the technology of mechanical performance of the asphalt pavement on the steel-bridge deck. As an effective research method, the multiscale model is widely used in the mechanical analysis of structures and bridges, but less in the analysis of the stress of different bridge deck pavements. Qian et al. puts forward the bridge-subsection pavement, a three-stage mechanical analysis technique of the bridge deck pavement, and applied it to the analysis of the bridge deck pavement of multiple bridges [19]. In order to extend the service life of SBDP, a long-life steel-bridge deck pavement (LLSBDP) was put forward [20]. The three-stage mechanical analysis technique was used to analyze the mechanical response law of SBDP considering bridge characteristics and uniformity [21]. Qian and Liu applied the stress-state transformation prestress of the first system to the local SBDP system and studied the influence of stress on the first system of steel-bridge deck on the stress of the SBDP layer [22]. Through large-scale model specimens, Zhang et al. demonstrated that setting the light concrete layer between the steel-bridge plate and asphalt pavement layer allowed stress to be equally distributed in the steel-bridge plate and improved the structural stiffness of the SBDP system [23]. Nevertheless, both structures can be simulated by a smaller model under vehicle load. The multiscale analysis approach is an important and useful tool to clarify the mechanical property of steel-bridge deck and pavement system.

In general, the multiscale analysis approach has been seldom used to study the influence of the bridge type on the mechanical behavior of SBDP, especially under random vehicle load. Therefore, this paper adopted the multiscale method to study the mechanical response of the whole bridge model under the action of random dynamic load through the case study. Taking the mechanical response of the whole bridge as the boundary condition, the critical girder segment model was established, and the influence of random dynamic load on the model was analyzed. Based on the girder segment model and in view of the effect of the multitower suspension bridge, the finite element refinement model of the steel-deck pavement composite structure was established. Finally, a local full-size bridge test model was established to verify the correctness of the finite element analysis results. The analysis results can provide guidance for the design and construction of the multitower suspension bridge and its SBDP part.

## 2. Case Information

*2.1. Project Survey.* Taizhou Bridge (TZB) is a highway bridge across the Yangtze River in China. The main bridge of the TZB is a three-tower and two-span continuous stiffening girder system. The side tower is made of the concrete structure, while the middle tower and stiffening girder are made of steel. The overall layout of the bridge is shown in Figure 1.

*2.2. Load Model and Analysis Approach.* The random vehicle load model was established, and the multiscale analysis approach was selected in this paper. A large-scale model was used to simulate the full-bridge model under working conditions, and a small-scale model was used to simulate the girder cross-section model and local detail model to study stress conditions. Furthermore, the SBDP synergy test model was designed to verify the results of the multiscale model in numerical simulation. The results of the hypothetical model were compared with those of the numerical model to study the cooperative working performance of the steel-bridge deck and pavement system.

*2.2.1. Random Vehicle Load.* Random vehicle load is greatly complex and random, containing the most unfavorable combination of load to match the actual working condition. It was applied to finite element analysis. The results lay a foundation for the establishment of a detailed SBDP system model with the full-bridge effect by numerical simulation and are also an important condition for the study of the SBDP system dynamic response under random vehicle load.

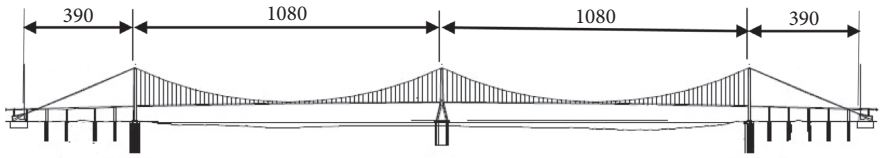


Figure 1: Overall layout of the Taizhou Yangtze river bridge (unit: M).

*2.2.2. Multiscale Analysis Approach.* In the current study of long-span bridge structures, such as multitower suspension bridges and cable-stayed bridges, the mid-girder model is usually used to simulate the full-bridge model. The bridge deck system was simulated in the girder element. The model is suitable for analyzing the dynamic and static characteristics of the bridge, and it reflects the distribution of internal forces and stress distribution along the main girder of the bridge. However, it is difficult to calculate the stress state of a specific girder cross-section. The cross-section of the large-size girder is usually simulated in the solid element or shell element. However, due to the limitation of the bridge size, it is difficult to accurately analyze the cm-level detail structure. On this basis, in order to meet the requirements of different scale analysis, multiscale analysis provides a method to solve this problem by controlling boundary conditions and associating different scale models.

The full-bridge multiscale analysis method, key beam segments, and orthogonal anisotropic plates were adopted to analyze the mechanical properties of the pavement layer, as shown in Figure 2.

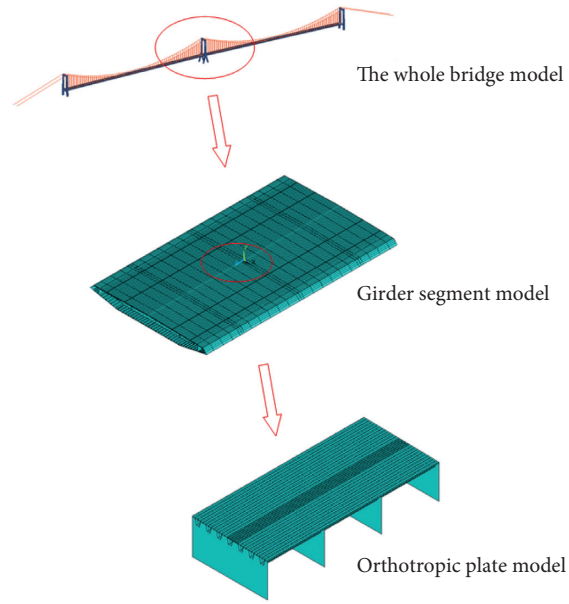


Figure 2: Schematic diagram of the three-stage analysis model.

*(1) Full-Bridge Model Analysis*. The full-size bridge model was the first stage of multiscale analysis. Firstly, the mechanical responses such as deflection, axial force, bending moment, and torque of the whole structure were analyzed. Secondly, the most unfavorable position of the girder segment was identified. Finally, the displacement response of the boundary part for the local refinement model was studied.

*(2) Subsection Model Analysis*. As a boundary condition, the response of the full-bridge model to the corresponding location of the local model was established. In this case, mechanical responses of the most unfavorable girder under the external load were calculated. Then, the influence of pavement structural stiffness on the most unfavorable girder segment was analyzed.

*(3) Finite Mixed-Element Model Analysis*. On the basis of size, structure, and analysis target, the orthotropic composite structure refinement model was established. Stress and strain of the pavement system under the most unfavorable force were extracted as the boundary conditions of the submodel.

*2.2.3. Test Model Design.* According to the selection of model structures, model tests can be divided into two types: full-scale model and small-scale model. The model of the full-scale model test is in good agreement with the prototype of the test structure, which can effectively avoid the error in reverse calculation, and the test results are accurate and reliable. Therefore, the full- scale model was selected. The idea of the design is shown in Figure 3. The main cable is consolidated at the anchorage, and the main cable is consolidated with the pylon. The boundary conditions of the FEM of the whole bridge are treated as follows: the pylon is set with vertical supports which can only slide along the bridge direction, and the pylon bottom is consolidated. The bridge design load is adopted as the load condition.

On the basis of analyzing the distribution characteristics of the SBDP stress response, the 3.2-meter-long longitudinal section and 2.4-meter-wide cross-section of the typical section were selected from the overall structure of the steel box girder. It was taken as the initial model of solid units under the synergistic effect of bridge deck and pavement, as shown in Figure 4.

## 3. Multiscale Numerical Model

*3.1. Full-Bridge Model.* The bending moment of the beam is the key to determine the most unfavorable beam. The deck pavement is constructed after the main bridge. Thus, mechanical analysis of the main bridge in the early stage should not be involved in the pavement, such as structural dead weight load and second-stage constant load. Main load originates from traffic load, temperature load, and wind load after completion of the bridge. Therefore, traffic load was taken as the main load, and vertical bending moment was taken as the main concern for internal forces for analysis in this paper. The most unfavorable girder segment of SBDP

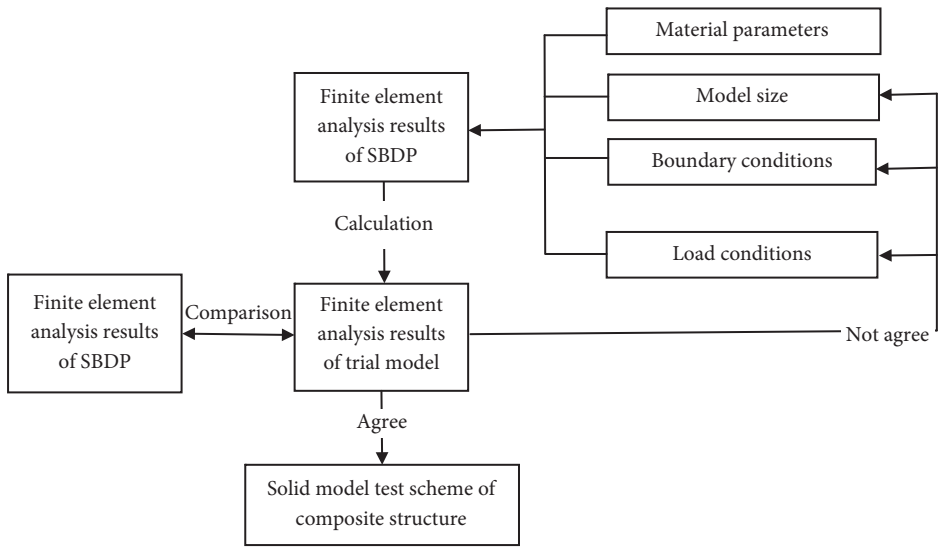


Figure 3: Design flow chart of the cooperative entity unit model for SBDP.

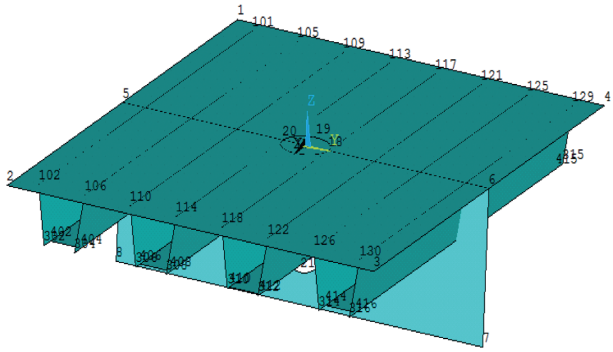

Figure 4: Three-dimensional FEM diagram of the initial model scheme of the solid element.

under live load was investigated. Analysis diagrams are shown in Figures 5 and 6.

The results showed that although the steel box girder of the middle tower was strengthened, the stress was still greater than that of the standard girder due to the excessive internal force. A 64-meter-long steel box girder segment in the mid-tower was identified as the most unfavorable. The length of the girder was 3.5 m relative to that of the steel box girder, which ensured the simulation accuracy of the middle section of the girder to its section. Then, the internal mechanical response on both sides of the girder was taken as the local boundary condition of the model.

### 3.2. Subsection Model

*3.2.1. Finite Mixed Element Method.* It is very important to accurately reflect the influence of the subsection model on the whole bridge so as to improve the accuracy of the model. The simulation of boundary conditions is the key to realize the overall effect of the bridge. To solve this problem, the boundary conditions of the girder segment model were simulated accurately by employing the finite mixed element method (FMEM), as shown in Figure 7.

*3.2.2. Critical Girder Segment Model.* There were four standard girder segments with 64 m in length and 39.1 m in width. It was simulated in the FMEM with ANSYS. The critical girder segment model is shown in Figure 8. Detailed structural size parameters of the steel box girder are shown in Table 1. There were two main materials in the subsection model. The other one was epoxy asphalt concrete, which is a temperature-sensitive material. Its elasticity modulus is a function of temperature, which decreases with the increase of temperature. Only normal temperature was considered, while modeling. Material parameters were selected on the basis of this temperature. The major material and structural parameters are listed in Tables 1 and 2.

### 3.3. Subelement Model

*3.3.1. Submodel Method.* Submodel method, also known as the cutting boundary displacement method or specific boundary displacement method, is realized by the cutting local model based on the analysis of the coarse mesh model. Mesh refinement can be divided and calculated in the submodel. The submodel method is a secondary analysis process, the key of which is the boundary cutting and data transmission of the submodel. The submodel method is suitable for the simulation of a large bridge to transmit the full-bridge data from the girder segment model to the next model, such as the orthotropic plate model.

*3.3.2. Orthotropic Composite System Model.* In order to improve the accuracy of the model and obtain the detailed rules of local stress, the orthogonal anisotropic plate at the key stress position of SBDP was intercepted on the basis of analyzing the model of the main beam segment. Therefore, the influence of the full-bridge effect on the deck pavement is considered in the orthotropic plate model, which could conveniently reflect the stress of the pavement system and deck. In addition, the bridge deck, diaphragm, and stiffener

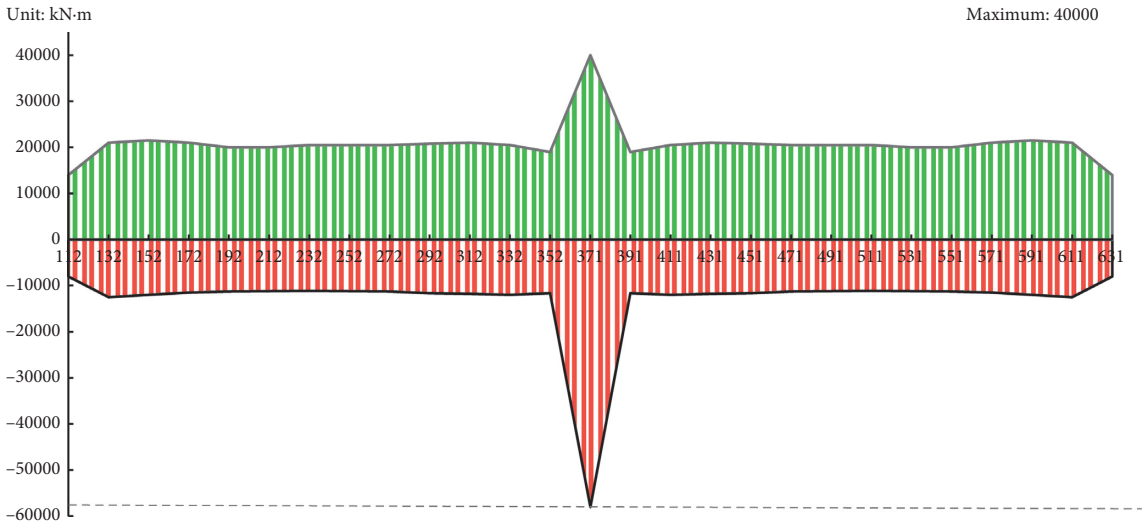


Figure 5: Bending moment envelope diagram of the girder under random traffic flow load.

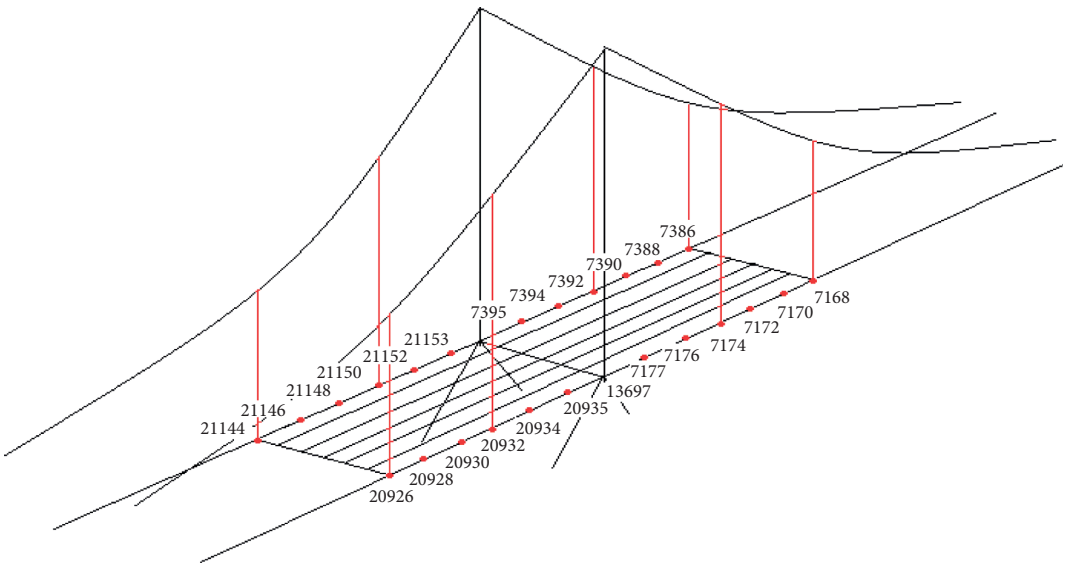


Figure 6: The most unfavorable beam diagram.

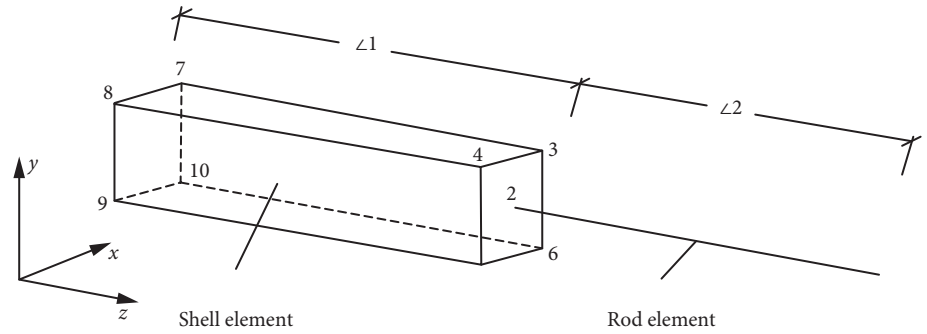


Figure 7: Diagram of the FMEM.

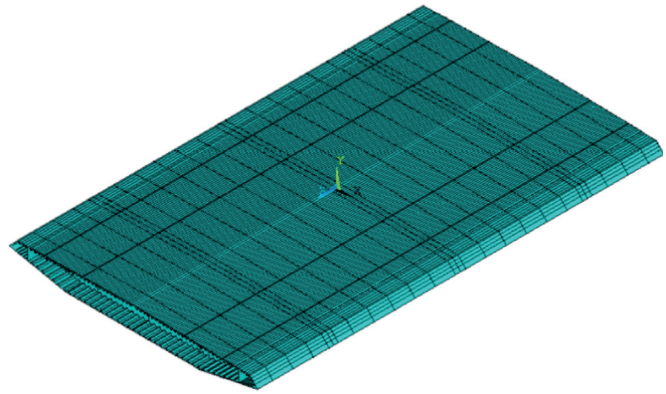

Figure 8: Critical segment model diagram.

Table 1: Material parameters used in the segment model.

| Steel | | Epoxy asphalt concrete | |
|---|---|---|---|
| Item | Value | Item | Value |
| Elasticity modulus | 210000 MPa | Elasticity modulus | 9000 MPa |
| Poisson's ratio | 0.3 | Poisson's ratio | 0.25 |

were simulated by the shell element and the pavement layer by the solid element. The orthotropic bridge model is shown in Figure 9.

### 3.4. Results' Analysis

#### 3.4.1. Girder Segment Model

*(1) Effect of the Deck Pavement to the Steel Box Girder*. The pavement layer actually contributes to the overall structural forces, especially anaphase loads such as vehicle load. The maximum vertical bending moment of standard middle-lane load was set as the girder segment model to study the contribution of the pavement layer to the entire bridge structure under vehicle load. The internal force of the roof in the pavement layer is shown in Figure 10.

As can be seen from the nephogram, the pavement layer plays an auxiliary role in the internal force of the roof. The maximum tensile stress decreased by 10% from 51 MPa to 44 MPa when there was the pavement. In order to confirm its influence on roof stress, the middle part of the bridge close to the inner pavement and the two longitudinal strips close to the edge of the bridge outside the pavement were selected for stress comparison, as shown in Figure 11. It can be concluded that the pavement layer has a greater impact on the roof stress not only limited to the pavement area but also on the whole structure. Under the action of moving load, the influence of the pavement layer on the roof was obvious.

*(2) Dynamic Random Vehicle Load*. In the full-bridge model, the calculation results of bending moment and torque on both sides of the steel box girder under the random dynamic load of the vehicle were quite different from those under lane load. The calculation results of internal forces under random dynamic load were applied to both sides of the main girder section. Traffic load on the center of the girder was taken as uniform load, as shown in Figures 12 and 13. It can be seen that when random dynamic load of the vehicle was applied, the longitudinal and transverse tensile stress peak values of the steel-box girder under the maximum bending moment envelope value were 1.65 MPa and 0.9 MPa, respectively, which increased by different extents compared with those under lane load. The longitudinal and transverse tensile stress peak value of the steel box girder under the maximum torque were 1.3 MPa and 0.86 MPa, respectively, higher than those under lane load.

For comparison, different results under traffic load and lane load were recorded, as shown in Table 3, indicating that the results of vehicles under random dynamic load increased to different degrees compared with those under lane load. The overall growth rate was about 40%, indicating that the simulation of increasing traffic volume was relatively lagging behind.

*3.4.2. Orthotropic Steel Plate Deck Model.* In order to analyze the influence of the characteristics of the whole bridge on the stress of the pavement layer, a high-rise analysis of the orthotropic steel plate was carried out without considering the influence of the whole bridge, that is, the conventional method was used for simulation without considering the initial boundary conditions. Dual-wheel load was transferred from middle span to diaphragm, as shown in Figures 14 and 15. The maximum longitudinal and transverse tensile stresses were 0.60 MPa and 0.93 MPa, respectively, appearing on both sides of the upper deck under dual-wheel load. The maximum longitudinal and interlaminar transverse shear stresses between the pavement layer and top deck of the steel box girder were 0.60 MPa and 1.24 MPa, respectively.

Considering the effect of the whole bridge, the results of the girder segment model were applied to the orthotropic plate model. The results of the orthotropic plate near mid-tower were selected to analyze the influence of the whole bridge on the high-rise model. As shown in Figures 16 and 17, the longitudinal tensile stress of the midspan pavement layer was about 0.14 MPa, and the maximum transverse tensile stress was 0.82 MPa when considering the effect of the whole bridge. When wheel load acted on the edge of the diaphragm, the longitudinal tensile stress was about 0.62 MPa, and the maximum

Table 2: Geometry dimensions of the subsection model.

| Project | Size (mm) | Project | Size (mm) |
|---|---|---|---|
| Steel box girder roof thickness | 14 | Thickness of steel box girder bottom plate | 10 |
| Diaphragm spacing | 3200 | Bottom-plate trapezoidal stiffening rib thickness | 6 |
| Diaphragm thickness | 12 | Floor stiffener lower-mouth width | 400 |
| U-shaped stiffener thickness | 6 | Floor stiffener spacing | 850 |
| U-shaped rib opening width | 300 | Floor stiffener height | 250 |
| U-shaped rib spacing | 600 | U-shaped rib height | 280 |

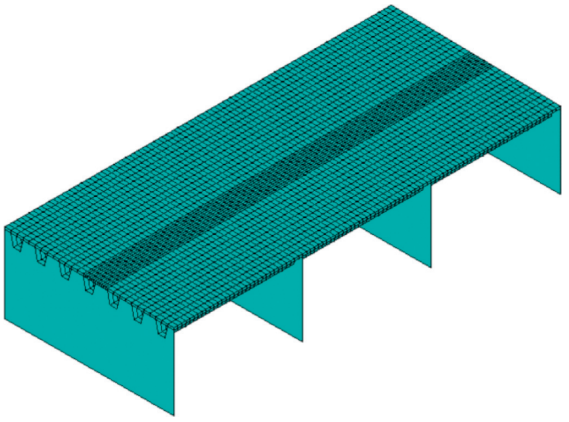

Figure 9: The orthotropic bridge model.

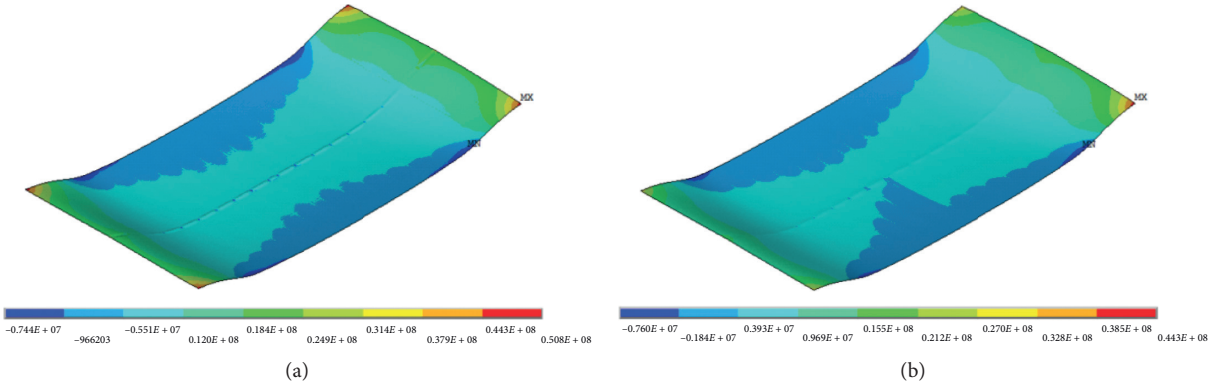


(a) (b)

Figure 10: Nephogram of the steel-box girder roof along the bridge. (a) The steel box girder without the pavement player. (b) The steel box girder with the pavement player.

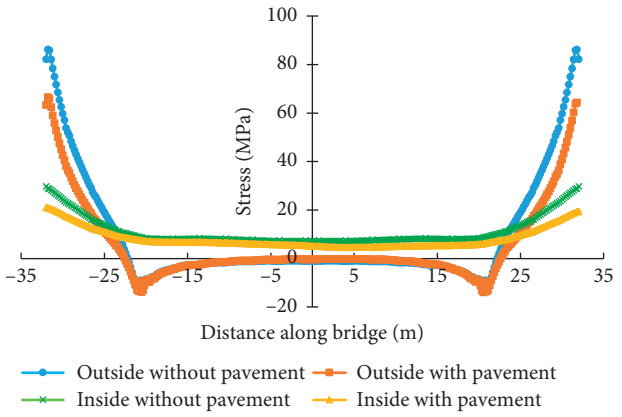


Figure 11: Impact of the pavement layer to steel box girder force.

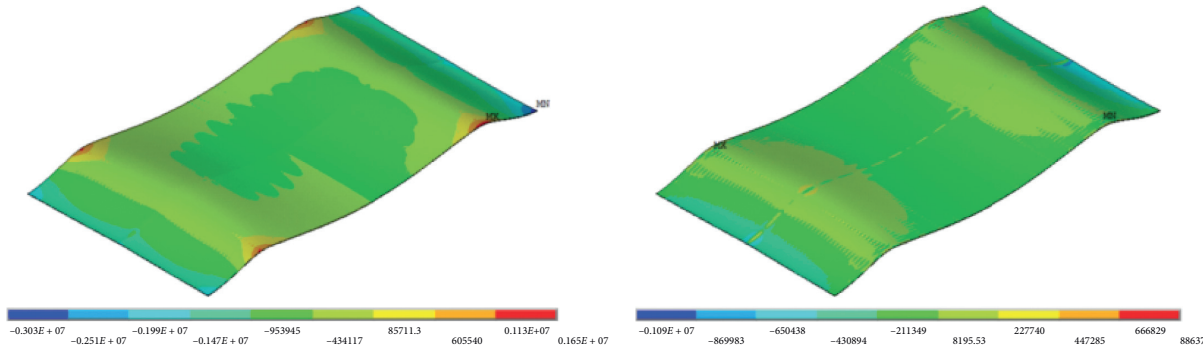


(a) (b)

Figure 12: The stress diagram of the pavement layer under the most unfavorable bending moment of the random traffic flow. (a) The longitudinal stress diagram. (b) The transverse stress diagram.

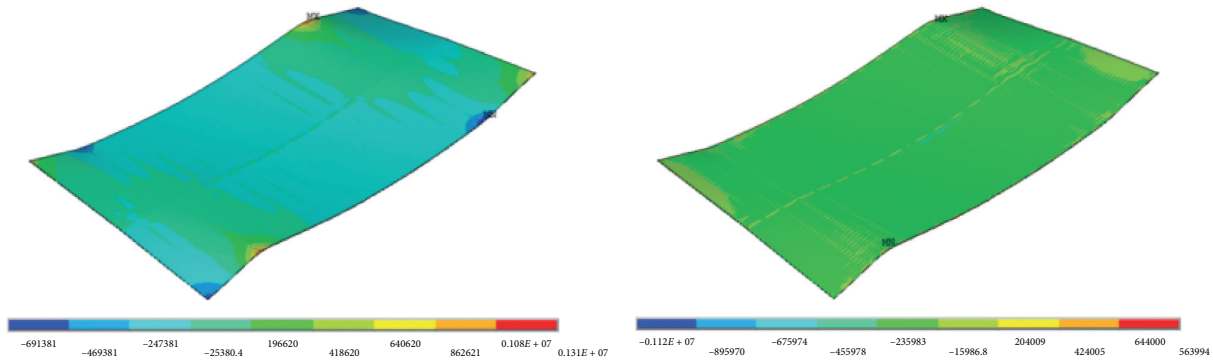


(a) (b)

Figure 13: The stress diagram of the pavement layer under the most unfavorable torque of the random traffic flow. (a) The longitudinal stress diagram. (b) The transverse stress diagram.

Table 3: Comparison of random traffic flow and lane load results.

| Moment | Stress | Load | Random traffic | Difference (%) |
|---|---|---|---|---|
| Bending moment | Longitudinal tensile stress | 1.18 | 1.65 | 39.83 |
| | Transverse tensile stress | 0.65 | 0.89 | 36.92 |
| | Main longitudinal tensile stress | 0.26 | 0.3 | 15.38 |
| | Transverse main tensile stress | 0.38 | 0.54 | 42.11 |
| Torque moment | Longitudinal tensile stress | 0.97 | 1.31 | 35.05 |
| | Transverse tensile stress | 0.64 | 0.86 | 34.38 |
| | Main longitudinal tensile stress | 0.3 | 0.56 | 86.67 |
| | Transverse main tensile stress | 0.2 | 0.47 | 135.00 |

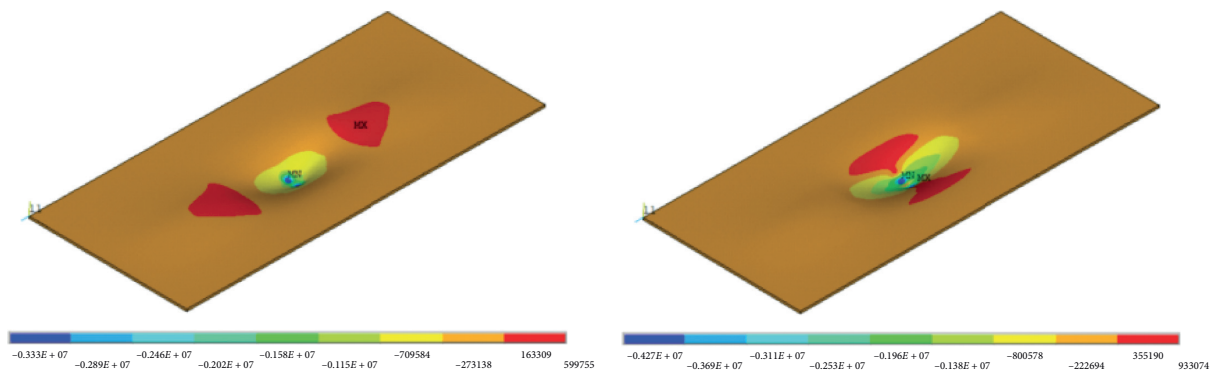


(a) (b)

Figure 14: The stress diagram of the midspan pavement layer under dual-wheel load. (a) The longitudinal stress diagram. (b) The transverse stress diagram.

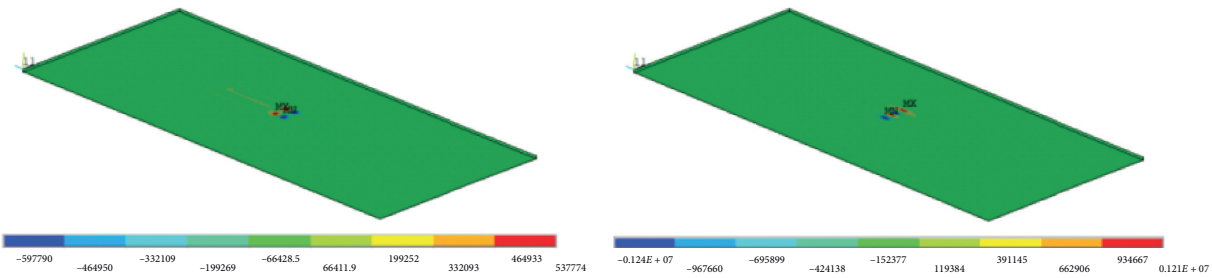


(a) (b)

Figure 15: The shear stress diagram of the midspan pavement layer under dual-wheel load. (a) Interlaminar longitudinal shear stress. (b) Interlaminar transverse shear stress.

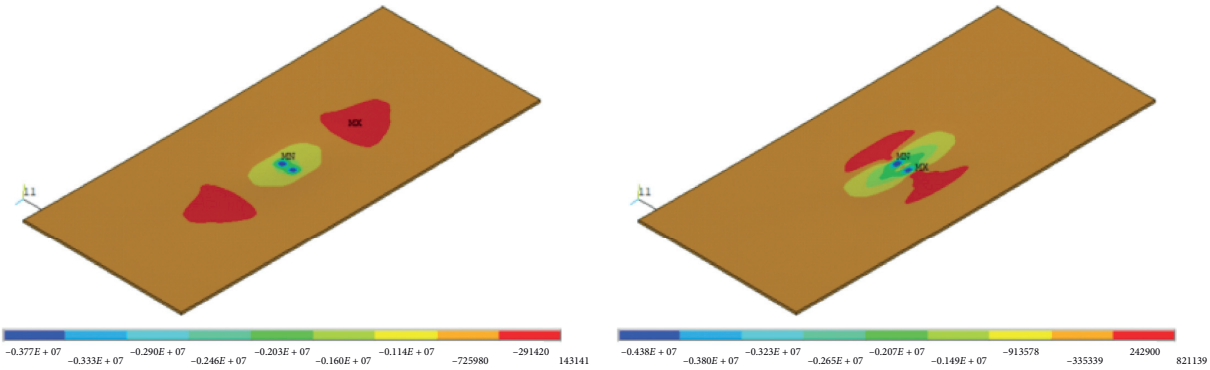


(a) (b)

Figure 16: The stress distribution diagram of the midspan pavement under wheel load under full-bridge action. (a) The longitudinal stress diagram. (b) The transverse stress diagram.

transverse tensile stress was 1.46 MPa. The results showed that the influence of the whole bridge on the orthotropic plate stress was very obvious, especially on the longitudinal stress. The longitudinal stress caused by wheel load could be offset by selecting the area with large positive moment, which also indicated that it is the same as the position with large negative moment. However, transverse stress was not significantly affected. When wheel load acted on the middle span of diaphragm, the maximum transverse stress decreased from 0.93 MPa to 0.82 MPa. In addition, when wheel load acted on the edge of diaphragm, the maximum transverse stress only decreased from 1.56 MPa to 1.46 MPa.

## 4. Experimental Program

*4.1. SBDP Synergy Test.* In order to verify the results of numerical simulation, a full-scale model was first established in the experimental stage. In order to study the dynamic response of the bridge deck pavement system, the random vehicle load system and multichannel strain-displacement measurement system are needed. Several key points were set both on the bare deck and paved deck. The dynamic response of the deck pavement of the multitower suspension bridge under dynamic load was studied by the data collected by sensors. Then, the calculated results were compared with the simulation results.

*4.1.1. The Establishment of the Full-Scale Model.* According to the structural parameters and geometric dimensions of the full-size structural test model (Figure 18), box-type stud welding Q390 large thick steel plates were used. In addition, they were cut to the relevant dimensions required by the full-size test model. Then, they were processed and installed. The processing process and post-installation model are shown in Figure 19.

*4.1.2. Load System.* In order to study the dynamic response of the bridge deck pavement, a load system which can realize the stochastic dynamic loading mode and has large load tonnage was required. Therefore, the large portal MTS hydraulic servo-loading system was selected as the load test system in this project.

*4.1.3. Multichannel Strain Displacement Testing System.* The length and width of the full-length structure are larger. The response characteristics of loads at different positions are also complex. In order to study the mechanical

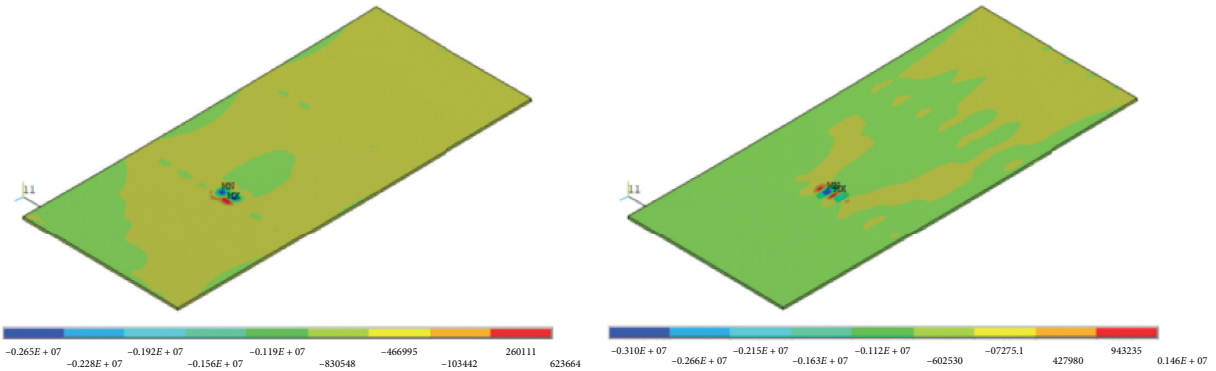


(a) (b)

Figure 17: The shear stress distribution diagram of the midspan pavement under wheel load under full-bridge action. (a) Interlaminar longitudinal shear stress. (b) Interlaminar transverse shear stress.

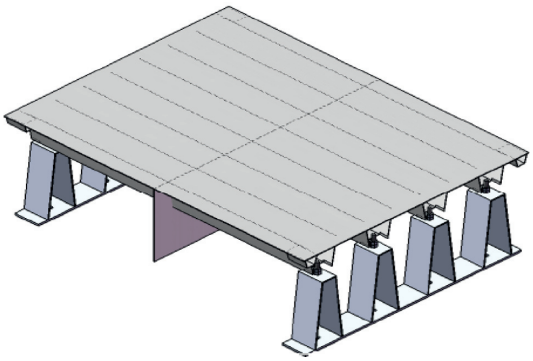

Figure 18: Effect diagram of the full-scale structure test model.

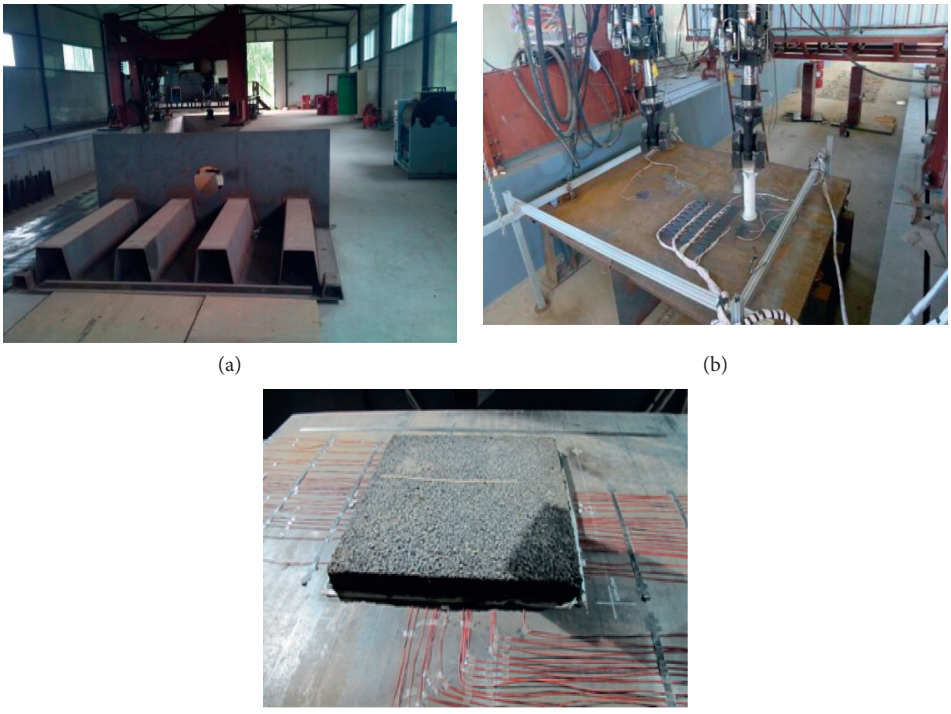

(a) (b)

(c)

Figure 19: Processing and installation process of the full-scale structural test model with the SBDP synergistic effect. (a) The orthogonal anisotropic bridge-panel model. (b) The full-scale test model after completion. (c) The full-scale test model with the pavement.

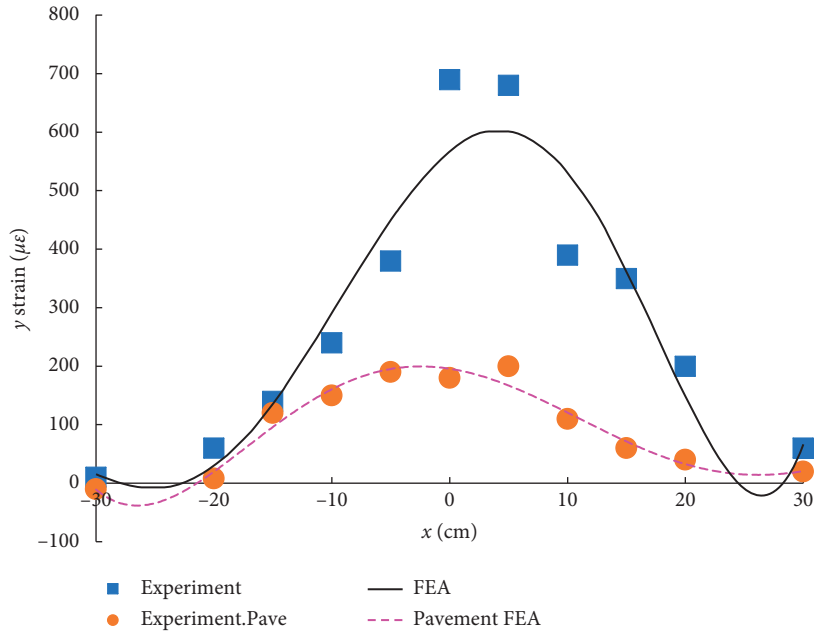


Figure 20: The strain at the top surface ($Y = +15$ cm) of the U-shaped stiffening rib-side plate.

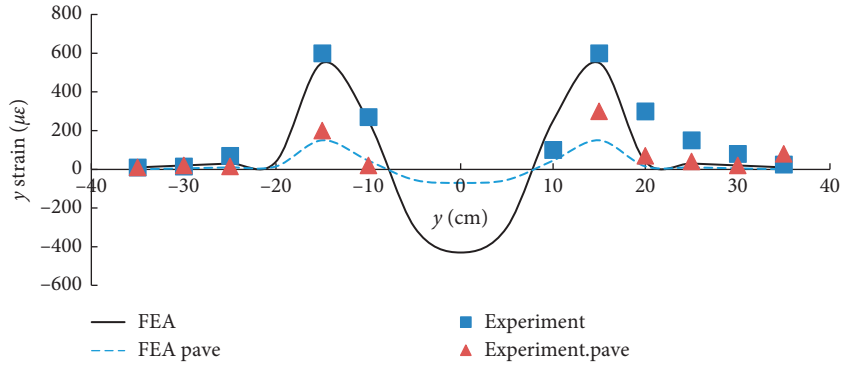


Figure 21: Strain at the transverse bridge section (i.e., $X = 0$ cm position) passing through the load center point.

characteristic points and sections of the full-scale model, a test system that could collect the load response, stress, strain, and displacement of different measuring points was needed.

*4.2. Comparative Analysis of Test and Numerical Simulations.* In order to study the multispan suspension characteristics of the deck pavement, the mechanical response of bare steel-box girder deck under the action of dynamic load was firstly studied. On this basis, the mechanical response characteristics of the composite structure of the steel-box girder bridge with the deck pavement under the action of dynamic load were studied. In the study, strains of several characteristic points were compared and analyzed, as shown in Figures 20 and 21.

It can be seen that the measured value of the steel-bridge deck pavement with the pavement layer was close to the calculated value of the finite element model, and the overall trend and rule were consistent, but there were certain deviations. According to the above calculation and analysis, the steel plate thickness and the constraint conditions of diaphragm exert a very important influence on the mechanical response of the whole model.

Due to the steel plate processing and welding used in the unit solid structure model, the thickness of the steel plate was not uniform, and the size deviation of different positions was large. Therefore, the unit entity structure model size and the thickness of the steel plate were measured. And, the elastic modulus of steel was tested. On the basis of the finite element numerical model, the related parameters were processed and further modified. The modification contents and methods are as follows:

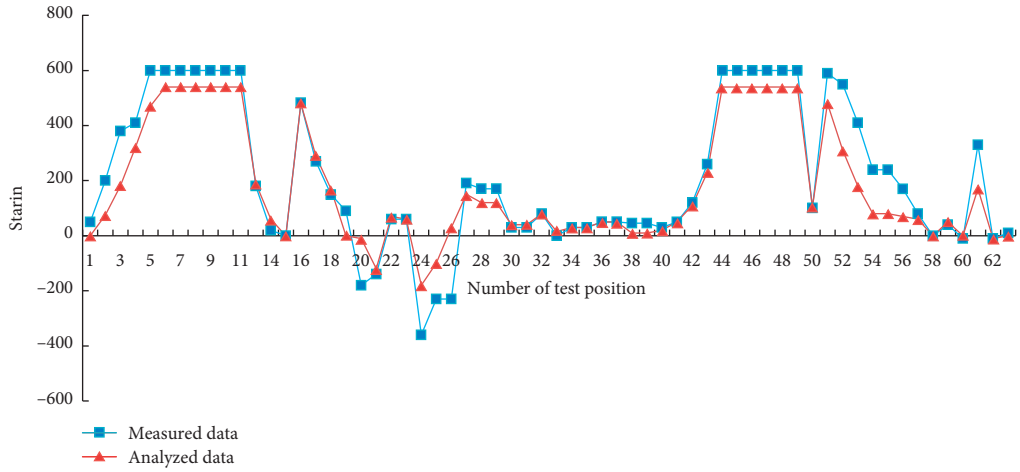


Figure 22: Comparison of measured and finite element numerical calculation results (strain).

(1) The measured structural dimensions and thickness of the steel deck element solid model were substituted into the finite element numerical model

(2) The elastic modulus of the processed steel plate was measured

(3) Boundary conditions with vertical constraints were adopted instead of the consolidation support

After the above modification of the finite element numerical model, a comparative analysis was conducted between the strain measured under the static load of the bare slab and the finite element numerical calculation results, as shown in Figure 22.

As can be seen from Figure 22, after the modification of the finite element numerical model, the experimental measured results of the full-size model had a very good correlation with the calculation results of the finite element numerical model. The variation trend of the data was completely consistent with the strain direction, and the numerical values were also very close.

## 5. Conclusion and Discussion

In this paper, the mechanical response of SBDP of the multitower suspension bridge under moving load was analyzed by multiscale numerical and experimental methods. Considering the full-bridge effect of the multitower-span suspension bridge, the three-stage finite element refinement model of the steel-bridge deck pavement composite structure was studied. Additionally, the full-scale experimental model was established to verify the simulation results. From the above analysis, the following conclusions can be drawn:

(1) The pavement layer contributes to the stress of the steel box girder. In the most unfavorable model of the bridge, the pavement layer reduces the maximum stress by about 10%.

(2) The mechanical response of the pavement layer under the random traffic flow is generally 40% larger than that under the standard load. It can be seen that the actual moving load is underestimated in the standard as the volume of traffic increases.

(3) Three-tower and two-span bridge structures have a great influence on the vertical deformation of the pavement under vehicle load. Therefore, the pavement material should have great deformation capacity.

(4) The full-bridge effect also has an obvious influence on the stress of the local orthotropic plate, especially the longitudinal stress, but has little influence on the transverse stress.

(5) The experimental measured results of the full-size model have a very good correlation with the calculation results of the finite element numerical model, which demonstrates the validity of multiscale numerical results.

The research results can provide guidance for the design and construction of SBDP in a multitower suspension bridge.

## Data Availability

The data used to support the findings of this study are included within this article.

## Conflicts of Interest

The authors declare that there are no conflicts of interest regarding the publication of this paper.

## Acknowledgments

This work was supported by Natural Science Foundation of Jiangsu (Grant no. BK20191267) and Fundamental Research Funds for the Central Universities (Grant no. 2242020R40094).

## References

[1] J. Cheng, H. Xu, and M. Xu, "Study on midtower longitudinal stiffness of three-tower four-span suspension bridges with steel truss girders," *Structural Engineering and Mechanics*, vol. 73, no. 6, pp. 641–649, 2020.

[2] S. B. Chai, R. C. Xiao, X. L. Wang, and X. Ren, "Analytic method for calculating anti-slip safety factor between main cable and saddle in multi-tower suspension bridge," *China Journal of Highway and Transport*, vol. 29, no. 4, pp. 59–66, 2016.

[3] W. Huang, "Integrated design procedure for epoxy asphalt concrete–based wearing surface on long-span orthotropic steel deck bridges," *Journal of Materials in Civil Engineering*, vol. 28, no. 5, Article ID 04015189, 2016.

[4] L. L. Chen, G. Liu, Z. D. Qian, and X. F. Zhang, "Determination of allowable rutting depth based on driving safety analysis," *Journal of Transportation Engineering Part B Pavements*, vol. 146, no. 2, Article ID 04020023, 2020.

[5] S. R. Chen and J. Wu, "Dynamic performance simulation of long-span bridge under combined loads of stochastic traffic and wind," *Journal of Bridge Engineering*, vol. 15, no. 3, pp. 219–230, 2010.

[6] J. M. Cai, "Better fitting for distribution of vehicles flow on road segment of city," *Journal of Shanghai University of Engineering Science*, vol. 20, no. 2, pp. 100–103, 2006.

[7] T. Wang, W. Han, F. Yang, and W. Kong, "Wind-vehicle-bridge coupled vibration analysis based on random traffic flow simulation," *Journal of Traffic and Transportation Engineering (English Edition)*, vol. 1, no. 4, pp. 293–308, 2014.

[8] P. F. Liu, J. Hu, H. Wang, F. G. Canon, D. Wang, and M. Oeser, "Influence of temperature on the mechanical response of asphalt mixtures using microstructural analysis and finite-element simulations," *Journal of Materials in Civil Engineering*, vol. 30, no. 12, Article ID 04018327, 2018.

[9] P. F. Liu, H. N. Xu, D. W. Wang, C. Schulze, and M. Oeser, "Comparison of mechanical responses of asphalt mixtures manufactured by different compaction methods," *Construction and Building Materials*, vol. 162, no. 2018, pp. 765–780, 2019.

[10] P. F. Liu, Q. Zhao, H. L. Yang et al., "Numerical study on influence of piezoelectric energy harvester on asphalt pavement structural responses," *Journal of Materials in Civil Engineering*, vol. 31, no. 3, Article ID 04019008, 2019.

[11] Q. H. Huang, Z. D. Qian, L. L. Chen, and M. Zhang, "Evaluation of epoxy asphalt rubber with silane coupling agent used as tack coat for seasonally frozen orthotropic steel bridge decks," *Construction and Building Materials*, vol. 241, no. 30, Article ID 117957, 2020.

[12] Q. H. Huang, Z. D. Qian, J. Hu, and D. Zheng, "Investigation on the properties of aggregate-mastic interfacial transition zones (itzs) in asphalt mixture containing recycled concrete aggregate," *Construction and Building Materials*, vol. 269, no. 1, Article ID 121257, 2021.

[13] Q. H. Huang, Z. D. Qian, Y. M. Yang, and D. Zheng, "Investigation of warm mix epoxy asphalt compaction with gyratory compactor and charge coupled photoelectric imaging," *Construction and Building Materials*, vol. 271, no. 15, Article ID 121506, 2021.

[14] F. J. Zhao, "The research on design method for steel deck asphalt pavement on large-pan steel box beam bridges", PhD Dissertation, Hunan University, Changsha, China, 2012.

[15] C. Wu, H. Y. Liu, Z. H. Zhang, and Y. Sun, "Influence of pavements temperature on fatigue life of orthotropic deck of steel bridge," *Journal of Tongji University (Natural Science)*, vol. 41, no. 8, pp. 1213–1218, 2013.

[16] S. Kainuma, Y.-S. Jeong, J.-H. Ahn, T. Yamagami, and S. Tsukamoto, "Behavior and stress of orthotropic deck with bulb rib by surface corrosion," *Journal of Constructional Steel Research*, vol. 113, pp. 135–145, 2015.

[17] S. Iglouli, N. Boumechra, and K. Hamdaoui, "Damage or change detection in a small scale model of steel bridge deck under static loading by extensometery," *IOP Conference Series: Materials Science and Engineering*, vol. 419, Article ID 012024, 2018.

[18] A. Kasprzak and A. Berger, "Strengthening and widening of steel single box girder bridge in Warsaw," *Structural Engineering International*, vol. 29, no. 4, pp. 533–536, 2019.

[19] Z. D. Qian, W. Huang, X. Du, and L. Yun, "Research on effects of shape of long-span cable-supported bridge on mechanical analysis of surfacing under vehicular load," *Strategic Study of CAE*, vol. 8, no. 9, pp. 35–41, 2006.

[20] L. L. Chen, Z. D. Qian, D. X. Chen, and Y. Wei, "Feasibility evaluation of a long-life asphalt pavement for steel bridge deck," *Advances in Civil Engineering*, vol. 2020, Article ID 5890945, 8 pages, 2020.

[21] L. L. Chen, Z. D. Qian, and C. Zhang, "Bridge structure effect in the crack analysis of the steel deck pavement," in *Proceedings of the Geo-Hubei 2014 International Conference on Sustainable Infrastructure*, Yichang Hubei, China, 2014.

[22] Z. D. Qian and Y. Liu, "Mechanical analysis of waterproof bonding layer on steel bridge deck under bridge-temperature-load coupling effect," *Journal of Southeast University (Natural Science Edition)*, vol. 42, no. 4, pp. 729–733, 2012.

[23] J. P. Zhang, S. W. Liu, and Y. J. Liu, "Large-scale model test on mechanics characteristics of composite pavement of steel bridge deck," *Journal of Tongji University*, vol. 41, no. 12, pp. 1837–1842, 2013.

Hindawi
Advances in Materials Science and Engineering
Volume 2021, Article ID 5572011, 16 pages
https://doi.org/10.1155/2021/5572011

*Research Article*

# Investigation on Durability Behaviour and Optimization of Concrete with Triple-Admixtures Subjected to Freeze-Thaw Cycles in Salt Solution

**Xuejiao Li**,[1] **Wensheng Wang**,[2] **Zhiqing Zhu**,[2] **and Kunkun Zheng**[3]

[1]*Changchun University of Architecture and Civil Engineering, Changchun 130604, China*
[2]*College of Transportation, Jilin University, Changchun 130025, China*
[3]*Guangdong Aohong Technology Co.,Ltd., Zhongshan 528437, China*

Correspondence should be addressed to Wensheng Wang; wangws@jlu.edu.cn and Zhiqing Zhu; zhuzqjlu@163.com

Received 6 January 2021; Revised 23 January 2021; Accepted 29 January 2021; Published 11 February 2021

Academic Editor: Qinglin Guo



In the seasonal frozen area of northeast China, cement concrete is usually in a working environment of cold climate and chlorine erosion coupling effect. In general, with a reasonable addition of air entraining agent (AEA) and multimineral admixtures such as fly ash, blast furnace slag, and silica fume, the durability of cement concrete under the effects of freeze-thaw and salt solution can be significantly improved in cold regions. However, due to several more compositions of cement concrete with multiple mineral admixtures, it would take excessive trial mixtures to select the desired mixture proportion based on the conventional method. This means a great deal of costs of raw materials and laboratory experimental time. In this paper, the experimental scheme of mixture proportion for air-entrained concrete with multimineral admixtures was designed based on the orthogonal experiment design method. Based on the compressive strength, rapid chloride permeability, and weight loss and relative dynamic elastic modulus after salt freeze-thaw cycles, the influence of different mineral admixtures and their dosages on the durability of concrete subjected to freeze-thaw in salt solution was analyzed. After that, based on genetic algorithm, an optimization of mixture proportion was proposed, which only requires less trial mixes and accessible optimization process. The test results indicated the superiority of air-entrained concrete with multimineral admixtures when serving in salt freeze-thaw environment. Eventually, it was also verified that the optimized concrete in this paper could achieve pleasurable durability performances under salt freeze-thaw cycles.

## 1. Introduction

With the advantages of high strength, considerable durability, and promising economy, concrete has been one of the most widely used building materials in civil engineering since the 20th century [1–6]. When optimizing mix proportion of concrete in many, if not most, engineering construction of China, the trial mix with highest strength is the chosen mix proportion [7–12]. Actually, the durability indexes of concrete deserve the same attention as the strength index, especially when the concrete is working in harsh environment [13–17]. In northeast China where the authors are located, as an example, de-icing salt has been invariably used to melt ice and snow on roads for decades [18–20]. Consequently, concrete pavements and bridges suffer from freezing and thawing environment strengthened by salt solution. A large number of cases have shown that the durability of concrete with rosy frost resistance will be greatly reduced when serving in this salt freeze-thaw condition. The presence of salt solutions eventually results in premature spalling of the concrete surface [21, 22], which gives rise to additional maintenance costs every year [23, 24].

The air entraining agent (AEA) is undoubtedly the most critical admixture in order to improve the frost resistance of concrete [25, 26]. The addition of air entraining agent brings a large number of tiny, enclosed bubbles inside the concrete. The work of Wellman et al. indicated that these bubbles block the growth of the bodies of ice and the generation of hydraulic pressure as water freezes in capillary cavities, effectively improving the frost resistance of concrete [27].

There are quite a few influential factors impacting air entrainment, in which bubble size and bubble distribution are decisive factors [28–30]. However, it is extremely difficult to obtain the bubble size and distribution in fresh concrete for engineering builders. As a rule, measuring the total air content as a quality control measure of air entrainment is practical [30]. Subsequently, much of research has suggested that the optimal air contents are invariably below 7% when giving consideration to concrete strength, frost resistance, and workability [31]. Recently, super air meter has become a popular tool for assessing air-void system of fresh concrete. Not only does the total air-void content matter but also the distance between different air bubbles plays an important role in controlling freeze-thaw damage in concrete. Powers indicated that the reason for that is the spacing factor of air voids rather than the air content, and concrete with spacing factor less than 200 $\mu$m should have a good freezing-thawing resistance [32]. Yuan et al. used CT to obtain the bubble structure distribution information and proposed the void-to-void distance as a factor to evaluate the freezing-thawing resistance with deicing salts performance of cement concrete [33].

On the other hand, environment-friendly mineral admixtures for concrete such as fly ash (FA), blast furnace slag (BFS), and silica fume (SF) are strongly recommended to improve salt freeze-thaw resistance because of their contributions to microstructure of concrete [34, 35]. Studies on mechanism for salt freeze-thaw have suggested that the invasion of chlorides is responsible for damage from salt crystals, high degree of saturation, and additional hydraulic pressure [36, 37]. This damage can be alleviated by rational addition of mineral admixtures, which are pozzolanic and finer than cement, filling pore structure, and interfacial transition zone of concrete. Consequently, the penetration coefficient of chloride ion would be reduced significantly [38]. Moreover, the reasonable combination of multimineral admixtures would enable concrete to show better performance than that of single mineral admixture [39, 40]. For instance, when being used together as the composite mineral admixtures in cement paste, FA can reduce the autogenous shrinkage, while SF can increase the autogenous shrinkage, making up each other accordingly [41]. In the case of addition of SF, BFS, and FA at the same time, Sun et al. believed that SF provides main prophase strength amongst these three types of mineral admixtures due to its highly early pozzolanic reaction [42]. Then, BFS begins to develop its pozzolanic effect during transitional period. After 28 days, FA also gradually exhibits its own properties and provides its contributions to the strength of concrete. In terms of improvement of resistance to concrete deteriorating factors, Bapat emphasized that the use of mineral admixtures in concrete is the cheapest alternative [43].

In northeast China, the design strength grade of C40 is sufficient for construction concrete in many cases. By contrast, the durability of concrete served in salt-frost environment has been more emphasized heavily recently. When taking the concrete technical factors such as design requirements, construction methods, times, and strength grade into consideration, the high-performance concrete might not be suitable for adoption. Accordingly, the air-entrained concrete with multimineral admixtures would be an overwhelmingly feasible and economical choice to improve the resistance of concrete to salt frost erosion. However, when using conventional method to design the mix proportion of air-entrained concrete with multimineral admixtures, a large number of trial mixes are required to select the desired combination of materials that meets special performance, which would be costly, time-consuming, and sometimes uneconomical and wasteful [44, 45]. From these considerations, a simple genetic algorithm was applied to optimize the mix proportion design of this multiconstituent concrete in this paper. The genetic algorithm is a global optimizing method which imitates biological evolution and has an advantage over many other methods on handling multiple objectives [46]. Actually, the fitness functions of different indices such as strength, slump, material price or else, have been adopted by researchers in order to obtain optimum mix proportions for target concrete properties through genetic algorithm [47, 48]. In this paper, aiming at improving the resistance of concrete to salt frost erosion, the mix proportion of air-entrained concrete with multimineral admixtures was designed based on genetic algorithm, in which the fitness functions of salt freeze-thaw resistance indices were adopted.

This paper discussed the mix proportion design of air-entrained concrete with multimineral admixtures based on genetic algorithm. Firstly, the authors earmarked the air content of concrete as a priority parameter and divided it into three feasible levels, because the influence of air entraining agent on the frost resistance of concrete is much more significant than that of mineral admixtures according to available literature and field experience. Then, the dosages of fly ash (FA), blast furnace slag (BFS), and silica fume (SF) were earmarked as secondary parameters, and the number of trial mixes with different dosages of mineral admixtures was reduced by orthogonal design. Subsequently, the salt freeze-thaw resistance indices such as strength, rapid chloride permeability, weight loss, and relative dynamic module of elasticity of concrete were tested and analyzed. Finally, fitness functions for testing results were derived through regression analysis and the optimum concrete mix proportions were obtained through genetic algorithm.

## 2. Materials and Methods

*2.1. Raw Materials.* All materials used in this paper were obtained from a concrete construction site in Jilin Province, China. The grade P.O. 42.5 ordinary Portland cement was procured from Jilin Yatai Dinglu Cement Ltd., and the physical properties meet the requirements of Chinese specification GB 175-2007. Studies have shown that concrete mixed with fly ash (FA), blast furnace slag (BFS), silica fume (SF), or air-entrainment agent (AEA) has better salt freeze-thaw resistance [49–52]. In order to achieve the reasonable application of mineral admixtures and AEA in concrete to improve the salt freeze-thaw resistance, FA, BFS, SF, and AEA were introduced into cement concrete. The properties and main chemical compositions of cement, FA, BFS, and SF are shown in Table 1.

Table 1: Properties and main chemical compositions of cement and mineral admixtures.

| Properties | Cement | FA | BFS | SF |
|---|---|---|---|---|
| Specific gravity | 3.12 | 2.19 | 2.83 | 2.18 |
| Surface area ratio ($m^2$/kg) | 358 | 420 | 450 | 18500 |
| $SiO_2$ (%) | 20.62 | 51.27 | 32.28 | 90.21 |
| CaO (%) | 65.07 | 3.21 | 40.23 | 0.23 |
| $Al_2O_3$ (%) | 5.14 | 28.92 | 12.92 | 0.61 |
| MgO (%) | 0.87 | 1.85 | 7.40 | 0.52 |
| $Fe_2O_3$ (%) | 3.96 | 7.63 | 2.25 | 0.22 |
| Loss on ignition (%) | 1.6 | 3.41 | 1.02 | 1.9 |

Triterpenoid saponin AEA with the type of SJ-2 was used to achieve different air contents in cement concrete. And naphthalene superplasticizer was also introduced into trial concrete mixes to keep consistent workability. Referring to the study of Rakinul Islam [53], natural sand with maximum size of 9.5 mm was used as coarse aggregate and well-graded river sand with fineness modulus of 2.0 was used as fine aggregate, which were obtained from Jilin Province, China. The specific gravities for natural gravel and river sand are 2.76 and 2.64, respectively. The sieving test results of coarse and fine aggregates are shown in Table 2.

*2.2. Mixture Proportion and Specimen Preparation.* In this paper, the reasonable dosages of AEA and multimineral admixtures were studied through the orthogonal experimental design [54–56]. Considering that the influence of AEA on the frost resistance of concrete is higher than that of multimineral admixtures [31], the AEA content was regarded as the priority parameter and divided into three feasible range levels of air content, i.e., $(2.5 \pm 0.5)\%$, $(4.5 \pm 0.5)\%$, and $(6.5 \pm 0.5)\%$. Then, the orthogonal experimental design for the dosages of multimineral admixtures at each range level of air content was carried out, which is presented in Table 3. In the orthogonal experimental design, based on the existing literature [54–57], the dosage of FA or BFS should be controlled within 30% by the total weight of cementitious materials, respectively. Meanwhile, the total dosage of FA and BFS was limited to less than 40% by the total weight of cementitious materials. By contrast, the dosage of SF was controlled not to exceed 10% due to its high activity and cost.

Table 3 provides an orthogonal experimental design with three factors at three levels, in which "A" means the total dosage of FA and BFS, "B" is the dosage ratio of FA to BFS, and "C" means the dosage of SF.

According to the orthogonal design in Table 3, a total of 9 groups of concrete proportions are listed in Table 4. Cement, FA, BFS, and SF were used as the main components of binders and the total binder content in all concrete specimens was kept at 423 kg/$m^3$. A target concrete strength grade of C40 was selected for pavement concrete mixtures, and the water-to-binder ratio was also kept constant at 0.40. After that, a concrete mixer was applied to mix all the raw materials, and naphthalene superplasticizer was carefully added to the mixture to maintain a slump range of 50–70 mm, as shown in Figure 1(a). In accordance with the Chinese specification JTG E30-2005, three groups of air content range levels, $(2.5 \pm 0.5)\%$, $(4.5 \pm 0.5)\%$, and $(6.5 \pm 0.5)\%$, were controlled and are illustrated in Figure 1(b). Then, the concrete specimens were casted and cured in the temperature and humidity control chamber for 28 days. Three replicates for each specimen were prepared for each test.

*2.3. Test Methods*

*2.3.1. Compressive Strength Test.* The compressive strength at the age of 28 days was tested according to the Chinese specification GB/T 50081-2019. The specimen sizes of compressive strength test are 100 mm × 100 mm × 100 mm and the universal testing machine was performed on three replicate specimens for the mechanical tests, as shown in Figure 2. For the compressive strength test, the loading rate was set as 0.5 MPa/s. During the whole process of test loading, the load and deflection of the specimens were recorded in real time. Then, the corresponding compressive strength ($S_c$) could be calculated as follows:

$$S_c = \frac{F_c}{A}, \tag{1}$$

in which $F_c$ and $F_f$ are the compressive and flexural failure loads, respectively, and $A$ is the area of the pressure surface of specimens; $A = 100^2$ mm$^2$ in this paper.

*2.3.2. Rapid Chloride Permeability Test.* The rapid chloride permeability test of cement concrete was carried out to evaluate the resistance to chloride ion penetration of concrete according to the Chinese specification GBT 50082-2009 (ASTM 1202). These specimens of rapid chloride permeability test were 100 mm in diameter and 50 mm in height. The side surfaces of all specimens were firstly coated with rapid setting epoxy. These specimens were placed inside an automatic vacuum water-soaking machine to saturate for 18 hours and then the rapid chloride permeability of concrete specimens was determined. The setups of surface resistivity test and rapid chloride permeability test are illustrated in Figure 3.

*2.3.3. Salt Freeze-Thaw Cycle Test.* For the purpose of making explicit the damage process of salt freeze-thaw, the concrete specimens with size of 40 mm × 40 mm × 160 mm were immersed in 3% concentration salt solution and exposed to freeze-thaw condition at the same time. A special freeze-thaw machine was adopted to create temperature conditions, as shown in Figure 4. The duration of one freeze-thaw cycle was 12 hours, in which the lowest and highest temperature were −18°C and 18°C, respectively. The freeze-thaw test was terminated when any specimen showed considerable surface damage or reduction in relative dynamic modulus of elasticity value of more than 80% of the initial value.

After multiple salt freeze-thaw cycles, the weight of concrete specimens and ultrasonic propagation speeds in

Table 2: Sieving results of coarse and fine aggregates.

| Size (mm) | | 9.5 | 4.75 | 2.36 | 1.18 | 0.6 | 0.3 | 0.15 |
|---|---|---|---|---|---|---|---|---|
| Cumulative sieve residue (%) | Coarse | 4 | 95 | 99 | — | — | — | — |
| | Fine | — | 3.44 | 15.25 | 27.62 | 46.70 | 77.84 | 95.65 |

Table 3: The orthogonal experimental design of concrete with multiadmixtures in this paper.

| Properties | Level I (L-I) | Level II (L-II) | Level III (L-III) |
|---|---|---|---|
| "A"-dosage of FA and BFS (%) | 10 | 25 | 40 |
| "B"-dosage ratio of FA/BFS | 1 : 3 | 2 : 2 | 3 : 1 |
| "C"-dosage of SF (%) | 3 | 6 | 9 |

Table 4: Mix proportions of concrete with multiadmixtures (kg/m$^3$).

| Group no. | A | B | C | Cement (kg/m$^3$) | Water (kg/m$^3$) | FA (%) | BFS (%) | SF (%) | Fine aggregate (kg/m$^3$) | Coarse aggregate (kg/m$^3$) |
|---|---|---|---|---|---|---|---|---|---|---|
| 1 | L-I | L-I | L-I | 368 | 170 | 2.50 | 7.50 | 3.00 | 584 | 1240 |
| 2 | L-I | L-II | L-II | 355 | 170 | 5.00 | 5.00 | 6.00 | 584 | 1240 |
| 3 | L-I | L-III | L-III | 343 | 170 | 7.50 | 2.50 | 9.00 | 584 | 1240 |
| 4 | L-II | L-I | L-II | 292 | 170 | 6.25 | 18.75 | 6.00 | 584 | 1240 |
| 5 | L-II | L-II | L-III | 279 | 170 | 12.50 | 12.50 | 9.00 | 584 | 1240 |
| 6 | L-II | L-III | L-I | 305 | 170 | 18.75 | 6.25 | 3.00 | 584 | 1240 |
| 7 | L-III | L-I | L-III | 216 | 170 | 10.00 | 30.00 | 9.00 | 584 | 1240 |
| 8 | L-III | L-II | L-II | 241 | 170 | 20.00 | 20.00 | 3.00 | 584 | 1240 |
| 9 | L-III | L-III | L-I | 228 | 170 | 30.00 | 10.00 | 6.00 | 584 | 1240 |

Note: the dosages of FA, BFS, and SF are the weight ratio by the total binder.

specimens were measured, as shown in Figure 4. Then, the variations of weight loss ($WL_v$) and relative dynamic elasticity modulus ($EM_v$) of specimens can be calculated by using equations (2) and (3), respectively:

$$WL_v = \frac{W_0 - W_v}{W_0} \times 100\%, \quad (2)$$

$$EM_v = \frac{E_v}{E_0} = \frac{(v_v)^2}{(v_0)^2} \times 100\%, \quad (3)$$

where $W_0$ and $v_0$ are the initial weight of concrete specimens and ultrasonic propagation speed in specimens before exposed to salt freeze-thaw condition, respectively, and $W_v$ and $v_v$ are the weight of concrete specimens and ultrasonic propagation speed in specimens after multiple salt freeze-thaw cycles, respectively.

## 3. Results and Discussion

### 3.1. Orthogonal Experimental Analysis

*3.1.1. Compressive Strength.* The range analysis results of compressive strength of concrete with triple-admixtures are shown in Figure 5. It can be seen from Figure 5 that the factors affecting the compressive strength of concrete with triple-admixtures are as follows in the order of primary and secondary: dosage of SF > dosage ratio of FA/BFS > dosage of FA and BFS. This shows that the dosage of SF has more influence on the compressive strength of concrete than the other two factors. On the whole, the compressive strength of concrete with triple-admixtures first increases and then decreases with the increase of dosage of FA and BFS. As the dosage ratio of FA/BFS increases, the compressive strength of concrete with triple-admixtures shows a downward trend. This may be due to the fact that BFS enhances the strength of concrete better than FA. However, the compressive strength of concrete with triple-admixtures increases significantly with the dosage of SF increasing. This is because SF contains a large amount of amorphous silica, which has a strong cementing force and can react with cement in a very short time to form a high-strength substance and then improve the strength of concrete. On the other hand, although the dosage of SF has the greatest impact on the compressive strength of concrete with triple-admixtures, the other two factors still have important effects that cannot be ignored. In addition, comparing the compressive strength results of concrete with different air contents, it can be seen that the compressive strength of concrete with triple-admixtures decreases with the increase of air contents.

(a) (b)

Figure 1: Parameters control of cement concrete during the specimen preparation. (a) Slump. (b) Air content.

Figure 2: Compressive strength test of cement concrete used in this paper.


Figure 3: Rapid chloride permeability test of cement concrete in this paper.

*3.1.2. Rapid Chloride Permeability.* The range analysis results of rapid chloride permeability of concrete with triple-admixtures are shown in Figure 6. It can be seen from Figure 6 that the factors affecting the rapid chloride permeability of concrete with triple-admixtures are as follows in the order of primary and secondary: dosage of SF > dosage of FA and BFS > dosage ratio of FA/BFS. Among them, the range results of the dosage of SF are much larger than those of the dosage of FA and BFS and their dosage ratio, which shows that the dosage of SF has an absolute influence on the

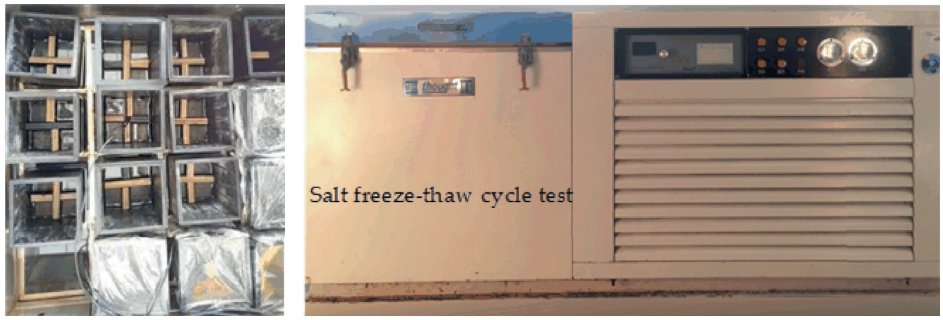


Figure 4: Salt freeze-thaw cycles test of cement concrete.

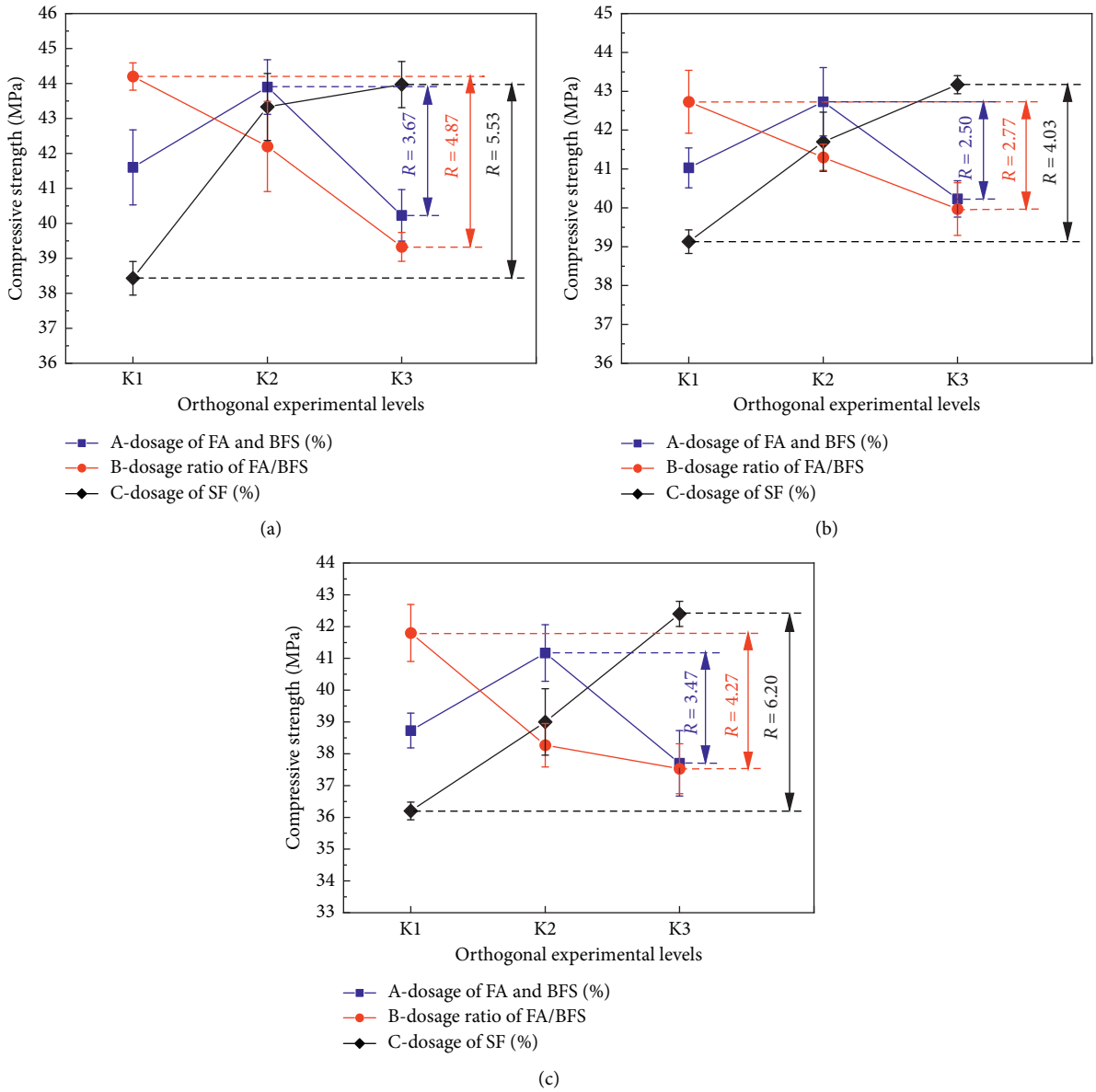


Figure 5: Range analysis between compressive strength and orthogonal experimental levels of cement concrete. (a) Air content of (2.5 ± 0.5)%. (b) Air content of (4.5 ± 0.5)%. (c) Air content of (6.5 ± 0.5)%.

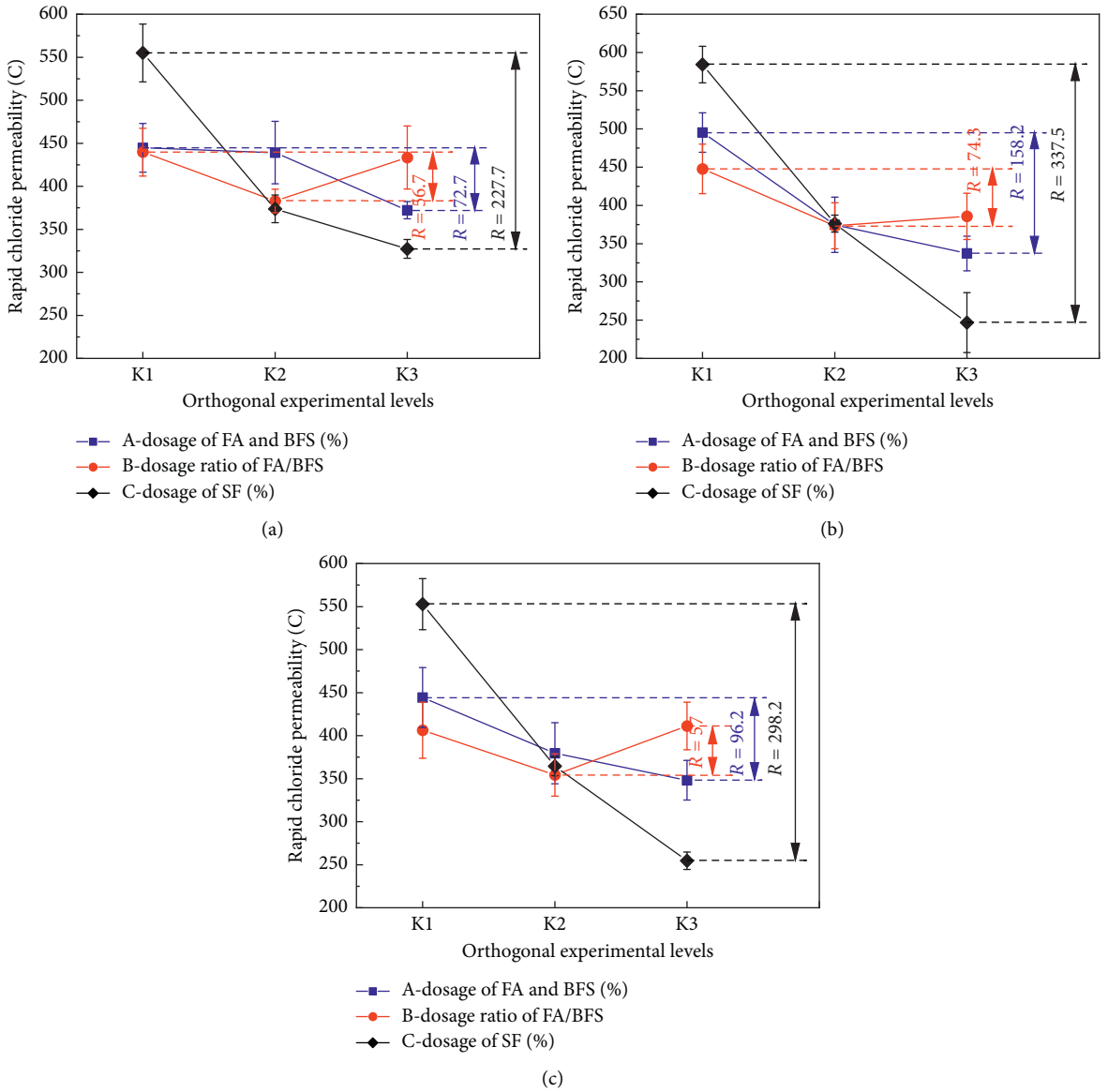


Figure 6: Range analysis between rapid chloride permeability and orthogonal experimental levels of cement concrete. (a) Air content of (2.5 ± 0.5)%. (b) Air content of (4.5 ± 0.5)%. (c) Air content of (6.5 ± 0.5)%.

rapid chloride permeability of concrete with triple-admixtures. Moreover, the rapid chloride permeability of concrete with triple-admixtures shows a downward trend as the dosage of SF increases. This is due to the small particle size of SF, which can change the size and number of air voids in concrete and effectively reduce the pore size. In addition, incorporating FA and BFS can also reduce the permeability of concrete, thereby improving its durability against salt and freeze-thaw cycles. Therefore, the rapid chloride permeability of concrete with triple-admixtures decreases with increase of dosage of FA and BFS as well as dosage ratio of FA/BFS. Simultaneously, comparing the rapid chloride permeability results of concrete with different air contents, it can be seen that the rapid chloride permeability of concrete with triple-admixtures decreases slightly with the increase of air contents.

*3.1.3. Weight Loss after 50 Salt Freeze-Thaw Cycles.* The range analysis results of weight loss after 50 salt freeze-thaw cycles of concrete with triple-admixtures are shown in Figure 7. It can be seen from Figure 7 that the factors affecting the weight loss after 50 salt freeze-thaw cycles of concrete with triple-admixtures are as follows in the order of primary and secondary: dosage of FA and BFS > dosage ratio of FA/BFS > dosage of SF. Among them, the range results of the dosage of FA and BFS are much larger than those of the dosage ratio of FA/BFS and dosage of SF, which shows that the dosage of FA and BFS has more influence on the weight loss after 50 salt freeze-thaw cycles of concrete with triple-admixtures. The weight loss after 50 salt freeze-thaw cycles of concrete with triple-admixtures shows a downward trend as the dosage of SF increases. The reason is mainly due to the small particle size of SF, which can participate in the

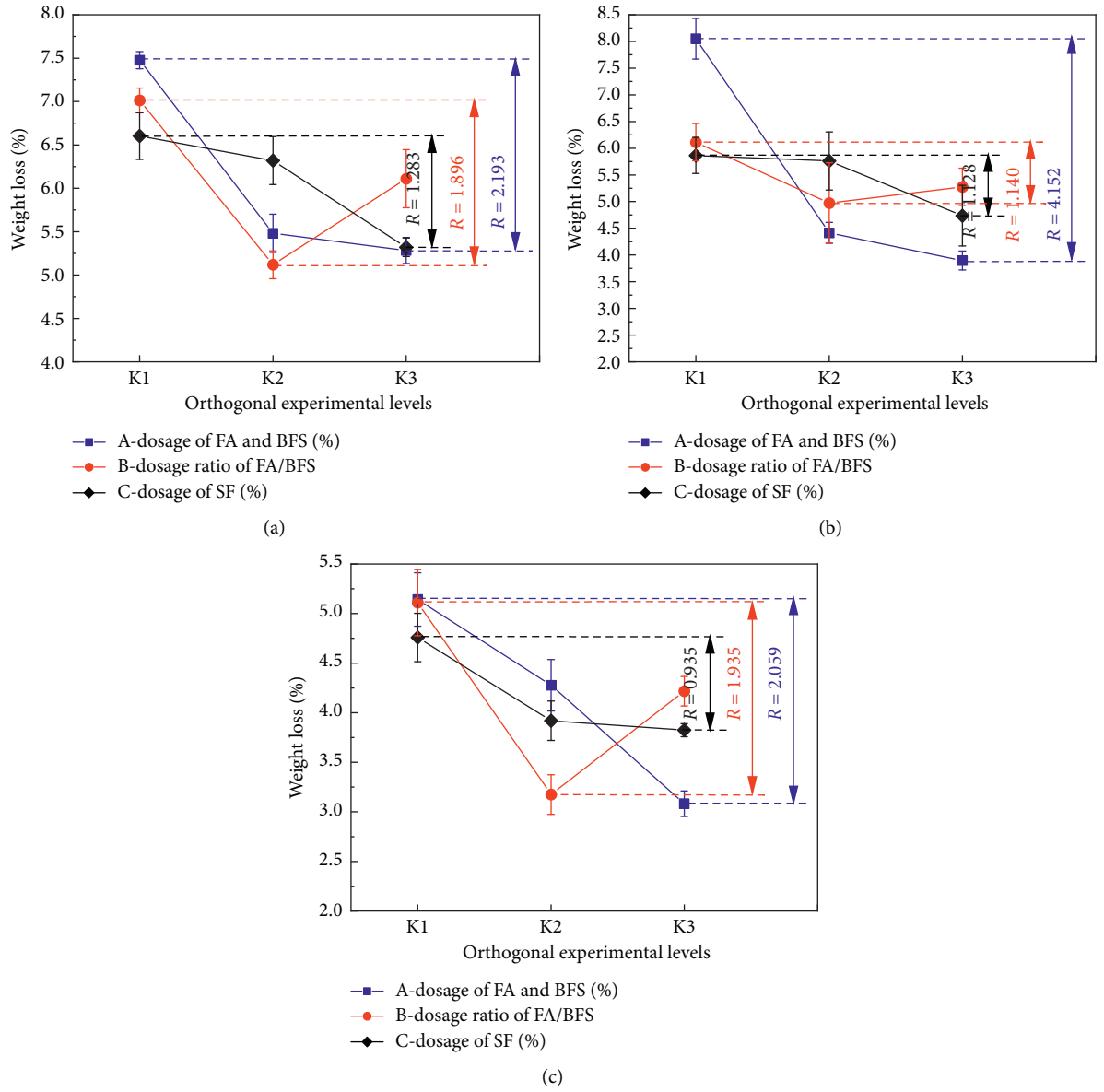


Figure 7: Range analysis between weight loss and orthogonal experimental levels of cement concrete. (a) Air content of (2.5 ± 0.5)%. (b) Air content of (4.5 ± 0.5)%. (c) Air content of (6.5 ± 0.5)%.

hydration reaction of cement to produce a hard and strong cementing substance, which improves the density of concrete and improves its resistance to chloride ion penetration. Moreover, the weight loss after 50 salt freeze-thaw cycles of concrete with triple-admixtures also decreases as the dosage of FA and BFS increases. However, as the dosage ratio of FA/BFS increases, the weight loss after 50 salt freeze-thaw cycles of concrete with triple-admixtures first decreases and then increases. The active $SiO_2$ in the FA will react with the cement hydration product CH to form C-S-H gel to fill the pores of the interface layer between the aggregate and the cement paste and improve its durability. Overall, comparing the weight loss after 50 salt freeze-thaw cycles of concrete with different air contents, it can be seen that the weight loss of concrete with triple-admixtures decreases slightly with the increase of air contents.

*3.1.4. Relative Dynamic Elasticity Modulus after 50 Salt Freeze-Thaw Cycles.* The range analysis results of relative dynamic elasticity modulus after 50 salt freeze-thaw cycles of concrete with triple-admixtures are shown in Figure 8. It can be seen from Figure 8 that the factors affecting the weight loss after 50 salt freeze-thaw cycles of concrete with triple-admixtures are as follows in the order of primary and secondary: dosage of FA and BFS > dosage ratio of FA/BFS > dosage of SF. Among them, the range results of the dosage of FA and BFS are much larger than those of the dosage ratio of FA/BFS and dosage of SF, which shows that the dosage of FA and BFS has more influence on the relative dynamic elasticity modulus after 50 salt freeze-thaw cycles of concrete with triple-admixtures. The relative dynamic elasticity modulus after 50 salt freeze-thaw cycles of concrete with triple-admixtures shows a

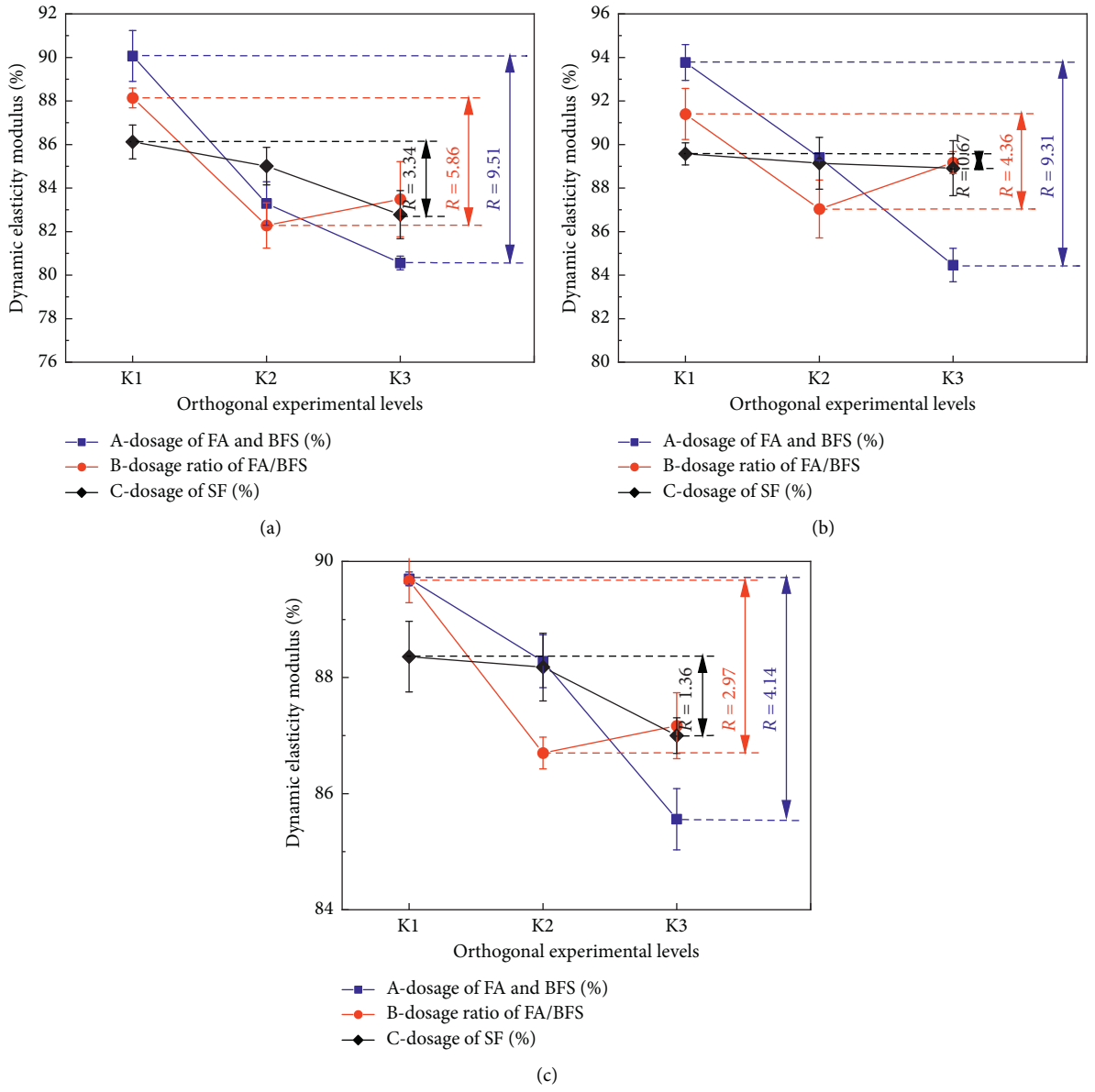


Figure 8: Range analysis between relative dynamic elasticity modulus and orthogonal experimental levels of cement concrete. (a) Air content of (2.5 ± 0.5)%. (b) Air content of (4.5 ± 0.5)%. (c) Air content of (6.5 ± 0.5)%.

downward trend as the dosage of SF as well as FA and BFS increases. However, as the dosage ratio of FA/BFS increases, the weight loss after 50 salt freeze-thaw cycles of concrete with triple-admixtures first decreases and then increases. The reinforcing effect of the secondary hydration reaction of active $SiO_2$ in the FA with cement is greater than the reinforcing effect of BFS and SF on concrete. Meanwhile, comparing the relative dynamic elasticity modulus after 50 salt freeze-thaw cycles of concrete with different air contents, it can be seen that the relative dynamic elasticity modulus of concrete with triple-admixtures decreases slightly with the increase of air contents.

### 3.2. Influence Analysis of Salt Freeze-Thaw Cycles on Durability of Concrete

*3.2.1. Weight Loss versus Salt Freeze-Thaw Cycles.* During the salt freeze-thaw test in this study, the index of weight loss rate most directly reflected the process of the gradual surface erosion of concrete specimens subjected to freeze-thaw cycles in salt solution. The test results of weight loss at each air content range level varying with the number of salt freeze-thaw cycles are demonstrated in Figure 9.

In Figures 9(a)–9(c), the weight loss of concrete with triple-admixtures increases with the number of salt freeze-thaw cycles. Generally, in the conventional freeze-

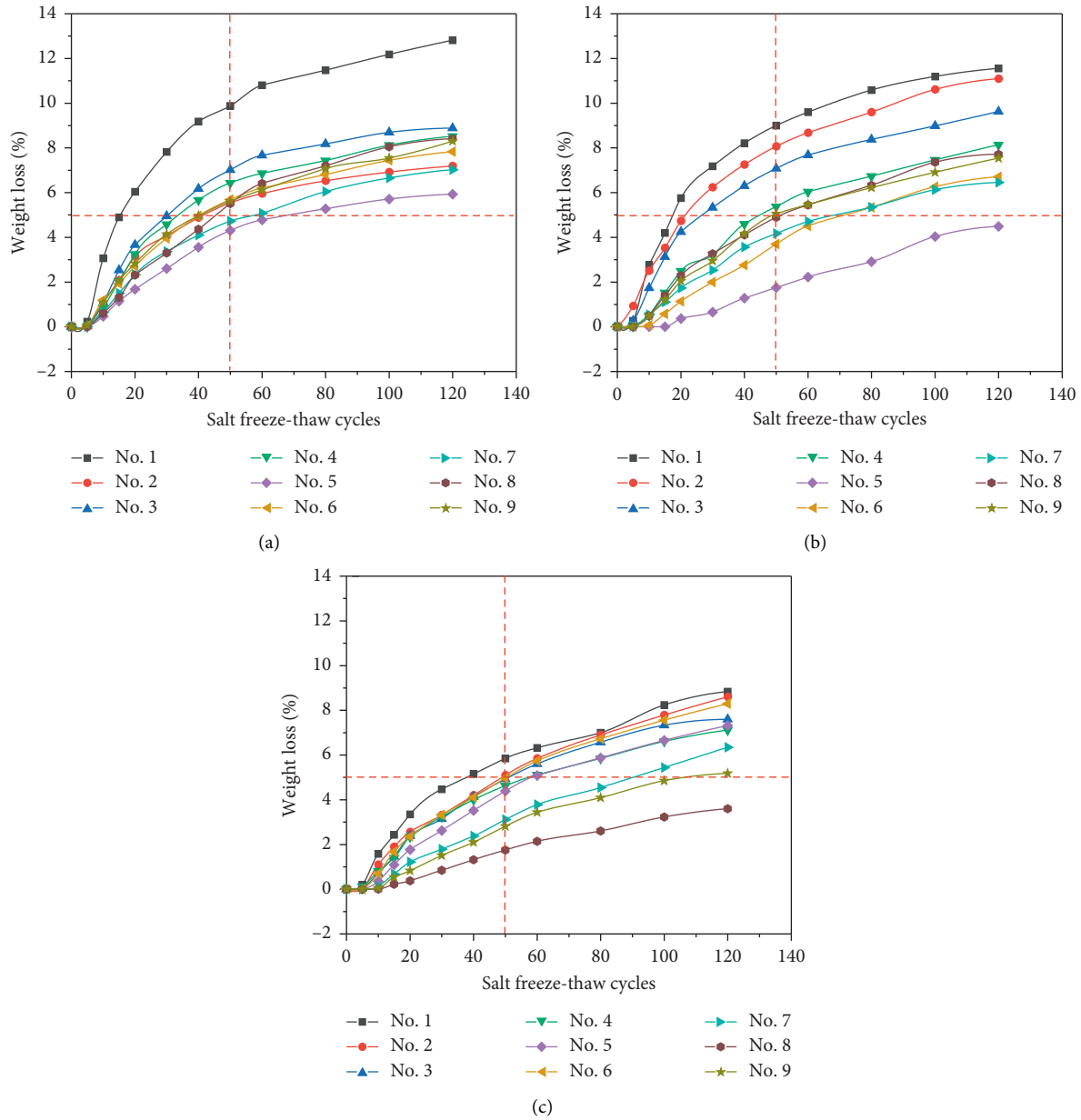


Figure 9: Weight loss of concrete with triple-admixtures versus salt freeze-thaw cycles. (a) Air content of (2.5 ± 0.5)%. (b) Air content of (4.5 ± 0.5)%. (c) Air content of (6.5 ± 0.5)%.

thaw cycle of concrete, the value 5% of weight loss is used as the evaluation index of concrete frost resistance. By comparing the 9 groups of weight loss results designed by orthogonal experiments, it can be seen that the weight loss increases with the increase in the number of salt freeze-thaw cycles. The addition of mineral admixtures can reduce the weight loss of concrete during the salt freeze-thaw process to a certain extent, which is beneficial to improve the resistance to salt freeze-thaw cycles of concrete. At the same time, the changes in the weight loss of concrete with different dosages of mineral admixtures are consistent with the range analysis results in Section 3.1.3. In addition, by comparing the weight loss of concrete with different air contents, it is obvious that the weight loss decreases with the increase of air content. This shows that adding AEA to increase air content can improve the salt freeze-thaw resistance of concrete.

*3.2.2. Relative Dynamic Elasticity Modulus versus Salt Freeze-Thaw Cycles.* On the other hand, the relative dynamic modulus of elasticity can also characterize the performance changes in concrete during the salt freeze-thaw cycles. The test results of relative dynamic modulus of elasticity at each air content range level varying with the number of salt freeze-thaw cycles are demonstrated in Figure 10. In Figures 10(a)–10(c), the relative dynamic modulus of elasticity of concrete with triple-admixtures

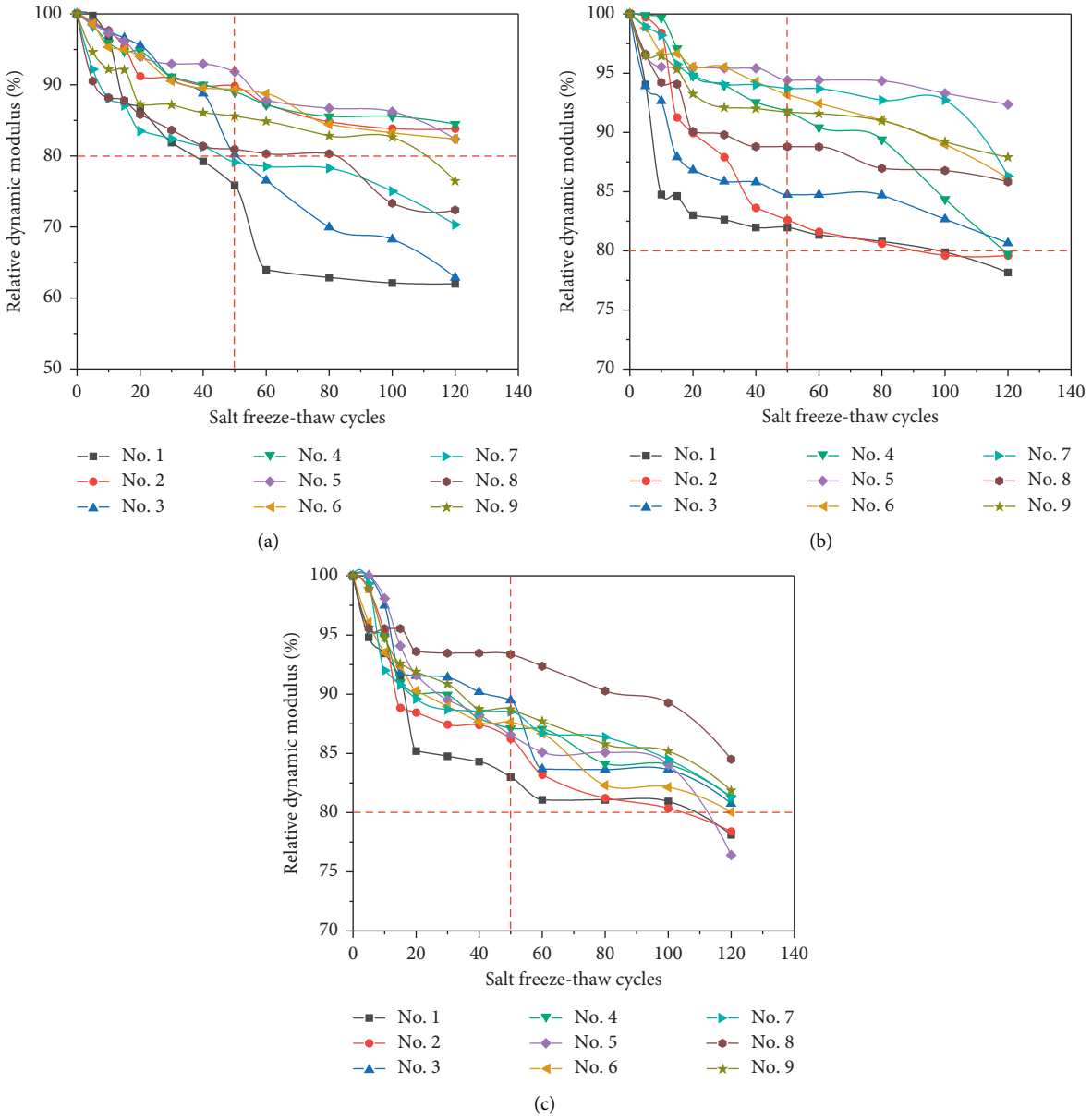


Figure 10: Relative dynamic modulus of concrete with triple-admixtures versus salt freeze-thaw cycles. (a) Air content of (2.5 ± 0.5)%. (b) Air content of (4.5 ± 0.5)%. (c) Air content of (6.5 ± 0.5)%.

decreases with the number of salt freeze-thaw cycles. The value 80% of relative dynamic modulus of elasticity is used as the evaluation index of concrete frost resistance. By comparing the 9 groups of relative dynamic modulus results designed by orthogonal experiments, it can be seen that the relative dynamic modulus decreases with the increase in the number of salt freeze-thaw cycles. Meanwhile, the addition of mineral admixtures can reduce the variation of relative dynamic modulus of concrete during the salt freeze-thaw process to a certain extent, which is also beneficial to improve the resistance to salt freeze-thaw cycles of concrete. Besides, the changes in the relative dynamic modulus of concrete with different dosages of mineral admixtures are consistent with the range analysis results in Section 3.1.3 and the change law in Section 3.2.1. Apart from this, by comparing the relative dynamic modulus of concrete with different air contents, it is obvious that the relative dynamic modulus increases with the increase of air content. This shows that adding AEA can improve the salt freeze-thaw resistance of concrete.

*3.3. Mixture Proportion Optimization Based on Genetic Algorithm.* In order to reflect the relationship between durability and mix proportion of concrete, the variance test fitting equation results are shown in Tables 5–7, which characterize the weight loss of concrete specimens after 120 salt freeze-thaw cycles. And the fitting results have been proved to be effective through significance test.

Table 5: Fitted quadratic equations of weight loss after 120 salt freeze-thaw cycles at air content of (2.5 ± 0.5)%.

| Group no. | Degree of freedom | Estimated value | $F$-value | $p$-value | Significant |
|---|---|---|---|---|---|
| A | 1 | −43.44 | 34.77 | <0.0001 | Yes |
| B | 1 | −0.69 | 3.08 | 0.0065 | Yes |
| C | 1 | −63.46 | 7.20 | <0.0001 | Yes |
| $A^2$ | 1 | 51.62 | 16.2 | <0.0001 | Yes |
| $B^2$ | 1 | −0.59 | 9.23 | <0.0001 | Yes |
| A × B | 1 | 11.15 | 40.9 | <0.0001 | Yes |
| A × C | 1 | 167.23 | 7.48 | <0.0001 | Yes |
| B × C | 1 | 18.93 | 9.65 | <0.0001 | Yes |
| Intercept | 1 | 14.30 | 439.1 | <0.0001 | Yes |

Table 6: Fitted quadratic equations of weight loss after 120 salt freeze-thaw cycles at air content of (4.5 ± 0.5)%.

| Group no. | Degree of freedom | Estimated value | $F$-value | $p$-value | Significant |
|---|---|---|---|---|---|
| A | 1 | −1.25 | 1.01 | 0.3271 | No |
| B | 1 | 0.52 | 2.31 | 0.0330 | Yes |
| C | 1 | −216.31 | 24.52 | <0.0001 | Yes |
| $A^2$ | 1 | −14.23 | 4.47 | 0.0003 | Yes |
| $B^2$ | 1 | −0.54 | 8.44 | <0.0001 | Yes |
| A × B | 1 | −4.09 | 15.03 | <0.0001 | Yes |
| A × C | 1 | 566.20 | 25.31 | <0.0001 | Yes |
| B × C | 1 | 55.85 | 28.46 | <0.0001 | Yes |
| Intercept | 1 | 12.16 | 450.12 | <0.0001 | Yes |

Table 7: Fitted quadratic equations of weight loss after 120 salt freeze-thaw cycles at air content of (6.5 ± 0.5)%.

| Group no. | Degree of freedom | Estimated value | $F$-value | $p$-value | Significant |
|---|---|---|---|---|---|
| A | 1 | 0.81 | 0.65 | 0.5258 | No |
| B | 1 | 5.22 | 23.35 | <0.0001 | Yes |
| C | 1 | −17.56 | 1.99 | 0.0618 | No |
| $A^2$ | 1 | −3.78 | 1.19 | 0.2505 | No |
| $B^2$ | 1 | −0.89 | 13.74 | <0.0001 | Yes |
| A × B | 1 | −2.32 | 8.54 | <0.0001 | Yes |
| A × C | 1 | 174.15 | 7.79 | <0.0001 | Yes |
| B × C | 1 | −9.01 | 4.59 | 0.0002 | Yes |
| Intercept | 1 | 2.84 | 487.87 | <0.0001 | Yes |

The genetic optimization was applied to find the optimum mix proportion in this section based on the effective quadratic equations of test results on concrete with different mix proportions. Considering that the purpose of this paper is to improve the resistance to salt frost erosion, quadratic equations of weight loss in Tables 5–7 were chosen as the fitness functions of genetic algorithm. In this paper, it is a simple genetic algorithm optimization problem with the input variables "A," "B," and "C" and output variable "weight loss." The population size was regulated as 1000, mutation rate was 0.001, recombination rate was 0.5, and the number of generations was 300. The experimental simulation results at each air content range level are given in Figure 11.

As it can be seen from the above results, the weight loss values tend to be stable with the increasing of generation number. And the optimum variables obtained from the genetic algorithms are listed in Table 8.

To verify the usefulness of the genetic algorithm programs, the optimum variables in Table 8 were substituted into the fitted quadratic equations; the corresponding values of compressive strength and rapid chloride permeability at each air content range level could be obtained, respectively. The results and mix proportions are shown in Table 9.

It is observed that higher air content would contribute to the reduction of weight loss. However, when the air content is raised up to (6.5 ± 0.5)%, the compressive strength of concrete decreases significantly. The optimum mix proportion of concrete with air content of 6%–7% has the minimum dosage of mineral admixtures, and it shows the rapid chloride permeability about three times that of other groups, which means a lower chloride ion penetration resistance. Therefore, the final recommended optimum mix proportion of concrete with multimineral admixtures in this paper is that the dosage of FA is 5.06%, dosage of BFS is 6.75%, dosage of SF is 7.77%, and the air content should be controlled at the range of (4.5 ± 0.5)%.

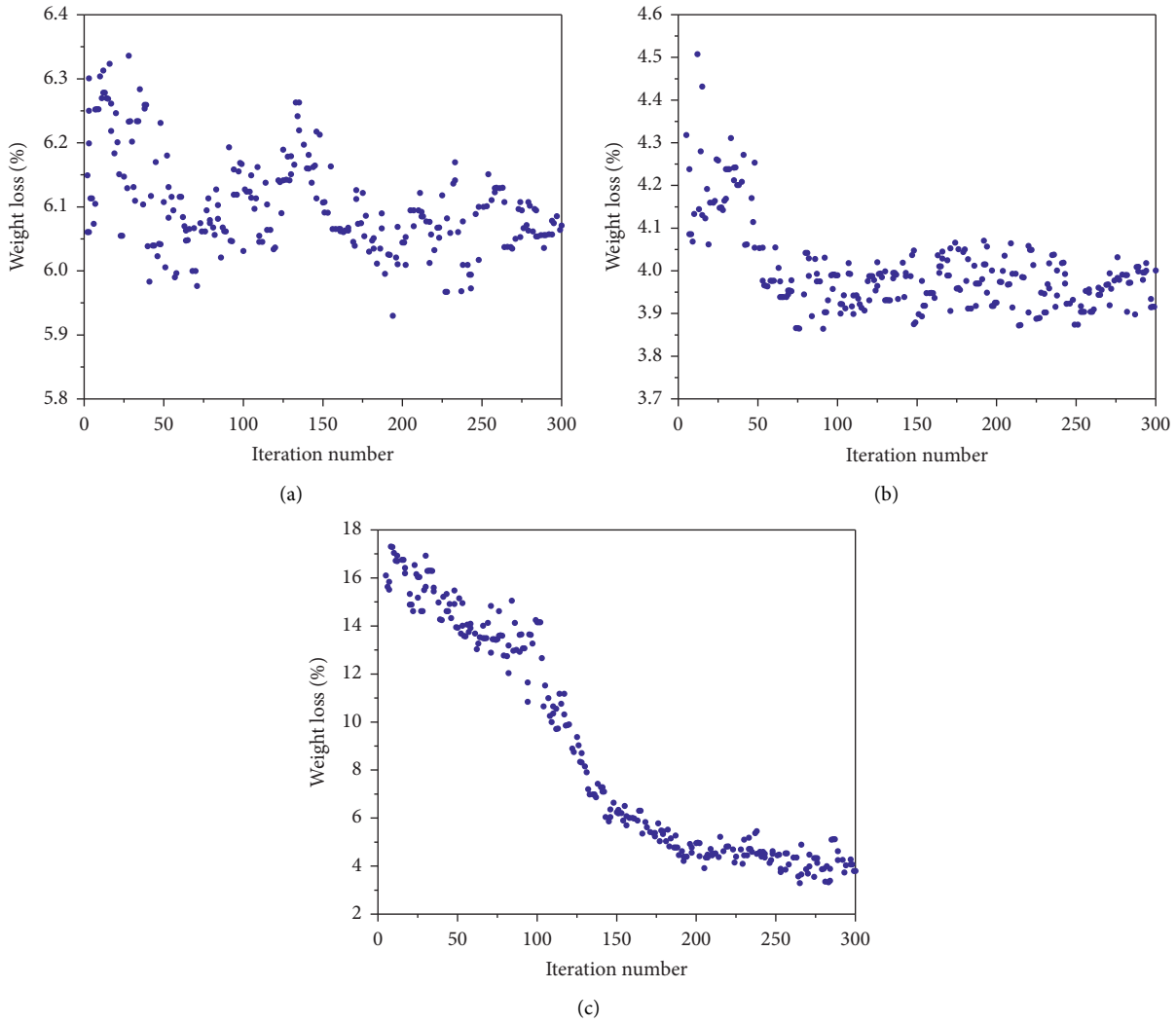


Figure 11: Relative dynamic modulus of concrete with triple-admixtures versus salt freeze-thaw cycles. (a) Air content of (2.5 ± 0.5)%. (b) Air content of (4.5 ± 0.5)%. (c) Air content of (6.5 ± 0.5)%.

Table 8: The optimum variables obtained from the genetic algorithms.

| Air content | Iteration number | A | B | C | Weight loss (%) |
|---|---|---|---|---|---|
| (2.5 ± 0.5)% | 178 | 24.2 | 0.343 | 8.8 | 5.92 |
| (4.5 ± 0.5)% | 248 | 11.8 | 0.748 | 7.8 | 3.86 |
| (6.5 ± 0.5)% | 283 | 10.3 | 0.338 | 3.3 | 3.28 |

Table 9: The optimum mix proportions and predicted values of concrete under salt freeze-thaw cycles.

| Air content | Compressive strength (MPa) | Chloride permeability (C) | Weight loss (%) | FA (%) | BFS (%) | SF (%) |
|---|---|---|---|---|---|---|
| (2.5 ± 0.5)% | 51.94 | 202.36 | 5.97 | 6.19 | 18.02 | 8.84 |
| (4.5 ± 0.5)% | 49.17 | 234.37 | 3.32 | 5.06 | 6.75 | 7.77 |
| (6.5 ± 0.5)% | 37.44 | 631.77 | 4.92 | 2.60 | 7.70 | 3.04 |

## 4. Conclusions

The object of this research is to propose a mix proportion design method for air-entrained concrete with multi-admixtures, which would improve the durability of concrete serving in salt freeze-thaw condition. Firstly, the orthogonal experiment about different dosages of three kinds of mineral admixtures was designed to reduce the number of trial mixes and three range levels of air content were taken into consideration simultaneously. Then, the salt freeze-thaw resistance

indices of concrete such as compressive strength, rapid chloride permeability, weight loss, and relative dynamic modulus of elasticity were tested. Finally, the test results were fitted into quadratic equations and an ordinary genetic algorithm was applied to optimize the mix proportion. Based on the results of this research, the following conclusions are reached.

(1) In order to evaluate the salt freeze-thaw resistance of concrete, indices such as compressive strength, rapid chloride permeability, weight loss, and relative dynamic modulus of elasticity should be considered at the same time, which reflect the basic strength, chloride ion penetration resistance, surface erosion resistance, and internal defects resistance of concrete suffering from freeze-thaw environment.

(2) Combined with engineering experience and correlative study, applying orthogonal design would reduce the number of trial mixes significantly. Quadratic fitting and genetic algorithm are both practical methods to analyze and optimize data for the problem discussed in this paper. The method proposed by the authors will considerably improve the quantity and efficiency of mix proportion design for this kind of multiconstituent concrete.

(3) It may cause obvious difference in salt freeze-thaw resistance of concrete when changing the proportions of mineral admixtures and air content. An appropriate amount of mineral admixtures would improve pore structures and chloride ion penetration resistance of concrete, while overmuch mineral admixtures, especially FA, would bring negative impact on strength and surface erosion resistance. On the other hand, the addition of AEA could prominently improve salt freeze-thaw durability of concrete, while overmuch air content will cause obvious decrease in concrete strength.

(4) Finally, the recommended optimum mix proportion of air-entrained concrete with multimineral admixtures in this paper is that the dosage of FA is 5.06%, dosage of BFS is 6.75%, dosage of SF is 7.77%, and the air content should be controlled at the range of $(4 \pm 0.5)\%$.

This study only evaluated the macroscopic durability behaviour of concrete with triple-admixtures subjected to freeze-thaw cycles in salt solution and did not conduct in-depth analysis from the aspect of microscopic mechanism, which is also the future direction of this research work.

## Data Availability

The data used to support the findings of this study are available from the corresponding author upon request.

## Conflicts of Interest

The authors declare that they have no conflicts of interest.

## Acknowledgments

This work was partially financially supported by the Scientific and Technological Project of Science and Technology Department of Jilin Province (grant number 20190303052SF) and the Innovation Special Project of Zhongshan Science and Technology Bureau (grant number 2019AG001).

## References

[1] Y. B. Jiao, Y. Zhang, M. Guo, L. Zhang, H. Ning, and S. Liu, "Mechanical and fracture properties of ultra-high performance concrete (uhpc) containing waste glass sand as partial replacement material," *Journal of Cleaner Production*, vol. 277, Article ID 123501, 2020.

[2] C. S. Poon, S. C. Kou, and L. Lam, "Compressive strength, chloride diffusivity and pore structure of high performance metakaolin and silica fume concrete," *Construction and Building Materials*, vol. 20, no. 10, pp. 858–865, 2006.

[3] F. Pacheco-Torgal, Y. N. Ding, and S. Jalali, "Properties and durability of concrete containing polymeric wastes (tyre rubber and polyethylene terephthalate bottles): an overview," *Construction and Building Materials*, vol. 30, pp. 714–724, 2012.

[4] H. B. Liu, G. B. Luo, H. B. Wei, and H. Yu, "Strength, permeability, and freeze-thaw durability of pervious concrete with different aggregate sizes, porosities, and water-binder ratios," *Applied Sciences-Basel*, vol. 8, no. 8, p. 1217, 2018.

[5] G. Tan, Z. Zhu, W. Wang et al., "Flexural ductility and crack-controlling capacity of polypropylene fiber reinforced ecc thin sheet with waste superfine river sand based on acoustic emission analysis," *Construction and Building Materials*, vol. 277, Article ID 122321, 2021.

[6] X. J. Shi, P. Park, Y. Rew, K. Huang, and C. Sim, "Constitutive behaviors of steel fiber reinforced concrete under uniaxial compression and tension," *Construction and Building Materials*, vol. 233, 2020.

[7] W. S. Wang, Y. C. Cheng, and G. J. Tan, "Design optimization of sbs-modified asphalt mixture reinforced with eco-friendly basalt fiber based on response surface methodology," *Materials*, vol. 11, no. 8, p. 1131, 2018.

[8] K. Amini, P. Vosoughi, H. Ceylan, and P. Taylor, "Effect of mixture proportions on concrete performance," *Construction and Building Materials*, vol. 212, pp. 77–84, 2019.

[9] H. B. Liu, S. Q. Liu, P. L. Zhou, Y. Zhang, Y. Jiao et al., "Mechanical properties and crack classification of basalt fiber rpc based on acoustic emission parameters," *Applied Sciences-Basel*, vol. 9, no. 18, 2019.

[10] W. J. Long, K. H. Khayat, A. Yahia, and F. Xiang, "Rheological approach in proportioning and evaluating prestressed self-consolidating concrete," *Cement & Concrete Composites*, vol. 82, pp. 105–116, 2017.

[11] X. J. Shi, A. Mukhopadhyay, D. Zollinger, and Z. Grasley, "Economic input-output life cycle assessment of concrete pavement containing recycled concrete aggregate," *Journal of Cleaner Production*, vol. 225, pp. 414–425, 2019.

[12] X. J. Shi, A. Mukhopadhyay, and K. W. Liu, "Mix design formulation and evaluation of portland cement concrete paving mixtures containing reclaimed asphalt pavement," *Construction and Building Materials*, vol. 152, pp. 756–768, 2017.

[13] H. J. Wu, Z. Diao, and K. Z. Fan, "Study on durability of non-dispersible concrete in seawater environment," *International Journal of Structural Integrity*, vol. 11, no. 3, pp. 443–452, 2020.

[14] N. Xie, M. Akin, and X. M. Shi, "Permeable concrete pavements: a review of environmental benefits and durability," *Journal of Cleaner Production*, vol. 210, pp. 1605–1621, 2019.

[15] G. Dimitriou, P. Savva, and M. F. Petrou, "Enhancing mechanical and durability properties of recycled aggregate concrete," *Construction and Building Materials*, vol. 158, pp. 228–235, 2018.

[16] H. B. Liu, G. B. Luo, Y. F. Gong, H. Wei et al., "Mechanical properties, permeability, and freeze-thaw resistance of pervious concrete modified by waste crumb rubbers," *Applied Sciences-Basel*, vol. 8, no. 10, 2018.

[17] W. S. Wang, G. J. Tan, C. Y. Liang, Y. Wang, and Y. Cheng, "Study on viscoelastic properties of asphalt mixtures incorporating sbs polymer and basalt fiber under freeze-thaw cycles," *Polymers*, vol. 12, no. 8, 2020.

[18] N. Xie, X. M. Shi, and Y. Zhang, "Impacts of potassium acetate and sodium-chloride deicers on concrete," *Journal of Materials in Civil Engineering*, vol. 29, no. 3, 2017.

[19] Y. Farnam, M. Krafcik, L. Liston et al., "Evaluating the use of phase change materials in concrete pavement to melt ice and snow," *Journal of Materials in Civil Engineering*, vol. 28, no. 4, 2016.

[20] Z. H. Sun and G. W. Scherer, "Measurement and simulation of dendritic growth of ice in cement paste," *Cement and Concrete Research*, vol. 40, no. 9, pp. 1393–1402, 2010.

[21] J. Yuan, H. Lu, Q. B. Yang, and J. Ling, "Mechanisms on the salt-frost scaling of concrete," *Journal of Materials in Civil Engineering*, vol. 29, no. 3, 2017.

[22] B. Lei, W. G. Li, Z. Tang, V. W. Y. Tam, and Z. Sun, "Durability of recycled aggregate concrete under coupling mechanical loading and freeze-thaw cycle in salt-solution," *Construction and Building Materials*, vol. 163, pp. 840–849, 2018.

[23] Q. L. Guo, Q. Liu, P. Zhang et al., "Temperature and pressure dependent behaviors of moisture diffusion in dense asphalt mixture," *Construction and Building Materials*, vol. 246, 2020.

[24] Q. L. Guo, G. Y. Li, Y. Gao et al., "Experimental investigation on bonding property of asphalt-aggregate interface under the actions of salt immersion and freeze-thaw cycles," *Construction and Building Materials*, vol. 206, pp. 590–599, 2019.

[25] G. J. Ke, J. Zhang, B. Tian, and J. Wang, "Characteristic analysis of concrete air entraining agents in different media," *Cement and Concrete Research*, vol. 135, 2020.

[26] F. L. Huang, H. J. Li, Z. L. Yi, Z. Wang, and Y. Xie, "The rheological properties of self-compacting concrete containing superplasticizer and air-entraining agent," *Construction and Building Materials*, vol. 166, pp. 833–838, 2018.

[27] D. M. Wellman, K. E. Parker, L. Powers et al., "Effect of iron and carbonation on the diffusion of iodine and rhenium in waste encasement concrete and soil fill material under hydraulically unsaturated conditions," *Applied Geochemistry*, vol. 23, no. 8, pp. 2256–2271, 2008.

[28] G. C. Shan, S. Zhao, M. Qiao et al., "Synergism effects of coconut diethanol amide and anionic surfactants for entraining stable air bubbles into concrete," *Construction and Building Materials*, vol. 237, 2020.

[29] M. Khoshroo, A. A. S. Javid, and A. Katebi, "Effect of chloride treatment curing condition on the mechanical properties and durability of concrete containing zeolite and micro-nano-bubble water," *Construction and Building Materials*, vol. 177, pp. 417–427, 2018.

[30] L. X. Du and K. J. Folliard, "Mechanisms of air entrainment in concrete," *Cement and Concrete Research*, vol. 35, no. 8, pp. 1463–1471, 2005.

[31] S. Chatterji, "Freezing of air-entrained cement-based materials and specific actions of air-entraining agents," *Cement & Concrete Composites*, vol. 25, no. 7, pp. 759–765, 2003.

[32] Z. C. Liu and W. Hansen, "Pore damage in cementitious binders caused by deicer salt frost exposure," *Construction and Building Materials*, vol. 98, pp. 204–216, 2015.

[33] J. Yuan, Z. Y. Du, Y. Wu, and F. P Xiao, "Freezing-thawing resistance evaluations of concrete pavements with deicing salts based on various surfaces and air void parameters," *Construction and Building Materials*, vol. 204, pp. 317–326, 2019.

[34] P. Duan, Z. H. Shui, W. Chen, and C. Shen, "Efficiency of mineral admixtures in concrete: microstructure, compressive strength and stability of hydrate phases," *Applied Clay Science*, vol. 83-84, pp. 115–121, 2013.

[35] H. B. Liu, G. B. Luo, L. H. Wang, and Y. F. Gong, "Strength time-varying and freeze-thaw durability of sustainable pervious concrete pavement material containing waste fly ash," *Sustainability*, vol. 11, no. 1, p. 176, 2019.

[36] J. J. Valenza and G. W. Scherer, "Mechanism for salt scaling of a cementitious surface," *Materials and Structures*, vol. 40, no. 3, pp. 259–268, 2007.

[37] B. Amini and S. S. Tehrani, "Simultaneous effects of salted water and water flow on asphalt concrete pavement deterioration under freeze-thaw cycles," *International Journal of Pavement Engineering*, vol. 15, no. 5, pp. 1–9, 2014.

[38] S. H. Han, "Influence of diffusion coefficient on chloride ion penetration of concrete structure," *Construction and Building Materials*, vol. 21, no. 2, pp. 370–378, 2007.

[39] Q. Yuan, D. J. Zhou, B. Y. Li, H. Huang, and C. Shi, "Effect of mineral admixtures on the structural build-up of cement paste," *Construction and Building Materials*, vol. 160, pp. 117–126, 2018.

[40] C. Wu, L. Li, W. Wang, and Z. W. Gu, "Experimental characterization of viscoelastic behaviors of nano-tio2/caco3 modified asphalt and asphalt mixture," *Nanomaterials (Basel)*, vol. 11, no. 1, 2021.

[41] Y. Li, J. L. Bao, and Y. L. Guo, "The relationship between autogenous shrinkage and pore structure of cement paste with mineral admixtures," *Construction and Building Materials*, vol. 24, no. 10, pp. 1855–1860, 2010.

[42] W. Sun, Y. S. Zhang, S. F. Liu, and Y. M. Zhang, "The influence of mineral admixtures on resistance to corrosion of steel bars in green high-performance concrete," *Cement and Concrete Research*, vol. 34, no. 10, pp. 1781–1785, 2004.

[43] J. D. Bapat, "Performance of cement concrete with mineral admixtures," *Advances in Cement Research*, vol. 13, no. 4, pp. 139–155, 2001.

[44] C. H. Lim, Y. S. Yoon, and J. H. Kim, "Genetic algorithm in mix proportioning of high-performance concrete," *Cement and Concrete Research*, vol. 34, no. 3, pp. 409–420, 2004.

[45] C. Liang, X. Xu, H. Chen et al., "Machine learning approach to develop a novel multi-objective optimization method for pavement material proportion," *Applied Sciences*, vol. 11, no. 2, p. 835, 2021.

[46] M. Shahnewaz, R. Machial, M. S. Alam, and A. Rteil, "Optimized shear design equation for slender concrete beams reinforced with frp bars and stirrups using genetic algorithm

and reliability analysis," *Engineering Structures*, vol. 107, pp. 151–165, 2016.

[47] S. Kim, H. B. Choi, Y. Shin, G. H. Kim, and D. S. Seo, "Optimizing the mixing proportion with neural networks based on genetic algorithms for recycled aggregate concrete," *Advances in Materials Science and Engineering*, vol. 2013, Article ID 527089, 10 pages, 2013.

[48] W. J. Park, T. Noguchi, and H. S. Lee, "Genetic algorithm in mix proportion design of recycled aggregate concrete," *Computers and Concrete*, vol. 11, no. 3, pp. 183–199, 2013.

[49] H. Yazici, "The effect of silica fume and high-volume class c fly ash on mechanical properties, chloride penetration and freeze-thaw resistance of self-compacting concrete," *Construction and Building Materials*, vol. 22, no. 4, pp. 456–462, 2008.

[50] C. W. Chung, C. S. Shon, and Y. S. Kim, "Chloride ion diffusivity of fly ash and silica fume concretes exposed to freeze-thaw cycles," *Construction and Building Materials*, vol. 24, no. 9, pp. 1739–1745, 2010.

[51] A. Mardani-Aghabaglou, G. I. Sezer, and K. Ramyar, "Comparison of fly ash, silica fume and metakaolin from mechanical properties and durability performance of mortar mixtures view point," *Construction and Building Materials*, vol. 70, pp. 17–25, 2014.

[52] H. Ziari, P. Hayati, and J. Sobhani, "Airfield self-consolidating concrete pavements (asccp): mechanical and durability properties," *Construction and Building Materials*, vol. 72, pp. 174–181, 2014.

[53] M. J. Islam, M. S. Meherier, and A. K. M. R. Islam, "Effects of waste pet as coarse aggregate on the fresh and harden properties of concrete," *Construction and Building Materials*, vol. 125, pp. 946–951, 2016.

[54] W. S. Wang, Y. C. Cheng, H. P. Chen, G. J. Tan, Z. Lv, and Y. S. Bai, "Study on the performances of waste crumb rubber modified asphalt mixture with eco-friendly diatomite and basalt fiber," *Sustainability*, vol. 11, no. 19, p. 5282, 2019.

[55] Q. L. Guo, L. L. Li, Y. C. Cheng, Y. Jiao, and C. Xu, "Laboratory evaluation on performance of diatomite and glass fiber compound modified asphalt mixture," *Materials & Design*, vol. 66, pp. 51–59, 2015.

[56] Q. L. Guo, H. Y. Wang, Y. Gao, Y. Jiao, F. Liu, and Z. Dong, "Investigation of the low-temperature properties and cracking resistance of fiber-reinforced asphalt concrete using the dic technique," *Engineering Fracture Mechanics*, vol. 229, 2020.

[57] Q. Guo, Z. Chen, P. Liu et al., "Influence of basalt fiber on mode i and ii fracture properties of asphalt mixture at medium and low temperatures," *Theoretical and Applied Fracture Mechanics*, vol. 112, 2021.

Hindawi
Advances in Materials Science and Engineering
Volume 2021, Article ID 6622628, 10 pages
https://doi.org/10.1155/2021/6622628

*Research Article*

# An Accurate Measurement Method for Tension Force of Short Cable by Additional Mass Block

**Shuichang Li**,[1] **Longlin Wang**,[2,3] **Hua Wang**,[3,4] **Peihua Shi**,[3] **Riyan Lan**,[5,6] **Changxia Wu**,[3] **and Xirui Wang**[3]

[1]*Guangxi Nantian Expressway Co.,Ltd., Nanning 530007, China*
[2]*Southeast University, Nanjing 211189, China*
[3]*Guangxi Transportation Science and Technology Group Co.,Ltd., Nanning 530007, China*
[4]*Guangxi Beibu Gulf Investment Group Co.,Ltd., Nanning 530029, China*
[5]*Central South University, Changsha 410012, China*
[6]*Guangxi Xinfazhan Communication Group Co.,Ltd., Nanning 530029, China*

Correspondence should be addressed to Hua Wang; wanghua15@mails.jlu.edu.cn

Received 3 December 2020; Revised 5 January 2021; Accepted 16 January 2021; Published 27 January 2021

Academic Editor: Qinglin Guo



The equivalent effective length parameter is introduced into the vibration equation of short cable; that is, the boundary condition that affects the test accuracy of short cable force is equivalent to the calculated length of cable. By attaching an additional mass block to the cable, new parameters are introduced to identify the tension force. Vibration differential equations are established for cable with and without addition mass block, taking new parameters into account, such as equivalent effective length and added mass. By solving the equations using the RITZ method, the analytical relationship between the natural frequency of cable and equivalent effective length before and after a mass block is added can be developed. It can also develop an analytical method to identify the equivalent effective length depending on whether the added mass block is attached. Then, tension force of short length cable can be evaluated by measuring its natural frequency based on equivalent effective length. The method is verified by field tests. The tests results indicate the new method mentioned in this paper is going to largely improve the accuracy of tension force measurement of short length cable.

## 1. Introduction

In recent years, China's infrastructure has made rapid development; especially in the transportation infrastructure, it has made remarkable achievements [1–3]. In order to ensure the safe operation of traffic infrastructure, nondestructive testing technology has been paid more and more attention [4, 5]. In the long-span bridges that have been built, the cable-type bridges occupy a very important proportion. Among them, the cable is an important force transmission component. No matter in the design, construction, or maintenance stage, the cable force is a very important parameter [6, 7].

The common methods used in cable force tests are the pressure sensor method and frequency method. The pressure sensor method can only test the cable force with the pressure sensor installed in advance in the construction and cannot be used without sensors after the bridge is completed [4]. The frequency method [8–11] is widely used because of its simple equipment, high reliability, and accuracy of cable force results, which can meet the requirements of repeated tests in engineering. The main steps are as follows: the natural frequency of the cable is firstly analyzed by vibration signal of the cable; next one brings the natural frequency into the relationship between the cable force and the natural frequency and then obtains the cable force. It should be noted that the relationship between the cable force and the natural frequency in the existing technology is derived based on the string tension. For long cable (the ratio of cable length to diameter is more than 200 times), the cable force obtained

by this relationship can meet the requirements of the project. However, for the short cable, the error of cable force may be very large, and even the wrong result will be obtained. It is mainly due to the anchorage conditions, casing, shock absorber, cable stiffness, and other factors that will have a greater impact on cable frequency. How to accurately test the short cable force is always an unsolved engineering problem. In order to solve this problem, many scholars have proposed some approximate algorithms or solved this problem by the finite element method [12] and the difference method [13].

In 1996, Zui et al. [14] put forward a practical formula, which can be used to calculate the cable force using the widely used fundamental frequency and the second-order frequency. In 1998, Mehrabi and Tabatabai [15] proposed a practical formula that can consider the cable sag effect and bending stiffness, which assumes that both ends of the cable are consolidated. The formula has high accuracy for cables with a sag parameter less than 3.1 and a bending stiffness parameter greater than 50. Fang and Wang [16] obtained the numerical relationship among flexural rigidity, length, linear density, and vibration frequency based on the transverse vibration equation of the beam under axial tension. In 2002, Zui et al. [17] proposed the Kalman filtering method to identify the tension and bending stiffness of the suspender according to the cable vibration caused by an external force. Roman et al. [18] proposed that the changing trend of each frequency should be considered in the calculation of cable force, so as to achieve the consistency between the high-order frequency value and the low-order frequency value and meet the shortcomings that the low-order frequency may be difficult to measure in the actual engineering. Kim and Park [19] proposed a parameter identification method based on frequency sensitivity correction to identify the bending stiffness and cable force of the cable. Through the comparison of the calculation results of three different methods, i.e., finite element method, experiment, and example, it shows that the cable force calculated by this method has high accuracy. In 2010, Park et al. [20] proposed a parameter identification method based on the suspension bridge, which can identify bending stiffness and tensile stiffness parameters. In 2015, Kyu-Sik et al. [21] proposed a systematic identification method for the finite element model to avoid the occurrence of large deviation of the short cable and proved that the finite element model is more accurate than the calculation result of the practical formula on the basis of parameter identification through examples. Yan et al. [22] established an innovative framework for the cable force estimation considering complex boundary conditions, from the perspective of the zero-amplitude points of cable mode shapes. Considering the complexity of the vibration-based cable tension estimation, Ehsan et al. [23] proposed a simple novel framework to estimate the cable tension based on artificial neural networks and verified the accuracy of the method through the Ironton–Russell Bridge.

It can be seen from the existing research work that there is a good solution to the identification of the cable force for long cable at present, while for short cable, researchers usually use the finite element method combined with parameter identification technology to consider the influence of bending stiffness, boundary conditions, etc., which has a high technical requirement for engineers and is not conducive to the engineering application. By analyzing on vibration characteristics of cables, a new parameter named equivalent effective length is introduced to solve the issue in this paper. There will be more parameters to be measured by adding added mass block on cables in order to combine the concept of equivalent effective length and parameter of an added mass block. The analytical method for calculating equivalent effective length is established by measuring the difference of vibration frequency of cable before and after addition mass block is applied. Then, tension force of short length cable can be identified based on the equivalent effective length and measured vibration frequency. Finally, the reliability and practicability of this method are verified by practical engineering application.

## 2. Equivalence of Effective Cable Length

Nowadays, one of the most popular and convenient ways to identify cable tension in engineering projects depends on the measurement of the cable's vibration frequency and the following calculation. For those cables which are not equipped with a pressure sensor or other instruments, frequency method is the most efficient and economical way during the service stage. The theory is to simplify a cable as a simply supported cable, where $L$ is the effective length, $T_0$ is the cable tension, and $EI$ is the bending stiffness of cable. The simplified model is shown in Figure 1.

Figure 2 shows a microscopic mechanics model of a cable with transverse vibration, where $y(x, t)$ is the horizontal movement varied with location $x$ and time $t$, $m$ is the weight of cable per unit length, $M$ is the bending moment, and $V$ is the shear force. Here, the bending stiffness of cable is taken into consideration.

The vibration equation can be developed based on the equilibrium of force and moment:

$$EI\frac{\partial^4 y(x,t)}{\partial x^4} + m\frac{\partial^2 y(x,t)}{\partial t^2} - T_0\frac{\partial^2 y(x,t)}{\partial x^2} = 0. \quad (1)$$

Having solved equation (1) by the Galerkin procedure, the natural frequency of cable is given as

$$\omega_n = \sqrt{\frac{EI}{m}\left(\frac{n\pi}{L}\right)^4 + \frac{T_0}{\rho A}\left(\frac{n\pi}{L}\right)^2} \quad (n = 1, 2, 3, \ldots), \quad (2)$$

where $\omega_n$ is the $n$-order natural frequency.

From equation (2), one can solve the tension force once the natural frequency of cable is measured since bending stiffness of cable $EI$, weight per unit length $m$, and effective length $L$ are known. Bending stiffness $EI$ and mass per unit length $m$ can be known right after cable installation. For effective length $L$, it is determined by boundary conditions of cable such as distance between two anchoring points or damper conditions at the two ends. For cable with long length, the ratio of influence in terms of boundary conditions on effective length $L$ is not so large so that the accuracy of tension force measurement is still acceptable. However,

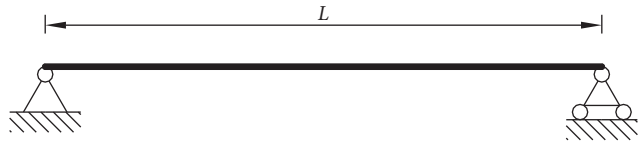


Figure 1: Simplified mechanics model of a cable.

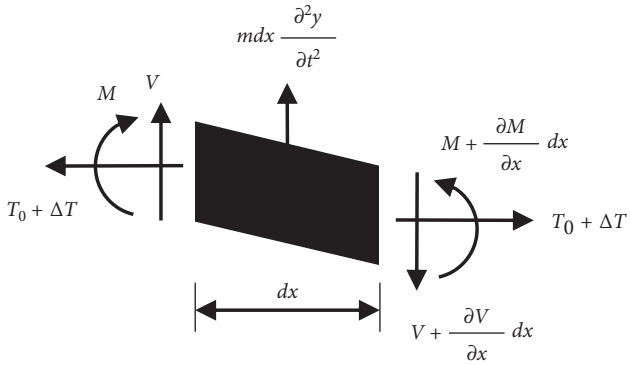


Figure 2: A microscopic mechanics model of a vertical stretched cable with consideration of bending stiffness.

when cable length becomes short, boundary conditions will have a large effect on the accuracy of cable tension measurement. And the error and accuracy are not accepted, sometimes even lead to misjudgment.

From the analysis above, for short length cable, the main factor influencing the accuracy of tension force measurement by using the frequency method is the boundary conditions. The effect can be equivalent to the influence on effective length. Now define $L$ as the distance between two anchoring points, two dampers are installed, respectively, from anchoring point with distance $d$, and the stiffness of damper is $k$. The force diagram of cable is simplified as Figure 3.

From the mechanical equilibrium of force and moment, one can obtain the vibration equilibrium of cable:

$$EI\frac{\partial^4 y(x,t)}{\partial x^4}+m\frac{\partial^2 y(x,t)}{\partial t^2}-T\frac{\partial^2 y(x,t)}{\partial x^2}+ky(x,t)\cdot\delta_1(x-d)++ky(x,t)\cdot\delta_2(x-d+L)=0, \tag{3}$$

where $EI$ is the stiffness of cable, $m$ is the cable weight per unit length, $T$ is the tension force, and $\delta_1(x-d)$ and $\delta_2(x-d+L)$ are the Dirac equation, i.e.,

$$\begin{aligned}\delta_1(x-d)&=\begin{cases}1, & x=d,\\ 0, & x\neq d,\end{cases}\\ \delta_2(x-d+L)&=\begin{cases}1, & x=L-d,\\ 0, & x\neq L-d.\end{cases}\end{aligned} \tag{4}$$

Equation of free vibration for cable is

$$y(x,t)=\phi(x)\sin(\omega t+\theta), \tag{5}$$

where $\phi(x)$ is the vibration function of cable, $\omega$ is the natural frequency of cable, and $\theta$ is the phase angle.

By using the RITZ method, the total kinetic energy of cable vibration at a moment is

$$E_k=\frac{1}{2}\int_0^L m\left(\frac{\partial y}{\partial t}\right)^2 dx=\frac{1}{2}m\omega^2\cos^2(\omega t+\theta)\int_0^L[\phi(x)]^2 dx. \tag{6}$$

From the equation above, one can get the maximum total kinetic energy

$$E_{k\max}=\frac{1}{2}m\omega^2\int_0^L[\phi(x)]^2 dx. \tag{7}$$

And the total potential energy of cable at a moment is

$$\begin{aligned}V_k&=\frac{1}{2}\int_0^L EI\left(\frac{\partial^2 y}{\partial x}\right)^2 dx+\frac{1}{2}\int_0^L T\left(\frac{\partial y}{\partial x}\right)^2 dx+\frac{1}{2}k[y(d,t)]^2+\frac{1}{2}k[y(L-d,t)]^2\\ &=\frac{1}{2}EI\sin^2(\omega t+\theta)\int_0^L[\phi''(x)]^2 dx+\frac{1}{2}T\sin^2(\omega t+\theta)\int_0^L[\phi'(x)]^2 dx+\frac{1}{2}k\sin^2(\omega t+\theta)[\phi(d)]^2\\ &\quad+\frac{1}{2}k\sin^2(\omega t+\theta)[\phi(L-d)]^2.\end{aligned} \tag{8}$$

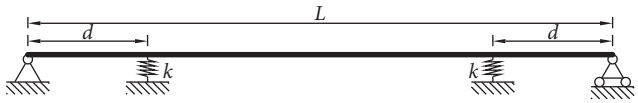


Figure 3: Simplified force diagram of cable influenced by stiffness of damper.

From the equation above, the maximum total potential energy could be obtained as follows:

$$V_{k\max} = \frac{1}{2}EI\int_0^L [\phi''(x)]^2 \mathrm{d}x + \frac{1}{2}T\int_0^L [\phi'(x)]^2 \mathrm{d}x + \frac{1}{2}k[\phi(d)]^2 + \frac{1}{2}k[\phi(L-d)]^2. \tag{9}$$

When the stiffness of damper is small, vibration mode of cable can be approximated as a vibration of a simply supported beam, which is

$$\phi(x) = \sin\left(\frac{n\pi x}{L}\right). \tag{10}$$

According to the RITZ method, for cable vibration, the maximum total kinetic energy is equal to the maximum potential energy:

$$E_{k\max} = V_{k\max}. \tag{11}$$

Based on equations (7) and (9), one can solve the natural frequency of cable

$$\omega^2 = \frac{EI\int_0^L [\phi''(x)]^2 \mathrm{d}x + T\int_0^L [\phi'(x)]^2 \mathrm{d}x + k[\phi(d)]^2 + k[\phi(L-d)]^2}{m\int_0^L [\phi(x)]^2 \mathrm{d}x}. \tag{12}$$

Taking equations (10) into (12) has

$$\omega^2 = \frac{EI}{m}\left(\frac{n\pi}{L}\right)^4 + \frac{T}{m}\left(\frac{n\pi}{L}\right)^2 + \frac{4k}{mL}\sin^2\left(\frac{n\pi d}{L}\right), \tag{13}$$

where $\sin^2(n\pi d/L)$ is a constant. Define $\beta = \sin^2(n\pi d/L)$, and (13) becomes

$$\omega^2 = \frac{EI}{m}\left(\frac{n\pi}{L}\right)^4 + \frac{T}{m}\left(\frac{n\pi}{L}\right)^2 + \frac{4k\beta}{mL}. \tag{14}$$

Now, one can transform the force diagram in Figure 3 into a new equivalent force diagram with an equivalent effective length $L_{eq}$ of pin-supported cable, as shown in Figure 4.

Then, the natural frequency of cable after equivalence is

$$\omega^2 = \frac{EI}{m}\left(\frac{n\pi}{L_{eq}}\right)^4 + \frac{T}{m}\left(\frac{n\pi}{L_{eq}}\right)^2. \tag{15}$$

Since the natural frequency does not change before and after equivalence, by taking equations (14) and (15) into consideration, one has

$$\frac{EI}{m}\left(\frac{n\pi}{L}\right)^4 + \frac{T}{m}\left(\frac{n\pi}{L}\right)^2 + \frac{4k\beta}{mL} = \frac{EI}{m}\left(\frac{n\pi}{L_{eq}}\right)^4 + \frac{T}{m}\left(\frac{n\pi}{L_{eq}}\right)^2. \tag{16}$$

Here, if the influence of bending stiff of cable is ignored, one can derive the relationship between original length and equivalent effective length of cable:

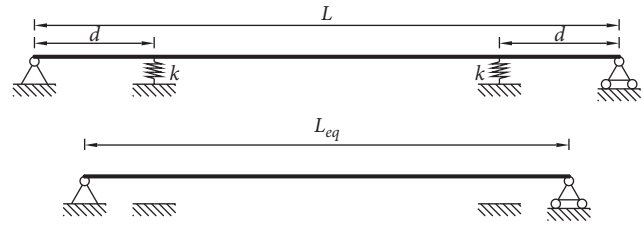


Figure 4: Equivalent model of cable.

$$L_{eq} = L\sqrt{\frac{1}{1+\left(4Lk\beta/Tn^2\pi^2\right)}}. \tag{17}$$

From the above equation, it is obvious that the equivalent length of cable is shorter compared to the original cable length because the effect of damper stiffness. Based on the theoretical derivation above, for a cable with a damper, its effective length can be equivalent by using an equivalent effective length to identify the cable tension force.

## 3. Using Added Mass to Identify the Effective Length of Short Length Cable

In equation (14), stiffness of cable $EI$ and mass per unit length $m$ are determined by design, and natural frequency of cable $\omega_n$ can be measured by vibration testing instrument. Therefore, it is only necessary to figure out the equivalent effective length $L_{eq}$ in order to obtain the cable tension force $T$ based on measured vibration frequency $\omega_n$.

To figure out the $L_{eq}$, an added mass $M$ is applied on cable on purpose, away from bottom end of cable by a distance $L_m$. Then, the cable can be simplified as the model shown in Figure 5, where $L_m' = L_m - (L - L_{eq}/2)$.

Here, the vibration equilibrium of cable becomes

$$EI\frac{\partial^4 y(x,t)}{\partial x^4} + [m + M\delta(x - L_m')]\frac{\partial^2 y(x,t)}{\partial t^2} - T\frac{\partial^2 y(x,t)}{\partial x^2} = 0, \tag{18}$$

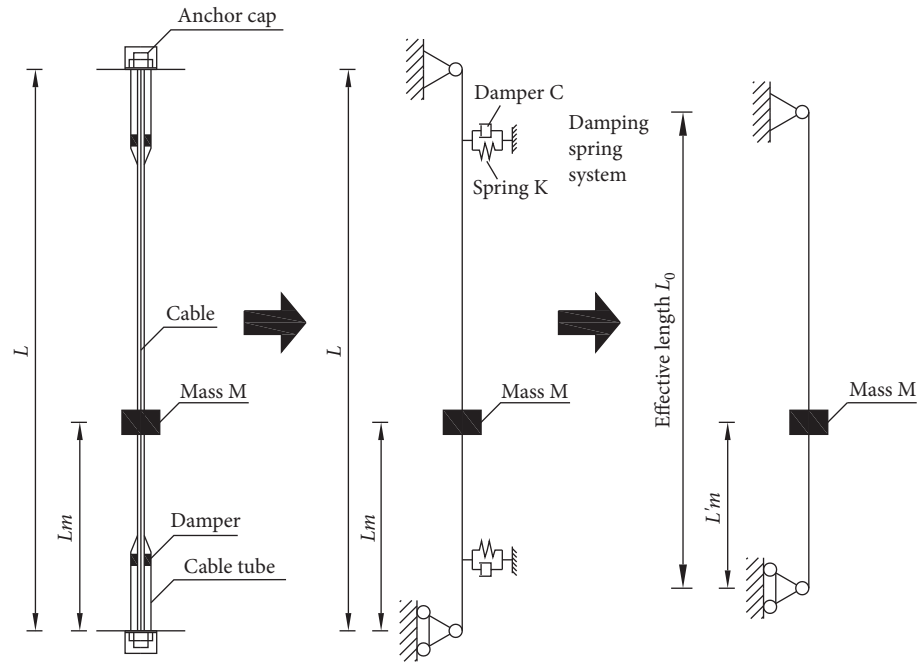


Figure 5: Simplified diagram of cable with added mass.

where $\delta(x - L'_m) = \begin{cases} 1 & x = L'_m \\ 0 & x \neq L'_m \end{cases}$.

The free vibration equation of cable might be defined as

$$y(x,t) = \phi(x)\sin(\omega_m t + \theta), \tag{19}$$

where $\phi(x)$ is the vibration model function, $\omega_m$ is the natural frequency of cable after added mass block is applied, and $\theta$ is the phase angle.

Also, use the RITZ method to solve the vibration equilibrium of cable in equation (19). Now the total kinetic energy of cable vibration at a moment is

$$\begin{aligned} E_k &= \frac{1}{2}\int_0^L m\left(\frac{\partial y}{\partial t}\right)^2 \mathrm{d}x + \frac{1}{2}M\left(\frac{\partial y(L'_m,t)}{\partial t}\right)^2 \\ &= \frac{1}{2}m\omega_m^2\cos^2(\omega_m t + \theta)\int_0^L [\phi(x)]^2\mathrm{d}x + \frac{1}{2}M\omega_m^2\cos^2(\omega_m t + \theta)[\phi(L'_m)]^2. \end{aligned} \tag{20}$$

Then, the maximum total kinetic energy $E_{k\max}$ is

$$E_{k\max} = \frac{1}{2}m\omega_m^2\int_0^L [\phi(x)]^2\mathrm{d}x + \frac{1}{2}M\omega_m^2[\phi(L'_m)]^2. \tag{21}$$

And the total potential energy of cable vibration at a moment is

$$\begin{aligned} V_k &= \frac{1}{2}\int_0^L EI\left(\frac{\partial^2 y}{\partial x}\right)^2 \mathrm{d}x + \frac{1}{2}\int_0^L T\left(\frac{\partial y}{\partial x}\right)^2 \mathrm{d}x \\ &= \frac{1}{2}EI\sin^2(\omega_m t + \theta)\int_0^L [\phi''(x)]^2\mathrm{d}x + \frac{1}{2}T\sin^2(\omega_m t + \theta)\int_0^L [\phi'(x)]^2\mathrm{d}x. \end{aligned} \tag{22}$$

Then, the maximum total potential energy is

$$V_{k\max} = \frac{1}{2}EI\int_0^L [\phi''(x)]^2\mathrm{d}x + \frac{1}{2}T\int_0^L [\phi'(x)]^2\mathrm{d}x. \tag{23}$$

When the added mass is small, vibration mode of cable can be approximated as the vibration of a simply supported beam, which is

$$\phi(x) = \sin\left(\frac{n\pi x}{L_{eq}}\right). \tag{24}$$

According to the RITZ method, for cable vibration, the maximum total kinetic energy is equal to the maximum potential energy:

$$E_{k\max} = V_{k\max}. \tag{25}$$

Based on equations 21 and (23), one can solve the natural frequency of cable after an added mass block is applied:

$$\omega_m^2 = \frac{EI\int_0^L [\phi''(x)]^2 dx + T\int_0^L [\phi'(x)]^2 dx^2}{m\int_0^L [\phi(x)]^2 dx + M[\phi(L_m')]^2}. \tag{26}$$

Bring equations (24) into (26), one has

$$\omega_m^2 = \frac{1}{1+\left(2M/mL_{eq}\right)\sin^2\left(nL_m'/L_{eq}\right)}\left(\frac{EI}{m}\left(\frac{n\pi}{L_{eq}}\right)^4 + \frac{T}{m}\left(\frac{n\pi}{L_{eq}}\right)^2\right). \tag{27}$$

The natural frequency of cable before applying an added mass block is

$$\omega^2 = \frac{EI}{m}\left(\frac{n\pi}{L_{eq}}\right)^4 + \frac{T}{m}\left(\frac{n\pi}{L_{eq}}\right)^2. \tag{28}$$

Using the 1st order of natural frequency to analyze, by comparing equations (26) and (27), one has

$$\left(\frac{\omega_1}{\omega_{m1}}\right)^2 = 1 + \frac{2M}{mL_{eq}}\sin^2\frac{\pi L_m'}{L_{eq}} = 1 + \frac{2M}{mL_{eq}}\sin^2\frac{\pi\left(2L_m - L + L_{eq}\right)}{2L_{eq}}. \tag{29}$$

$\omega_1$ and $\omega_{m1}$, the 1st order of natural frequency of cable before and after added mass is applied, can be measured by instrument. The weight of an added mass $M$ and its location $L_m$ can also be measured and determined. Consequently, based on the 1st order of natural frequency of cable before and after an added mass block is applied, the equivalent effective length of cable can be derived by equation (28). If the added mass block is applied at the middle of cable, which means $L_m = (L/2)$, then from equation (29), one has

$$\left(\frac{\omega_1}{\omega_{m1}}\right)^2 = 1 + \frac{2M}{mL_{eq}}. \tag{30}$$

Or it can be written as

$$L_{eq} = \frac{2M}{\left[\left(\omega_1/\omega_{m1}\right)^2 - 1\right]m} \tag{31}$$

## 4. Using Equivalent Effective Length to Identify Cable Tension Force

Taking equivalent length $L_{eq}$ into equation (28), one can obtain the equation of cable tension force $T$, i.e.,

$$T = m\left(\frac{\omega_1 L_{eq}}{\pi}\right)^2 - EI\left(\frac{\pi}{L_{eq}}\right)^2 = \frac{16M^4\omega_1^2 - \left[\left(\omega_1/\omega_{m1}\right)^2 - 1\right]^4\pi^4 mEI}{4\left[\left(\omega_1/\omega_{m1}\right)^2 - 1\right]^2\pi^2 M^2 m}. \tag{32}$$

The equation above is an accurate method to identify the tension force of short length cable, depending on $\omega_1$ and $\omega_{m1}$, the 1st order of natural frequency of cable before and after added mass block is applied.

## 5. Practical Engineering Verification

In order to illustrate the accuracy and applicability of the cable tension force calculation method proposed in this

paper, three arch bridges are selected as a case study. Firstly, the pressure sensors need to be installed on the cable during bridge construction to obtain the tension force of cable, and consider this value as a reference value. Then, combined with the measured frequency, the tension force of the short cable is calculated by the method of additional mass block proposed in this paper and compared with the reference value.

*5.1. Project 1.* Liujing Yujiang superbridge (as shown in Figure 6) in Guangxi, which was built in 1997 and completed in 1999, is a superlarge bridge across Yujiang on Liuzhou Nanning Expressway. In 2018, it was repaired and reinforced, replacing the original 61 $\varphi$ 7 galvanized parallel steel wire with 55 $\varphi$ 7 galvanized parallel steel wire.

In the process of replacing the suspender, the no. #4 short suspender with a length of 6.93 m at the upstream side is selected as the verification example of the proposed method in this paper. The new suspender adopts OVMLZM 7-55 III type PES (FD) low-stress anticorrosive cable body and adopts double-layer HDPE protection. Its strength grade is 1670 mpa, the breaking load is 3535 kN, modulus of elasticity is greater than $1.9 \times 105$ MPa, the anchorage at the arch rib end adopts the cold cast anchor lzm-55, and other end adopts the anchorage form of steel tie rod and parallel steel wire connector with a ball stranding device.

After the installation of the new suspender, the lower end of the suspender is tensioned with a jack and the tension was 450 kN. Then, the cable force is identified by this method. The processes are as follows:

(1) The velocity pick-up is installed at 5 m from the lower end of the suspender, and the velocity time-history curve of the suspender is obtained by means of environmental random excitation. FFT analysis is carried out on the time-history curve, and then, the obtained 1st order frequency of the suspender is 13.36 Hz.

(2) A 30.4 kg mass block (as shown in Figure 7) 2.275 m away from the lower end of the suspender was installed. Repeat step 1, the 1st order frequency of the suspender with lumped mass block is 11.41 Hz.

(3) The effective length of the suspender could be calculated according to equation (28) whose corresponding parameters are shown in Table 1. One can obtain effective length of suspender is 5.81 m.

Then, the cable force is 436.13 kN by taking the effective length into equation (31), and its deviation from the actual cable force is only 3.08%, which meets the requirements of the project.

*5.2. Project 2.* The Pumiao Bridge, shown in Figure 8, is located in Pumiao County, Yongning District, Nanning City, and crossed the Yongjiang River. It was completed in July 1996. The main bridge is a half-through-type steel frame reinforced concrete arch bridge with a 312 m span. 27 suspenders are arranged for each arch rib of the main bridge.

Figure 6: Liujing Yujiang superbridge.

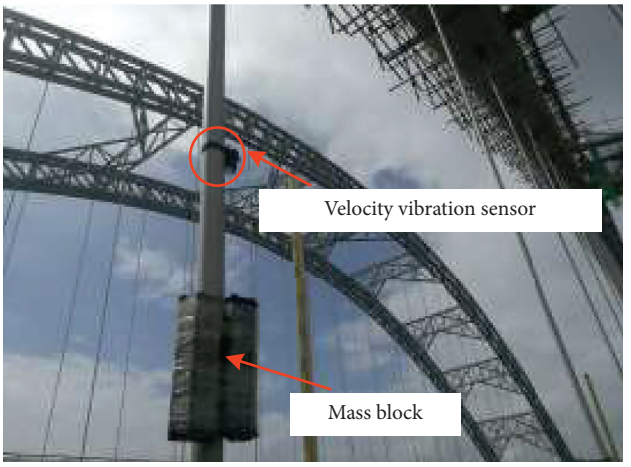


Figure 7: Field test of cable force with lumped mass.

Table 1: Parameter table of equivalent length calculation.

| Parameters | $\omega_1$ (rad/s) | $\omega_{m1}$ (rad/s) | M (kg) | m (kg/m) | $L_m$ (m) | $L$ (m) |
|---|---|---|---|---|---|---|
| Value | 13.36 | 11.41 | 30.4 | 18.43 | 2.275 | 6.93 |

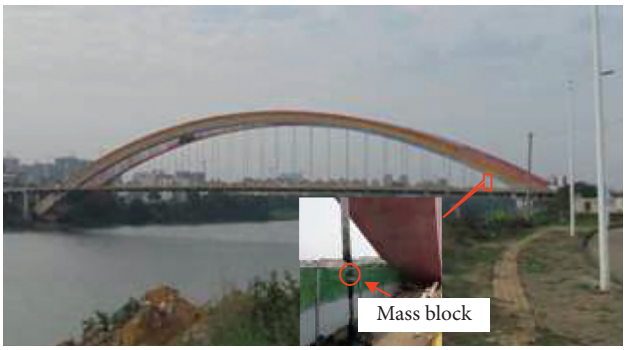


Figure 8: Pumiao Bridge.

Table 2: Comparison results of cable forces.

| Position | Frequencies without mass block (Hz) | Frequencies with mass block (Hz) | Tensioning force (kN) |
|---|---|---|---|
| Upstream | 9.91 | 9.70 | 1174.51 |
| Downstream | 9.86 | 9.65 | 1185.55 |

Table 3: Comparison results of cable forces under different test methods.

| Method | Upstream | | Downstream | |
|---|---|---|---|---|
| | Cable force (kN) | Relative deviation (%) | Cable force (kN) | Relative deviation (%) |
| Pressure sensor method | 1174.51 | — | 1185.55 | — |
| Conventional method | 1711.93 | 45.76% | 1695.18 | 42.99% |
| This paper | 1149.64 | −2.12% | 1184.28 | −0.11% |

The original suspender is made of 27 Φ 7 high-strength steel wire wrapped with PE. Due to the cracks of PE sheath of some suspenders and the corrosion of lower anchor head, the suspenders of the whole bridge were replaced in 2018. 1860 grade 27 Φ 15.2 mm epoxy coated unbonded steel strand is selected as the new suspenders and wrapped with PE. The outer diameter of the cable body is Φ 126 mm, the nominal breaking force is 7031 kN, and the unit weight of the cable body is 36.81 kg/m.

The 2nd suspenders are typical short suspenders, of which the cable force is tested to verify the correctness of this method.

First, the acceleration signal of the suspender without mass was tested. Then, the iron block with a mass of 20.75 kg (as shown in Figure 8) was bound at the middle position of the suspender, and the 1st order frequency of the cable could be obtained through FFT transformation, as shown in Table 2. Finally, the cable force of the suspender, as shown in Table 2, can be obtained by taking the frequency into equation (31). Simultaneously, the results of the cable force calculated by the conventional method are also shown in Table 3.

It can be seen from Table 1 that, due to the constraint of the additional mass, the first-order frequency decreases to some extent. According to the comparison results in Table 2, one can see the following: (1) there is a large deviation between the cable force identified by the conventional method and the actual cable force, and the upstream and downstream errors are 45.76% and 42.99%, respectively, which cannot meet the engineering requirements. (2) The upstream and downstream cable force errors identified by the method in this paper are very small, i.e., −2.12% and −0.11%, respectively, which can meet the engineering requirements.

*5.3. Project 3.* Yuanjiang Bridge in Wuzhou is a 3-span half-through concrete-filled steel tubular tied arch bridge (as shown in Figure 9). It is 695 m long and 25.6 m wide. The span composition of the main bridge is $(40 + 175 + 40)\ m$, and the rise height is 43.75 m. The length of the 5th suspender is 10.38 m, tensile stiffness is 109.76 kN, and cable unit length mass is 20.88 kg/m.

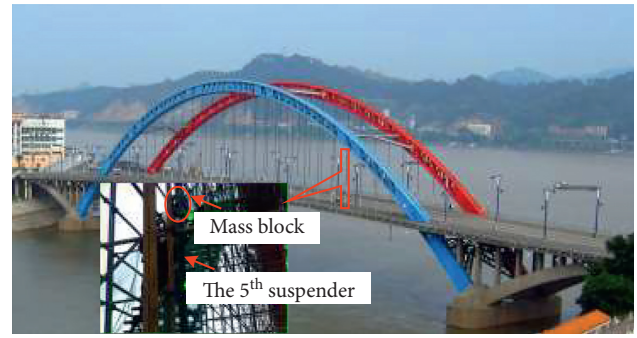


Figure 9: Yuanjiang Bridge.

When installing the 5th suspender (shown in Figure 9), the method in this paper is verified. Firstly, the acceleration pick-up is installed at the position 3 m away from the anchor head below. The acceleration signal of the suspender is tested, as shown in Figure 10(a), and the 1st order frequency of the cable is 13.497 Hz through FFT transformation (shown in Figure 10(b)). Then, the iron block with a weight of 20.75 kg is bound at the middle position of the suspender (as shown in Figure 9) to simulate the concentrated mass block. The collected acceleration signal is as shown in Figure 11(a), and the first-order frequency is 12.087 Hz through spectrum analysis of acceleration signal, as shown in Figure 11(b).

Finally, the effective length of the suspender could be calculated according to equation (29) which corresponding parameters are shown in Table 4. It can be obtained that an effective length of suspender is 8.06 m. The cable forces of the suspender can be obtained by taking the frequencies into equation (32). Simultaneously, the accurate cable force value of the suspender is obtained by the pressure sensor installed at the anchor head, and the cable force calculated by the conventional calculation method is also shown in Table 5, respectively.

From the data in Table 5, it can be seen that the cable force value obtained by the conventional method has a great error with the actual cable force value, reaching 72.45%, while by the method in this paper, the test accuracy can reach within 5%, meeting the engineering requirements.

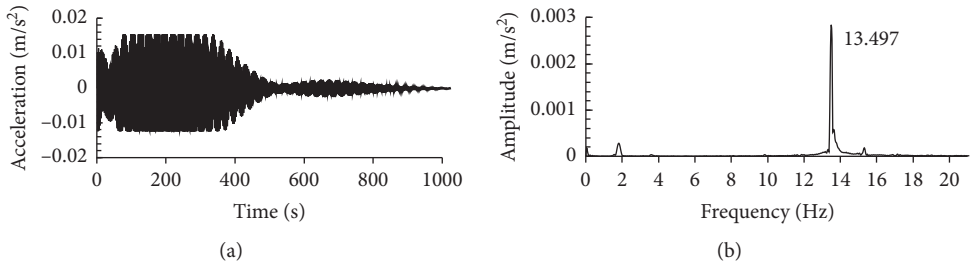


Figure 10: (a) Acceleration time-history curve of suspender without additional mass; (b) frequency spectrum without additional mass.

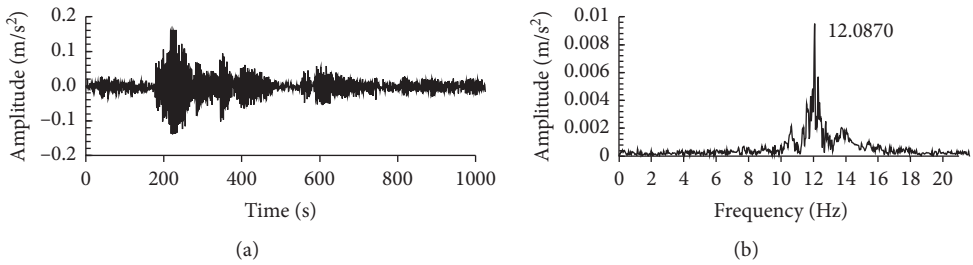


Figure 11: (a) Acceleration time-history curve of suspender with additional mass; (b) frequency spectrum with additional mass.

Table 4: Parameters table of equivalent length calculation.

| Parameters | $\omega_1$ (rad/s) | $\omega_{m1}$ (rad/s) | M (kg) | m (kg/m) | $L_m$ (m) | $L$ (m) |
|---|---|---|---|---|---|---|
| Value | 13.497 | 12.087 | 20.75 | 20.88 | 5.19 | 10.38 |

Table 5: Comparison results of cable forces.

| Method | Force (kN) | Relative deviation (%) |
|---|---|---|
| Pressure sensor method | 935.00 | — |
| Conventional method | 1612.39 | 72.45 |
| This paper | 974.59 | 4.23 |

## 6. Conclusion

Considering that the traditional frequency method has a large error in calculating short cable tension force, this paper presented a novel calculation method to improve the accuracy of the results. Firstly, the identification method of the effective cable length considering the mass block was deduced, and combined with the natural frequency, the calculation equation of the short cable force was established. Then, three practical projects were used to illustrate the analysis process of the proposed method. The following conclusions are drawn:

(1) Since the bending stiffness and boundary conditions have a greater impact on the accuracy of the short cable tension force measurement, the concept of equivalent effective length is presented to consider the influence. By installing two dampers on the cable to simulate the change in boundary conditions, the vibration equation of the cable is established. Then, the equivalent effective length of shore cable can be obtained through the RITZ method and the principle of constant natural frequency.

(2) In order to effectively and accurately identify the equivalent effective length of short cable, a mass block is installed at a certain position from the anchor cap on the cable. Then, the equivalent effective length identification method considering the mass block is deduced. Combining the natural frequency and the deduced effective length, a novel measurement method of the short cable tension force considering the mass block is proposed.

(3) Three suspender arch bridges are selected as case study. The velocity vibration sensor and the mass block are, respectively, installed on the tested short cable, and the time-history vibration signals collected can be converted into the natural frequency of the short cable through FFT transformation. The conventional method and the new method proposed in this paper are used to calculate the short cable tension force, respectively. By comparing with the theoretical cable tension force obtained by the pressure sensor method, the maximum relative error obtained by the method proposed in this paper is 3.08%, −2.12%, and 4.23%, respectively, which has high accuracy and reliability.

## Data Availability

The data used to support the findings of this study are included within the article.

## Conflicts of Interest

The authors declare that they have no conflicts of interest.

## Acknowledgments

This research was sponsored by the Nanning Excellent Young Scientist Program (no. RC20180108), Nanning Excellent Young Scientist Program and Guangxi Beibu Gulf Economic Zone Major Talent Program (no. RC20190206), Science and Technology Base and Talent Special Project of Guangxi Province (no. AD19245152), and "Yongjiang Plan" of Nanning Leading Talents in Innovation and Entrepreneurship (no. 2018-01-04).

## References

[1] Q. Guo, L. Li, Y. Cheng, Y. Jiao, and C. Xu, "Laboratory evaluation on performance of diatomite and glass fiber compound modified asphalt mixture," *Materials & Design (1980-2015)*, vol. 66, no. 66, pp. 51–59, 2015.

[2] H. B. Liu, H. Wang, G. J. Tan et al., "Effect of temperature and spring-mass systems on modal properties of Timoshenko concrete beam," *Structural Engineering and Mechanics*, vol. 65, no. 4, pp. 389–400, 2018.

[3] Q. Guo, Y. Bian, L. Li, Y. Jiao, J. Tao, and C. Xiang, "Stereological estimation of aggregate gradation using digital image of asphalt mixture," *Construction and Building Materials*, vol. 94, no. 94, pp. 458–466, 2015.

[4] L. Wang, H. Wang, L. Li, T. Hao, and C. Wu, "An adjustment method for the suspender tension of CFSTTTHAB based on influence matrix of single suspender," *Advances in Civil Engineering*, vol. 2020, no. 6, pp. 1–10, 2020.

[5] Q. L. Guo, Q. Liu, P. Zhang, Y. Gao et al., "Temperature and pressure dependent behaviors of moisture diffusion in dense asphalt mixture," *Construction and Building Materials*, vol. 2020, no. 246, Article ID 118500.

[6] Seaoc, *Conceptual Framework for Performance-Based Seismic Design*, pp. 393–416, Structural Engineers Association of California, 1996.

[7] K.-S. Kim and H. S. Lee, "Analysis of target configurations under dead loads for cable-supported bridges," *Computers & Structures*, vol. 79, no. 29-30, pp. 2681–2692, 2001.

[8] J. R. Casas, "A combined method for measuring cable forces: the cable-stayed alamillo bridge, Spain," *Structural Engineering International*, vol. 4, no. 4, pp. 235–240, 1994.

[9] S. Kangas, A. Helmicki, V. Hunt, R. Sexton, and J. Swanson, "Cable-stayed bridges: case study for ambient vibration-based cable tension estimation," *Journal of Bridge Engineering*, vol. 17, no. 6, pp. 839–846, 2012.

[10] W. Y. Liao, Y. Q. Ni, and G. Zheng, "Tension force and structural parameter identification of bridge cables," *Advances in Structural Engineering*, vol. 15, no. 6, pp. 983–995, 2012.

[11] A. C. Marcelo and A. P. Carlos, "Determination of the axial force on stay cables accounting for their bending stiffness and rotational end restraints by free vibration tests," *Journal of Sound and Vibration*, vol. 317, no. 1-2, pp. 127–141, 2008.

[12] Y. Q. Ni, J. M. Ko, and G. Zheng, "Dynamic analysis of large-diameter sagged cables taking into account flexural rigidity," *Journal of Sound and Vibration*, vol. 257, no. 2, pp. 301–319, 2002.

[13] A. B. Mehrabi and H. Tabatabai, "Unified finite difference formulation for free vibration of cables," *Journal of Structural Engineering*, vol. 124, no. 11, pp. 1313–1322, 1998.

[14] H. Zui, T. Shinke, and Y. Namita, "Practical formulas for estimation of cable tension by vibration method," *Journal of Structural Engineering*, vol. 122, no. 6, pp. 651–656, 1996.

[15] A. B. Mehrabi and H. Tabatabai, "Unified finite difference formulation for free vibration of cables," *Journal of Structural Engineering*, vol. 124, no. 11, pp. 1313–1322, 1998.

[16] Z. Fang and J.-q. Wang, "Practical formula for cable tension estimation by vibration method," *Journal of Bridge Engineering*, vol. 17, no. 1, pp. 161–164, 2012.

[17] H. Zui, Y. Hamazaki, and Y. Namita, "Study on tension and flexual rigidity identification for cables having large ratio of the diameter and the length," *Doboku Gakkai Ronbunshu*, no. 703, pp. 141–149, 2002.

[18] G. Roman, D. R. Guido, and P. Johannes, "Cable force determination for the Danube channel bridge in Vienna," *Structural Engineering International*, vol. 15, no. 3, pp. 181–185, 2005.

[19] B. H. Kim and T. Park, "Estimation of cable tension force using the frequency-based system identification method," *Journal of Sound and Vibration*, vol. 304, no. 3-5, pp. 660–676, 2007.

[20] T. Park, D. Hyung Lee, and B. Hwa Kim, "Estimation of tension force in double hangers by a system identification approach," *Inverse Problems in Science and Engineering*, vol. 18, no. 2, pp. 197–216, 2010.

[21] P. Kyu-Sik, S. Taek-Ryong, and N. Myung-Hyun, "Feasibility study on tension estimation technique for hanger cables using the FE model-based system identification method," *Mathematical Problems in Engineering*, vol. 2015, Article ID 512858, 12 pages, 2015.

[22] B. Yan, J. Yu, and M. Soliman, "Estimation of cable tension force independent of complex boundary conditions," *Journal of Engineering Mechanics*, vol. 141, no. 1, 2014.

[23] H. A. M. Z. S. Ehsan, M. Norouzi, R. Allemang et al., "Vibration-based cable condition assessment: a novel application of neural networks," *Engineering Structures*, vol. 177, pp. 291–305, 2018.

Hindawi
Advances in Materials Science and Engineering
Volume 2021, Article ID 6611691, 12 pages
https://doi.org/10.1155/2021/6611691

*Research Article*

# Study on the Accurate Measurement and Quantitative Evaluation Methods of Aggregate Surface Roughness

**Luoke Li**,[1] **Meng Guo**,[2] **and Cong Zeng**[3]

[1]*Faculty of Civil Engineering and Mechanics, Kunming University of Science and Technology, Kunming 650500, China*
[2]*The Key Laboratory of Urban Security and Disaster Engineering of Ministry of Education, Beijing University of Technology, Beijing 100124, China*
[3]*School of Civil Engineering and Architecture, Northeast Electric Power University, Jilin 132012, China*

Correspondence should be addressed to Meng Guo; gm@bjut.edu.cn

Received 4 November 2020; Revised 15 December 2020; Accepted 28 December 2020; Published 20 January 2021

Academic Editor: Qinglin Guo



In this work, to quantitatively analyze the roughness of the surfaces of road aggregates, the contact measurement technique and contactless scanning technique were, respectively, used to capture the coordinate data of point clouds on the aggregate surface, which were then used to reconstruct the digital elevation models of aggregate particles. Then, the joint roughness coefficient (JRC) was used as an evaluation index, and the quantitative calculation methods of the two-dimensional (2D) contour line roughness and three-dimensional (3D) contour surface roughness of aggregate particles were, respectively, studied. Finally, the anisotropic characteristics and size effect of the roughness coefficients of aggregates with different lithologies were, respectively, investigated, based on which the practicability of the 3D roughness coefficient index was proven. The results demonstrate that the roughness of a road aggregate surface can be quantitatively described by the point cloud data. The 2D roughness of aggregate profile lines exhibits anisotropy, while the 3D roughness of the aggregate contour surface indicates the size effect. The subtle morphological changes of the surface textures of aggregates can be accurately described by the 3D joint roughness coefficient ($JRC^{3D}$) calculated by the feature parameter method.

## 1. Introduction

Rock aggregates are commonly used raw materials in the field of road engineering, and their surface roughness significantly affects the performance of asphalt mixtures [1]. The rough surface is beneficial to increasing the contact area between the aggregate and asphalt, thereby creating a certain penetration depth of the asphalt, increasing the thickness of the asphalt film, and enhancing the physical adsorption of the two materials on the contact surface [2–6]. Additionally, there are many fine protrusions on the surfaces of aggregates, which is conducive to the formation of the aggregate skeleton structure of the asphalt mixture during the mixing process, thereby endowing asphalt concrete with good shear strength and ultimately improving the rutting resistance of the road surface [7–9].

From the aspect of the collection of aggregate surface morphology data, with the continuous development of measurement technology, a variety of measurement methods have been applied to obtain the characteristic information of the surfaces of rock materials. According to the acquisition method, these methods can be divided into contact contour measurement methods and noncontact optical measurement methods. Additionally, according to the dimension, the data can be divided into two-dimensional (2D) contour line coordinate data and three-dimensional (3D) contour surface coordinate data [10, 11]. To quantitatively evaluate the roughness coefficient of road aggregates, the accuracy requirements must first be met. Moreover, the measurement instruments, test methods, and calculation processes should not be too complicated and should be characterized by a fast measurement speed and convenient statistical analysis. Therefore, the contact measurement method was commonly used to quickly calculate the 2D roughness of the profile contour of the aggregate surface and

the 3D topography data can also be obtained via a large amount of 2D contour data interpolation [12, 13]. In contrast, the high-precision noncontact measurement technology based on the optical principle has several advantages for obtaining data on the surface topography of rock materials [14]. A 3D scanning device can quickly obtain point cloud data describing the 3D features of the aggregate particles. These data can be used for the physical reconstruction of the aggregate and the quantification of 3D morphological parameters [15].

The quantitative evaluation methods for the characterization of aggregate surface roughness primarily include the fractal mathematics method and statistical parameter method [16]. In the fractal mathematics method, more attention is paid to the correlation between the characteristic fractal dimension of the surface topography of the rock structure and the roughness and mechanical properties [17]. In contrast, in the statistical parameter method, quantitative evaluation is conducted by establishing the regression relationship between the characteristic parameters of the surface topography of rock materials and the roughness index [15]. The joint roughness coefficient (JRC) recommended by the International Society of Rock Mechanics was commonly used as the evaluation index of the surface texture roughness of the rock aggregate [18]. In geotechnical engineering research, roughness is often used to analyze the correlations between the rock surface profile and the interface mechanics and seepage characteristics [19]. In road engineering, the roughness coefficient can also be used as an important index to analyze the surface texture roughness of aggregate particles and the correlation between asphalt and aggregate adhesion.

Therefore, in this study, the collection methods for aggregate surface morphology data and the applicability of the joint roughness coefficient (JRC) to the evaluation of the changes of the mesostructure of the aggregate surface texture are investigated. First, the measurement and quantitative evaluation method of the 2D roughness of the aggregate surface based on contact measurement is studied, and the anisotropic characteristics of aggregate surface texture roughness are analyzed. Second, the measurement and quantitative evaluation method of the 3D roughness of the aggregate surface based on 3D scanning technology is studied, and the size effect and resource characteristics of the aggregate surface texture roughness are analyzed. In addition, a polishing test of the aggregate was conducted to explore the influences of the resource characteristics and polishing degree on the surface roughness of aggregates.

## 2. Materials and Methods

*2.1. Materials.* Four types of coarse aggregates with different lithologies were obtained from the Highway Science and Technology Research Institute of Yunnan Province. The aggregate particle size range was 16–19 mm, and the aggregates were produced using jaw and counterattack crushers. The technical indices of the raw materials were obtained according to the Chinese specification "Test Methods of Aggregate for Highway Engineering" (JTG E42-2005). The technical indices of the coarse aggregates are listed in Table 1.

*2.2. Evaluation Index of Surface Roughness.* To quantitatively analyze the roughness of the surfaces of road aggregates, the joint roughness coefficient (JRC) was used as an evaluation index in this study. Combining engineering experience and experimental research results, Barton (1977) presented 10 typical rock surface contour lines with values ranging from 0 to 20 to evaluate the JRC value [20], as shown in Table 2.

*2.3. Aggregate Surface Topography Feature Data Collection*

*2.3.1. Collection Method of 2D Contour Line.* A Kasaka FGA51 high-precision stylus profiler, which operates on the principle of the needle-tracing method [21], was used to obtain the 2D profile curves of the aggregate surface (see Figure 1(a)). The $x$-axis measurement accuracy of the profiler is 1.2 $\mu$m, the grating resolution is 0.1 $\mu$m, the $Z_1$ measurement accuracy is 1.0 $\mu$m, the resolution is 0.05 $\mu$m, and the measurement speed range is 0.02–4 mm/s; these characteristics meet the requirements of aggregate surface topography measurement (see Figure 1(b)). During the measurement process, the aggregate was fixed on a precision linear motion guideway in the $x$-direction so that the stylus was in contact with the surface of the specimen. Then, the stylus movement speed was set to 0.5 mm/s, the fluctuation range was set to ±0.02 mm/s, the sampling step was set to 2 $\mu$m, and the sampling line distance was set to 10 mm. By setting the parameters of the measurement system, the measurement command was issued, and the computer accepted the command to drive the control instruction to make the stylus move to the moving guideway. When the aggregate moved at the sampling interval along the $x$-axis, the $x$-coordinate of the measurement point was obtained at the position to be measured, and the stylus moved up and down with the fluctuation of the surface profile, causing the $z_1$-axis digital sensor to output electrical signals. The signals were transmitted to the computer for processing via the photoelectric conversion processing circuit, and the $z$-coordinate could then be determined. This process was repeated for the observation section of the aggregate surface presented in Figure 1(c) to obtain the corresponding 2D profile curve. Finally, the data from the effective test length of 10 mm were filtered and digitized and were drawn in proportion to the coordinate grid. The roughness coefficients $JRC^{2D}$ of 9 contours of the aggregate surface were estimated from the visual comparison with the 10 typical rock surface contour lines shown in Table 2, as presented in Figure 1(d).

*2.3.2. Collection Method of 3D Contour Surface.* An EinScan-S 3D scanner was used to obtain the point cloud data that contain information about the surface geometric characteristics of the aggregate particles. The resolution of the profiler lens is 3264×2488, the scanning size is 200 × 200 mm, the measurement accuracy is 20 $\mu$m, there are 8 million effective 3D points, and omnidirectional scanning

Table 1: Technical indices of the coarse aggregates.

| Lithology | Crushing value (%) | Wear value (%) | Polishing value | Water absorption rate (%) | Apparent relative density (g/cm$^3$) |
|---|---|---|---|---|---|
| Granite | 18.1 | 21.5 | 46 | 0.37 | 2.654 |
| Diabase | 12.6 | 10.0 | 65 | 0.77 | 2.765 |
| Basalt | 10.5 | 8.9 | 58 | 0.63 | 2.724 |
| Limestone | 21.5 | 19.4 | 42 | 0.72 | 2.698 |

Table 2: Barton standard roughness contours.

| Value range of *JRC* | Typical rock surface roughness contour |
|---|---|
| 0 ~ 2 | |
| 2 ~ 4 | |
| 4 ~ 6 | |
| 6 ~ 8 | |
| 8 ~ 10 | |
| 10 ~ 12 | |
| 12 ~ 14 | |
| 14 ~ 16 | |
| 16 ~ 18 | |
| 18 ~ 20 | |

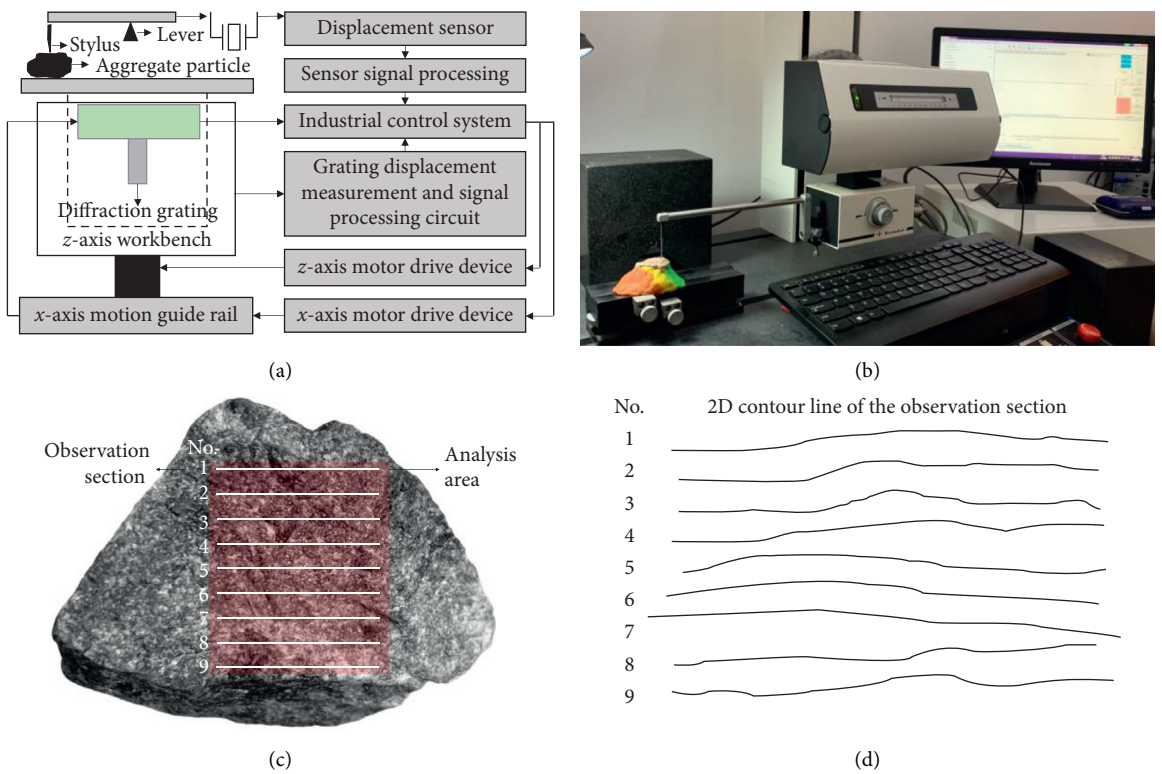


Figure 1: Collection method of 2D profile curves of the aggregate. (a) Principle of the needle-tracing method. (b) High-precision stylus profiler. (c) Observation section of the aggregate surface. (d) 2D profile curve of the observation section.

is supported; these characteristics meet the requirements of aggregate surface topography measurement (see Figure 2(a)).

The 3D scanner system operates on the principle of white-light interferometry [22, 23]. During the measurement process, the aggregate sample was placed on the stage, the white-light emitted by the light source was refracted by the lens and the beam splitter and was irradiated to the rough textured surface of the aggregate. Then, the white-light intensity of the light source was adjusted according to the light

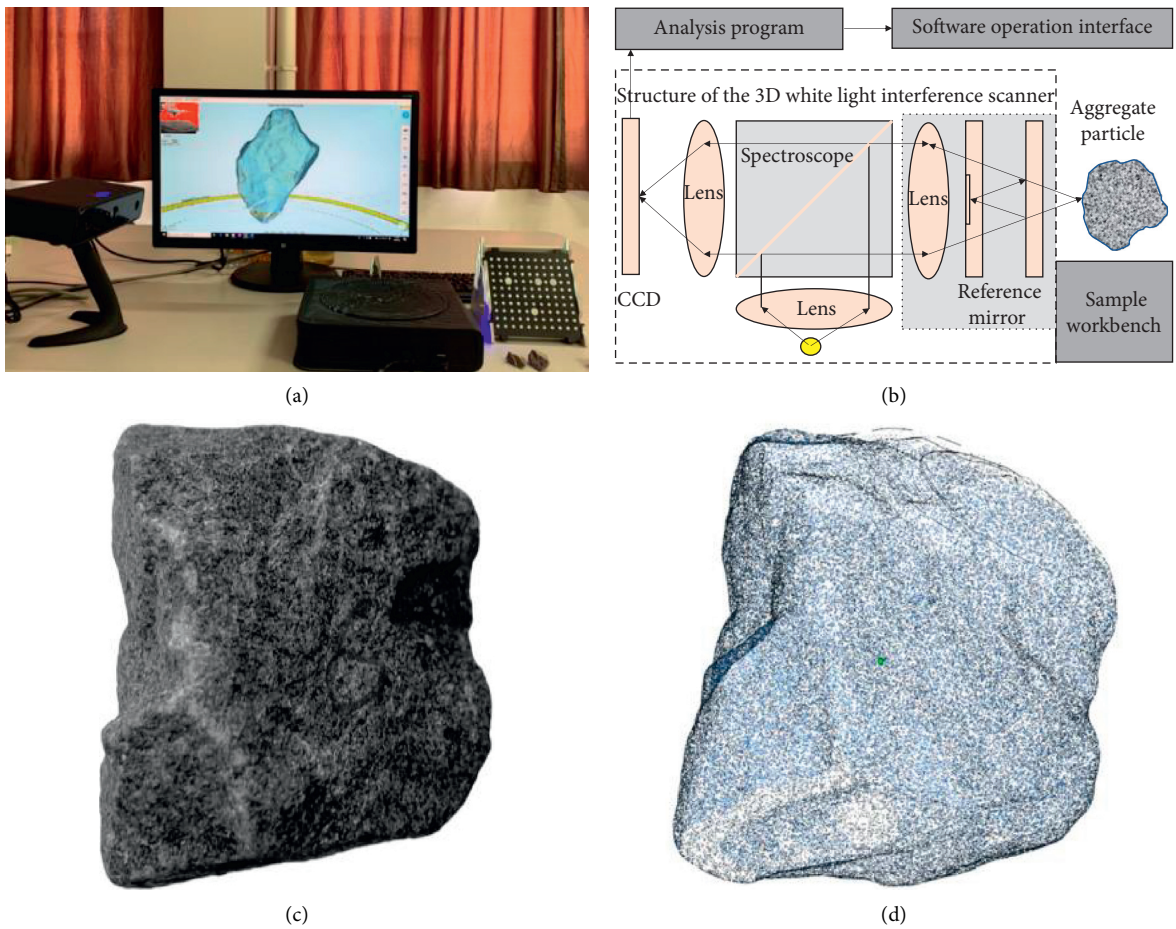


Figure 2: Point cloud data acquisition instrument and 3D scanning principle. (a) EinScan-S 3D scanner. (b) Principle of 3D scanning technology. (c) Coarse aggregate particle. (d) 3D coordinate lattice model.

intensity and color temperature of the room, and the carrier table was simultaneously adjusted for calibration until the interference image of the aggregate surface captured by the charge-coupled device (CCD) camera in the visual interface of the software met the analysis accuracy requirements. After setting the scanning range, sampling step length, and number of frames, multiframe images of interference fringes on the 3D contour surface of the aggregate were obtained via the CCD, and the 3D scanning point of the aggregate surface in the coordinate system of the scanner was calculated by the analysis software. The principle of 3D scanning technology is presented in Figure 2(b).

After scanning the 3D contour surface of the aggregate test sample from multiple angles (see Figure 2(c)), the iterative closest point (ICP) algorithm in the Imageware software was used to register the point cloud of multiple scans. The purpose of the ICP algorithm was to determine the rotation and shift parameters of the point cloud scans from different angles to register the dataset and obtain an optimal match for the data with different incident angles due to changes in the light source [24].

The registered dataset was imported into the PCL library to eliminate outliers and noise. This library is a large cross-platform open-source C++ programming library containing many algorithms and data structures related to point clouds, including point cloud acquisition, filtering, segmentation, registration, retrieval, feature extraction, recognition, tracking, surface reconstruction, and visualization [25]. The VoxelGrid filter was used for noise reduction. A 3D mesh of the aggregate particle was generated after eliminating 96% of the point cloud data (see Figure 2(d)).

### 2.4. Quantitative Characterization of the Surface Roughness

#### 2.4.1. Calculation Method of 2D Contour Line Roughness

*(1) Characteristic Parameter Method.* To quantitatively analyze the roughness of the two-dimensional profiles of the rock materials, a least-squares midline running through the sampling length was used as the baseline [26, 27], as shown in Figure 3.

The regression equation of the relationship between the geometric characteristic parameters and roughness proposed by Tse and Crude is generally used to calculate the 2D roughness ($JRC^{2D}$) of the surface profile of rock materials [28] and is defined as follows:

$$JCR^{2D} = 32.2 + 32.47 \lg Z_2. \quad (1)$$

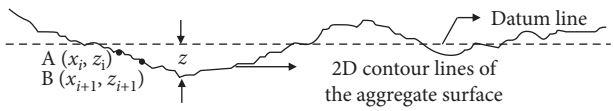


Figure 3: Characteristic parameter of the 2D profile curve.

The parameter $Z_2$ is a characteristic parameter of the slope of the rock surface that is not affected by the position of the calculated reference line [29] and is expressed as follows:

$$z_2 = \frac{1}{L}\sqrt{\int_{x=0}^{x=L}\left(\frac{\mathrm{d}y}{\mathrm{d}x}\right)^2 \mathrm{d}x}. \tag{2}$$

When using 3D point cloud data to calculate the roughness of the 2D contour of an aggregate surface, equation (2) can be approximately expressed as follows:

$$z_2 = \frac{1}{L}\sqrt{\sum_{i=1}^{n-1}\frac{(z_{i+1}-z_i)^2}{x_{i+1}-x_i}}, \tag{3}$$

$$L = \sum_{i=1}^{n-1}(x_{i+1}-x_i), \tag{4}$$

where $L$ is the total length of the 2D profile contour line, $n$ is the number of calculated samples, and $x_\mathrm{i}$ and $z_\mathrm{i}$ are the point cloud coordinates on the contour line.

*(2) Trace Length Characterization Method.* To quantitatively evaluate the roughness coefficient of road aggregates in practical engineering applications, the accuracy requirements must first be met. Moreover, the measurement instruments, test methods, and calculation processes should not be too complicated and should be characterized by a fast measurement speed and convenient statistical analysis. Therefore, the trace length characterization method proposed by Soudan was used to quickly calculate the 2D roughness of the profile contour of the aggregate surface [30] and is defined as follows:

$$R_p = \frac{\sum_{i=1}^{n-1}\left[(x_{i+1}-x_i)^2+(y_{i+1}-y_i)^2\right]^{(1/2)}}{L}, \tag{5}$$

where $R_p$ is the ratio of the actual length of the profile line to its straight-line length and $x_\mathrm{i}$, $x_{\mathrm{i}+1}$, $y_\mathrm{i}$, and $y_{\mathrm{i}+1}$ are the relative coordinates of point $i$ and point $i$+1, as indicated by the subscripts.

Table 3 presents the functional relationship between $R_\mathrm{p}$ and $\mathrm{JRC}^{2\mathrm{D}}$ under different sampling intervals [29].

*(3) Evaluation Accuracy of 2D Contour Line Roughness.* According to the relative coordinate data of the measured curve exhibited in Figure 1(d), the roughness coefficients $\mathrm{JRC}^{2\mathrm{D}}$ of 9 contours of the aggregate surface were first calculated based on the characteristic parameter method. The measurement point data of each contour curve were then sampled at 0.5 mm intervals and substituted into equation (5) to determine the elongation rate $R_p$ of the contour line. The roughness coefficient $\mathrm{JRC}^{2\mathrm{D}}$ of each 2D profile contour line was calculated by the functional relationship between $R_p$ and $\mathrm{JRC}^{2\mathrm{D}}$ at a sampling interval of 0.50 mm. The calculation results of the two analysis methods are reported in Table 4.

Table 3: The relationship between $R_p$ and JRC.

| Sample interval (mm) | Functional relation | Correlation coefficient |
|---|---|---|
| 0.25 | $\mathrm{JCR} = 558.68\sqrt{R_p} - 557.13$ | 0.951 |
| 0.50 | $\mathrm{JCR} = 559.73\sqrt{R_p} - 597.46$ | 0.945 |
| 1.00 | $\mathrm{JCR} = 702.67\sqrt{R_p} - 699.99$ | 0.951 |

From the calculation results, it can be seen that the characteristic parameter method and the trace length method can both quantitatively characterize the roughness coefficient of the 2D profile of the aggregate texture, and the calculation deviation was within 13%. Similarly, other test samples were also governed by the same law, and a good correlation was found. The comparative evaluation results demonstrate that the calculation deviation of the two roughness characterization methods was mainly caused by the difference in the sampling interval. Compared with that of the characteristic parameter method (0.002 mm), the sampling interval of the trace length method was 0.5 mm. Under the relatively large sampling interval, a portion of the mesomorphological changes of the measurement curve could not be collected, resulting in the overall low roughness value.

*2.4.2. Calculation Method of 3D Contour Surface Roughness.* The 2D roughness coefficient of the aggregate cannot fully reflect the geometric shape of the aggregate surface, so it is necessary to use the 3D roughness coefficient to characterize the geometric characteristics of the rough texture of the aggregate profile. In the calculation of 3D roughness, the weighted average method and characteristic parameter method are typically used.

(1) Weighted Average Method. The roughness $\mathrm{JRC}^{2\mathrm{D}}$ of a large number of 2D contours on the surface of a rock material can be measured, and the 3D average roughness $\overline{\mathrm{JRC}}$ of this area can be calculated by the weighted average method, as follows:

$$\overline{\mathrm{JCR}} = \frac{1}{m}\sum_{i=1}^{m}\mathrm{JRC}_i^{2D}, \tag{6}$$

where $\overline{\mathrm{JRC}}$ is the 3D average roughness, $\mathrm{JRC_i}^{2\mathrm{D}}$ is the roughness of each 2D undulating curve, and $m$ is the number of section lines.

(2) Characteristic Parameter Method. It is assumed that the coordinates of the point cloud on the rough surface of a rock are continuously differentiable. The root mean square $Z_{2\mathrm{s}}$ of the 3D characteristic

Table 4: Roughness evaluation of form line based on trace length method.

| Number of 2D contour lines | | 1 | 2 | 3 | 4 | 5 | 6 | 7 | 8 | 9 |
|---|---|---|---|---|---|---|---|---|---|---|
| Characteristic parameter method | $JRC^{2D}$ | 13.1 | 14.0 | 19.4 | 12.3 | 14.2 | 11.1 | 10.8 | 18.7 | 17.8 |
| Trace length method | $R_p$ | 1.186 | 1.188 | 1.207 | 1.183 | 1.189 | 1.179 | 1.177 | 1.206 | 1.203 |
| | $JRC^{2D}$ | 12.0 | 12.7 | 17.5 | 11.4 | 12.9 | 10.5 | 9.7 | 17.3 | 16.6 |

parameter of the relative height fluctuation can be calculated as follows [31]:

$$Z_{2s} = \left\{ \frac{1}{L_x L_y} \int_0^{L_x} \int_0^{L_y} \left[ \left( \frac{\partial z(x,y)}{\partial x} \right)^2 + \left( \frac{\partial z(x,y)}{\partial y} \right)^2 \right] \mathrm{d}x\mathrm{d}y \right\}^{(1/2)}. \tag{7}$$

When using the 3D point cloud data to calculate the 3D profile roughness coefficient $JRC^{3D}$ of an aggregate surface, the *approximate* formula is as follows:

$$Z_{2s} = \left\{ \frac{1}{(N_x - 1)(N_y - 1)} \left[ \frac{1}{\Delta x^2} \sum_{j=1}^{N_x - 1} \sum_{i=1}^{N_y - 1} \frac{\left(z_{i+1,j+1} - z_{i,j+1}\right)^2 + \left(z_{i+1,j} - z_{i,j}\right)^2}{2} + \frac{1}{\Delta y^2} \sum_{j=1}^{N_y - 1} \sum_{i=1}^{N_x - 1} \frac{\left(z_{i+1,j+1} - z_{i+1,j}\right)^2 + \left(z_{i,j+1} - z_{i,j}\right)^2}{2} \right] \right\}^{(1/2)}, \tag{8}$$

where $N_x$ is the number of point clouds on the $x$-axis in the length direction of the rock profile, $N_x$ is the number of point clouds on the $y$-axis in the height direction, $\Delta x$ is the sampling spacing of point clouds on the $x$-axis, $\Delta y$ is the sampling spacing of point clouds on the $y$-axis, and $Z_i$ and $Z_{i+1}$ are the coordinates of the $i$-th point and the ($i$+1)-th point in the $z$-axis direction of the roughness height, respectively. The relevant parameters are presented in Figure 4.

(3) Evaluation Accuracy of 3D Contour Surface Roughness. According to the roughness coefficient $JRC^{2D}$ of 9 contours of the aggregate surface, the 3D average roughness $\overline{JRC}$ of the analysis area of the aggregate surface was calculated to be 14.6 via equation (6). The texture feature of the analysis area was then evaluated by the 3D contour surface roughness $JRC^{3D}$. After scanning the 3D contour surface of the aggregate test sample from multiple angles, the data point cloud of the analysis area (Figure 1(c)) of the aggregate fracture surface was sampled at intervals of $10 \times 10$ mm, that is, $\Delta x = \Delta y = 0.25$ mm. Equation (8) was used to calculate the characteristic parameter $Z_{2s}$, and the 3D contour surface roughness $JRC^{3D}$ of the analysis area of the aggregate surface was then calculated to be 13.8 via equation (1). The differences and correlations between the two calculation methods for the calculation of the 3D roughness are discussed in the subsequent section.

*2.5. Change Method for the Surface Roughness of the Aggregate.* An aggregate polishing test was designed to test the accuracy of the roughness coefficient *JRC* for the analysis of changes of the aggregate surface roughness. In the test, 1200# carborundum with a 95% alumina content was used as an abrasive, and a vibrating polishing machine was employed to change the mesostructures of the surface textures of the four aggregates with different lithologies. The steps of the aggregate polishing test were as follows:

(1) After fully soaking the abrasive in water, it was drained with a basket and poured into the vibrating polishing machine.

(2) The power was turned on and the wet water-drained aggregate was arranged in the abrasive in the vibrating polishing machine to be polished from different directions one-by-one.

(3) After the carborundum was uniformly added to the mixture, the polishing time was set according to the polishing requirements; after the polishing test was completed, the carborundum in the mixture was washed with clean water.

At the end of each polishing test, the profile point cloud data of the particle surface were collected again, and the changes of the aggregate surface roughness under different polishing conditions were compared and analyzed.

## 3. Results and Discussion

*3.1. Anisotropy Analysis of Aggregate Surface Roughness.* To analyze the differences in the roughness of the 2D contour line of the aggregate surface in different directions and angles, coarse aggregates with a particle size between 16 and 19 mm were used as the research object, and the size of the aggregate fracture surface was $10 \times 10$ mm. The range was used as the analysis area, as shown in Figure 5(a). Twelve observation cross sections were, respectively, set up along the $x$- and $y$-axes at equal intervals of 0.8 mm, as shown in Figures 5(b) and 5(c). The origin of the coordinates and the direction of 0° in

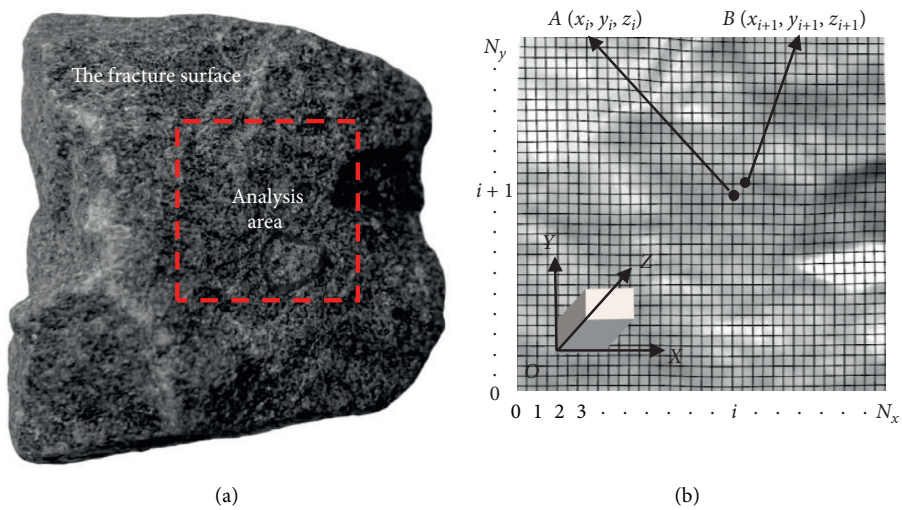


Figure 4: 3D contour surface of the aggregate. (a) Analysis area. (b) Contour surface point cloud.

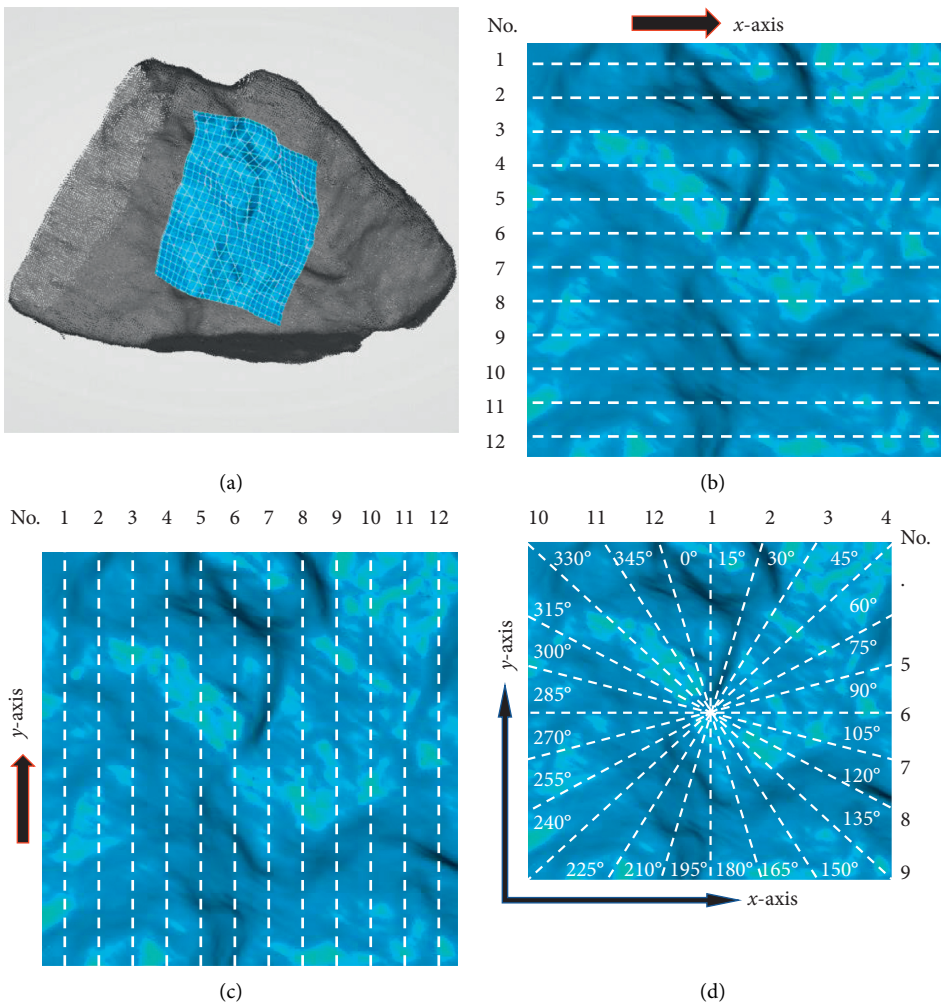


Figure 5: Observation sections of the aggregate surface. (a) Analysis area of the aggregate fracture surface. (b) 2D profile position distribution along the *x*-axis. (c) 2D profile position distribution along the y-axis. (d) 2D profile position distribution along the circumference.

the analysis area was defined with the direction of 0° as the reference line, and an observation section was set up every 15° through this point for a total of 12 observation sections, as shown in Figure 5(d).

The characteristic point coordinate data of the observation section contour lines were measured from the contact stylus profiler, and the 2D contour curve was drawn. According to the functional relationship in the characteristic parameter method, the $JRC^{2D}$ value of each curve was programmed in MATLAB, as reported in Tables 5–7.

The test results demonstrate that, under different observation section sampling rules, the roughness of the 2D contour lines of the aggregate particle surface was different, and the apparent morphologies were quite different and had no correlation with the sampling direction or angle, thereby exhibiting anisotropy. When the $JRC^{2D}$ index is used to characterize the roughness characteristics of the texture of aggregates, the randomness of the selection of the observation cross sections will lead to deviations in the evaluation of roughness. Therefore, the 2D roughness index cannot describe the overall morphology of the aggregate surface, and it is necessary to use the 3D roughness index to comprehensively characterize the spatial geometric characteristics of the aggregate particle profile.

*3.2. Influence of the Size Effect on Aggregate Surface Roughness.* To analyze the roughness of the different observation areas with the same centroid and different dimensions of the aggregate fracture surface, the weighted average method and the characteristic parameter method were used to calculate the 3D average roughness of the analysis area of the aggregate fracture surface.

Via the weighted average method, equation (5) was used to calculate the 3D average roughness of the analysis area of the aggregate fracture surface. The calculation results of the sampling methods for the three observation sections along the $x$-axis, $y$-axis, and circumference were 13.2, 10.6, and 12.2, respectively.

Using the characteristic parameter method, the data point cloud of the analysis area of the aggregate surface was sampled at intervals of 0.1 mm, that is, $\Delta x = \Delta y = 0.1$ mm. In MATLAB, equation (7) was used to calculate the characteristic parameter $Z_{2s}$, and the 3D contour surface roughness $JRC^{3D}$ of the analysis area of the aggregate surface was then calculated to be 12.6 by equation (1). This calculation result is closer to the average roughness coefficient of the 12 observation sections taken along the circumference calculated by the weighted average method.

The weighted average method (12 observed sections along the circumference) and the characteristic parameter method were used to study the influence of the area difference of the aggregate surface analysis on the roughness calculation results. The 3D roughness of the four analysis areas with the same centroid and different dimensions of the aggregate fracture surface was, respectively, calculated, as presented in Figure 6.

The calculation results reveal that the rough texture of the aggregate surface was characterized not only by anisotropy at the 2D level but also by the size effect at the 3D level. With the increase of the observation range of the aggregate surface, the 2D profile roughness of each observed section and the 3D profile roughness of the analysis area exhibited decreasing trends. The anisotropic characteristics

Table 5: 2D roughness of contour lines along the $x$-axis.

| Number | 2D contour line of aggregate fracture surface | $JRC^{2D}$ |
|---|---|---|
| 1 | | 8.4 |
| 2 | | 10.3 |
| 3 | | 12.7 |
| 4 | | 13.4 |
| 5 | | 14.3 |
| 6 | | 15.7 |
| 7 | | 14.3 |
| 8 | | 15.1 |
| 9 | | 16.2 |
| 10 | | 11.6 |
| 11 | | 12.6 |
| 12 | | 13.8 |

Table 6: 2D roughness of contour lines along the $y$-axis.

| Number | 2D contour line of aggregate fracture surface | $JRC^{2D}$ |
|---|---|---|
| 1 | | 12.7 |
| 2 | | 11.4 |
| 3 | | 13.7 |
| 4 | | 12.1 |
| 5 | | 10.6 |
| 6 | | 9.3 |
| 7 | | 8.6 |
| 8 | | 9.0 |
| 9 | | 8.3 |
| 10 | | 9.9 |
| 11 | | 10.4 |
| 12 | | 11.3 |

Table 7: 2D roughness of contour lines along the circumference.

| Number | 2D contour line of aggregate fracture surface | $JRC^{2D}$ |
|---|---|---|
| 1 | | 14.1 |
| 2 | | 12.8 |
| 3 | | 12.3 |
| 4 | | 10.6 |
| 5 | | 9.4 |
| 6 | | 10.8 |
| 7 | | 11.6 |
| 8 | | 12.3 |
| 9 | | 13.2 |
| 10 | | 13.0 |
| 11 | | 13.5 |
| 12 | | 12.9 |

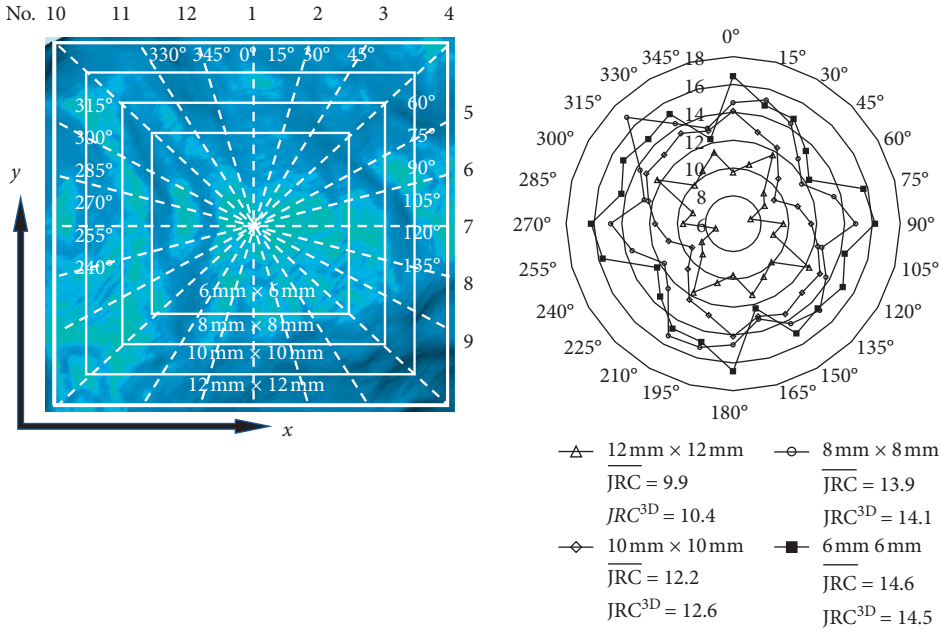


Figure 6: The size effect of the roughness of the aggregate surface.

displayed certain similarities in different observation ranges, but no correlation was found. Similarly, other test samples were also governed by the same law. Therefore, when evaluating the 3D roughness of an aggregate surface, the analysis area of the aggregate surface should be maintained at a constant value during the test to ensure the comparability of the evaluation results.

*3.3. Influence of Lithology Characteristics on the Aggregate Surface Roughness.* The point cloud data of aggregates with four different lithologies were obtained by 3D white-light interferometry, and the weighted average method (observation data were collected every 15° along the circumference) and the characteristic parameter method were used to evaluate the fracture surface of each aggregate within the range of 10 × 10 mm. The roughness results are presented in Table 8.

The test results demonstrate that when the weighted average method and the characteristic parameter method are used to evaluate the 3D roughness in the same analysis area, the difference between the calculation results can be controlled below 10%, and the results, therefore, exhibit a good correlation. Under the experimental conditions of this study, the average 3D roughness value of the limestone aggregate sample was the highest, that of granite was the lowest, and those of basalt and diabase were in the middle. When the weighted average method was used to evaluate the 3D roughness of the aggregate surface, the $\overline{\text{JCR}}$ values of the granite samples were found to range from 8 to 16, and the roughness among the samples varied greatly. In contrast, when the characteristic parameter method was used, the $\text{JRC}^{3D}$ values of the granite samples ranged from 9 to 14, the variation of roughness among the samples was relatively small, and the other test samples were also governed by the same law. The comparative evaluation results demonstrate that the calculation deviation of the two roughness characterization methods was mainly caused by the differences in the test methods and data accuracy. During the process of contact measurement, factors such as the excessive hardness of the contact probe, unstable moving speeds, and easy lateral sliding will affect the measurement accuracy. In contrast, 3D noncontact measurement technology based on the optical principle is used to obtain the contour surface feature information of an object and has obvious advantages in the collection of the surface topography data of rock-like materials.

*3.4. Influence of Polishing on the Aggregate Surface Roughness.* To test the accuracy of the 3D roughness coefficient $\text{JRC}^{3D}$ for the analysis of changes of the aggregate surface roughness, an aggregate polishing test was designed. Carborundum with a 95% alumina content was used as an abrasive, and a vibrating polishing machine was employed to change the mesostructures of the surface textures of the four aggregates with different lithologies. At the end of each polishing test, the 3D profile point cloud data of the particle surface were collected again, and the changes of the aggregate surface roughness under different polishing conditions were compared and analyzed. The results are reported in Table 9. The changing trend of the roughness of each lithologic aggregate test sample under different polishing times is shown in Figure 7.

It is evident from the test data that the average roughness of the fracture surface of the limestone aggregate sample was the highest, that of granite was the smallest, and that of basalt and diabase were in the middle. With the increase in polishing time, the rough texture surface of aggregate gradually wore away, which shows that the roughness of the coarse

Table 8: The basic properties of aggregates.

| Lithology | Number of aggregate samples | 3D average roughness ($\overline{JCR}$) | | | 3D topographic roughness ($JRC^{3D}$) | | |
|---|---|---|---|---|---|---|---|
| | | Max | Min | Average | Max | Min | Average |
| Granite | 50 | 15.7 | 8.3 | 11.9 | 13.6 | 9.7 | 11.5 |
| Diabase | 50 | 16.4 | 11.7 | 13.8 | 17.4 | 12.2 | 14.6 |
| Basalt | 50 | 16.4 | 10.2 | 13.7 | 15.7 | 11.0 | 13.1 |
| Limestone | 50 | 18.2 | 12.0 | 15.1 | 18.3 | 11.1 | 15.8 |

Table 9: The variation of the $JRC^{3D}$ values of aggregates with different lithologies with the polishing time.

| Polishing time (h) | Number of aggregate samples | Granite | | | Diabase | | | Basalt | | | Limestone | | |
|---|---|---|---|---|---|---|---|---|---|---|---|---|---|
| | | Max | Min | Average | Max | Min | Average | Max | Min | Average | Max | Min | Average |
| 0.0 | 20 | 13.6 | 9.7 | 11.5 | 17.4 | 12.2 | 14.6 | 15.7 | 11.0 | 13.1 | 18.3 | 11.1 | 15.8 |
| 0.5 | 20 | 13.1 | 9.5 | 11.0 | 16.5 | 11.7 | 13.7 | 15.1 | 10.5 | 12.4 | 16.01 | 9.63 | 14.1 |
| 1.0 | 20 | 12.9 | 9.2 | 10.7 | 15.5 | 11.4 | 13.2 | 14.4 | 10.2 | 12.1 | 14.85 | 8.77 | 12.4 |
| 1.5 | 20 | 12.8 | 9.1 | 10.5 | 14.7 | 11.0 | 13.0 | 13.9 | 10.0 | 11.8 | 14.09 | 8.08 | 11.1 |
| 2.0 | 20 | 12.5 | 9.2 | 10.4 | 14.6 | 10.7 | 12.8 | 13.3 | 10.0 | 11.4 | 13.50 | 7.11 | 9.8 |

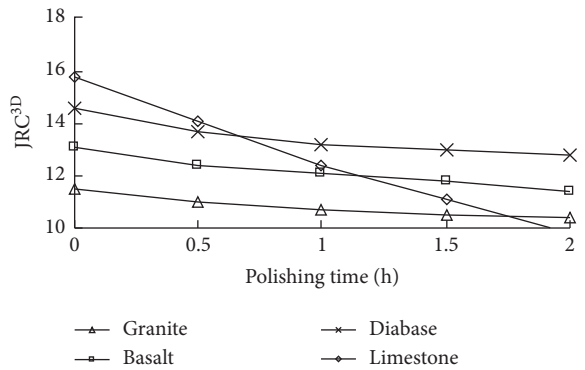


Figure 7: Variation trend of aggregate roughness.

aggregate surface of different lithologies decreases with the increase in polishing time. Among them, the average roughness of the fracture surface of limestone decreases the most, followed by basalt and diabase, while the roughness of granite decreases the least. The results show that the wear resistance of the surface texture of granite aggregate was obviously better than that of limestone aggregate, and the wear resistance of diabase aggregate was similar to that of basalt, which was consistent with the attenuation law of the mechanical index of road aggregate in practical engineering.

Under the experimental conditions of this study, when the 3D roughness of aggregate profile $JRC^{3D} \geq 11.0$, there were many pores and cracks on the aggregate surface, and the texture was uneven, which was beneficial to the formation of good physical adsorption between asphalt and aggregate on the contact surface. The test results demonstrate that the 3D profile roughness coefficient $JRC^{3D}$ has good sensitivity in the evaluation of the mesostructure changes of the aggregate surface texture and that this coefficient can be used as an evaluation index of the 3D roughness of road aggregate surfaces.

## 4. Conclusions

Based on the stylus contact measurement method and optical noncontact measurement method, the 2D and 3D quantitative evaluation methods of aggregate surface roughness were studied using the roughness coefficient *JRC* as the evaluation index. The following conclusions can be drawn.

(1) By using contact measurement technology based on the principle of the needle-tracing method, the 2D profile curves of the aggregate surface can be obtained and can be used to quantitatively characterize the roughness coefficient of the 2D profile of the aggregate texture obtained by the characteristic parameter method. By using noncontact 3D scanning technology based on the principle of white-light interferometry, the 3D coordinate data of the analysis area of the aggregate surface can be obtained by the point cloud, which can be used to calculate the 3D roughness indexes of the aggregate surface after data processing.

(2) When using the $JRC^{2D}$ index to evaluate the contour roughness of an aggregate surface, it is necessary to consider that the randomness of the selection of observation sections will lead to the anisotropy of the 2D roughness evaluation results. The evaluation index of 2D roughness cannot reflect the overall roughness of an aggregate surface.

(3) Under the experimental conditions of this study, the average 3D roughness value of the limestone aggregate sample was the highest, that of granite was the lowest, and those of basalt and diabase were in the middle. When the weighted average method was used to evaluate the 3D roughness of the aggregate surface, the difference between the calculation results

can be controlled below 10%, and the results, therefore, exhibit a good correlation. The calculation deviation of the two roughness characterization methods was mainly caused by the differences in the test methods and data accuracy.

(4) The 3D profile roughness $JRC^{3D}$ calculated by the characteristic parameter method can be used to quantitatively evaluate the morphological characteristics of the aggregate particle surface. It is sufficiently sensitive to describe the microlevel structure of the aggregate texture and can be used as an evaluation index of the 3D roughness of road aggregate surfaces.

(5) The calculation results of the 3D roughness of the aggregate surface are affected by the size effect. It is therefore suggested that when evaluating the surface roughness of the same batch of aggregates with the same particle size, the observation range of the analysis area should be fixed to avoid the deviation of the roughness evaluation results caused by the size effect.

## Data Availability

The data used to support the findings of this study are available from the first author upon request.

## Conflicts of Interest

The authors declare that they have no conflicts of interest.

## Acknowledgments

The research was funded by the National Natural Science Fund (51708267).

## References

[1] D. Kuang, B. Zhang, Y. Jiao, H. Chen, and L. Wang, "Impact of particle morphology on aggregate-asphalt interface behavior," *Construction and Building Materials*, vol. 132, pp. 142–149, 2017.

[2] I. S. Fang, T. F. CasteloBranco, J. B. Soares et al., "Aggregate shape properties and their influence on the behavior of hot-mix asphalt," *Journal of Materials in Civil Engineering*, vol. 27, no. 7, Article ID 04014212, 2015.

[3] M. Guo and Y. Tan, "Interaction between asphalt and mineral fillers and its correlation to mastics' viscoelasticity," *International Journal of Pavement Engineering*, vol. 22, no. 1, pp. 1–10, 2021.

[4] M. Guo, H. Liu, Y. Jiao et al., "Effect of WMA-RAP technology on pavement performance of asphalt mixture: a state-of-the-art review," *Journal of Cleaner Production*, vol. 266, Article ID 121704, 2020.

[5] J. Jin, Y. Gao, Y. Wu et al., "Rheological and adhesion properties of nano-organic palygorskite and linear SBS on the composite modified asphalt," *Powder Technology*, vol. 377, p. 212, 2021.

[6] J. Jin, Y. C. Gao, Y. R. Wu et al., "Performance evaluation of surface-organic grafting on the palygorskite nanofiber for the modification of asphalt," *Construction and Building Materials*, vol. 268, Article ID 121072, 2020.

[7] P. Li, J. Su, and S. Ma, "Effect of aggregate contact condition on skeleton stability in asphalt mixture," *International Journal of Pavement Engineering*, vol. 21, no. 2, pp. 196–202, 2020.

[8] S. Dong, E. Yenera, F. Hattatoglu, and S. Akbuluta, "Correlation between shape of aggregate and mechanical properties of asphalt concrete," *Road Materials and Pavement Design*, vol. 12, no. 2, pp. 239–262, 2011.

[9] Z. Hinislioglua, P. Li, X. Wu et al., "Evaluation of the contact characteristics of graded aggregate using coarse aggregate composite geometric indexes," *Construction and Building Materials*, vol. 247, Article ID 118608, 2020.

[10] D. Ünlüsoy and M. L. Süzen, "A new method for automated estimation of joint roughness coefficient for 2D surface profiles using power spectral density," *International Journal of Rock Mechanics and Mining Sciences*, vol. 125, Article ID 104156, 2020.

[11] M. O. Idrees and B. Pradhan, "Geostructural stability assessment of cave using rock surface discontinuity extracted from terrestrial laser scanning point cloud," *Journal of Rock Mechanics and Geotechnical Engineering*, vol. 10, no. 3, pp. 524–544, 2018.

[12] W. J. Pan, H. S. Li, L. Y. Ling et al., "Investigation of tangential contact damping of rough surfaces from the perspective of viscous damping mechanism," *ASME*, 2015.

[13] M. Sharafisafa, L. Shen, and Q. Xu, "Characterisation of mechanical behaviour of 3D printed rock-like material with digital image correlation," *International Journal of Rock Mechanics and Mining Sciences*, vol. 112, pp. 122–138, 2018.

[14] Z. Q. Xiong, Q. Jiang, Y. H. Gong et al., "Modeling natural joint of rock mass using three dimensional scanning and printing technologies and printing technologies and its experimental verification," *Rock and Soil Mechanics*, vol. 36, no. 6, pp. 1566–1572, 2015.

[15] Z. R. Tang, M. Z. Liu, Y. Jiang et al., "Point cloud registration algorithm based on canonical correlation analysis," *Chinese Journal of Lasers*, vol. 46, no. 4, pp. 173–181, 2019.

[16] N. Babanouri, M. Asadizadeh, and Z. H. Alizade, "Modeling shear behavior of rock joints: a focus on interaction of influencing parameters," *International Journal of Rock Mechanics and Mining Sciences*, vol. 22, Article ID 104449, 2020.

[17] S. R. Nayak, J. Mishra, and G. Palai, "Analysing roughness of surface through fractal dimension: a review," *Image and Vision Computing*, vol. 89, pp. 21–34, 2019.

[18] R. Tse and D. M. Cruden, "Estimating joint roughness coefficients," *International Journal of Rock Mechanics and Mining Sciences & Geomechanics Abstracts*, vol. 16, no. 5, pp. 303–307, 1979.

[19] Z. Y. Yang, S. C. Lo, and C. C. Di, "Reassessing the joint roughness coefficient (JRC) estimation using Z 2," *Rock Mechanics and Rock Engineering*, vol. 34, no. 3, pp. 243–251, 2001.

[20] N. Barton and V. Choubey, "The shear strength of rock joints in theory and practice," *Rock Mechanics*, vol. 10, no. 1-2, pp. 1–54, 1977.

[21] P. Jerónimo, R. Resende, and E. Fortunato, "An assessment of contact and laser-based scanning of rock particles for railway ballast," *Transportation Geotechnics*, vol. 22, Article ID 100302, 2020.

[22] K. G. Larkin, "Efficient nonlinear algorithm for envelope detection in white light interferometry," *Journal of the Optical Society of America A*, vol. 13, no. 4, pp. 832–843, 1996.

[23] Z. Lei, X. Liu, L. Chen, and S. Chang, "A novel surface recovery algorithm in white light interferometry," *Measurement*, vol. 80, pp. 1–11, 2016.

[24] A. Lu, H. Ogawa, and K. Kitagawa, "Fast surface profiler by white-light interferometry by use of a new algorithm based on sampling theory," *Applied Optics*, vol. 41, no. 23, pp. 4876–4883, 2002.

[25] J. Schauer and A. Nüchter, "Removing non-static objects from 3D laser scan data," *ISPRS Journal of Photogrammetry and Remote Sensing*, vol. 143, pp. 15–38, 2018.

[26] Y.-H. Lee, J. R. Carr, and D. J. Barr, "The fractal dimension as a measure of the roughness of rock discontinuity profiles," *International Journal of Rock Mechanics and Mining Sciences & Geomechanics Abstracts*, vol. 27, no. 6, pp. 453–464, 1990.

[27] J. Haas, "Joint surface matching and shear strength part B: JRC-JMC shear strength criterion," *International Journal of Rock Mechanics and Mining Sciences*, vol. 34, no. 2, pp. 179–185, 1997.

[28] A. J. Beer, D. Stead, and J. S. Coggan, "Technical note estimation of the joint roughness coefficient (JRC) by visual comparison," *Rock Mechanics and Rock Engineering*, vol. 35, no. 1, pp. 65–74, 2002.

[29] G. Zhang, M. Karakus, H. Tang, and L. Zhang, "A new method estimating the 2D joint roughness coefficient for discontinuity surfaces in rock masses," *International Journal of Rock Mechanics and Mining Sciences*, vol. 72, pp. 191–198, 2014.

[30] S. M. Ge, "Profilometric analysis of fractures," *Metallography*, vol. 11, no. 3, pp. 247–336, 2008.

[31] T. Belem, F. Homand-Etienne, and M. Souley, "Quantitative parameters for rock joint surface roughness," *Rock Mechanics and Rock Engineering*, vol. 33, no. 4, pp. 217–242, 2000.

Hindawi
Advances in Materials Science and Engineering
Volume 2021, Article ID 6660915, 13 pages
https://doi.org/10.1155/2021/6660915

*Research Article*

# Damage Identification of Prefabricated Reinforced Concrete Box Culvert Based on Improved Fuzzy Clustering Algorithm and Acoustic Emission Parameters

**Yafeng Gong, Siyuan Lin, Feng He, Yang He, and Jiaxiang Song**

*College of Transportation, Jilin University, Changchun 130025, China*

Correspondence should be addressed to Feng He; hefeng@jlu.edu.cn

Received 23 November 2020; Revised 19 December 2020; Accepted 2 January 2021; Published 18 January 2021

Academic Editor: Yubo Jiao



Prefabricated box culvert is a new structure in road engineering, whose health is very important to road safety. The use of acoustic emission (AE) as a detection method and the use of other improved algorithms to evaluate the damage of prefabricated box culverts are still insufficient. In this paper, two kinds of prefabricated box culverts are tested and studied, and the damage process of the box culverts is analysed based on the AE parameters of the box culvert using the traditional fuzzy C-means method (FCM). In addition, an improved algorithm based on the combination of grid density and distance (G-DFCM) was proposed, which was simulated and applied to the AE data analysis of the prefabricated box culvert. The research results show that the application effect of the G-DFCM algorithm is good, which not only overcomes the shortcomings of the original algorithm but also improves the effectiveness of the algorithm. This work can provide a supplement to the damage identification of fabricated box culverts.

## 1. Introduction

As an important part of roadbed engineering, culverts are often buried under underground roadbeds as water passages or traffic interruptions. Common culvert structure types include box type, pipe type, and arch type. Box culverts can be divided into the integral cast-in-situ type and prefabricated assembled type according to the construction method. Integral cast-in-situ box culverts are suitable for various projects due to their high strength and rigidity and relatively low cost. Based on factory-based manufacturing, prefabricated assembled type box culverts have fast construction speed and stable quality and conform to the characteristics of green and ecological construction, which have attracted more and more attention in modern engineering construction methods. The research on the acoustic emission (AE) characteristics and damage identification methods of the integrally assembled box culvert and the four-component assembled box culvert in the prefabricated assembled box culvert is slightly insufficient.

Scholars around the world have carried out related research on the structure of prefabricated box culverts. Park et al. [1] simulated the influence of vehicle load and temperature load on the maximum tensile stress and cracking of the box culvert through the finite element method and proposed the optimal slab length and hinge position of different types of box culverts. Liu and Chen [2] made relevant studies on the design parameters, structural requirements, reinforcement types, and construction methods of prefabricated assembled culverts and provided a reference for the design of prefabricated box culverts.

Acoustic emission is a common method of non-destructive testing. Since its discovery, it has attracted more and more attention due to its convenience of detection [3, 4], and accuracy of the positioning [5, 6]. Modern AE technology originated from the discovery of the Kaiser effect [7] and the Felicity effect [8]; then, some scholars continued to conduct in-depth research on the phenomenon of acoustic emission. Bhuiyan et al. [9] studied the AE waveforms of thin aerospace specimens, explained the correlation between the waveform evolution and the physical boundaries of cracks, and studied the growth mechanism of fatigue cracks. Madarshahian et al. [10] studied the problem of inverse

source location in specific areas and proposed a method to determine the true arrival time based on probability theory.

Other scholars have also made relevant research on the damage identification method of determining the structure by AE signal. Krivosheev and Ivanov [11] proposed a trend statistical method for the AE signal of rock masses, described the statistical change criteria used to identify the flow, and gave the use of these criteria. Yang et al. [12] analysed the characteristics of the AE signal during the staged loading of concrete materials and used the activity coefficient ACT to indicate the activity of the AE activity. The results showed that the energy average exceeded 100 mV·ms and the activity coefficient ACT was in the range of 20~70 when the concrete material was destroyed.

It should be pointed out that the existing acoustic emission analysis is often used in ordinary concrete specimens, concrete beams, or other concrete specimens [13, 14], while the research on other types of models, especially box culvert and prefabricated box culvert, is slightly insufficient [15]. In addition, as a common method for processing AE data, the fuzzy C-means (FCM) clustering method has the inability to identify noise in processing data [16], and clustering is easy to fall into the local optimal situation [17]. Therefore, it is necessary to monitor, analyse damage process of the prefabricated assembled box culvert model, and optimize the damage identification process of the prefabricated assembled box culvert model. In this paper, aiming at the shortcomings of the existing literature in these aspects, the AE signals of the two prefabricated box culverts during the static load test loading and unloading process were collected through experiments. The damage process of the box culvert was analysed based on the test signals, and a damage identification algorithm based on FCM was proposed. This algorithm was compared and analysed with the traditional FCM method, statistical information grid-based (STING) method, and density-based spatial clustering of applications with noise (DBSCAN) method, in the meantime applying to the prefabricated box culvert scale model. The study can fill the problem of insufficient research on damage identification of prefabricated box culverts and provide a reference for the research process of damage identification of prefabricated box culverts.

## 2. Materials and Methods

*2.1. Materials and Equipment.* There are two types of common prefabricated box culverts: one is the integrally prefabricated culvert, and the other is the four-component prefabricated culvert. Integrally prefabricated culvert means that the culvert facade becomes a whole, and the assembly work only occurs between the culverts, while the four-component prefabricated culvert is composed of the top plate, two side walls, and the cast-in-situ bottom plate. The assembly work of four-component prefabricated culvert is carried out not only between the culverts, but also between the various components in each culvert. In this experiment, based on the similar theorems [18–20] and the dimensional analysis, under the condition of ensuring that the prototype and the model had the same mechanical properties, the scale used in this experiment is 1 : 4. At the same time, to ensure that the model and the prototype had the same material properties, the concrete compressive strength was 40 MPa, which was the same as the prototype. The main reinforcement of the integrally assembled model was 20Φ6, and the stirrup was 87Φ2; for the four-component fabricated model, the main reinforcement was 20Φ6, and the stirrup was 80Φ2. The completed two box culvert model sizes are shown in Figures 1 and 2.

The SAEU2S acoustic emission system produced by Beijing Shenghua Testing Company was used in the test. The AE system was composed of an AE sensor, a preamplifier, and a computer. The AE sensor collected and converted the internal acoustic signal of the structure into an electrical signal and then transmitted it to the preamplifier. After being amplified by the preamplifier, the signal was transmitted to the computer for subsequent analysis work. The detailed technical parameters of the system are shown in Table 1. The HC-CK101 crack width observer produced by Beijing Haichuang Hi-Tech Company was used in the test. The detailed technical parameters of the instrument are shown in Table 2. Besides, the test loading equipment comes from the T-PMC microcomputer-controlled electro-hydraulic servo loading system produced by Changchun Xiaoxiu Metrology Technology Company. The parameters are shown in Table 3.

*2.2. Test Scheme.* In this test, a hydraulic Jack and an I-type beam were utilized for the four-point bending test. Three AE sensors were stuck on the culvert façade: one was on the middle span and the other two were near hinges of the culvert facade with scotch tape. Because the facade of the concrete box culvert was rough and uneven, the surface of the concrete was polished as smooth as possible with abrasive paper. In order to fix AE sensors well, Vaseline was used as a coupling agent to smear the contact surface between the sensor and the concrete. The schematic diagram of the loading device and AE sensors layout is shown in Figure 3.

The cyclic loading and unloading scheme was adopted in the test. According to the previous similar experiment experience of the research group and the conclusions of related documents [16, 21, 22], the loading level interval was 3 kN, and each level of load was uniformly loaded and unloaded. For a whole cycle, the load was applied from 0 to the loading level in 200 s, which was held in the next 300 s. Then, it was unloaded to 0 kN in 200 s and the interval between cycles was 1000 s. During the loading period and after completely unloading, the crack observation instrument was employed to observe the cracks. This loading system repeatedly loads and unloads the model until it was destroyed. The AE data and crack data of the top plate of the model were observed and recorded; subsequent analysis was performed.

*2.3. Current Status of Damage Identification Research.* Fuzzy C-means clustering (FCM) is a mathematical method based on the optimal solution of the function, through continuous iterative calculation, to separate the difficult-to-

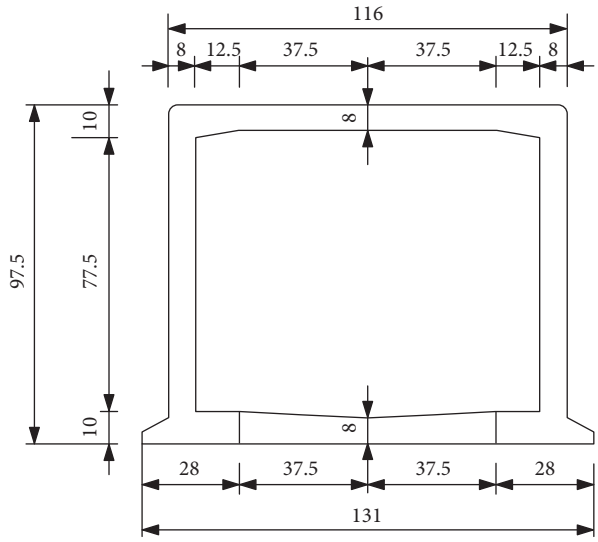


Figure 1: Dimension diagram of integrally assembled box culvert model.

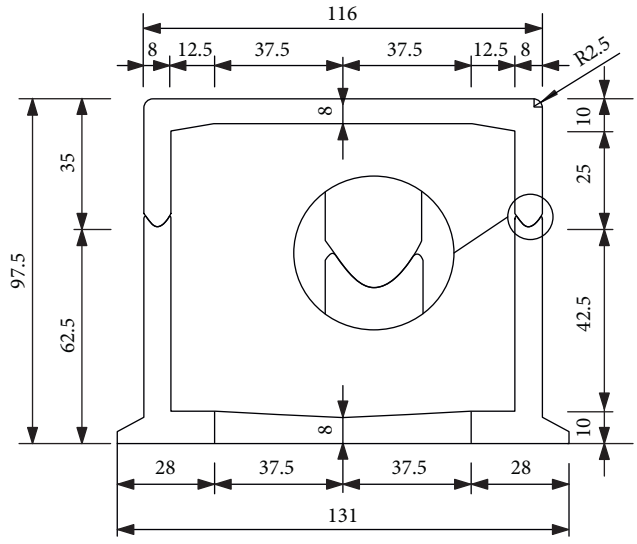


Figure 2: Dimensions of four-component fabricated box culvert model.

segment data set into visible and distinct data clusters. The process is usually achieved through the following 5 steps.

(1) The objective function is the sum of squared deviations, expressed by

$$J(U,P)=\sum_{j=1}^{n}\sum_{i=1}^{c}[u_{ik}]^{m}(d_{ik})^{2}, \tag{1}$$

where $u_{ik}$ is the membership degree of the $k$-th data point to the $i$-th cluster center, $m$ is smoothing parameter, and $(d_{ik})^2$ is the Euclidean distance of the $k$-th data point to the $i$-th cluster center.

(2) The sample data is normalized to the [0, 1] interval to eliminate the difference in data scale. Normalization is expressed by

$$x^{*}=\frac{x_{\max}-x}{x_{\max}-x_{\min}}. \tag{2}$$

(3) Initialize the membership degree matrix; the membership degree matrix is expressed by

$$\begin{aligned}&\sum_{i=1}^{t}u_{ik}=1,\quad 1\le k\le c,\\&\sum_{n=1}^{c}u_{ik}>0,\quad 1\le i\le t,\\&u_{ik}\ge 0,\ 1\le i\le t,\ 1\le n\le c.\end{aligned} \tag{3}$$

(4) Enter the number of clusters, smoothing parameter, maximum number of iterations, and convergence criteria.

Under the constraints of equation (3), the minimum value of formula (1) is obtained by applying the Lagrange multiplier method to equation (1)and taking the derivative to obtain the elements of the membership matrix and cluster centers in each iteration through calculating. The cluster centers and elements of the membership matrix are expressed by

$$P_i=\frac{\sum_{k=1}^{n}[u_i(x_k)]^{m}x_k}{\sum_{j=1}^{n}[u_i(x_j)]^{m}},\quad i=1,2,\ldots,k, \tag{4}$$

$$u_{jt}=\left[\sum_{i=1}^{c}\left(\frac{d_{jt}}{d_{it}}\right)^{(2/m-1)}\right]^{-1}. \tag{5}$$

(5) Iteratively calculate the cluster centers and adjust the updated membership matrix until the convergence criterion is reached. At this time, the objective function reaches the minimum, and the final cluster center matrix and membership degree matrix are taken as the basis for drawing the clustering results.

As a commonly used soft clustering method, the traditional FCM method is often used to analyse the AE data of the structure. Based on the acoustic emission method and using the FCM method, Shao [23] monitored the damage process of steel tube constrained reinforced concrete columns and obtained the damage type and cracking mode of the structure. Zhao et al. [24] used principal component analysis (PCA) and FCM to cluster the AE signals collected during the torsion test of the 3D braided composite shaft. The study found the material failure mode and mechanism by analysing the structural damage. Zhao and Zhou [25] used AE and FCM methods to evaluate the damage process of carbon/glass fiber reinforced hybrid composite materials and obtained the characteristics of the three damage modes of the material, which provided a reference for the health monitoring of the material. But due to the random generation of its initial membership matrix, it was easy to cause a

Table 1: Technical parameters of acoustic emission system.

| Name | Model | Test frequency range (kHz) | Noise minimum threshold (dB) | Maximum signal amplitude (dB) |
|---|---|---|---|---|
| Acoustic emission system | SAEU2S | 3~2000 | 10 | 100 |

Table 2: Technical parameters of creak observation equipment.

| Name | Model | Magnification | Range (mm) | Minimum indexing (mm) |
|---|---|---|---|---|
| Crack width observer | HC-CK101 | 40 | 0~2 | 0.02 |

Table 3: Technical parameters of microcomputer-controlled electro-hydraulic servo loading system.

| Name | Model | Range (kN) |
|---|---|---|
| Microcomputer-controlled electro-hydraulic servo loading system | T-PMC | 0~100 |

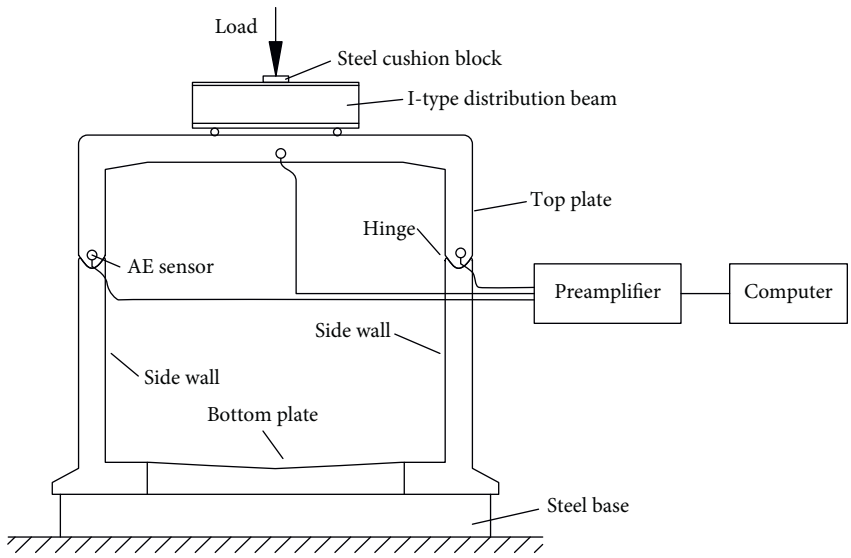


Figure 3: Diagram of loading device and AE sensors layout.

local optimal situation [26]. To solve this problem, Liang and Xue [27] used a method that combines an improved artificial bee colony algorithm and KFCM algorithm to improve the problem. The results showed that, compared to the IABC-GFCM algorithm, the algorithm could effectively improve the cluster validity index.

The basic idea of the STING method is to grid the data space and analyse the data with space as the basic unit. The advantage is that the calculation speed is faster, but the disadvantage is that the space complexity is high when the mapping path is long and the dimensions are uneven [28].

The density-based algorithm represented by the DBSCAN algorithm has been applied in many fields by scholars due to its effectiveness in filtering noise and flexibility in processing data [29, 30], but it was more sensitive to input parameters [31]. The density peak clustering algorithm proposed by Rodriguez and Laio [32] was based on the spatial hierarchical relationship and provides two methods for different users. It was extremely flexible, but its complexity was high, and it had poor adaptability to high-dimensional data [33].

Aiming at the shortcomings of the above three algorithms and drawing on their advantages and inspired by the above algorithms, this paper proposes a grid-based fuzzy C-means clustering analysis method based on the combination of density and distance (G-DFCM).

*2.4. G-DFCM Clustering Method.* The G-DFCM algorithm aims at solving the fuzzy C-means clustering easy to fall into the local optimal and cannot identify the noise situation. First, select the first clustering center grid according to the peak density, calculate the membership grid matrix, and use it as the initial membership matrix to replace the matrix which is the first step to initialize the membership randomly in the normal fuzzy C-means algorithm, to solve the occurrence of local optimal conditions. Secondly, for the case that the original algorithm cannot identify noise, the relative grid average density parameter is proposed to distinguish the noise data in the original data. Finally, a two-step method is used to reduce the sample space and optimize the original objective function. The optimized objective function is based

on the grid. The membership degree of the grid is substituted for the degree of membership of the point, and the Euclidean distance of the point is replaced by the grid distance, and the relative grid average density parameter is introduced to reduce the number of iterations and reduce the calculation time. It is convenient for the objective function to converge to the minimum value as soon as possible. The following describes the foundation and detailed steps of the algorithm.

*2.4.1. G-DFCM Algorithm Foundation.*

*Definition 1.* Grid density:

$$R_i = \frac{\sum_{j=1}^{k} \rho_j}{k}, \tag{6}$$

where $R_i$ is the grid density of the $i$ grid, $k$ is the amount of data in the $i$ grid, and $\rho_j$ is the local density of the point, which can be calculated according to

$$\rho_j = \sum_{j=1}^{n} \chi\left(d_{ij} - d_c\right), \tag{7}$$

where $\rho_j$ is the local density of point $j$, $n$ is the amount of data, $\chi(x)$ is the indicator function, $\chi(x) = \begin{cases} 1, & x < 0 \\ 0, & \text{others} \end{cases}$, $d_{ij}$ is the Euclidean distance of point $j$ to the center $i$, and $d_c$ is the cutoff distance, which is defined by the user. When defining the local density, keep it greater than the minimum point value.

*Definition 2.* Relative grid average density:

$$R_{ij} = \frac{R_j}{R_i}. \tag{8}$$

*Definition 3.* G-DFCM algorithm objective function:

$$J(U, V) = \sum_{i=1}^{c} \sum_{j=1}^{n} \left[u_{ij}\right]^m \left(d_{ij}\right)^2 R_{ij}. \tag{9}$$

Use the Lagrange multiplier method to find the partial derivative of the objective function:

$$u_{ij} = \left[\frac{\left(d_{ij}\right)^2 R_{ij}}{\sum_{k=1}^{c} \left(d_{kj}\right)^2 R_{kj}}\right]^{-(1/m-1)}, \tag{10}$$

$$C_i = \frac{\sum_{j=1}^{n} \left[u_{ij}\right]^m R_{ij} x_j}{\sum_{j=1}^{n} \left[u_{ij}\right]^m R_{ij}}, \tag{11}$$

where $u_{ij}$ is the membership degree of grid $j$ relative to the center grid of $i$, $R_{ij}$ is the average density of the relative grid, $d_{ij}$ is the Euclidean distance of grid $j$ relative to the center grid of $i$, and $C_i$ is the $i$-th cluster center grid.

*2.4.2. The Specific Operation Steps of the G-DFCM Algorithm.* The specific operation steps of the G-DFCM algorithm are as follows:

Data normalization: use normalization methods to adjust the data to [0, 1] to eliminate the difference in data point scale.

Data gridization: grid the region, and assign the data to the corresponding grid according to its location.

Calculate the parameters of the points in the grid: calculate the local density parameters of all data according to equation (7).

Datapoint classification: according to the density calculation result of equation (6), the effective point and the noise point are distinguished, and the noise point is removed from the original data after the noise point is output to facilitate the subsequent steps.

Screening of grid density: screen all grids, and use the average density of all points in the grid as the grid density of the grid.

Calculation of grid average density: calculate the relative grid average density according to equation (8).

Enter the number of clusters, the maximum number of iterations, smoothing parameter, and convergence criterion.

Calculate the initial membership matrix: take the highest grid density as the clustering center, and calculate the membership matrix once according to equation (9), and use it as the initial membership matrix to replace the randomly generated membership in the original algorithm membership grid matrix.

Continue to iteratively calculate the membership degree matrix and the clustering center matrix according to equations (10) and (11) until the objective function equation (9) reaches the minimum value.

Output the final membership degree matrix, cluster center matrix, objective function value, iteration calculation times, running time, and noise points.

*2.5. G-DFCM Simulation Experiment.* The performance of the G-DFCM method was tested. The test environment was built as a platform: Core i7-4710HQ (2.5 GHz) processor, 8 GB memory, and Windows 10 operating system. This algorithm was developed and tested in Matlab R2018a. The test data set used the open data sets Iris [34] and Glass [35] in the UCI data set. The relevant information of the two data sets is shown in Table 4. Since the two data sets do not contain noise data, the Balance-scale data set and the Cmc data set with the same dimensions were manually introduced as noise data, and the relevant information of the two data sets is shown in Tables 4 and 5. The test aimed to compare the effectiveness of noise discrimination, convergence speed, and clustering effectiveness with the normal FCM algorithm, STING algorithm, and DBSCAN algorithm through this algorithm.

When calculating with G-DFCM, the following parameters need to be entered: number of clusters, cutoff distance, the minimum number of points, and three common data maximum iterations, smoothing parameter, and convergence criterion. Among them, the first three data sets

Table 4: Related information of the two data sets.

| Data set | The amount of data | Dimension | The amount of clusters |
|---|---|---|---|
| Iris | 150 | 4 | 3 |
| Glass | 214 | 9 | 6 |

Table 5: Related information of the two noise data sets introduced.

| Data set | The amount of original data | The amount of data introduced | Dimension |
|---|---|---|---|
| Balance-scale | 625 | 30 | 4 |
| Cmc | 1473 | 30 | 9 |

have a greater impact on the clustering speed and accuracy, and different values should be selected for different data sets, and the last three data sets can generally use common values. The value assignment of each parameter is shown in Table 6.

## 3. Results and Discussion

*3.1. Parameter Analysis of Acoustic Emission in the Model Test.* When a load is applied to the structure, the AE parameters generated by the structure will change drastically. Through the model test, the AE data of the integrally assembled box culvert and the four-component assembled box culvert were collected, including amplitude, ringing count, duration, rising count, rising time, energy, etc. Among them, amplitude, ringing count, and energy are the most commonly used analysis parameters. The amplitude represents the maximum amplitude of the AE signal waveform, which directly reflects the strength of the signal. The ringing count represents the number of oscillations in the AE signal waveform that exceed the threshold, and it also reflects the strength and frequency of the signal. Amplitude and ringing count are both important indicators to measure the intensity of AE. Energy represents the amount of energy released by changes in the energy level of the stress wave and reflects the relative strength of the signal. Due to the particularity of the ringing count, the ringing count was used as the representative parameter to analyse the AE parameters. In the subsequent analysis, three common parameters are also selected as clustering data.

Figures 4 and 5 are graphs of the ringing count and cumulative ringing count of the two prefabricated box culvert models over time. Table 7 is crack data of four-component assembly box culvert in model test.

$N_i$ was used to represent the ringing count of the integrally assembled box culvert, and $N_f$ was used to represent the ringing count of the four-component assembly box culvert. The following can be known from the figure:

(1) In the initial loading stage of the integrally assembled box culvert (the first five loading stages), the structural acoustic emission phenomenon was not obvious, and occasionally a slightly stronger acoustic emission activity occurred. At this time, the highest value of the ringing count was $N_{i,\max 1} = 597$, and the cumulative ringing count rose slowly. However, the initial loading of the four-component assembly box culvert was shorter (the first two loading stages), and the highest ringing count was $N_{f,\max 1} = 1023$. Combined with the crack observation instrument to observe the two box culverts, no cracks occurred. Therefore, this stage of the two box culverts was the initial structural compaction and internal slippage of the structure, and the internal damage of the structure was in the cumulative stage. Occasionally, a slightly stronger acoustic emission activity was the release of energy when the internal pores were closed under pressure or the internal structure of the structure slips.

(2) In the mid-loading period of the integrally prefabricated box culvert (the sixth and seventh loading stages), the structural acoustic emission phenomenon was very violent and peaks were generated, the highest ringing count was $N_{i,\max 2} = 973$, and the cumulative ringing count was suddenly increased. Combined with the crack observation instrument, two cracks were generated, which were located in the middle of the top plate and a quarter of the span, whose length was 4.0 cm and 3.5 cm, respectively, and width was 0.28 mm and 0.14 mm, respectively. The loading period of the four-component assembly box culvert was slightly longer (the third to sixth loading stages), the maximum ringing count was $N_{f,\max 2} = 1527$, and the cumulative ringing count was rising steadily. Combined with the observation of the crack observer, one crack was generated, which was located at the middle of the top plate, whose length was 6.8 cm and width was 0.3 mm. Therefore, in the mid-loading period of the two box culverts, the internal damage accumulation limit was reached, and the process of releasing accumulated energy in the form of cracks began.

(3) At the end of the loading stage (the eighth and ninth loading stage) of the integrally prefabricated box culvert, the acoustic emission activity produced a secondary peak, accompanied by frequent acoustic emission phenomena. Combined with the observation of the crack observation instrument, two new cracks were generated, located between the right quarter span and the middle span and another quarter of the span, whose length was 2.9 cm and

Table 6: Parameter value assignment table.

| Name of parameters | Data set | Value assignment |
|---|---|---|
| Number of clusters | Iris | 4 |
| | Glass | 9 |
| Cutoff distance | Iris | 0.4 |
| | Glass | 1.0 |
| Minimum number of points | Iris | 30 |
| | Glass | 30 |
| Maximum iterations | | 100 |
| Smoothing parameter | | 2 |
| Convergence criterion | | $1E-5$ |

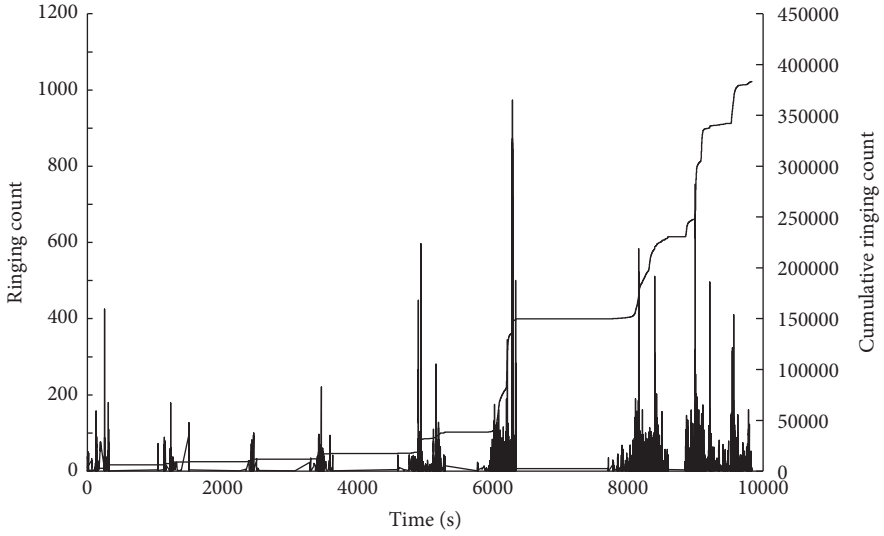


Figure 4: The change diagram of integrally assembled box ringing count and cumulative ringing count over time.

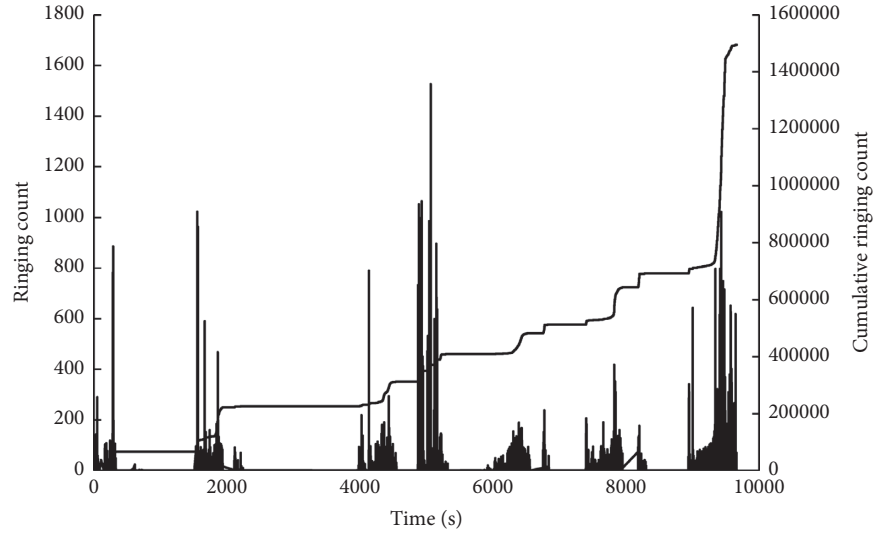


Figure 5: Four-component assembly box ringing count and cumulative ringing count change with time.

3.6 cm, respectively, and width was 0.09 mm and 0.18 mm, respectively. The loading end of the four-component assembly box culvert was slightly shorter (the seventh loading stage) and was also accompanied by frequent ringing counting signals and two cracks were generated in the right quarter span and

Table 7: Crack data of four-component assembly box culvert in model test.

| Load level (kN) | Loading/unloading | Crack number | Crack starting point (cm) | Crack width (mm) | Crack length (cm) |
|---|---|---|---|---|---|
| 3.0 | Loading | — | — | — | — |
| 6.0 | Loading | — | — | — | — |
| 9.0 | Loading | 1 | (63.8, 0) | 0.30 | 6.8 |
| | Unloading | 1 | (63.8, 0) | 0.04 | 6.8 |
| 12.0 | Loading | 1 | (63.8, 0) | 0.48 | 8.0 |
| | | 2 | (37.0, 0) | 0.44 | 6.4 |
| | Unloading | 1 | (63.8, 0) | 0.18 | 8.0 |
| | | 2 | (37.0, 0) | 0.30 | 6.4 |
| 15.0 | Loading | 1 | (63.8, 0) | 1.26 | 8.0 |
| | | 2 | (37.0, 0) | 0.54 | 6.4 |
| | Unloading | 1 | (63.8, 0) | 0.59 | 8.0 |
| | | 2 | (37.0, 0) | 0.28 | 6.4 |
| 18.0 | Loading | 1 | (63.8, 0) | 1.50 | 8.0 |
| | | 2 | (37.0, 0) | 0.58 | 6.4 |
| | | 3 | (84.0, 0) | 0.05 | 7.5 |
| | Unloading | 1 | (63.8, 0) | 0.72 | 8.0 |
| | | 2 | (37.0, 0) | 0.28 | 6.4 |
| | | 3 | (84.0, 0) | 0.03 | 7.5 |
| 21.0 | Loading | 1 | (63.8, 0) | 9.00 | 8.0 |
| | | 2 | (37.0, 0) | 2.26 | 6.4 |
| | | 3 | (84.0, 0) | 1.70 | 7.5 |
| | Unloading | 1 | (63.8, 0) | 5.10 | 8.0 |
| | | 2 | (37.0, 0) | 1.08 | 6.4 |
| | | 3 | (84.0, 0) | 0.73 | 7.5 |

The origin of the coordinates is set at the imaginary intersection point between the lower edge of the top plate and the outer edge of the side wall.

left quarter span, whose length was 6.4 cm and 7.5 cm, respectively, and width was 0.08 mm and 0.05 mm, respectively. Therefore, at the end of loading of the two box culverts, cracks and deformations continued to be used to release the accumulated energy to the full, and the structure tended to be destroyed until the bearing capacity was completely lost. Other acoustic emission signals showed a tendency to change synchronously with the ring count.

(4) In terms of cumulative ringing count performance, the overall prefabricated box culvert model generally presented a "three-stage" upward trend, and the two inflection points were located at 66.67% and 77.78% of the ultimate load, respectively. The four-member prefabricated box culvert generally presents a "two-stage" upward trend, and the only inflection point was near the ultimate load. This showed that the overall prefabricated box culvert was more sensitive to load than the four-member prefabricated box culvert. As long as the damage accumulates to a certain degree, energy would be released through cracks appearance. The crack data of the four-member box culvert model is shown in Table 4.

(5) The two box culvert models from the early to mid-loading stage were both in the transition period from the elastic stage to the plastic stage. The difference was that the integrally prefabricated box culvert had a longer elastic phase (the first five loading phases), and the four-member prefabricated box culvert had a longer plastic phase (third to sixth loading phases). Therefore, corresponding to the actual structure, the integrally assembled box culvert structure had a longer elastic stage and could work for a long time without cracks under the low load level, so the performance would be more excellent. Under the action of great load level, because the four-member prefabricated box culvert had a longer plastic phase, it could continue to work for a longer time with cracks. For larger loads, due to the stronger ultimate bearing capacity of the integrally assembled box culvert, the integrally assembled box culvert was more reliable under extreme conditions.

*3.2. FCM Analysis of Acoustic Emission in the Model Test.* Although the use of AE parameter analysis can preliminarily characterize the damage of the two box culverts, because this method uses single factor analysis in the reanalysis process and is mixed with some subjective wishes, it is easy to draw one-sided conclusions [36, 37]. For making a distinction among the damage stages more reasonably, the fuzzy C-means clustering method is used to comprehensively analyse the collected three acoustic emission representative signals, namely, amplitude (dB), ringing count, and energy (mV·$\mu$s); these parameters can reflect the meaning represented by the AE signal from different angles. The relevant parameters given in this analysis are as follows: the number of clusters is 3, the smoothing parameter is commonly used as 2 [38], the maximum number of iterations is 100, and the convergence criterion is $1E-5$. Among them, the

smoothness index affects the clustering mode. The closer the parameter is to 1, the closer the clustering result is to the traditional hard clustering method. The smoothness index is generally of a common value 2. Convergence criteria and the maximum number of iterations affect the tolerance of the clustering results; the larger the maximum number of iterations or the smaller the convergence criterion value, the higher the clustering accuracy and the longer the calculating time. The convergence criteria and maximum number of iterations are generally of a common value $1E-5$ and 100, respectively. Substitute the acoustic emission data and four parameters into equations (1)~(5) until the change value of the calculation result of equation (1) reaches the convergence criterion before reaching the maximum number of iterations.

The clustering results after FCM calculation are shown in Figures 6 and 7. The following can be known from the figure:

(1) For low-energy (less than $1E4$ mV·$\mu$s [39]) data, the results of the two prefabricated culverts were similar: cluster 1 had the characteristics of low amplitude and low ringing count, and the amplitude range was located at 40.1~45.9 dB and 40.1~46.1 dB, and the ring count interval was 1~425 and 1~964, respectively. Observing with the crack observer, no macroscopic cracks were generated, and the influence of laboratory environment noise was taken into account, which meant it was related to the accumulated damage inside the model or the noise signal that cannot be filtered. Compared with cluster 1, cluster 2 had a higher amplitude and ringing count. The amplitude ranges were 42.4~55.3 dB and 43.3~56.4 dB, and the ring count ranges were 1~720 and 1~1079. There are no macroscopic cracks measured by the crack observer, so this was related to the relative slippage inside the model and the initiation and formation of micro-cracks. Compared with cluster 2, the amplitude and ringing count of cluster 3 increased again. The amplitude ranges were 47.2~99.6 dB and 52.2~100 dB, and the ringing count ranges were 7~973 and 3~1527. There were still no macroscopic cracks after observation with the crack observer, but the environmental noise would not reach such a high level and would not have such a significant impact on the structure, so this was related to the development of micro-cracks inside the model.

(2) For high-energy data (higher than $1E4$ mV·$\mu$s), there was a big difference between the two types of fabricated culverts: the overall fabricated culvert had high-energy AE signals while simultaneously having a high amplitude and high ringing counts. The amplitude range was higher than 99.0 dB and the ringing count range was higher than 612. At the same time, combined with the crack observer, it observed the cracks on the lower edge of the upper roof plate and found a crack in the middle of the span with a width of 0.50 mm and a length of 5.8 cm. A crack was found in a quarter span with a width of 0.14 mm and a length of 4.8 mm, so this was related to the sudden release after the cumulative damage, which directly produces visible cracks; it indicated that the destruction of the integrally fabricated culvert was relatively sudden, and the precursor features were not obvious, while the four-component assembled culvert model had a wider range of high-energy signal values. It not only had a large number of data points in the high-amplitude area, but also had a certain number of data points in the other two groups. This was related to the increasing cumulative damage, but the slow generation of macroscopic cracks, indicating that the failure process of the four-member assembly culvert was relatively slow and the precursor characteristics were obvious.

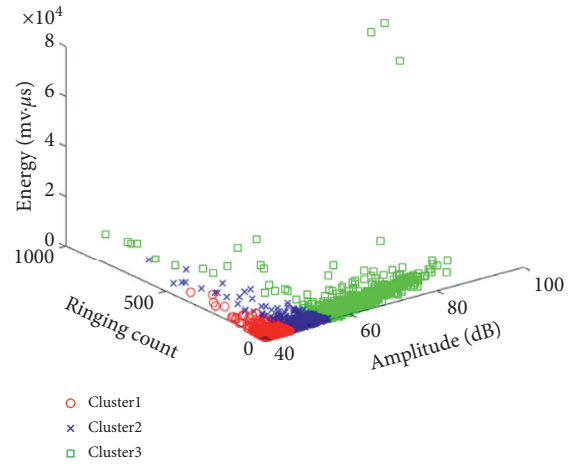


Figure 6: The direct clustering results of the whole assembled box culvert model.

*3.3. Results of G-DFCM Simulation Experiment.* According to the above-mentioned G-DFCM method to calculate the results of the simulation experiment, the experimental results are as follows: the noise calculation results are shown in Table 8 and the number of convergences and operation time in the calculation process are shown in Table 9 and Figures 8 and 9.

Analyse the accuracy of the G-DFCM clustering algorithm. Since the XB index considers the geometric structure information and membership degree of the data set at the same time [40], the XB index is used to verify the clustering effectiveness of the above method, and the XB index can be expressed by the following equation [41]:

$$XB^{(-)} = \frac{\sum_{i=1}^{K}\sum_{j=1}^{n}\mu_{ij}^{m}d\left(x_j, v_i\right)}{n \times \min\limits_{i\neq j} d\left(v_i, v_j\right)}, \tag{12}$$

where (−) indicates that the index is a minimum index; that is, the smaller the value, the higher the clustering effectiveness.

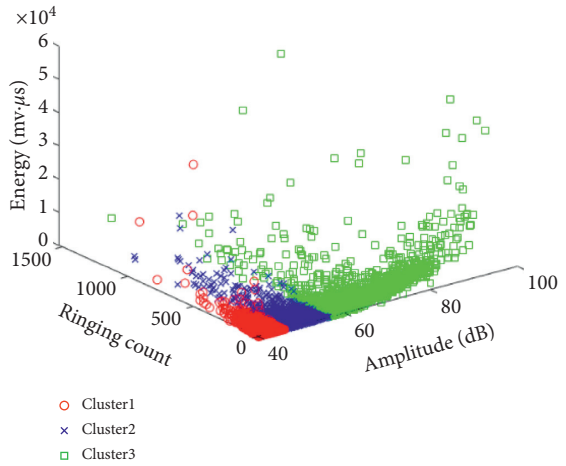


Figure 7: The direct clustering results of four-component assembled box culvert model.

Table 8: Data set noise calculation results.

| Calculation method | Data set | The amount of total data | The amount of noise point calculation | The amount of noise accurate calculation | Accuracy (%) |
|---|---|---|---|---|---|
| G-DFCM | Iris + Balance-scale | 180 | 30 | 30 | 100.00 |
| | Glass + Cmc | 244 | 32 | 30 | 93.75 |
| DBSCAN | Iris + Balance-scale | 180 | 39 | 30 | 76.92 |
| | Glass + Cmc | 244 | 32 | 32 | 52.63 |
| FCM | Iris + Balance-scale | 180 | —[1] | — | — |
| | Glass + Cmc | 244 | — | — | — |
| STING | Iris + Balance-scale | 180 | —[2] | — | — |
| | Glass + Cmc | 244 | — | — | — |

[1]FCM algorithm cannot identify noise. [2]The STING algorithm is not suitable for high-dimensional data.

Table 9: Comparison of data set calculation process.

| Calculation method | Data set | Number of convergence iterations | Operation time (s) |
|---|---|---|---|
| G-DFCM | Iris + Balance-scale | 16 | 0.368 |
| | Glass + Cmc | 35 | 0.363 |
| DBSCAN | Iris + Balance-scale | — | 1.030 |
| | Glass + Cmc | — | 0.995 |
| FCM | Iris + Balance-scale | 16 | 0.309 |
| | Glass + Cmc | 43 | 0.286 |
| STING | Iris + Balance-scale | —[1] | — |
| | Glass + Cmc | — | — |

[1]The STING algorithm is not suitable for high-dimensional data.

Table 10 and Figure 10 show the XB index values of the two fuzzy algorithms.

From Table 8 and Figure 10, it can be concluded that the G-DFCM algorithm not only identifies noise points but also improves the effectiveness of clustering through almost the same or lower number of iterations, while only increasing a small amount of computing time.

*3.4. G-DFCM Analysis of Acoustic Emission in Model Test.* The G-DFCM algorithm is used to analyse the AE data of the test integrated box culvert. The clustering results are shown in Figure 11.

Figure 11 indicates that the clustering result of acoustic emission data using the G-DFCM algorithm has clearer boundaries and more obvious differences between clusters.

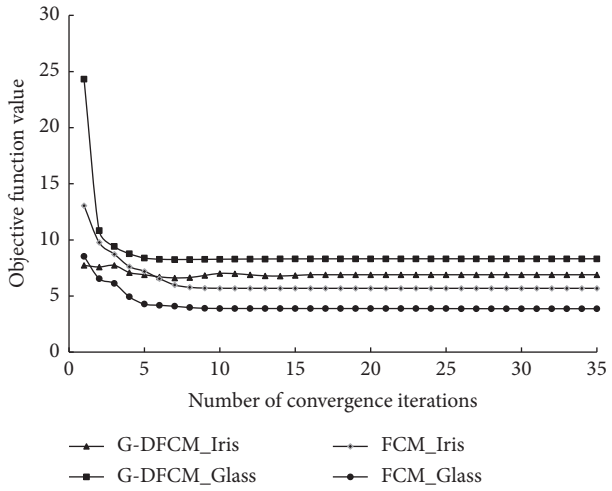


Figure 8: Comparison of iteration times.

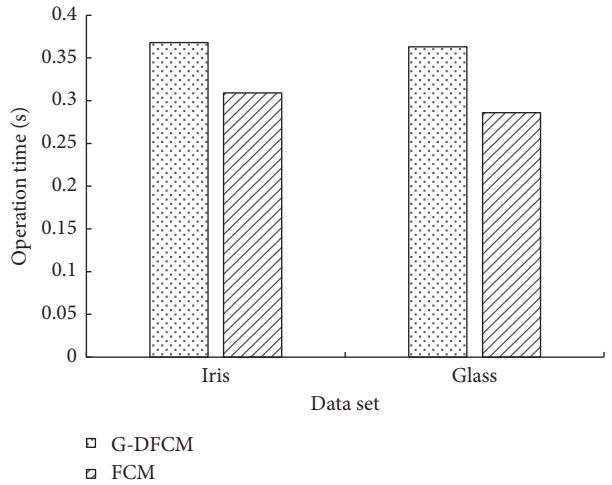


Figure 9: Comparison of operation times.

Table 10: Data set XB index comparison.

| | Data set | |
|---|---|---|
| Calculation method | Iris | Glass |
| G-DFCM | 0.023 | 0.057 |
| FCM | 0.108 | 0.143 |

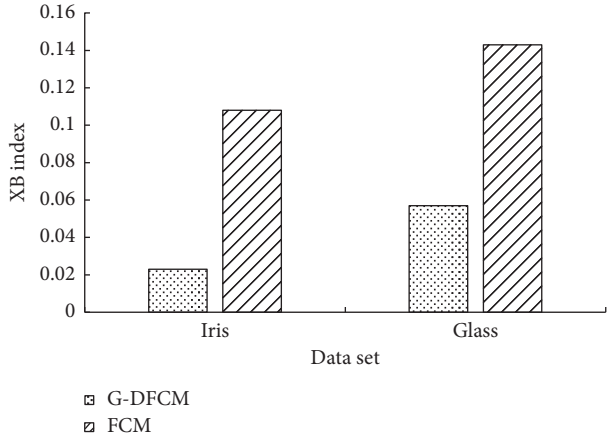


Figure 10: XB index comparison.

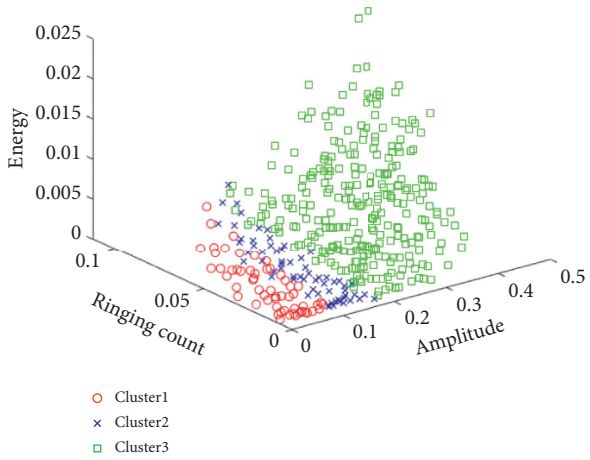


Figure 11: The G-DFCM method clustering results of the acoustic emission of the integrally assembled box culvert.

This is mainly due to the higher clustering effectiveness of the algorithm.

## 4. Conclusions

Aiming at the deficiencies in the research on the structure of the prefabricated box culvert and the damage identification method, this paper had made and tested the scaled model of the prefabricated box culvert; the AE data during the test were collected and analysed; a grid-based fuzzy C-means clustering analysis method was proposed based on the combination of density and distance (G-DFCM), and the algorithm was simulated to verify its effect, and it was applied to the damage identification process of the assembled box culvert. Through the analysis of the research results in the experiment, the main conclusions of this paper are as follows:

(1) The failure process of both culvert models includes three stages, namely, the accumulation of internal damage and internal structural slippage, the formation and development of micro-cracks, and the formation and development of macro-cracks. But the difference is that the destruction process of the integrally fabricated culvert is more sudden and the stage is more obvious; the failure process of the four-member fabricated box culvert is slower and the precursors are obvious.

(2) For low-energy signals, the acoustic emission amplitude range of 40~46 dB corresponds to the accumulation of structural internal damage; amplitude range of 43~56 dB corresponds to the internal structure slip; amplitude range of 49~99.8 dB corresponds to the formation and development of structural micro-cracks. For high-energy signals, they are often accompanied by high amplitude and high ringing count (amplitude interval higher than 99.0 dB, ringing count interval higher than 612). Such signals usually correspond to structural macroscopic cracks.

(3) Compared with the FCM algorithm, the G-DFCM algorithm improves the clustering effectiveness by 69.4% and can identify noise while the calculation time and the number of iterations are similar, and has the ability to identify the noise. The G-DFCM algorithm is used to cluster the AE data of the prefabricated box culvert. It can be found that this method can make the clustering boundary clearer and the clustering effect more obvious.

## Data Availability

The Iris, Balance-scale, Glass, and Cmc data used to support the findings of this study have been deposited at http://archive.ics.uci.edu/ml/index.php. Additionally, raw data generated during the study are available from the corresponding author upon request.

## Conflicts of Interest

The authors declare that there are no conflicts of interest regarding the publication of this paper.

## Acknowledgments

This work was funded by the National Natural Science Foundation of China (Project no. 51978309), the Transportation Technology Program of Jilin Province of China (Grant no. 2018-1-9), the Education Department's "13th Five-Year" Science and Technology Program of Jilin Province (Grant no. JJKH20190015KJ), the Special Funding for Basic Scientific Research Operation Fees of Central Universities, the Scientific and Technological Developing Scheme Program of Jilin Province (Grant no. 20200403157SF), and the Transportation Technology Program of Jilin Province of China (Grant no. 2018ZDGC-16).

## References

[1] J.-Y. Park, D.-S. Sohn, J.-H. Lee, and J.-H. Jeong, "A study on joint position at concrete pavement with box culverts," *Journal of the Korean Society of Road Engineers*, vol. 14, no. 2, pp. 45–53, 2012.

[2] S. Liu and M. Chen, "Design and construction of prefabricated cover passage and culvert," *Highway*, vol. 2002, no. 7, pp. 94-95, 2002.

[3] Q. Zhang and Y. Zhang, "Research status and prospect of concrete acoustic emission technology," *Applied Mechanics and Materials*, vol. 170–173, pp. 470–473, 2012.

[4] D. Soulioti, N. M. Barkoula, A. Paipetis, T. E. Matikas, T. Shiotani, and D. G. Aggelis, "Acoustic emission behavior of steel fibre reinforced concrete under bending," *Construction and Building Materials*, vol. 23, no. 12, pp. 3532–3536, 2009.

[5] A. Olszewska, "Location of partial discharge sources in oil transformer with the use of analysis of acoustic emission signals in various frequency bands," *Przeglad Elektrotechniczny*, vol. 86, no. 11B, pp. 63–65, 2010.

[6] Q. Wang and X. Liu, "Acoustic emission sensors circular array for concrete structure damaging source DOA estimation," *Structural Health Monitoring 2011: Condition-based Maintenance and Intelligent Structures*, vol. 2, no. 1, pp. 2189–2194, 2013.

[7] P. Ziehl, *Monitoring of the Bonnet Carre Spillway Bridge during Extreme Overload*, Department of Civil and Environmental Engineering, Tulane University, New Orleans, LA, USA, 2003.

[8] R. S. Gostautas, G. Ramirez, R. J. Peterman, and D. Meggers, "Acoustic emission monitoring and analysis of glass fiber-reinforced composites bridge decks," *Journal of Bridge Engineering*, vol. 10, no. 6, pp. 713–721, 2005.

[9] M. Y. Bhuiyan, B. Lin, and V. Giurgiutiu, "Acoustic emission sensor effect and waveform evolution during fatigue crack growth in thin metallic plate," *Journal of Intelligent Material Systems and Structures*, vol. 2017, no. 1, pp. 1276–1284, 2017.

[10] R. Madarshahian, P. Ziehl, and J. M. Caicedo, "Acoustic emission Bayesian source location: onset time challenge," *Mechanical Systems and Signal Processing*, vol. 123, no. 123, pp. 483–495, 2019.

[11] I. A. Krivosheev and G. A. Ivanov, "Statistical method for processing acoustic emission signals in rock mass," *Russian Journal of Nondestructive Testing*, vol. 38, no. 2, pp. 127–129, 2002.

[12] Y. Yang, J. Liu, R. Xue, and Y. Gao, "Analysis of acoustic emission characteristics in the process of graded loading of concrete materials," *Journal of Agricultural University of Hebei*, vol. 41, no. 1, pp. 100–105, 2008.

[13] C.-L. Wang, Z. Chen, Z.-F. Liao et al., "Experimental investigation on predicting precursory changes in entropy for dominant frequency of rockburst," *Journal of Central South University*, vol. 27, no. 10, pp. 2834–2848, 2020.

[14] S. W. Hu, J. Lu, and X. Zhong, "Study on characteristics of acoustic emission property in the normal concrete fracture test," *Advanced Materials Research*, vol. 189–193, pp. 1117–1121, 2011.

[15] R. Birgul, F. M. W. Al-shammari, and I. O. Yaman, "Acoustic emission evaluation of concrete culverts," *Research in Nondestructive Evaluation*, vol. 15, no. 4, pp. 191–208, 2004.

[16] X. Xu, Y. Zhang, and X. Li, "Research on damage identification method of reinforced concrete beams based on acoustic emission and depth confidence network," *Journal of Building Structures*, vol. 39, no. S2, pp. 400–407, 2008.

[17] A. Chen and H. Yan, "An improved fuzzy C-means clustering for brain MR images segmentation," *Journal of Medical Imaging and Health Informatics*, vol. 11, no. 2, pp. 386–390, 2021.

[18] L. A. Zadeh, "Similarity relations and fuzzy orderings," *Journal of Information Science*, vol. 3, no. 2, pp. 177–200, 1971.

[19] F. Ma, Z. Li, R. Xue, and G. Luo, "NIOS model materials and their application in geomechanical similar model test," *Journal of Hydroelectric Engineering*, vol. 2004, no. 1, pp. 48–51, 2004.

[20] N. S. Kim, J. H. Lee, and S. P. Chang, "An equivalent multiphase similitude law for pseudodynamic test on small-scale RC models: verification tests," *Journal of the Earthquake Engineering Society of Korea*, vol. 7, no. 6, pp. 834–846, 2004.

[21] S. H. Kim, B. S. Shin, and I. J. Park, "Model test on concrete placement method of tunnel lining due to tunnel size," *Journal of Korean Tunnelling& Underground Space Association*, vol. 11, no. 3, pp. 213–221, 2009.

[22] R. M. Bennett, S. M. Wood, E. C. Drumm, and N. R. Rainwater, "Vertical loads on concrete box culverts under high embankments," *Journal of Bridge Engineering*, vol. 10, no. 6, pp. 643–649, 2005.

[23] J. Shao, *Investigation on Damage Mechanisms of Civil Structures Based on Acoustic Emission Technique*, Dalian University of Technology, Dalian, China, 2017.

[24] G. Zhao, L. Zhang, C. Tang, W. Hao, and Y. Luo, "Clustering of AE signals collected during torsional tests of 3D braiding composite shafts using PCA and FCM," *Composites Part B: Engineering*, vol. 161, no. 1, pp. 547–554, 2019.

[25] W.-z. Zhao and W. Zhou, "Cluster analysis of acoustic emission signals and tensile properties of carbon/glass fiber-reinforced hybrid composites," *Structural Health Monitoring*, vol. 18, no. 5-6, pp. 1686–1697, 2019.

[26] Z. Han, D. Li, and J. Zhao, "Image segmentation algorithm based on improved genetic fuzzy clustering and level set," *Computer Engineering and Design*, vol. 40, no. 5, pp. 1390–1393, 2019.

[27] B. Liang and H. Xue, "Kernel fuzzy C-means clustering based on improved artificial bee colony algorithm," *Journal of Computer Applications*, vol. 34, no. 9, pp. 2600–2604, 2017.

[28] A. Amini, T. Y. Wah, and H. Saboohi, "On density-based data streams clustering algorithms: a survey," *Journal of Computer Science and Technology*, vol. 29, no. 1, pp. 116–141, 2014.

[29] K. M. Jones and M. Lacy, "Measuring the clustering around normal and dust-obscured quasars at 2 in the spitzer extra-galactic representative volume survey," in *Proceedings of the American Astronomical Society Meeting*, Boston, MA, USA, June 2014.

[30] S.-J. Horng, M.-Y. Su, Y.-H. Chen et al., "A novel intrusion detection system based on hierarchical clustering and support vector machines," *Expert Systems with Applications*, vol. 38, no. 1, pp. 306–313, 2011.

[31] Z. Li and Y. Zhang, "Analysis and evaluation of cluster analysis algorithm," *Electronic Technology and Software Engineering*, vol. 153, no. 7, p. 172, 2019.

[32] A. Rodriguez and A. Laio, "Clustering by fast search and find of density peaks," *Science*, vol. 344, no. 6191, pp. 1492–1496, 2014.

[33] Y. Chen, L. Shen, and C. Zhong, "Survey on density peak clustering algorithm," *Journal of Computer Research and Development*, vol. 57, no. 2, pp. 378–394, 2020.

[34] F. Liu, Y. Liang, and T. Hou, "Research and improvement of fuzzy C-harmonic mean algorithm on unbalanced data," *Journal of Jilin University (Engineering and Technology Edition)*, 2020.

[35] A. Seal, A. Karlekar, and O. Krejcar, "Fuzzy c-means clustering using Jeffreys-divergence based similarity measure," *Applied Soft Computing*, vol. 88, pp. 1–11, 2020.

[36] W. Zhao, *Composite Deformation Damage Monitoring and Acoustic Emission Characteristic Signal Clustering Analysis*, Hebei University, Baoding, China, 2018.

[37] R. L. Cannon, J. V. Dave, and J. C. Bezdek, "Efficient implementation of the fuzzy c-means clustering algorithms," *IEEE Transactions on Pattern Analysis & Machine Intelligence*, vol. 8, no. 2, pp. 248–255, 2009.

[38] A. A. A. Ahmed and A. A. H. B. Assem, "Classification of damage in self-consolidating rubberized concrete using acoustic emission intensity analysis," *Ultrasonics*, vol. 100, pp. 1–10, 2020.

[39] M. Wang, *Study on Flexural Fracture Resistance and Acoustic Attenuation Characteristics of Basalt Fiber Concrete Based on Acoustic Emission Parameters*, Jilin University, Changchun, China, 2017.

[40] K. Zhou, S. Yang, and S. Ding, "Summary of clustering validity research," *Systems Engineering Theory and Practice*, vol. 34, no. 9, pp. 2417–2431, 2014.

[41] X. L. Xie and G. Beni, "A validity measure for fuzzy clustering," *IEEE Transactions on Pattern Analysis and Machine Intelligence*, vol. 13, no. 8, pp. 841–847, 1991.

Hindawi
Advances in Materials Science and Engineering
Volume 2020, Article ID 6617742, 10 pages
https://doi.org/10.1155/2020/6617742

*Research Article*

# Real-Time Evaluation of Compaction Quality by Using Artificial Neural Networks

**Weidong Cao,[1] Shutang Liu,[1] Xuechi Gao,[2] Fei Ren,[3] Peng Liu,[2] and Qilun Wu[1]**

[1]*School of Qilu Transportation, Shandong University, Jinan 250061, Shandong Province, China*
[2]*Shandong Hi-Speed Group Co. Ltd., Jinan 250101, Shandong Province, China*
[3]*School of Mechanical and Automotive Engineering, Qilu University of Technology (Shandong Academy of Sciences), No. 3501, Daxue Road, Changqing District, Jinan 250353, Shandong Province, China*

Correspondence should be addressed to Fei Ren; ren87@outlook.com

Received 27 October 2020; Revised 9 December 2020; Accepted 13 December 2020; Published 23 December 2020

Academic Editor: Yubo Jiao



The primary goal of this study is to find an easy and convenient way to estimate the degree of compaction in real time for compaction quality control. In this paper, an artificial neural network classifier is developed to identify the different characteristic patterns of drum vibration and classify them according to the different compaction levels. At first, a field compaction experiment is designed and performed in a construction site, and the degree of compaction and the vibration are measured. Then, the vibration signals collected from the experiment are processed to extract the features of vibration patterns and labeled with the compaction level to train the artificial neural network model. At last, the performance of the artificial neural network classifier is verified against the degree of compaction measured by using a nuclear density gauge. It can be found that artificial neural networks show good performance and huge potential for the problem of compaction quality control.

## 1. Introduction

The compaction process plays an important role in improving the strength and bearing capacity of materials for use in road construction. The existing compaction quality control relies on spot tests, such as sand replacement method, falling weight deflectometer (FWD), and plate bearing test. These traditional manual measurements have several drawbacks [1, 2]: (1) the measurements are usually time consuming and may interrupt the subsequent construction operation; (2) test samples are collected at limited test points, and the testing results cannot indicate the overall pavement quality; (3) the measurements are performed after compaction; thus, it is impossible to provide real-time compaction quality information for the operator, which may lead to under or over compaction. To address these problems, intelligent compaction (IC) technique is proposed to provide real-time compaction quality assurance during compaction.

So far, there are several equipment manufacturers around the world offering IC rollers to compact subgrade and aggregate materials. Several intelligent compaction measurement values (ICMV) are set up to evaluate the compaction quality, such as Compaction Meter Value (CMV), Compaction Control Value (CCV), Resonance Meter Value (RMV), Machine Drive Power (MDP), vibration modulus (Evib), and soil stiffness (Ks) [2, 3]. CMV is widely accepted for quality assurance, and it is computed by the amplitude of vertical drum acceleration at the operating frequency and first harmonic. CCV and RMV further consider the high-order harmonics. Considering the nonlinearity vibration induced by the periodic loss of contact between soil and drum, Anderegg et al. [4, 5] develop a feedback control system to automatically adjust the compaction parameters (vibration frequency, vibration amplitude, and driving speed) during construction. Due to the development of these helpful IC technologies, roller operator can optimize the compaction process timely according to the

updated compaction information, and the compaction quality is improved effectively.

However, recent research studies found that there are still some uncertain correlations between ICMVs and compaction quality. Firstly, CMV, as a harmonic-based indicator, is easily influenced by many factors. Zhu et al. [6] test a multilayer structure and find that CMV is sensitive to the characteristic of underlying layers, such as stiffness and moisture content of the layers. White et al. [7] indicate that CMV is dependent on the vibration amplitude; therefore, a higher excitation force amplitude generally yields a greater CMV at a constant soil modulus. Wersäll et al. [8] conduct full-scale tests to study the influence of variable frequencies on compaction control. The results indicate that the resonant frequency is about 17 Hz, and the optimum compaction frequency is about 18 Hz, while the standard operating frequency of the roller is about 31 Hz. This means that there is no direct correlation between the excitation force and compaction quality. Secondly, the mechanical-based ICMVs related to soil stiffness and vibration modulus manifest unstable changes due to their amplitude dependence. Mooney and Rinehart [9, 10] demonstrate that soil stiffness on the soft layer decreases with increasing excitation force, while on the stiffer layer exhibits conversely. Further analysis by Mazari et al. [11] shows that roller type, machine operation setting variation, and instability of the machine in practicing operation commonly affect the accuracy of ICMVs. Furthermore, some researchers [12–16] use operational modal analysis (OMA) for the structural health monitoring of engineering. Different from the experimental modal analysis methods, OMA uses the output-only response to identify the structure properties; thus, the input excitation measures can be avoided.

Recently, an artificial intelligence-based intelligent compaction analyzer (ICA) was developed by Barman et al. [17–19]. The frequency characteristics of drum vibration can be analyzed by the ICA, and amounts of field testing show that the results correlate well with subgrade modulus. Zhang et al. [20, 21] utilize acoustic wave detection techniques to evaluate rock-fill compaction status, and a genetic algorithm-based optimization procedure was proposed to optimize the overall compaction process.

The recent IC techniques are largely based on the vibration analysis of pavement during compaction, trying to build the correlation between the vibration of pavement and compaction quality. However, the development of IC technique is blocked by the complication of vibration during compaction. From another point of view, the development of IC technique can be considered as a problem of signal processing and recognition. Fourier transform and artificial neural networks (ANN) have been widely used for signal processing and recognition nowadays, especially for speech recognition [22–25]. Zhan et al. [26] also use the ANN for radar waveform recognition. These studies provide many references on the applications of Fourier transform and ANN. However, few studies have been conducted on the compaction quality control by using the ANN. In the research studies by Barman et al. [17–19], the ANN is tried to analyze the correlation between the vibration pattern and subgrade stiffness. For the development of IC technique, neural networks can bypass some difficulties which cannot be solved easily by traditional methods, showing huge potential.

Generally, degree of compaction is the most direct index for the compaction quality evaluation. The main objective of this study is to find an easy and convenient way to estimate the degree of compaction in real time. In this research, the compaction analysis is based on a hypothesis that the vibratory roller and pavement form a coupled system during compaction. The coupled response is determined by the excitation frequency and natural vibration modes of the coupled system. The variations in the degree of compaction will affect the response and will lead to different patterns of vibrations of the drum. Therefore, the compaction quality can be estimated by using the mapping between the vibration pattern and degree of compaction.

In reality, however, the vibration pattern of the drum usually includes the information of the noise, which means some of the features of the vibration pattern reflect the system and others reflect the noise. The vibration pattern features reflecting the system can be used to estimate the compaction quality, but these useful features cannot be recognized and extracted easily. In this paper, an artificial neural network (ANN) classifier is developed to identify the different characteristic patterns of drum vibration and classify them according to the different compaction levels. A field compaction experiment is designed and performed in a construction site, and the degree of compaction and the vibration are measured. The vibration signals collected from the experiment are processed to extract the features of vibration patterns and then labeled with the compaction level to train the ANN model. At last, the performance of the ANN classifier is verified against the degree of compaction measured by using a nuclear density gauge (NDG).

## 2. Experimental Program and Signal Processing

It is assumed that the vibratory roller and pavement underneath form a coupled system during compaction. The variations in degree of compaction affect the coupled response and lead to different vibration patterns of the drum. To analyze and make use of the mapping relationship between the vibration pattern and degree of compaction, a field compaction experiment is designed and performed in a construction site to collect the data of the vibration signal and degree of compaction.

*2.1. Experimental Program.* A field test is performed on the extension project of G2 expressway in Shandong Province, China. The typical pavement structure used in the project is shown in Table 1, which consists of three hot-mix asphalt (HMA) surface layers, one flexible base layer, two semirigid base layers, one sub-base layer, and the subgrade, in that order, from top to bottom. The vibrating compaction test is implemented at the cement-stabilized gravel base layer with a thickness of 18 cm. The aggregate used for cement-stabilized base layer is limestone, and the details of the mixture and equipment are shown in Tables 2 and 3.

Table 1: Pavement structure in the project.

| | |
|---|---|
| HMA surface layers | 4 cm SMA-13<br>6 cm AC-20<br>8 cm AC-25 |
| Flexible base layer | 12 cm LSPM-25 |
| Semirigid base layer | 2 × 18 cm cement-stabilized aggregate |
| Sub-base layer | 18 cm cement-stabilized weathered sands |
| Subgrade | Compacted natural soil |

Table 2: Details of the base layer.

| Layer | Materials | Depth (cm) | Cement mass percent (%) | Maximum dry density (g/cm$^3$) | Optimum moisture content (%) |
|---|---|---|---|---|---|
| Base | Cement-stabilized gravel | 18×2 | 4.5 | 2.348 | 4.9 |

Table 3: Details of equipment.

| Roller type | Drum width (m) | Static weight (kg) | Speed (m/s) | Operation frequency (Hz) | Amplitude (mm) | Excitation force (KN) | Sample frequency |
|---|---|---|---|---|---|---|---|
| Single drum | 2.13 | 2000 | 0.5~0.7 | 33 | 1.2 | 290 | 2000 Hz (acceleration) |

Two wireless accelerometers are mounted on the axle of the roller drum on both sides to monitor the vibration acceleration signals in the vertical direction, as shown in Figure 1. The compaction is carried out on ten test lanes, and each test lane has a length of 60 m. The width of each test lane is 2.13 m, the same as the width of the roller. Figure 2 shows the roller pass trajectory on each test lane, and a total of 8 passes are performed for each lane. The degree of compaction is measured by using nuclear density gauge for each pass and computed as follows:

$$\rho_d = \frac{\rho_w}{1+w}, \qquad \mathrm{DOC} = \frac{\rho_d}{\rho_E} \times 100\%, \tag{1}$$

where DOC is the degree of compaction, $\rho_E$ is maximum dry density, $\rho_w$ and $w$ are wet density and moisture content measured by nuclear density gauge, and $\rho_d$ is dry density. For each test lane, two different locations are tested, as shown in Figure 2, and the relationship between the number of roller passes and degree of compaction is investigated.

The relationship between the number of passes and degree of compaction is plotted in Figure 3. Here, the open circles denote the degree of compaction obtained from the experiment by using NDG, and the solid circles denote the average degree of compaction for each pass. Ten test lanes are investigated and each test lane has two test locations; therefore, there are 20 experimental results for each pass. For the cement-stabilized gravel base, the minimum requirement of degree of compaction is 98% and about 6 passes are needed to reach the requirement.

*2.2. Signal Processing.* The vibration signals are collected continuously from two accelerometers when the vibratory roller moves on the test lane. The length of the test lane is 60 m, the velocity of the roller is about 0.6 m/s, and it takes about 100 s for one pass. Therefore, we can get a 100-second long vibration signal from one accelerometer in one pass, and a total of 160 long signals can be collected since we have ten test lanes and two accelerometers. Theoretically, the vibration signals from two accelerometers have the same frequency components, even though their amplitudes may be different.

The vibration is sampled at a 2 kHz sampling frequency. The long vibration signal of one pass is divided into lots of 0.5-second short signals. Each short signal includes 1000 contiguous data samples having an overlap with 500 previous values. Each short signal is converted to frequency domain representation using a fast Fourier transform (FFT). Since the vibration is sampled at 2 kHz, the Nyquist frequency is 1 kHz. Therefore, a single-sided FFT provided a frequency spectrum distributed between 0 and 1 kHz, and the output of the single-sided FFT for each short signal is an array of 500 elements, expressed as $a = (a_1, a_2, \ldots, a_{500})$. By using a FFT, the features of the vibration signal are expressed as the frequency components. Amplitude is not considered as a kind of feature in this study; array $a$ should be normalized to eliminate the effects of amplitudes. The normalized array $x$ is obtained as follows:

$$\overline{a} = \ln(a), \qquad x = \frac{\overline{a}}{|\overline{a}|_{\max}}. \tag{2}$$

Here, the logarithmic operation in equation (2) is used to amplify some inconspicuous frequency components. The signal processing method in this section is shown in Figure 4 and summarized as the following steps:


Figure 1: Accelerometer-equipped vibratory roller during compaction.

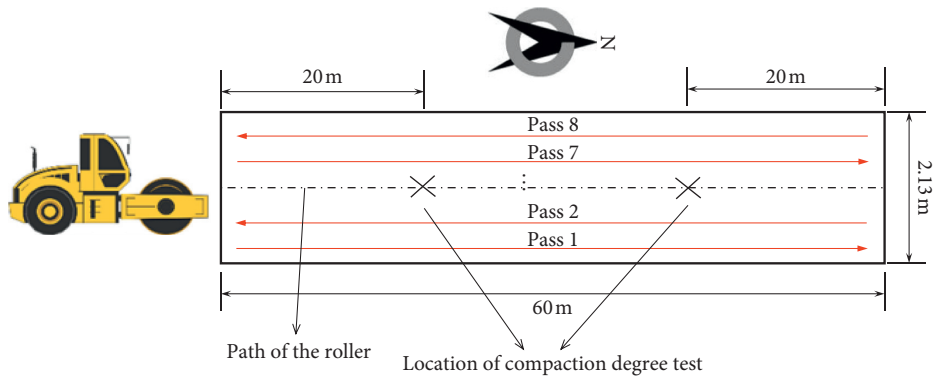


Figure 2: Test lane.

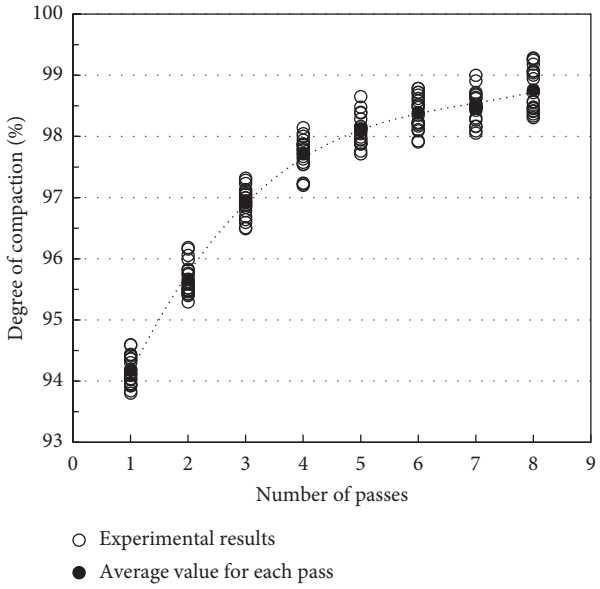


Figure 3: Influence of number of passes on the degree of compaction.

(1) The long vibration signal from the accelerometer in one pass is divided into lots of 0.5-second short signals

(2) Each short signal is converted to frequency domain representation by using a single-sided FFT to extract the frequency features

(3) The output of the single-sided FFT for each short signal is normalized by using equation (2) to eliminate the effects of amplitudes and amplify the inconspicuous frequency components

(4) The processed signals are input to ANN for training or for predicting the degree of compaction

The frequency features of vibration signals are extracted by this method, and the processed arrays will be used as input data for training the ANN model. In the following discussion on the ANN, the input array $x$ is called "sample," and the element of $x$ is called "feature." In this study, therefore, each sample has 500 features.

Before being used for training the ANN, each sample should be labeled with a target class. In this research, we use four target classes to represent four compaction levels, as shown in Table 4. According to the experimental results of

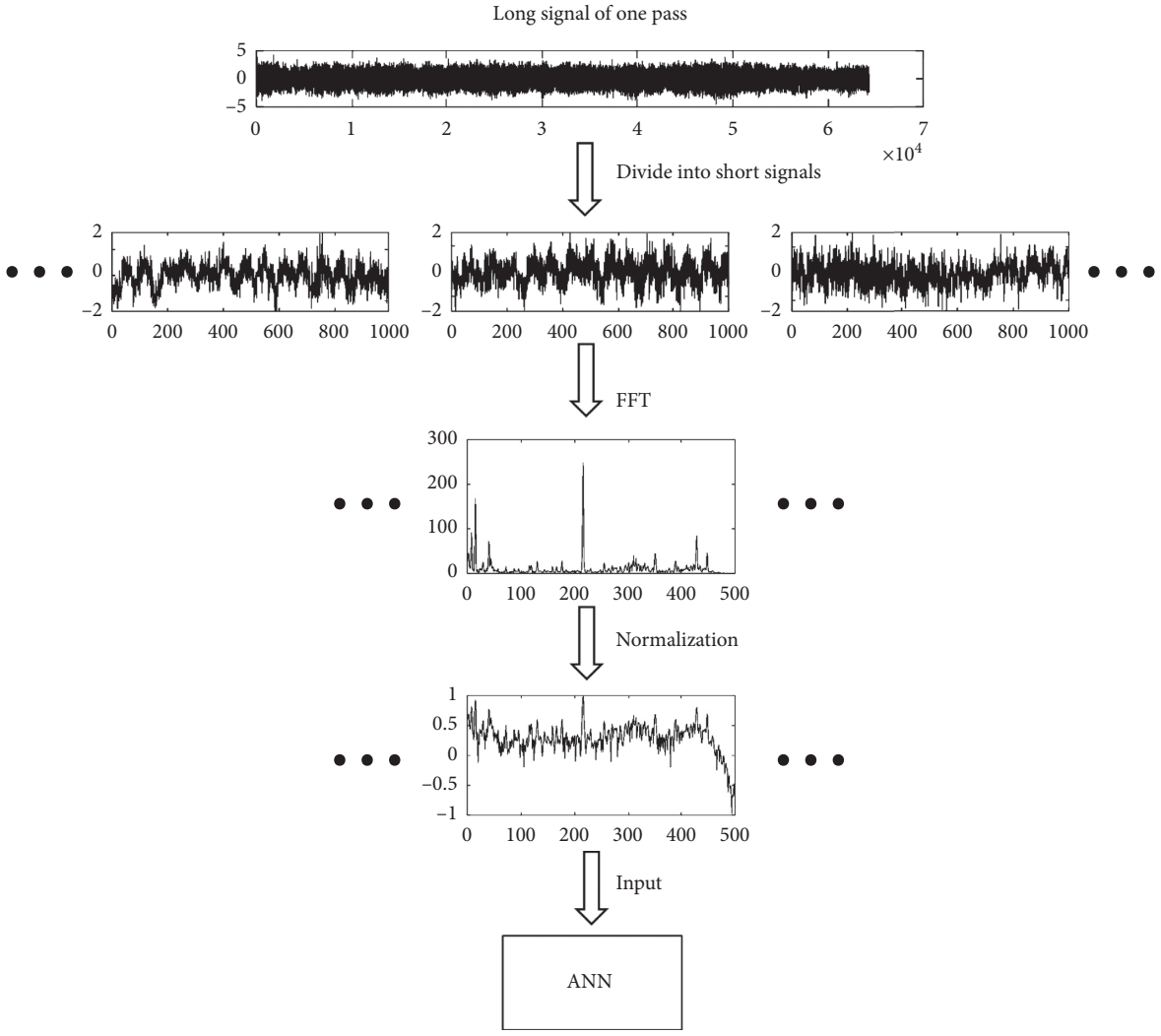


Figure 4: Signal processing.

Table 4: Target class and compaction level.

| | Level no. | Degree of compaction (%) | Target array |
|---|---|---|---|
| Target class 1 | 1 | <94 | (1, 0, 0, 0) |
| Target class 2 | 2 | 94~96 | (0, 1, 0, 0) |
| Target class 3 | 3 | 96~98 | (0, 0, 1, 0) |
| Target class 4 | 4 | >98 | (0, 0, 0, 1) |

the degree of compaction (Figure 3), the samples are labeled with the corresponding compaction level, forming the dataset for the ANN training.

## 3. Development of the ANN Model

A multilayer perceptron (MLP) feedforward neural network is used in this research. Figure 5 shows the structure of the network. The network consists of one input layer, two hidden layers, and an output layer. There are 500 nodes in the input layer since each sample has 500 features. The first and second hidden layers contain 44 and 10 nodes, respectively. The output layer contains four nodes representing four classes of the compaction level. Figure 5(b) shows the schematic of a single neuron. Each node is governed by the following equation:

$$x_{s,j}^{(l+1)} = f\left(\sum_{i=1}^{k} x_{s,i}^{(l)} w_{i,j}^{(l)} + b_{0,j}^{(l)}\right), \tag{3}$$

where the subscript $s$ denotes the $s$th sample, $k$ denotes the number of nodes in layer $l$, $x_{s,i}^{(l)}$ is the $i$th input of layer $l$, and $x_{s,j}^{(l+1)}$ is the $j$th output. Meanwhile, $x_{s,j}^{(l+1)}$ is also the $j$th input of layer $l+1$. $w_{i,j}^{(l)}$ is the weight value from the $i$th input to the $j$th output. $b_{0,j}^{(l)}$ is the weight value from the bias term of layer $l$ to the $j$th output. All the bias terms are "+1" in this research. $f()$ is the activation function, a softmax function, $\mathrm{Sof}(z_j) = (e^{z_j} / \sum_{i=1}^{4} e^{z_i})$, is used in the output layer to ensure the predictions for each sample are in the range of $[0, 1]$ and sum to 1, and a sigmoid function, $\mathrm{Sig}(z) = (1 + e^{-z})^{-1}$, is used in the rest of the layers.

## 4. Training of the ANN Model

A supervised learning method is used to train the ANN. The network can be trained to classify inputs according to target

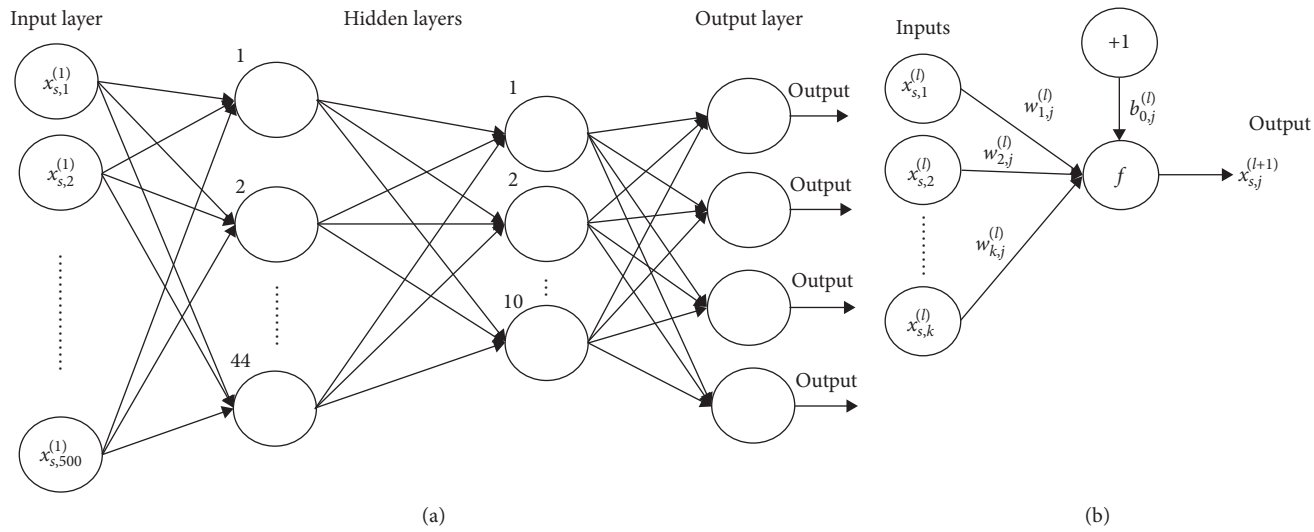


Figure 5: (a) Structure of the MLP feedforward ANN and (b) schematic of a neuron.

classes. The target data should consist of arrays of all 0 values except for a 1 in element $c$, where $c$ is the class they are to represent, as shown in Table 4.

The cross-entropy is used as the loss function to measure the network's performance. The loss associated with the $s$th prediction would be

$$\mathrm{CE}_s = -\sum_{c=1}^{4} y_{s,c} \ln\left(\widehat{y}_{s,c}\right), \tag{4}$$

where $y$ is the target array, $\widehat{y}$ is the output array of the output layer, the subscript $s$ denotes the $s$th sample, and $c$ denotes the $c$th element of the target or output array. The cross-entropy loss of the entire training dataset would be the average $\mathrm{CE}_s$ over all samples.

In this work, the scaled conjugate gradient (SCG) algorithm [27] is used to perform training. SCG is based on a class of optimization algorithms called Conjugate Gradient Methods (CGM), but this algorithm avoids the line-search per learning iteration by using a Levenberg–Marquardt approach to scale the step size. SCG can train any network as long as its weight, net input, and activation functions have derivative functions. Backpropagation is used to calculate derivatives of the loss function with respect to the weights.

To avoid overfitting during neural network training, the dataset is randomly divided into three subsets: training set, validation set, and test set. The training set is used for computing the gradient and updating the network weights. The validation set is aimed to avoid the overfitting problem. The error on the validation set normally decreases during the initial phase of the training, as does the error on the training set. When the network begins to overfit the data, the validation error typically begins to increase. When the validation error increases for several iterations, the training should be stopped. In this work, when the validation error keeps increasing for six iterations, the training is stopped and the weights at the minimum of the validation error are returned. The test set is not used during the training, but it is used as a completely independent test of network generalization. In this study, validation and test datasets are each set to 15% of the original data.

The data of the test lanes 1 to 8 are used for the training in this work. The signals collected in these eight test lanes are processed by using the method mentioned in Section 2.2, forming the dataset for the training. The order of samples in the dataset matrix is arranged randomly since samples are considered to be independent of each other. The data of test lane 9 and 10 are used to test the validity and performance of the ANN model.

The training performance of the ANN is shown in Figure 6. The performance is also visualized in the form of confusion matrix in Figure 7. In the confusion matrix in Figure 7, the rows correspond to the output predicted class, and the columns correspond to the target class. The diagonal cells correspond to samples that are correctly classified. The off-diagonal cells correspond to incorrectly classified samples. Both the number of samples and the percentage of the total number of samples are shown in each cell. The column on the far right of the plot shows the percentages of all the samples predicted to belong to each class that are correctly and incorrectly classified. The row at the bottom of the plot shows the percentages of all the samples belonging to each class that are correctly and incorrectly classified. The cell in the bottom right of the plot shows the overall accuracy.

## 5. Test Results of the ANN Classifier

A good training performance of the ANN can be seen in Figure 7. Combining the signal processing method and ANN model, we can get an ANN classifier, as shown in Figure 8. We input a 0.5-second signal, the ANN classifier outputs an estimated compaction level.

In this section, the data of test lane 9 and 10 are used to test the validity and performance of the ANN classifier. As mentioned in Section 2, a total of 32 long vibration signals

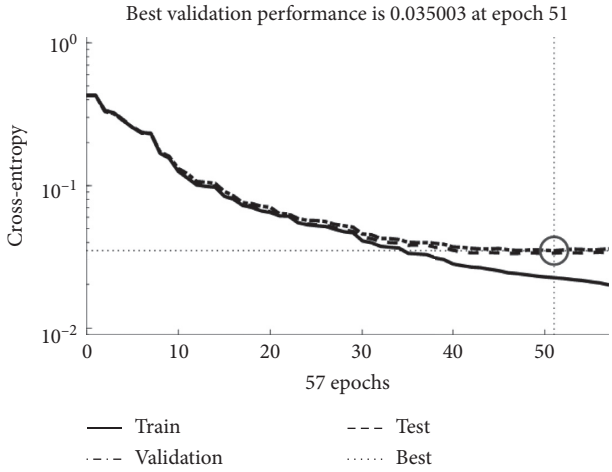


Figure 6: Output prediction error of the ANN after each training cycle.

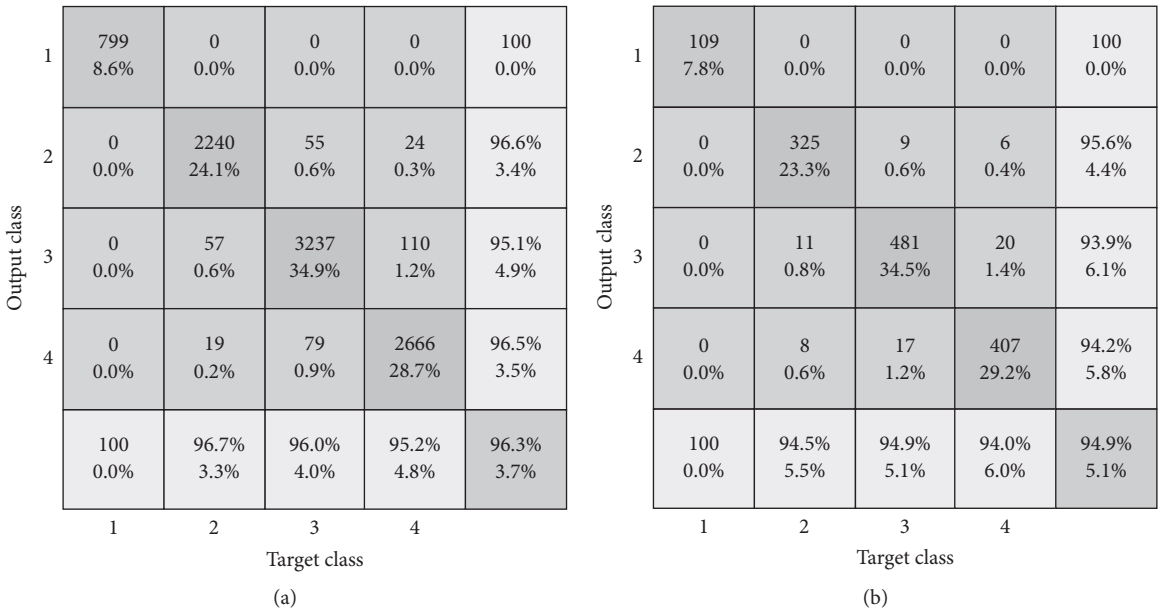


Figure 7: Confusion matrix of training performance: (a) for all dataset and (b) for test set.

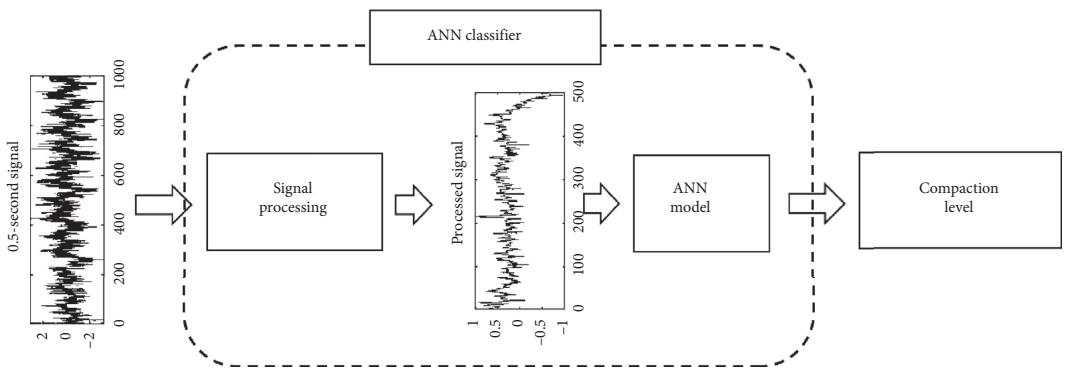


Figure 8: The ANN classifier.

are collected on these two test lanes. Considering that, under the actual working condition, the signal samples may be not collected continuously or in order during the real-time estimation of the compaction quality, we randomly capture some 0.5-second short signals from the long signals as the inputs of the ANN classifier. The output accuracy of the ANN classifier is shown in Figure 9. We can believe that the ANN classifier is accurate enough for the real-time estimation of the compaction quality.

## 6. Discussion on Roller Moving Direction during Compaction

The analysis in this paper mainly focuses on the compaction of cement-stabilized gravel base. The main intention of this study is to find an easy way to estimate the degree of compaction in real time. The ANN classifier developed in this paper partly achieves this goal by using vibration pattern recognition. In fact, it is difficult to analyze the vibration of cement-stabilized gravel base layer by using traditional methods because of the inhomogeneity and anisotropy. Therefore, the authors try to use neural networks. Although neural network is a black box for the user, it does work well in this study.

From the experimental results shown in Figure 3, it can be seen that the degree of compaction increases slowly from pass 5 to 8. In the "sight" of neural network, the vibration signals of pass 5 to 8 should look similar since the values of the degree of compaction have little differences (they are in the same compaction level). In this section, we try to label the samples with the number of passes, and the network is trained to classify the input samples according to 8 target classes. The training performance is shown in Figure 10. Some samples of pass 5 are misclassified as target class 7, and some samples of pass 6 are misclassified as target class 8. However, the ANN has good performances on the classification between class 5 and 6 and between class 6 and 7 as well. The ANN thinks some vibration signals of pass 5 look like the signals of pass 7, but signals of pass 5 and 6 are completely different. This is weird because the values of the degree of compaction of pass 5 and 6 are closer, and signals of pass 5 and 6 should look more similar. Similarly, the ANN thinks some signals of pass 6 look like the signals of pass 8, but not signals of pass 7.

The roller moving direction may be the reason for this weird phenomenon. During compaction, in Figure 2, the roller moves to the north in pass 1, 3, 5, and 7, to the south in pass 2, 4, 6, and 8. Due to the inhomogeneity and anisotropy, the cement-stabilized gravel base layer shows different properties and vibration responses in different roller moving directions. The effect of roller moving direction may be paid attention to for the vibration analysis of compaction in future studies.


Figure 9: Output accuracy of the ANN classifier.

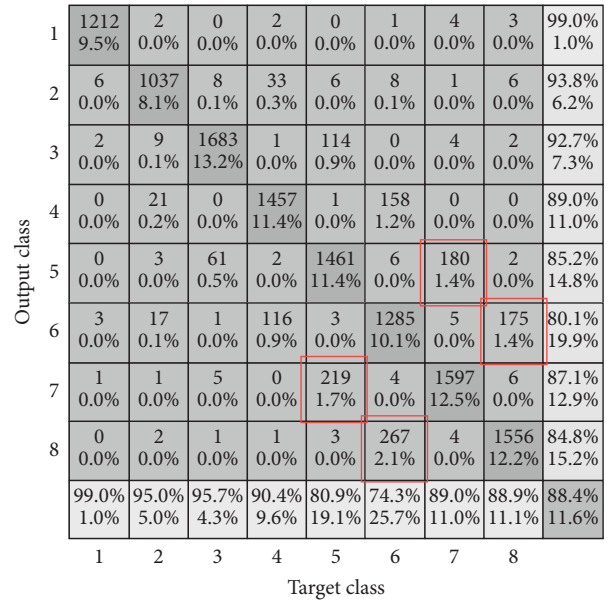


Figure 10: Classification according to the number of passes.

## 7. Conclusions and Outlooks

The primary goal of this paper is to find an easy and convenient way to estimate the degree of compaction in real time. The ANN classifier developed in this paper partly achieves this goal. Some main conclusions and findings of this research are as follows:

(1) A signal processing method is proposed. The signals collected in the experiment are converted to frequency domain representation by using a single-sided FFT. The frequency features of the vibration signal are extracted and expressed in the logarithmic form to amplify some inconspicuous frequency components. The vibration signals are also normalized to eliminate the effects of amplitudes.

(2) An ANN model is designed and trained to identify the different vibration patterns of drum and classify them according to the different compaction levels. The correlation between vibration patterns and the compaction quality is built by the ANN model.

(3) An ANN classifier is developed by combining the signal processing method and ANN model together. The ANN classifier can estimate the compaction quality in real time according to the input vibration signal. From the testing results, it can be found that the ANN classifier shows a good performance on the compaction quality real-time estimation.

(4) The effect of roller moving direction during compaction is observed and analyzed by using the ANN. This effect may be important and should be considered in future studies.

Essentially, the development of IC technique is based on the idea that the compaction quality can be evaluated by identifying the vibration patterns of pavement. Therefore, IC technique can be regarded as a problem of pattern recognition, and the ANN is very suitable for this problem. However, the works in this paper still have room for improvement. To improve the performance of the ANN classifier, a large number of training data are required. Moreover, different pavement materials (such as the pavement structure in Table 1) have different properties; therefore, training different ANN models for different materials is necessary. More projects and materials will be included in our future studies.

## Data Availability

The data required to reproduce these findings cannot be shared at this time as the data also forms part of an ongoing study.

## Conflicts of Interest

The authors declare that there are no conflicts of interest regarding the publication of this paper.

## Acknowledgments

This work was supported by Science and Technology Plan of Shandong Transportation Department (Grant no. 2019B48).

## References

[1] O. Jeongho, "A review on intelligent compaction techniques in railroad construction," *International Journal of Railway*, vol. 7, no. 3, pp. 80–84, 2014.

[2] D. Liu, Y. Wang, J. Chen, and Y. Zhang, "Intelligent compaction practice and development: a bibliometric analysis," *Engineering, Construction and Architectural Management*, vol. 27, no. 5, p. 1213, 2019.

[3] M. Mooney and D. Adam, "Vibratory roller integrated measurement of earthwork compaction: an overview," in *Proceedings of the 7th International Symposium on Field Measurements in Geomechanics*, Boston, MA, USA, 2007.

[4] R. Anderegg and K. Kaufmann, "Intelligent compaction with vibratory rollers: feedback control systems in automatic compaction and compaction control," *Transportation Research Record: Journal of the Transportation Research Board*, vol. 1868, no. 1, pp. 124–134, 2004.

[5] R. Anderegg, D. A. von Felten, and K. Kaufmann, "Compaction monitoring using intelligent soil compactors," in *Proceedings of the GeoCongress 2006: Geotechnical Engineering in the Information Technology Age*, Atlanta, GA, USA, 2006.

[6] X. Zhu, S. Bai, G. Xue et al., "Assessment of compaction quality of multi-layer pavement structure based on intelligent compaction technology," *Construction and Building Materials*, vol. 161, pp. 316–329, 2018.

[7] D. J. White, P. K. R. Vennapusa, and H. H. Gieselman, "Field assessment and specification review for roller-integrated compaction monitoring technologies," *Advances in Civil Engineering*, vol. 2011, Article ID 783836, 15 pages, 2011.

[8] C. Wersäll, I. Nordfelt, and S. Larsson, "Soil compaction by vibratory roller with variable frequency," *Géotechnique*, vol. 67, no. 3, pp. 272–278, 2017.

[9] M. A. Mooney and R. V. Rinehart, "In situ soil response to vibratory loading and its relationship to roller-measured soil stiffness," *Journal of Geotechnical and Geoenvironmental Engineering*, vol. 135, no. 8, pp. 1022–1031, 2009.

[10] M. A. Mooney and R. V. Rinehart, "Field monitoring of roller vibration during compaction of subgrade soil," *Journal of Geotechnical and Geoenvironmental Engineering*, vol. 133, no. 3, pp. 257–265, 2007.

[11] M. Mazari, J. Beltran, R. Aldouri, and S. Nazarian, "Variability of intelligent compaction data on embankment and subgrade geomaterials," in *Proceedings of the Geotechnical Frontiers 2017*, Orlando, FL, USA, 2017.

[12] E. Reynders, "System identification methods for (operational) modal analysis: review and comparison," *Archives of Computational Methods in Engineering*, vol. 19, no. 1, pp. 51–124, 2012.

[13] B. Li and A. Der Kiureghian, "Operational modal identification using variational Bayes," *Mechanical Systems and Signal Processing*, vol. 88, pp. 377–398, 2017.

[14] K. H. Hsieh, M. W. Halling, and P. J. Barr, "Overview of vibrational structural health monitoring with representative case studies," *Journal of Bridge Engineering*, vol. 11, no. 6, pp. 707–715, 2006.

[15] G. F. Sirca Jr. and H. Adeli, "System identification in structural engineering," *Scientia Iranica*, vol. 19, no. 6, pp. 1355–1364, 2012.

[16] C. Devriendt, G. De Sitter, S. Vanlanduit, and P. Guillaume, "Operational modal analysis in the presence of harmonic excitations by the use of transmissibility measurements," *Mechanical Systems and Signal Processing*, vol. 23, no. 3, pp. 621–635, 2009.

[17] M. Barman, S. A. Imran, M. Nazari, S. Commuri, and M. Zaman, "Use of intelligent compaction in detecting and remediating under-compacted spots during compaction of asphalt layers," in *Proceedings of the 2018 Civil Infrastructures*

*Confronting Severe Weathers and Climate Changes Conference*, Hangzhou, China, 2018.

[18] S. A. Imran, M. Barman, S. Commuri et al., "Artificial neural network–based intelligent compaction analyzer for real-time estimation of subgrade quality," *International Journal of Geomechanics*, vol. 18, no. 6, Article ID 04018048, 2018.

[19] M. Barman, M. Nazari, S. A. Imran et al., "Quality control of subgrade soil using intelligent compaction," *Innovative Infrastructure Solutions*, vol. 1, no. 23, 2016.

[20] Q. Zhang, T. Liu, Z. Zhang, Z. Huangfu, Q. Li, and Z. An, "Compaction quality assessment of rockfill materials using roller-integrated acoustic wave detection technique," *Automation in Construction*, vol. 97, pp. 110–121, 2019.

[21] Z. An, T. Liu, Z. Zhang et al., "Dynamic optimization of compaction process for rockfill materials," *Automation in Construction*, vol. 110, Article ID 103038, 2020.

[22] P. Dighe, A. Asaei, and H. Bourlard, "Sparse modeling of neural network posterior probabilities for exemplar-based speech recognition," *Speech Communication*, vol. 76, pp. 230–244, 2016.

[23] R. V. Darekar and A. P. Dhande, "Emotion recognition from Marathi speech database using adaptive artificial neural network," *Biologically Inspired Cognitive Architectures*, vol. 23, pp. 35–42, 2018.

[24] S. Mirsamadi and J. H. L. Hansen, "Multi-domain adversarial training of neural network acoustic models for distant speech recognition," *Speech Communication*, vol. 106, pp. 21–30, 2019.

[25] D. Palaz, M. Magimai-Doss, and R. Collobert, "End-to-end acoustic modeling using convolutional neural networks for HMM-based automatic speech recognition," *Speech Communication*, vol. 108, pp. 15–32, 2019.

[26] M. Zhan, M. Diao, L. Gao et al., "Neural networks for radar waveform recognition," *Symmetry*, vol. 9, no. 5, p. 75, 2017.

[27] M. F. Møller, "A scaled conjugate gradient algorithm for fast supervised learning," *Neural Networks*, vol. 6, no. 4, pp. 525–533, 1993.